

**Quantitative modelling of fluvial sedimentary architecture
and its application to evaluating suitability of subsurface
reservoir successions for carbon sequestration**

Jose Miguel Montero

Submitted in accordance with the requirements for the degree of
Doctor of Philosophy

The University of Leeds
Institute of Applied Geosciences
School of Earth and Environment

July, 2023

The candidate confirms that the work submitted is his/her own, except where work which has formed part of jointly-authored publications has been included. The contribution of the candidate and the other authors to this work has been explicitly indicated below. The candidate confirms that appropriate credit has been given within the thesis where reference has been made to the work of others.

Chapter 3 - Published

Montero J.M., Colombera L., Yan, N., Mounthey N. P. (2021) A workflow for modelling fluvial meander-belt successions: Combining forward stratigraphic modelling and multi-point geostatistics, *Journal of Petroleum Science and Engineering*, 201, 108411.

<https://doi.org/10.1016/j.petrol.2021.108411>.

- Montero, J.M. – Main author. Data Analysis and parametrisation, simulations, manuscript preparation and figure illustrations.
- Colombera, L. – Field area introduction, SGeMS software induction, manuscript review and edits, discussion.
- Yan, N. – Induction to PB-SAND software, Manuscript review and edits, discussion.
- Mounthey N.P. – Manuscript review and edits, discussion.

This copy has been supplied on the understanding that it is copyright material and that no quotation from the thesis may be published without proper acknowledgement. The right of Jose Miguel Montero to be identified as Author of this work has been asserted by him in accordance with the Copyright, Designs and Patents Act 1988.

© 2023 The University of Leeds and Jose Miguel Montero

Acknowledgements

First and foremost, I would like to express my deep and sincere gratitude to my supervisors Nigel Mountney and Luca Colombera. Nigel, thank you for giving me the opportunity to do this research. It has been an honour, a privilege and a vital experience I will always cherish. I am deeply indebted to you for it. I am also extremely grateful for the innumerable scientific discussions and the countless lessons learned from you to carry out this investigation and to present the results. Luca, thank you for always making the time to support me and your guidance over the years. Your vision, sincerity and motivation has always inspired me and provided invaluable knowledge throughout this research. This project would not have been accomplished without your support.

My warmest thanks to Na Yan and Enrique Yuste who also collaborated in parts of the wider underpinning programme of research. Also, I am thankful to the FRG sponsors who funded this project; Aker BP, Areva, Cairn India, BHP Billiton, Conoco Phillips, Murphy, NERC, Nexen, PDS, CNOOC, Saudi Aramco, Tullow, Shell, Woodside, and YPF.

Moreover, I would like to thank Richard Collier, Paul Glover and Nigel Mountney who introduced me to teaching opportunities. Special thanks to past and present members of the FRG who gave me the best experience in Leeds. Ricardo, Marco, Gia, Dave, Ru and Simon - it was great meeting you all!

Additionally, I am truly thankful to those who recommended and endorsed me to do research. Thanks to Enrique (Quique) Rojas, Lorenzo Serra, Jorge Navarro, Carlos Rossi and specially to Gonzalo Ruiz.

To my family, words will never express how much you all mean to me, and how grateful I am to have had your support. To my partner and my baby daughter - your unwavering belief in me has always uplifted me. I owe it all to you – thank you for everything.

Abstract

The creation of fluvial reservoir models that are geologically realistic remains challenging. A workflow has been developed for modelling reservoir successions that comprise fluvial meander-belt deposits, based on algorithms that employ multi-point statistics (MPS). A library of training images from which MPS modelling algorithms can borrow geological patterns for modelling meandering fluvial systems has been built. The training images incorporate sedimentary architectures relating to various types of point-bar deposits as observed in high-sinuosity river systems and their preserved deposits in the geologic record. The training images are applied to two widely employed MPS modelling algorithms: SNESIM and DEESSE. Solutions to common issues encountered in MPS modelling workflows have been established through optimisation of modelling settings.

Facies models that incorporate different levels of heterogeneities for meandering fluvial systems have been produced. The created facies models are used to simulate the injection of a CO₂ plume applied into a carbon capture and storage (CCS) process, allowing a comparison between macroscale 3-facies models and mesoscale levels of heterogeneities as 5-facies models, incorporating intra-point-bar stratigraphic features. An analogue database (PAFD, Petrophysical Analogue Fluvial Database) is developed including petrophysical data related to fluvial successions. PAFD is used to support property static modelling, whose outputs are applied in property models. With more than 4,000 records, PAFD can be employed to inform subsurface modelling in data-poor situations.

The study demonstrates how CO₂ dynamic simulations related to a CCS context are influenced by the underlying facies framework in a reservoir model. Important implications regarding the redistribution of pressures in the reservoir, caprock pressure relief phenomena, horizontal distribution and differences on capillary trapping mechanisms only emerge from models that consider meso-scale features. Furthermore, geological realism in terms of an accurate facies model proved to be fundamental in controlling the CO₂ plume displacement, injection rates and the cumulative injected volumes.

Table of Contents

Acknowledgements	iii
Abstract	iv
Table of Contents	v
List of Tables	xi
List of Figures	xii
List of Abbreviations	xvii
Preface	xviii
1. Introduction	1
1.1 Background	1
1.2 Statement of Research Problem	6
1.3 Rationale	8
1.4 Aim and Objectives	10
1.5 Thesis Layout.....	11
2. Geological Modelling of Subsurface Successions	15
2.1 Reservoir Model: Scopes and Characteristics.....	15
2.1.1 Model Concept	21
2.1.2 Project Scoping.....	22
2.1.3 Input Data (Hard, Soft and Analogue Data).....	24
2.1.4 Structural Modelling.....	25
2.1.5 Grid Configuration	26
2.1.6 Facies Modelling	27
2.1.7 Property Modelling	28
2.1.8 Volumetrics	30
2.1.9 Upscaling	31
2.1.10 Dynamic Models: Numerical Simulations	34
2.1.11 History Matching	37
2.1.12 Uncertainties	38
2.2 Reservoir Modelling: Meandering Fluvial Systems.....	40
2.2.1 Fluvial Heterogeneities (Scales).....	48
2.3 Geostatistics and Applications to Fluvial Reservoirs	50
2.3.1 Stationarity	51
2.3.2 Variograms.....	52
2.3.3 Variogram-based Modelling	55
2.3.4 Object-based Modelling.....	55

2.3.5 Texture-based Modelling.....	56
2.3.5.1 Training Images and Stationarity.....	57
2.4 MPS Simulations.....	59
2.4.1 SNESIM	59
2.4.2 DEESE	62
2.5 Carbon Capture and Storage Applications.....	64
3. A Workflow for Modelling Fluvial Meander-belt Successions: Combining Forward Stratigraphic Modelling and Multi-Point Geostatistics.....	69
3.1 Introduction	69
3.2 Sedimentary Heterogeneities in the Deposits of Meandering River Systems.....	71
3.2 Methodology.....	74
3.2.1 PB-SAND	75
3.2.2 FAKTS.....	75
3.2.3 Construction of Training Images	76
3.2.4 Training-Image Selection	78
3.2.5 MPS Algorithms: SNESIM and DEESSE	80
3.2.6 Auxiliary Variables (Trends)	82
3.2.7 Model Configuration and Input Tuning	85
3.3 Results	86
3.3.1 Case 1: Meander Expansion (3 facies)	87
3.3.2 Case 2: Meander Expansion (4 facies)	88
3.3.3 Case 3: Meander Expansion (5 facies)	89
3.3.4 Case 4: Meander Translation (3 facies)	91
3.3.5 Case 5: Meander Translation (4 facies)	92
3.3.6 Case 6: Meander Translation (5 facies)	93
3.3.7 Stationarity Testing.....	94
3.3.7.1 Case 7 (3 Facies).....	96
3.3.7.2 Case 8 (5 Facies).....	97
3.3.7.3 Case 9 (3 Facies).....	99
3.3.7.4 Case 10 (5 Facies).....	100
3.3.7.5 Case 11: Point-Bar Expansion (Stationary Sample) (3 Facies).....	101
3.3.7.6 Case 12 (5 Facies).....	103
3.4 Discussion.....	104
3.5 Conclusions.....	108

4. Petrophysical Analogue Fluvial Database (PAFD) for Characterisation of Controls on Petrophysical Properties in Fluvial Successions: Development, Structure, and Data Population.....	110
4.1 Introduction	110
4.2 Aim and Objective	115
4.3 PAFD Structure and Content.....	115
4.3.1 Metadata	117
4.3.2.1 References.....	117
4.3.3.2 Sample Source.....	117
4.3.3.3 Data Types.....	119
4.3.3.4 Type of Analysis	120
4.3.3.5 Well Name.....	121
4.3.3.6 Field Name.....	122
4.3.3.7 Latitude and Longitude.....	122
4.3.3.8 Country.....	122
4.3.3.9 Basin Name.....	122
4.3.2 Stratigraphy	123
4.3.2.1 Chronostratigraphy.....	123
4.3.2.2 Lithostratigraphy.....	124
4.3.3 Basin Classification	124
4.3.3.1 Relative Plate Movement	125
4.3.3.2 Basin Type	126
4.3.3.3 Primary Tectonic Force Type	128
4.3.4 Petrography.....	128
4.3.4.1 Lithological Classification	128
4.3.4.2 Grain Size	129
4.3.4.3 Sorting.....	130
4.3.4.3 Roundness	130
4.3.4.3 Maturity	130
4.3.5 Fluvial System Classification.....	131
4.3.5.1 Geomorphic Settings I.....	132
4.3.5.2 Geomorphic Settings II.....	133
4.3.5.3 Depositional Environment	134
4.3.5.4 Dominant Process Influence	136
4.3.5.5 Dominant Formative River Planform	138

4.3.5.6	Depositional Elements.....	139
4.3.5.7	Channel Association.....	140
4.3.5.8	Channel Body Type.....	141
4.3.5.9	Architectural Elements	143
4.3.5.10	Lithofacies	145
4.3.5.11	Discharge Regime.....	147
4.3.5.12	Climate	147
4.3.6	Diagenesis	148
4.3.6.1	Physical Compaction.....	148
4.3.6.2	Mineral Precipitation (Timing).....	150
4.3.6.3	Mineral Association	150
4.3.6.4	Main Clay Type	151
4.3.6.5	Secondary Porosity	152
4.3.7	Depth References	152
4.3.8	Petrophysical Properties	153
4.3.8.1	Porosity	154
4.3.8.2	Permeability	156
4.3.8.3	Hydrocarbon Phase	158
4.3.8.4	Other	159
4.4	Discussion.....	159
4.5	Conclusions.....	162
5.	Assessing the Role of Sedimentary Heterogeneity in Fluvial Successions for CO₂ Injection Using Property Models Constrained on MPS Facies Distributions	164
5.1	Introduction	164
5.2	Aim and Objectives	166
5.3	Methodology: Property Modelling.....	166
5.3.1	The Latrobe Group.....	171
5.3.2	Porosity Models (3-Facies Simulations)	174
5.3.3	Porosity Models (5-Facies Simulations)	177
5.3.4	Permeability Models (3-Facies Simulations)	180
5.3.5	Permeability Models (5-Facies Simulations)	181
5.4	Dynamic Modelling.....	184
5.4.1	Dynamic Model Configuration	184
5.4.2	3Dynamic Models (3-Facies Simulations)	187
5.4.2.1	Pressure Distribution	192

5.4.3 Dynamic Models (5-Facies Simulations)	194
5.4.3.1 Pressure Distribution	201
5.5.4 Storage and Injection Rates	203
5.6 Discussion	208
5.7 Conclusions.....	211
6. Discussion	214
6.1 Challenges and Limitations of MPS Geomodelling	214
6.2 PAFD Applications	220
6.2.1 Model Conceptualisation	221
6.2.1.1 CASE 1: Model Conceptualisation for Prospect Definition	222
6.2.2 Porosity and Permeability Inputs for Reservoir Modelling.....	227
6.2.2.2 CASE 2: Porosity-Depth Trends.....	227
6.2.2.3 CASE 3: Porosity vs Depth Applied to “CASE-1” ..	229
6.2.2.4 CASE 4: Porosity and Permeability Trends (Transforms).....	230
6.2.2.5 CASE 5: Porosity-Permeability Trends (Applied to “CASE-1”).....	232
6.2.2.6 CASE 6: Thresholds (Cut-off) Selection.....	233
6.3 Meandering Fluvial Systems and CCS Suitability	235
7. Conclusions.....	240
7.1 Overview	240
7.2 Facies Modelling Workflow.....	240
7.2.1 Training-Image Library Development (Objective 1)	241
7.2.2 Application of Training Images to SNESIM and DEESSE Codes (Objective 2)	242
7.2.3 Modelling Heterogeneity in Meandering Fluvial Systems (Objective 3)	243
7.2.4 Strengths, Weaknesses and Opportunities	246
7.3. PAFD, Petrophysical Analogue Fluvial Database	246
7.3.1 The Development of a Petrophysical Database (Objective 4).....	247
7.3.2 Petrophysical Database for Fluvial Successions (Objective 5).....	247
7.3.3 Strengths, Weaknesses and Opportunities of the Database.....	248
7.4 Property and Dynamic Models of CO ₂ Injection	249

7.4.1 CO ₂ Property and CO ₂ Dynamic Model building (Objective 6).....	249
7.4.2 CO ₂ Dynamic Model Assessment (Objective 7)	250
7.4.3 Strengths, Weaknesses and Opportunities of CO ₂ Modelling.....	253
7.4.4 Suitability of Reservoir Successions for CCS and Other Applications (Objective 8)	253
7.5 Suggested Future Works.....	255
References.....	258
Appendix A: 48 Case-studies Included in the Database (References)	295
Appendix B: Published Version of Chapter 3	303
Appendix C: Supplementary Files	318

List of Tables

Table 2.1 Type of reservoir model, applications, and purpose.	17
Table 3.1 The parameters employed in the simulations	86
Table 3.2 Parameters employed in the additional MPS models of section 3.3.6.....	95
Table 5.1 Summary for simulations performed for porosity and permeability models.....	169
Table 5.2 Query 1: Analogue identification (Point-Bars)	170
Table 5.3 Query 2: Porosity-Depth (3 facies)	174
Table 5.4 Query 3: Porosity-Depth (5 facies)	177
Table 5.5 Query 4: Porosity-Permeability trend (5 facies).	182
Table 6.1 MPS modelling recipes (meandering fluvial systems)	219
Table 6.2 Thickness and width comparison	236
Table 6.3 Classification for reservoir heterogeneities (clastic reservoirs).....	237

List of Figures

Figure 1.1 Static and Dynamic models.....	2
Figure 1.2 Reservoir Model dependencies on Facies model.....	3
Figure 1.4 Analogue Data Applied to Reservoir Modelling.....	13
Figure 2.1 Field Lifecycle.....	15
Figure 2.2 Type of Data for Reservoir and associated scales.....	18
Figure 2.3 Gridded vs Gridless approaches in geomodelling.....	19
Figure 2.4 Reservoir Modelling Workflow.	20
Figure 2.5 Reservoir Concept	21
Figure 2.6 Reservoir Purposes (Screening, Visualisation, Simulation).....	22
Figure 2.7 Petrophysical Interpretation (Example).....	25
Figure 2.8 Upscaling (Grid Example).....	32
Figure 2.9 Dynamic Model	34
Figure 2.10 Monte-Carlo simulation example	39
Figure 2.11 Confined meandering fluvial system (incised valley)	41
Figure 2.12 Fluvial meandering system (Channel-belt architecture)....	43
Figure 2.13 Modern examples showing neck cut-off, chute cut-off and oxbow lakes among other meandering features.....	44
Figure 2.14 Different types of meander bend transformations.	45
Figure 2.15 Point-Bar Types.....	47
Figure 2.16 Scales of fluvial reservoirs.....	49
Figure 2.17 The Variogram	53
Figure 2.18 CO ₂ phase diagram.	66
Figure 3.1 Simulation Workflow.....	71
Figure 3.2 Expansion and translation processes (point bars)	72
Figure 3.3 Training image building workflow.	77
Figure 3.4 Production of 2 training images.....	78
Figure 3.5 Example of a probability grid.	84
Figure 3.6 Case 1: Meander Expansion (3 facies)	87
Figure 3.7 Case 2: Meander Expansion (4 facies)	89
Figure 3.8 Case 3: Meander Expansion (5 facies)	90
Figure 3.9 Case 4: Meander Translation (3 facies)	91
Figure 3.10 Case 5: Meander Translation (4 facies)	92
Figure 3.11 Case 6: Meander Translation (5 facies)	94
Figure 3.12 Case 7 (3 Facies)	97

Figure 3.13 Case 8 (5 Facies)	98
Figure 3.14 Case 9 (3 Facies)	99
Figure 3.15 Case 10 (5 Facies)	101
Figure 3.16 Case 11 (3 Facies)	102
Figure 3.17 Case 12 (5 Facies)	103
Figure 4.1. Horizontal and vertical depth of investigation vs sedimentary structures and fluid flow baffles within genetic units relationships.	112
Figure 4.2. Flowchart indicating a representative workflow from which PAFD can be utilised.	114
Figure 4.3 Graphical chart. Database build.....	116
Figure 4.4 PAFD (Petrophysical Analogues Fluvial Database) Structure Table.....	118
Figure 4.5 Metadata. References, Well Names and Field Names	119
Figure 4.6 Sample Source, Type of Analysis and Data Type charts ...	121
Figure 4.7 Wells/Outcrops count and map location charts	123
Figure 4.8 Era, Period, Epoch and Stage charts.....	124
Figure 4.9 Formation Rocks count in the database	125
Figure 4.10 Relative Plate Movement, basin Type and Tectonic Force type charts	127
Figure 4.11 Lithological Classification charts	129
Figure 4.12 Petrographic charts	131
Figure 4.13 Geomorphic Settings I Charts.....	133
Figure 4.14 Geomorphic Settings II Charts.....	135
Figure 4.15 Depositional Environment Charts.....	136
Figure 4.16 Dominant Process Charts.....	137
Figure 4.17 Formative River Planforms Charts	139
Figure 4.18 Fluvial Architecture Classification Diagram	140
Figure 4.19 Facies Architecture Charts.....	142
Figure 4.20 Architectural Elements Charts	144
Figure 4.21 Lithofacies Classification	145
Figure 4.22 Architectural Elements and Lithofacies Charts.....	146
Figure 4.23 Discharge and Climate Charts	148
Figure 4.24 Porosity vs Depth vs Compaction	149
Figure 4.25 Mineral Association, Precipitation and Main Clay Type Charts.....	151
Figure 4.26 Depth References Charts.....	153

Figure 4.27 Porosity Charts.....	155
Figure 4.28 Permeability Charts.....	159
Figure 5.1 Four realisations selected for property modelling.	167
Figure 5.2 Porosity-Permeability Trends Dataset (Point-bars).....	171
Figure 5.3 Petroleum Production facilities. Gippsland Basin	172
Figure 5.4 Latrobe Group (Stratigraphic units).....	173
Figure 5.5 Porosity vs Depth Trends (compaction Regimes).....	175
Figure 5.6 Porosity Models (3 Facies – SNESIM & DEESE).....	176
Figure 5.7 Porosity vs Depth Trends (Point-bar base and Point-bar top)	178
Figure 5.8 Porosity Models (5 Facies – SNESIM & DEESE).....	179
Figure 5.9 Permeability Models (3 Facies – SNESIM & DEESE).....	180
Figure 5.10 Depth-Porosity and Porosity-Permeability trends.....	181
Figure 5.11 Permeability Models (5 Facies – SNESIM & DEESE).....	183
Figure 5.12 Relative Permeability for Point-bar facies.....	186
Figure 5.13 Dynamic Models - Summary (3 Facies – SNESIM & DEESE).....	187
Figure 5.14 Plume evolution (Horizontal sections) (3-facies SNESIM and DEESSE models).....	188
Figure 5.15 Plume shape (Vertical sections) at 5 years of injection (3-facies SNESIM and DEESSE models).	189
Figure 5.16 Plume shape (Horizontal sections) (3-facies SNESIM and DEESSE models) after 10, 15 and 30 years of injection.	190
Figure 5.17 Plume shape (Vertical sections) after 10, 15 and 30 years of injection (3-facies SNESIM and DEESSE models).....	191
Figure 5.18 Pressure distribution over the area of investigation (3-facies SNESIM and DEESSE models) after 5, 15 and 30 years of injection.....	193
Figure 5.19 Dynamic simulations (5-Facies SNESIM & DEESSE models)	194
Figure 5.20 Plume shape (Horizontal sections) (5-facies SNESIM and DEESSE models) for early injection stages.	195
Figure 5.21 Plume shape (horizontal sections) compared with permeability model sections for early injection stages.....	196
Figure 5.22 Plume shape (vertical sections) (5-facies SNESIM and DEESSE models) for early injection stages compared with permeability model sections.....	197
Figure 5.23 Plume shape analysis (horizontal sections) compared with permeability model sections (10- 15 years of injection).....	199

Figure 5.24 Plume shape (Vertical sections) (10- and 15-years injection-5-facies-SNESIM and DEESSE).....	200
Figure 5.25 Plume shape in horizontal and vertical sections at 30 years of injection (5-facies SNESIM and DEESSE models).....	201
Figure 5.26 Pressure distribution over the area of investigation over time (5 facies SNESIM and DEESSE)	202
Figure 5.27 Cumulative injected volume and injection rate plots (3-facies models)	203
Figure 5.28 Perforated intervals associated with INJ-1 and INJ-2 for the four static models.	204
Figure 5.29 Injection cumulative and Gas Injection rate plots (5 facies models)	205
Figure 5.30 Cumulative injected volumes and injection rates through time (3 facies vs 5 facies models)	206
Figure 5.31 Perforated intervals associated with each of the dynamic models in INJ-1 well.	207
Figure 6.1 Training-image library (examples)	215
Figure 6.2 Case 1: Mobile Channel Belt	222
Figure 6.3 Model Elements identification	223
Figure 6.4 Facies Recognition (Braided).....	224
Figure 6.5 Porosity and permeability charts.....	225
(6) Figure 6.6 Porosity and permeability charts shows a porosity-permeability cross-plotted for different <i>Compaction</i> categories. (B) shows boxplots for porosity distributions associated with different types of cementation processes (<i>Mineral Association</i>). The same filters as used in the query described in Figure 6.4 are applied. N=661 for both cross-plot (A) and boxplot (B).....	226
(6) Figure 6.7 Uncertainty Analysis (Data source) shows a histogram plot where different sample sources are represented. (B) shows a histogram plot for the different <i>Type of Analysis</i> included in the database Same filters used in the query described in Figure 6.4 applies. N=661 entries for both histogram plots.	226
(6) Figure 6.8 Depth-Porosity trends Porosity values as a function of depth based on the entire database. Two trend-lines are calculated. (B) Porosity-depth plot in which depths are binned into 100 m classes and median (e.g., P50), P10 and P90 porosity are shown (N=2,294).....	228
Figure 6.9 Depth-Porosity trends.....	229
Figure 6.10 Porosity-Permeability trends.....	231
Figure 6.11 Porosity-Permeability trends (Case-1).....	232

Figure 6.12 Porosity-Permeability trends (Porosity cut-off identification).....	233
(6) Figure 6.13 Porosity-Permeability trends (Permeability cut-off(A) calculated porosity values for the depth ranges (1200-1400 m). (B) porosity statistical evaluation for the depth range 1200-1400 m. (C) porosity-permeability trend used for the determination of a permeability cut-off based on 16.6% porosity and related to the Permian trend-line. N=489	234
Figure 7.1. Graphical workflow summarising this Thesis research....	257

List of Abbreviations

- 1D** – One dimensions / one dimensional
- 3D** – Three dimensions / three dimensional
- CCS** – Carbon Capture and Storage
- CCUS** – Carbon Capture and Underground Storage
- CO₂** – Carbon Dioxide
- DEESSE** – Direct Sampling algorithm
- FAKTS** - Fluvial Architecture Knowledge Transfer System
- Fm** – Formation rock
- GDE** – Gross Depositional Environment
- GRFS** - Sequential Gaussian Random Function Simulation
- HFU** – Hydraulic Flow Units
- IOR/EOR** – Improved Oil Recovery / Enhanced Oil Recovery
- K** - Permeability
- LWD** – Logging While Drilling
- MPS** – Multi-point Statistics
- PAFD** – Petrophysical Analogue Fluvial Database
- PB-SAND** - Point-Bar Sedimentary Architecture Numerical Deduction
- PHI (Φ)** - Porosity
- QC/QA** – Quality Control / Quality Assurance
- SGS** – Sequential Gaussian Simulations
- SIS**- Sequential Indicator Simulations
- SNESIM** - Single Normal Equation SIMulation algorithm
- TI** – Training Image
- USA** – United States of America
- WAPIMS** - Western Australia Department of Mines, Industry Regulations and Safety Database

Preface

*“All models are wrong,
but some are useful.”*

George E. P. Box, British statistician, (1919-2013)

1. Introduction

1.1 Background

Lithological variability expressed as sedimentary architecture acts as a primary control on the hosting of resources within subsurface sedimentary successions. In assessing the nature of lithological variability and its impact on subsurface resource analysis, quantitative representations of key aspects of sedimentary architecture are commonly used to erect a framework from which predictive reservoir models are built. The recognition and appropriate consideration of lithological heterogeneities are key to establishing and defining reservoir models that are used to condition reservoir volumes and to predict how fluids will move through subsurface host reservoir rock bodies (Walker, 1984; Hickin, 1993; North, 1996; Brandsaeter et al., 2001)

The three-dimensional characterisation of sedimentary architecture and the lithological heterogeneity associated with it has been shown to exert a fundamental primary control on the performance of subsurface resource plays (Reading, 2001; Lunt et al., 2004). Traditionally, resource plays have been developed dominantly in the exploitation of subsurface hydrocarbon (oil and gas) reserves (e.g., Volve Field, Norway, Equinor 2014), but also of water aquifers (e.g., San Bernardino Groundwater modelling, USA, Danskin et al., 1992), amongst other subsurface resources. Since the 1990s, the analysis of lithological heterogeneities – and the description of the facies units and architectural elements that constitute these heterogeneities within reservoir rocks – has also become important in application to emerging and ongoing low-carbon technologies, such as carbon capture storage (CCS) (Ringrose et al., 2015), development of medium- to high-enthalpic sedimentary geothermal reservoirs, subsurface hydrogen storage in sedimentary reservoirs (Bishoff et al., 2021), and underground radioactive waste repositories (Atabek, 2021). Furthermore, the evaluation of these play types is expected to become increasingly important as the energy transition progresses in coming years and decades.

Reservoir models are built to gain improved understanding of the subsurface and may take many forms. However, overall, such models seek to quantify geological processes, notably aspects relating to sedimentation, tectonic basin evolution, hydrothermal diagenesis, and paleoenvironmental evolution.

In addition, reservoir models are applied to estimate rock volumes and improve production planning with respect to resource exploitation strategies (Ringrose and Bentley, 2015). Of particular note, the net rock volume will typically be assigned an economic potential based on its internal sedimentary anatomy, which is itself a function of lithological heterogeneity.

Reservoir models may be static or dynamic in type. A static model includes rock and fluid properties arising from primary depositional and post-depositional processes. These are normally variables that do not change over time (e.g., stratigraphy, geometry, size, lithologies, structure, initial porosity and permeability, temperature, etc). Static models serve as the basis to account for structural and stratigraphic characteristics and within which lithological heterogeneity is represented. On the contrary, dynamic models quantify the properties that experience variable changes throughout the life of a field (e.g., fluid saturation, fluid contacts, flow rates, pressure, etc). A dynamic reservoir model describes, predicts and accounts for the displacement of fluids through the rocks over time (**Figure 1.1**).

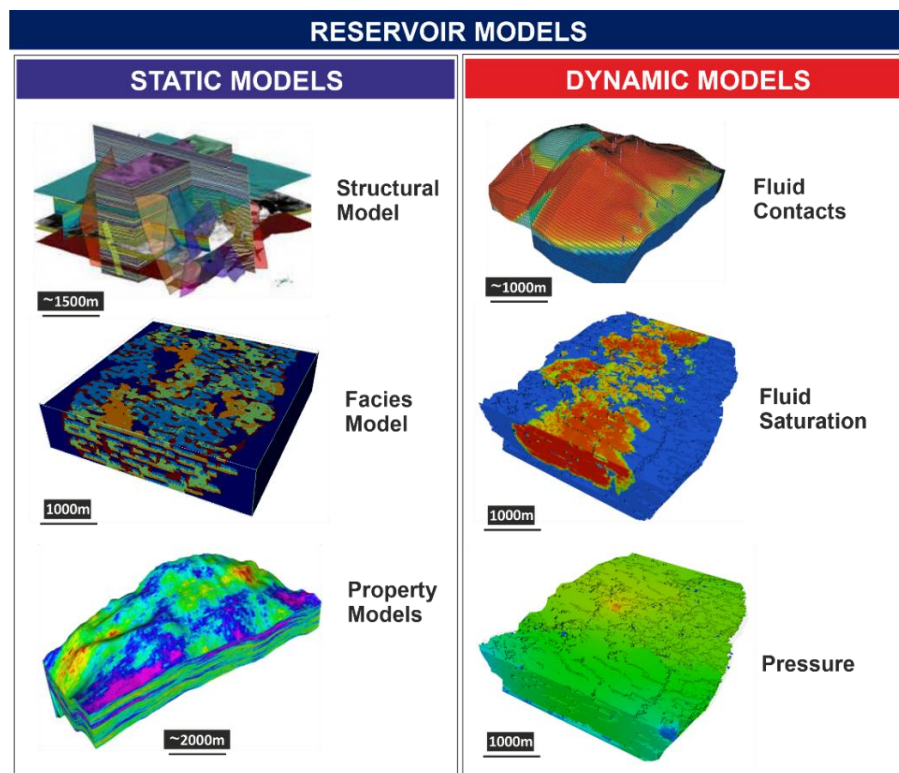


Figure 1.1 Static and Dynamic models

Examples of static and dynamic types that exist in reservoir modelling. Structural model and fluid contacts courtesy of Paradigm's SKUA GoCAD® website. Property model courtesy of Schlumberger's Petrel®.

Facies models are an integral part of a static model that itself incorporates various geological features relating to structural and sedimentary geology. Static models encapsulate, depict and predict the distribution of primary lithological heterogeneities associated with the main type of lithofacies (henceforth *facies*). Poor characterisation of facies within a static model result in a weak definition of the rock types that constitute the main model elements. Commonly, misrepresentations at the stage of determining the facies model are a root cause for discrepancies between volumetric analysis and production forecasting against actual production results (history-matching discrepancies) (Caers and Zhang, 2004). This is particularly important because the economic viability of a resource play will depend on an appropriate definition of reserve and production estimations (Gilman et al., 2013). Dependencies from the facies model as the framework provider to inform different properties can be seen in **Figure 1.2**.

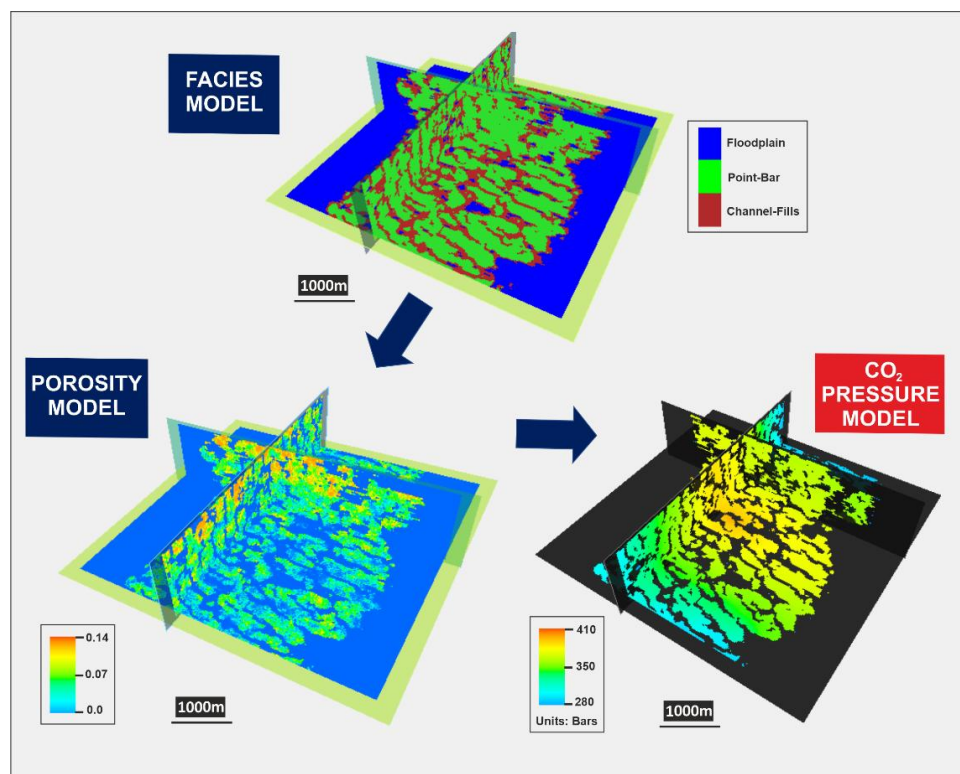


Figure 1.2 Reservoir Model dependencies on Facies model

Illustration where the facies model constitutes the framework from which other static models (e.g., a porosity model) and dynamic models (e.g., CO₂ saturation, CO₂ pressure) are built.

This Thesis focusses on the facies modelling of high-sinuosity systems and their preserved successions, with particular emphasis on successions at the

scale of complexes of multiple meandering river elements and their accumulated sedimentary successions that are characterised by the presence of sedimentary deposits within and beyond the limits of a formative river. In relation to channelized sedimentary systems, including rivers and submarine channel, a meander is one of the bends observed along the channel in planview. Curved channel reaches representing meanders are commonly regular in form and sinuous. The most commonly applied quantitative measure of degree of meandering of the channel of a river (or other channel forms) is its sinuosity. The sinuosity of a watercourse is the ratio of the length of the centreline of the channel to the straight line down-stream distance. Rivers with a single channel and sinuosities of 1.5 or more are commonly referred to as meandering rivers ([Schumm, 1963](#); [Bluck, 1971](#)). Facies models will provide a good approximation for architectural and compositional trends.

Meandering river behaviour results in the generation of a complex arrangement of geo-bodies of different dimensions: some composed principally of sandstone; others of mudstone or other lithology types ([Miall, 1985, 1988, 2016](#); [Dreyer et al., 2009](#); [Gibling 2006](#); [Bridge, 2003](#)). The spatial distribution of channel elements and associated barform elements (as well as elements representing the deposits of splays, crevasse channels, floodplain lakes and floodplain soil profiles), and the connectivity between these different geobodies – some of which tend to be more sand prone than others – can be difficult to predict. This is due to the inherent complexity of architecture associated to the style of the fluvial system, climatic regime and other factors, such as basin setting and rate of subsidence-driven accommodation generation and filling ([Priddy and Clarke, 2021](#)). Meandering fluvial systems are one of the most challenging sedimentary depositional environments to model numerically due to the high geometric variability (e.g., the presence of sinuous channel paths) and the topological arrangement of a complex array of architectural elements. A major challenge is to design workflows to enable such elements to be incorporated effectively within 3D geocellular models where their misrepresentation would have an impact during subsequent modelling stages (e.g., property modelling where petrophysical parameters such as porosity and permeability are spatially dependent).

Two different types of heterogeneity scales are represented in many reservoir models: macroscale and mesoscale ([Friend, 1983](#); [Tyler and Findley, 1991](#); [Issautier et al., \(2013\)](#); [Riordan et al., 2004](#)). The macroscale records

lithological variability observable at the “interwell” scale (>1km to several km in lateral extent); it is commonly characterised by the recognition of depositional or architectural elements (e.g., [Colombera et al., 2013](#)). At this scale, static reservoir models seek to represent the arrangement of sandbody deposits encased or embedded in a “background” of “mudrock” (relatively fine-grained deposits). In reservoir models of meandering fluvial sedimentary successions, the sand-prone deposits are typically representative of channels and barforms, whereas the fine-grained mud-prone parts of the succession are typically representative of floodplain and abandoned channel-fill deposits (mud plugs) ([Miall, 1985](#)) (**Figure 1.3**). The mesoscale records lithological variability observable in more detail (metres to tens or a few hundreds of metres laterally) and refers to the architectural elements that occur nested within the larger-scale depositional elements in the system (e.g., channel fills and point-bar deposits). Within these architectural elements – and also at the mesoscale – many architectural elements are themselves internally composed of beds and bedsets, commonly arranged in a predictable order within their parent architectural elements. At a smaller scale, additional lithological heterogeneities (centimetric and smaller) are present.

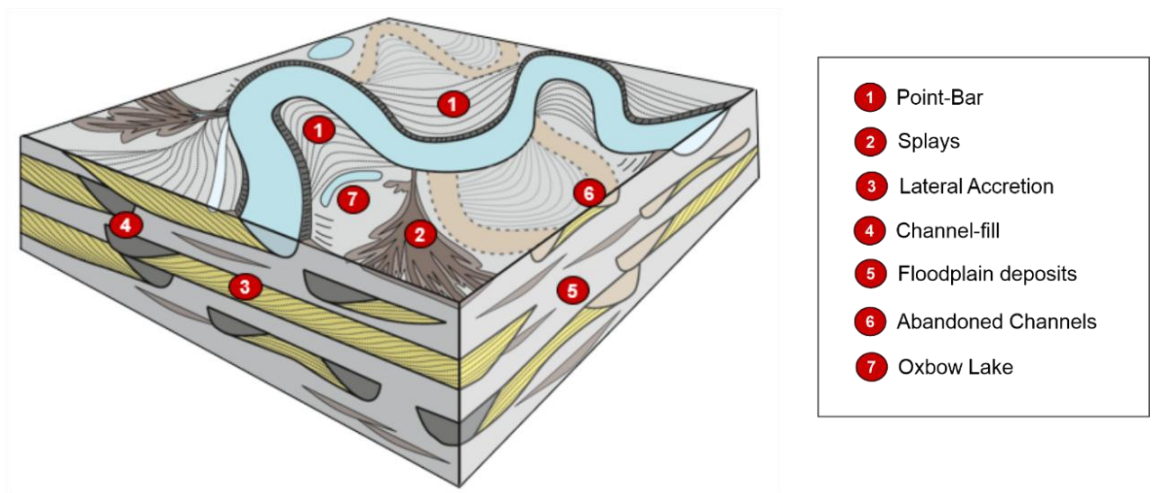


Figure 1.3 Meandering Fluvial System

Block diagram of a meandering fluvial system showing different architectural elements. Expansional point-bars are developed (three bends). Compartments are shown in the vertical sections where sandbodies arising from lateral accretion in response to channel migration occur between relatively non-permeable channel-fill (mud plug) and floodplain deposits. ([Modified from Ghazi and Mountney, 2009; Shiers et al., 2014](#)).

The accurate definition and representation of macroscale and mesoscale heterogeneities in 3D reservoir simulations determines the ability of a model to effectively map and predict recovery/injection efficiency and the storability volume in reservoirs (Willis and Sech, 2018a and b; Cabello et al., 2018; Puig et al., 2019). These concepts apply to both the production of fluids from reservoirs, such as water and hydrocarbons, and the injection of fluids into reservoirs, such as supercritical CO₂ (Soltanian et al., 2016; Nguyen et al., 2017; Eiken et al., 2011).

The most evident characteristic in meandering rivers is the development of channel bends (meander loops) and point-bars, which form due to a combination between erosion of the outer channel bank with deposition on the inner bank, leading to lateral migration of the channel over space and time, and to eventual cut-off of tightening meander loops (Ghinassi, 2011). The repetition of lateral-accretion events, the different combinations of point-bar types, and heterogeneities within point-bar elements, collectively act to generate a highly heterogeneous sedimentary system that will typically contain multiple preserved point-bar elements compartmentalised or truncated by relatively non-permeable channel-fill deposits (**Figure 1.3**). Successions of meandering fluvial systems modelled as part of this research ideally exhibit several of these features, notably point-bar accumulations compartmentalised by channel-fill and floodplain deposits, and lithological heterogeneities associated with them, and which themselves act as important controls on fluid-flow.

1.2 Statement of Research Problem

Historically, a variety of geostatistical methods have been used to model the accumulated deposits of meandering fluvial systems. Geostatistical modelling algorithms are recurrently used in facies modelling where predictions of categories (facies) associated with spatial phenomena in a grid are required (Cannon, 2018). However, each of these approaches faces challenges in the reproduction of highly sinuous features typical of mud-prone abandoned channel elements and closely associated “circular” (discoid in 3D) or “elliptical” (ellipsoid) features typical of sand-prone point-bar elements (Colombera et al., 2017).

Classic variogram-based methods, which use indicator kriging, seek to generate a conditional probability distribution field (e.g., Sequential Indicator Simulations – SIS). Such methods have been shown to be largely ineffective at representing commonly observed meandering fluvial geometries ([Deutsch and Journel, 1998](#)). Object-based or Boolean methods, where each model element is represented by a discrete entity, deliver better results than variogram-based models in their attempt to simulate channel and point-bar geometries. However, object-based, Boolean methods encounter numerous issues in their attempt to honour conditional well data, most notably, the so-called funnelling effect whereby specific objects are forced towards certain regions in the grid) ([Haldorsen and MacDonald, 1987](#); [Holden et al., 1988](#); [Larue and Hovadik, 2006](#)). By contrast, texture-based methods, or multipoint statistical techniques (MPS) use conceptual geological models as training images to integrate geological information into reservoir models. This class of model combines the ability of pixel-based variogram methods to fully honour well data with the capability to reproduce complex meandering shapes as achieved with object-based methods ([Guardiano and Srivastava, 1993](#); [Liu et al., 2004](#)). These advantages mean that MPS methods are generally well-suited to modelling fluvial systems with sinuous channels and channel belts. However, MPS methods currently remain underutilised within the geomodelling community due to problems relating to the creation of geologically sensible training images, and to issues relating to a complicated parametrisation process that is specific of each MPS algorithm. As a result, to date, geomodellers have tended to rely on object-based models or classic variogram-based methods.

A failure to deliver accurate facies models to serve as frameworks in posterior reservoir modelling stages will lead to unreliable property and dynamic models that cannot rigorously account for different types of heterogeneity at the macroscale and mesoscale. In the case of CO₂ reservoirs, as an important fluid to be monitored in simulations, it remains unclear how the displacement of a CO₂ plume, injection rates and storage capacity will behave in highly heterogeneous sedimentary successions, especially those of meandering fluvial systems. Thus, special attention is currently being given to this topic by the scientific community (e.g., [Norouzi et al., 2022](#); [Sun et al., 2021b](#); [2022c](#); [2023](#)).

1.3 Rationale

This study has devised and applied a novel workflow for modelling reservoir successions that comprise fluvial meander-belt deposits, based on algorithms that employ multi-point statistics (MPS). The workflow includes details from which training images are created using two existing technologies: i) information on multiple sedimentary rock analogues included within a relational database storing information on many fluvial sedimentary successions (FAKTS, the Fluvial Architecture Knowledge Transfer System – (Colombera et al., 2012a, b; 2013, 2017); and ii) a forward stratigraphic modelling software tool (PB-SAND, The Point-Bar Sedimentary Architecture Numerical Deduction model – Yan et al., 2017) that simulates fluvial meander-bend evolution and resulting point-bar facies organisation. A library of training images developed as part of this research are included within an MPS code to deliver facies realisations.

This research utilises two different MPS codes to model realistic meandering fluvial facies models. One is SNESIM (Single Normal Equation SIMulation) (Strebelle, 2002), a well-established code included in major software packages (e.g., Schlumberger Petrel®). The other is DEESSE (Direct Sampling) (Mariethoz et al., 2010), a newer MPS code that may offer better performance in the delivery of facies simulations. Solutions to common issues encountered in MPS modelling workflows have been sought through optimisation of modelling settings for SNESIM and DEESSE. Auxiliary variables are used to simulate common facies trends and control channel density (proportions).

The application of different training images, each incorporating different types of lithological heterogeneities, is represented in modelling scenarios that incorporate 3, 4 and 5 facies types. These training images are applied to the developed workflow where the SNESIM and DEESSE codes are tested. The sensitivity of unconditional simulation results to input parameters are analysed to define modelling recipes consisting of sets of appropriate modelling parameters for use with each training image and modelling algorithm. Then, the generated 3 and 5-facies models, which correspond to macroscale and mesoscale heterogeneity respectively, are used as frameworks for the creation of property models (porosity and permeability) and most importantly

for the creation of dynamic reservoir models where a plume of CO₂ is simulated to be injected within each of the scenarios.

The choice of CO₂ as the fluid to model dynamically stems from the recent rise in the scientific investigation and commercial evaluation of carbon sequestration projects (CCS) as a solution for reducing the effects of anthropogenic CO₂-induced global warming and planetary climate change (Bachu 2001; Gibson-Poole et al., 2008). The evaluation and development of commercial CCS projects is expected to serve as a major solution to mitigate the effects of the ongoing climate crisis in coming decades (Global CCS Institute, 2020).

Many former oil and gas operators are now dedicating substantial resources to provide knowledge for the underground storage of CO₂. Many new commercial opportunities are arising, in some cases supported by national governments, where operators contribute to the safe and long-term underground storage of CO₂ in reservoir rock successions in a cost-effective manner as part of an environmentally aware and sustainable procedure. Examples for already completed or ongoing CCS projects are the Big Sky in Montana (USA), Sleipner (Norway) and the Southwest Hub project (Australia). For each of these projects, injection of CO₂ has been ongoing for more than two decades (e.g., the Sleipner project started in 1996); one million metric tonnes of CO₂ approximately are stored per year in each of these projects (William and Chadwick, 2017).

The reservoir modelling workflow developed in this research has been enabled via reference to analogue data describing aspects of sedimentary meandering fluvial systems and their preserved successions stored in a geological database, which includes records of petrophysical parameters related to fluvial facies characteristics (PAFD, Petrophysical Analogues Fluvial Database). PAFD is used as a tool to feed property and dynamic models with quantitative data (hard data), but it has also the potential to deliver soft data (conceptual) for use at different stages in the process of reservoir model construction.

1.4 Aim and Objectives

The aim of this research is to develop novel approaches for creating geologically valid static models of the lithological and petrophysical heterogeneity of high-sinuosity fluvial successions. This aim is achieved by addressing the following specific objectives:

- **Objective 1:** The development of a library of training images – from which MPS modelling algorithms can borrow geological patterns for modelling meandering fluvial systems – based on forward stratigraphic modelling software.
- **Objective 2:** The application of the training images to two widely employed MPS modelling algorithms: SNESIM and DEESSE.
- **Objective 3:** The creation of fluvial meandering reservoir models that consider scenarios encompassing macroscale and mesoscale levels of sedimentary heterogeneity.
- **Objective 4:** The development of a database (PAFD, Petrophysical Analogue Fluvial Database) that can be applied to describe fluvial characteristics in terms of quantitative petrophysical properties.
- **Objective 5:** The utilisation of the created database (PAFD) as a tool that delivers petrophysical analogue data linked to fluvial deposits for the development of realistic property models that can be later utilised to simulate CO₂ fluid-flow through each of the model elements.
- **Objective 6:** The creation of dynamic models for the analysis of injected supercritical CO₂ fluid-flow within a highly heterogeneous succession produced by a fluvial meandering system.
- **Objective 7:** An assessment of how variability in the geological realism of facies models impacts petrophysical properties (porosity and permeability) and ultimately influences the results of dynamic simulations of CO₂ injection. Determination of plume behaviour, injection rates and storage behaviour for scenarios considering macroscale mesoscale heterogeneities.
- **Objective 8:** Evaluation of the effectiveness of meandering fluvial successions as potential storage reservoirs for the long-term, safe sequestration of anthropogenically generated CO₂, thereby reducing and mitigating the effects of anthropogenic CO₂ emissions to the atmosphere.

1.5 Thesis Layout

The thesis comprises seven chapters: i) introduction, ii) literature review and background, iii) the investigation of new applications of quantitative analysis of fluvial sedimentary architecture to improve facies and reservoir modelling workflows, iv) the development of a database to quantitatively inform property and dynamic models, v) assessing the role of sedimentary heterogeneity in fluvial successions on CO₂ injection using property models constrained on MPS facies distributions. vi) discussion, vii) conclusions.

Chapter 2 corresponds to the literature and background section where an overview of reservoir model practices is given related to the requisites needed to simulate meandering fluvial systems. The chapter also presents an overview of the most important geostatistical modelling methods, with special emphasis on MPS modelling techniques and the SNESIM and DEESSE algorithms. The motivation for capturing anthropogenic CO₂ from industrial activity as a key action recommended by the International Energy Agency is also summarised.

Chapter 3 describes a novel workflow for building facies models for meandering fluvial systems. A library of training images is developed from which MPS modelling algorithms can borrow geological patterns. The training images incorporate sedimentary architectures relating to point-bar deposits accumulated by fluvial meander-bend expansion and translation, as observed in high-sinuosity river systems and their preserved deposits in the geological record. The training-image library has been developed using a forward stratigraphic modelling software (PB-SAND) that simulates fluvial meander-bend evolution and resulting point-bar facies organisation, and which has been constrained using sedimentological data from geological analogues. The training images are applied to two widely employed MPS modelling algorithms: SNESIM and DEESSE. Solutions to common issues encountered in MPS modelling workflows have been established through optimisation of modelling settings for SNESIM and DEESSE. Auxiliary variables are used to simulate common facies trends. Application of the training-image library through the developed workflows for SNESIM and DEESSE has been tested. The sensitivity of unconditional simulation results to input parameters has been analysed to define modelling recipes, consisting of sets of appropriate modelling parameters for use with each training image and modelling

algorithm. The principal methods and findings of this chapter are published in [Montero et al., \(2021\)](#).

Chapter 4 presents a tool designed to facilitate the search of suitable analogue data on petrophysical properties of fluvial deposits. With more than 4,000 records, PAFD (Petrophysical Analogue Fluvial Database) has been developed to enable derivation of statistical outputs that can be utilised in subsurface workflows for constraining property models. Database-derived analogue petrophysical summaries and predictions can be used where well data do not exist or are insufficient for purposes of model building ([Weber, 1987](#); [Dreyer et al., 1990](#); [1993](#); [Miall and Tiller, 1991](#); [Keogh et al., 2007](#); [2014](#); [Gibling, 2006](#); [Engie and Howell, 2010](#); [labourdette, 2011](#); [Colombera et al., 2012](#); [Luthi and Flint, 2013](#); [Pranter et al., 2013](#); [Cannon, 2018](#)). Different test applications were undertaken to demonstrate the value of the created database, which are included in Chapter 6 (Discussion). The developed database can be applied at different stages of a reservoir-modelling workflow, by providing hard data (quantitative measures) and soft data (conceptual relationships) depending on requirements (**Figure 1.4**).

Chapter 5 applies the facies models produced as part of the work of Chapter 3 as frameworks on the basis of which CO₂ injection is simulated. The Latrobe Group located in the Gippsland basin (Australia) and penetrated by the Tarwhine-1 well located in a depleted gas field is used to deliver hard and soft data to complement property and CO₂ dynamic models. Four different facies realisations are selected from those presented in Chapter 3 representing different “levels” of heterogeneities (macroscale and mesoscale) using SNESIM and DEESSE. The additional heterogeneity information included within the mesoscale models is compared against the macroscale counterparts where the CO₂ plume behaviour, injection rates and storage capacity are also evaluated. The investigation addresses the role of macro- and mesoscale heterogeneities in controlling the injection of CO₂ in meandering fluvial systems ([Issautier et al., 2013](#); [Milliken et al., 2008](#); [Frykman et al., 2009](#); [Sun et al., 2023](#)).

Chapter 6 presents a comprehensive discussion of the results of chapters 3, 4 and 5, which are debated in an applied perspective, placing an emphasis on additional applications of the developed database (PAFD) (**Figure 1.4**).

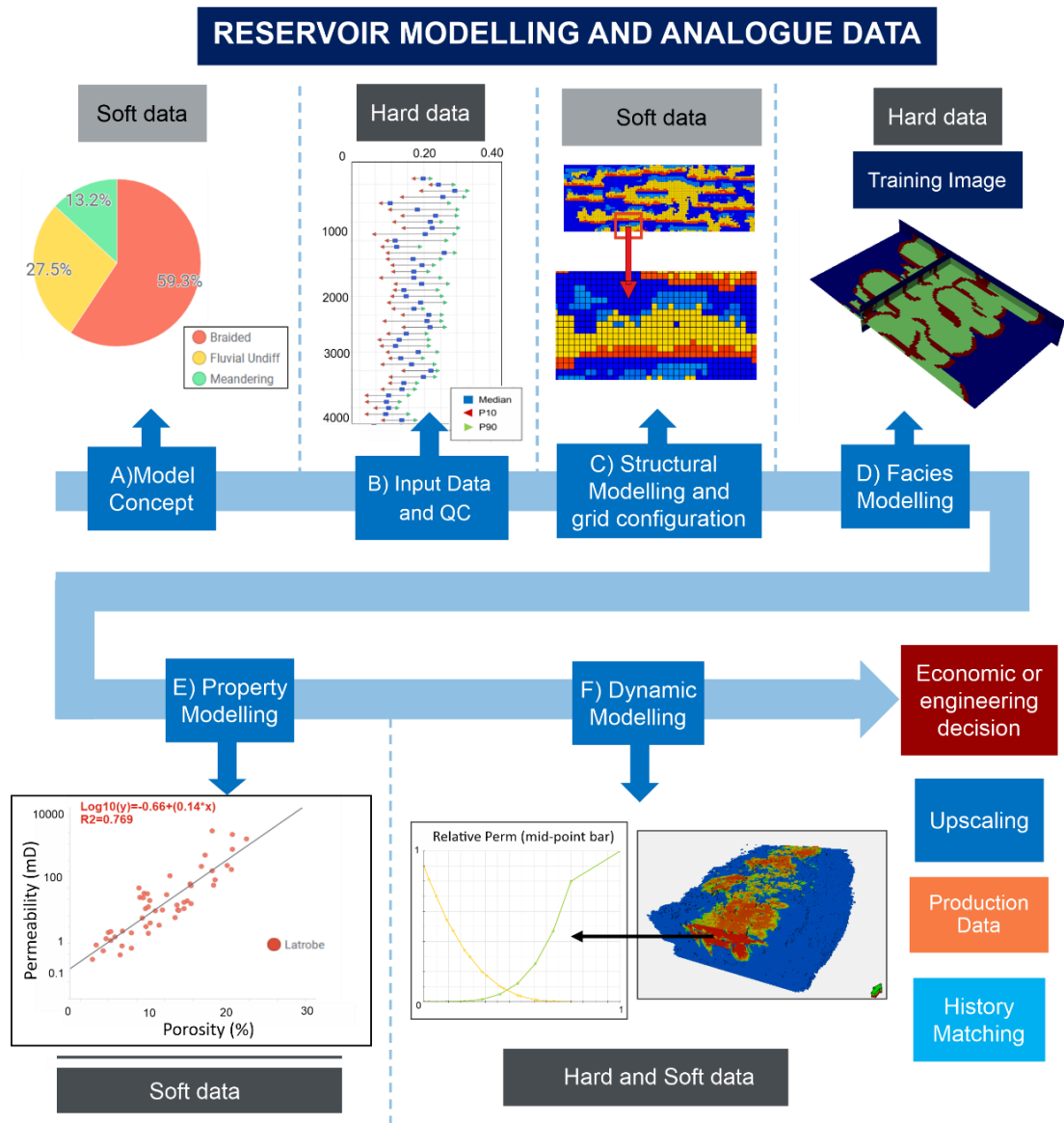


Figure 1.3 Analogue Data Applied to Reservoir Modelling

The different type of analogue data (hard and soft) that PAFD (Petrophysical Analogue Fluvial Database) can deliver corresponding to different model stages within the reservoir model workflow. PAFD does not content analogue data applicable to upscaling, production, or history matching purposes.

These are as follows. i) Model concept applications corresponding to the first stage of reservoir modelling, where main approaches are envisioned to guide the development of geocellular models (stratigraphy, depositional environment, facies architecture, etc). ii) Input Data and QC stage, where hard and soft data provided by analogue rocks can contribute to fill data gaps in early exploration and appraisal phases.

Finally, Chapter 7 presents the conclusions of the Thesis, summarising the most important findings of this research with respect to the importance of appropriate levels of heterogeneity modelling when dealing with meandering fluvial systems and its significance for CO₂ sequestration projects. Furthermore, limitations are considered, and future research opportunities regarding the developed facies modelling workflow are suggested.

2. Geological Modelling of Subsurface Successions

2.1 Reservoir Model: Scopes and Characteristics

Reservoir models are 3D representations of the geological features that exist in a subsurface volume of applied interest (Yarus and Chambers, 1994; Pycz and Deutsch, 2002; Tyson, 2007; Ringrose and Bentley, 2015). Such models may take many forms and be based on a variety of quantitative and qualitative approaches to geological characterisation. Reservoir modelling most commonly involves the construction of a digital model that can be utilised for different purposes (e.g., field management, forecasting, etc) (Deutsch, 1992). The employment of reservoir models has become a central requirement in designing and implementing field management strategies affecting the feasibility of a project throughout its entire life cycle (Figure 2.1) (Holden et. Al., 1998).

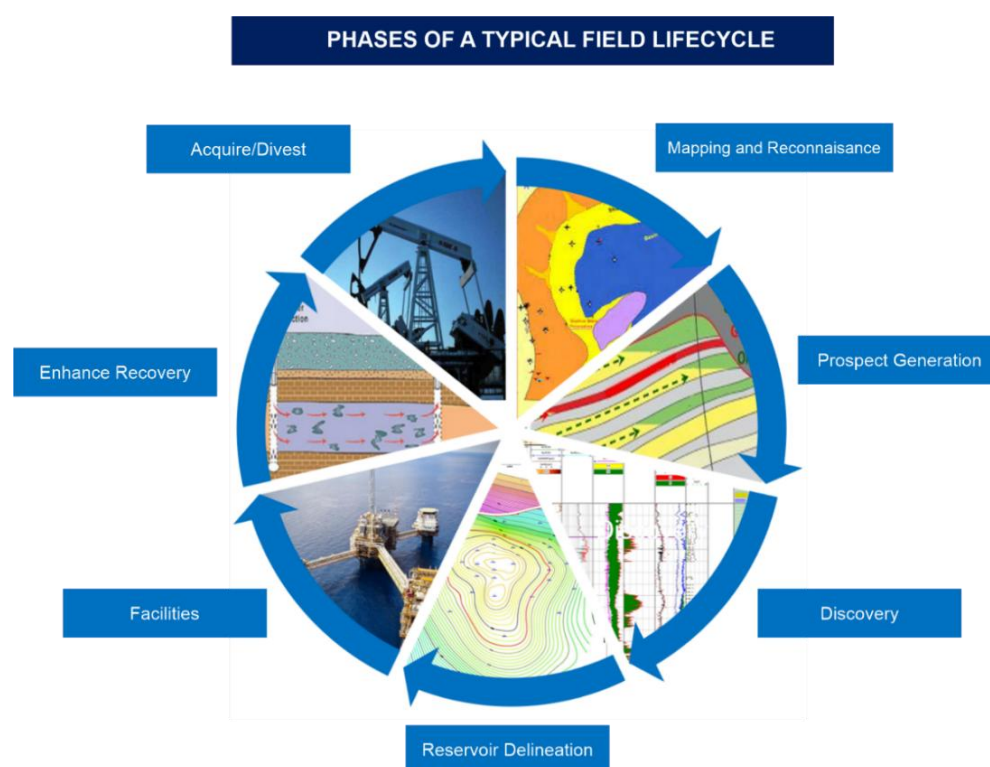


Figure 2.1 Field Lifecycle

A typical field life cycle includes 7 phases. These are: mapping and reconnaissance, prospect generation, discovery, reservoir delineation, facilities, enhance recovery and finally the acquire/divest phase. The reservoir model plays a fundamental role in each of them. Images in figure taken from different sources (GDE map, delineation map and cross-section - Getech website; logplot - Interactive Petrophysics® website)

The reservoir model is also employed to condition the upstream process where the phases of exploration, appraisal, development, and abandonment/decommissioning are included (Ma et al., 2014). As an example, during appraisal and development phases, reservoir models are commonly used for optimising well locations; during the production phase, models are built for monitoring and to predict and test performance (Labourdette, 2008). Reservoir modelling approaches are employed routinely in different industries (oil and gas, carbon capture and underground storage (CCS), hydrogeology, the geothermal industry, etc.) and are specifically needed to assist in developing, managing, monitoring and optimising field performance (Ringrose et al., 2011).

Reservoir models are also one of the most important tools used in reservoir characterisation procedures. Therefore, the construction and design of reservoir models are crucial tasks that determine the digital representation of the subsurface (Pyrzcz and Deutsch, 2014). Knowledge and workflows from different disciplines (geophysics, geology, petrophysics, reservoir engineering, etc) provide the critical understanding and knowhow for the construction of a three-dimensional model describing and accounting for the distribution of the reservoir heterogeneity and petrophysical properties (Lucia et al., 2003). Steps in this process require knowledge of static and dynamic reservoir characteristics. Static models characterise existing rock and fluid properties, which do not change markedly (if at all) during the entire life cycle of a field (Pyrzcz and White, 2015). These properties refer to the primary depositional and post depositional processes controlling the structural framework (structural model) and petrophysical parameters (property models). On the contrary, dynamic models consider changing parameters throughout the life cycle of a field, such as pressure or fluid saturations.

Reservoir models are used to support important reservoir evaluations and engineering decisions, as summarised in the following points (Soleimani and Shokri, 2015): i) volumetrics (estimation of fluid volumes in place in a given reservoir rock; ii) production forecasting; iii) the definition of sweet spots or well targets corresponding with highly ranked net-pay sections or zones; iv) well-planning and design for appraisal and development drilling plans; v) reservoir production optimisation (e.g., Improved Oil Recovery-IOR/Enhanced Oil Recovery-EOR planning) (**Table 2.1**).

	Static Modelling				Dynamic Modelling	
	Model Concept	Structural Modelling	Facies modelling	Property Modelling		
Management/Definition	●	●	● ●	● ● ●	● ● ●	
Volumetrics			●	● ● ●	● ● ●	
Well Planing			●	●	● ●	
Flow Simulations						● ● ●
Forecasting						● ● ●
IOR/EOR			●	● ● ●		

● Visualization
 ● Screening
 ● Simulations

Table 2.1 Type of reservoir model, applications, and purpose.

The different stages of a reservoir model (static: model concept, structural model, facies model, property model and the dynamic model) compared against its main applications (management/definition, volumetrics, well planning, flow simulations, forecasting and IOR/EOR) and its purpose (visualisation, screening, and simulation).

The majority of reservoir models (but not all) are built using computational approaches. Of these reservoir models, the majority (but again not all) are represented using geocellular grids made of discrete cells associated with various physical properties (Weber and Geuns, 1990). Grids can be regular or irregular. The physical attributes associated with each cell may be determined from the analysis of different data types: well-logs (wireline, LWD-logging while drilling), core analysis, well-production data, geophysical and geological data, and analogue data are analysed by different professionals and are used as input to reservoir models (Serra, 1986).

However, with the exception of seismic data sets that might typically image several hundreds of millions of cubic metres of reservoir volume, most of the data are limited to well data representing a very small portion of the reservoir and effectively restricted to one spatial dimension (1D) (Figure 2.2) (Weber et al., 1978). Therefore, geostatistical methods are routinely utilised to fill the gaps within the model space between the different sites of known deterministic well data in the area of investigation.

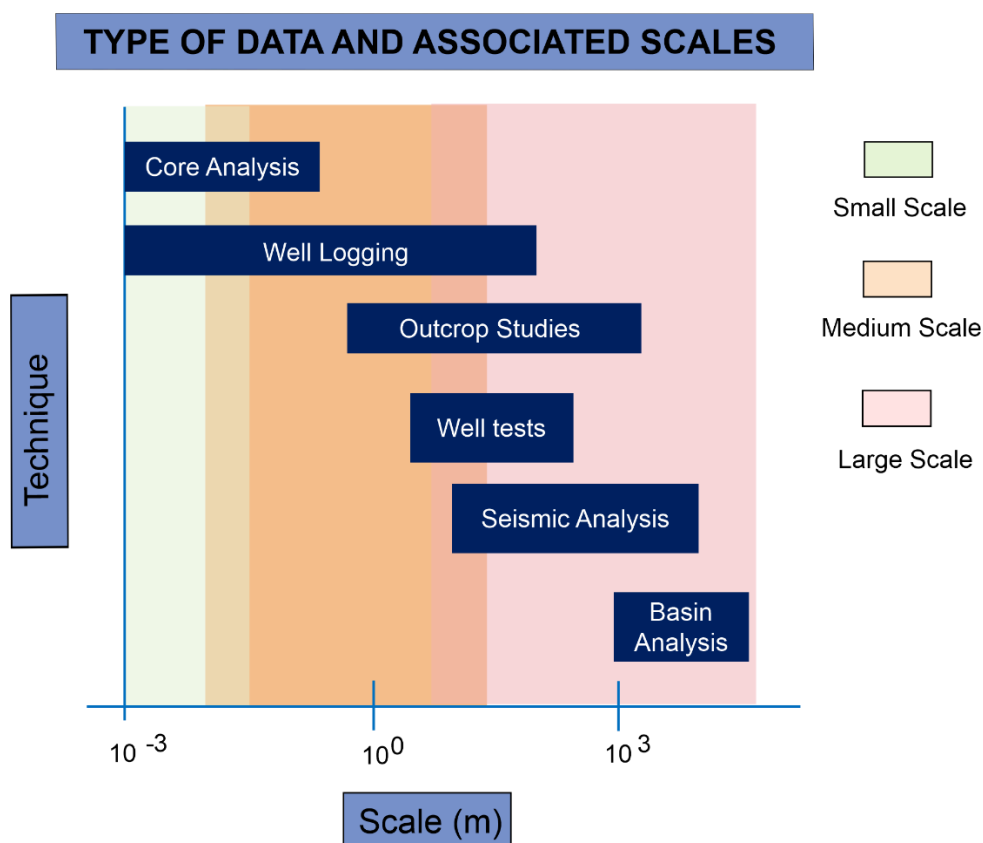


Figure 2.2 Type of Data for Reservoir and associated scales

Scales related to different investigation evaluation techniques from small scale (i.e, pore scale) to large scale (i.e, basin scale).

Apart from classical grid-based methods, gridless (e.g., point-vector) approaches for geomodelling are also employed (**Figure 2.3**). Gridless modelling approaches allow reservoir models to be built within a volume that includes a plurality of data points in the absence of a grid that would otherwise be restrictive for the purposes of geological characterisation (Maucec et al., 2012; Mirzadeh et al., 2014; Carvajal et al., 2014). Gridless methods resolve many common geocellular issues related with the parameterisation of the cellular volume, cell dimensions and layering styles, which tend to make classical gridded methods very time-consuming processes (Maucec et al., 2012). Computation speed is also enhanced in gridless models where multiple realisations can be run at unmatched speed when compared to more conventional gridded models (typically 95% more efficient) (Maucec et al., 2012; Yarus et al., 2010; 2016). However, numerous issues remain to be addressed regarding usability and the successful integration of gridless models with dynamic models that are designed for gridded inputs; there are many compatibility issues and challenges (Yarus, et al., 2016).

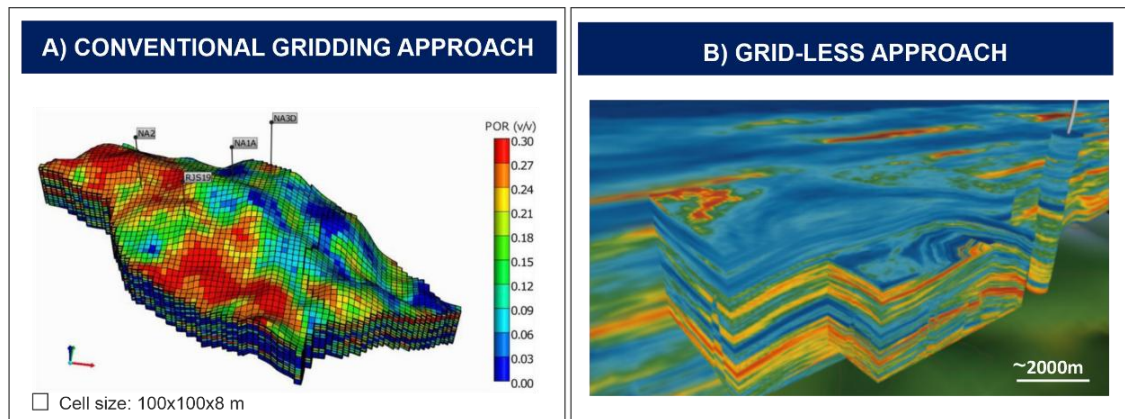


Figure 2.3 Gridded vs Gridless approaches in geomodelling.

(A) Porosity model using a conventional grid approach with a regular cell size (Santos and Schiozer, 2017). (B) an example for a gridless approach (Landmark SEM-Scalable Earth Modelling®) where no cells are present in the model.

Data from geological analogues may be also considered at different stages of reservoir modelling, especially in the early exploration phases when subsurface data are limited (Dreyer et al., 1990; 1993; Miall and Tiller, 1991). As the field lifecycle progresses and the first wells are drilled, well logs are acquired (gamma ray, neutron-density, resistivity, etc.) to provide indications of rock and fluid properties in the wellbore. Cores can also be retrieved from selected intervals and more advanced types of logging can be undertaken (e.g., image log analysis, nuclear magnetic resonance - NMR). Production tests, such as well tests, are also performed to determine potential flow rates and pressures, in order to derive data on flow characteristics that can be employed to refine a reservoir model (Serra, 2010).

A reservoir model is built by following a workflow that can be summarised in different stages where static and dynamic models are built. These are i) model concept, ii) input data and quality check (QC), iii) structural modelling, iv) grid configuration, v) facies modelling, vi) property modelling, vii) volumetrics, viii) upscaling and ix) dynamic simulations (Figure 2.4). A reservoir model is frequently updated depending on the availability of new data (e.g., new wireline data coming from a recently drilled well during the appraisal phase). Therefore, a reservoir model's accuracy varies throughout the field lifecycle. A history matching process is also performed in many cases, whereby initial input parameters in static and dynamic models are reviewed to ensure that they match with production data.

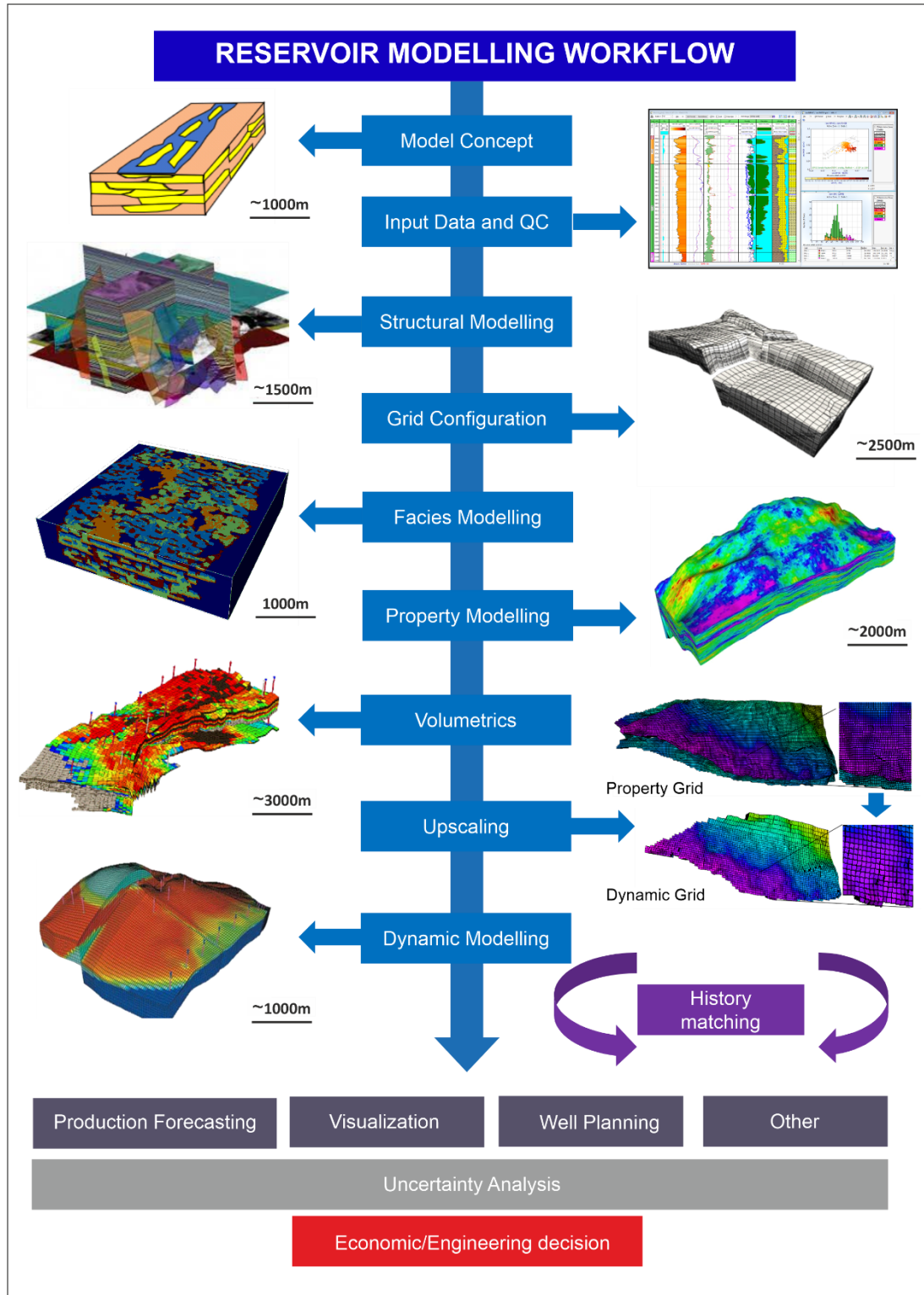


Figure 2.4 Reservoir Modelling Workflow.

Summary of the most important steps for building a reservoir model. Different stages are differentiated which eventually will lead to an economic/engineering decision. Structural modelling figure taken from Paradigm's SKUA GoCAD. Grid configuration figure taken from Araujo et al., 2016. Property modelling, upscaling and volumetrics figures taken from Petrel® (Schlumberger) manual. Dynamic modelling taken from Eclipse® (Schlumberger).

Reservoir models are commonly constructed using commercially available software for reservoir characterisation studies (Yarus et al., 2016). These software platforms allow rapid analysis of large datasets for exploration and production, for the construction of 3D digital models and their use for reservoir simulation purposes. Examples of industry-standard commercial software platforms used for the construction of reservoir models are Petrel® (Schlumberger) or Decision Space® Geoscience (Halliburton). Other non-commercial software, like SGeMS® (Stanford University, Boucher, 2009), are also commonly used by geomodellers.

2.1.1 Model Concept

Conceptual models are initially developed by geoscientists to present a thorough understanding of the area of investigation (Ringrose et al., 2011). At first, the model concept can be conceived as a sketch, an outcrop panel, satellite photos or an analogue reservoir case study, for example. The geoscientist will include in this conceptual model all available geological data of the reservoir (stratigraphy, depositional environment, facies architecture, etc). This information will serve as a guide to the construction of the quantitative geocellular representation that will include the most relevant model elements (building blocks or main architectural elements in a digital 3D model) (Brandsaeter et al., 2001; Journel, 1993) (Figure 2.5).

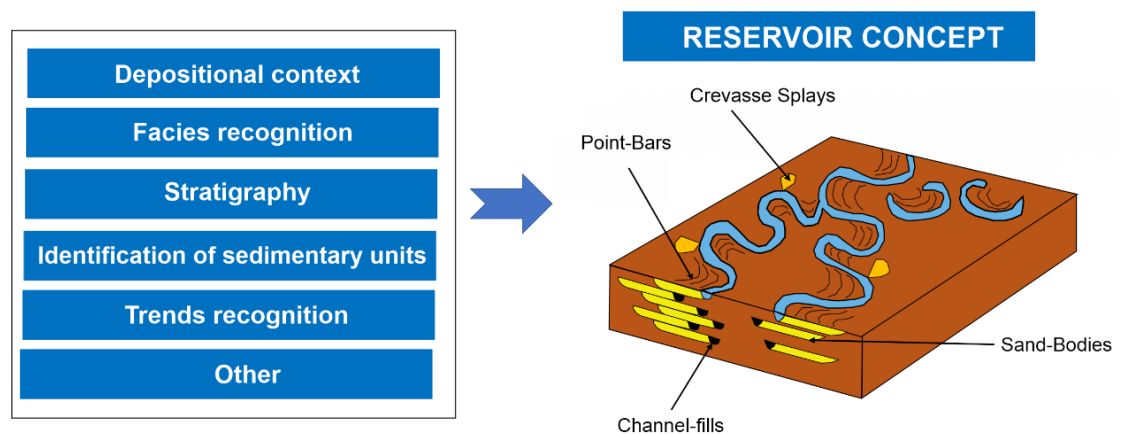


Figure 2.5 Reservoir Concept

A conceptual reservoir model is defined by considering the characteristics included in the left-hand side table. In this case a meandering fluvial system sketch is represented including different model elements (point-bar sandbodies, crevasse splays, channel-fills and flood-plain deposits). Vertical scale: $\sim 10^1$ - 10^2 m. Horizontal scale: $\sim 10^3$ - 10^4 m.

During the model concept phase, outcrop analogue studies are commonly used to acquire both soft (conceptual) and hard (quantitative) data that may be relevant to the reservoir succession under investigation (Pranter et al., 2013; Cannon, 2018). These are useful to determine different aspects of reservoir heterogeneity, notably sedimentary architectures and resulting reservoir properties, and attributes such as horizontal connectivity and petrophysical properties (including porosity and permeability) (Nordahl et al., 2014; Keogh et al., 2014).

2.1.2 Project Scoping

Reservoir models may have different purposes, which will guide their design. There are three different types of project scopes: i) reservoir screening, ii) visualisation and iii) reservoir simulation (Figure 2.6).

Screening. Reservoir models made for screening purposes are used for different reasons. The most important one is commonly the determination of initial volumetrics and its variations in the different phases of appraisal and development (Ringrose and Bentley, 2015). Reservoir models should provide the most accurate estimation of the volume of a resource (e.g., oil, gas, water) in place. Also, the 3D model can incorporate the estimated positions of fluid contacts in the reservoir, which will evolve throughout the field life cycle (Deutsch, 2002).

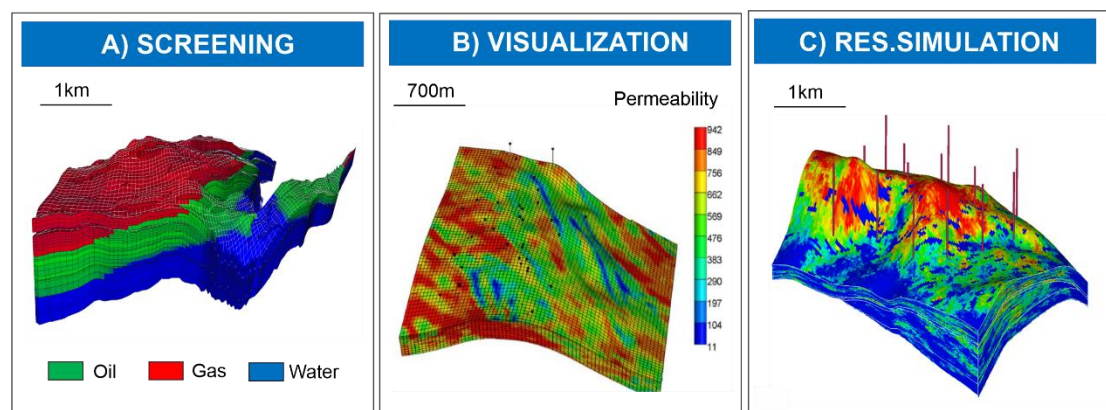


Figure 2.6 Reservoir Purposes (Screening, Visualisation, Simulation)

(A) Shows an example for screening in which the oil, gas and water zones are monitored after production started (Rasmussen et al., 2001). (B) Permeability model for visualisation purposes (Al-Mudhafar et al., 2015). (C) Reservoir simulation modelling example taken from Reservoir Simulation (SOS-spacialoilfield.com/services/reservoir simulation).

Visualisation/Definition. Reservoir models can be also created to visualise different type of properties (static and dynamic), in support of business decisions. These properties are associated with the different rock bodies, which constitute the building blocks of a reservoir. This can be the analysis of various rock types and their relationships with different petrophysical properties (Caers, 2008). For purposes of visualisation, the 3D model will help communicate the conceptual understanding of the reservoir, for example highlighting sweets spots in the area of investigation. Visualisation models should have sufficient resolution to represent vertical and horizontal heterogeneity at different scales. These can be at the scales of a single well, multiple wells, field scale and less commonly, to regional inter-field (play) scales (Deutsch and Wang, 1996). Different examples for visualisation purposes are given below.

- 3D (digital) visualisation of a conceptual model of the reservoir.
- Visualisation of the structural framework used for subsequent analyses. The model should reflect the location of faults determined from seismic data analysis and of geologically meaningful reservoir zones (e.g., prerift, synrift and postrift intervals). Also, 3D models apply seismic models that translate geophysical properties into rocks and fluid properties. An example for this is the visualisation of Direct Hydrocarbon Indicators (DHIs).
- Visualisation of properties (e.g., porosity, permeability, water saturation, etc.) highlighting areas corresponding with high net-pay. This type of visualisation often serves to support decisions related to the targeting of different plays or to validate an appraisal or development campaign.
- Visualisation of well paths for the well planning and geosteering strategies. These models should include all factors that will impact the drilling of wellbores. An example of this can be a 3D model which focuses on pore pressure prediction for the determination of mud pressure in each of the planned wells. 3D models applied to well planning can be used in real-time and can guide the reorientation of perforations when needed.

Simulation. Static models are required as input for reservoir flow simulation (Jackson et al., 2003). For example, permeability values are required as input for the purpose of constraining dynamic reservoir simulation forecasts. Therefore, special attention should be taken in the definition of permeability

fields if the purpose of the 3D model is to serve as a dynamic representation of the flow behaviour of the reservoir volume (Nghiem et al., 1991). Models for simulation purposes are particularly important to be applied to IOR (Improved Oil Recovery) and EOR (Enhanced Oil Recovery) activities, which require time-lapse 3D outputs for informing the choice of reservoir-flooding method (Nordahl et al., 2014).

2.1.3 Input Data (Hard, Soft and Analogue Data)

Many different data types are included in 3D reservoir models. Surfaces bounding rock volumes, sequence stratigraphy picks, electrical logs and core data are some examples of features used by geomodellers, and which need to be referenced in a common coordinate system (Alexander, 1993). Modelling inputs must be as accurate as possible, and operators make sure a QC process exists to minimise the risk of error of each of these inputs. The availability of input data changes throughout the field lifecycle. During early exploration stages, very little data may exist; even during more advanced stages of appraisal, where several wells might have been drilled, geomodellers might still face challenges in relation to conditioning the inter-well volume of a reservoir model (Howell et al., 2014; Tarek, 2020).

Well data will provide information at high resolution, but in one dimension (1D) only. The resolution can increase further if core data are available. Petrophysical interpretations will tie continuous recorded logs to core data in a process called core-to-log reconciliation (Serra, 2008). Petrophysical data are used as deterministic hard data in a model. Petrophysical interpretations are made using electrical logs to infer properties such as porosity, permeability, water saturation, etc. (**Figure 2.7**). On the contrary, seismic data will cover larger areas but their vertical resolution is small (approximately 25 m for many vintage seismic acquisitions and at best ~7 m for modern 3D surveys), meaning that internal heterogeneities of geobodies that control fluid flow will not typically be imaged (e.g., smaller abandoned channel-fill deposits) (Nanda, 2016; Kearey et al., 2013). Production data from well tests can also provide detailed information regarding heterogeneities but cannot confidently be interpreted in terms of geological architectures (Oliver et al., 2008). Therefore, geological analogue data have long been used in reservoir modelling to improve understanding of reservoir rocks (Keogh et al., 2007;

Alexander, 1993; Flint and Bryant, 1993). This topic is discussed in more detail in Chapter 4.

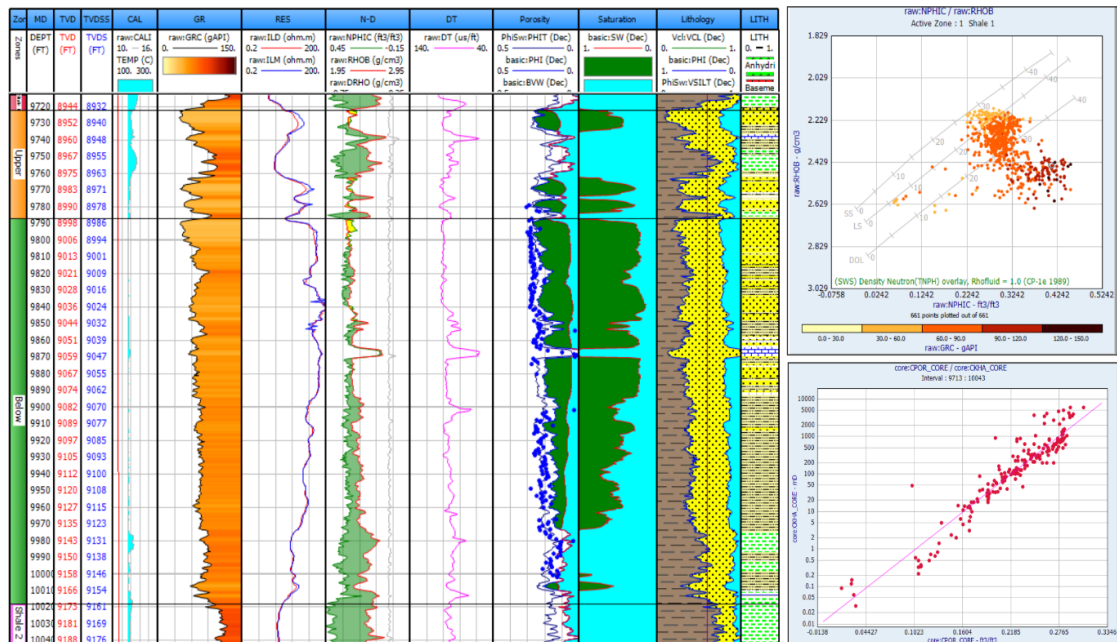


Figure 2.7 Petrophysical Interpretation (Example)

Petrophysical Interpretation showing some calculated parameters (Effective Porosity-PHIE, Bulk Volume Water-BVW, Volume of Clay-VCL, Saturation Water-SW, Lithology, etc) using raw logs (Gamma Ray-GR, Resistivity-RES, Neutron-Density and Sonic log-DT). A neutron-density plot cross plotted to gamma ray is shown in the upper right corner and a porosity-permeability chart (core) relationship is shown in the lower right corner. Logplot made with Interactive Petrophysics® software.

Data acquisition issues or inconsistencies in interpreted or calculated data are cautiously scrutinised by different professionals in order to assure the highest data quality is pushed to the model. Examples of such issues, which are often found during the data input and QC stages, are large uncertainty values for specific petrophysical parameters (e.g., $\pm 5\%$ porosity). Usually, Monte-Carlo simulations are used to constrain uncertainties in 1D logs which have been interpreted from raw data and can be useful to understand and detect anomalies in reservoir models (Serra, 2007; 2008; 2010; Glover, 2022).

2.1.4 Structural Modelling

Structural modelling – also called framework modelling – must capture both i) zonation (e.g., inputs on division in stratigraphic intervals) and ii) faulting (e.g.,

structural inputs) (Pyrz and Deutsch, 2014; Al-Badawi, 2015). With regard to zonation (stratigraphical inputs), the frameworks must capture surfaces that separate different stratigraphic intervals. Zonations are based in part on seismic interpretations, tied to well logs where possible. There are different types of zonations that can be taken into consideration by geomodellers; lithostratigraphic, biostratigraphic, chronostratigraphic, or sequence stratigraphic, for example (Van Wagoner et al., 1990).

With regard to faulting, the structural frameworks should capture all major faults that form compartments in the reservoir. Similar to the zonation, faults are also typically most obviously identified via seismic interpretation. Zonation and faulting interpretation tasks are usually interpreted by geophysicists and geologists. The structural framework is typically built prior to gridding, where raw depth-converted seismic surfaces and fault sticks needs to be geometrically and spatially well represented in the grid (Altameemi and Alzaidy, 2018).

2.1.5 Grid Configuration

The model should account for the size of the volume being investigated. This means that the number and sizes of cells included in an x, y and z grid space should be allocated with consideration of the size of the reservoir volume. The selected 3D gridding approach needs to adequately represent the different geological features that will be modelled, such as onlap, downlap and other stratal geometries, as well faults, where appropriate. The cell size can be regular or irregular. In some cases, where more definition is required in depth (z) dimension, irregular cell sizes are utilised. This can be a case where certain vertical variations in heterogeneity need to be captured in the model (Araujo et al., 2016; Lasseter, 2022).

Currently, field-scale reservoir models are typically in the order of 10^6 - 10^7 cells with horizontal cell sizes of 50-100 m and vertical cell sizes of about 1-10 m (Pickup et al., 2000). The grid configuration is usually a compromise between the detail and complexity of the features that are required to be modelled and the available computation resources.

2.1.6 Facies Modelling

Facies modelling – also called rock modelling – incorporates the geological knowledge that has been acquired by geologist from the rock record analysis (Caers, 2008; Remy, 2009; Strebelle 2002; Miall, 2016; Canon, 2018). It handles the building blocks from which a reservoir model is constructed, corresponding to different model elements that will control the distribution and flow of fluids in a reservoir model (De Vries et al., 2009; Colombera et al., 2012a). There are different types of model elements. Some examples are listed below.

- Lithologies. Fundamental rock units defined by their sedimentological attributes, e.g., sandstones, limestones, mudstones, the latter in some cases referred to as shales (Reading, 1986).
- Lithofacies and facies associations including rock types distinguished on the basis of various characteristics including sedimentary textures, and physical, chemical and biological structures (e.g., cross-bedded sandstones, black organic-rich mudstones) (Tucker, 1996, Miall, 1986) (Figure 2.8).
- Rock types with contrasting hydraulic properties and petrophysical and engineering characteristics (e.g., porosity, permeability, water saturation) (Serra, 2007; Glover, 2022; Tiab et al., 2003).
- Genetic units related to a particular set of depositional processes (e.g., parasequences) (Van Wagoner, 1990).

It is common for a geologist to include geological data coming from different sources (e.g., sedimentological core descriptions, cuttings descriptions, master log descriptions, etc.) into the rock models. However, this can overcomplicate the model (Haldorsen and Damsleth, 1990). The geomodeller may thus select what types of data should be included into the model, noting that some data types can be superfluous for the purpose of informing engineering decisions (Caers 2001; 2003). The decision to choose specific types of model elements should be underpinned by knowledge of the degree of heterogeneity thought to be significant and requiring incorporation into the reservoir model. It is a combination of geology and flow physics that leads geomodellers to select rock types with consideration of their influence on flow behaviour (Corbett et al., 2012). For this, petrophysical and geological analyses are required to determine both rock-type permeability variations and

architectures of model elements (Bentley and Eliot, 2008; Ringrose and Bentley, 2015). Therefore, petrophysical rock types are usually picked by geomodellers to constrain corresponding building blocks associated with similar hydraulic flow behaviour (HFU-Hydraulic Flow Units) (Serra, 2007; Abbaszadeh et al., 1996).

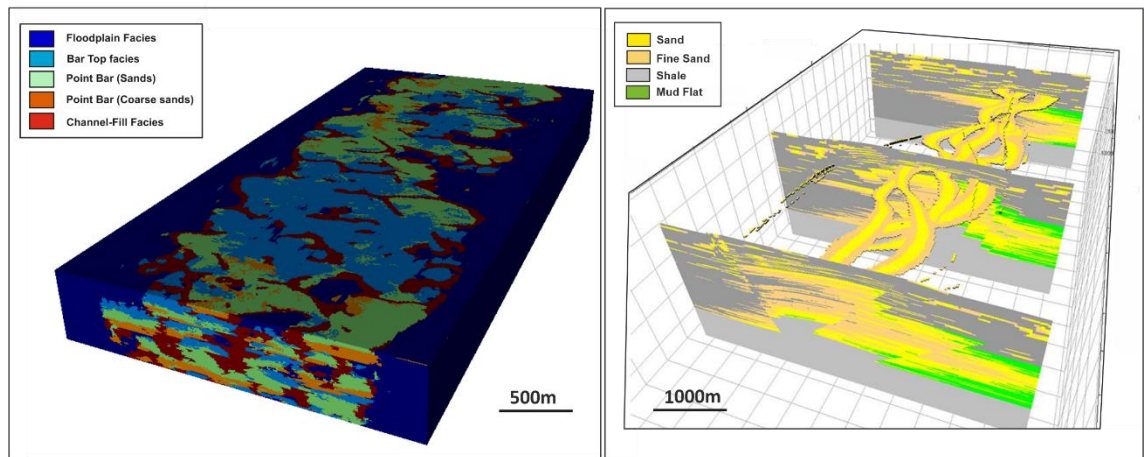


Figure 2.8 Example of facies model.

Facies models where different types of lithofacies are included for a meandering fluvial system. Left-hand image displays a facies model produced using SGEMS® software (Chapter 3). Right-hand shows a facies model produced by Petrel® (From Schlumberger website).

The facies modelling stage involves stochastic techniques applied to determine the best facies distribution in the space, conditioned by well log data (Deutsch, 2002). Secondary data (e.g., porosity-permeability transforms, probability maps, etc) may be applied to conditioned simulations too. This Thesis focuses on the application of facies models for tasks of subsurface characterisation and prediction. As such, special attention is herein given to the different stochastic approaches, with emphasis on those that are commonly used for facies modelling, and in particular those based on multipoint statistics (Guardiano and Srivastava, 1993; Strebelle and Journel, 2001; Montero et al., 2021). More information regarding geostatistics can be found in **section 2.3**.

2.1.7 Property Modelling

Property modelling seeks to incorporate, in previously created facies models, different petrophysical engineering, geophysical, geomechanical, and related

properties (Hohn, 1999). The most important properties modelled within the petrophysical domain are: i) porosity (Φ), ii) permeability (K), iii) water saturation (S_w), iv) volume of clay (V_{cl}), v) net-to-gross ratio, vi) net reservoir, vii) net pay, viii) bulk density and ix) formation resistivity (Consentino, 2001).

In property modelling, as in facies modelling, data from well logs are incorporated to add local determinism. However, the continuous log properties, which are included within the intersected cells, need to be upscaled or averaged to the existing cell size. This upscaling process is different from the upscaling that occurs prior to numerical or dynamic modelling (**section 2.1.9**) (Isaaks and Srivastava, 1989; Corbett, 1992). As an example, 1D well log recordings, which are acquired/calculated to cm scale during the petrophysical analysis (current sample rate standards for various tools reach 0.1524 m or 0.5 ft) need to be related to a specific cell dimension. After this blocking process, a stochastic method is commonly employed to populate properties in the inter-well space (Journel, 1986). For petrophysical modelling the sequential gaussian simulation (SGS) technique is often used to reproduce the spatial structure of a given property (e.g., porosity, permeability) (Deutsch, 2002). The permeability model, given its non-additive characteristics, is more complicated to model than the other properties (Desberats, 1987). Permeability models can be derived from porosity-permeability transforms (trend/regression function) where a correlation between both exists (Altameemi, and Alzaidy, 2018).

Another petrophysical property that is often modelled is the initial water saturation (S_{wi}) within the porosity of the formation rock, which must be determined at this stage to estimate the hydrocarbon initially in place (Bierkins, 1996). There are different ways to calculate it. The simplest workflow could be co-simulations with K or Φ using SGS as a relationship exist between S_{wi} , K and Φ (Pickup et al., 1995). However, j-functions (a series of P_c curves -capillary pressure- that can be converted to a single curve relating S_w , K and Φ to corresponding rock types) calculated from core/log based and applied after upscaling can achieve better results (Leverett, 1941; Serra, 2010). Also, saturation height functions are calculated to deliver a thorough understanding of how saturation varies with height in the reservoir tied to each of the rock types (Cardwell, 1945; Bryant and Blunt, 1992; Al-Baldawi, 2015). A competent saturation water model is expected to yield information on the

free water level (FWL) and the oil-water/gas water contact associated with the previously interpreted rock typing (Worthington, 2001).

2.1.8 Volumetrics

The volumetrics assessment seeks to understand how much resource (e.g., oil or gas) is located in a given reservoir, one of the most important objectives in reservoir modelling (Pan, 2000). In other cases, as in carbon capture projects (CCS), volumetric analysis consists in understanding how much supercritical CO₂ could be stored in a given reservoir rock (Ringrose et al., 2011). Volumetric evaluations can be performed in 3D in the reservoir model to deliver potential reserves estimations for determining economic profitability (Dean, L., 2008). As an example, for volumetrics analysis, hydrocarbon in place equations (HIIP) are run for each of the cells included in the reservoir model, which include the following variables:

$$HIIP = \frac{(GRV \times Net \times \phi \times (1 - S_w))}{FVF}$$

- GRV (Gross Rock Volume) corresponds to volume of rocks, determined by geophysical procedures.
- Net refers to the net-to-gross which in the volumetric stage usually correspond with a given Net Pay. The Net Pay portion of the reservoir where hydrocarbons are found in an economical proportion is calculated by the application of various petrophysical cut-offs. Mainly effective porosity (ϕ_e), water saturation (S_w) and permeability (K).
- Porosity (ϕ), and more specifically the effective porosity that has been determined for each specific cell (average value).
- Water Saturation (S_w) corresponding to the fraction of effective porosity in the formation rock which is filled with water. Water saturation values are averaged for each cell.
- FVF or Formation Volume Factor indicates the ratio of the volume of hydrocarbons at reservoir conditions compared with the volume of hydrocarbons at surface conditions (different temperature and pressure). It is usually calculated from fluid compositions and reservoir pressure (often using offset wells).

Volumetrics calculations may yield results (e.g., predictions) that vary significantly due to the different input datasets (core versus log porosity, different S_w values based on different equation parameters or lowest known oil versus highest known water are some examples), and also with the number of wells that perforate the reservoir volume (Carlson, 2006; Fanchi, 2001). This means that, in early exploration stages where no wells or only one well has been drilled, the volumetrics calculations will be based on input ranges for variables that have significant uncertainties. By contrast, as the field is gradually further appraised and developed, more deterministic data will become available, and the volumetric estimation will become more accurate (Aziz and Settari, 2002). During the volumetrics stage, several realisations will typically be used to understand uncertainties. Results are evaluated using Monte Carlo Simulations that rank statistically the various realisations delivered by simulations and their probability (p10, p50, p90, etc.) (Pan, 2000).

2.1.9 Upscaling

The process of upscaling corresponds to the conversion of information at small scale to a larger-scale equivalent included in a coarser 3D grid used in flow simulator software (Barker and Thibeau, 1997). The goal is to create a coarser grid for numerical simulations using properties derived from a finer grid (facies and property models). Facies and property models are usually in the order of millions of cells, whereas dynamic simulations tend to be run on grids in the order of few hundred thousand of cells (Towler, 2002). The coarsening of the geocellular grid in numerical models is a limitation imposed by computational power and run time. Nevertheless, the upscaling process must ensure that upscaled models capture those finer-scale properties that are explicitly related to fluid-flow characteristics (heterogeneities) (Figure 2.8).

Different scales related to flow and heterogeneities are identified. These are defined based on the concept of Representative Elementary Volume (REV) (Bear, 1972), which provides the basis for understanding the impact of measurement scales and geological variability. These are: i) pore-scale or microscopic; ii) mesoscopic and macroscopic, which better represents the geological heterogeneity included in the model elements, and iii) megascopic, which represent regional or field-scale variations. In a given model, there must be a defined purpose for the inclusion of specific types of heterogeneities

(Bourbiaux, 2002; Jackson et al., 2003). For an optimum upscaling process, thorough geological knowledge of the different types of reservoir heterogeneities, rock architecture and controls on flow properties is required (Ekran and Aasen, 2000).

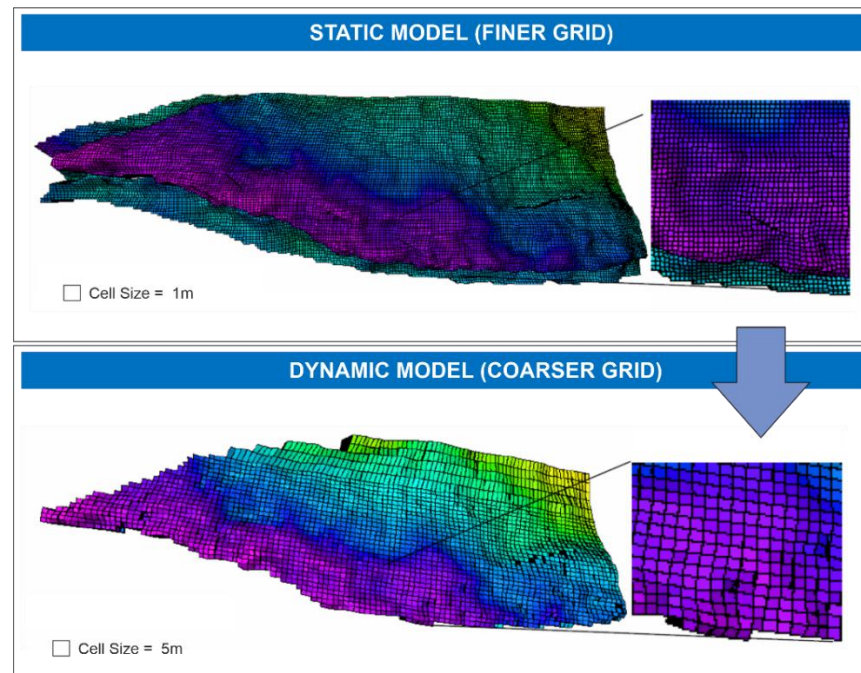


Figure 2.8 Upscaling (Grid Example)

Upscaling reduces the number of cells so that simulation run times are reasonable. From 2.5 million cells in the static model to 150,000 cells in the dynamic model (Modified from Petrel® Advanced guide).

Geomodellers will then deal with the types of upscaling which may correspond to i) the pore to lithofacies scale, where pore-scale behaviour is applied to the lithofacies architecture domain; ii) the lithofacies to geomodel, where larger heterogeneity characteristics are considered; and finally, iii) the upscaling process that may be needed to make a static model usable by a dynamic simulator (Ringrose and Bentley, 2015). The pore to lithofacies scale and the lithofacies to geomodel scales are normally considered to take part into static models as part of the facies modelling stage (section 2.1.6). A rock typing analysis based on the characterisation of hydraulic flow units (HFU) may calibrate well these scales (Abbaszadeh, et al., 1996; Corbett et al., 1992). It is widely recognised that the rock type/lithofacies concept adjusted to hydraulic flow units (HFU) fits best to the REV concept applied to geological variability (Corbett, 1992; Abbaszadeh et al., 1996; Nordahl et al., 2005; Serra 2007; Ringrose and Bentley, 2015; Glover, 2022; Tiab et al., 2003).

The dynamic model grid, even if coarser than the facies/rock model, should be able to allocate the determined rock type heterogeneities. The upscaling process, which in many cases involves a major transition in scale, should deliver representative average values corresponding to local variations and associated with previously defined hydraulic flow units (King and Mansfield, 1999). There are different types of mathematical approaches for upscaling (Durlofsky, 1991; 2003).

- **Well data averaging into the flow simulation grid:** continuous well logs related with different flow properties (Φ_e , S_w , K , etc.) and corresponding to smaller-scale measurements are upscaled or averaged to the existing cell size (larger scale). This leads to a very particular challenge, as flow properties can vary drastically over a wide range of length scales (Renard and de Marsily, 1997; Haldorsen, 1986). This approach is fast and simple but ignores the criteria for smaller-scale structures and flow. However, it can be useful for homogeneous and permeable rock sequences. Different averaging methods can be used and are usually adopted in the property model stage. These are the arithmetic, the geometric and the harmonic average. The geometric average is often considered as the most suitable averaging method for more heterogeneous types of rocks (Ringrose and Bentley, 2015).
- **Single phase upscaling:** Single phase upscaling can take place only in Z vertical planes or in the XY planes. For the upscaling in Z vertical planes, and assuming a simulation grid with the same cell size for X and Y, the method uses averaging methods to ensure thin layers acting as baffle or barriers to the flow in the axis Z are properly represented. The method is often used where complex structures or fine-scale layering take place and control fluid flow. For single phase upscaling occurring in X, Y and Z planes, the process takes place using diagonal tensor or full tensor methods in a multi-scale context where flow properties are required to be upscaled in X, Y and Z. However, multiphase flows are ignored in this method (Barker and Thibeau, 1997).
- **Multi-phase upscaling:** Effective in large-scale models where flow properties need to be upscaled in X, Y and Z using a steady state solution to multiphase flow scaling problems (Pickup and Stephen 2000).

A quality control for the upscaled variables takes place through a comparison between the property models and the upscaled values in the new coarser grid

(dynamic model). This can be done as i) comparison between previous HIIP volumes in the volumetric analysis versus the dynamic volumetrics, ii) statistics related to certain properties delivered during the property modelling and compared with the dynamic model, and iii) random property checks using pseudo-wells. Also, streamline simulations for breakthrough times, streamline patterns or time-to-producer values can be compared for dynamic vs static property modelling alongside with the preservation of heterogeneities. Once upscaling has been performed, flow simulations use mathematical approaches to calculate flows and pressures in the grid cells.

2.1.10 Dynamic Models: Numerical Simulations

In most cases when a static model is built, it is used to “feed” a dynamic model that will be used for various purposes (Tchelepi, 2005). The dynamic model uses inputs from the static model on dynamic properties that may change during the oilfield lifecycle (Weber, 1986). These are fluid saturations, contacts, compositions, pressures, and others. Porosity and permeability, which are commonly considered as static properties, may also change as reservoir pressures are modified over time or reactions between minerals occur when different fluids are injected in the reservoir (King, 1999; Dake, 2001).

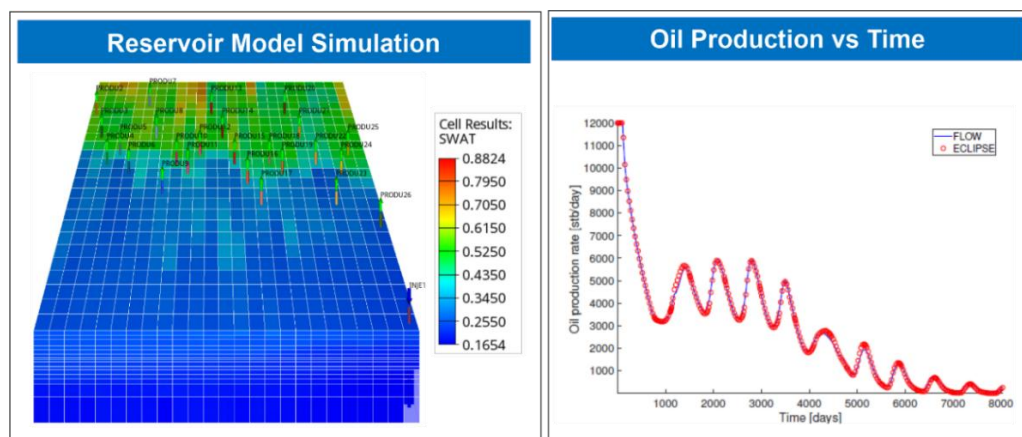


Figure 2.9 Dynamic Model

The left-hand figure shows a gas saturation simulation after production by wells at the rate shown in the red curve in the chart on the right-hand side. The red curve indicates the Eclipse® simulation results which agree with the computation of another reservoir modelling software called OPM Flow®. Modified from Rasmussen et al., (2019). Cell size= 24x25x15 ft (7x7x4.5 m).

The main outputs to consider in dynamic models are: i) fluid saturation, ii) fluid-flow rates, iii) fluid contacts, iv) pressure properties, v) acoustic properties (seismic) and fluid compositions (including gas-to-oil ratio [GOR] and water-to-oil ratio [WOR]) (**Figure 2.9A**).

Dynamic models are the end-goal of the reservoir modelling workflow and will deliver outputs for the following purposes.

- Visualisation: Dynamic models will allow reservoir engineers to understand the location and spatial distribution of oil, water and gas saturations in a given reservoir so reservoir engineers can plan or justify engineering or economic decisions.
- Well planning (field development): After understanding the reservoir characteristics with respect to fluid accumulations, decision relating to the producibility of the field will be made. The location of well producers and injectors is discussed and chosen based on the dynamic models ([Fanchi, 2001](#)).
- Well completion: Downhole equipment corresponding to the different type of well design will also consider the dynamic model for decision-making of different tools and technologies to be applied ([Mattax and Dalton, 1990](#)).
- Facilities layout. The dynamic model will calculate the pressure/saturation distribution into the reservoir, so that production engineers can design and plan the required facilities to successfully manage the produced fluids from the reservoir rock (platform/rig type, compression capacity, separation capacities, sequence of well drilling, etc) ([Ertekin et al., 1990](#)).
- Reservoir simulations (recovery process). Dynamic models are made to simulate the entire life of a reservoir rock considering different strategies for production and different parameters applied related with the optimisation and depletion plans (**Figure 2.9A**). Reservoir simulations can be applied at any stage in the oilfield lifecycle ([Aziz and Settari, 2002](#)). As an example, for mature field, the reservoir models can be very important for the evaluation of different development options. At this stage the engineers already have production history, pressures, cumulative oil, water cuts, GOR's, etc so history matchings are possible, as well as a better tuned reservoir model. Furthermore, water/gas injection rates or field reservoir pressures are some of the parameters identifiable from the dynamic model and that will contribute to the definition of reliable forecasting activities ([Crichlow, 1978](#)).

- Production forecasting is also delivered from dynamic models. Simulations using different parameters (e.g., Pressure, temperature, etc) take place and results are ranked in terms of production profiles vs time (Fanchi, 2001). Important business decisions are made taking production profiled vs time (**Figure 2.9B**).
- Reservoir performance. Dynamic models will provide important information regarding the drive mechanism (e.g., aquifer-controlled field natural depletion, waterflood mechanisms, etc) (Ringrose and Bentley 2015).

Mathematical techniques used in reservoir simulation include numerical methods such as finite difference, finite volume, finite elements, etc. (Chierici, 1994). Different laws are used by reservoir modelling software. These are conservation of mass, conservation of momentum and conservation of energy (Jensen et al., 2000). Although they all use variations from standard classical equations, the following forms are considered in the majority of simulators:

- Conservation of mass expressed as a function of “u” (velocity), “ρ” (density), “A” (area) and “t” (time):

$$\{u\rho A\}_x - \{u\rho A\}_{x+\Delta x} = \frac{\partial}{\partial t} \{\phi A \Delta x \rho\}$$

or

$$\left\{ \begin{array}{l} \text{Mass into the} \\ \text{element at } x \end{array} \right\} - \left\{ \begin{array}{l} \text{Mass out of the} \\ \text{element at } x + \Delta x \end{array} \right\} = \left\{ \begin{array}{l} \text{Rate of change of mass} \\ \text{inside the element} \end{array} \right\}$$

- The conservation of momentum, governed by the Navier-Stokes equations, is normally simplified for low velocity flow in porous materials to be described by the semi-empirical Darcy’s equation which for single phase, one dimensional, horizontal flow is defined as a function of “μ” (viscosity), “ρ” (density) and “k” (permeability). See equation below:

$$u = \frac{k}{\mu} \frac{\partial p}{\partial x}$$

- Regarding the conservation of energy law, this refers to the total energy of an isolated system remaining constant (Feynman, 1970) and can be expressed as follows (example for saturation “S” as a function of “B” (formation volumetric factor, FVF), “K” (permeability) and “P” (pressure)). See equation below:

$$\frac{\partial}{\partial t} \frac{\phi S_o}{B_o} = \frac{\partial}{\partial x} \left[\frac{k k_{ro}}{\mu B_o} \left[\left(\frac{\partial P_o}{\partial x} \right) - \rho_o g \frac{\partial z}{\partial z} \right] \right]$$

Geomodellers select different types of numerical simulators based on the type and behaviour of the original reservoir fluids and on the predominant process controlling the reservoir production and hydrocarbon recovery (Chierici, 1994). Examples for three of the most important flow simulators can be the following. i) The compositional model simulator that calculates the PVT (Pressure, Volume and Temperature) properties of hydrocarbons included within the equation of state (EOS) which is used to dynamically monitor the flow of different fluids and phases in the field (Haldorsen, 1986). ii) Black-oil simulator where the phases are treated as components to model natural depletion and most secondary recovery process. The black oil simulator is valid to model two or three immiscible phases of flow in porous media. iii) Thermal simulators that compute fluid phase behaviour and the Darcy approximation of fluid flow through porous media (Aziz and Settari, 2002).

Parameter changes for the three phases (water, gas, oil) are quantified in each of the cells in the model at increased cost in setup time, compute time, and computer memory. Also, well controls, such as injection rates and bottom-hole pressure constraints, drive dynamic models. However, for successful dynamic modelling, the static should be able to capture the permeability heterogeneity which is defined in the rock facies model and the property model and that will significantly impact reservoir performance (Mallet, 2008).

2.1.11 History Matching

A successful and reliable reservoir model should honour production history (history matching) with a representative set of realisations coming from the dynamic model and referring to field and individual wells, cumulative production, water cuts, well bottom-hole pressure, production flow rates, etc (Alessio et al., 2005; Bentley and Woodhead, 1998). The history matching process typically requires that dynamic well parameters be adjusted in the search for the closest match to known production data. An iterative procedure is employed. This will be considered finished when a final model includes the best (or at least a satisfactory) match to original recordings and production data (Tchelepi, 2005). The dynamic model can then be employed for purposes of drilling planning and production forecasting. The history matching process

will identify weaknesses and defects associated with certain input parameters in the initial dynamic model but also related to the static model. Once these non-accurate parameters have been replaced with more reliable entries, simulations should most closely reflect better and more trustworthy results (Oliver et al., 2008). The calibration process involved in history matching can last from few days to several months; analysis related to the uncertainty of the input parameters are also very important values that are usually included in dynamic simulation outputs related with a history matching process (**Figure 2.9B**).

2.1.12 Uncertainties

Uncertainty analyses applied to reservoir evaluations are conducted by studying the statistical variations associated with the multiple realisations that are run at different stages in the reservoir modelling workflows (Caers, 2011). A variety of different methods can be selected and applied by geomodellers. A typical approach consists in the selection of a base case, (e.g., a reference estimate based on different realisations delivered by a number of simulations). The base case may also be associated with a quantification of uncertainty (e.g., $\pm 10\%$ of the base case facies proportions) (Arnold et al., 2019). A different yet also commonly applied method employs multiple stochastic approaches from different modelling stages (facies models, property models, etc.) where deterministic inputs are used as boundary conditions (Yarus and Chambers, 1994). Realisations are then compared to a deterministic model (a best-estimate case) defined from a conceptual model considered as the base case (Caers, 2011). Both above-described methods rely on the selection of a best guess to determine uncertainties. The best guess should be validated – as far as possible – by professional experts from different disciplines. In cases where this cannot be accomplished using objective criteria, the uncertainty analysis loses credibility (Mintzberg, 1990).

Despite each of these approaches having limitations, these methods are commonly used in the subsurface resource exploration and production industry (Rojas et al., 2012). Scenarios can also be generated via deterministically driven models (geological, geophysical, petrophysical and dynamic) of possible development outcomes. Scenarios can link technical aspects of a model with commercial outcomes where a change in any element

of a model results in a quantitative and measurable change of specific outputs (e.g., volumetrics). (Wynn and Stephens, 2013).

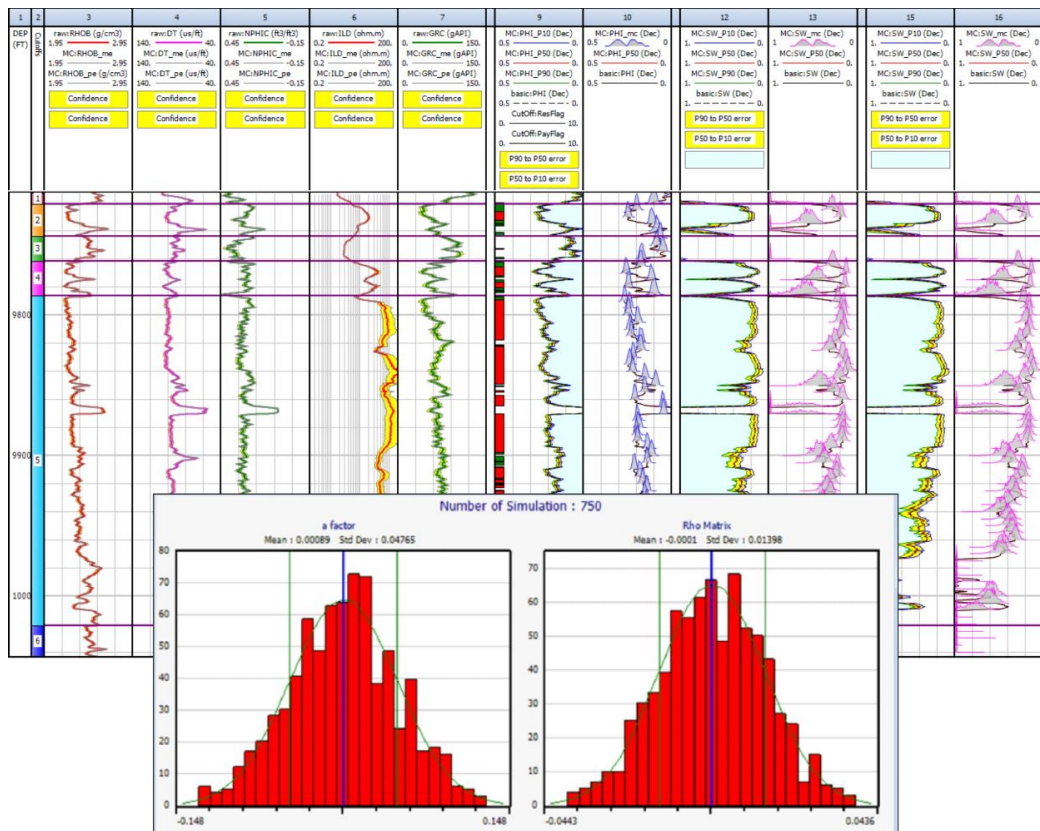


Figure 2.10 Monte-Carlo simulation example

Monte-Carlo simulation applied to the determination of uncertainties with respect to different output parameters in a petrophysical interpretation. Deliveries can be included in logplots, tables and histograms as the example for the “a factor” and the “Rho matrix” (histograms below). Interactive Petrophysics® software.

Monte-Carlo simulations are run to understand in quantitative terms uncertainties related to realisation variability but also to well log/parameters which can be incorporated into different scenarios (**Figure 2.10**) (Gilman et al., 1998).

Monte-Carlo simulations consider the distribution of possible errors associated with uncertainties in values of input parameters. Monte-Carlo simulations use random sampling according to a predefined probability distribution (density function) that define error distribution with respect to the input parameters. As a result, multiple iterations generate repeated random

sampling to compute a probabilistic result. The results for each simulation are compounded and a distribution of the results is delivered (Li and Friedman, 2001).

2.2 Reservoir Modelling: Meandering Fluvial Systems

To build a reliable reservoir model applied to a fluvial sedimentary succession, the geomodeller should properly understand the particularities associated with fluvial systems and their sedimentary deposits. Fluvial deposits mostly comprise clastic detritus transported and deposited by rivers in a continental environment (Miall, 1996). Via progressive accumulation within subsiding sedimentary basins, fluvial deposits are buried deeper over geological time and ultimately may become economic reservoir rocks, and in some cases may act as source and/or seal rocks (Leeder, 1978). Different fluvial features result from the processes of sediment transport and subsequent deposition in a specific depositional environment. The lateral continuity of sediment bodies, their geometries, orientation, shapes, sizes and net values (net reservoir, net pay) are all dependent on the modes of sediment erosion, transport and deposition, which in turn are dictated by physical geological factors, such as environmental energy, depositional processes, basin types, tectonic settings, or sea-level fluctuations, among others (Walker, 1984). Sedimentation processes that occur in a fluvial environment leave behind deposits characterised by distinctive lithological properties. The texture and fabric of a given rock directly determine the pore network. Moreover, stratigraphic features, such as laminae and bed geometries, will have an impact on the mechanics of fluid flow and reservoir performance.

This Thesis is focused principally on meandering fluvial systems and the development of geological models that describe the key attributes of such heterogeneous successions. These attributes are determined by the evolution and behaviour of rivers, which may display high-sinuosity channel features. Therefore, it is important to summarise their geological characteristics and how they may be represented in a 3D reservoir model. Posamentier (2001) separates meandering systems into two classes: meandering rivers confined and developed within incised valleys (**Figure 2.11**) and non-confined meandering rivers that are potentially free to traverse across low-relief alluvial plains, which themselves might be very broad (**Figure 2.12**).

Confined meandering systems associated with incised valleys are commonly formed as a result of tectonic change, climate change or sea-level change that lead to falls in base-level that cause a river to carve into underlying and pre-existing strata (Summerfield, 1985; Posamentier and Allen, 1999; Wakefield and Mountney, 2013). The channel may occupy just the base of the incised valley as erosion continues transporting sediment downstream away from the valley confines (Blum and Törnqvist, 2000).

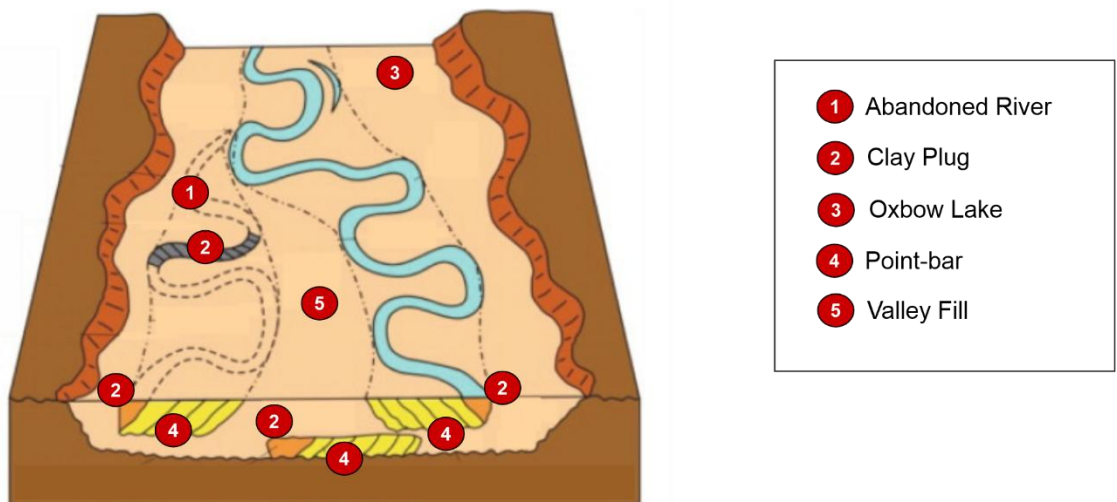


Figure 2.11 Confined meandering fluvial system (incised valley)

Diagram depicting the distribution of a fluvial meandering system in an incised valley. The fluvial system rests incised within pre-existing strata. Lateral migration takes place horizontally within the limits of the valley confines. Modified from Weimer (1992). Typical vertical scale: $\sim 10^1$ - 10^2 m. Typical horizontal scale: $\sim 10^3$ - 10^4 m.

In the following stage, when accommodation generation resumes, accumulation takes place via aggradation (vertically) and lateral accretion (horizontally), filling the valley (Holbrook et al., 2006). At this point, the river may escape from the confinement of the infilled valley. The valley filling process may be quite complicated, notably in cases where it occurs in response to multiple cycles of base-level fall and rise. In lower alluvial plains (close to coastlines) the style of valley filling may be associated with relative sea-level change that affects continental shelves, coastal plains, and the development of estuaries in the nearshore environments (Zaitlin et al., 1994). Conceptual, experimental and numerical models, as well as database-driven statistical analyses, have sought to investigate the geological controls on the geometry of incised-valley fills (Hooke, 1979, 1980; Nanson and Hickin, 1983;

Fielding and Crane, 1987). The degree and rate of river incision, the river size and mobility, tectonic controls, sea-level changes, climate and the extension of slope breaks are each important controlling factors (Wang et al., 2019).

Non-confined meandering systems mostly exist where topographic gradients are low. These are commonly located in the downstream (lowland) sections of a river drainage system where the streambed is gentler as the flow velocity decreases and the river tends to meander. (**Figure 2.12**). In some cases, deposition of finer-grained fractions may be dominant in lower river reaches, in contrast with the commonly coarser deposits of steeper-gradient braided rivers. Furthermore, fluvial channels may be subject to nodal avulsions whereby entire channel reaches may episodically jump to new positions across a basin floor. As such, over time, channel complexes may expand laterally to generate extensive sheet-like sedimentary bodies (Walker, 1984; Miall, 1996; 2016; Ielpi and Ghinassi, 2014).

The most important characteristic in meandering rivers is the development of channel bends (meander loops) and point-bars, which are the primary type of sand-prone deposit in most meandering systems (**Figure 2.12**). Point bars and their accumulated deposits are a particular type of architectural element. Point bars most commonly form on the inner bank of river bends, principally due to the interaction between water flowing around a curved channel and the channel banks and floor.

The curved geometry of the channel produces a helical flow, via centrifugal force, in which water moves from the outer to the inner bank from the channel floor upwards (Bluck, 1971; Miall, 1996; Posamentier, 2001; Miall, 1996). Over time, this process leads to the erosion of the bank on the outer bend of a channel and deposition on the inner bend. This induces the lateral migration of a meandering channel (Nanson, 2009). Synchronous with this, deposition of sediment occurs at the channel's inner bank where the flow velocity is reduced (Allen, 1963; Miall, 1996) (**Figure 2.12B and 2.12C**). In their simplest form, point-bar architectural elements are characterised by the lateral accretion of deposits on inner banks of channel beds. Such accreted deposits are expressed as accumulations that are curved in planview.

Multiple accretion packages amass to form a point bar. These are successions defining the former positions of the inner bank of an expanding river channel bend (**Figure 2.12A**). In cross-section, point-bar elements preserve inclined bedding geometries (epsilon cross-bedding, *sensu* Allen, 1963) which records the progressive building (lateral accretion) of the bar as it develops (Schumm, 1963; Bluck, 1971; Willis 1989; 2019).

Internal point-bar sedimentary architectures commonly display a vertical trend corresponding to a heterogeneous upward shift in lithological character based on grain texture and fabric, and sedimentary structures. This trend is typically dominated by a basal scour contact, cross-stratified gravel and/or sand deposits in the lower sections and ripple cross-laminated fine sand or silt deposits in the upper sections. This trend is expressed vertically as a generally fining-upward facies profile (Allen, 1964; 1965a; Bridges and Leeder, 1976) (**Figure 2.12D**).

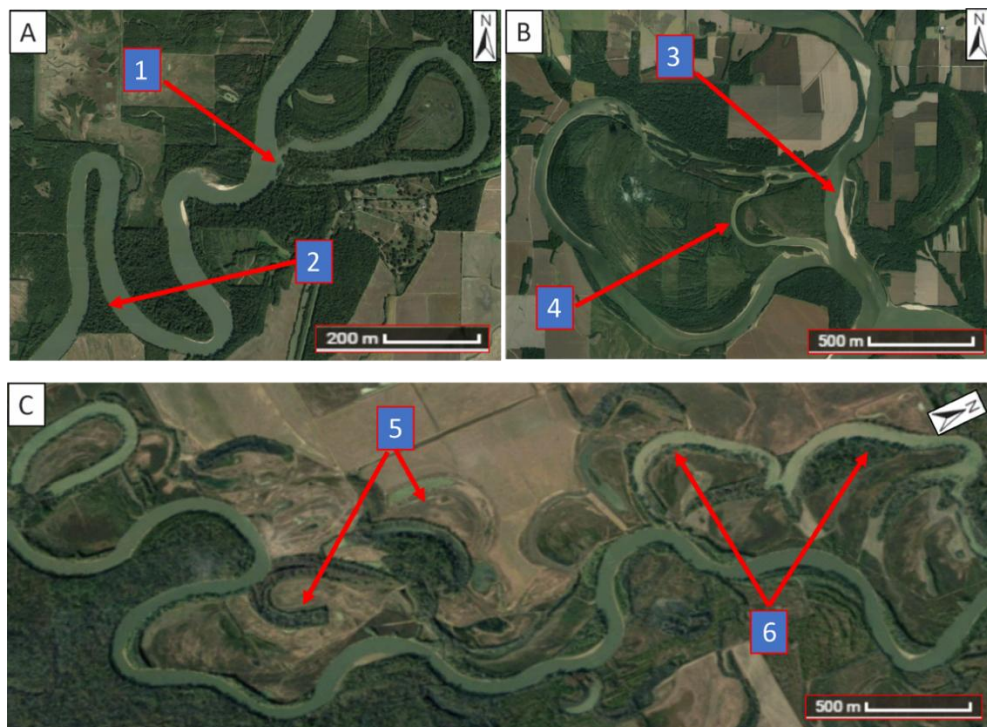


Figure 2.13 Modern examples showing neck cut-off, chute cut-off and oxbow lakes among other meandering features.

(A) White River (USA) (35.100712, -91.445168). 1: Neck cut-off occurrence creating an oxbow lake. 2: Meander bend close to a neck-cut off onset. (B): Wabash River (USA) (37.816673, -88.055439). 3: First chute cut-off development. 4: Second chute cut-off event development. (C) Black River (USA) (35.727818, -91.326290). 5: Old oxbow lakes (vegetated). 6: Oxbow lakes.

The fining-upward trend existing internally within the fill of a point-bar element exerts a significant influence on the porosity and permeability properties of preserved fluvial point-bar architectural elements (Hubbard, 2011). Commonly, a point bar and its associated meander bends will continue to evolve via lateral migration processes to a state whereby the shape of the meander loop becomes highly exaggerated, and a narrow neck develops. Eventually – commonly in the aftermath of a flood event - the meander loop will be cut off as the narrow neck is breached. A new short-cut path is established, and old meander loop becomes “cut-off” (Figure 2.13).



Figure 2.14 Different types of meander bend transformations.

Four basic types of meander-bend transformation (modern rivers). The arrows show the migration direction of meander bends. (A) Powder River (USA) (35.100712, -91.445168). (B): Chubut River (Argentina) (-42.011285, -71.144233). (C) Powder River (USA) (46.280540, -106.328747). (D) Rio Negro, Argentina (39°49' S, 64°56' W). Images from Google Earth®.

Via this process a channel-abandonment process is initiated. Meandering fluvial channels can be abandoned via neck cut-off (as described above) or chute cut-off where a flood channel grows across the surface of the point bar to eventually become the main channel (Stolum 1996; Ghinassi, 2011). Abandoned channel segments that have been cut-off commonly form oxbow lakes (Miall, 1996) (**Figure 2.13C**). These abandoned channel segments tend to slowly infill with fine-grained deposits washed over the floodplain during flood events (else blown in via aeolian processes), thereby creating abandoned channel-fill elements that are commonly described as abandonment mud plugs (Gay et al., 1998; Ielpi and Ghinassi, 2014) (**Figure 2.13C** and **Figure 2.12B**).

Furthermore, a meander bend and its associated point bar may undertake multiple and varied growth episodes (events) during its lifetime. Expansion, rotation, and translation processes (or combinations thereof), in some cases with adjustments from one type to another, may result in the generation of complex depositional patterns, many of which are difficult to model (**Figure 2.14**) (Brice 1974; Ielpi and Ghinassi, 2014; Hubbard et al., 2011; Yan et al., 2017; 2020a).

As a meandering river channel migrates laterally over time, they build channel belts (Leopold and Wolman, 1960; Gibling, 2006). The accumulation of all previous flow paths in the horizontal and vertical sections (subsurface) creates the channel belt (**Figure 2.12C** and **Figure 2.13C**) where net-depositional features are located. However, reservoir performance is controlled by the occurrence of certain preserved architectural elements (mainly point-bar elements) accumulated within a meandering fluvial succession. The preservation of point-bar elements and other fluvial features deposited in channel-belts will vary significantly in relation with the evolution of the fluvial system. This is because a meandering fluvial system will go through different stages of growth from which different types of bend transformations, including lateral expansion and downstream translation in combination with bend-apex rotation (Hagstrom et al., 2019). Furthermore, point-bar deposits can be partly eroded, reworked and overprinted leading to a preservation of potentially complex mosaics of accretion patterns (**Figure 2.15A**).

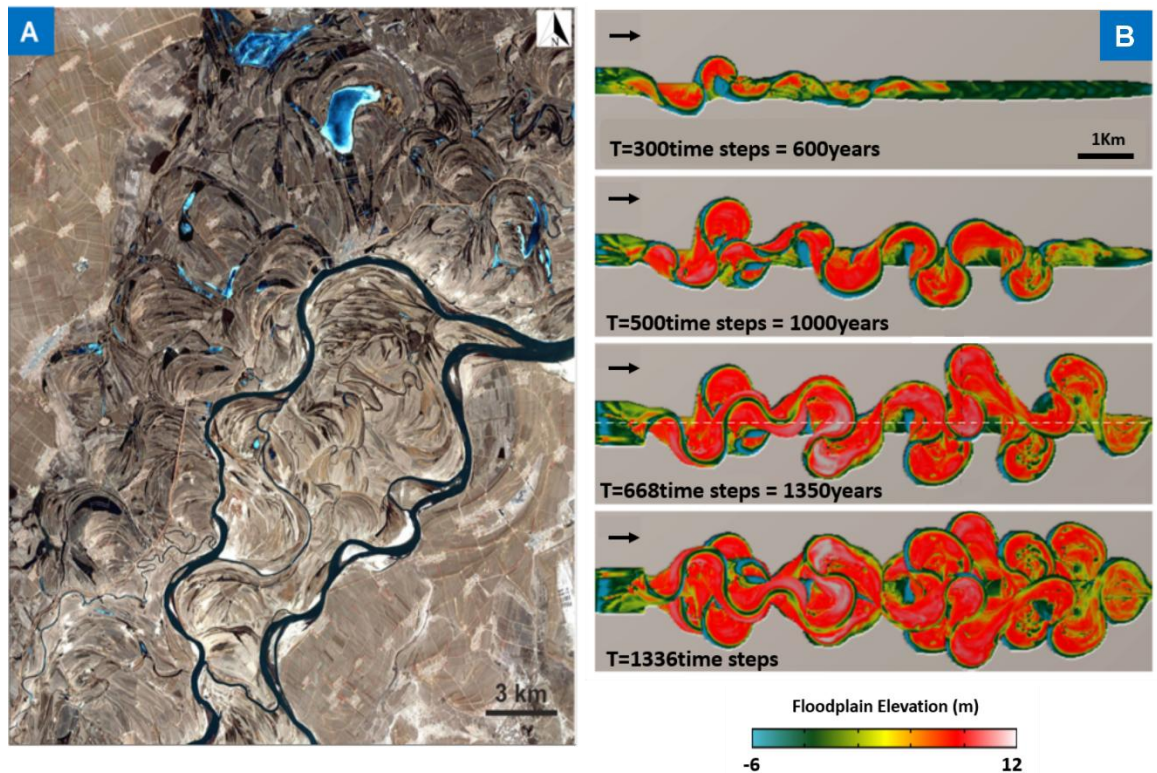


Figure 2.15 Point-Bar Types

(A) Fluvial meandering system (planview satellite image-NASA) for the Songhua River, China. Different loops are observed developing point-bars by the active current channels as well as many abandoned channels and some oxbow lakes. (B) Depiction of four events of meander belt formation in a simulation model where point-bar deposition and preservation can be observed in planview (Van de Lageweg et al., 2016).

In summary, the preservation of meandering river features has been related to different factors: i) intra-meander erosion associated with downstream translation or point-bar rotation (Durkin et al., 2015; 2017); ii) a progressive increase in the sinuosity of a meandering river reach related to bend expansion and lateral accretion (Johnston & Holbrook, 2019); iii) changes in the rate of vertical aggradation (Strick et al., 2018); iv) the lifespan of a channel reach; and v) changes in the rate of sediment supply (Willis & Sech, 2019).

Detailed investigations of meander-belt development by Yan et al., (2023), reveal the role of different morphodynamic processes in controlling point-bar preservation over a range of timescales. The study determined that preservation and accretion rates are rendered complicated by threshold processes of meander transformation change and bend cut-off. Van de Lageweg et al., (2016) also studied different morphodynamic models to

quantify the effect of bed aggradation and lateral migration on the preservation of meander morphologies using numerical methods. They determined that the primary control for deposit thickness is the variability in morphology (different types of bend-transformations) and not the aggradation rate. They also conclude that main architectural variations are expected laterally rather than vertically, even for highly aggradational meandering systems (**Figure 2.15B**).

2.2.1 Fluvial Heterogeneities (Scales)

It is critical to incorporate the identified heterogeneities in a fluvial reservoir model to ensure its realism ([Bridge, 1979](#); [Tyler and Finley, 1991](#); [Colombera et al., 2016](#)). In fluvial successions, heterogeneities of different types occur over different lateral and vertical scales as a hierarchy (**Figure 2.16**).

- **Megascale.** These are basin-scale heterogeneities reflecting large-scale regional geometries at the level of the depositional environment ([McDonnell, 1978](#)). These heterogeneities occur on a scale larger than the field size; typically, many kilometres in lateral extent. Seismic reflections, production data or even well correlations may help to describe them.
- **Macroscale.** These are features corresponding to the interwell scale, >1km to several km in lateral extent ([Friend, 1983](#); [Colombera, 2013](#)). They relate with the vertical and horizontal continuity of each of the model elements included in a model. Macroscale features correspond with the minimum level of heterogeneities that stochastic methods should be able to resolve where interconnections between major permeable units take place. Applied to fluvial meandering deposits, this level of heterogeneities corresponds to channel-belt scale features such as depositional elements. Macroscale heterogeneities can be generated, for example, by the migration and avulsion of river channels located in the channel-belt area over the floodplain. At this scale, the deposits of fluvial systems can lead to reservoir compartmentalisation due to flow barriers and baffles between different type of rocks with significant contrasts in porosity and permeability values ([Bridge, 2006](#); [Miall, 2016](#); [Colombera et al., 2016](#))
-
- **Mesoscale.** Heterogeneities at this scale correspond to architectural elements and lithofacies units (metres to tens or a few hundreds of metres laterally) ([Tyler and Findley, 1991](#)). They are features that may be identifiable in well logs and core data. For fluvial meandering deposits, these heterogeneities relate to intra point-bar features in meandering systems. They include vertical and lateral trends due to the variation of grain size and sorting (e.g., the point-bar base, mid-

point-bar and point-bar top components, that collectively are expressed as a fining-upward trend) (Miall, 2014). Distinctive sedimentary structures that take place within each of the architectural elements are also classified within the mesoscale domain (Tyler and Findley, 1991). These are heterogeneities corresponding to lithofacies units (Fm, Fl, Sp, Gp, etc.) (Miall, 1977; 1978; 1996). Vertical and horizontal heterogeneities at mesoscale level play a significant role in reservoir performance. It is recommended that stochastic facies models have a resolution that enables incorporation of these heterogeneities (Riordan et al., 2004).






SEDIMENTARY SCALES AND HETEROGENEITIES		
MEGA	Basin Scale (>10Km)	
MACRO	Channel-belt Depositional Elements (1- 10Km)	
MESO	Bed Scale Architectural Elements (>1m - 1Km)	
	LithoFacies (0.1m - 1m)	
MICRO	Microscopic Heterogeneity (0.01-1mm)	

Figure 2.16 Scales of fluvial reservoirs.

Scales of fluvial reservoirs compared with different types of heterogeneity (Adapted from Tyler and Finley, 1991).

- Microscale.** Pore-scale heterogeneities are expressed as variability in the detrital and diagenetic mineralogy of a given rock sample and have significant impact on how petrophysical properties behave (porosity, permeability, capillarity, etc.). Microscale heterogeneities can be responsible for several orders of magnitude of variation of permeability for a given porosity (Corbett and Mousa 2010; Medici et al., 2019). An example of this is the presence of a relatively small amount of diagenetic illite occluding pore throats, which may act to markedly reduce permeability (North, 1996). Well logs and core data may reach this level of resolution (Glover, 2022; Tiab et. Al., 2003). However, in conventional models, features and heterogeneities at the microscale tend to be later upscaled, with summarised results then incorporated into later models.

2.3 Geostatistics and Applications to Fluvial Reservoirs

Geostatistics is the study of phenomena that vary in space and/or time (Deutsch, 2002). It offers a way of describing the spatial continuity of natural phenomena providing adaptation of classical regression techniques to take advantage of this continuity (Isaaks and Srivastava, 1989). This section provides a brief summary of geostatistics and its applications, with a special focus on its use for the characterisation of fluvial sedimentary systems.

Geostatistical methods were initially developed in the mining industry in the early 1950s (Krige, 1951a; Sichel, 1952), when Matheron (1960) formalised Krige's innovative concepts. Geostatistical methods began to be used extensively in the oil and gas industry in the 1970s, and in this decade the first commercial software was developed (Bluepack, Delfiner et al., 1978). However, it was not until the advent and more widespread availability of increased computing power in the late 1980s and early 1990s that the use of geostatistical techniques became widespread throughout both industry and academia (e.g., Farmer, 1988; Haldorsen and Damsleth 1990; Journel and Alabert, 1990; Deutsch, 1996; Deutsch and Journel, 1997; Holden et al., 1988). Since then, the use of geostatistics has become an essential component in the representation, assessment, and analysis of rock heterogeneities in hydrocarbon reservoir models (filling the inter-well 3D space); geostatistical methods are also used to quantitatively evaluate uncertainties (Yarus and Chambers, 1994; Caers, 2001; 2008; Cannon, 2018; Pyrcz, 2014). Geostatistics is also applied to other domains different from mining and the oil and gas industry. Hydrogeology, soil science, ecology, and epidemiology are other sciences where geostatistical methods are widely applied (Danskin et al., 1992).

There are different stages in a geostatistical analysis. Prior to the application of stochastic methods, a data analytics process of available deterministic data takes place (Pen and Gupta, 2005; Yarus, 2016). This is an important step, as deterministic data are fundamental for conditioning the outputs of geostatistical methods. However, in many industrial applications, such as in the exploitation of oil and gas reserves or in hydrogeology, spatial data corresponding to deterministic sources (e.g., well log data) are limited and often expensive to obtain. In all cases, a geomodeller will need to find an equilibrium between deterministic and probabilistic inputs to be included in a

given model (Ringrose and Bentley, 2015). However, deterministic data should always be honoured in the models and used to condition stochastic outputs. A model can be considered “data-driven” when it includes a large amount of deterministic data. On the contrary, a “concept-driven” model is mostly based on conceptual features reproduced by stochastic methods in a grid. The models presented in this study fall in the concept-driven domain, since conceptualisations of geological architectures of fluvial systems are incorporated in digital representations of reservoir rocks (e.g., training images).

Statistical analysis related to deterministic data is undertaken. For example, normalisation or truncation of values of different properties (e.g., porosity) are often required prior to the application of a geostatistical method (Ma, 2019). From this first stage a spatial continuity analysis can be also performed where trends, anisotropies or patterns related to stationarity are identified. In this stage, variograms and covariance are used to measure spatial continuity prior to their application in the geostatistical modelling phase (Isaaks and Srivastava, 1989). The second step is to define the search neighbourhood that will be used by an algorithm to gather and use control points during the population of data in the model space. The search neighbourhood, also called mask or template, can be circular (isotropic) or an ellipsoid (anisotropic) and should adapt to the spatial variations of the model (Caers, 2011).

The geostatistical modelling phase starts with the selection of an appropriate stochastic algorithm that best fits a specific case study (Caers, 2011). The choice should be made based on the model elements that are used to populate the 3D volume (Olea, 1999). There are different types of stochastic methods for facies modelling: variogram-based methods (e.g., based on two-point statistics), object-based methods and texture-based methods (based on multi-point statistics, MPS). The algorithm is then executed (run), and the grid is populated with the desired properties. A quality-check process takes place so that the user can evaluate the quality of the realisations qualitatively and quantitatively (Yarus and Chambers, 1994).

2.3.1 Stationarity

Stationary in space is observed when a given property (e.g., mean, variance, etc.) behaves consistently at all locations of the spatial domain under study.

An example of stationarity, albeit in time, may be temperature measurements taken at the same location over a period of time. Statistical measurements such as mean and variance will be constant over time. By contrast, ergodicity refers to the property of a stochastic process where the time average of a process is equal to the ensemble average over all possible realisations of the process. A gas in a container may represent well an example of ergodicity. The ensemble average of the position of the gas is equal to the long-term time average of the position of the gas particles. This means that the long-term time average of a process is equal to the average of all possible realisations of the process.

Geostatistical algorithms assume stationarity and ergodicity as a prerequisite as they consider elements as randomly and homogeneously distributed in the 3D volume by default (Deutsch and Journel, 1997; Chiles and Delfiner, 1999). This is because estimations of random variables depend on stationarity rules where the same operation can be applied/repeated in every single grid cell whose property requires estimation or simulation (Caers and Zhang 2004). However, geological processes are non-stationary by nature. An example of non-stationarity is the fining-upward trend that exists in point-bar deposits in meandering fluvial systems.

2.3.2 Variograms

A variogram is used to define the way two values are correlated in space (Deutsch, 2002). It delivers a quantitative representation of the variation in a property as a function of the distance between data points (Deutsch and Journel, 1997; Goovaerts, 1997; Kelkar and G. Perez, 2002). Variogram analysis require the data to be stationary. The variogram considers i) similarity of two values next to each other, and ii) how far apart two values need to be so that they share no relationship with each other at all (Deutsch, 2002). The variogram can be expressed numerically. However, since a geometrically measure is required, the semi-variogram form is represented in a chart where the semi-variance is usually plotted in the Y-axis against some distance classes or “lag” in the X-axis (e.g., a lag of 10 m means the calculation of the semi-variance between all pairs of data that are spaced every 10 m) (**Figure 2.17A**). The semi-variogram (γ) where the number of pairs (N) found at the distance vector (h) and conditioned by the available data of variable Z at location u is defined numerically below:

$$y(h) = \left(\frac{1}{2N}\right) \sum [Z(u) - Z(u - h)]^2$$

In the geomodelling community, in both industry and academia, the term variogram is in most cases used to talk about the semi-variogram. The plotted semi-variogram of a given sample data is also known as the experimental variogram.

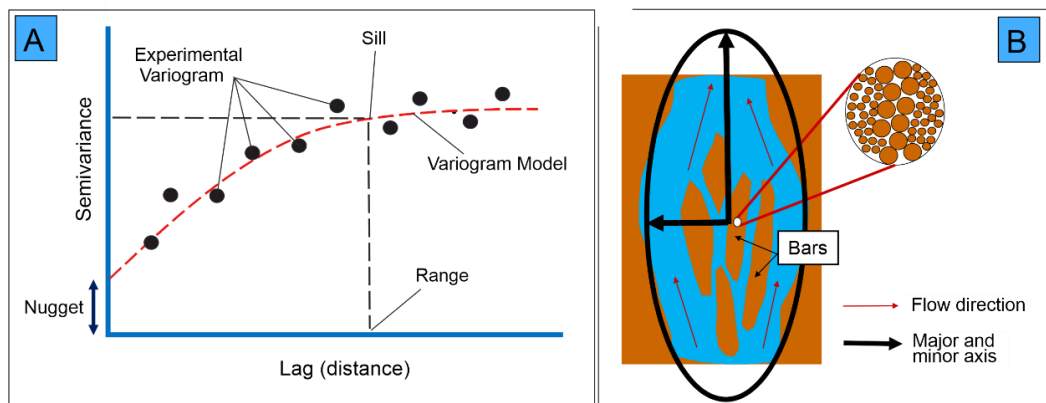


Figure 2.17 The Variogram

(A) Semivariogram where the variogram model is fitted (dashed line) to the experimental variogram. The sill, the nugget and the range are indicated. An exponential fit is selected to calibrate the experimental variogram. (B) A braided river representation with various bars of anisotropic behaviour defined by an elliptic semivariogram. A microscopic zoom to the sediment deposition also reveals an anisotropic behaviour for porosity.

The experimental variogram, also known as a sample variogram, is calculated for a sample dataset using a direction and separation distance usually defined by the indicator variogram. It contributes to find pairs of data with similar separation distances and calculating the degree of dissimilarity between the pairs. The calibration of an experimental variogram usually follows three parts: i) the determination of the orientation and direction of the variogram by the configuration of the vertical, major and minor ranges – also known as the indicator variogram (**Figure 2.17B**); ii) the calculation of the experimental variogram for each direction (vertical and horizontal); and iii) the creation of the model variogram fitted to the experimental variogram in each direction (**Figure 2.17B**). The “range”, the distance at which pairs of data have no relation with each other and the “sill”, the constant value of sampling variance reached at the “range” are also defined in this process. Different variogram

models are fitted using different standard functions ([Journel, 1993](#)). The most common are spherical, gaussian, exponential, nugget, power, and hole model. The variogram model is fitted manually by the user as a requirement ([Deutsch and Journel, 1992](#)). The semi-variogram is required for different purposes:

- Geostatistical algorithms. Certain geostatistical algorithms (e.g., SIS, SGS, etc) require a variogram input as the primary weight function during modelling. The variogram is also used as a quality control measurement for comparison before and after modelling process.
- Determination of heterogeneities in vertical directions. Definition of accurate vertical ranges are particularly important to capture facies variations in the wells. The range of a vertical variogram is a good indicator that defines the layering increment within a specific zone.
- Determination of anisotropy in the horizontal direction with respect to particular facies deposition.

Sometimes a property may exhibit different variogram ranges in different directions. In this case the spatial correlation is anisotropic (e.g., porosity has high correlation ranges in the direction of bar depositions and low correlation ranges perpendicular to them) (**Figure 2.17B**) ([Deutsch and Wang, 1996](#)). On the contrary, when the mean value of a property changes from one location to another following a specific pattern, a trend exists (e.g., vertical changes of porosities related with fining-upward sequences in a point-bar).

Anisotropic variograms and the input of trends are usually required for fluvial modelling to manipulate the intrinsic complexity derived from different scales of heterogeneities (**section 2.2.1**) ([Rojas et al., 2012](#); [Honarkhah & Caers, 2010](#)). This is the case for braided rivers where an anisotropic orientation is found in the deposition of bars (mesoscale level of heterogeneity) and also in the texture of the rocks (microscale level of heterogeneity) (**Figure 2.17B**). However, in the case of meandering systems where the orientation of high-sinuosity channels leads to the deposition of seemingly randomly distributed sandy deposits in multiple directions, an isotropic configuration of the experimental indicator variogram may yield more realistic results ([Pyrzcz et al., 2008](#)). This is the reason why variogram-based stochastic algorithms tend not to be well suited to fluvial facies models.

2.3.3 Variogram-based Modelling

Variogram-based approaches are a type of pixel-based modelling method that populates data in the grid according to a cell-by-cell routine, and which are constrained using two-points statistics (Cressie, 1993). There are different stochastic algorithms that apply variogram models. The first developed method was deterministic kriging applied to continuous variables (Matheron, 1963). However, a simulation algorithm underpinned by kriging called Sequential Indicator Simulation (SIS) is now widely used for reservoir modelling. SIS uses indicator kriging to generate conditional distribution functions describing the likelihood of occurrence of facies in a certain cell, which are then sampled with a Montecarlo algorithm to assign a specific facies type stochastically (Journel and Alabert, 1990).

Geomodellers commonly rely on pixel-oriented facies-modelling tools based on two-point statistics, which are constrained on indicator variogram models that describe the spatial continuity of the modelling categories ('facies') (Pyrz and Deutsch, 2002). However, limitations of variogram-based methods applied to fluvial deposits are important. Discrete shapes and well-defined geometries (e.g., meandering channel loops) associated with channel features are not reproduced by these methods. This is because the variogram is merely a measure of continuity, and does not capture significant geological characteristics, such as shape, facies transitions and connectivity (Caers and Zhang, 2004). This is especially problematic, for example, when modelling sinuous channelised bodies. Therefore, it is recommended not to use this type of method to model the architecture of fluvial systems (Ringrose, 2015).

Variogram-based stochastic methods are also use for property modelling. The variant Sequential Gaussian Simulation (SGS) is most widely used for modelling continuous petrophysical properties (Wackernage, 2003).

2.3.4 Object-based Modelling

This type of approach populates discrete Boolean objects or bodies (ellipsoids, crescents, channels, etc) in a 3D volume of defined background (Holden et al., 1998; Bridge and Leeder, 1979; Haldorsen and Damsleth, 1990; more, 1991). The bodies are placed in the space randomly filling the inter-well volume until specified proportions or object numbers are reached

(Alabert and Massonnat, 1990). Well data are used to constrain the model. Most object-based algorithms assume stationarity; the geometries of the bodies are defined prior to the simulation. Inputs for the definition of the bodies may come from different sources. As an example, channel bodies can be defined based on analogue data where information regarding thickness, width or length of the channels can be found (Colombera et al., 2012).

Object-based algorithms are also popular within the geomodelling community to model fluvial facies. They successfully render the complex geometries of geobodies that are common in fluvial, deltaic and turbiditic successions. However, this approach suffers from various limitations related to the control of the morphologies of channelised units leading to the population of non-realistic features in the inter-well areas (Journel and Alabert, 1990). For example, where channels are funnelled in certain areas, the algorithm may struggle to honour well data (Pickup et al., 1994). This is especially problematic in cases where data are heavily distributed, as in the case of dense well arrays where it may be difficult or impossible to condition the models to subsurface data (Ringrose and Bentley, 2015). In this situation the discrete continuous shapes produced by the algorithms may bear little resemblance with the real geometry of certain elements (Srivastava, 1994).

2.3.5 Texture-based Modelling

Texture-based methods are more recent than object-based and variogram-based methods. First attempts at using stochastic methods based on multipoint statistics (MPS) in the geosciences were made by Farmer (1988) using Markov Chain Monte Carlo methods (MCMC), followed by Caers and Journel (1988), Deutsch (1992) and Xu (1996). However, it was Guardiano and Srivastava (1993) who proposed a direct (non-iterative) algorithm for stochastic MPS modelling. Initial incarnations of MPS modelling algorithms were highly demanding on CPU time, and this issue significantly limited the use of the method. However, Strebelle and Journel (2000) implemented the efficient SNESIM (Single Normal Equation SIMulation) algorithm, which made the approach become practical by significantly decreasing CPU demand. Many other MPS algorithms have been created since; examples include IMPALA (Straubhaar et al., 2013) and DEESSE (Mariethoz et al., 2010). In this project, both SNESIM and DEESSE are used in the devised modelling workflows presented in Chapter 3. MPS methods, which are also considered

another type of pixel-based methods, capture textures by considering more than two points (cells) simultaneously, allowing the reproduction of complex, non-linear spatial correlation (Strabelle and Journel, 2001).

The most important input by MPS algorithms is the so-called 'training image', which can be defined as a 2D or 3D cellular model that includes a digital representation of the reservoir interval that is going to be modelled (Pyrzcz et al., 2008). The algorithm will scan the training image to draw patterns that can be replicated in the simulation grid. Once statistical patterns are acquired from the training image, MPS assigns conditional probability distributions using a geometric template including random variables referring to different positions of specific elements contained in the training image (Strebelle, 2000). The simulation grid is then populated according to the likelihood of a particular cell having a particular model content, previously identified in the training image.

Overall, the MPS approach combines the strengths of other pixel-based methods (e.g., perfect conditioning to subsurface data) and of object-based methods (e.g., the ability to reproduce complex geological shapes) (Guardiano and Srivastava, 1993; Liu et al., 2005), making them generally better suited for modelling fluvial systems with sinuous channel fills and belts, in comparison to other methods. However, MPS simulation methods are not currently as popular as object- and variogram-based methods, among geomodellers. Numerous authors have pointed out important limitations when attempting the creation of MPS models. One of the most important drawbacks refers to the tedious and time-consuming process related to the parametrisation process where training images are coupled with MPS code requirements (de Vries et al., 2009; Pyrcz et al., 2008; Strebelle, 2000; 2001; 2002; Riou and Hocker, 2015). The construction of training images requires also additional work prior to model building (Maharaja, 2008).

2.3.5.1 Training Images and Stationarity

The training image is a numerical description of the perceived geological heterogeneity, which should match the conceptual model of the type of heterogeneities present in the reservoir under investigation (Journel and Zhang, 2006). The training image will describe geometries, proportions, spatial structures, connectivity and other geological features of a reservoir. It should be an idealised and simplified representation of the most important

patterns that need to be represented in the model and, importantly, it should be compatible with the type of MPS algorithm that will be used (Strebelle, 2000; 2002). The training image replaces the variogram (a description of two-point statistics) reflecting the variability of different points in the space separated by a vector “h”, independent of the specific location “u”. Repeated patterns of heterogeneity, shape of the geobodies and facies relationships are obtained by the MPS algorithms by scanning the training image (Pyrz et al., 2008). The conditional probabilities for each cell are taken from the training image based on the data available in the surrounding of the cell being modelled at each step (Wang et al., 2019). However, similar to two-point statistical methods, MPS algorithms work better when the training image includes certain levels of stationarity and ergodicity. To meet the assumption of stationarity, training images must have the following attributes:

- Spatial patterns should be reasonably homogeneous and consistent over the entire training image (Caers and Zhang, 2004; Maharaja, 2008).
- Patterns should be repeated in a form whereby the algorithm is able to capture sufficient information to enable replication. The simulation quality will be dependent directly on the form of the training image. The more explicit the repeatability of a pattern within a training image, the greater the chance of pattern recognition (Meerschman et al., 2013).
- Sedimentological features in the form of facies units and their properties should ideally not be confined to specific locations within parts of a training image but should instead be distributed throughout the training image grid (Caers and Zhang 2004).

Dealing with geological non-stationarity is one of the main issues faced by geomodellers who employ MPS methods for facies modelling. Since most geological processes in nature result in non-stationary patterns in the distribution of geological features, the creation and application of suitable training images is one of the main factors limiting the uptake of MPS modelling algorithms for purposes of subsurface modelling. This is due to the depositional facies patterns resulting from geological processes that are often location-specific, tend to vary in space and are non-repetitive (Journel and Zhang, 2006; de Vries et al., 2009). Therefore, complex non-stationary

geological trends (vertical and horizontal) are not directly reproducible in the resulting reservoir models using MPS algorithms (Comunian et al., 2013; Chugunova and Hu 2008; Huysmans and Dassargues 2010; Le Coz et al., 2011). However, to enable the reproduction of realistic stratigraphic architectures, MPS modelling inputs include various types of secondary data (auxiliary variables) that can be employed to reproduce spatial trends (Remy et al., 2009; Straubhaar et al., 2011).

Training images can be built using stochastic algorithms (variogram-based and object-based), using analogue data (e.g., satellite images of modern rivers), a sketch representing different features, or a combination of analogue data and forward stratigraphical model outputs, as is proposed and demonstrated by this research. In all these cases, the training images need to be suitable for use in the different MPS codes, meaning that they will also need to be stationary. The construction of training images can therefore also be time consuming in itself.

2.4 MPS Simulations

Facies models based on Multipoint Statistics have been built in this study. The algorithms used were SNESIIM (Strebelle 2002) and DEESE (Mariethoz et al., 2010). SNESIM was run in SGeMS v2.5b; DEESSE was run from a command prompt and resulting realisations were visualised in SGeMS. SNESIM is an MPS modelling code included in multiple geoscience software packages used in the oil and gas industry (e.g., Petrel®). DEESSE is a code developed by the University of Neuchatel (Switzerland) made available via an academic licence to the University of Leeds. The code was run using the ASCII driver file and using the command prompt in Windows. The next two sections describe the functioning of the two codes and offer a comparison.

2.4.1 SNESIM

SNESIM (Single Normal Equation SIMulation) (Strebelle, 2002) works in two different phases: i) training image scanning phase and ii) grid simulation phase. During the scanning phase the training image is scanned using a search mask (size and shape defined manually by the user), resulting in a search tree that stores the statistical information that is required for the

simulation phase (conditional probability of the occurrence [cdf] of a pattern). Extracted patterns from the scanning process are analysed for replicates and the determination of the cumulative distribution function (cdf) of the central pattern (random variable X) is calculated. The SNESIM code, contrary to its predecessors, runs the scanning process in a CPU/RAM efficient manner making the SNESIM algorithm several orders of magnitude faster than previous attempts that require the training image to be re-scanned every time a modelling-grid cell is visited. The simulation phase in SNESIM starts assigning the conditional or hard data to the grid. Then the population of the grid cells starts from a preselected seed number that initiates a random path. Then, the search mask or template will be used now to scan the patterns in the training image nodes to find matching replicates of the patterns that have been previously recognised and stored. Finally, a category that matches the previously defined surrounding nodes is found and the corresponding mode is assigned that category. SNESIM needs the following inputs.

- Number of Facies and Proportions

The numbers of facies in the training images have a significant impact in the computational time used by the algorithm. Proportions of the different facies included in the training images are also a requirement to be input (fraction). This proportions refers to the percentage (or fraction) of each facies that are included in the training images. In SNESIM, the “servosystem” parameter controls the matching between original facies proportions and the simulation proportions.

- Number of Informed Nodes (N)

The number of nodes is intimately related to the configuration of the search mask/template. The greater the number of informed nodes, the greater the number of cells that will be used during the scanning and simulation phases.

- Search Mask

The training image need to be scanned in order to obtain patterns from which the algorithm will work in the simulation process. The scanning process take place by the application of a search mask or template. The Search Mask is a geometrical template that is defined as a set of cells with a defined centre, which can have an elliptical, circular, or rectangular shape. It is defined by the x , y and z axis, an angle for each of the axis (a_1 , a_2 , a_3) and by its azimuths, strike, and rake. The selection of the appropriate shape and radius is a crucial stage at multi-point statistic. It will be the criteria to find out the frequency of

instances of a model element (facies) occurring next to similar and different elements.

- Multigrids and Subgrids

Multigrids and subgrids are used in the SNESIM algorithm to configure the search mask to store the conditional probability within the template in a more efficient way. The purpose is to capture large-scale structures using a relatively small search mask with relatively small number of nodes, which can be more CPU efficient. The bigger the multigrid size the less nodes are considered in a particular grid.

- Number of Replicates

Before categories are populated in the simulation grid, SNESIM tries to locate equal conditioning data events in the search tree with those that the search mask is scanning. A particular number of data events need to be recognised to enable continuation of the population of facies/category. This is controlled by the “number of replicates” parameter. On some occasions, the algorithm may not be able to find enough replicates in the search tree to compute a conditional probability. In this case, the algorithm will define a smaller data event by dropping the furthest away informed node and repeat the search until those replicates are found.

- Auxiliary Variable Maps: TAU Models

The application based on TAU models remains a practical solution for the application of auxiliary variables in the SNESIM code ([Journel, 2002](#)). The probability of A jointly conditioned on B and C becomes a function of the marginal probability of A and the two probabilities of A separately conditioned on B and on C. This function depends on a parameter “ τ ” that measures the degree of redundancy between events B and C with respect to event A ([Krishnan et al., 2005](#)).

$$P(A|B, C) = f_{\tau}[P(A), P(A|B), P(A|C)]$$

Probability maps, as a type of soft data (which may be based on seismic attributes), are grids of continuous properties which apply to a domain where the soft probability is a relative weighting of the influence of the simulated probability against any soft probability input. Generally, the higher the TAU2

values (relative to the TAU1 values), the greater the influence of the soft probability data in the simulations.

2.4.2 DEESE

DEESSE ([Mariethoz et al., 2010](#)) also known as “Direct Sampling” is the other MPS algorithm used in this research. The code addresses technical difficulties and runtime cost associated with computing the conditional cdf one cell at a time. Reduction in simulation runtime is achieved mainly through the ability to scan the training image while simultaneously populating the simulation grid and thanks to CPU parallelisation (up to 4 cores). The direct scanning-simulation process means that no search tree is created to store the training image probabilities. The probability of training image values is stored in a catalogue prior to simulations. DEESSE scans the training image based on a search window or search neighbourhood of size defined by the user and the lag vectors in the simulation grid and starting from a random location, the training image is scanned for the specific lag vectors and the specific search window until a data event is matched building the cdf. Simultaneously, the population of the simulation grid starts from closest nodes to the included conditional data (hard data). If conditional data are not present a random or unilateral path is defined in the simulation grid controlled by a preselected seed number. Afterwards, the population of the simulation grid proceeds at the closest node already informed in the grid.

DEESSE also includes a recursive syn-processing algorithm to enhance the quality of the pattern reproductions in the simulations. Once a data event is matched, a mismatching distant event is run on the training image and the simulation grid with three different outcomes. I) If the data event is smaller than a specific distance threshold “t”, the value at the central node is pasted to “x” (the unknown location in the grid). li) If the distance threshold “t” is the smaller measured to that point, this information is stored. lii) If after running several iterations, no data event is found for the predetermined threshold distance “t” value, the lowest distance is assigned as informed value. These steps represent a significant difference with SNESIM, as DEESSE does not drop successive data points from the data event when a specific data event is not found. The distant threshold “t” helps reduce computation time. Finally, for each “x” or unknown location in a grid, a simulated value is drawn from a

cumulative distribution “ f ” conditioned to a local data event. Inputs include the following.

- Number of Facies and Proportions

Similar to SNESIM, the numbers of facies and their proportions included in the training images are required as input to DEESSE.

- Number of Informed Nodes (N)

“N” is defined as the number of nodes or neighbours that are closest to the central point “x” (data event) within the defined search area. It is strictly related to the search neighbourhood parameters. Commonly, the higher the n, the more nodes the algorithm will count to calculate the cdf and more accurate will be the calculations (until a threshold is reach and no more improvements are found in the realisations).

- Search Neighbourhood

A search mask similar to SNESIM will be defined selecting an appropriate search radius, anisotropy values and angles. The mask defines the search radius associated with the maximum search distance and it is one of the most important parameters to fit. The size of the radius will depend on the number of nodes (N) included in the simulation. Differently from SNESIM, the shape of the data event and the size of the search window can be modified at each simulated node (original search window size different from the actual search window size). Therefore, the data events are always adapted to the simulation path. However, the size of the data event is limited by the size of the training image and is controlled by a specific number of nodes given by the radius.

- Distant Threshold (t or DT)

A particular training image pattern matching a specific data event needs to be assigned. The distant threshold “t” plays a fundamental role defining distances from a data event called “x” (the unknown location in the grid). Similar to the number of replicates in SNESIM, the distance threshold in DEESSE plays a fundamental role for the recognition of previously identified data events. Starting from a random location, the training image is scanned for the specific lag vectors and the specific search window until the data event is matched. If the data event is smaller than a specific distance threshold, the value at the central node is incorporated in the simulation grid. If a specific is pattern is recognised at a given distance and that distance is the smaller measured so far, this particular information is stored; if after running several iterations no

data event is found for the predetermined threshold value, the lowest distance is assigned as informed value.

- Scanning Fraction (F)

“F” refers to the maximum scanning fractions performed on the training image. It describes the maximum fraction of training image to be scanned. Ranges from “0” (no scan) to “1” (scan full training image). If the scanning fraction is set to “1” and still no pattern with a distant smaller than “t” is found, the pattern located in the node scanned from the training image with the lowest distance is pasted at the location x.

- Auxiliary Variable Maps (Supported Radius-SR, Actual Supported Radius-RA)

The algorithm will randomly select a location “x” in the simulation grid and it will compare that specific data event with the patterns in the training images, the previously populated categories in the simulation grid and the probabilities stored in the auxiliary map. A supported radius (SR) will be used to identify patterns in the nodes that have been previously informed (N). If within the “SR” there are more informed nodes than the number “N”, the nodes closest to “x” will be the ones that will be populated in the realisations. At the beginning of the simulation when no “n” has been informed the algorithm populates facies that have been recognised straight from the training image conditioned from the probabilities in the probability map. At this stage the supported radius (SR) is equal to the actual supported radius (RA), However, at the end of the simulation when most of the simulation grid is populated with informed nodes, the actual search radius “RA” is less than “SR”. Then, at this moment if the “RA” < “t” (Deactivation threshold radius), the probability constraint mechanism is stopped. The support radius will be used to identify pattern and matching facies proportions from the training image and to reduce noise.

2.5 Carbon Capture and Storage Applications

Carbon sequestration projects are increasingly recognised by the international community as a solution for controlling and reducing the concentration of anthropogenic carbon dioxide (CO₂) in the atmosphere. According to the U.S. Energy Information Administration (2021), most CO₂ emissions come from fossil fuel combustion. Burning of fossil fuels is estimated to account for 73% of total greenhouse gas emissions and for 92% of total U.S. anthropogenic

CO₂ emissions. In domestic terms, the UK used a total of almost 170 million tonnes of oil equivalent (Mtoe) of energy in 2020, with the majority of this (78%) coming from fossil fuels (heating and electricity production activities) ([Office for National Statistics, 2023](#)). As an outcome of the Paris Agreement ([UNFCCC, 2022](#)), 194 countries showed commitment with their Nationally Determined Contributions (NDC) to implement new low-carbon technologies, and Carbon Capture and Storage (CCS) practices were mentioned among the most important mitigation pathways. Many CCS projects currently exist around the world (e.g., Big Sky in Montana, USA; Sleipner, Norway; the Southwest Hub project, Australia) and large-scale efforts are currently underway in many other countries including China, the largest CO₂ emitting country in the world (e.g., the Ordos basin project) ([Global CCS institute, 2020](#)).

The concept is simple: separation of CO₂ from the emissions of industrial processes prior to its release into the atmosphere and its storage permanently within underground geological formations ([Larsen et al., 2003](#)). This process allows industrial processes to continue to operate whilst emitting fewer greenhouse gases to the atmosphere. However, the process of capturing, transporting and storing CO₂ must be done safely, and in a way that is environmentally sustainable and economically viable. Many energy companies are dedicating substantial resources to develop programmes of underground storage of CO₂ (CCS).

For a CCS project to be successful, an underground carbon storage complex should provide the following. i) Sufficient space (volume) to store compressed CO₂ in a way that is economically viable. ii) Capability to sustain specific injection rates (directly related with the permeability of the formation and connectivity of porous volumes). iii) Ability to sustain and confine CO₂ safely without leaking to overlying formations (topseal integrity) but also to preserve wellbore stability ([Espinoza, 2017](#)). iv) Capacity to inject at a sufficient depth where the CO₂ can exist as a supercritical fluid. Supercritical CO₂ is stable at a temperature higher than 31.1°C (88°F) and pressures of 72.9 atm (about 1,057 psi) ([Ambrose et al., 2008](#)) (**Figure 2.18**). Supercritical CO₂ has characteristics that are intermediate to those of liquids and gases: it is as dense as a brine but with the viscosity of a gas. Supercriticality delivers significant advantages in terms of storing CO₂ as required storage volume is

significantly less than if the CO₂ were at “standard” surface conditions (Alcalde et al., 2018; 2019).

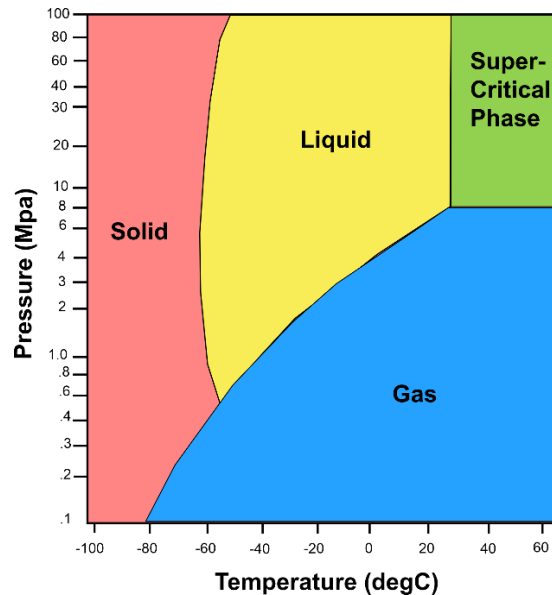


Figure 2.18 CO₂ phase diagram.

Solid, liquid, gas and supercritical phases with respect temperature and pressure. Modified from Voormeij and Simandl (2003).

Several important mechanisms act to trap CO₂ in the subsurface. i) Structural or stratigraphic trapping of CO₂ in the reservoir rock. This is the most important trapping mechanism in terms of volume of CO₂ stored and depends on the structures and heterogeneities of the reservoir rock (Iglauer, 2018). ii) Solubility trapping volumes of CO₂ that can be assimilated by the reservoir brine within the pore space (Riaz et al., 2014). iii) Residual trapping where CO₂ stays confined in pore spaces between rock grains (Gershenzon, et al., 2016). iv) Mineral trapping due to the chemical reactions of CO₂ with minerals in the reservoir rock. The latter process may involve the previously dissolved CO₂ in brine, weak carbonic acid (H₂CO₃) and eventually bicarbonate (HCO₃⁻) that will precipitate to permanently sequester that portion of the injected CO₂ (Al-Khdheawi et al., 2017a and b).

Different types of reservoir rocks have been identified as suitable for carbon storage. For instance, the U.S. Department of Energy (DOE) includes five types of geological formations: saline aquifers, oil and gas reservoirs,

unmineable coal seams, organic-rich shales and basalts (Kumar et al., 2017). In this study, the scenario of a depleted gas storage is examined. The oil and gas extracted from the reservoir rock leaves a permeable and porous volume that can potentially be filled with CO₂. Furthermore, such reservoir volumes are a proven record of geological storage as they previously contained hydrocarbons over geological timescales (Spiteri et al., 2005; Bennion and Bachu 2006). Selecting already depleted oil or gas reservoirs also offers an advantage in terms of gathered knowledge throughout many years of production. Data on reservoir properties, final well reports, interpretative data records, production data, and even reservoir models may already exist. This may mean that no (or only modest) additional data acquisition is required, and infrastructures and facilities already in place may be converted for re-use. In addition, locations of depleted oil and gas reservoirs are already known, so no exploration phase is required.

Similar to conventional reservoir management routines, accurate understanding of reservoir rocks in which to store CO₂ is required. Skills and practices associated with the investigation of conventional hydrocarbon reservoirs can be transferred. However, it is also clear that new learnings with respect to differences in fluid properties and flow processes of CO₂ through reservoir rocks are still needed. Reservoir modelling will play a significant role in the quantification of volumetrics, injection rates, integrity, and CO₂ supercriticality and injected-plume behaviour (Bachu et al., 2007; Budinis et al., 2018).

Robust facies models built using appropriate modelling algorithms, and incorporating detailed characterisation of sedimentary architecture and heterogeneity are important for modelling the behaviour of a CO₂ plume in the subsurface and for ensuring the success of CO₂ storage projects (Soltanian et al., 2016; Nguyen et al., 2017; Eiken et al., 2011; Dai et al., 2014; Stalker et al., 2014; Singh et al., 2010). This is because facies geometries and distributions may affect the behaviour and shape of CO₂ plumes more than other factors, such as pressure conditions at the wellbore location (Nguyen et al., 2017; Flett et al., 2007). Special attention should be given to issues of stratigraphic compartmentalisation, which may influence the lateral propagation of injected CO₂. Furthermore, reservoir properties and relative permeability curves for different rock types have been observed to significantly impact CO₂ plume dynamics (Nguyen et al., 2017; Juanes et al., 2006). It is

therefore a fundamental requirement to “feed” accurate permeability values to dynamic models and to select suitable relative permeability functions that best represent a given rock type ([Spiteri et al., 2005](#); [Flett et al., 2004](#)).

3. A Workflow for Modelling Fluvial Meander-belt Successions: Combining Forward Stratigraphic Modelling and Multi-Point Geostatistics

3.1 Introduction

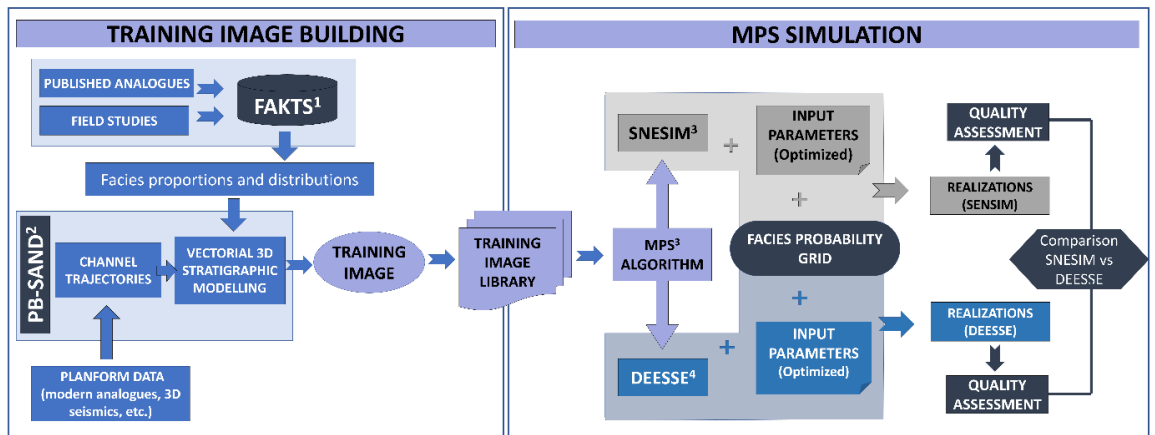
Static models depicting the sedimentary architecture of subsurface successions are required to visualise the possible distribution of different properties associated with the rock volume being characterised (Ringrose and Bentley, 2015) (section 2.1.6). Facies models are used to display the distribution and the geometry of rock types and constitute the framework on which petrophysical parameters are populated in a digital three-dimensional grid (Caers, 2005; Cannon, 2018; Honarkhah et al., 2010). Facies models simplify lithological heterogeneity, but nevertheless provide a reasonable framework with which to model flow properties (Harding et al., 2004; Walker et al., 1979). To address the considerable uncertainty regarding properties of the bulk reservoir volume, including uncertainty associated with geological heterogeneities at multiple scales, stochastic modelling methods are routinely employed (Ma, 2019; Caers, 2001).

Since the 1980s, geomodellers have relied preferentially on variogram- and object-based methods to model different depositional environments, using indicator variograms and Boolean objects, respectively (Guardiano and Srivastava, 1993). However, techniques based on two-point statistics are not especially effective at capturing and reproducing complex geological patterns, such as curvilinear shapes (Journel, 1993; Strebelle, 2000; Strebelle and Journel, 2001). By contrast, object-based methods do permit the reproduction of bodies with complex shapes, but commonly are unable to honour conditioning well data, particularly for densely drilled reservoirs (Deutsch et al., 1996). Techniques based on multi-point statistics (MPS) allow reproduction of complex geological patterns while simultaneously honouring well data, but require suitable and realistic training images to be used as simplified digital representations of the heterogeneities of a reservoir rock (Strebelle and Journel, 2001) (section 2.3.5). A library of suitable training images should, ideally, incorporate stationary features, e.g., patterns that are homogeneous, repeated and not confined to specific locations in the grid (section 2.3.1). However, the geological bodies that training images seek to model are inherently non-stationary, because the properties of rock types are variable in space (Caers and Zhang, 2004). To enable the reproduction of

geological non-stationarity through the application of stationary training images, MPS modelling algorithms employ auxiliary variables that describe how geological properties should vary in space; this permits the incorporation of geological trends in the modelling grids (**section 2.4**) (Chuginova et al., 2008).

A workflow that incorporates an MPS approach, a library of training images constructed using analogue data and forward stratigraphic modelling and the use of auxiliary variable maps has here been developed to support the construction of facies models for a common type of hydrocarbon reservoirs: high-sinuosity meandering fluvial successions (**Figure 3.1**). These facies models incorporate geological features that are commonly difficult to reproduce with traditional subsurface modelling workflows. The application of training images has been optimised for two MPS algorithms: SNESIM (Strebelle, 2002) and DEESSE (Mariethoz et al., 2010); these algorithms are adopted in this work because they are widely used in the hydrocarbon industry, thanks to their availability in commercial software (**section 2.4.1** and **2.4.2** respectively). For the construction of the training images, a stratigraphic forward modelling approach to simulating geological complexity in meandering fluvial systems and their accumulated successions has been employed (Yan et al., 2017), constrained with data from a wide range of known geological analogues (Colombera et al., 2012a; b).

The aim of this chapter is to develop and employ a workflow for the generation of unconditional reservoir models that capture the complex lithological heterogeneity inherent in meandering fluvial reservoir successions at multiple scales. Primary research objectives of this chapter are as follows: i) creation of a library of training images that incorporate the main sedimentological and stratigraphic features of meandering fluvial systems and their accumulated deposits; ii) demonstration of how the training images included in the library can be constrained in terms of their geological realism through the use of data from many known examples stored in a relational database, and of how suitable examples can be selected from the library according to the specifications of different geomodelling cases; iii) development of an efficient modelling workflow whereby appropriate training images are selected from the library and used to undertake MPS-based simulations.



1: FAKTS: Colombera et al. 2012a, b; 2: PB-SAND: Yan et al. (2017); 3: SNESIM: Strebelle and Journel (2000); 4: DEESSE: Mariethoz et al. (2010)

Figure 3.1 Simulation Workflow.

Workflow describing the process for building a training-image library for MPS facies simulations and its application to two different MPS algorithms. The workflow consists of two stages: i) the creation of training images and ii) their application to SNESIM (Single Normal Equation Simulation) and DEESSE (DS, Direct Sampling) (Strebelle, 2002; Mariethoz et al., 2010). The left-hand side of the workflow demonstrates how the training images are built through a novel approach for the synthesis of geological knowledge of the sedimentary architecture of successions deposited by meandering fluvial systems, by using a forward stratigraphic model (PB-SAND) (Yan et al., 2017) constrained using analogue data from a sedimentological database (FAKTS) (Colombera et al., 2012a, b). The box on the right-hand side summarises the application of the training images for MPS modelling, as undertaken in this work, utilising input parameters and facies-probability grids that are optimised for the reproduction of features of reservoir architecture typical of meandering fluvial systems. As part of this work, assessment of algorithm outputs and comparisons between realisations of SNESIM and DEESSE are also undertaken.

3.2 Sedimentary Heterogeneities in the Deposits of Meandering River Systems.

Different sedimentary heterogeneities applied to meandering fluvial facies models have been attempted to model in these studies. The most important patterns that a geomodeller will expect to observe at a range of spatial scales (macroscale and mesoscale; section 2.2.1) are:

- Stratigraphic architecture determined by the distribution of channel-belt and floodplain deposits.

- Internal architecture of channel-belts determined by the distribution of channel-fill and point-bar deposits.
- Intra-bar variations in the relative proportion of sand and mud, vertically and horizontally. Such lithological heterogeneities have long been recognised in the deposits of meandering rivers (Jackson, 1976). From an applied perspective, such lithological heterogeneities are important because they affect fluid-flow behaviour over a range of scales (Corbett et al., 2012; Hovadik and Larue, 2007).

Some common examples of complex sedimentary architectures that give rise to the configuration and the lithological heterogeneity in the deposits of meandering fluvial systems are depicted in **Figure 3.2**; their origins and form are summarised below.

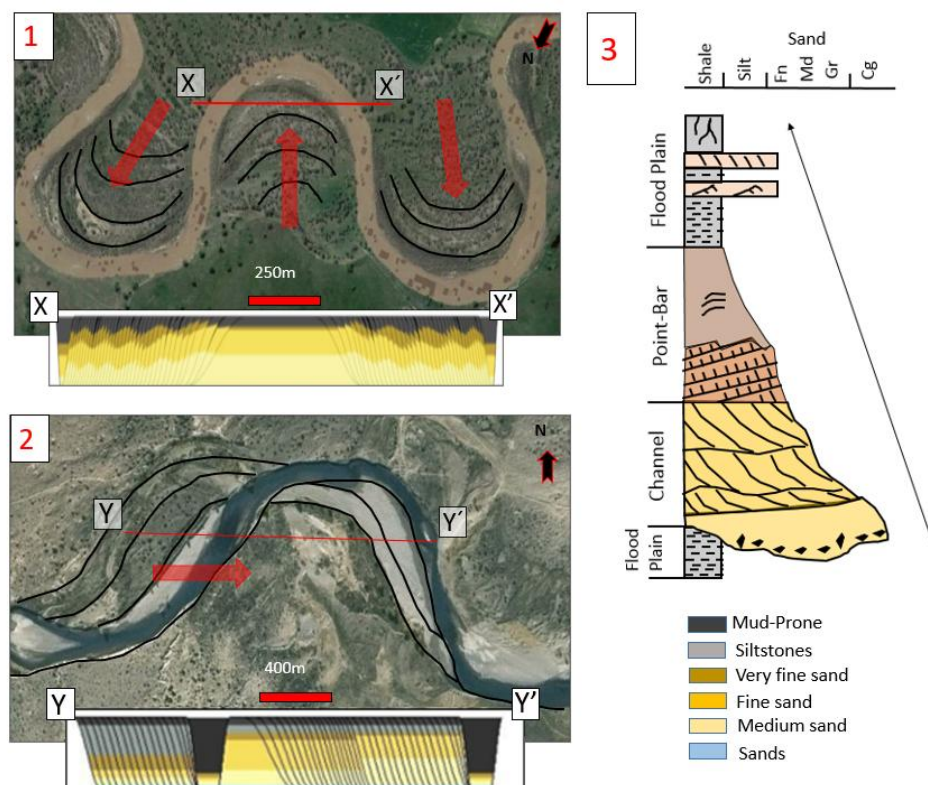


Figure 3.2 Expansion and translation processes (point bars)

Two examples of point bars and their deposits associated with meanders undergoing expansion and translation processes. 1-expansion (Powder River, US ($45^{\circ}19'34.43''\text{N}$ - $105^{\circ}31'43.43''\text{W}$) and 2-translation (Chubut River, Argentina ($42^{\circ}31'26.33''\text{S}$ - $70^{\circ}32'53.24''\text{W}$)). Cross-sections resulting from PB-SAND forward stratigraphic model runs (X-X' and Y-Y') show accreted deposits with typical fining-upward trends (3). Red arrows indicate the accretion trajectory of point bars associated with the different types of meander transformations.

- The migration of river channels over time results in erosion of sediments from the outer bank and sedimentation occurring via accretion on the inner bank. The gradual lateral accretion of successive units forms a point bar on the inner part of a developing meander loop. In sand-rich fluvial systems, resultant accumulated lateral-accretion architectural elements commonly form volumetrically significant sand-bodies with good reservoir potential composed internally of a coset of lateral-accretion units. Each lateral-accretion unit may be separated from its neighbouring unit within the overall point-bar element by thin lower-permeability beds. Commonly, such beds take the form of drapes on successive bar-front surfaces, which themselves accumulate during episodes of reduced flow in the aftermath of flood events ([Miall, 2016](#)).
- Some lateral-accretion units are characterised by 'inclined heterolithic stratification' (IHS), a term introduced to describe shallow-dipping heterogeneous point-bar deposits whose strata show original depositional dip ([Thomas et al., 1987](#)). Muddy IHS, in either fluvial or tidally influenced channels, may represent baffles that can hinder or impede fluid flow in otherwise sand-prone point-bar deposits ([Hubbard, 2011](#)).
- Different styles of baffling can be developed within a laterally accreting point-bar element. The distribution of intra-bar-scale heterogeneities is dependent, in part, on the growth mechanisms of the point bars and on the trajectories of the formative meanders. For example, unlike meanders undergoing simple expansion (e.g., lateral growth), translating (e.g., downstream migrating) meanders are characterised by areas where deposition takes place on concave banks, leading to the deposition of mud-prone counter-point-bar deposits ([Ielpi and Ghinassi, 2014](#); [Nanson and Page, 1983](#)).
- High-sinuosity fluvial-channel deposits commonly display fining-upward sequences in which the coarsest-grained sediment accumulations are deposited in the lower portions of point-bar units. These results from energy dissipation associated with the helical flow in the channel ([Miall, 2016](#)). Moreover, sediments forming point-bar deposits also commonly display a trend of downstream decrease in

grain size, especially downstream of a meander-bend apex, in relation to changes in flow direction around the bend (Bluck, 1971 and Wood 1989).

These commonly occurring types of lithological heterogeneity give rise to different forms and degrees of non-stationarity, which need to be accounted for i) in training images that seek to depict the range of architectural styles common in point-bar deposits associated with meandering-river succession, ii) by means of auxiliary variable maps (trends) intended to enable effective training-image application, and iii) in resulting MPS models (de Vries et al., 2009).

3.2 Methodology

A workflow has been developed for the creation of training images and their application to MPS simulations. A detailed explanation of the steps undertaken for building the training images is provided. Six different training images are then utilised to demonstrate their use in MPS simulations with SNESIM and DEESSE, making use of auxiliary variables to achieve the desired trends in facies distribution and orientation.

To construct training images that include fundamental features of the facies architecture of fluvial point bars and meander belts, a workflow has been established (**Figure 3.3**) whereby a forward stratigraphic model of meander-belt sedimentary architectures (Point-Bar Stratigraphic Architecture Numerical Deduction; PB-SAND; Yan et al., 2017; 2019; 2020) has been informed by sedimentological data drawn from a relational database (Fluvial Architecture Knowledge Transfer System; FAKTS; Colombera et al., 2012a; 2012b; 2013; 2017). The joint application of PB-SAND and FAKTS allows reproduction of the sedimentological features of interest in this particular study. Of note, training images have been created that embody different styles of sedimentary architecture that are common in high-sinuosity fluvial environments, associated with different modes of meander transformation. Utilising this workflow, a training-image library has been created that includes different training images representing idealised stratigraphic architectures applicable to different modelling scenarios.

3.2.1 PB-SAND

The Point-Bar Sedimentary Architecture Numerical Deduction (PB-SAND), coded in Matlab and C#, is a forward stratigraphic model designed to reconstruct and predict the complex spatial-temporal evolution of a variety of meandering river behaviours. The software simulates the complex spatio-temporal migratory evolution of fluvial meanders, their generated bar forms and the associated lithofacies distributions that accumulate as heterogeneous fluvial successions (Yan et al., 2017). PB-SAND can be applied to explore and gain improved understanding of relationships between evolutionary channel trajectories and preserved lithofacies distributions, allowing reproduction of the stratigraphic heterogeneity of meandering fluvial systems at different temporal and spatial scales and in three spatial dimensions.

Based on time-lapse plan-view trajectories of channel courses (e.g., as captured from satellite images, **Figure 3.3** and **Figure 3.4**) PB-SAND can reconstruct the channel-belt sedimentary architectures that arise from the complex spatio-temporal evolution of meandering rivers. Facies characteristics in the modelled architectures reflect the type of meander-bend transformation, the channel sinuosity, the stream-wise distance away from meander apices, and the position of inflection points of a meander loop (Yan et al., 2019). In addition to the centrelines that track the course of a river channel at different times, PB-SAND requires definition of several other parameters, which vary depending on the type of meander-bend transformation, and which include the river-channel hydraulic geometry (maximum bankfull depth, width) and descriptions of the types and arrangement of lithologies forming point-bar and channel-fill deposits (Yan et al., 2021). Inputs to constrain channel-form and bar geometries can be acquired from different sources such as well data (electrical logs, core data, etc), field-based measurements from outcrops and modern systems, satellite images, or – as done in this study – from a relational database (FAKTS) that stores the required inputs.

3.2.2 FAKTS

The Fluvial Architecture Knowledge Transfer System (FAKTS) is a MySQL relational database that stores quantified sedimentological data from modern systems and analogue ancient fluvial successions (Colombera et al., 2012a, b; 2013; 2017). FAKTS satisfies the long-recognised need for inclusion of

quantitative inputs in facies models, which improves the value of facies models as a reference for comparison, interpretation and subsurface prediction.

The FAKTS database uses end-member styles of fluvial geomorphology to classify facies models by type of facies, facies associations and facies relationships that tend to occur in a particular environment. FAKTS allows determination of appropriate geological analogues to subsurface reservoir successions (Colombera et al., 2012a). This is the case that applies for this particular research where FAKTS provides the required inputs to PB-SAND.

3.2.3 Construction of Training Images

The training images constructed in this work are scale-independent, hence only a relative scaling between channel-fill and barform deposits is specified, on the basis of analogue data from FAKTS (Colombera et al., 2012a; b; 2013, 2017; 2018). In PB-SAND outputs, the stratigraphic complexity of point-bar deposits is characterised by bar-accretion geometries and the presence of genetically related channel fills, sitting in a background of fine-grained overbank deposits. By default, a representative fining-upward point-bar succession is modelled, though the facies trends can be customised. PB-SAND incorporates a number of facies types specified by users, and which relate to different grain size categories (e.g., gravel, clay). Additional lithofacies types include the following: i) mud that is deposited on accretion surfaces to form drapes during stages of low energy or slack water; ii) mud that accumulates in undisturbed floodplain areas between point-bar elements; and iii) conglomerates or breccias that accumulate on the channel thalweg floor as a result of localised reworking of channel banks (e.g., intraformational mud-clast breccias) (Miall, 1996).

In this study, training images that incorporate three, four or five facies were created for the purpose of testing different geomodelling scenarios. PB-SAND outputs are vector-based, grid-free graphics. This output is converted to a 3D geocellular grid, which can be outputted as an ASCII format text file or GSLib file for importing into industry-standard software applications. The resulting training images are idealised and scale independent. Examples of the produced training images can be seen in **Figure 3.3**.

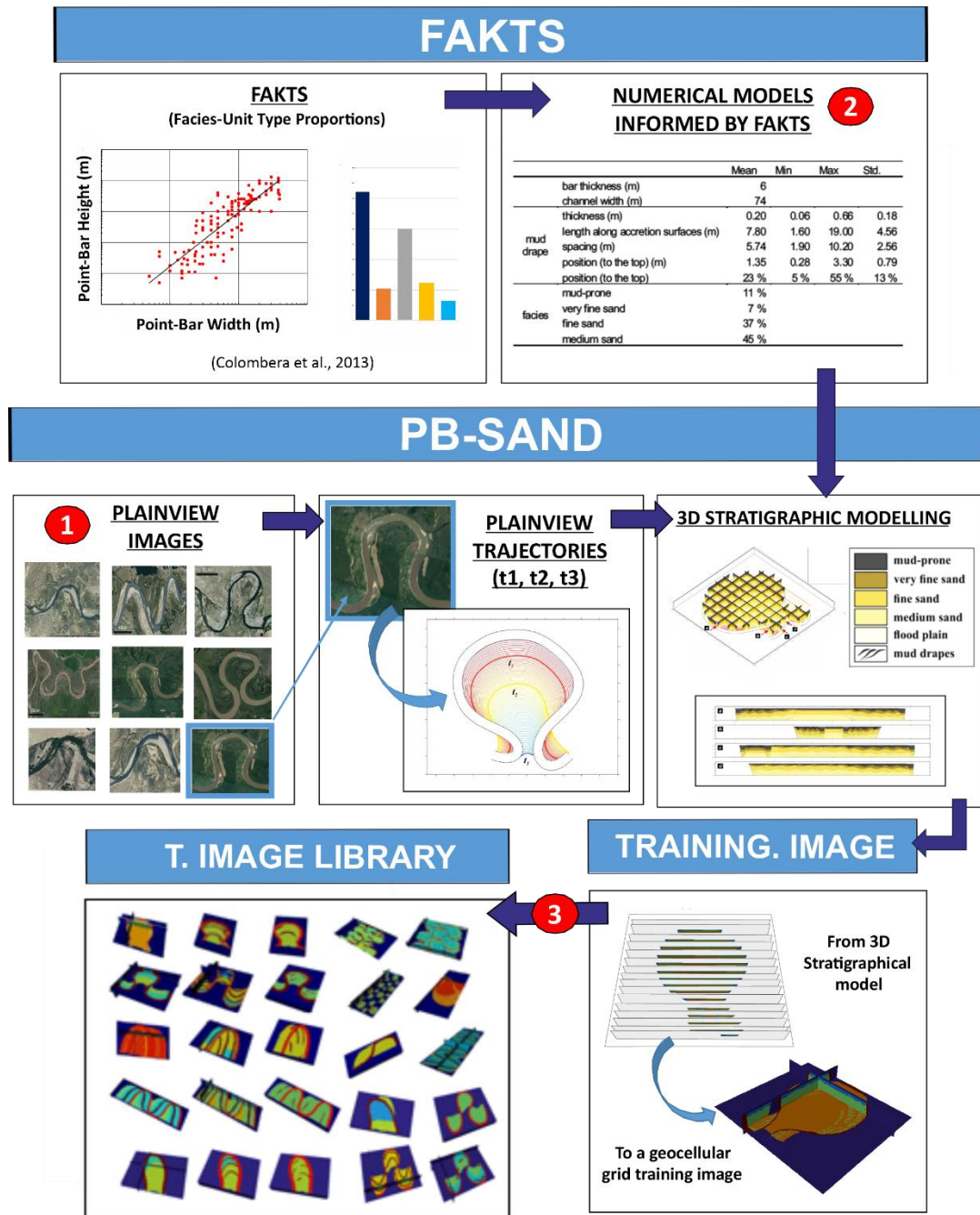


Figure 3.3 Training image building workflow.

A training image is created following a three-step process, as follows: (1) derivation of quantitative information on facies architecture from geological analogues stored in FAKTS (e.g., facies proportions, channel geometry), to be employed as input to PB-SAND; (2) specification of trajectories tracking channel planform evolution (e.g., as captured from time-lapse satellite images), to be fed as input to PB-SAND; (3) PB-SAND simulation of meander-belt facies architectures, whereby geometries of bar accretion are modelled deterministically and facies distributions are simulated stochastically. 3D vector models produced by PB-SAND are then converted into gridded geocellular models that can be used as MPS training images. A set of training images is created using this workflow that serves as a training-image library.

Although MPS modelling codes are known to work best with stationary training images, all the 3D training images created for the purpose of this research represent inherently non-stationary fluvial architectures. This means that some of the lithological trends (e.g., point-bar fining-upward) are incorporated in the training image itself. However, the reproduction of other forms of non-stationarity (e.g., spatial variations in proportions of deposits) is only attempted through the application of auxiliary variables when performing MPS simulations.

3.2.4 Training-Image Selection

From PB-SAND outputs, two geometric frameworks were selected that are representative of meander-belt architectures associated with meander translation and expansion, respectively (**Figure 3.4**). For each of these two architectural frameworks, a set of three alternative training images were created using a different number of facies.

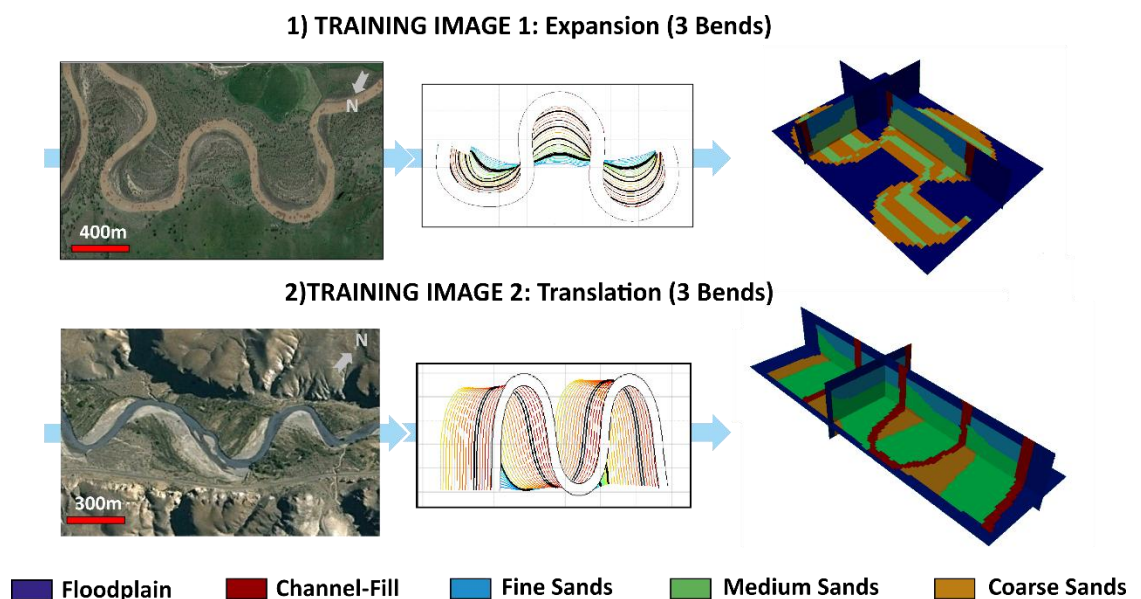


Figure 3.4 Production of 2 training images.

Two training images selected from the training-image library, which incorporate channel-belts associated with two different scenarios of meander transformation: (1) meander expansion (mean sinuosity 1.55) and (2) meander translation (mean sinuosity 3.03). PB-SAND outputs of reconstructed planform evolution are also shown in the middle, showing the plan-view expression of accretion surfaces resulting from channel migration through time. The legend at the bottom applies to the gridded Training images shown on the right-hand side. Satellite imagery of meanders undergoing expansion and translation are shown for comparison.

The aim of this is to simulate different categories of lithology and different types of facies trends, each of which serves a different geomodelling purpose.

- Three-facies training image. In this case, the training image only incorporates lithological categories representing point-bar (sand-prone), floodplain (mud-prone) and channel-fill (mud-prone) deposits. A training image of this type is applicable in contexts of prospect evaluation (macroscale level of heterogeneity, **section 2.2.1**), or where intra-point-bar sedimentary heterogeneity is considered negligible or not important.
- Four-facies training image. In addition to the previously mentioned facies, training images of this type also include a separate category for muds that are deposited as drapes on the bar fronts and that are thus oriented along lateral-accretion surfaces. Therefore, these training images include: point-bar (sand-prone), floodplain, channel-fill and bar-front-mud (all mud-prone) facies. A training image of this type is applicable in contexts requiring assessment of intra-point-bar compartmentalisation (macro-mesoscale level of heterogeneity, **section 2.2.1**).
- Five-facies training image. Three additional types of sandy facies within point-bar (meander expansion and translation) and counterpoint-bar (meander translation) deposits are defined in terms of grain size (coarse, medium and fine sands) to portray fining-upward (meander expansion and translation) and downstream-fining (meander translation) trends. A training image of this type is applicable in situations where prediction of intra-point-bar petrophysical heterogeneity is deemed important (mesoscale, **section 2.2.1**)

The size of the geobodies that are to be modelled in the simulation grid is determined by the number of cells and the cell size of the training image, in accordance with the number of cells and cell size of the simulation grid. Vector-based output from PB-SAND can be rasterised at any resolution. The larger the size and/or resolution (number of cells) of the training image, the longer it will take to complete a realisation using it. Since an objective of this study is to develop a workflow that delivers a realisation in less than 10 minutes – a runtime considered to be standard in industry – using a standard

desktop computer (of 2019 vintage), upscaling of the training images is required. Training-image grid upscaling may result in significant loss of sedimentological detail, but the training images included in the library are all scale-independent, allowing users to set a resolution that preserves the desired features.

3.2.5 MPS Algorithms: SNESIM and DEESSE

The training images have been applied in workflows for the simulation of meandering fluvial systems using the modelling algorithms SNESIM (Strebelle, 2002) and DEESSE (Mariethoz et al., 2010). A calibration process based on trial and error has been employed to determine appropriate inputs for parameters that control training image scan and grid simulation, for both SNESIM and DEESSE. This has been achieved by trialling different values for input parameters, with consideration of runtime performance. Some of these parameters are similar or equivalent for SNESIM and DEESSE (e.g., search mask/neighbourhood) others are unique and only apply to a particular code (e.g., number of replicates in SNESIM, distance threshold “t” in DEESSE).

The numbers of facies in the training images have a significant impact on the computational time of both SNESIM (Strebelle, 2002) and DEESSE (Mariethoz et al., 2010). Input parameters have been adjusted to a runtime target of 10 minutes or less. The same facies proportions for the different facies included in the training images have been specified as the target proportions for realisations of both SNESIM and DEESSE. In SNESIM, the modelled facies proportions are allowed to vary from the input facies proportions if the servosystem value ‘ λ ’ is different from 0, or if a trend is included using an auxiliary variable. For this study, the servosystem value was set to 0.5, and probability grids were employed, so a discrepancy between target and output proportions is expected.

The number of nodes considered during scan and simulation depends on the size and shape of the search mask or neighbourhood, e.g., of geometric templates defined as a set of cells with elliptical, circular or rectangular shape, and specified in terms of radius, azimuth, strike and rake. The larger the search mask, the longer the time per realisation (Meerschman et al., 2013). In DEESSE, the radius of the search neighbourhood can vary according to the number of nodes that are being simulated. (e.g., the size of the radius will

progressively decrease when the number of simulated nodes increases). A number of strategies have been introduced for optimizing search-mask or search neighbourhood definition. [Riou et al., \(2015\)](#), in application to channelised architectures, proposed the application of a search radius of 1.5 times the width of the largest channel units, and recommended isotropic search neighbourhoods as the most robust option for capturing some of the patterns expected in meandering fluvial systems.

In SNESIM, so-called 'multigrids' and 'subgrids' are used to configure the search mask to store the conditional probabilities efficiently. The purpose is to capture large-scale structures using a relatively small search mask with a relatively small number of nodes. The larger the multigrid size the fewer the nodes that need to be considered in a particular grid. In this study, four multigrids have been used to run the simulations, as preliminary work indicated that this setting results in reasonably short runtime; the four multigrids have each been divided into four subgrids, which allow locating a larger number of conditioning data during simulation. The runtime increases with increasing minimum number of replicates ([Strebelle, 2002](#)); a minimum number of replications between 5 and 10 has been chosen.

In the training image scan process performed by DEESSE, a distance threshold 't' is used to define the tolerance within which a pattern is recognised to match; the maximum fraction of training image to scan ('f') can also be specified ([Mariethoz et al., 2010](#)). Runtime increases with decreasing values of 't' and increasing values of 'f' ([Meerschman et al., 2013](#)). In DEESSE, the combination of number of nodes (n), distance threshold (t), and maximum scanned fraction (f) will have a significant impact on computation time. Therefore, changes to these parameters will need to be considered jointly. According to [Meerschman et al., \(2013\)](#) important considerations can be made as follows: i) pattern-reproduction performance improves when 'n' is larger, 't' is closer to 0, and 'f' is closer to 1, but at the expense of realisation runtime; ii) variations in 't' and 'n' influence significantly the degree to which the patterns from the training image are reproduced in the simulation grid. However, 'f' has a much smaller effect on the simulation quality; iii) reducing the scanned fraction 'f' of the training image allows substantial computational gains without degrading pattern reproduction as long as the training image contains a large enough number of reproducible patterns; iv) a small 'f' value may lead to training image under-sampling and thus affect simulation results,

but usually results in large computation gains without substantial decrease in simulations quality. The choice of input parameters to DEESSE was guided by these considerations. **Table 3.1** includes all the parameters used for every simulation presented in this study.

3.2.6 Auxiliary Variables (Trends)

To employ the training images for modelling the stratal architecture of a particular fluvial meandering system, a hierarchical approach to facies modelling has been taken. This is in part achieved through the use of auxiliary variables as means to force the incorporation of expected or desired geological features within the models.

For obtaining representative statistics, MPS algorithms commonly require stationary training images. However, sedimentary bodies and associated facies characteristics and distributions tend to vary in space, e.g., are non-stationary. To be able to incorporate – at least in part – non-stationary features in the simulations, auxiliary variable grids ([Chugunova et al., 2008](#)) have been employed. Auxiliary variables are gridded properties that describe a spatial trend in the property being modelled. They also facilitate the reproduction of nested architectures, whereby simulations are undertaken at multiple scales, to enable reproduction of heterogeneities.

Auxiliary variables in the form of 2D or 3D grids are routinely used for forcing the reproduction of spatial variations in modelled properties at different levels (e.g., in mean body thickness, grain size). These auxiliary variables allow resultant models to account for non-stationarity relating to scaling effects (scaling maps that describe variations in space of the scale of certain features), variations in orientations of architectural elements (rotation maps), variations in the facies proportions (probability maps), and differentiation of regions characterised by different types of lithological heterogeneities (region maps). Probability maps are used as part of the proposed workflow to facilitate the reproduction of geological features associated with the channel belts of meandering rivers.

In the proposed workflow, probability maps have also been used to ensure realistic spatial transitions between facies, particularly between channel belt

and floodplain facies, and the reproduction in the simulations of specific sedimentological features, such as planform cut-bank geometries, and variations in facies proportions. Auxiliary variables also facilitate the incorporation of relationships between small-scale and large-scale features in a reservoir model.

Auxiliary variable grids have been used in the developed workflow, consisting of grids that specify the probability of modelling categories. The object-based modelling tool of Schlumberger Petrel® was used to create probability regions. These regions represent: i) the axial part of a sand fairway that could represent an amalgamated channel belt or valley fill (90% probability of channel deposits); ii) an area that can only be occupied by floodplain deposits (100% probability of occurrence of mud-prone overbank sediments); and iii) a buffer area that is defined with the scope to reproduce realistic channel-to-overbank transitions, whereby the channel belts would have some rugosity in planform and mud plugs would border the outer side of the belts (**Figure 3.5**). The same probability grids have been applied to all simulations, but a total of 3 different grids for each of the 3 training-image types (3, 4 and 5 facies) have been created, which will differ with respect to probability values assigned to each region (cf. tables in **Figure 3.5**).

The functioning of probability grids differs between SNESIM and DEESSE. In SNESIM, auxiliary variables are applied based on TAU models ([Journel, 2002](#)). The probability of A jointly conditioned on B and C becomes a function of the marginal probability of A and of the two probabilities of A separately conditioned on B and C. This function depends on a parameter τ that measures the degree of redundancy between events B and C with respect to event A ([Krishnan et al., 2005](#)). Parameters that act as weights, named Tau2 and Tau1, can be controlled so that the higher Tau2 relative to Tau1 the higher is the influence of soft-probability data in controlling simulation results.

In DEESSE two main parameters control simulation outputs: the support radius (SR) and the deactivation threshold radius (DTR). The simulation process will randomly pick a data event "X" (e.g., a pattern formed by a certain number of cells) in the simulation grid and will then try to find a similar data event considering i) the patterns in the training images, ii) the previously populated categories in the simulation grid, and iii) the probabilities stored in

the probability map. SR is used to identify patterns in the nodes that have been previously populated. If within the SR distance there are more informed nodes than the number of nodes, the nodes closest to “X” are those that will be populated in the realisations.

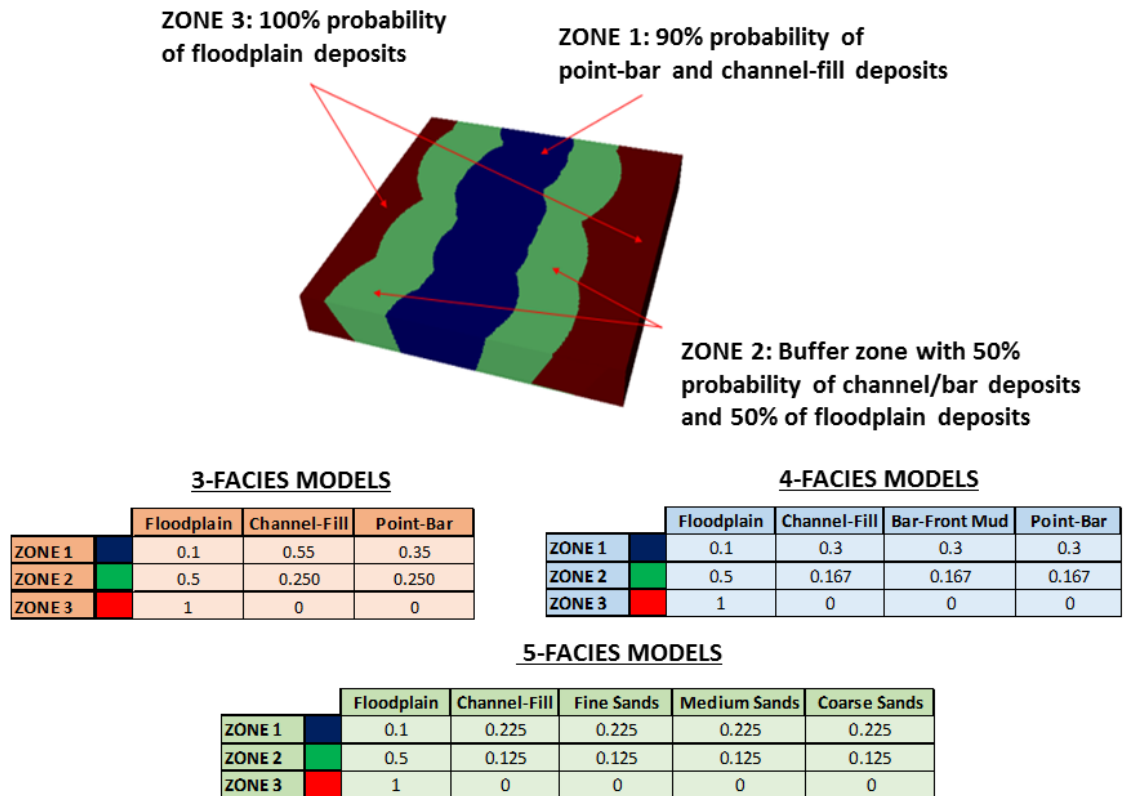


Figure 3.5 Example of a probability grid.

Example of a probability grid that may be applied to reproduce facies distributions in a channel-belt or valley-fill unit. In the grid, 3 different zones are created, within which the probability of occurrence of the facies varies. The tables represent the 3 different probability scenarios that will be used in the application of training images that include 3, 4 and 5 facies (see main text and **Table 3.2**).

At the beginning of the simulation, prior to any cells being populated in the simulation grid, the algorithm populates facies that are recognised directly from the training image conditioned on the probabilities in the probability grid. At this stage the SR is equal or smaller than the actual search radius (RA). However, towards the end of the simulation, when most of the simulation grid is populated with informed nodes, if the RA is smaller than the DTR distance, the probability constraint mechanism is stopped. The selection of appropriate

SR and DTR is a critical step when dealing with auxiliary variables in DEESSE, as it significantly affects the quality and the computation time per realisation.

3.2.7 Model Configuration and Input Tuning

Training images have been used that incorporate the two channel-belt geometries shown in **Figure 3.4**, which are representative of channel-belt reaches composed of three meander bends and associated point-bar and channel-fill deposits, placed in a background of fine-grained floodplain sediment. The two architectural frameworks represent simple meander belts that are respectively undergoing meander expansion and translation. For each of these two frameworks, three different sets of modelling categories (hereafter termed 'facies', for sake of simplicity) have been considered (**Table 3.1**). Each of these sets involves different number and types of facies. The three cases are as follows: i) 3-facies case (point-bar, channel-fill and floodplain deposits); ii) 4-facies case (point-bar deposits, channel-fill deposits, continuous bar-front muds and floodplain deposits); and iii) 5-facies case (coarse point-bar sands, medium point-bar sands, fine point-bar sands, channel-fill and floodplain deposits). These facies configurations have been selected to run unconditional simulations, such as those that would be run for modelling undrilled prospects, since unconditional realisations are ideal for assessing the degree to which training image patterns are reproduced ([Rojas et al., 2012](#); [Manchuk et al., 2011](#); [Manchuk and Deutsch, 2012](#)).

Unconditional simulations were performed to establish preferred modelling recipes that can be paired to each training image and to each MPS modelling algorithm. SNESIM and DEESSE were run on a simulation grid with the following dimensions: 250 cells along X, 250 cells along Y and 50 cells along Z. The cell size for the simulation grid was set to X:Y:Z ratios of 20:20:0.25. The parameters selected for every simulation in SNESIM and DEESSE, based on trial and error and aiming for a runtime below 10 minutes, are shown in **Table 3.1**.

Results are analysed and discussed according to qualitative criteria that allow evaluation of aspects of sedimentary architecture whose reproduction in the simulations is desirable. These are: i) planform sinuosity and continuity of deposits with curvilinear geometries such as channel fills and bar-front muds; ii) cross-sectional channelised geometry and adjacency to point-bar facies for

channel-fill deposits, which act to compartmentalise point-bar sands; iii) vertical fining-upward trends in point-bar deposits, in cases where different grain size categories of point-bar sediments are considered; iv) planform concavity of abandoned channel-fills being oriented towards the belt axis when placed at the transition to the overbank domain; and v) outward fining in point-bar elements associated with expansional meanders. Additionally, for training images embodying the products of meander translation, the presence of counter-point-bar deposits (which are typically finer grained than corresponding point-bar deposits) associated with concave-bank accretion is also evaluated.

		SNESIM input parameters							DEESSE input parameters					
		SM	N	Serv	Rep	MG	SG	Tau	SN	N	DT	F	SR	DTR
Meander expansion	Case 1	2000x 2000y 10z	60	0.5	10	4	4	2, 1	20x 20y 8z	30	0.15	0.3	7	5
	Case 2	2000x 2000y 10z	60	0.5	10	4	4	2, 1	20x 20y 8z	30	0.2	0.3	10	8
	Case 3	4000x 3000y 4z	60	0.5	10	4	4	2, 1	20x 20y 4z	30	0.2	0.3	10	6
Meander Translation	Case 4	5000x 5000y 10z	60	0.5	5	4	4	2, 1	20x 20y 5z	30	0.2	0.5	12	10
	Case 5	5000x 5000y 10z	60	0.5	5	4	4	2, 1	18x 18y 4z	35	0.15	0.5	10	7
	Case 6	5000x 5000y 5z	60	0.5	5	4	4	2, 1	15x 15y 5z	40	0.15	0.5	10	8

Table 3.1 The parameters employed in the simulations

SM: Search Mask, SN: Search Neighbourhood N: Nodes, Serv: Servosystem, Rep: Number of replicates, MG: Multigrids, SG: Subgrid, Tau: Tau Model weight values, SN: Search Neighbourhood, DT: Distance Threshold, F: maximum fraction of training image to scan, SR: Support Radius and DTR: Deactivation Threshold Radius.

3.3 Results

Here, an evaluation of the modelling outputs that would be generated upon application of training images created using the proposed workflow is presented. Results are shown below for the six cases that result from applying i) the two sets of training images reflecting contrasting channel-belt accretion geometries and ii), for each set, three facies configurations, as explained in **Section 3.2.7**. The training images were retrieved from the training-image library constructed following the workflow explained in **Section 3.2.4**. The

application of training images in MPS simulations was tested using SNESIM and DEESSE, constrained through the parameters and auxiliary variable described in **Section 3.2.6**. Outputs of SNESIM and DEESSE are compared in terms of degree of pattern reproduction and CPU performance.

Twenty realisations were generated for each of the six simulation cases. In the figures (**Figures 3.6-3.11**), only one of these realisations is presented for each of the six cases. The results of the qualitative assessment of modelling outputs are also indicated.

3.3.1 Case 1: Meander Expansion (3 facies)

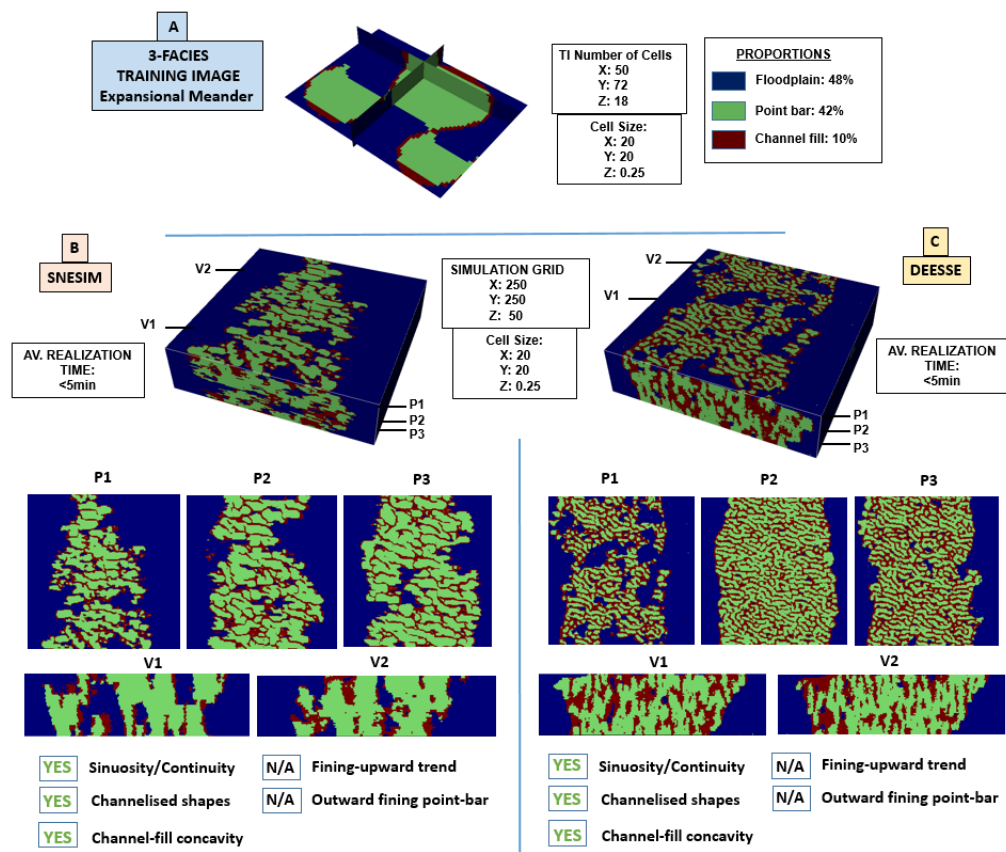


Figure 3.6 Case 1: Meander Expansion (3 facies)

Representative simulation results for the 3-facies training image for meander belts with expansional meanders (case 1). (A) Employed training image. Number of cells, cell size and proportions are indicated. Simulations performed for SNESIM (B) and DEESSE (C) are presented as block models in perspective view, together with 3 plan-view sections (P1, P2 and P3) and 2 vertical sections (V1 and V2) for each. A summary of the number of cells for the simulation grid is reported between part B and C. Below the vertical sections, a qualitative assessment of the realisations is presented for each simulation method.

Upon application of this training image, in both SNESIM and DEESSE realisations (**Figure 3.6**) sinuous channel-fill deposits appear relatively continuous, locally display loop geometries, and compartmentalise the sand-fairway zone where point-bar deposits are located. Stratigraphic compartmentalisation created by sinuous channel-fill deposits is also evident in vertical sections of realisations delivered by SNESIM. DEESSE realisations appear slightly different in vertical sections, in which more vertically elongated features are present. Overall, both SNESIM and DEESSE successfully reproduce meandering loops typical of mud-filled plugs representing abandoned channel-fill segments over a sand fairway (fluvial channel belt).

3.3.2 Case 2: Meander Expansion (4 facies)

Case 2 was simulated using a larger training image (number of cells: 165 along x, 175 along y, 60 along z) to test the effects of image resolution in populating geobodies with better defined geometries in the selected simulation grid (**Figure 3.7**). SNESIM simulations delivered results in less than 7 minutes, on average. However, for simulations performed according to the devised workflow using DEESSE, in order to complete simulations within the 10-minute runtime target, the training image had to be set to a lower resolution (76x80x30).

Although DEESSE realisations contain geobodies that are significantly smaller than those generated by SNESIM due to the different size of the training image, realisations are relatively similar in terms of geological patterns they incorporate. Curvilinear shapes are evident in plan-view sections, corresponding to channel-fill deposits and mud-front facies. Channel-fill deposits create compartments separating volumes of point-bar facies but lack the expected continuity in both SNESIM and DEESSE realisations. Plan-view sections show bar-front muds that are sinuous and delineate a second type of compartments within the point-bar facies, separating different sand-prone packages. Compartmentalisation by thick mud-prone packages that drape accretion surfaces are also evident in most of the realisations. In vertical sections, channel-fill deposits exhibit a channelised shape. However, both channel-fill and bar-front-mud bodies are excessively elongated vertically in DEESSE simulations, similarly to Case 1.

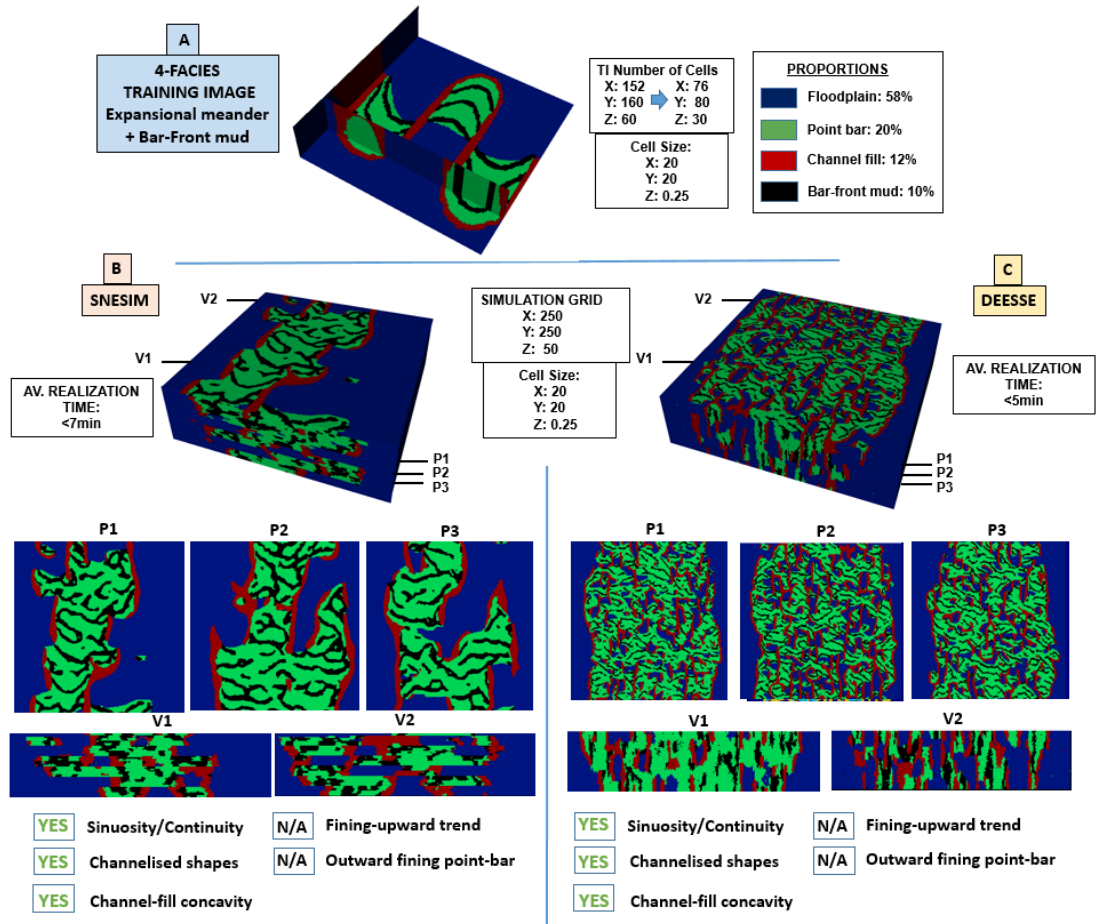


Figure 3.7 Case 2: Meander Expansion (4 facies)

Representative simulation results for the 4-facies training image for meander belts with expansional meanders (case 2). (A) Employed training image. Number of cells, cell size and proportions are indicated. Simulations performed for SNESIM (B) and DEESSE (C) are presented as block models in perspective view, together with 3 plan-view sections (P1, P2 and P3) and 2 vertical sections (V1 and V2) for each. A summary of the number of cells for the simulation grid is reported between part B and C. Below the vertical sections, a qualitative assessment of the realisations is presented for each simulation method.

3.3.3 Case 3: Meander Expansion (5 facies)

These simulations attempted to model different types of sandy point-bar facies including the characteristic fining-upward trend common in expansional point-bar elements (**Figure 3.8**).

In horizontal sections, realisations created by both SNESIM and DEESSE demonstrate the simulated lateral juxtaposition of different point-bar elements deposited through the sand-fairway region. Channel-fill deposits are seen as

remnant channel-fill plugs that have limited continuity and sinuosity; these only locally compartmentalise point-bar sands, as is common in many documented successions. Vertically, a fining-upward trend has been successfully reproduced by both SNESIM and DEESSE, with channel-deposits located at the margins of point-bar units. Model outputs are characterised by vertically stacked bar-and-channel deposits locally separated by remnants of overbank deposits, such that point-bar tops are mostly preserved. In general terms, realisations performed using both SNESIM and DEESSE show aspects of geological realism; it is possible to differentiate different types of sand-prone units located in isolated compartments. No major differences in runtime were observed between SNESIM and DEESSE.

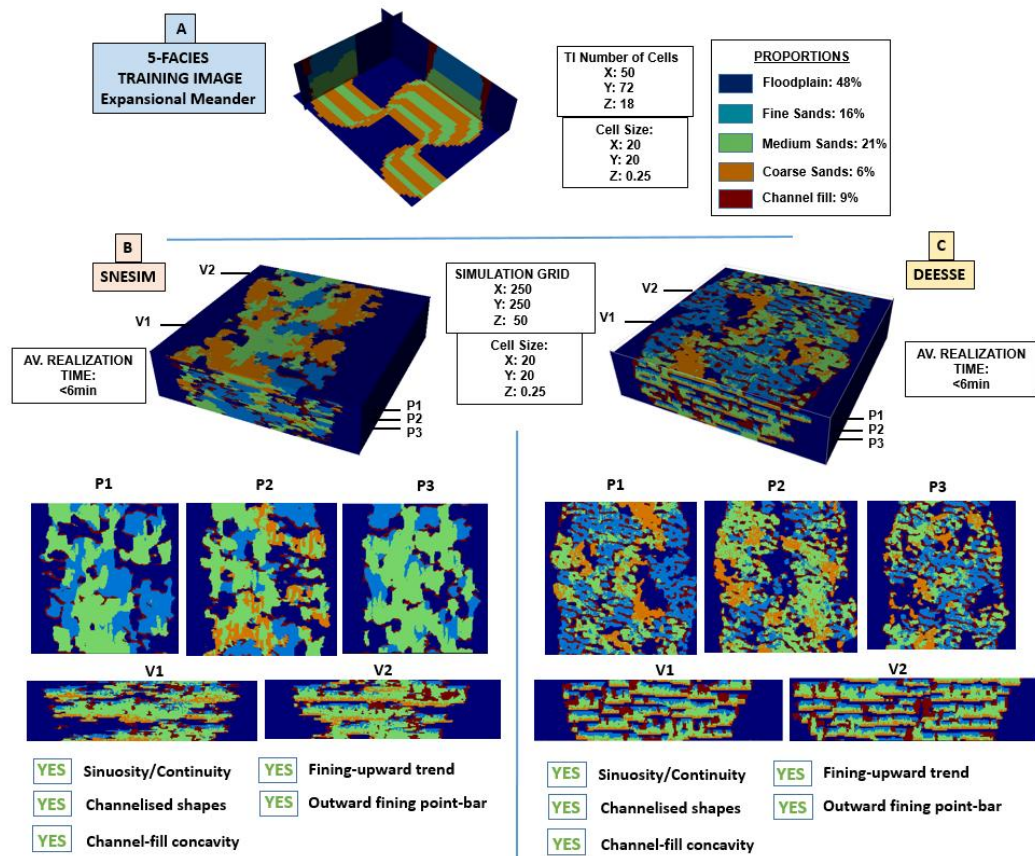


Figure 3.8 Case 3: Meander Expansion (5 facies)

Representative simulation results for the 5-facies training image for meander belts with expansional meanders (case 3). (A) Employed training image. Number of cells, cell size and proportions are indicated. Simulations performed for SNESIM (B) and DEESSE (C) are presented as block models in perspective view, together with 3 plan-view sections (P1, P2 and P3) and 2 vertical sections (V1 and V2) for each. A summary of the number of cells for the simulation grid is reported between part B and C. Below the vertical sections, a qualitative assessment of the realisations is presented for each simulation method.

3.3.4 Case 4: Meander Translation (3 facies)

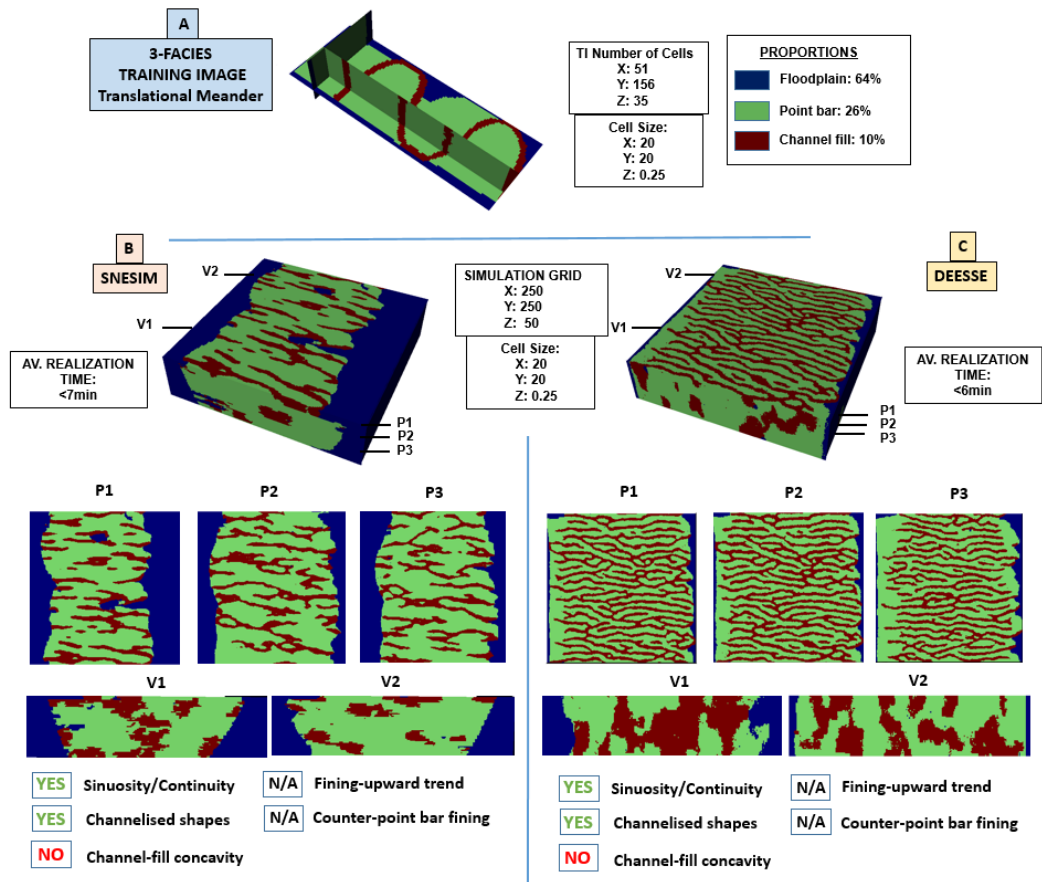


Figure 3.9 Case 4: Meander Translation (3 facies)

Representative simulation results for the 3-facies training image for meander belts with downstream translating meanders (case 4). (A) Employed training image. Number of cells, cell size and proportions are indicated. Simulations performed for SNESIM (B) and DEESSE (C) are presented as block models in perspective view, together with 3 plan-view sections (P1, P2 and P3) and 2 vertical sections (V1 and V2) for each. A summary of the number of cells for the simulation grid is reported between part B and C. Below the vertical sections, a qualitative assessment of the realisations is presented for each simulation method.

On horizontal planes, simulations performed using both SNESIM and DEESSE demonstrate channel-fill geobodies that appear as low-sinuosity linear features that are oriented perpendicular to the direction of the sand-fairway axis (**Figure 3.9**) and that are laterally discontinuous. Compartments are locally created by the channel-fill deposits, which do not however exhibit loop geometries. In vertical sections, channelised features are recognisable as channel deposits in simulations delivered by SNESIM. However, DEESSE realisations include oversized channel-fill geobodies. Overall, geometries of

geobodies produced by SNESIM and DEESSE differ from the ones in the original training image. Notably, channel-fill deposits appear overly elongated along a direction that is perpendicular to the sand-fairway axis.

3.3.5 Case 5: Meander Translation (4 facies)

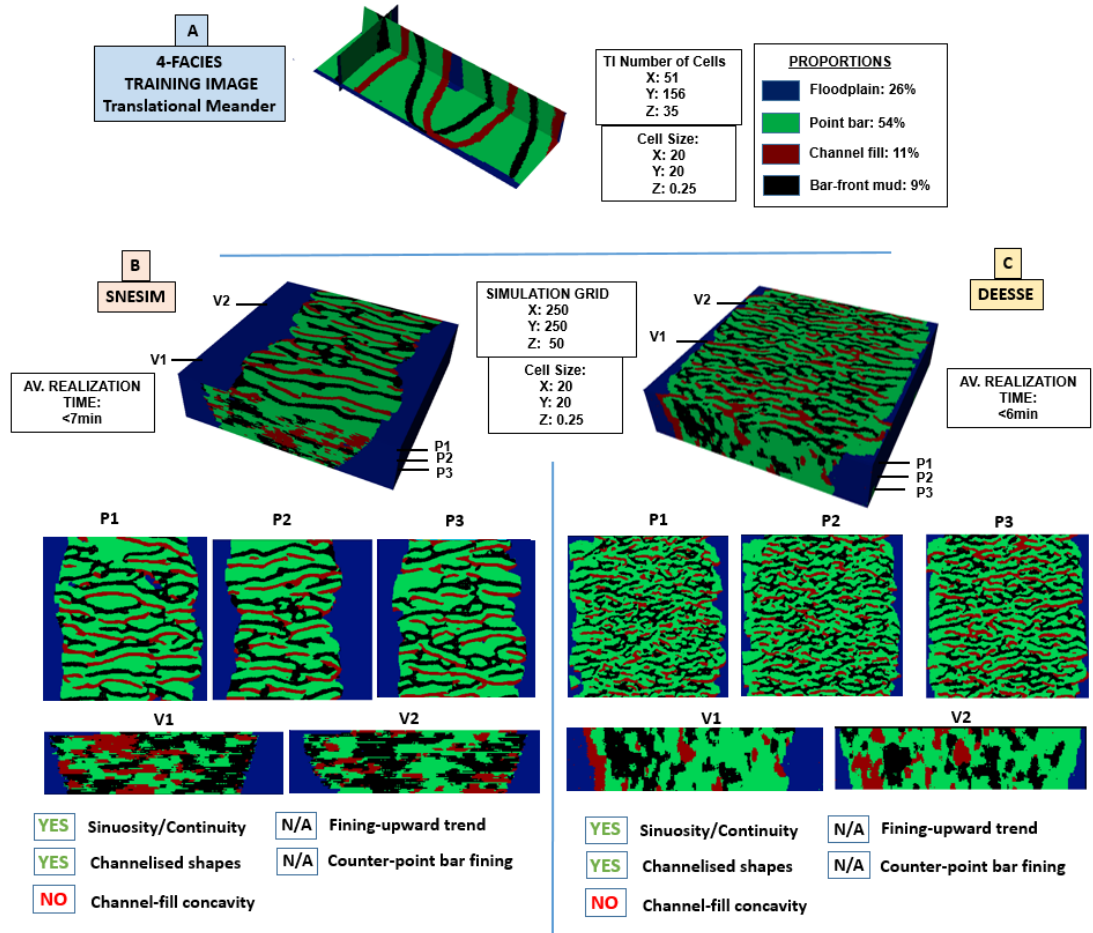


Figure 3.10 Case 5: Meander Translation (4 facies)

Representative simulation results for the 4-facies training image for meander belts with downstream translating meanders (case 5). (A) Employed training image. Number of cells, cell size and proportions are indicated. Simulations performed for SNESIM (B) and DEESSE (C) are presented as block models in perspective view, together with 3 plan-view sections (P1, P2 and P3) and 2 vertical sections (V1 and V2) for each. A summary of the number of cells for the simulation grid is reported between part B and C. Below the vertical sections, a qualitative assessment of the realisations is presented for each simulation method.

Similar to Case 4, considerable time was required to satisfactorily tune input parameters to DEESSE. Both SNESIM and DEESSE realisations produced

using this TI (**Figure 3.10**) include channel-fill geobodies and mud-prone packages that appear as low-sinuosity ribbons elongated perpendicularly to the sand-fairway axis, similarly to Case 4. Both mud-prone packages and channel-fill deposits interrupt the continuity of sandy point-bar deposits. However, similarly to the 3-facies scenario, channel-fill meander-loop elements are rarely reproduced, since channel fills appear as continuous features perpendicular to the channel-belt axis. Furthermore, delivered realisations included sharp transitions between floodplain and channel-belt facies, and in most of the cases simulations incorporated less than 50% of floodplain facies, as embodied in the probability grid selected for this simulation. In vertical sections, channel-fill deposits rendered by DEESSE have more unrealistic shapes and aspect ratios than those generated by SNESIM.

3.3.6 Case 6: Meander Translation (5 facies)

These realisations include different types of bar deposits (grain size categories) located within the channel belt (**Figure 3.11**). Compartmentalisation determined by muddy abandoned channel-fill deposits is oriented dominantly perpendicular to the channel-belt axis. However, similarly to cases 4 and 5, the continuity of abandoned channel-fill elements is limited. Sinuous abandoned channel-fill features are absent in both SNESIM and DEESSE outputs.

Similar to previous cases, considerable time was required for effective parameterisation. For DEESSE, the chosen values for SR (Search Radius) and DTR (Deactivation threshold radius) gave rise to patchy and chaotic geobodies and resulted in proportions of floodplain facies in the sand-fairway region that do not honour the probability grid (e.g., floodplain deposits represent over 10% of this region).

Vertical sections display sandbody compartmentalisation by channel-fill deposits. The point-bar fining-upward trend is not typically evident in either SNESIM or DEESSE outputs. The lack of a clear differentiation between different point-bar bodies makes it difficult to ascertain the reproduction of downstream facies trends within them. Overall, the geobodies bear little resemblance to the patterns present in the training images.

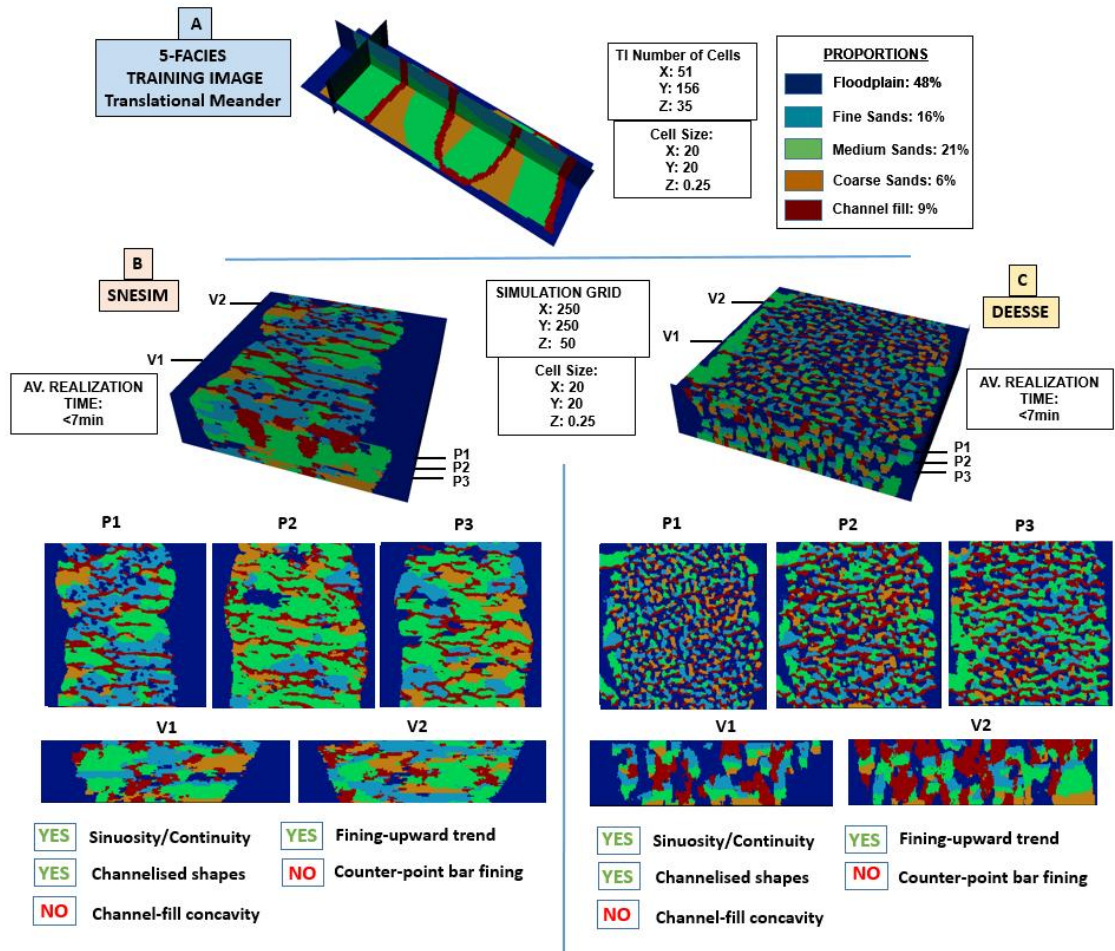


Figure 3.11 Case 6: Meander Translation (5 facies)

Representative simulation results for the 5-facies training image for meander belts with downstream translating meanders (case 6). (A) Employed training image. Number of cells, cell size and proportions are indicated. Simulations performed for SNESIM (B) and DEESSE (C) are presented as block models in perspective view, together with 3 plan-view sections (P1, P2 and P3) and 2 vertical sections (V1 and V2) for each. A summary of the number of cells for the simulation grid is reported between part B and C. Below the vertical sections, a qualitative assessment of the realisations is presented for each simulation method.

3.3.7 Stationarity Testing

In addition to the previously described cases (cases 1-6; [Montero et al., 2021](#)), extra MPS models using different training images were created. The purpose of these was to better understand the impact of i) variable stationarity of the training images, and ii) related inputs to SNESIM and DEESSE. A workflow similar to the one described above was followed, which included the application of auxiliary variable maps following the settings reported in [section 3.2.6](#).

Training Image names and case number		SNESIM input parameters						DEESSE input parameters						
		SM	N	Serv	Rep	MG	SG	Tau	SN	N	DT	F	SR	DTR
Repeated Meandering Expansional Features	Case 7	2000x	70	0.5	20	4	4	2, 1	15x	45	0.15	0.5	7	6
		2000y							15y					
		8z							5z					
	Case 8	2000x	70	0.5	20	4	4	4, 1	20x	35	0.25	0.1	5	4
		2000y							20y					
		15z							8z					
Point Bar Expansion	Case 9	2000x	60	1	20	4	4	2, 1	15x	35	0.25	0.1	5	4
		2000y							15y					
		15z							5z					
	Case 10	2000x	60	0.5	20	4	4	3, 1	20x	35	0.25	0.1	5	4
		2000y							20y					
		15z							10z					
Point Bar Expansion (Stationary)	Case 9	4000x	70	5	20	4	4	3, 1	25x	45	0.15	0.5	7	5
		4000y							25y					
		10z							8z					
	Case 10	5000x	60	0.5	20	4	4	4, 1	25x	35	0.25	0.1	5	4
		5000y							25y					
		15z							8z					

Table 3.2 Parameters employed in the additional MPS models of section 3.3.6.

SM: Search Mask, SN: Search Neighbourhood N: Nodes, Serv: Servosystem, Rep: Number of replicates, MG: Multigrids, SG: Subgrid, Tau: Tau Model weight values, SN: Search Neighbourhood, DT: Distance Threshold, F: maximum fraction of training image to scan, SR: Support Radius and DTR: Deactivation Threshold Radius.

Table 3.2 describes the model configuration for both SNESIM and DEESSE for each of the additional cases (Case 7-12). Three different training images are used, which respectively incorporate:

- i) A meander-belt composed of multiple point-bar elements accreted by meander expansion – Case 7 and 8 (**Figure 3.12** and **Figure 3.13**).
- ii) A point-bar and channel-fill architecture resulting from meander expansion – Case 9 and 10 (**Figure 3.14** and **Figure 3.15**) and
- iii) Two parallel, identical meander belts in which point-bar and channel-fill architecture results from meander expansion – Case 11 and 12 (**Figure 3.16** and **Figure 3.17**).

3.3.7.1 Case 7 (3 Facies)

A training image is employed that includes a meander-belt composed of multiple point-bar elements grown by meander expansion (**Figure 3.12**). The aim is to test the impact of repeated features (increased stationarity) in the training image on realisations for a 3-facies scenario.

In horizontal sections of the output realisations, sinuous channel-fill deposits are recognised. They appear relatively continuous exhibiting loop geometries, sometimes delineating stratigraphic compartments, in both SNESIM and DEESSE outputs. Some of the geometries included in the original training image are reproduced in the horizontal plane, but geobody dimensions appear smaller in the DEESSE simulations. In vertical sections, realisations display channel-fill deposits forming barriers between multiple stratigraphic compartments in both SNESIM and DEESSE outputs. However, deformation on channel-fill geometries with respect original training image patterns are easily recognised in the DEESSE realisations.

Realisations were obtained in less than 5 minutes in all cases. The realisations shown in **Figure 3.12** are applied for property modelling in Chapter 5 (**section 5.3**).

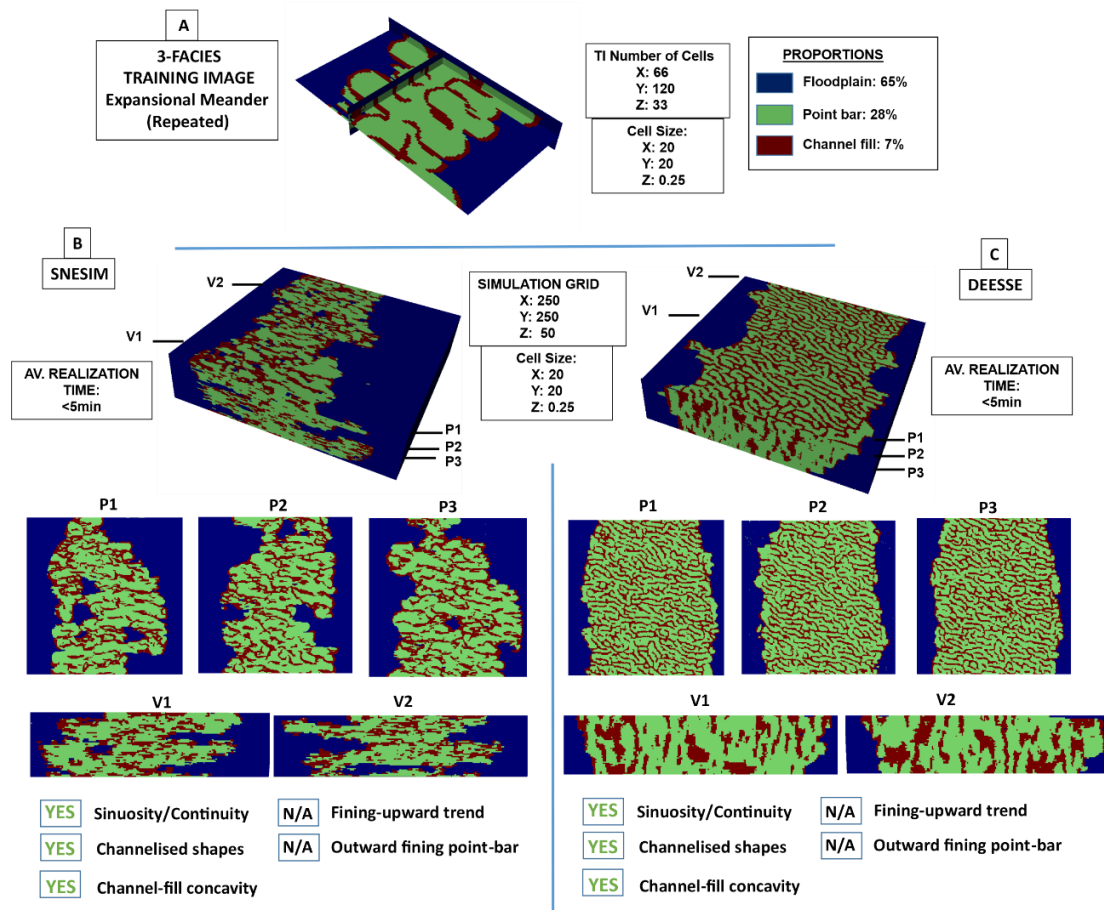


Figure 3.12 Case 7 (3 Facies)

Representative simulation results for the 3-facies training image for meander belts with multiple point-bar elements produced by meander expansion (Case 7). (A) Employed training image. Number of cells, cell size and proportions are indicated. Simulations performed for SNESIM (B) and DEESSE (C) are presented as block models in perspective view, together with 3 plan-view sections (P1, P2 and P3) and 2 vertical sections (V1 and V2) for each. A summary of the number of cells for the simulation grid is reported between part B and C. Below the vertical sections, a qualitative assessment of the realisations is presented for each simulation method.

3.3.7.2 Case 8 (5 Facies)

A training image is employed that reflects the architecture of the one in Case 7, but which additionally includes mesoscale features as intra point-bar heterogeneities (**Figure 3.13**).

Horizontal sections of the output realisations show multiple stratigraphic compartments caused by the presence of channel-fill deposits. However clear meander loops are not recognised. Also, similarly to Case 6 (**section 3.3.6**),

outputs are characterised by patchy and chaotic features. With respect to vertical sections, vertical facies trends in point-bar elements are reproduced in both SNESIM and DEESSE realisations. Stratigraphic compartmentalisation and point-bar amalgamation is also seen in multiple instances. Based on results observed in vertical sections, DEESSE outputs exhibit more realistic depositional geometries. Results were delivered within 5 minutes. As for Case 7, realisations obtained from Case 8 were used to constrain property models in Chapter 5.

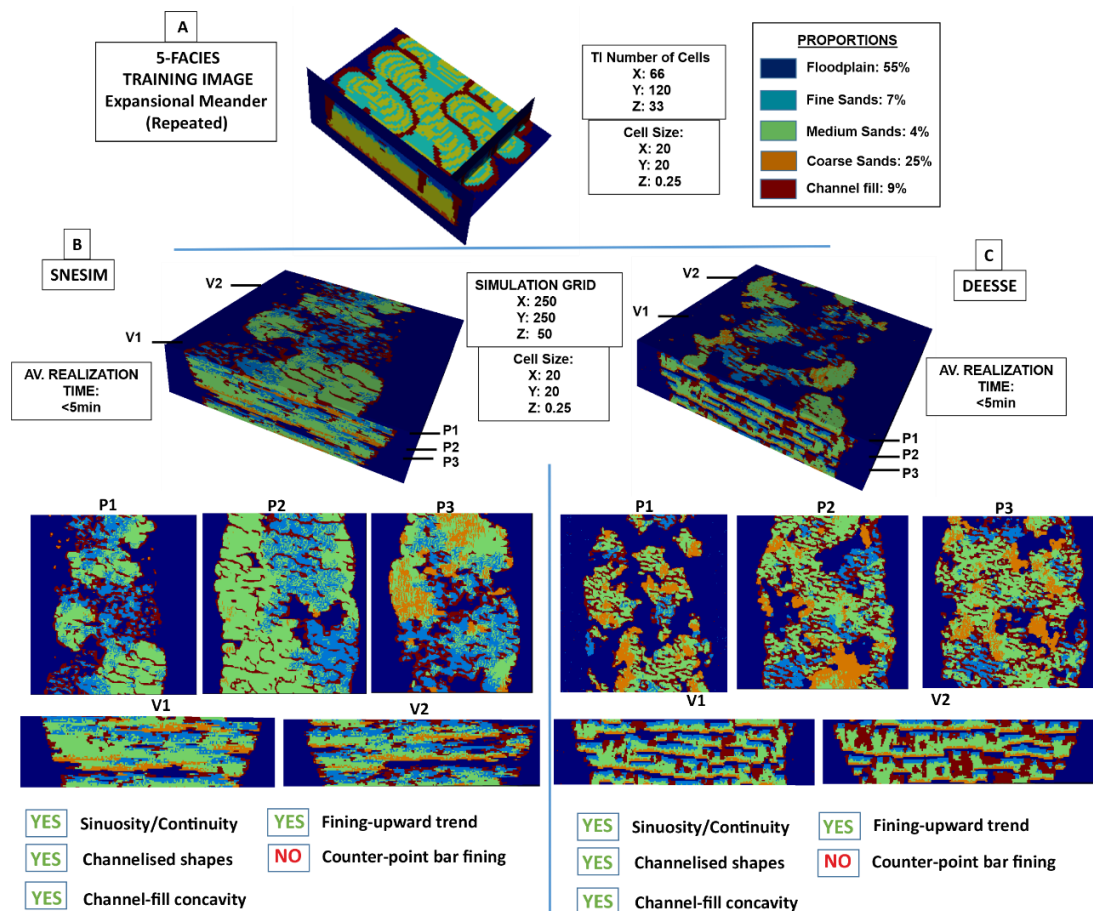


Figure 3.13 Case 8 (5 Facies)

Representative simulation results for the 5-facies training image for meander belts with multiple point-bar elements produced by meander expansion (Case 8). (A) Employed training image. Number of cells, cell size and proportions are indicated. Simulations performed for SNESIM (B) and DEESSE (C) are presented as block models in perspective view, together with 3 plan-view sections (P1, P2 and P3) and 2 vertical sections (V1 and V2) for each. A summary of the number of cells for the simulation grid is reported between part B and C. Below the vertical sections, a qualitative assessment of the realisations is presented for each simulation method.

3.3.7.3 Case 9 (3 Facies)

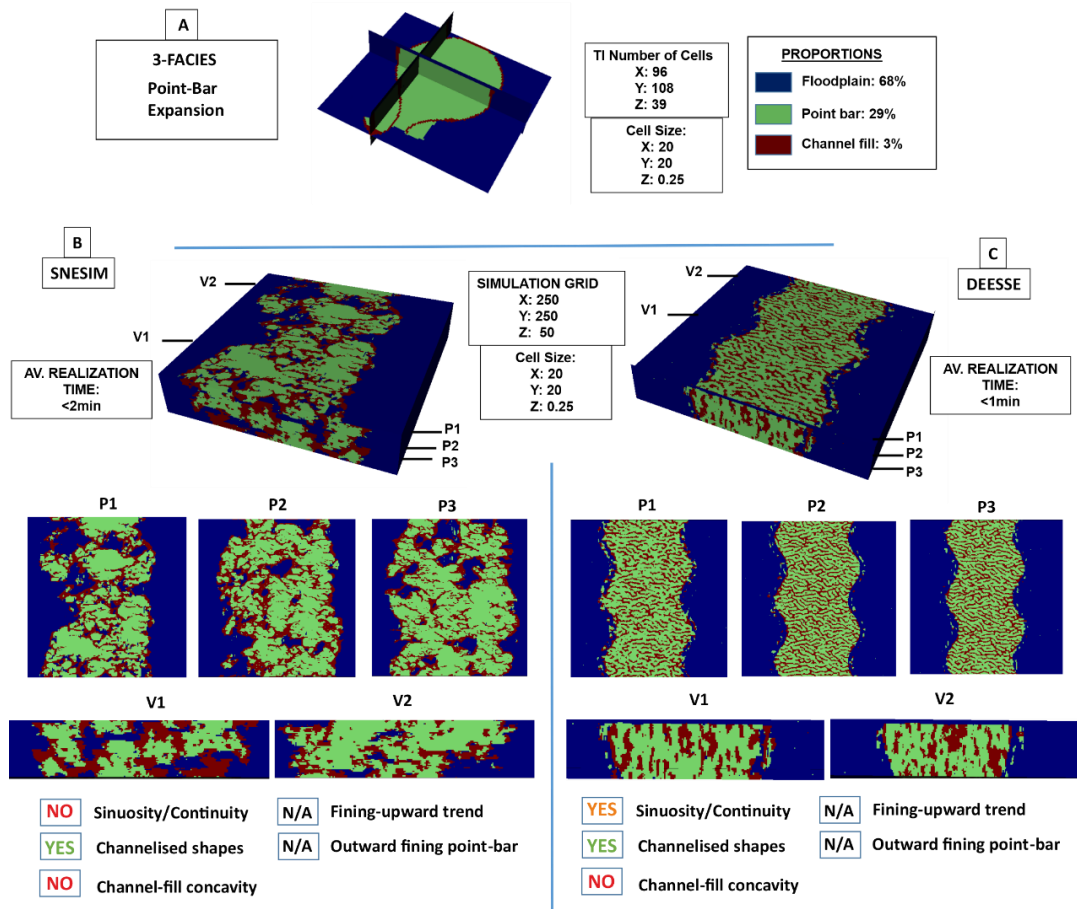


Figure 3.14 Case 9 (3 Facies)

Representative simulation results for the 3-facies training image for point-bar and channel-fill architectures resulting from meander expansion (Case 9). (A) Employed training image. Number of cells, cell size and proportions are indicated. Simulations performed for SNESIM (B) and DEESSE (C) are presented as block models in perspective view, together with 3 plan-view sections (P1, P2 and P3) and 2 vertical sections (V1 and V2) for each. A summary of the number of cells for the simulation grid is reported between part B and C. Below the vertical sections, a qualitative assessment of the realisations is presented for each simulation method.

In contrast with the training image used in Case 7 and Case 8, a training image with very limited stationarity is used for Case 9. The training image corresponds to the architecture produced by a single meander bend and includes a single fully represented point-bar element with its genetically related channel-fill deposits, all surrounded by floodplain facies. Also, contacts between the point-bar category and the floodplain category exists in this

training image, in contrast with Case 7 and Case 8 where the channel-fill deposit was found between point-bar and floodplain facies (**Figure 3.14**).

Horizontal sections for both SNESIM and DEESE show significant differences. Although sinuous features are recognised in the SNESIM realisations, channel-fill features are bigger and thicker than in the DEESSE realisations. Also, these features tend to notably vary in size, especially in SNESIM realisations, and to exhibit various geometries, which differ from those included in the training image. In DEESSE realisations the sizes of the geobodies are relatively homogeneous, and their shapes tend to be elongated. Some of the patterns included in the training image are not reproduced in realisations of either algorithms. In vertical sections, both SNESIM and DEESSE realisations display stratigraphical compartments.

Regarding run time, realisations were performed below the 5 minutes threshold in all cases.

3.3.7.4 Case 10 (5 Facies)

A 5-facies training image with the same geometric framework as the ones used for Case 9 but that incorporates intra point-bar heterogeneities is used in Case 10 (**Figure 3.15**).

Horizontal sections of the realisations show poor reproduction of the geometries of channel-fill deposits. Patterns related to point-bar accretion by meander expansion are not evident, and no clear stratigraphic compartmentalisation is observed in outputs of either algorithms. Furthermore, the three different lithologies of the point-bar features are displayed in patches, and in the case of the DEESSE models they appear very small. In vertical sections, the fining-upward trend and the amalgamation of point-bar elements are hardly recognised in both SNESIM and DEESSE realisations. Geometries of the units also appear to be unrealistically elongated.

Realisations were obtained in less than 5 minutes in all cases.

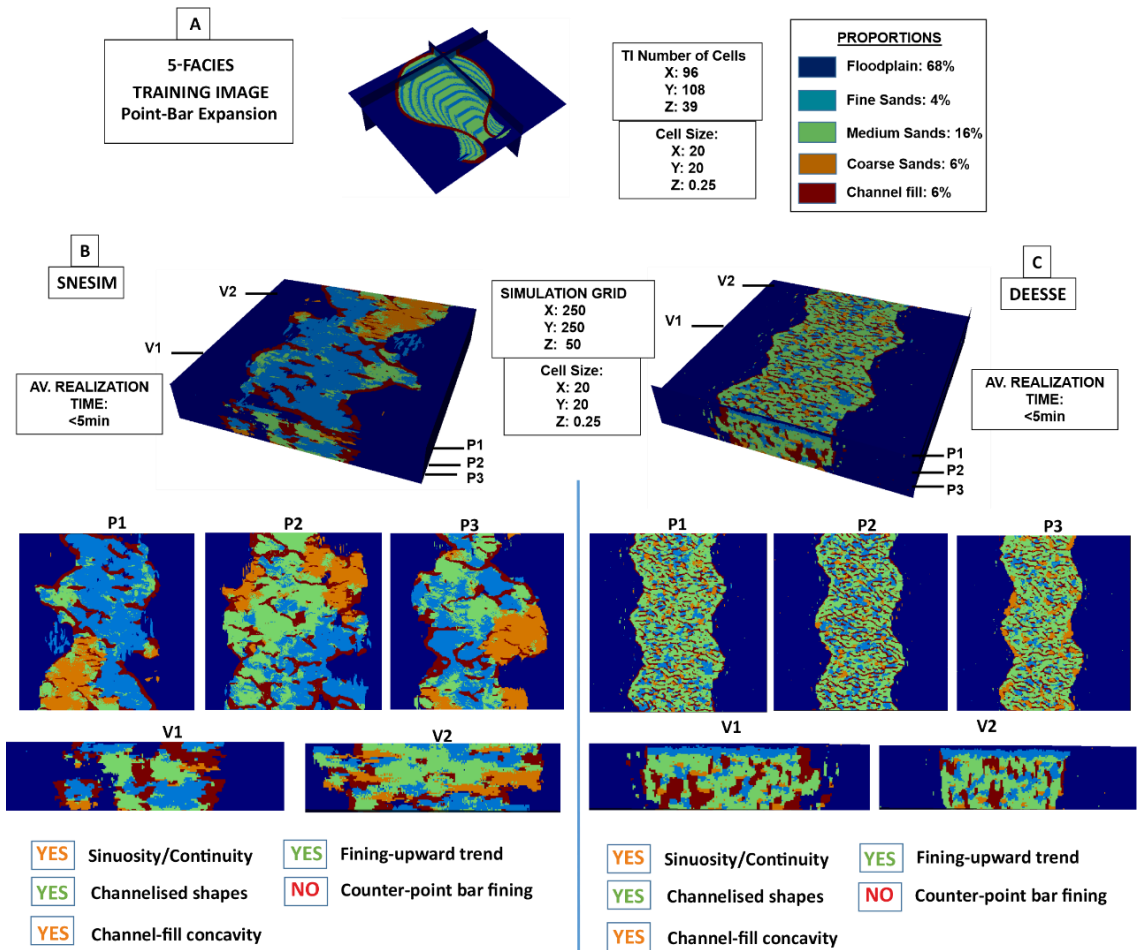


Figure 3.15 Case 10 (5 Facies)

Representative simulation results for the 5-facies training image for point-bar and channel-fill architectures resulting from meander expansion (Case 10). (A) Employed training image. Number of cells, cell size and proportions are indicated. Simulations performed for SNESIM (B) and DEESSE (C) are presented as block models in perspective view, together with 3 plan-view sections (P1, P2 and P3) and 2 vertical sections (V1 and V2) for each. A summary of the number of cells for the simulation grid is reported between part B and C. Below the vertical sections, a qualitative assessment of the realisations is presented for each simulation method.

3.3.7.5 Case 11: Point-Bar Expansion (Stationary Sample) (3 Facies)

Case 11 is based on the use of a more stationary (but rather geologically unrealistic) training image, including two channel belts, each of them made of repeated point-bar elements produced by meander expansion. The simulations were also carried out using a relatively bigger training image grid comparing with previous cases (**Figure 3.16**).

In the horizontal sections, the continuity and shape of the modelled channel-fill deposits do not differ significantly in comparison with previous cases. This is observed in both SNESIM and DEESSE outputs. Smaller features are observed in realisations delivered by DEESSE in comparison with those by SNESIM. Vertical sections of SNESIM realisations demonstrate more realistic channel-fill geometries. In the case of DEESSE, the shapes are elongated along the vertical direction and differ markedly compared to the original patterns in the training image.

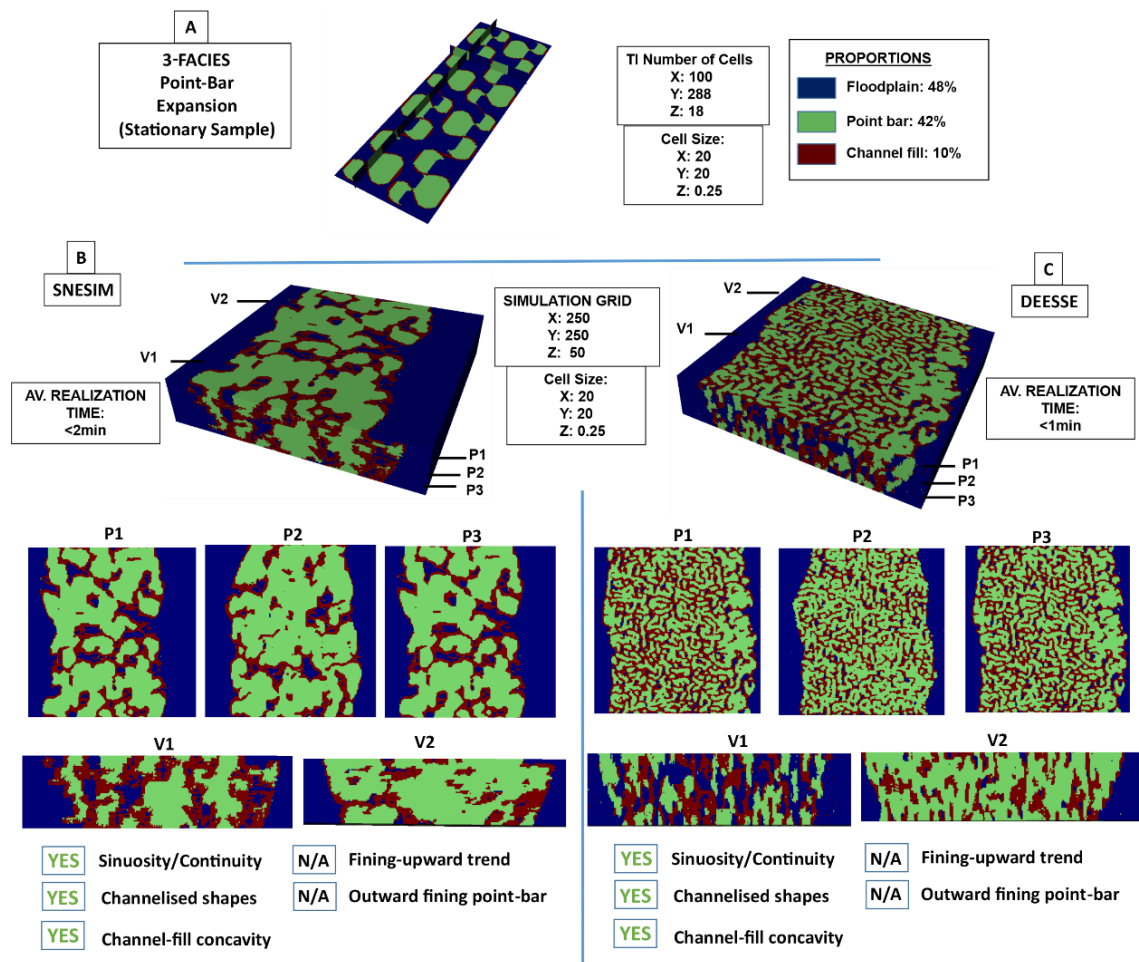


Figure 3.16 Case 11 (3 Facies)

Representative simulation results for the 3-facies training image for two parallel meander belts in which point-bar and channel-fill architecture results from meander expansion (Case 11). (A) Employed training image. Number of cells, cell size and proportions are indicated. Simulations performed for SNESIM (B) and DEESSE (C) are presented as block models in perspective view, together with 3 plan-view sections (P1, P2 and P3) and 2 vertical sections (V1 and V2) for each. A summary of the number of cells for the simulation grid is reported between part B and C. Below the vertical sections, a qualitative assessment of the realisations is presented for each simulation method.

Even though the training image was significant bigger than those used for the previous cases, the time required to obtain the outputs was below the 5 minutes threshold.

3.3.7.6 Case 12 (5 Facies)

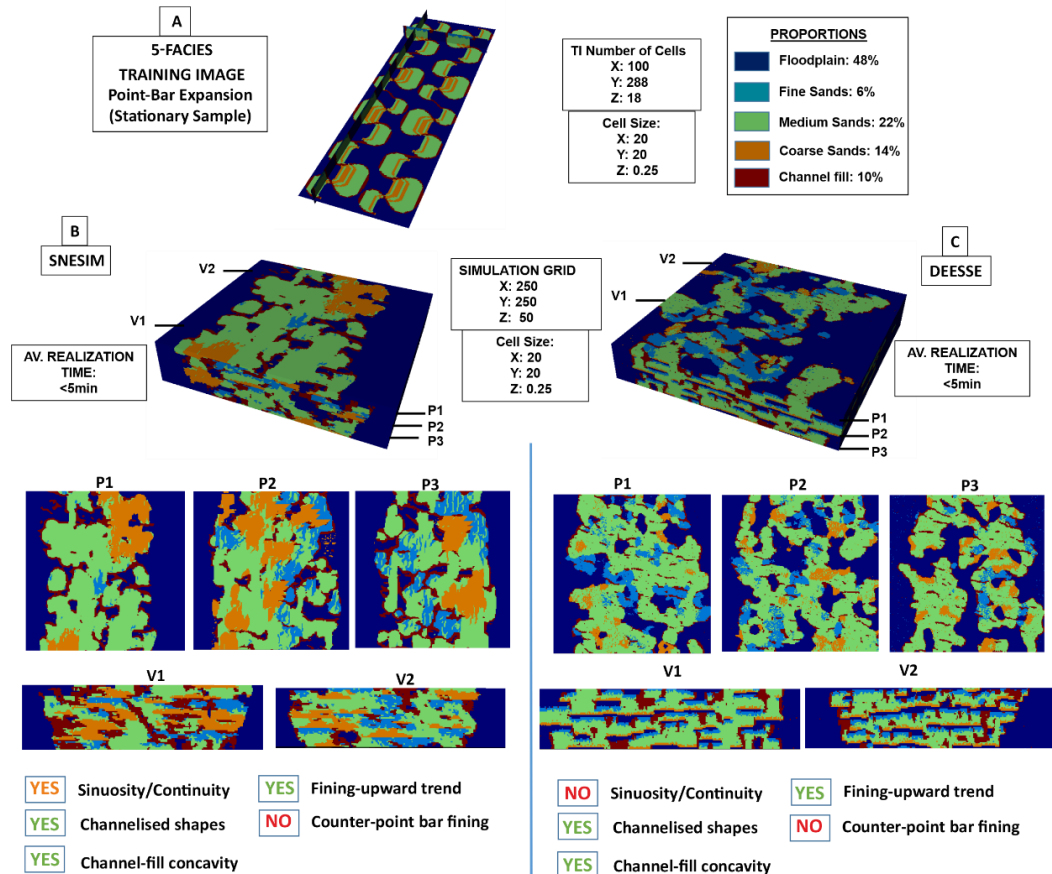


Figure 3.17 Case 12 (5 Facies)

Representative simulation results for the 5-facies training image for two parallel meander belts in which point-bar and channel-fill architecture results from meander expansion (Case 12). (A) Employed training image. Number of cells, cell size and proportions are indicated. Simulations performed for SNESIM (B) and DEESSE (C) are presented as block models in perspective view, together with 3 plan-view sections (P1, P2 and P3) and 2 vertical sections (V1 and V2) for each. A summary of the number of cells for the simulation grid is reported between part B and C. Below the vertical sections, a qualitative assessment of the realisations is presented for each simulation method.

A training image with the same geometric framework as that one employed for Case 11, but which incorporates mesoscale features, was applied to obtain 5-facies models of Case 12 (**Figure 3.17**).

Horizontal sections demonstrate more limited continuity in channel-fill deposits compared with the realisations of Case 11, and no clear meander loops are seen. Moreover, no patterns found in the original training images can be clearly recognised in realisations delivered by SNESIM and DEESSE. The orientation of the point-bar elements considered in the training image is not identified in the realisations either. Vertical sections demonstrate the reproduction of (i) stratigraphic compartments due to the presence of channel-fill deposits and (ii) fining-upward trends in point-bar elements, in both SNESIM and DEESSE outputs.

Outputs were obtained in less than 5 minutes. The DEESSE models were delivered more rapidly than the SNESIM ones.

3.4 Discussion

The intent of this research was not to test modelling algorithms through a systematic assessment of their performance, with the aim to provide definitive guidance on parameter tuning; work of this type already exists, as applied to both SNESIM and DEESSE (Liu et al., 2004; Meerschman et al., 2013). Rather, we determined the ability of these MPS modelling methods to reproduce the types of geological architectures that are characteristic of successions deposited by meandering fluvial systems, since this is a geological context to which MPS is often applied (Rojas et al., 2012; Manchuk et al., 2011; Manchuk and Deutsch, 2012; Arnold et al., 2019), but which is characterised by heterogeneities that are intrinsically non-stationary (Nanson and Page, 1983; Thomas et al., 1987; Alpak and Barton, 2014; Russell et al., 2019). Concurrently, this work demonstrates the following.

- Provides a test of the suitability of the proposed forward stratigraphic modelling software (PB-SAND; Yan et al., 2017; 2019; 2020; Colombera et al., 2018) as a training-image creator, which allows producing trends that would not be readily generated using general-purpose tools (e.g., Maharaja, 2008).
- Outlines a workflow that is applicable in cases where a framework exists of the macro and mesoscale architecture of a fluvial succession, consisting

of the distribution of channelised geobodies representing channel belts or valley fills, within which sedimentary heterogeneity needs to be predicted. In reservoir-modelling situations, this framework may be established based on outputs of other modelling efforts (e.g., object-based modelling) linked with MPS in a hierarchical fashion, or by defining channelised geobodies recognisable in 3D seismic cubes; in this way, regions of the reservoir volumes can be defined that can be utilised in the same manner as the probability grids adopted to generate the unconditional realisations discussed in this work.

As applied to SNESIM and DEESSE using training images that incorporate 3 facies only (representing point-bar, channel-fill and overbank deposits) and that relate to channel-belt architectures associated with simple meander expansion, the proposed workflows were effectively employed to model the distribution of channel-fill deposits. The resultant simulated outputs reveal the presence and expected distribution of compartments within meander-belt deposits.

Similar results were observed when using 4-facies training images for expansional point bars, where thick accumulations of mud are also simulated within the point-bar compartments. The successful application of training images incorporating 3 and 4 facies are particularly important as these types of simulation are the preferred scenarios for many simulations of fluvial reservoir successions. When feeding a dynamic simulation, these static models will effectively discriminate facies that act as barriers to fluid flow (floodplain, channel-fill and bar-front mud) from more permeable reservoir volumes (point-bar deposits).

By contrast, the application of training images that incorporate 3, 4 and 5 facies relating to channel-belt architectures associated with meander translation returned realisations that contained discontinuous string-shaped channel-fill geobodies arranged perpendicular to the axis of the sand fairway, rather than units that are continuous and sinuous in planform, as was expected. Also, trends incorporated in the training image, such as downstream or upward fining, do not seem to be well replicated by either SNESIM or DEESSE. This highlights limitations in the application of these codes to reproduction of trends of this type.

The 5-facies simulations were performed for the two different types of training images. Contrary to the 3-facies training images, the aim for this set of model runs was to simulate a scenario where three different types of bar deposits (sands forming reservoir units) can be differentiated from two types of mud-prone units (channel-fill and floodplain facies – typically non-net reservoir). For both SNESIM and DEESSE, the implemented fining-upward trend is recognised in all the realisations, allowing effective differentiation of different vertically stacked, genetically related bars and channel fills. Channelised shapes are also recognised in the vertical section. However, a decrease in sinuosity and continuity of channel-fill deposits has been acknowledged in the horizontal planes. Loops are rarely distinguished, unlike in 3- and 4-facies simulations obtained using the training images related to expansional meanders. Moreover, simulations appear patchy where different types of point-bar facies are populated in sandy compartments. Runtime for these types of simulations were significantly higher than for the 3- and 4-facies simulations. However, all realisations were still generated in less than 10 minutes based on the chosen inputs.

Based on the qualitative criteria of geological realism considered in this work, an algorithm – SNESIM or DEESSE – that performs consistently better cannot be indicated. Rather, the manner in which features incorporated in the training images are reproduced by either algorithm appears to depend on a combination of input parameters, type of architecture being modelled, and number and types of facies considered.

The simulations performed in this research are not associated with a specific physical scale. The size and resolution of the training images were important factors in the simulations for dictating geological realism and runtime. The relative size of the training image (number of cells) with respect to the size of the simulation grid was calibrated to the size of geobodies to be reproduced in the realisations. For example, the reproduction of large-scale patterns requires training images whose size might be close to the size of the simulation grid. Modelled channelised features will tend to be discontinuous in planform if the training image is smaller than the modelling grid. However, if the training image includes small-scale features that must be reproduced in the simulation grid, a larger number of cells is required (Caers and Zhang, 2004). However, the greater the number of cells in the training image, the greater the runtime needed to perform the simulations in both SNESIM and

DEESSE. The size of the geobodies is controlled by the number of cells in the training image with respect to the number of cells in the simulation grid.

Differences were observed in runtime when SNESIM and DEESSE needed to handle training images with larger number of cells. An example of the differences can be seen in cases 2 and 5 where DEESSE realisations required significantly longer runtime than those created using SNESIM. In these cases, the input parameters employed initially resulted in runtime that exceeded the established 10 minutes threshold per realisation, so a further upscaling was performed to create a coarser training image for use in DEESSE simulations.

The iterative process by which parameters are optimised in order to deliver relatively realistic realisations within the target runtime is time-consuming, and likely represents a barrier to the widespread uptake of this method by geomodellers. From the experience acquired through this work, some recommendations can be made that can be used to guide modelling practice, as follows.

- Both the Search Mask (SNESIM) and the Search Neighbourhood (DEESSE) should be set to a size that is sufficiently large to allow the algorithm to borrow the required patterns from the training image along horizontal axes. This study always considered search masks and search neighbourhood values that span the number of cells needed to cover the full amplitude of a meander bend (point bar). Working with large 3D training images often results in excessive runtime.
- To speed up the modelling effort, it is recommended that parameter tuning is initially performed on 2D grids with any given orientation (X, Y or Z).
- Calibrating the use of the probability grids in DEESSE can be time-consuming. Unlike SNESIM, which only requires the choice of a TAU model, DEESSE demands setting the weight of the probability grid in the simulations, which requires a search radius (SR) and deactivation threshold radius (DTR) to be optimised simultaneously. A recommendation can be made for a calibration of probability grids starting from values of SR and DTR that are relatively high (>10); smaller values for SR and DTR resulted in excessive runtime.

3.5 Conclusions

A hierarchical workflow for the application of MPS modelling algorithms (SNESIM and DEESSE) has been devised and tested by modelling sedimentary architectures that are characteristic of high-sinuosity meandering fluvial systems. The hierarchical approach involves the use of 3D training images for two different scenarios (associated with fluvial systems development via bar expansion and translation respectively), each incorporating either 3, 4 or 5 facies. Training images were built using an established forward stratigraphic model (PB-SAND) partly conditioned on geological-analogue data borrowed from a sedimentological database (FAKTS), together with auxiliary variables that describe facies probability and input parameters to the algorithms that are optimised for delivering realisations in less than 10 minutes on a standard desktop personal computer. The proposed workflow can be employed in real-world reservoir modelling scenarios through the use of probability grids constrained on seismic geobodies, or through linkage to outputs of object-based modelling.

The comparison between unconditional realisation generated using SNESIM and DEESSE enables evaluation of their performance in modelling fluvial successions, assuming a target runtime of up to 10 minutes. Realisations have been assessed qualitatively against i) the training images, and ii) known characteristics of sedimentary architectures of high-sinuosity river systems. Analysis of simulation results indicate what geological features of meandering fluvial successions arising from expansional and translational point-bar development are reproduced.

Planform curvilinear and channelised geometries in the cross-section are sometime evident in modelled channel-fill deposits. Furthermore, under certain modelling inputs, modelled sand-prone point-bar facies take the form of compartments that are juxtaposed horizontally and vertically. This modelling set up is applicable to simulate the architecture of meandering reservoir successions requiring prediction of the degree of stratigraphic compartmentalisation of effective net reservoir units by mud plugs. Fining-upward trends incorporated in the 5-facies training image for expansional bars are successfully reproduced by both SNESIM and DEESSE. This modelling approach finds application to reservoir models requiring finer-scale petrophysical characterisation of point-bar deposits, especially in contexts of

enhanced oil recovery or CO₂ injection. However, for simulations based on training images associated with translational meanders, the desired differentiation of counter-point bar fines and the geometry of channel-fill meander loops were not readily replicated.

Geomodelling workflows that employ MPS simulations recommend use of stationary training images and incorporation of trends by using auxiliary variable maps. This study demonstrates that geological trends that are incorporated in the training image itself (e.g., point-bar fining-upwards) can be reproduced in some circumstances. Moreover, this research highlights the potential value of a comprehensive training-image library for fluvial depositional systems (cf. [Pyrzcz et al., 2008](#)), from which geomodellers could select training images and associated modelling recipes based on types of heterogeneities that need to be modelled and target runtime.

4. Petrophysical Analogue Fluvial Database (PAFD) for Characterisation of Controls on Petrophysical Properties in Fluvial Successions: Development, Structure, and Data Population

4.1 Introduction

Populating 3D models with realistic distributions of petrophysical properties is an important part of an industry-wide, routinely employed workflow that seeks to provide a better understanding of reservoir-rock volumetrics, productivity and containment (Ringrose and Bentley, 2015; Cannon, 2018; Caers, 2008; Pyrcz and Deutsch, 2014). Certain fluvial sedimentary bodies (architectural elements) tend to be characterised by distinctive petrophysical properties. This is because sedimentary lithological heterogeneity at the scale of the facies units that comprise such bodies are often linked to petrophysical heterogeneity determined by fundamental sedimentary processes of erosion, transport and deposition (Miall, 1996). Thus, the evaluation of the petrophysical properties of genetic sedimentary units of fluvial origin, which constitute the building blocks of larger-scale geological models, is important for the characterisation and prediction of reservoir quality of larger rock volumes, and hence for assessing overall reservoir quality (see **section 2.1**)

Rock successions of fluvial and alluvial origin are a common subsurface reservoir type (Allen, 1965). These dominantly siliciclastic sedimentary successions exhibit considerable heterogeneity in mineral composition, sediment texture, structure, porosity and permeability distributions (Miall, 2014). These rocks are the product of sedimentation in a wide range of fluvial and alluvial environments whereby river and overbank landforms, and their deposits are emplaced, reworked, eroded and/or preserved through erosion, transport, and deposition of sediment (Evans, 2018). As a consequence, accumulated and preserved fluvial sedimentary bodies possess distinctive petrophysical properties at a hierarchy of different sedimentary scales (basin scale, channel-belt scale, architectural-element scale, facies-unit scale, bedding and lamina scale, and pore scale). These properties arise from the action of primary depositional processes that govern the development of different types of heterogeneities (Bridge, 1993; Priddy and Clarke, 2021). Moreover, following the deposition of fluvial strata, secondary processes, notably associated with sediment compaction and a range of diagenetic events, commonly occur. These also influence petrophysical characteristics

that develop, in addition to those arising as a consequence of primary depositional processes. Collectively, the ultimate petrophysical characteristics of a rock volume are determined by the combination of all of these effects (Pola et al., 2012; Aretz et al., 2015; Weydt et al., 2018a; Mordensky et al., 2018; Durán et al., 2019).

Several types of data (and sources thereof) may be considered and utilised to acquire and catalogue attributes describing the petrophysical properties of rock volumes. Principal amongst these are seismic data, well-log data, cuttings, core plugs and associated rock samples, thin sections, and well-test data. For seismic data, innovative seismic acquisition, processing and interpretation techniques can help to relate impedances, amplitudes and signal frequencies directly to facies types, petrophysical properties (e.g., porosity) or fluid content (Serra, 2008; Tiab et al., 2003; Cannon, 2015). However, the vertical resolution associated with this class of data collection is limited to an extent which usually exceeds the scale of significant lithological reservoir heterogeneities; for example, the vertical resolution of seismic reflection data is typically limited to no better than 20 m for conventional survey data (Xu, et al., 1992). Additional data from well-log analysis are usually required to attain information at the vertical resolution required for appropriate reservoir analysis at the scale of facies units (e.g., beds) and architectural elements (**Figure 4.1**). Well-logging techniques enable analysis of formations and reservoirs with a vertical resolution that can reach centimetric scales, depending on the type of tool and local environmental effects (Deutsch, 1992). An example of commonly employed and informative combination of wireline tools is the so-called Triple-Combo® (Schlumberger): gamma-ray, resistivity and neutron-density tools are commonly combined in an attempt to derive reliable petrophysical interpretations (Serra, 2008).

Estimates of the majority of petrophysical parameters can be obtained from well-log evaluation and through petrophysical interpretations that can be complemented by rock samples coming from analysis of core sections and rock cuttings. Properties from these sample sources are evaluated to gain an accurate understanding of different parameters (notably porosity, permeability, grain composition). Finally, well tests can provide valuable information related to the type of fluids filling the pore space, pressure, determination of fluid contacts and reservoir geometries (Tiab et al., 2003; Cannon, 2015). However, during exploration, appraisal or early stages of field

development, directly acquired petrophysical rock properties for the relevant target formations are commonly not available because appropriate and broadly distributed well data or core samples will have been acquired at these stages. As such, subsurface prediction commonly relies on analogue data from other sources (Serra, 1986; Colombera et al., 2012a; Cannon, 2018).

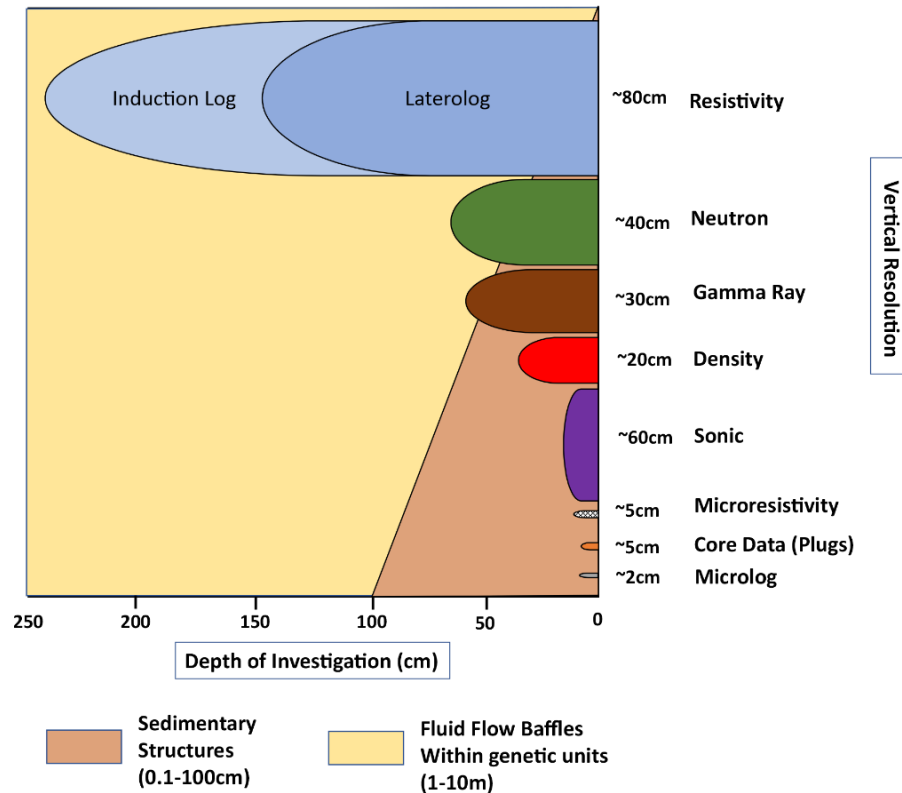


Figure 4.1. Horizontal and vertical depth of investigation vs sedimentary structures and fluid flow baffles within genetic units relationships.

Depth of investigation and vertical resolution of different petrophysical logs. The graph also differentiates the logs which will be able to resolve sedimentary structures and fluid flow baffles within genetic units (meso and microscale resolution). Petrophysical logs also can resolve many mega-scales features when entire sections (well log analysis) are evaluated, and interpretations can be delivered. Note that measures for core data (plugs) are restricted to the physical conditions of the plugs. Horizontal and vertical resolution can be enhanced if thin sections are obtained from them and hence being able to reach the micro-scales analysis.

Databases of geological analogues that can be applied to the characterisation of property models in data-poor contexts are useful to several industries and for different purposes (e.g., oil and gas resources, geothermal, mining, hydrogeology, carbon capture and storage – CCS) (Bär et al., 2020; Weydt,

et al., 2020). Specialised sedimentary analogue databases with which to assist particular aspects of reservoir characterisation already exist and are routinely applied in industrial workflows (e.g., the P3 – Petrophysical Property Database, Bar et al., 2019; the BritGeothermal database hosted by the British Geological Survey (BGS), or the National Geothermal Data System (NGDS) hosted by the United States Geological Survey (USGS)). However, there are currently no large-scale publicly available databases that bring together a large volume of analogue data on petrophysical properties in a way that enables such properties to be linked directly to fluvial lithofacies characteristics. Such a resource is of value as both a research tool and as a tool for subsurface evaluations by industry. Furthermore, existing published resources that attempt to relate rock properties, notably porosity and permeability, with fluvial facies characteristics are limited in their scale and scope. They are also commonly based on attributes that are poorly or inconsistently defined, else which draw upon data that are distributed over multiple sources. This has led to the following problems:

- the utilisation of generalised or assumed values, which are highly uncertain or unreliable, and which do not necessarily relate to posterior history matching records (Brierley, 1996);
- the need to obtain core data from the prognosed penetrations, acquisition of which is costly and also subject to high degrees of uncertainty as core data sample only a very small portion of the total reservoir volume of a target succession, and effectively do so only in one dimension (Miall, 2014).

Data corresponding to rock petrophysical properties of ancient and recent fluvial deposits are abundant in the published literature. However, relevant data tend to be dispersed across hundreds of publications, dissertations or reports, which makes data collection, standardisation and management challenging and cumbersome (Tarek, 2020). A recent study has determined that some industry geoscientists spend up to 80% of their working time on these routine tasks (CrowdFlower report, 2016). Also, data inconsistency, due to the existence of many types of datasets and the use of different nomenclatures, hinders comparisons between analogues and subsurface successions (Baas et al., 2005; Colombera et al., 2012a). Hence, sourcing and checking suitable analogue data is a very time-consuming process; as a result, geoscientists often use assumed or generalised datasets without necessarily appropriately considering uncertainties or geological

heterogeneities that may only have local expression (Bär et al., 2020). In addition, existing public-domain databases commonly include large amounts of data relating to petrophysical properties but for which only very limited metadata information is recorded alongside. This makes it difficult to extract other important information related to specific formations of interest, such as geological age, fluvial sedimentary architecture and palaeoenvironment (Vakarelov, et al., 2010).

The need to inform previously built facies models, such as those developed in Chapter 3, with meaningful petrophysical data has been the driver for the development of the Petrophysical Analogue Fluvial Database (PAFD) as part of this research. Moreover, a motivation beyond this scope exists and intends to fill a gap in geoscience: more informatively relating quantitative aspects of fluvial facies units with petrophysical parameters. PAFD mainly relates outcrop, core and well-log data associated with fluvial sedimentary deposits; it includes both hard and soft data for modern and ancient fluvial systems, obtained from public-domain sources (Figure 4.2).

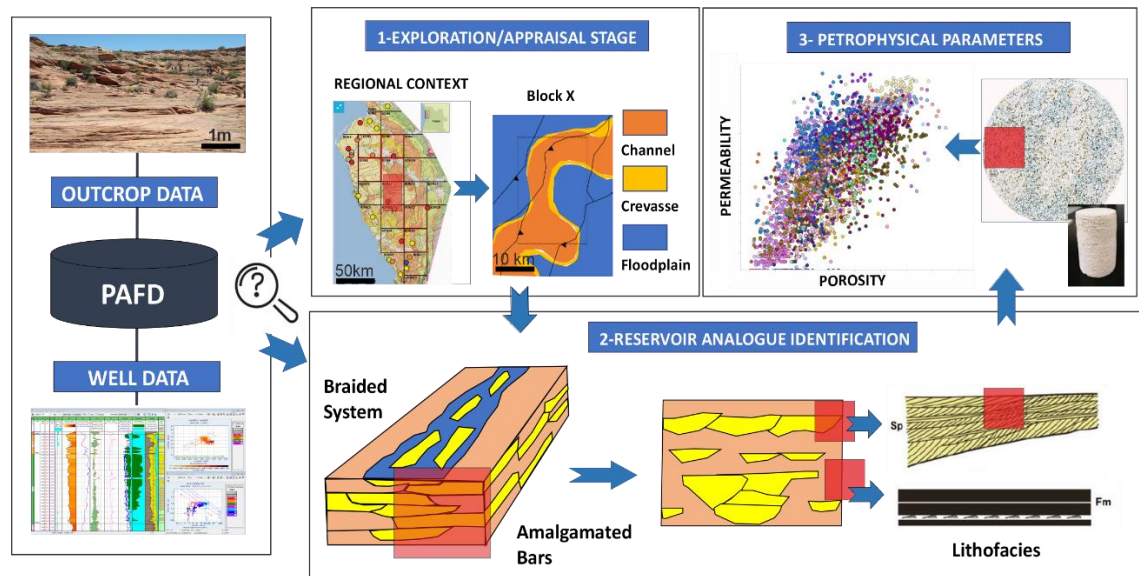


Figure 4.2. Flowchart indicating a representative workflow from which PAFD can be utilised.

PAFD includes outcrop and well data recordings (left-hand side of the image) and can be interrogated to retrieve regional and local information (1). Further filters can be applied to the database relating a specific fluvial depositional environment and corresponding lithofacies (2). Then, associated petrophysical parameters are delivered for different purposes (3). Sp and Fm lithofacies figure modified from Miall (1985).

PAFD incorporates more than 4,000 records associated with fluvial deposits. Porosity, permeability and other petrophysical parameters are related to numerous associated fields, such as sedimentary structure, petrographic composition, lithofacies type, parent architectural-element type, age of deposit, formative palaeoenvironment, and associated metadata.

Results delivered as the outcome of database queries can be used to gain improved understanding and address fundamental problems in reservoir analysis. PAFD can be employed to make better informed subsurface characterisations in cases where direct well-log data are not abundant or available (see **section 6.2**).

This study also finds inspiration from another class of sedimentary architectural database: FAKTS (Fluvial Architecture Knowledge Transfer System) of [Colombera et al., \(2012a\), \(2012b\); \(2013\); \(2017\)](#) and SMAKS (Shallow-Marine Architecture Knowledge Store) of [Colombera et al., \(2016\)](#).

4.2 Aim and Objective

The aim of Chapter 4 is to develop a database which relates fluvial characteristics associated to metadata, stratigraphy, petrography, facies classification, diagenesis and petrophysical properties and that can condition property models based on previously developed fluvial facies models. **Figure 4.3** displays a graphical visualisation of the steps performed to build the database. Specific objectives of this chapter are as follows: i) to explain and demonstrate the structure and design of the Petrophysical Analogue Fluvial Database (PAFD), ii) to illustrate the data standardisation procedure and entry routine and iii) to showcase the type and volume of data included in the database, notably in the form of plots of example outputs that demonstrate the usefulness and versatility of PAFD.

4.3 PAFD Structure and Content

At the time of writing, PAFD contains data from 48 case studies obtained from public domain sources, including different types of quantitative (hard) and

qualitative (soft) data. Numbers cited here and in the following text refer to the content of the database at the time of writing of this chapter (July 2023).

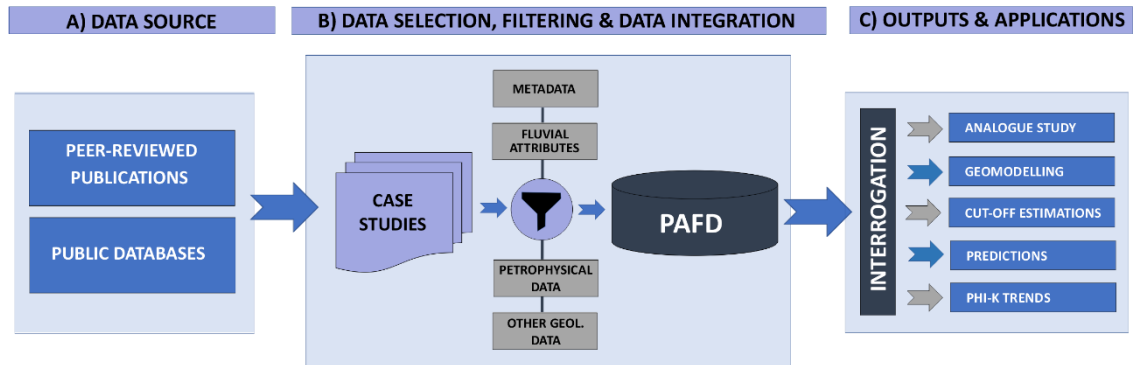


Figure 4.3 Graphical chart. Database build

Graphical visualisation of the steps performed for the building of PAFD and some of its more important applications. Three stages are identified: (A) Data Source, where the information included in the database is derived; (B) Data Selection, Filtering, and Data Integration, which include the section where the case studies are prepared to finally be included with the database; and (C) Outputs and Applications of the database after of interrogation.

Key data were extracted from fluvial successions studies. All data extracted from the 48 examined case studies were retrieved from different peer-reviewed publications and public databases. For those case studies whose data source belonged to databases, the information was extracted from Well Completion Reports. The data from the 48 case studies were collected and classified in a manner that promotes accurate recording of rock properties related to specific fluvial system units complemented by metadata. To achieve this, PAFD has been standardised using a common nomenclature that assists in the filtering of rock properties based on different attributes describing the successions and their formative fluvial systems. For ease of use, PAFD is here presented as a Microsoft Excel spreadsheet, but it could readily be structured as a relational database. However, overall, this investigation has no requirement for a more sophisticated tool (see discussion in Chapter 6. **Section 6.2**). Spotfire® software was used for both data analytics and data visualisation purposes.

The spreadsheet includes 4,262 records or entries (rows) and 75 columns organised in three hierarchy levels (see **Figure 4.4**):

- **Groups.** The groups relate to the highest rank of the hierarchy. There are seven groups in the database. Each of them including several subgroups. To facilitate the rationale of the database to the reader, groups are indicated capitalised in this manuscript (e.g., Metadata).
- **Subgroups.** Subgroups are single columns in the database (71 in total), which record major characteristics for the rock samples represented by categories. Subgroups are displayed capitalised and in italics style in this text (e.g., *Lithology*).
- **Categories.** Categories correspond to the lowest hierarchy level in the database; they record information referring to different attributes. They are shown with quote marks and italics in this document (e.g., “*core-plug data*”).

4.3.1 Metadata

PAFD includes meta-information, which is used to enable data filtering according to the context, type and quality of the data. The metadata group of fields includes information regarding the nature of the data dividing the entries into 9 subgroups: *References*, *Sample Source*, *Data Types*, *Type of Analysis*, *Well Name*, *Field Name*, *Latitude and Longitude*, *Country* and *Basin Name*.

4.3.2.1 References

The *References* subgroup stores the bibliographic reference of the peer-reviewed publication from where the source data were extracted, else a URL link to the data source itself. The references included in this subgroup correspond to the 48 case studies included overall. This subgroup includes bibliographic references extracted from public domain sources (**Figure 4.5**).

4.3.3.2 Sample Source

The subgroup *Sample Sources* specifies the particular type of data presentation in the original data source from which data were extracted. Types of data included are from sources that take several forms: i) tabulated statistical summaries or “*tables*” (e.g., maximum, minimum, average total porosity). ii) “*logplot scanned*” that have been digitised or from which porosity values can be read directly for specific depth points. iii) “*Xplot scanned*” where relationships can be acquired (typically with values relating to porosity vs permeability) and “*boxplot scanned*” (**Figure 4.6**).



Figure 4.4 PAFD (Petrophysical Analogues Fluvial Database) Structure Table

PAFD includes 7 major groups (capitalised names) displayed by different colours. Associated subgroups (capitalised and italic style) are summarised in this table and are described in detail in the subsequent sections, as are the various categories (sentence-case names) included in each subgroup.

The majority of data in PAFD were extracted from scanned sources (cross-plots, logplots and boxplots) (**Figure 4.6**). The open-source software DataThief® was used to digitise this data from different type of plots. This was a semi-manual process whereby plots were first cropped from the data source, then fitted to specific “x” and “y” scaled axes; data included in the cross-plots, boxplots, logplots, etc were then picked individually. Checks were made for data integrity as each record was acquired.

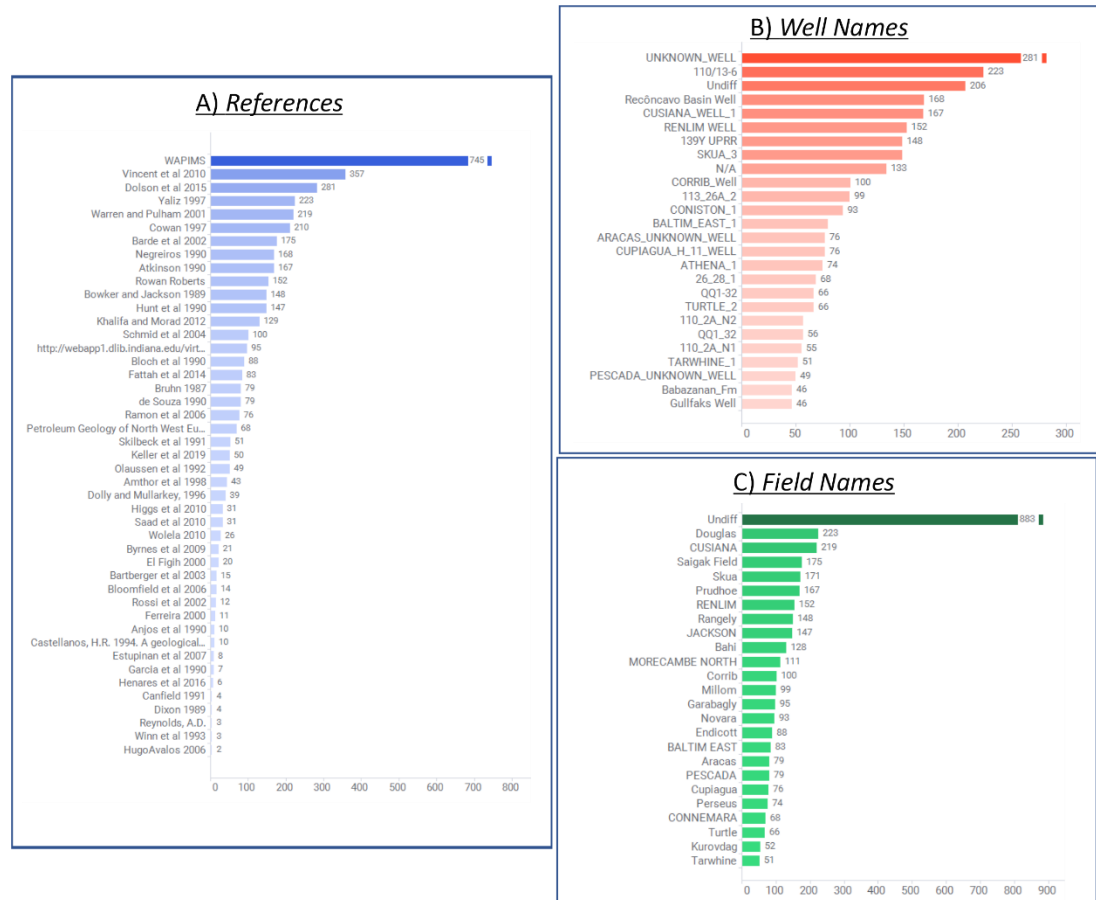


Figure 4.5 Metadata. References, Well Names and Field Names

(A) List of all bibliographic references that contribute more than one entry in the database. (B) The 20 well names that contribute the largest number of entries in the database. (C) The 20 field names that contribute the largest number of entries in the

4.3.3.3 Data Types

Each entry is classified in terms of data types, an attribute that takes one of two categories: i) “*outcrop*” (3.1%, 134 entries) and ii) “*well*” (>96.9%, 4,128 entries) (**Figure 4.6**).

4.3.3.4 Type of Analysis

Both outcrop data and well data are associated with different types of analysis. These types are described by an attribute that takes one of the following categories: i) “*core data (plug)*”, for data acquired via analysis of plugs coming from core data; ii) core data from undifferentiated type of analysis (“*core undiff*”); iii) “*log analysis*”; iv) “*sidewall core*”; v) “*thin section*”. Undifferentiated types are also recognised in the database with the category of “*undiff*” (**Figure 4.6**).

The “*core data plug*” and “*core undiff*” data categories incorporate data derived from recovered core sections, to enable thorough geological analysis over a specific cored interval. These core plugs provide information at a microscopic scale (grain and pore size) and allow different types of analysis that can be conducted from plugs, notably Routine Core Analysis (RCA), and Special Core Analysis (SCAL) (Dolson, 2016). Routine Core Analysis and Special Core Analysis samples are classified in the “*core data (plug)*” data category in this database. Where no indication is provided regarding the type of analysis conducted on a sample, database entries are classified as “*core undiff*” (core data from undifferentiated type of analysis).

Retrieved core data may also incorporate erroneous readings due to recovery issues (Hovadik and Larue, 2007). Samples can be damaged due to the release of stresses after their extraction from the barrels and the type of processing (cleaning, drying, etc) they endure in the lab. These data are not always removed from datasets, but an attempt has been made in this study not to include data that are clearly associated with damaged plugs. This check has been implemented by eliminating core data from larger sample sets where such data values represent clear outliers with respect to a trend observed in available properties (e.g., regression line of porosity versus permeability). The deleted outliers were related with different types of issues: broken plugs, wrong calculated log outputs associated with environmental raw logs issues, etc.

The “*log analysis*” data category identifies database entries whose values result from well-log analysis coming from wireline logging or logging-while-drilling operations (LWD). Well-log analysis allows geoscientists to fill the gap represented by the lack of representative rock samples and they are obtained

from raw electrical data (Serra, 2003). The “*sidewall core data*” category refers to those samples extracted from the walls of the borehole with the aid of a rotary or a bullet core barrel, which runs with a wireline (obtained after drilling). They can be located to an accurate depth, and they are smaller samples than those retrieved by core barrels (Tiab et al., 2003). The category “*thin-section*” corresponds to the quantitative estimations by modal analysis obtained from the microscopic examination of sedimentary-rock composition, texture and structure. In the case of porosity, the point-counting technique is commonly applied for at least 300 counted points per thin section. The “*core plug*” data and the “*core undiff*” categories correspond with the bulk of entries in the database adding up to nearly 75% of the total number of samples (3,122 entries in total) in the database.

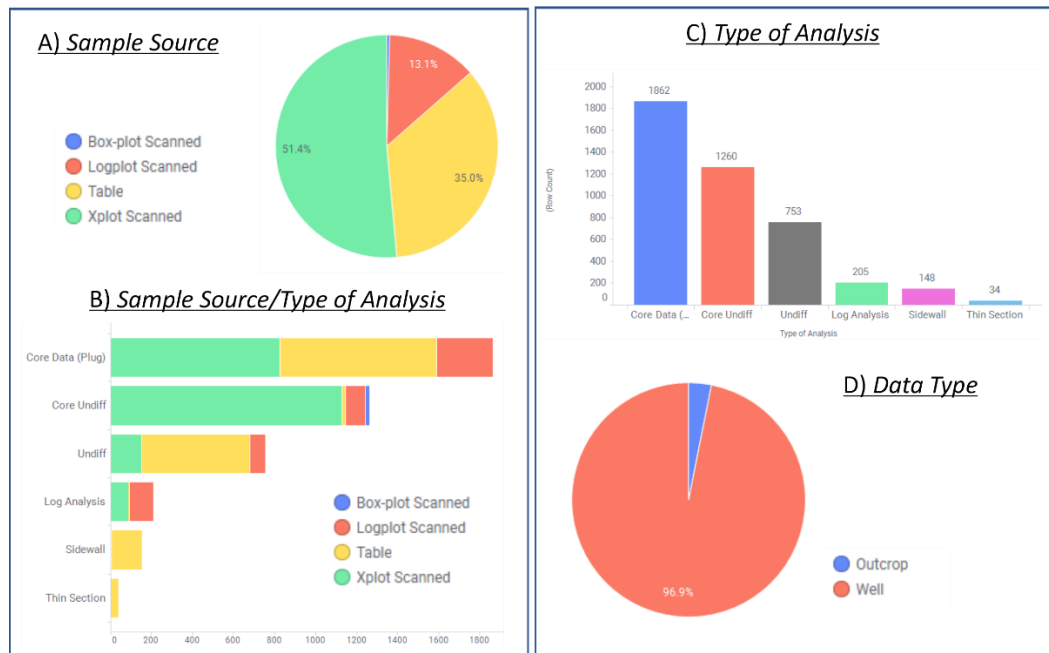


Figure 4.6 Sample Source, Type of Analysis and Data Type charts

(A) Pie chart indicating the volume for the four categories included in the *Sample Source* subgroup as percentages. (B) Bar chart showing a data count for the *Sample Source* stacked to the *Type of Analysis* categories. (C) Bar chart showing the categories associated to the *Type of Analysis* subgroup where core data is indicated as the most abundant category in the database. (D) Pie chart indicating that most of the data is included in the “*well data*” category: (>96%) in the database.

4.3.3.5 Well Name

The *Well Name* subgroup indicates the name of the well to which corresponding samples are associated. The nomenclature of the well name in

this database follows the “common well name” format (also called “popular name”). In those cases where the “common well name” is not mentioned by the original authors, the numeric designated naming for that specific area/basin/territory is included (e.g., Common well name: Titan or 34/8-13A). A total of 568 wells are included in the database. An “*unknown-well*” category is assigned for wells that have no name associated with them (**Figure 4.5**).

4.3.3.6 Field Name

For entries that correspond to subsurface successions, the corresponding field name where the specific well is located is included in the dataset. PAFD includes a total of 125 fields (**Figure 4.5**).

4.3.3.7 Latitude and Longitude

The *Latitude and Longitude* of each sample is included where possible. For entries of unknown coordinates, this field is left empty to indicate a NULL value. The position of the samples in terms of longitude and latitude are given in decimal degrees and relative to the reference system WGS84. **Figure 4.7** displays the position of the well data and outcrop data included in the database. It is noteworthy that PAFD was designed to include well and outcrop data that are spread geographically wide, whilst also covering the main basin types and important geological provinces associated with fluvial systems around the world.

4.3.3.8 Country

The recorded sample data originate from 22 countries, of which Australia, the USA and the United Kingdom are the top three contributors; collectively these three countries account for 73% of samples (3,122 out of a total of 4,262 entries or records) included in the database (**Figure 4.7**).

4.3.3.9 Basin Name

Samples included in PAFD are from a total of 76 sedimentary basins associated with hydrocarbon plays and linked to fluvial reservoir successions. The most important basins in terms of number of entries included in the database are the Irish Sea basin (United Kingdom), South Caspian basin (Azerbaijan) and Los Llanos basin (Colombia) (**Figure 4.7**).

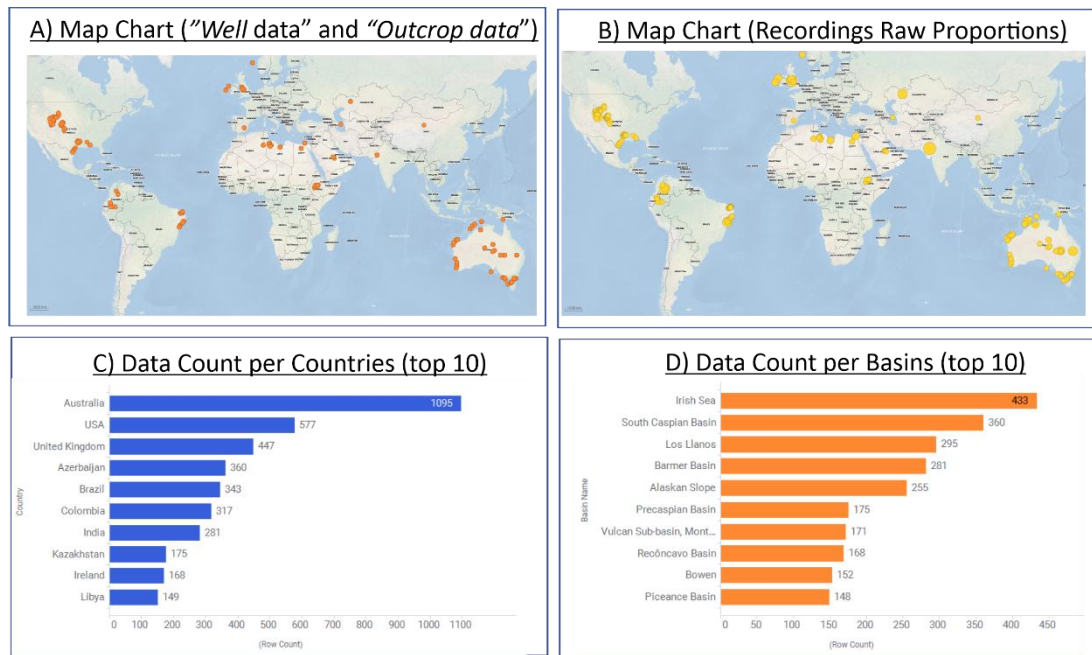


Figure 4.7 Wells/Outcrops count and map location charts

(A) Map chart indicating the geographic location for the different dataset (well and outcrop data) included in the database. (B) Map chart displaying various spot sizes proportional to the sample size associated to different geographic locations (C) Bar chart indicating the data count of the 10 countries contributing with the largest amount of data. (D) Bar chart indicating the data count of the 10 basins contributing the largest amount of data.

4.3.2 Stratigraphy

In the Stratigraphy group of data fields, the data are organised in order and relative position of strata, and their relationship to geological timescales (Miall, 2016; Brookfield, 2008; Sheets et al., 2002). The different entries included in PAFD are classified in terms of chronostratigraphy, and lithostratigraphy.

4.3.2.1 Chronostratigraphy

Geological age is recorded in terms of chronostratigraphic divisions (*Era*, *Period*, *Epoch* and *Stage*). PAFD stores chronostratigraphic attributions as reported in the evaluated publications. The 2021 chronostratigraphic chart made by the International Commission on Stratigraphy has been utilised as a reference for assigning chronostratigraphic classes in the database (Figure 4.8).

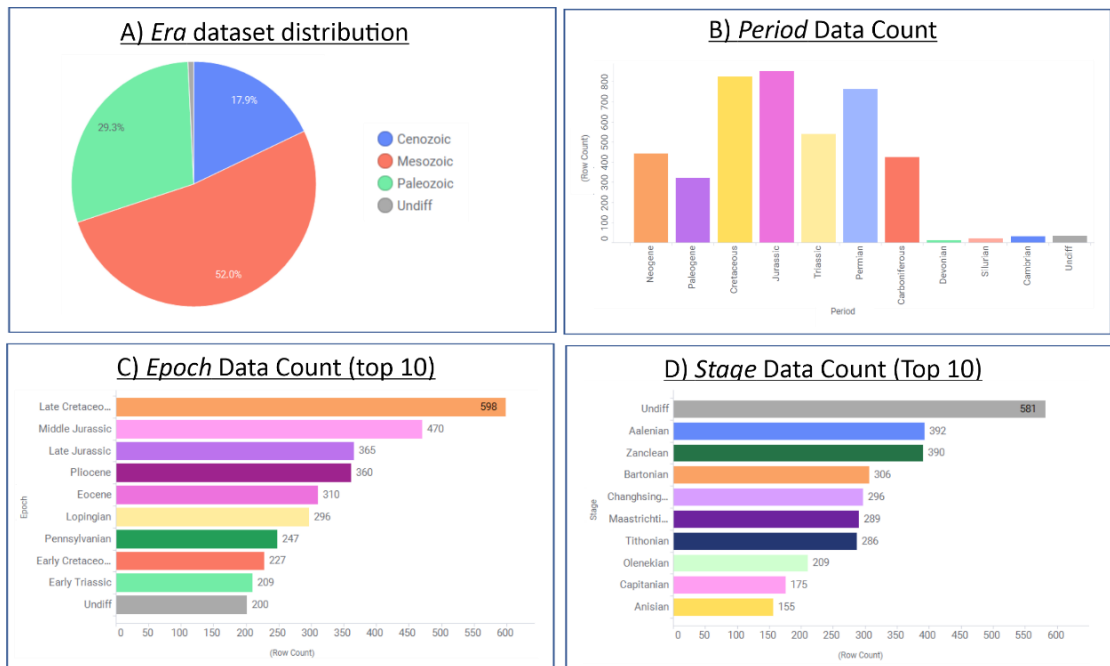


Figure 4.8 Era, Period, Epoch and Stage charts

(A) Pie chart indicating the *Era* subgroup distribution in the database. (B) Bar chart showing a data count for the *Period* subgroup and its respective subdivisions organised by geological chronology. (C) Bar chart indicating the data count distribution for the top 10 *Epoch* subdivisions in the database. (D) Bar chart indicating the data count of the top 10 *Stages* subdivisions included in the database.

4.3.2.2 Lithostratigraphy

Lithostratigraphic nomenclature for each entry is recorded in PAFD including the following subgroups: *Group*, *Formation*, *Member* and *Informal Units* names. **Figure 4.9** shows the number of entries corresponding to the 20 formations yielding most entries in the database.

4.3.3 Basin Classification

The Basin Classification group classifies sedimentary basins according to tectonic processes and settings (Ingersoll and Busby, 1995). In PAFD, these are characterised with respect to i) *Relative Plate Movement*, ii) *Basin Type* and iii) *Primary Tectonic Forces Type*.

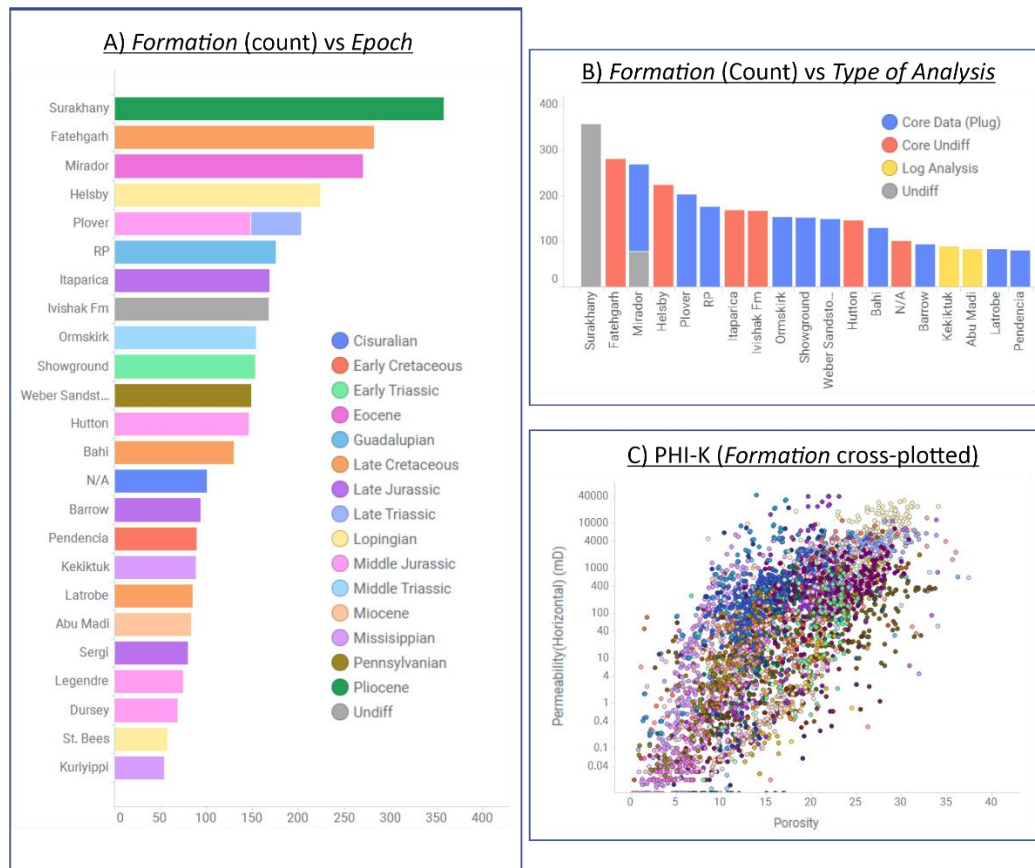


Figure 4.9 Formation Rocks count in the database

(A) Bar chart including a count for the 25 *Formation* rocks more numerous in the database. The chart stacks the corresponding *Epoch* categories for each of the formation rocks in the chart. (B) Chart including the 20 most numerous formation rocks stacked to the *Type of Analysis* subgroup. Most of the data included for this *Formation* rocks were extracted from “core data (plug)”. (C) Porosity-Permeability cross-plot with colour-coded scheme representing each of the formation rocks that include porosity and associated permeability records in the database (3,809 recordings) Each colour in (C) represents the 102 formation rock names included in the database.

4.3.3.1 Relative Plate Movement

The subgroup *Relative Plate Movement* describes plate kinematics in five different categories: “*divergent*”, “*intraplate*”, “*convergent*”, “*transform*” and “*hybrid*” settings. The “*divergent*” setting relates to active (mantle-convective-drive) or passive (lithospheric-driven) rifting processes (Sengor and Burke, 1978). If divergence continues further beyond the initial rifting stage, an oceanic basin paired with intraplate margins will be generated, in a rift-to-drift transition process (Dickinson, 1974b; 1976a; Ingersoll, 1988; Bond et al., 1995; Ingersoll and Busby, 1995). In other cases, “*convergent*” boundaries are associated with two or more lithospheric plates colliding against each

other leading to the formation of mountain ranges and depressed forelands (Dickinson and Seely, 1979; Dewey, 1980). “transform” boundaries develop in strike-slip contexts where two plates move laterally relative to each other along the plate boundary; a subordinate component of vertical motion may occur as well (Dickinson, 1974a). “hybrid” settings correspond principally to those of reactivated fossil rifts in orogenic belts (Ingersoll and Busby, 1995). **Figure 4.10** shows a pie chart and a data count for the distribution of these five categories, of which the “divergent” category includes ~45% of the entries in the database. Another category “undiff” is included in the database for those undifferentiated entries which cannot be related to any of the above-described categories.

4.3.3.2 Basin Type

The subgroup *Basin Type* follows the classes described by Ingersoll and Busby (1995). A total of eight categories are recorded: “terrestrial rift valley”, “intracratonic basins”, “continental embankment”, “dormant ocean”, “foreland”, “back-arc”, “transtensional”, “transpressional” and “aulacogens” (**Figure 4.10**).

For divergent settings, the only category included is that of the “terrestrial rift valley”, corresponding to elongated- linear shaped lowlands or troughs formed by subsidence due to extensional tectonics. This classification includes grabens and half-grabens. For “intraplate” settings, PAFD includes three categories: “intracratonic” basins represent the surface expression of failed rifting (Sengor, 1995) and other mechanisms of subsidence generation, such as dynamic topography or thermal relaxation; “continental embankments” exist where the shelf edge has prograded over oceanic crust because the maximum sediment thickness allowed by isostatic loading has been reached inland of the shelf edge (Kinsman, 1975); and “dormant ocean” basins are floored by oceanic crust that is neither spreading nor subducting (Ingersoll and Busby, 1995). Basins from convergent settings are represented in this database by “foreland” basins and “back-arc” basins. Foreland basins are characterised by relatively low-relief regions adjacent and parallel to mountain ranges, resulting from lithospheric flexure driven by crustal thickening and loading.

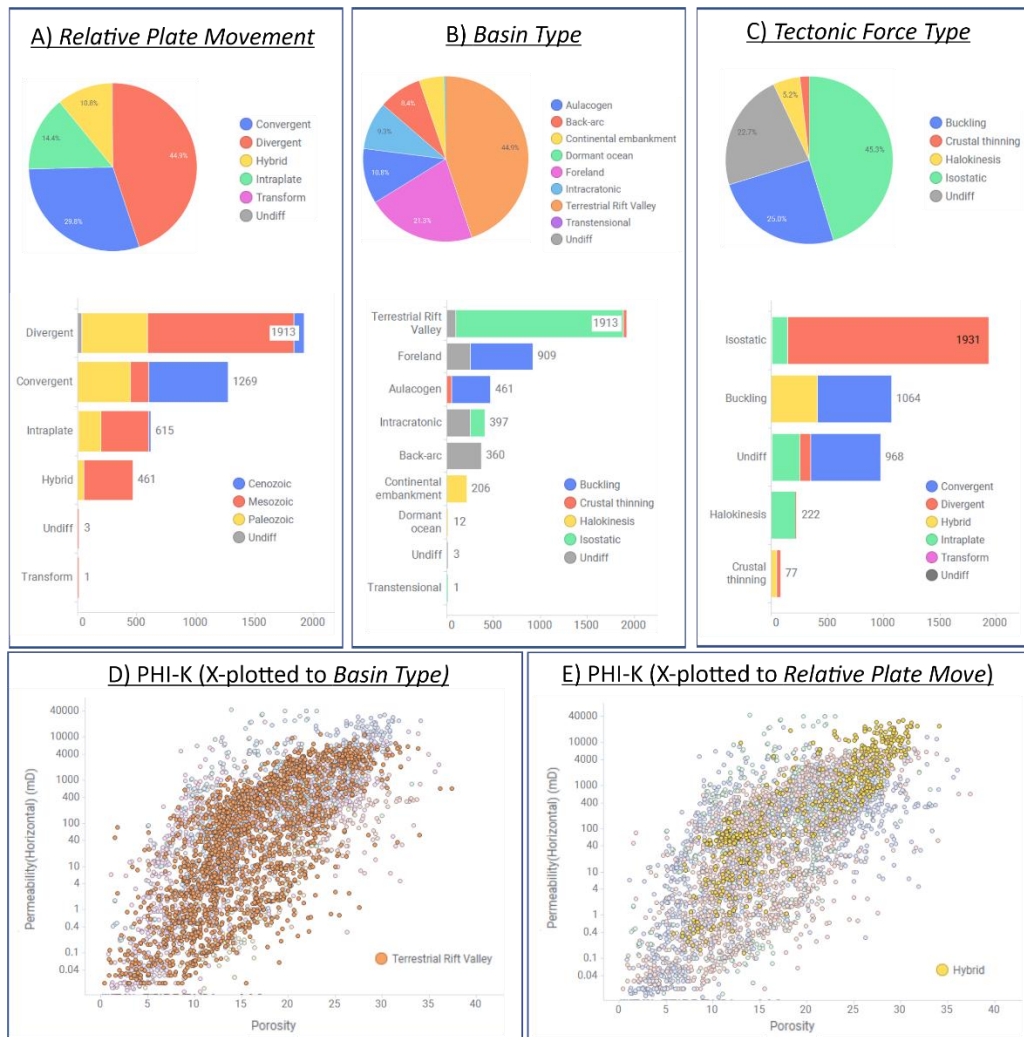


Figure 4.10 Relative Plate Movement, basin Type and Tectonic Force type charts

(A) Pie chart including the *Relative Plate Movement* categories proportions and a bar chart with the *Relative Plate Movement* categories stacked to the *Period* categories. (B) Pie chart showing the category proportion regarding the *Basin Type* subgroup and a bar chart for the *Basin Type* stacked to the *Tectonic Force Type* categories. (C) Pie chart including the *Tectonic Force Type* proportions and a stacked bar chart for *Tectonic Force Type* and *Relative Plate Movement*. Finally, two cross-plots for porosity and permeability showing the “terrestrial rift valley” category (D) and the “hybrid” tectonic force type in (E) over the entire data population included in the database (greyed out points).

“back-arc” basins are island arcs associated with subduction zones and resulting from tensional forces caused by oceanic trench rollback and the collapse of the edge of the continent (Ingersoll and Busby, 1995). In transform settings, basins can be “transtensional” or “transpressional”, if extensional or compressional components of motion respectively exist (Ingersoll and Busby, 1995). “aulacogens”, associated with failed rift branches in triple junctions, are

basins that belong to hybrid settings where former failed rifts were reactivated during convergent tectonic events (Ingersoll and Busby, 1995). Entries associated with the “*terrestrial rift valley*” category are the most numerous in the database; they account for ~45% of the total number of samples. An additional category for unknown basin types is recorded in the database with the name of “*undiff*”.

4.3.3.3 Primary Tectonic Force Type

The subgroup for *Primary Tectonic Forces Types* specifies the dominant processes that acted to drive the formation of the basin. Four categories are recorded in PAFD; these summarise the dominant tectonic process at the time of deposition of relevant sedimentary units. i) “*isostatic forces*” causing regional lithospheric flexure due to sedimentary, eustatic and tectonic loading; ii) “*lithospheric buckling*” driving the creation of highlands and lowlands near convergent margins; iii) “*halokinesis*” due to the presence of mobile evaporites in the subsurface causing the formation of localised depocentres; and iv) “*crustal thinning*” induced by stretching, erosion, and magmatic withdrawal (Ingersoll and Busby, 1995).

4.3.4 Petrography

In the Petrography group, attributes regarding the mineral content and textural relationships for each of the rock samples in PAFD are delivered in five subgroups: *Lithological Classification*, *Grain Size*, *Sorting*, *Roundness*, and *Maturity*.

4.3.4.1 Lithological Classification

The classification method adopted in PAFD is the approach developed first by Pettijohn et al., (1973), itself modified from Dott (1964) and Folk (1968); it enables lithotype classification based on proportions of quartz, feldspars and lithic fragments, with a variable mud component in the rock matrix. Sandstones are classified according to seven categories, which refer to the proportions of quartz, feldspars and lithic component in the rock matrix (QFL). These are the: “*quartzarenite*”, “*sublitharenite*”, “*litharenite*”, “*quartzarenite/subarkose*”, “*subarkose*”, “*subarkose/arkose*” and “*arkose*”. A category for those samples which do not have associated petrographical data were classified as “*undiff*” (Figure 4.11).

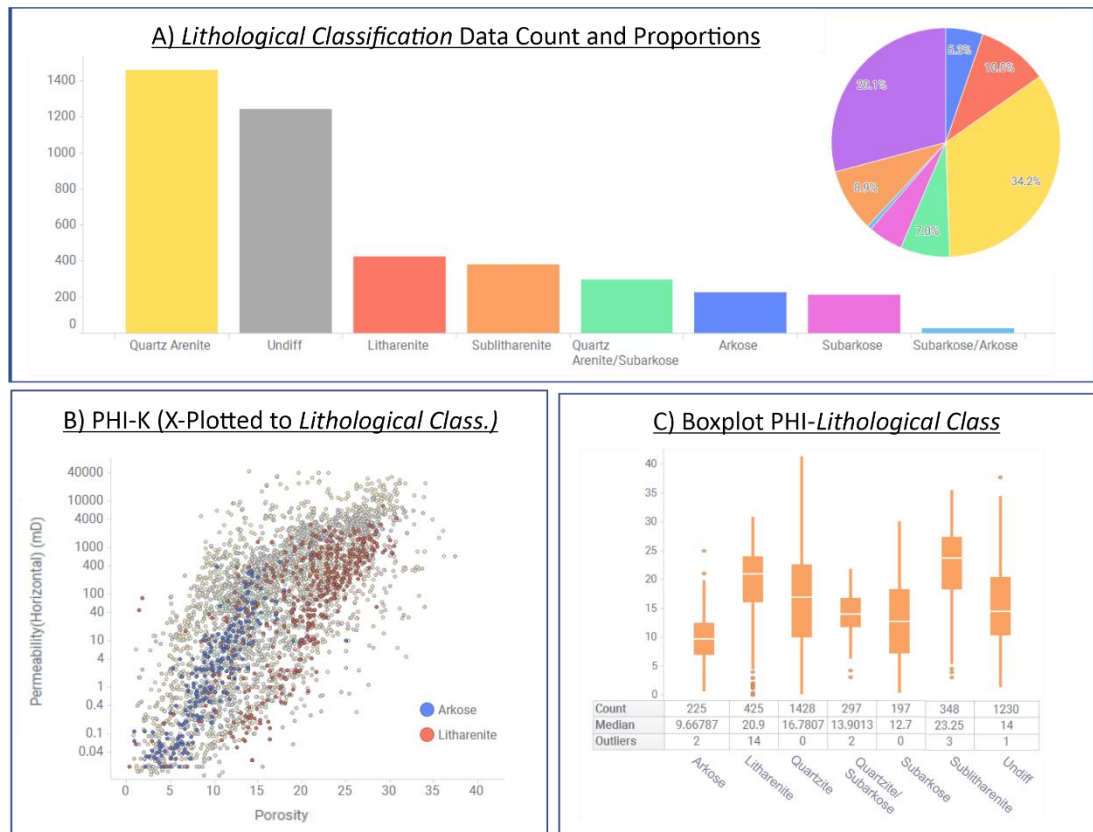


Figure 4.11 Lithological Classification charts

(A) Bar chart and pie chart showing a data count and proportions for the *Lithological classification* subgroup and its respective categories. (B) Porosity and permeability cross-plot highlighting the “arkose” and “litharenite” categories over the rest of porosity and permeability recordings including in the database (greyed out points). (C) Boxplot displaying the statistical distribution for all categories in the *Lithological Classification* subgroup.

4.3.4.2 Grain Size

Sediment texture is represented by the shape and size of sediment grains, and their degree of sorting. Textural parameters are important because they directly influence the following traits: i) the porosity, ii) the size of the pores and connecting pore-throats (tortuosity), which also influences the permeability, and iii) the fluid saturation. In the database, grain size is classified based on the [Wentworth \(1922\)](#) scale. PAFD separates samples in two subgroups: i) samples where an average grain size has been assigned; and ii) samples where a range of grain sizes is given. For the first subgroup *Grain Size* the following categories are identified: “clay and silt”, “very fine”, “fine”, “medium”, “coarse”, “very coarse” and “granule”, where the various fine, medium, and coarse classes refer to sand. A category for those samples where no average grain size has been identified by the authors is recognised

as “*undiff*” (undifferentiated). For the samples where a “*range*” of grain sizes has been recognised by the authors in the data source, the database includes two columns for the “*minimum grain size*” and the “*maximum grain size*” where these specific grain sizes are included. (**Figure 4.12**).

4.3.4.3 Sorting

Grain sorting, describing the variance in particle sizes present in a sediment sample, is classified with the following categories: “*well sorted*”, “*moderately to well sorted*”, “*moderately sorted*”, “*moderately to poorly sorted*”, and “*poorly sorted*” following the definition summarised by Tucker (1996). A category for undifferentiated types of sorting is also available (“*undiff*”). All categories included in this subgroup correspond to averages of sorting described by the authors in their publications referring to specific formation rocks but also to deterministic points where core data was obtained, and plugs were evaluated. **Figure 4.12** includes a pie chart where the proportions of sorting categories in the database are displayed.

4.3.4.3 Roundness

Roundness, referring to the degree of smoothing due to abrasion of sedimentary particles, is also recorded. Although roundness can be quantified, for practical reasons, roundness is only classified in seven categories: “*angular*”, “*subangular*”, “*subrounded*”, and “*well rounded*” (Folk, 1974), plus the categories “*subangular to subrounded*”, “*subrounded to rounded*” and undifferentiated roundness (“*undiff*”) (**Figure 4.12**).

4.3.4.3 Maturity

Sediment maturity is described by means of a single attribute that accounts for both compositional and textural maturity of the grains (this study does not further consider compositional maturity); two categories are used: i) “*mature*” where the grains in a sediment are well-sorted and well-rounded due to weathering or abrasion during transport (mature texture) and including stable minerals and components (e.g., quartz), and ii) “*immature*” where grains are, on the contrary, not well-round and not well-sorted, and are composed of a more diverse mineralogical composition (**Figure 4.12**).



Figure 4.12 Petrographic charts

(A) Bar chart displaying the count for each of the categories included in the *Grain Size* subgroup. A pie chart also shows the statistical proportions in the database. (B) A bar chart and a pie chart showing both a count and proportions for all *Sorting* categories within the database. The *Grain Size* subgroup includes the “*range*” category which stands for almost 1,000 entries which include a minimum and a maximum range for grain sizes. (C) Indicates a data count (bar chart) and proportions (pie chart) for the *Roundness* subgroup. Important to highlight the “*undiff*” category was removed from the chart as it represents 86.5% from the total of entries. (D) Similar to (C) shows a data and proportions count for *Maturity* categories where the “*immature*” and “*mature*” categories more than 400 entries.

4.3.5 Fluvial System Classification

The sedimentary units resulting from the deposition of sediments in fluvial systems determine the dimensions, connectivity, spatial variability, and

internal heterogeneities giving rise to the petrophysical properties of reservoir rocks (Jackson, 1976). PAFD contains the following classifications for fluvial systems: *Geomorphic Setting I*, *Geomorphic Setting II*, *Depositional Environment*, *Dominant Process Influence*, *Dominant Formative River Planform*, *Depositional Elements*, *Channel Association*, *Channel Body Type*, *Architectural Elements*, *Lithofacies*, *Discharge Regime* and *Climate*.

4.3.5.1 Geomorphic Settings I

PAFD separates settings based on dominant geomorphic fluvial processes, leading to the formation of “*mobile channel-belts systems*”, “*fixed channels*” or “*poorly channelised systems*” and “*non-channelised bodies*”. The database also includes a category for those undifferentiated categories (“*undiff*”). This characterisation of geomorphic settings has been recognised by different authors (Friend, 1983; Alexander, 1993; Gibling, 2006) (Figure 4.13).

The “*mobile channel belts systems*” category refers to fluvial systems which exhibit features arising from and related to systematic lateral migration of channels and associated repeated avulsion processes. They are commonly associated with superimposed channel-belt components that progressively develop across alluvial plains because of avulsion processes. Braided systems and meandering rivers with a certain degree of amalgamation of channel segments and clearly defined lateral accretion sets are included in this group (Gibling, 2006; Miall, 2014). On the contrary, the “*fixed channels or poorly channelised systems*” category refers to those samples in the database associated to a more laterally stable behaviour between episodes of abrupt switching where laterally accreted sets typically can be followed only a few meters to a few tens of meters (Friend, 1983) and those channel systems including a high proportion of sandy sheetflood deposits. An example of systems included in this group can be the distributary channels associated to a delta or an alluvial fan (Gibling, 2006). The “*non-channelised*” category corresponds to those samples deposited as a results or short-lived events of rapidly flowing water. It spreads sediments in a sheet-like continuous surface over an area that expands beyond the channel banks (Miall 2014).

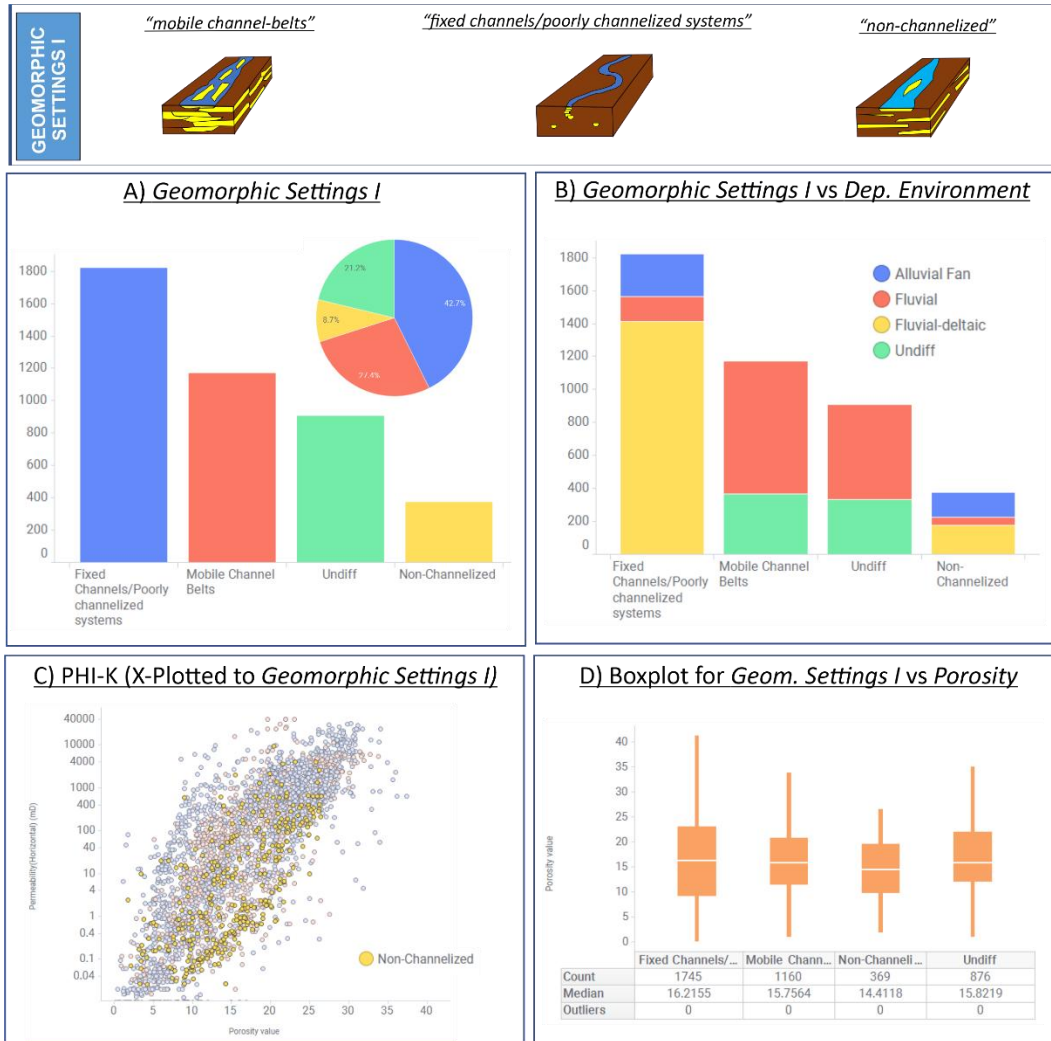


Figure 4.13 Geomorphic Settings I Charts

Upper part of figure shows a graphical representation for the 3 categories included in the *Geomorphic Settings I* subgroup (“*mobile channel-belts*”, “*fixed channels/poorly channelised*” systems and “*non-channelised*”). (A) A chart indicating a data count and a pie chart displaying proportions for each of the categories in the *Geomorphic Settings I* subgroup. (B) shows a stacked bar chart that shows the *Geomorphic Settings I* categories against the *Depositional Environment’s* categories. Important to highlight the big amount of “*fluvio-deltaic*” categories associated to the “*fixed/poorly channelised systems*” included in the database. (C) A cross-plots for porosity and permeability highlighting the “*non-channelised*” categories over the entire dataset in the database (greyed out points) (D) a boxplot showing the porosity statistical distribution for the four categories in the *Geomorphic Settings I*.

4.3.5.2 Geomorphic Settings II

The *Geomorphic Settings II* subgroup expand on the characteristics included in the previously described three categories within the *Geomorphic Settings I* subgroup. It includes more information by subdividing different classes for the

“mobile channel-belt” and the “fixed channels or poorly channelised systems” in the *Geomorphic Settings I* classification. With regards to the “mobile channel-belt” systems, the *geomorphic settings II* group includes two categories. These are: “low sinuosity” and “high sinuosity”. Both categories referring to the ratio of stream length with respect to valley length (straight-line length). Supporting the “fixed channels or poorly channelised systems” in the *Geomorphic settings I* subgroup, two categories are included. These are i) “Distributive channel” referring to those elongated, typically sinuous channel bodies with distributary patterns branches flowing away from a main river channel. Distributive channels can be related to different depositional environments (alluvial fans, delta, etc). ii) “fixed channels” referring samples that include channel bodies associated with isolated ribbon shapes (Gibling, 2006). The remaining entries in the database for this group are associated with “non-channelised” categories in the previous “*Geomorphic Settings I*” subgroup. These are the samples included in the “crevasse/avulsion elements” which refer to those overbank deposits, such as crevasse splays, that occur in response to flood events (which may display convex-upper surfaces), floodplain channels taking place as a single-event fills (in response to unconfined sheet-like flooding events), and channels being emplaced within otherwise aeolian-dominated settings. The database also includes a category for undifferentiated entries (“undiff”) (Figure 4.14).

4.3.5.3 Depositional Environment

The database contains three categories for classifying the depositional environment of fluvial-alluvial deposits: “fluvial”, “fluvio-deltaic” and “alluvial fan” (Figure 4.15). An additional category for undifferentiated (“undiff”) depositional environments is also included in the database. The “fluvial” category corresponds to sediments deposited by the flowing water of a stream channel in a subaerial plain. This occurs most obviously where a river loses energy and therefore cannot continue to carry the material it is transporting. Most rivers repeatedly entrain and deposit solid particles of rock and soil over their bed throughout their course (Nichols, 2009). The “fluvio-deltaic” depositional environment refers to the sediments deposited in a subaerial fluvial plain, coupled to a subaqueous delta. The deposition occurs chiefly by distributary channels that discharge into a body of standing water. The process can take place in a sea, permanent lake (fluvio-lacustrine) or into an ephemeral desert (playa) lake (Orton and Reading, 1993; Allen, 1978; Shiers et al., 2014).

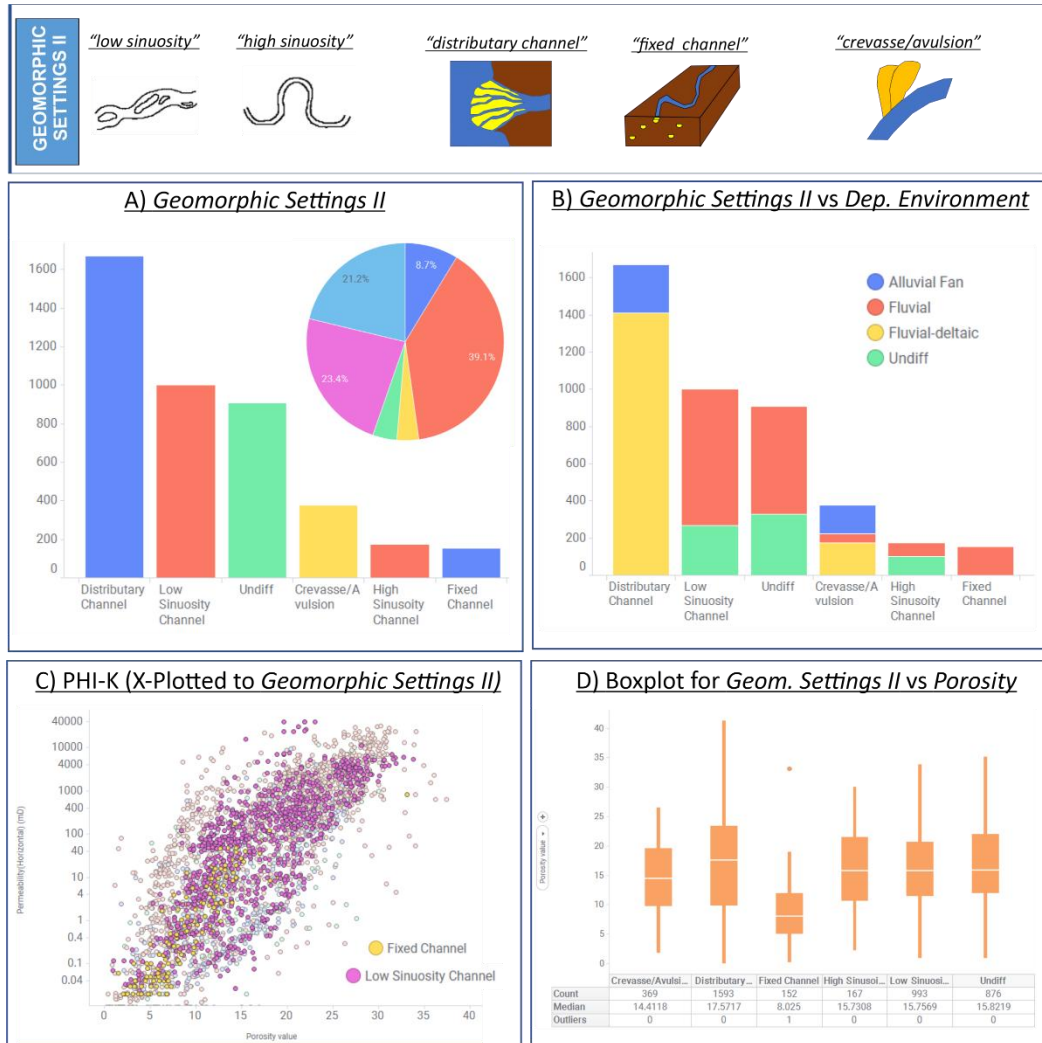


Figure 4.14 Geomorphic Settings II Charts

The *Geomorphic Settings II* categories are graphically represented in the upper part of the figure. (A) bar chart and pie chart representing both a count for entries included assigned to each category within the *Geomorphic Setting II* subgroup. (B) Bar chart showing the *Geomorphic Settings II* categories stacked to the *Depositional Environment* categories. (C) A cross-plot for porosity and permeability highlighting the trends defined by the “*fixed channel*” and the “*low sinuosity channel*” categories. (D) A Boxplot indicating the porosity distribution for the various *Geomorphic Settings II* categories.

Another important depositional environment included in the dataset is “*alluvial fans*” where alluvial (e.g., debris flows) and fluvial facies are deposited associated with distributive channels accumulating sediments that typically form fan-shaped (triangle-shaped) bodies. The deposition in this type of environment takes place in alternating streamflow processes with mass flow events resulting from ephemeral and flash flow events that lead to poor organisation of the sedimentary facies (Moscariello, 2020). **Figure 4.13** and

Figure 4.14 show examples of notable relationships of the depositional environment cross plotted to the *Geomorphic settings I* and *II* subgroups.

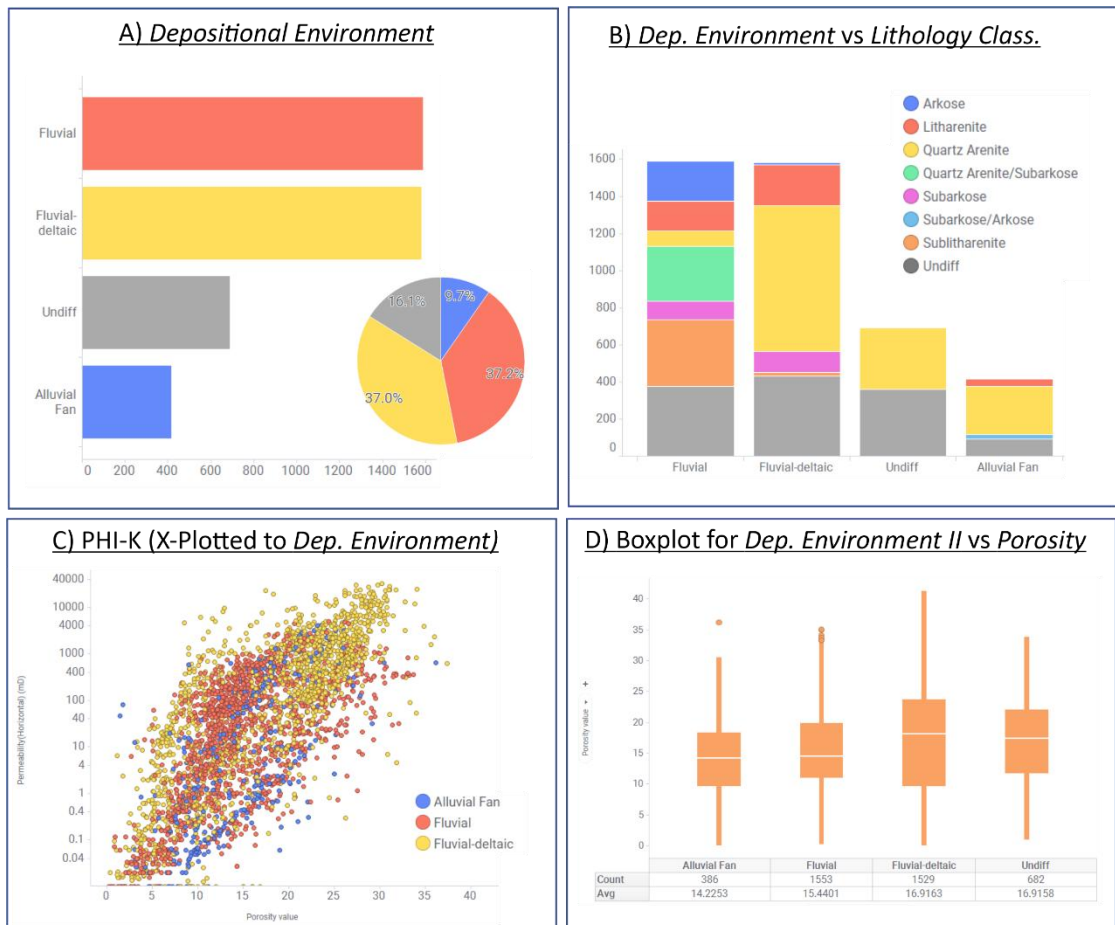


Figure 4.15 Depositional Environment Charts

(A) The count and proportions for the number of entries included within the *Depositional Environment* subgroup expressed in a bar chart and a pie chart. (B) Bar chart stacking the *Depositional Environment* categories against the *Lithological Classification* categories. (C) Cross-plot for porosity and permeability against the *Depositional Environment* category. (D) A boxplot showing the porosity variability for each of the categories within the *Depositional Environment* subgroup.

4.3.5.4 Dominant Process Influence

PAFD separates samples based on four different influences on sedimentary process and related to the depositional environment where these processes take place. These are the “*lacustrine*”, “*marine*”, “*aeolian mixed*” and “*fluvial*” categories. A category for undifferentiated (“*undiff*”) entries is also defined (Figure 4.16).

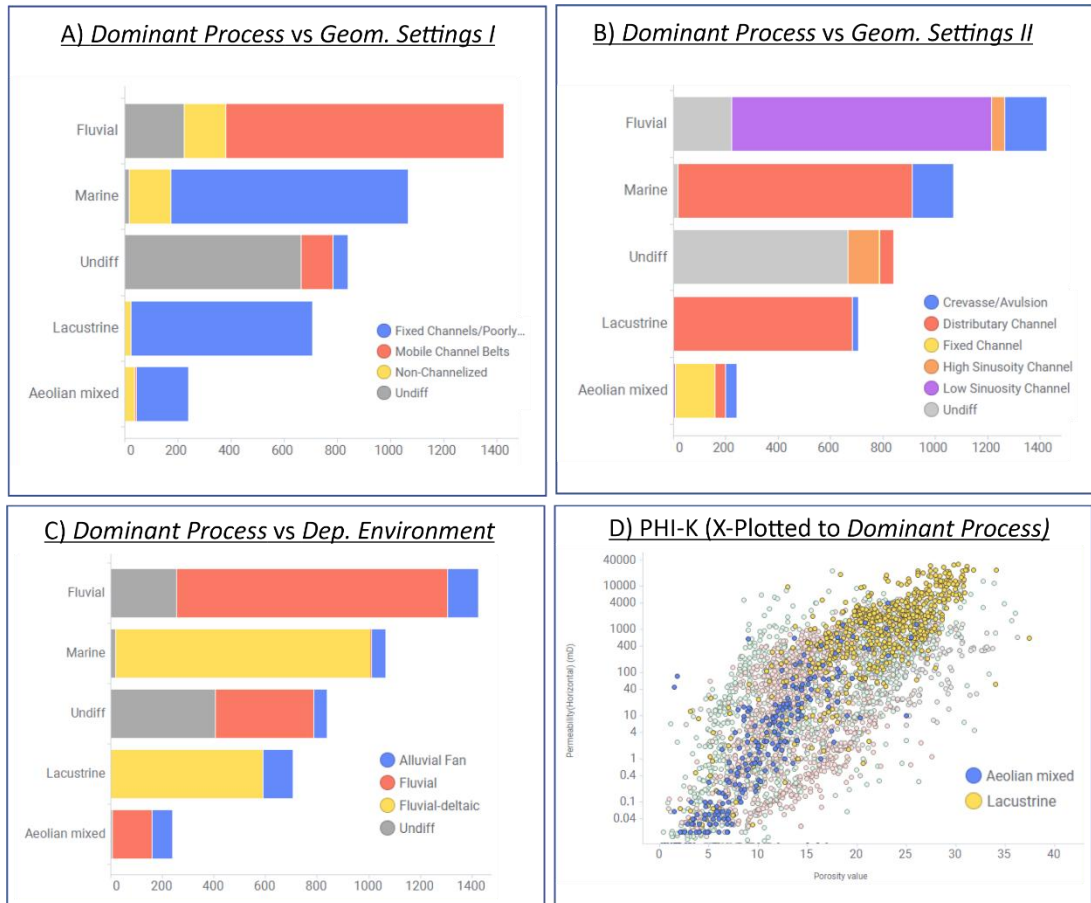


Figure 4.16 Dominant Process Charts

(A), (B) and (C) correspond to bar chart depicting the count of entries in the database for the *Dominant Process* categories and staked relationships against the *Geomorphic Settings I*, *Geomorphic Settings II* and the *Depositional Environment* categories. (D) indicates a porosity-permeability cross-plot where the “aeolian” and “lacustrine” categories are highlighted over the cloud of all porosity-permeability points available in the database (greyed out points).

“*lacustrine*” processes refer to those fluvial-lacustrine depositions of sediments in locations associated close to the margins of lakes where dominant environmental controls are related to axial and transverse influx of water and sediment by rivers. The deposition of sediment is also influenced by lake-level changes, which may impact the composition, texture, sorting and other properties of sedimentary lithofacies (Rust, 1982). Lacustrine processes commonly promote the construction of lacustrine deltas, which are formed at the point of entry of a river into a lake. The “*marine*” processes are those dominated by waves and tides, also influence fluvial depositions (Vakarelov and Ainsworth, 2013). Similar to lacustrine environments, deltas are also developed when deposition takes places just when a river enters into an

ocean (Miall, 1996; Jordan and Mountney, 2010). The “*aeolian mixed*” processes refer to depositions which involve erosion, transportation and deposition by the wind and may affect fluvial deposits developing distinctive rock types with high porosity and permeability values (Mountney et al., 1998; 2022; Cosgrove et al., 2021; Allaby, 2013). The “*fluvial*” category relates to deposits that are not influenced by a non-fluvial process regime.

4.3.5.5 Dominant Formative River Planform

The interpreted formative river planform category describes channel patterns, which are primarily controlled by stream power, grain size, bank stability and the amount of bed load carried (Allen, 1978). Three different morphologies are included in PAFD: “*braided*”, “*meandering*” and “*anastomosing*”. In addition, a category for those entries which cannot be classified in any of the previously mentioned classes is assigned under the name of “*undiff*” (undifferentiated).

“*braided*” rivers have multiple-thread channels, dominated by mid channel bars and commonly have relatively coarse-grained deposits. They commonly have mobile banks composed of largely non-cohesive sediment, and they are typically unstable with frequent lateral shifts, which commonly result in rearrangements of channel-belt morphology in the aftermaths of large flood events (Miall, 1996; Leeder, 1978). Compared with other formative river planforms, braided systems tend to have large width-to-depth ratios, often higher than 50 as defined by Fredsoe (1978). “*meandering*” rivers are single-thread channels with a distinctive sinuous planform. The formation of sinuous features is developed by eroding the sediment of an outer bank and depositing sediment on the inner bank (point bars). Small values for width-to-depth ratios (less than 50) are another important of meandering systems, together with the presence of cohesive banks, associated with levees, and fine-grained floodplain sediments (Mackey and Bridge, 1995; Ghazi and Mountney, 2009; Miall, 2014). “*anastomosing*” rivers are characterised by two or more interconnected, semi-permanent and stable channel belts associated with low energy conditions. Anastomosing rivers show high channel-bank stability, do not display mid-channel bars shifting and interconnected channels are separated by floodplain rather than by channel bars (Miall, 2014) (Figure 4.17).

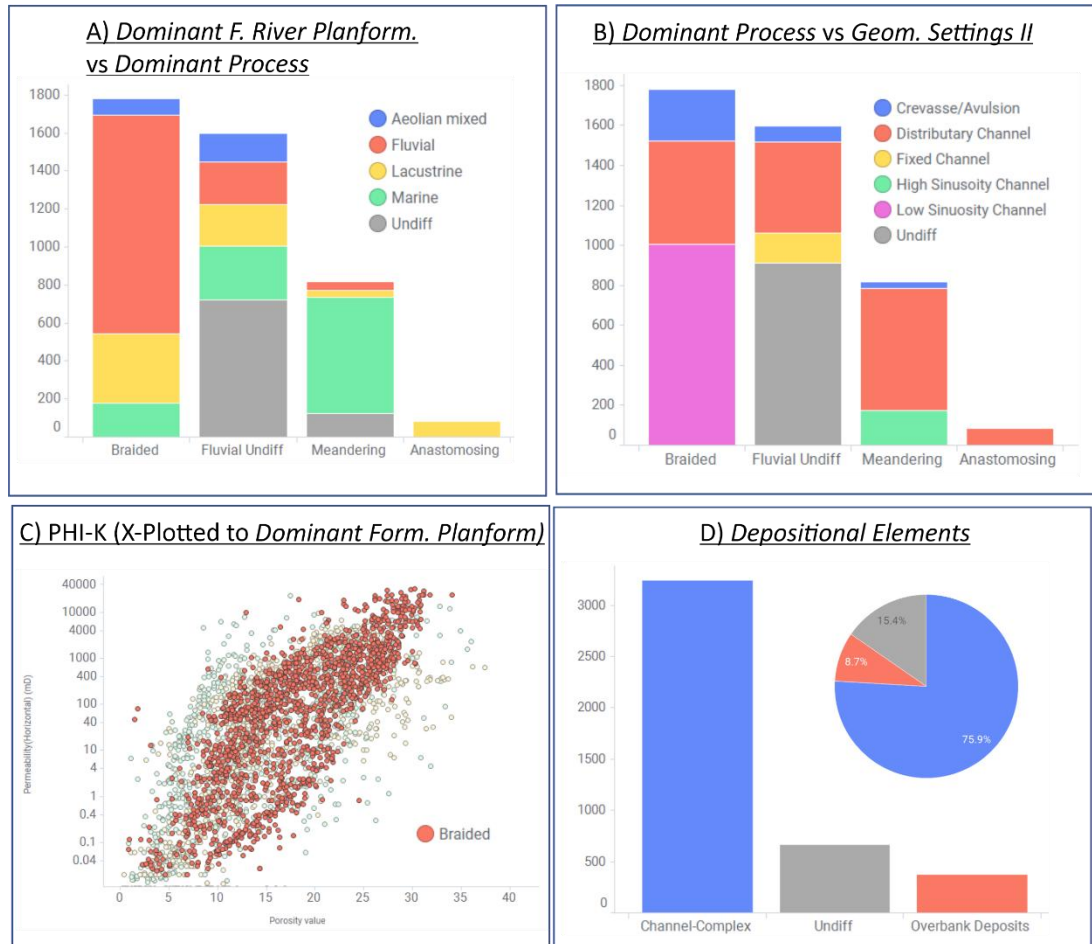


Figure 4.17 Formative River Planforms Charts

(A) A bar chart showing the number of entries associated to categories within the *Dominant Formative River Planform* categories stacked to the *Dominant Process* categories. (B) Similar to (A) shows a bar chart stacked to the *Geomorphic Settings II*. (C) A porosity-permeability cross-plot where the “braided” associated points are highlighted over the entire dataset in the database (greyed out points). (D) A bar chart and a pie chart indicating a data count and the volume of data corresponding to each category in the *Depositional Elements* subgroup.

4.3.5.6 Depositional Elements

For the *Depositional Elements* subgroup, two categories are distinguished: “overbank deposits” and “channel complex”. The differentiation of these two terms is important as the stratigraphic architecture is determined by the distribution of channel deposits forming channel bodies and overbank sediments (Miall, 1996; Walker, 1984). “overbank deposits” correspond to the sediment settled when the river water went beyond its normal boundaries or banks. “overbank deposits” form unconfined accumulations which display lateral grain-size trend, fining from locations close to the channel banks (generally coarser sediments) to distances located farther away from the river

(generally finer sediments) (Walker, 1984). The term “*channel complex*” is used to refer to the material deposited by a channel in a channel belt, within the bankfull elevation in a confined setting (Colombera and Mounthey, 2019). They commonly build lenticular bodies and tabular sheets including different types of complex bedding geometries and erosive bases (Miall, 1977; 1996; 2014). The depositional elements described above, are related in the definition of fluvial architecture in the database which is further subdivided in the *Channel Associations* and the *Channel Body Types* (Figure 4.18).

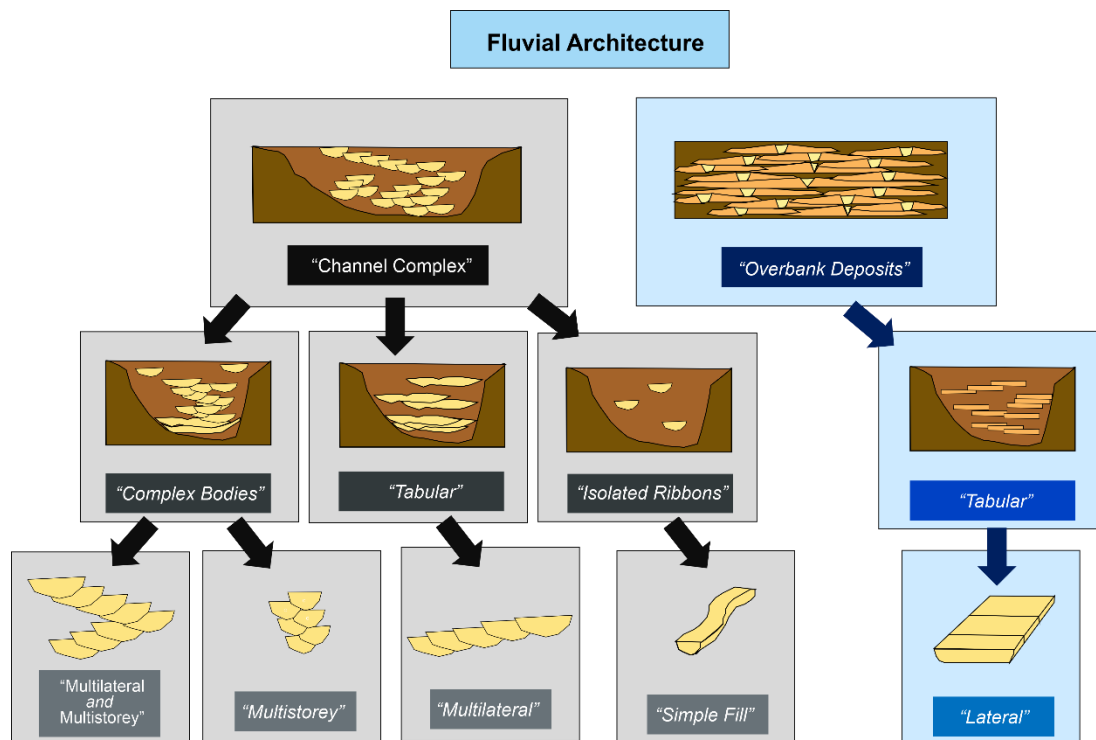


Figure 4.18 Fluvial Architecture Classification Diagram

Graphical summary depiction of the different subgroups and categories associated to the description of fluvial architecture in the database. The first row in the diagram corresponds to the categories included within the *Depositional Elements* subgroup. The second row relates with the *Channel Association* subgroup and the third row, includes the categories included within the *Channel Body Type* subgroup. The Diagram also separates in two colours the categories corresponding to both channel Complex (Grey) and overbank deposits (light blue).

4.3.5.7 Channel Association

The channel association subgroup complements the fluvial architecture classification adding a subdivision to the previously described *Depositional Element* subgroup. The categories “*complex bodies*”, “*isolated ribbons*” and

“*tabular*” are included here (**Figure 4.18**). Examples that cannot be classified or differentiated by the authors in any of these three classes are included as “*undiff*” in the database. The *Channel association* categories included in PAFD refer to the preserved fluvial style and external shape of large-scale architectural elements, based on a classification that follows those by Alexander (1992) and Giblin (2006).

For the “*complex bodies*” entries the database refers to those channel associations including different vertical and horizontal stacking patterns. They comprise two or more individual successions or storeys bounded by internal bounding surfaces (Allen, 1978; Tye, 2004). On the contrary, the “*isolated ribbons*” refers to those narrow, fixed channelised units with a ribbon shape architecture which do not exhibit major stacking patterns (Dreyer et al., 1993). The “*tabular bodies*” category includes those entries associated with sandbodies with an aspect ratio where its horizontal extension significantly exceeds its thickness (50:1) or vertical distribution defining tabular geometries. Sometimes, tabular shapes can be associated to various bodies attached to each other creating amalgamated shapes which also extend horizontally (Krynine, 1948) (**Figure 4.19**). Tabular bodies can be associated to both channel-complex and overbank deposits.

4.3.5.8 Channel Body Type

The *Channel Body Type* subgroup includes references associated to the morphologies created by sand bodies and corresponding stacking patterns. PAFD includes a classification of the type of internal architecture related with the previous *Channel Associations* categories described in the previous subgroup (**Figure 4.18**). This architecture classification considers the 3D forms associated with the existing channel bodies. It includes the following categories: “*multilateral*”, “*multistorey*”, “*multilateral and multistorey*” and “*simple fill*”. An “*undiff*” category also exist for entries that cannot be classified. “*Multilateral*” geometries in the database refer to those entries which correspond with horizontally migrating channels due to lateral migration of the active channel belt which generates stacked bodies (e.g., meandering system) (**Figure 4.19**) (Miall, 2014; Allen, 1978).

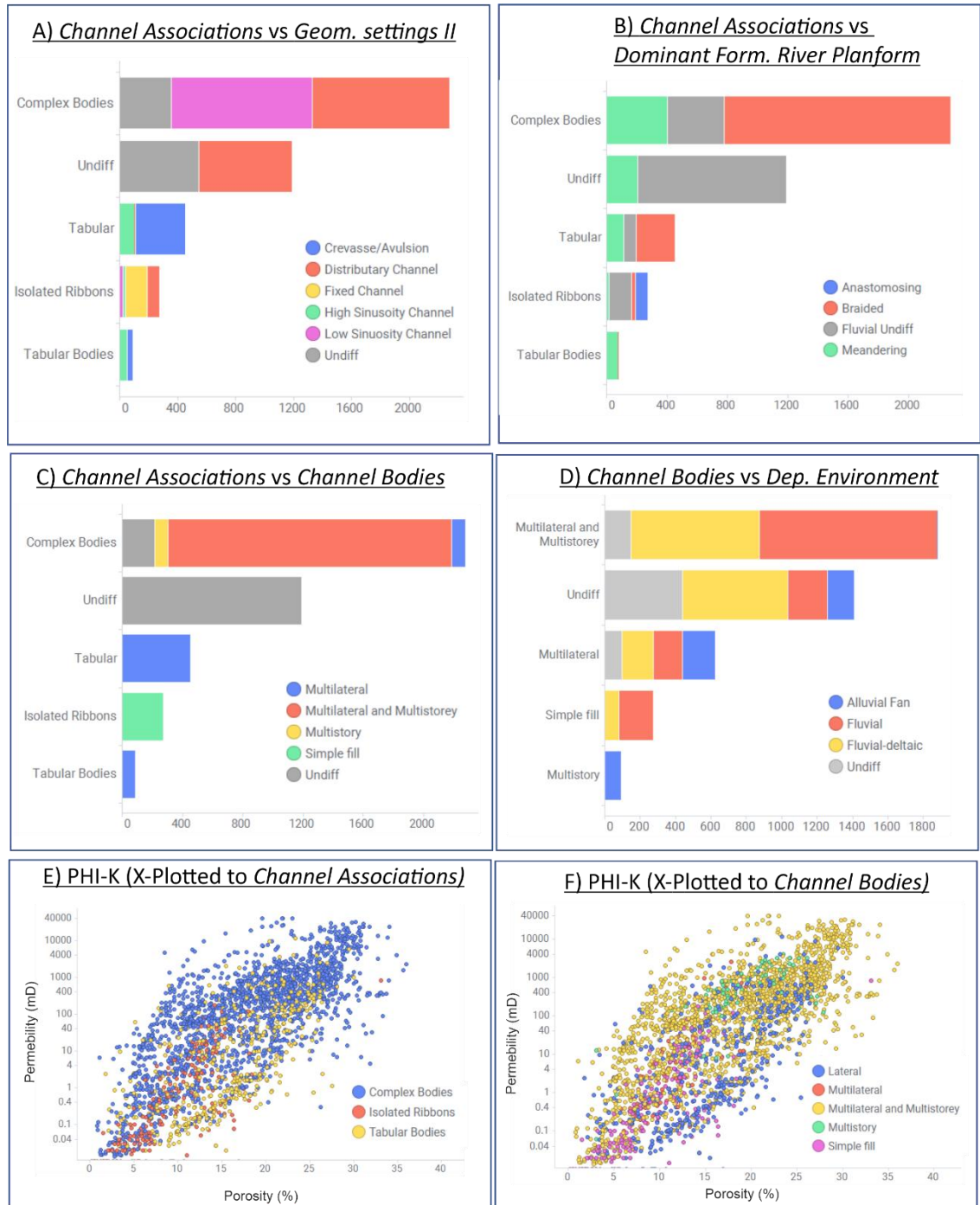


Figure 4.19 Facies Architecture Charts

(A) bar chart showing the number of entries associated to categories within the *Channel Associations* subgroup stacked to the *Geomorphic Settings II* categories. (B) Similar to (A) shows a bar chart stacked to the *Dominant Formative River Planform*. (C) Equal to (A) and (B) shows the *Channel Associations* categories stacked to the *Channel bodies* categories. (D) indicates the same type of chart previously defined but this time stacked the *Channel Bodies* subgroup to the *Depositional environment* subgroup. (E) and (F) are both porosity-permeability cross-plots which highlight different categories the *Channel Bodies* categories for both *Channel Associations* and *Channel Bodies* subgroups.

On the contrary, the class “*multistorey*” is applied to features where several sandbodies are in vertical superposition (Bridge and Mackey, 1992; Giblin, 2006). The “*multilateral and multistorey*” category includes examples which are located in a context where multilateral and multistorey geometries take place. The “*simple fill*” category refers to accumulations that infill a channel produced by accretion of sediment deposited by the water that has lost its transporting capacity (low energy). Simple fills may be produced during short periods of flow as a result of avulsion (**Figure 4.19**).

4.3.5.9 Architectural Elements

Architectural elements included in PAFD correspond to components of a fluvial depositional system associated to facies associations, architectures and individual sub-environments of deposition within formative river planforms. Categories are assigned based on criteria that include their bounding surfaces, geometry, scale and internal organisation, as proposed by Miall (1985; 1996). Four different types of architectural elements are being identified in the database. These are “*mid-channel bar*”, “*point-bar*”, “*bar undiff*”, “*channel-fill*”, “*splay*” and “*unconfined sheet body*”. Another category for samples that cannot be classified in any of the three previously mentioned classes is included under the name of “*undiff*” in the database (**Figure 4.20**).

The “*mid-channel-bar*” category groups different types of barforms developed wholly within a channel. These are predominantly downstream accretion barforms in which depositional increments are stacked at low angle with respect to paleoflow (DA) and downstream features including dominantly oblique accretion embodied by a combination of downstream accretion at their downstream ends and cross-bar accretion along their flanks (DLA) (Cant and Walker, 1978; Kirk, 1983; Bristow, 1987; Miall, 1996; Bridge, 2003; 2006; Colombera et al., 2013). The “*point-bar*” category includes elements related to lateral-accretion macroforms (LA) produced by migrating meander bends (Miall, 1978; 1996; Allen 1978). However, not all the defined “bars” by authors could be associated with specific categories. Therefore, these samples are grouped in the “*bar undiff*” category. The class “*channel fill*” includes the deposits of the aggradational infill of active channel forms (CH) (Miall 1985, 1996; Hobbrook, 2001; Colombera et al., 2012). The “*splays*” category corresponds to the crevasse splay (CS) type defined by several authors (Allen 1965a; Miall 1996; Bridge 2003; 2006; North and Davidson, 2012). It refers to

elongated tongue shaped bodies bordering channel-belt, which typically thin with increasing distance away from the channel margin into the floodplain. They are related with episodic unconfined flow from crevasse channels during floods.



Figure 4.20 Architectural Elements Charts

(A) A bar chart showing the number of entries associated to categories within the *Architectural Elements* subgroup. (B) A boxplot indicating the porosity distribution for each of the categories in the *Architectural Elements* subgroup. (C) Cross-plot highlighting the porosity and permeability points related to the “*mid-channel bar*” and “*channel-fill*” categories over the entire cloud of recordings included in the database. (D) A bar chart for the *Architectural Elements* categories stacked to the *Geomorphic Settings II* categories.

The “*unconfined sheet bodies*” include the Sandy sheetflood (SF) representing vertical aggrading areas controlled by bedload deposition from unconfined flows that may include sedimentary sheets forming terminal splays (Olsen, 1989; Miall, 1996; Colombera et al., 2013), and the overbank fines (FF) as defined by several authors which consist in elements with a tabular or prismatic fine-grained bodies associated to aggrading floodplains in which

suspension settling from subaerial unconfined flows is the dominant process (Miall, 1985; 1996; Ghazi and Mountney, 2009).

4.3.5.10 Lithofacies

This database organises different types of lithofacies according to Miall's scheme (Miall 1977; 1978; 1985; 1996). Each of the categories corresponds to distinctive genetic packages with different textural and lithostratigraphic characteristics. The adoption of this scheme enables use of mutually exclusive classes and of a well-established classification in the scientific community. Eleven categories are adopted, as follows: “*Gp*”, “*St*”, “*Sp*”, “*Sp-St*”, “*Sh*”, “*Sp-Sh*”, “*Sr*”, “*Sm*”, “*Fr*”, “*Fm*” and “*Fl*”. Another category for samples that cannot be classified in any of the previously mentioned classes under the name of “*undiff*” is included in the database (Figure 4.21).

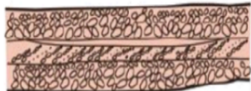








Code	LITHOFACIES DESCRIPTION	Image
Gm	Gravel to Boulders: Undefined textural and structural properties	 Gm Gp Gm
Gp	Gravel to Boulders: planar cross-stratified gravel	
St	Through cross-stratified sand	
Sp	Planar stratified sand	
Sh	Horizontal laminated sand	
Sr	Ripple cross-laminated sand	
Sm	Massive or faintly laminated sand	
Fr	Fine grained root bed	
Fm	Massive mud and silt	
Fl	Laminated sand, silt and mud	

Figure 4.21 Lithofacies Classification

Lithofacies classification describing all lithofacies included in the database (modified after Miall, 1996). Note the table does not include all lithofacies defined by Miall, 1996; only the ones included in the database developed in this work.

Categories included in PAFD are defined as follow: i) “*Gp*” as planar cross-stratified gravel. ii) “*St*” as a trough cross-stratified sand. iii) “*Sp*” as planar cross-stratified sand. iv) “*Sh*” as horizontally bedded sand. v) “*Sr*” for current ripple cross-laminated sand. vi) “*Sm*” for massive sand possibly locally graded or faintly laminated. vii) “*Fr*” as fine-grained root bed. viii) “*Fm*” for massive clay and “*Ff*” for interlaminated very fine, silt and clay. ix) “*Sp-St*” and “*Sp-Sh*” are also recognised in the database as separate entities as the samples which exhibit a mix or a gradation between “*Sp*” and “*St*” lithofacies (**Figure 4.22**).

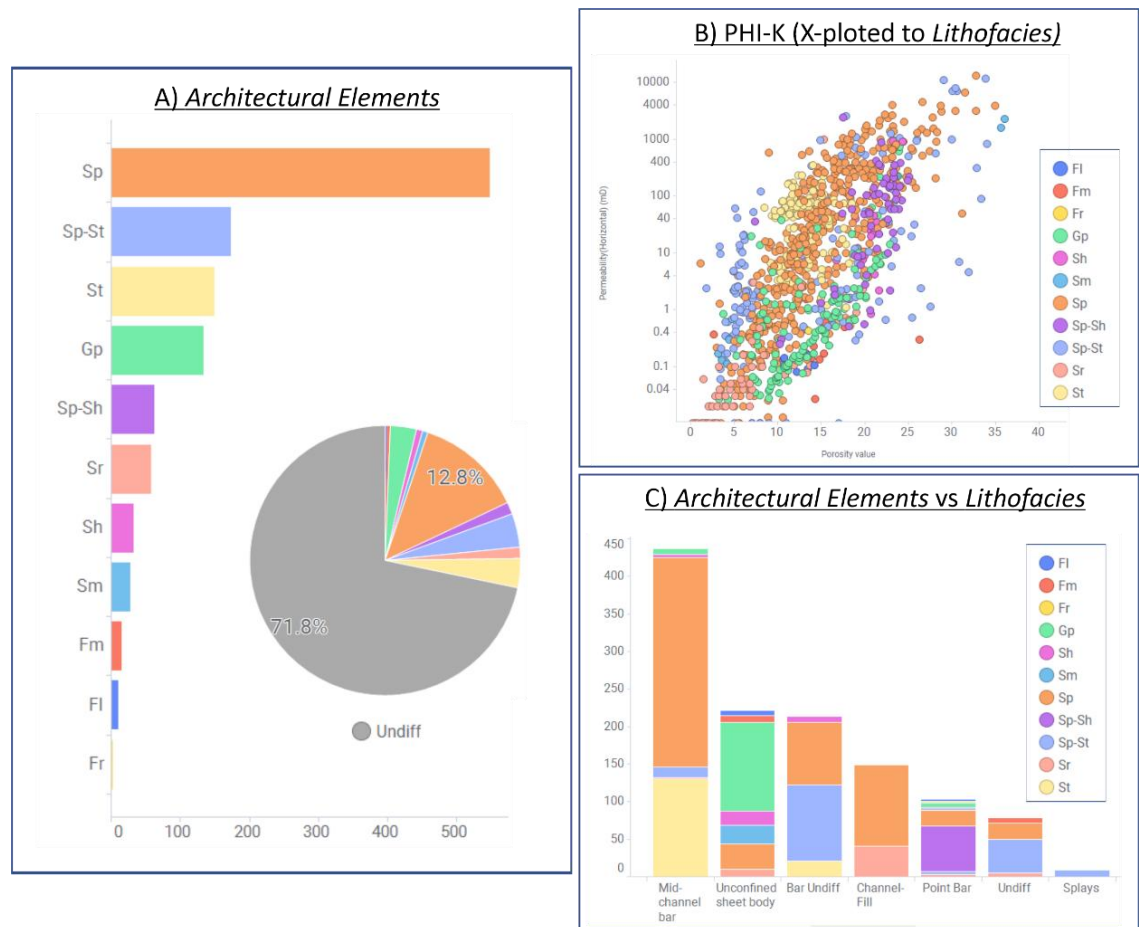


Figure 4.22 Architectural Elements and Lithofacies Charts

(A) Bar chart indicating the number of entries associated to each of the categories within the *Lithofacies* subgroup. The bar chart does not show the number of entries associated to the “*undiff*” category, which is 71.8% of the total of entries in the database, as shown in the pie chart. (B) Cross-plot showing the different trends for porosity-permeability depicted by each of the lithofacies included in the database. (C) A bar chart showing the *Architectural Elements* categories stacked to the *Lithofacies* categories.

4.3.5.11 Discharge Regime

Water discharge is the volume of water transported by a river per unit time (Buchanan and Somers, 1969). In the database, two categories are used to classify the discharge regime, as either “*intermittent*” or “*perennial*”. An “*undiff*” category is also included in the database when the discharge regime cannot be determined.

“perennial” streams or rivers have a constant flow of water throughout the year. Even for those periods where there is a prolonged or extreme drought, a perennial stream is supported by groundwater. On the contrary, “*temporary*” intermittent or non-perennial rivers are those which have no flow for at least a part of the year and are typically associated with arid climates where evaporation tends to be greater than precipitation (Oscar, 1923) (Figure 4.23).

4.3.5.12 Climate

Climate and its effects on rainfall and evaporation has a significant impact on fluvial processes. Rivers in wetter climate regimes tend to have a higher discharge as there is more water entering the system as the rate of erosion is also conditioned by the climate and tend to increase with higher discharge as it increases energy and transportation. Climate also affects the river processes as it influences evaporation rates. Other short-term weather events associated with climate, such as storms or drought, can also have an impact on fluvial processes. For instance, heavy rainfall drastically increases energy in fluvial systems leading to more erosion and changes in channel courses (Heller and Paola, 1996).

PAFD includes the following climatic categories as defined by Thornthwaite, (1931) and revised in 1948. This classification schemes separates groups on the basis of “precipitation effectiveness” criteria or, in its 1948 incarnation, of the “moisture index”. The database includes the following categories: “*arid*”, “*semi-arid*”, “*subhumid*” and “*humid*”. An “*undiff*” category is also included in the database for those entries that cannot be assigned to any of the aforementioned climate classes (Figure 4.23).

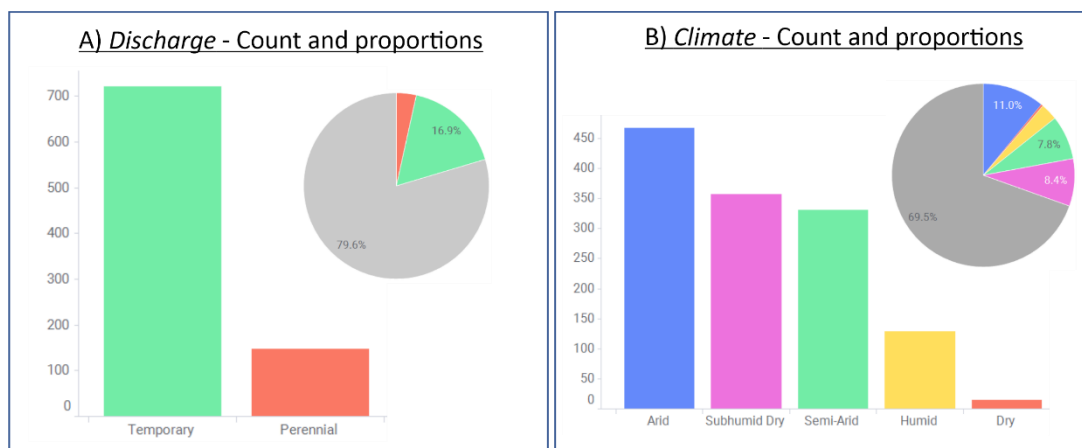


Figure 4.23 Discharge and Climate Charts

(A) and (B) show bar chart charts which indicate the number of entries for each of the categories within the *Discharge* and *Climate* subgroup. “undiff” categories are not shown in the bar chart but its volume in percentage is shown in the pie chart.

4.3.6 Diagenesis

Diagenetic processes have a great impact on the petrophysical properties and, hence, the quality of reservoir rocks. Reservoir quality, which is controlled by depositional facies and subsequent modifications by diagenetic alterations, is one of the critical aspects in understanding the basic elements of the play in sedimentary basins (Marshak, 2009). The majority of the rocks included in this database are sandstones and the diagenetic evolution of these types of rocks is controlled by a variety of interrelated parameters. These are the composition of framework grains, pore water chemistry, tectonic setting of the basin, and burial-thermal history of the succession (Morad et al., 2013; Stonecipher, 2000). Processes that occur during diagenesis fall mainly into three subgroups, which are accounted for in PAFD: i) *Physical Compaction*, ii) *Mineral Precipitation*, and iii) *Mineral Dissolution* (leading to the development of secondary porosity). The *Main clay type* present in the rock matrix is also recorded, as it can greatly influence reservoir quality.

4.3.6.1 Physical Compaction

Compaction is an indication of the decrease of porosity with depth and stress history in sedimentary basins. Understanding the compaction of siliciclastic sediment is very important in order to model different events that occur in the subsurface, such as subsidence, water expulsion along faults, diagenetic alterations and the formation of mineral and hydrocarbon deposit, etc.

(Ehrenberg, 1990; Lander and Walderhaug, 1999). Calculation of compactional porosity loss for characterising the diagenesis and porosity evolution can be done applying different techniques. A common technique is the one developed by Ehrenberg (1995), whereby the compactional porosity loss (COPL) is calculated for sandstone porosity. This calculation uses the present intergranular volume (IGV) (ideally measured from thin section analysis), compared with an assumed earlier original porosity (OP) (Figure 4.24).

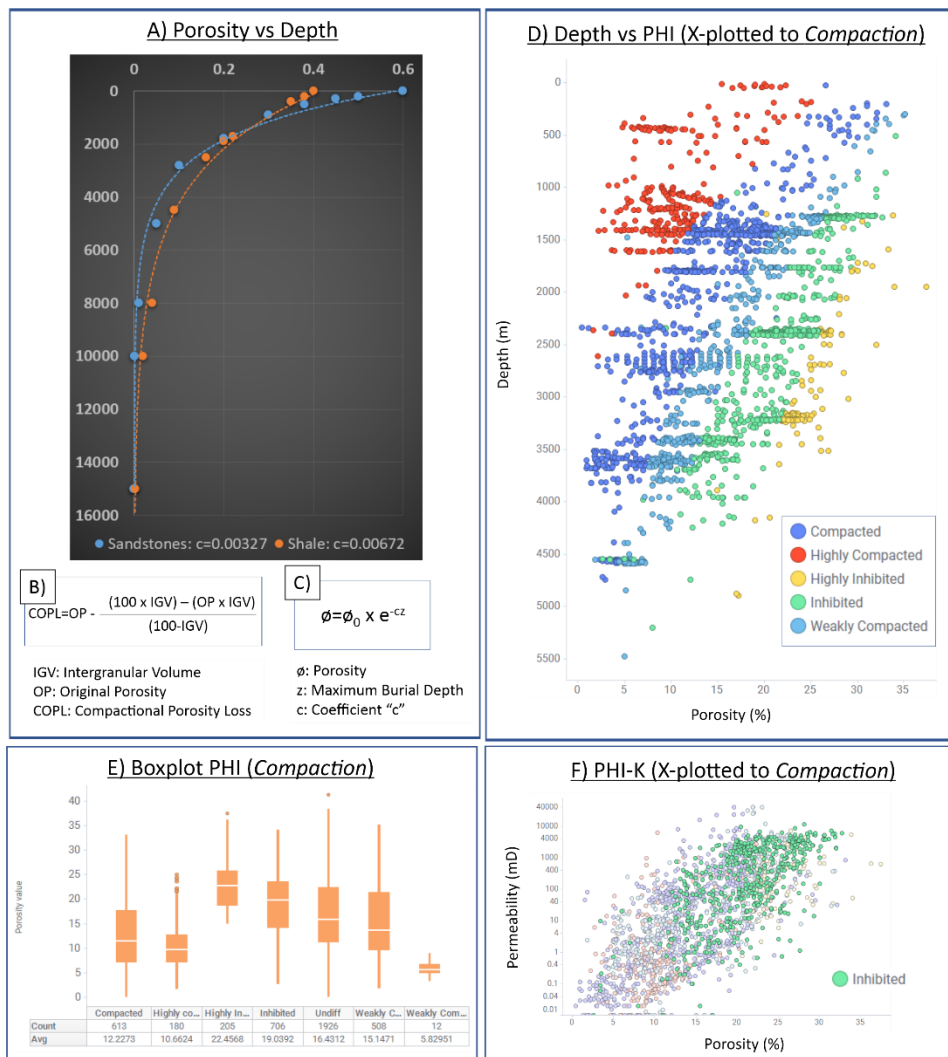


Figure 4.24 Porosity vs Depth vs Compaction

(A) shows a graph where porosity and depth distribution can be observed for sandstones and shales (modified from Sclater and Christie (1980). (B) and (C) correspond to the COPL from Ehrenberg, 1990 and Athy (1930) equations. (D) displays a chart where Depth and porosity are cross plotted to each of the categories located in the Physical Compaction subgroup. (E) Boxplot showing the porosity distribution of the various compaction categories. (F) A cross-plot for porosity and permeability depicting the "inhibited" category over the entire dataset.

For this study, the IGV value will be related with the actual measurement of porosity included in the database for each entry. However, for the OP, the [Athy \(1930\)](#) equation is applied which introduces an empirical compaction law relating the variation of porosity (ϕ) with the maximum burial (z) value (**Figure 4.24C**). The coefficient “c” varies with lithology. The value used for sandstones correspond to 0.000327 and for shales with 0.000672, as from [Sclater and Christie \(1980\)](#). Once the COPL is calculated is compared with the COPL categories which were defined for this compaction study. Values below 0 correspond with samples where compaction was inhibited (i.e., attenuated) for different reasons. On the contrary, when values are above 0, compaction took place in different levels. In the database, the following relationships are applied to form categories:

- If COPL < -10 the “*highly inhibited*” label is applied.
- If COPL = 0 and < -10 the “*inhibited*” label is applied.
- If COPL = 0 and < 5 the “*weakly compacted*” label is applied.
- If COPL > 5 and < 15 the “*compacted*” label is applied.
- If COPL >15 the “*highly compacted*” label is applied.
- The category “*undiff*” is used where no data are available.

4.3.6.2 Mineral Precipitation (Timing)

Diagenesis comprises a broad spectrum of physical, geochemical, and biological post-depositional processes by which original sedimentary mineral assemblages and their interstitial pore waters interact with each other to reach textural and thermodynamic equilibrium with their environment ([Worden and Burley, 2003](#)). In PAFD, a distinction is made between diagenetic processes that are inferred to have occurred in the earlier stages of a burial cycle, collectively known as “*eodiagenesis*” and processes that occurred during the subsequent “*mesodiagenesis*” where dehydration of clay minerals occurs, and the main development of oil genesis takes place ([Gier et al., 2008](#)). An additional category for samples which include patterns for both “*eodiagenesis and mesodiagenesis*” is also included in the database. A category for those samples which could not be classified in any of the previously mentioned category is recognised in the database as “*undiff*”. (**Figure 4.25**).

4.3.6.3 Mineral Association

Every sample in PAFD was also classified in terms of the most common mineral association related with geochemical processes which led to the

precipitation of different minerals. Although 1/3 of the samples could not be classified in any specific mineral association, this study includes 21 mineral groups where entries were classified (**Figure 4.25**).

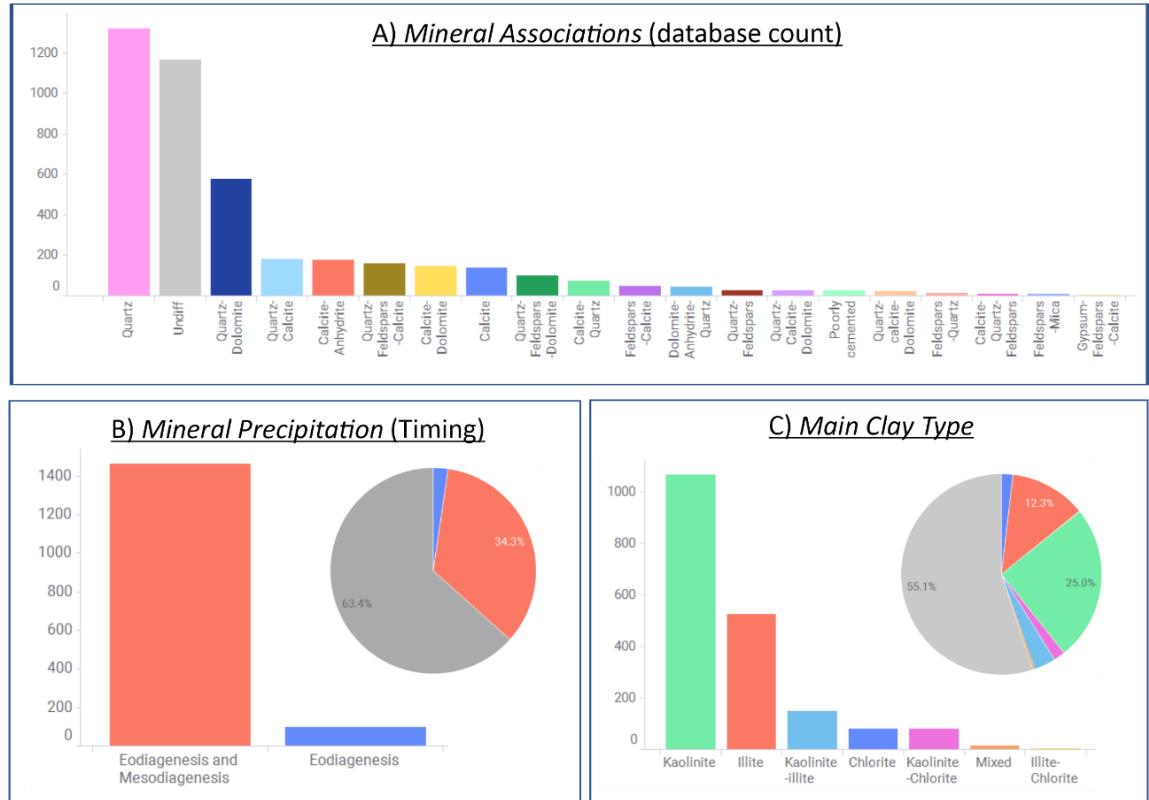


Figure 4.25 Mineral Association, Precipitation and Main Clay Type Charts

(A) Bar chart bar indicating the number of entries for the top 20 mineral associations categories included in the database. (B) and (C) bar chart bars showing the number of entries including in the categories for the *Mineral Precipitation (Timing)* and *Main Clay Type* subgroups respectively (excluding “undiff” category). A pie chart is also inserted indicating the volume proportions for each of the categories including the “undiff” category.

4.3.6.4 Main Clay Type

Furthermore, in the diagenesis section, the main and most abundant authigenic clay in the rock matrix is recorded. PAFD includes different type of clays: “kaolinite” (the most common clay mineral in sandstones reservoirs), “chlorite”, “illite” (which drastically contributes to permeability reduction), and combinations between these three such as “illite-chlorite”, “illite-kaolinite”, “kaolinite-chlorite”; the “undiff” category is also indicated in the database for

those entries where the most abundant authigenic clay was not indicated (**Figure 4.25**).

4.3.6.5 Secondary Porosity

The database includes a field to identify those sample where secondary porosity took place. PAFD includes 3 categories for this field: “yes” flags all entries where the authors indicated the occurrence of secondary porosity processes. “no” is instead used where publications explicitly indicate that no secondary porosity effects took place, and “undiff” where no information exists (**Figure 4.25**).

4.3.7 Depth References

An effort to select sufficient petrophysical entries linked to depths was made. These are depth recordings associated with petrophysical properties taken from subsurface data types where the depth is recorded. Depth references are important to recognise trends that might exist in the subsurface. Many parameters associated with the many categories in this database exhibit depth trends. An example of this is the previously mentioned physical compaction where porosity values are reduced for larger values of depths (**Figure 4.26**).

54% of the samples included in PAFD (>2,000 entries) include depth references. They are grouped in samples referenced to the “*ground level*” (referenced to Mean Sea Level), “*ground level and elevation*” (considering as elevation RT-Rotary table, KB-Kelly bushing, DF- Drilling Floor) and samples with “*no references associated*”.

The database also includes a field for “*burial depth*”, which records the maximum known depth to which the sample was buried during its geological history. However, the study recognises the challenge of inferring the burial depth to which such examples might have one been buried and assumes high uncertainty values for these records.

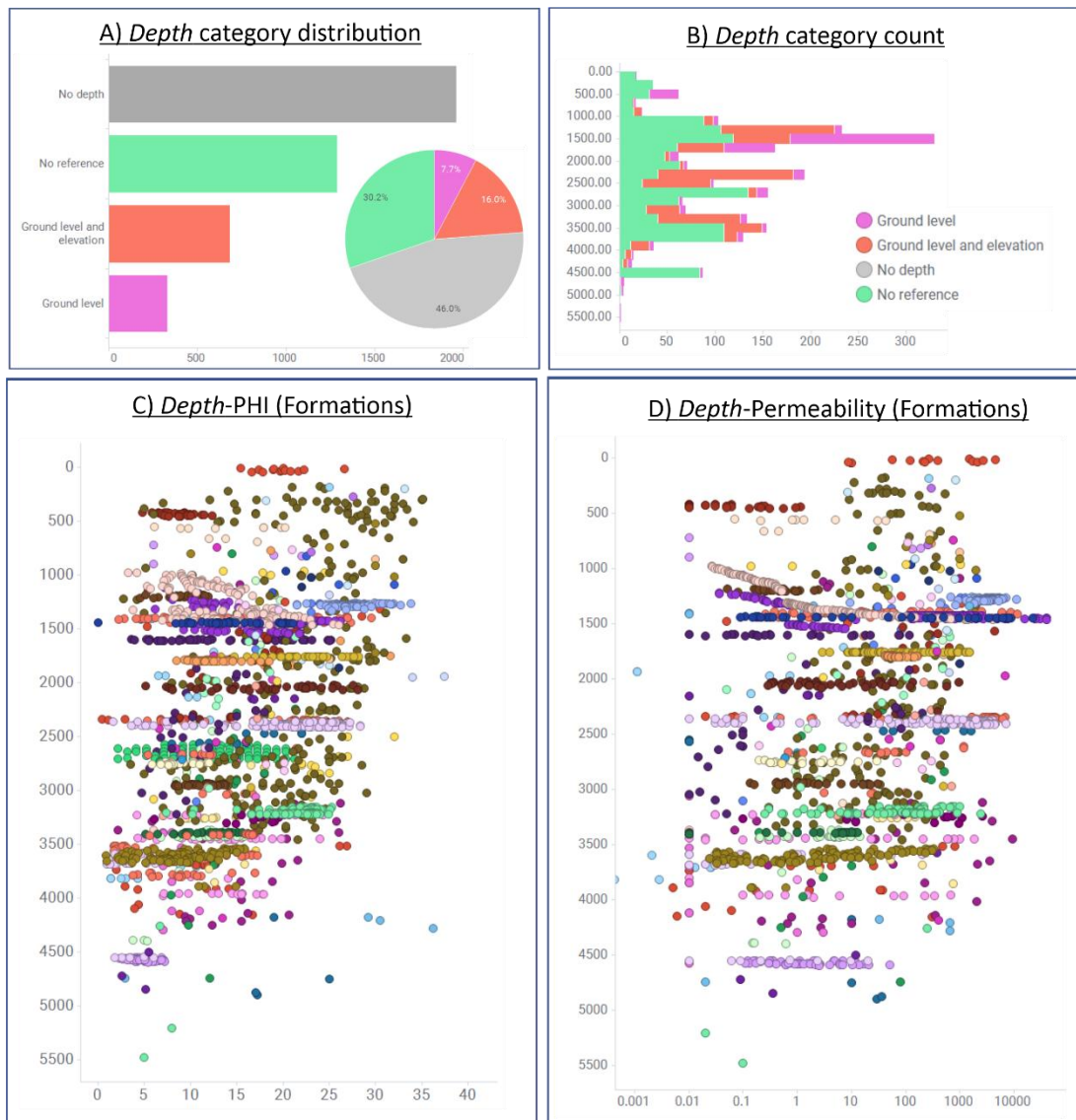


Figure 4.26 Depth References Charts

(A) Bar chart showing the number of entries for each of the categories in the *Depth Reference* subgroup. A pie chart also indicates the volume (percentage) for each category represented in the database. (B) Bar chart grouping depth intervals in bins cross plotted to the different depth references. (C) and (D) corresponds to cross-plots for *Depth-Porosity* (PHI) and *Depth-Permeability* respectively. Different colours represented in (C) and (D) correspond to the various *Formation* rocks included in the database and that covers a wide range of depths from close to the surface to approximately 5,500m.

4.3.8 Petrophysical Properties

Different petrophysical properties of rocks from fluvial successions are controlled by various intrinsic (intrabasinal) and extrinsic (extrabasinal) factors. Some of these factors include tectonics, base-level changes, climate and hinterland geology, which collectively control sediment deposition in

fluvial systems (Miall, 1996; Bridge, 2006; Priddy and Clarke, 2021). How the different units included in the fluvial systems are deposited will ultimately determine their petrophysical properties. Consequently, the petrophysical properties of a rock unit will depend on the properties of each sedimentary unit, themselves determined by characteristics such as mineral composition, texture (grain size, sorting, etc), internal structure (e.g., cross-bedded, massive, etc), diagenesis, etc (Tiab et al., 2003). Petrophysical parameters control the economic potential of a reservoir, and it is therefore imperative to determine them (Ballin, et al., 1997). PAFD primarily focused on the characterisation of porosity and permeability related to the rest of the categories and properties included in this study for fluvial reservoirs. The database approximately includes 4,000 readings where porosity and permeability values are jointly recorded.

4.3.8.1 Porosity

Porosity is the percentage of the bulk volume of a rock soil that is occupied by interstices, whether isolated or connected. In other words, the fraction of the total volume of rock that is not occupied by the rock matrix. There are several types of porosities: i) total porosity consisting of all the void spaces (pores, channels, molds, vugs, fissures, fractures, etc). ii) primary porosity which is the porosity developed during the final stages of sedimentation at the time of deposition. They can be intergranular or intercrystalline. iii) Secondary porosity corresponding to the porosity developed in a rock after its deposition. iv) interconnected porosity made up only of those spaces which are in communication. v) Effective porosity a term used specifically for log analysis corresponding to the one accessible to free fluids. vi) Potential porosity: the part of interconnected porosity in which the diameter of the connecting channel is large enough to allow flow (Serra, 2004; Crains, 2000; Glover P., 2019; Tiab et al., 2003). The porosity types depend on the rock type. In reservoirs of detrital or clastic origin like sandstones, the porosity is essentially intergranular in its origin, and is chiefly controlled by parameters such as sorting, packing and cement abundance (Ballin, et al., 1997).

PAFD includes several subgroups for different type of porosity values including *Porosity* values, *Average Porosity* values, *Minimum* and *Maximum* porosity. The samples are then classified according to the *Porosity type* where only “*total*” and “*effective porosity*” are included as categories. Metadata on

the acquisition of porosity measurements (*Porosity Sample Type*) are also recorded and include types such as Helium porosity (“*absolute*”, “*effective*” and “*undifferentiated*”), values derived from “*effective porosity and permeability regressions*”, “*SEM*” (scanning electron microscope), “*log analysis*”, “*thin section*” analysis and “*MICP*” samples. Mercury Injection Capillary Pressure (MICP) is a measure of the volume of mercury (Hg) that can invade pore volume of the rock as a function of the mercury pressure. The porosity system of a rock is interpreted as a system of tubes with variable diameter (pore throats). Each increment of this tubes has a flow constant (porosity-permeability) that is a function of the tube diameters squared (Bear, 1972) (Figure 4.27).

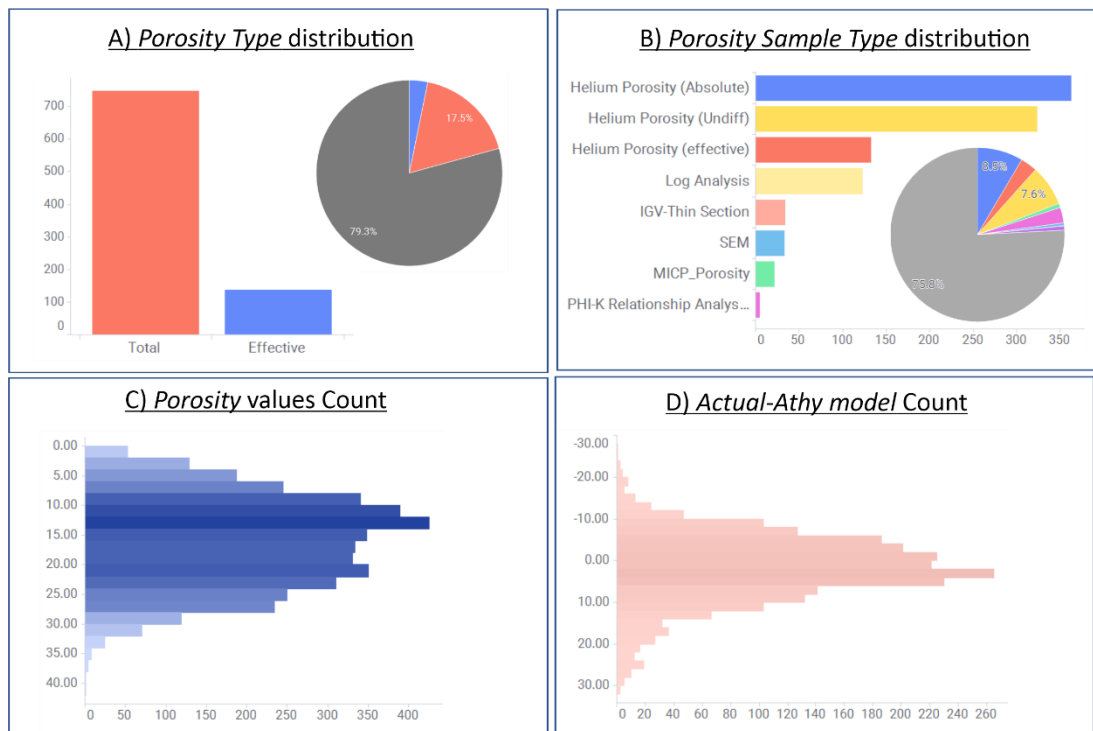


Figure 4.27 Porosity Charts

(A) Bar chart displaying the *Porosity Type* categories (“*total*” and “*effective*”). The bar chart excludes the undifferentiated (“*undiff*”) categories which are shown instead in the pie chart describing the volume in percentage. (B) Bar chart indicating the different *Porosity Sample Type* categories (count) and a pie chart showing the volume of *Sample Type* categories included in the database. Similar to (A), the “*undiff*” category is not shown in the bar chart but are represented in the pie chart instead. (C) A bar chart indicating the count for the porosity values. The data is binned grouping porosity values in groups. (D) Similar to (C), a bar chart displays binned porosity reduction data as per the different between the actual porosity recorded minus the Athy model.

The porosity section in the database also includes subgroups which refer to the porosity loss due to physical compaction (**Section 4.3.6.1**). Here we can find the following fields: i) The theoretical calculation of porosity loss assuming 40% porosity (sandstones) and 60% shales at surface conditions and its reduction at a specific depth as described by the Athy model represented in the **Figure 4.24C** (Athy, 1930). The resulting value is used for the calculation OP (original porosity) for the compaction calculations. ii) A comparison between the actual porosity measured and the previously porosity loss or original porosity (OP) which delivers additional insights for porosity reduction (Ehrenberg, 1995). In addition, to the previously described COPL in the compaction calculations, a column for the CEPL model (Cementation porosity model) (Ehrenberg, 1995) is also included in the porosity section. The CEPL model includes a measure of the 67 original porosity (OP) and only apply to a limited number of samples in the database included in the Estupinan et al., (2007) work. The CEPL equation includes the original porosity (OP), the compactional porosity loss (COPL) the volume percent of intergranular cements (CEM) and the intergranular volume (IGV) parameters (see equation below).

$$CEPL = (OP - COPL) \frac{CEM}{IGV}$$

4.3.8.2 Permeability

The permeability of a rock is a measure of the ease with which fluid of a certain viscosity can flow through it, under a pressure gradient. A permeable rock must have connected porosity. Furthermore, the permeability of a rock depends not only on the type of fluid in the connected porosity, the saturation condition by the fluids in the pores also affects this measurement. A single homogeneous fluid in the connected porosity with no chemical interactions with the rock refers to the absolute permeability of a rock and can be described by the Darcy's law where the instantaneous flow rate (q), permeability (k), viscosity (μ) and pressure drop (∇p) are represented (Darcy, 1856). See equation below:

$$q = -\frac{k}{\mu} \nabla p$$

Permeability can be measured in different ways. The most accurate permeability measurements can be taken from core. Tests are performed in the laboratory by flowing a fluid of known viscosity through a plug obtained from the core sample of a known dimensions at a set rate. The pressure drop is then measured across the core by setting the fluid to flow at a set pressure difference where the flow rate produced is measured.

The majority of the entries that include permeability values in PAFD refer to core-plug tests (Bear, 1972; Serra, 2004; Crains, 2000). The direction to which this pressure is measured from the core plug is also important (horizontal or vertical). Both measurements are useful to analyse the anisotropic component in a rock media. This is due to the depositional effects when clasts are sedimented and because of the in-situ stresses. In order to account for these two issues, tests are performed both parallel and perpendicular to bedding (Cannon, 2015). Gaseous fluids or liquids can be used for this procedure. If liquids are selected, the requirements for laminar flow and incompressibility of the fluid are almost always met at surface geological conditions.

On the other hand, if a gas is chosen there is a gas compression (or gas slippage or Klinkenberg effect) which needs to be addressed by the application of the Klinkenberg correction. Ignoring this correction in certain geological situations (tight rocks) can lead to errors and posterior corrections of up to 100%. For other settings such as high porosity and permeable rocks, the required correction is smaller (Klinkenberg, 1941).

Another way to calculate permeability refers to empirical methods which use various petrophysical inputs. An example of this is the Wyllie-Rose equation which uses porosity (Φ) and saturation water (S_{wi}) as inputs along with the parameters a , b and c . These are fixed values derived from specific lab experiments (e.g., Morris and Timur from the Western Atlas Chartbook or the Schlumberger Chart K3). See equation below:

$$k = a \frac{\phi^b}{S_{wi}^c}$$

In the database created in this study only 1% (122 entries) of the total permeability values correspond to log analysis.

PAFD accounts for permeability values corresponding to the following subgroups: i) *Specific Punctual Samples (Horizontal Permeability)*, ii) *Horizontal Average Permeability* values, iii) *Horizontal Minimum and Maximum* permeability values and *Vertical* permeabilities. The database includes a total of 3,831 permeability records. The permeability recordings can be associated with different *Types of Measurements*. These are samples coming from “liquid” tests indicating an accurate absolute permeability (“*liquid absolute*”) and samples where helium was chosen as the fluid to inject in the porosity (“*air- helium absolute*”). In the case of data on helium permeability, it was not possible to establish whether the Klinkenberg corrections were performed. A record of this relies on this information being present in the sources of permeability data where gas compressibility effects were considered. Another class of permeability measurements is termed “*air-Undiff*”, which is applied in cases where neither the nature of the fluid injected, nor the permeability type were documented. “*MICP*” samples are also differentiated in the database (**Figure 28A**).

The database also includes permeability values obtained from a porosity-permeability regression (“ *Φ -K relationship analysis*”), which is another common way to calculate permeability derived from a thorough petrophysical interpretation where porosity and saturation water were previously estimated. Finally, the ‘*undiff*’ category is applied to flag readings to which permeability measurement types are not described in the publications (**Figure 4.28B**).

4.3.8.3 Hydrocarbon Phase

The hydrocarbon phase encountered in the pore media is also included in this database. The database includes the following single-phase categories included in the Hydrocarbon phase (in conjunction with water): i) “*oil*”, ii) “*gas*” and iii) “*condensate*”. Also, PAFD includes 2 phases categories such as the “*oil and gas*”, the “*gas and condensate*” and the “*oil and condensate*”. The database also includes a category for those wells which didn’t find a hydrocarbon phase (water-bearing rocks) and as a result, they were plugged and abandoned. This is the “*dry (P&A)*” category. Entries where no data on the fluid phase occupying the existing porosity were tagged as “*undiff*” (**Figure 4.28C**).

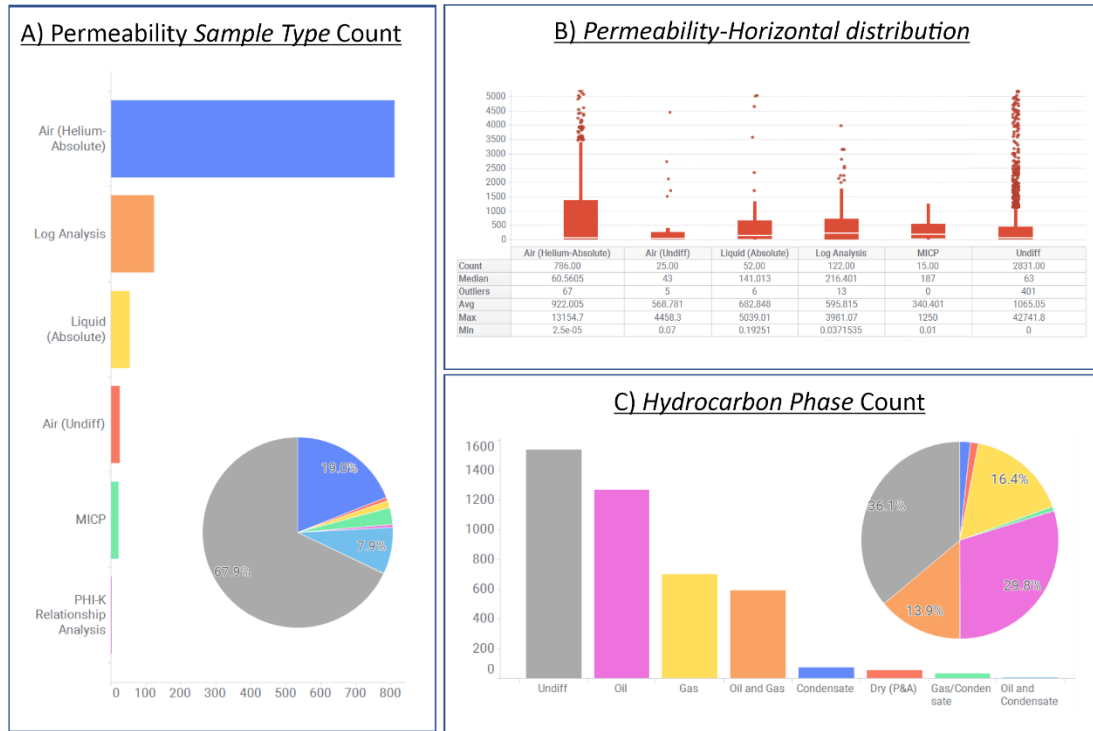


Figure 4.28 Permeability Charts

(A) Bar chart indicating the different *Permeability Sample Types* included in the database. The “undiff” (undifferentiated) category is excluded. The pie chart located in the lower right side shows the volumes in percentage for the same categories shown in the chart. (B) A boxplot displaying the permeability distribution for the horizontal permeability values stored in the database and (C) bar chart showing the different *Hydrocarbon Phase* categories in the database and a pie chart representing the volume percentages.

4.3.8.4 Other

Other petrophysical parameters, such as the *Bulk Density* recordings and *Volume of Clay*, are also included in the database. Furthermore, information for the reservoir Gross Thickness and the Net Reservoir thickness” recorded in metres are included in the database.

4.4 Discussion

PAFD allows the selection of several geological analogues to subsurface successions of economic interest. The ability to consider multiple alternative analogues to a formation rock enables effective consideration of geological uncertainty, which is crucial in subsurface workflows. The database ability to relate petrophysical properties to metadata (location, lithostratigraphy, etc.)

and geological attributes (petrography, stratigraphic architecture, tectonic settings, etc.) also enables the analysis of relationships between rock petrophysics and geological boundary conditions. Therefore, PAFD can be employed as a tool that facilitates meta-analysis, a research approach that has been proven to generate significant new insight in the earth sciences in recent years (e.g., [Colombera et al., 2012a](#); [2012b](#); [2013](#); [2015](#); [2016](#); [2017](#); [Bär et al., 2020](#); [Kenter and Harris, 2008](#); [Saunders et al., 2012](#); [Vakarelov et al., 2010](#); [Weydt et al., 2020](#)).

Although PAFD considers a broad range of petrophysical characteristics, special focus is on the characterisation of porosity and permeability values of fluvial facies. This is because these two properties are the most important for ranking reservoir rocks in terms of reservoir potential to hold hydrocarbons (porosity) and its capacity to be exploited adequately (permeability) ([Serra, 2004](#); [Crains, 2000](#); [Glover, 2019](#); [Tiab et al., 2003](#); [Cannon, 2015](#)).

In terms of applications, PAFD can be utilised for different purposes. In contexts of reservoir evaluation and modelling, different professionals (log analysts, geologists, petrophysicists, etc.) require a characterisation of likely rock properties for reserve calculations of a given asset and construction of a static geocellular model ([Rojas et al., 2012](#)). In these situations, queries to PAFD will help predict key rock properties derived from suitable outcrop and subsurface analogues. The main applications of the proposed database are summarised in the following points:

- **Conceptualisation.** The identification and location of suitable fluvial targets that may be associated with potential reservoir rock and the subsequently identification of its horizontal and vertical distribution in the subsurface ([Wood, 2004](#)). The devised database relates fluvial system characteristics with their corresponding geological context (e.g., tectonic setting, diagenetic history, depositional system) which may lead to the increase of the chance of succession prospect evaluation. An example for this application can be described in [Curry \(1972\)](#), where the location of successful wells improved once sufficient geological content was acquired by understanding the reservoir was located in a meandering fluvial system and a better understanding of its horizontal distribution was acknowledged. Also, Chapter 6 includes several examples where PAFD can greatly contribute to the model concept phase in a reservoir model workflow (**section 6.2.1**).

- **Modelling.** PAFD can effectively assist on the identification of analogue data suitable for a particular area of investigation where petrophysical values are needed to feed property models (porosity and permeability). This is the main purpose for the creation of this database where Chapter 5 validates its usefulness where trends and spatial variation are identified associated to petrophysical parameters (Chapter 5).
- **Net thickness determination.** Evaluation of effective vertical thickness by the determination of their net value. The determination of different net-to-gross values will determine the real thickness of the reservoir which combined with its lateral extent (see previously point 1) will determine the economic viability of a project (Serra, 2007). The created database can be applied to the determination of different cut-offs or thresholds on which net reservoir is defined. An example for the correct characterisation of a Net Pay thickness can be derived by the application of a combination of porosity and permeability values which can be easily calculated from a database-driven (section 6.2.2.6).
- **Porosity predictions.** PAFD can predict ranges of porosities that may exist at specific depths in the subsurface. Commonly, sandstone porosity decreases at a rate of 2.5-3 porosity units due to compaction (Ramm R., 1992), but might be also affected by other factors, such as sediment sorting or volume of clay (Scherer, 1987). The relationships between porosity and depth (subject to depth references: ground level, Kelly bushing, etc.) that can be drawn from this database allow the user to constrain the ranges of porosity at the depths where a play can be located, which can be employed in calculations of potential volumetrics of the reservoir rock unit (section 6.2.2.2 and 6.2.2.3).
- **Porosity and Permeability relationships.** Although in many circumstances, there is not a strong correlation between porosity and permeability, trends can often be observed, enabling users to obtain ranges of permeabilities for given porosity values (Serra, 2007). Prediction of porosity and permeability values can be very useful for subsurface evaluation and risk assessment related to early exploration phases (Tarek, 2020) (section 6.2.2.6).

Limitations associated with this database comes from different attributes which will be analysed in the following points:

- PAFD was created on a single Excel spreadsheet. Although this format allows users flexibility and simplicity to filter categories associated to different subgroups, has been proven easy-to-us, flexible and efficient at delivering meaningful outputs for multiple queries, the database is static, two-dimensional, may duplicate data and one-size-fits all views

make them though to use for more complex use-cases queries are more difficult to expand to complex searches related with fluvial systems as compared with relation databases.

- Uncertainties and errors in the original data sources. For instance, data originating from laboratory measurements tend to be more precise and reliable than those coming interpretations of wireline logs. For this limitation, the user has a simple way to understand uncertainties by interpreting the *Type of Analysis*.
- Wrong measures/interpretations for the entries extracted to public domain sources (publications and public databases) included in PAFD. Although this study did not attempt to identify errors in the original publications and relies on the assumption that the data they contained were already peer-reviewed and/or acquired according to the highest standards of quality, quick-look analysis were carried out to discard those outliers which do not fit to realistic trends. An example for the techniques applied was the usage of regression curve porosity-permeability which will deliver a realistic trend able to separate those reliable measures from those core data perhaps associated with fissured or fractures samples.
- A database as the one this study addressed can't never be completed. The amount of data which the database retrieves for a given query can be very variable and may deliver a number of results which can't be sufficient in terms of a reliable statistical population. This adds another degree of uncertainty which can only be solved with the addition of new data.

4.5 Conclusions

A database that encapsulates petrophysical data with fluvial characteristics in addition to associated metainformation has been built. Public domain data from peer-reviewed publication and other database have been used including both well and outcrop data including a total of 4,262 entries as of July 2023.

Porosity and permeability parameters included in the database allows users to objectively compare for different purposes discriminating different scales of observation and heterogeneity. The adopted database architecture prioritises speed for searches. The database can be applied for “quick-look” scenarios but more advanced queries can also be made where quantitative petrophysical parameters associated to fluvial characteristics and other

qualitative data are required. PAFD is sufficiently versatile to allow users to relate queries to single case-studies else to combine several case studies and to apply a series of one or more filters with respect to the various subgroups existing in the database. Moreover, the current architecture of PAFD allows easy modification and updating of the current data and most importantly enables the addition of new data for future expansion. Furthermore, the terminology used in the database is designed to be easy to be understood, not just by geoscientists, but also by other professionals such as petrophysicists, geomodellers and reservoir engineers.

PAFD is applied as a tool in Chapter 5 for better understanding and predicting the subsurface and to deliver meaningful property values applied to the previous stage of this PhD (Chapter 3) where facies models were created (Montero et al., 2021). However, there are numerous different potential fields of application for which PAFD can be interrogated. These are: i) the conceptualisation stage within the reservoir model workflow, ii) the identification of quantitative inputs to feed static models, iii) the determination of petrophysical cut-offs and thresholds associated with economic risk and uncertainties and iv) porosity and permeability predictions associated to fluvial characteristics. For these last three points some examples are included within Chapter 6 where the database is proven to be very useful at deliver important reservoir insights in the very early stages of exploration and during the appraisal phase.

Limitations of PAFD relate principally to the nature of the architecture and its design: the database is built as a single Excel spreadsheet, though it could readily be converted to a relational database format. Moreover, it relies on public-domain data which may have been wrongly extracted for the case of the quantitative petrophysical data, or subjectively interpreted for those fluvial characteristics and other metadata associated to the petrophysical data by the corresponding authors. Moreover, the amount of data associated to specific queries might not deliver the desired number of outputs considered as statically reliable.

5. Assessing the Role of Sedimentary Heterogeneity in Fluvial Successions for CO₂ Injection Using Property Models Constrained on MPS Facies Distributions

5.1 Introduction

Fluvial deposits of meandering river origin form important reservoir rocks that can host a variety of fluids (hydrocarbons, water, CO₂, etc) (**section 2.2**). An assessment of the suitability of rock volumes formed of the accumulated successions of meandering fluvial systems requires a series of studies to be performed, the objectives being to define the three-dimensional geometry, the spatial distribution, the orientation, and most importantly the total volume of the reservoir associated with a type of net, including assessment of the volume of the effective net component of the reservoir. For this purpose, petrophysical properties play a fundamental role because they define quantitatively the economic viability of a reservoir rock volume ([Cosentino, 2001](#)).

Petrophysical (property) modelling is undertaken after the construction of a facies model, by assigning cells within a 3D grid discrete or continuous properties using deterministic and/or stochastic methods ([Deutsch, 2002](#)). Properties of interest include porosity (Φ), permeability (K), volume of clay (Vcl), water saturation (S_w), net-to-gross ratio (NTG), density (ρ), seismic properties, geomechanical properties, amongst others (**section 2.1.7**). Porosity and permeability are a particular focus in many property models since these properties are especially important in determining fluid-flow properties within the main reservoir model elements ([Abbaszadeh and Fujimoto, 1996](#)). Well-log data, including 1D petrophysical data and different types of secondary data, are commonly used to ensure accurate representation of spatial trends within the overall model. Such secondary data include, for example, transforms associated with particular model elements, which may describe relationships between different properties (e.g., porosity-permeability transforms) ([Journel et al., 1986](#)).

In Chapter 3, the geological realism of facies models built using two MPS algorithms (SNESIM and DEESE) in application to highly heterogeneous fluvial successions were assessed ([Montero et al., 2021](#)). However, an assessment of the impact of geological realism of these facies models on

dynamic flow behaviour remains to be demonstrated. In this chapter, the facies models developed and presented in Chapter 3 are populated with petrophysical properties (porosity and permeability) derived from the database introduced in Chapter 4 (PAFD, Petrophysical Analogue Fluvial Database) to better quantify the impact of different types of lithological heterogeneity. Given that the facies models introduced in Chapter 3 were built in absence of any conditioning data, the database developed and summarised in Chapter 4 will be used to derive representative petrophysical hard data and other related soft data that can be employed in the property and dynamic modelling. Multiple filters are applied to PAFD to select appropriate petrophysical properties (porosity and permeability) with which to constrain the property models. This methodology is comparable to the use of analogue data for the construction of outcrop-based property models applicable for flow simulations (Chandler et al., 1989; Barton et al., 2004). The approach can also leverage on the use of database outputs for i) predicting ranges for porosity and permeability as a function of depth and resulting compaction, and ii) the determination of different net-category thresholds.

This Chapter seeks to understand how variability in the geological realism of facies models may impact dynamic flow behaviour, which is herein specifically considered with regards to a CO₂ plume injected in a host reservoir-rock volume. This type of application is of broad significance because it will elucidate the behaviour of a CO₂ plume injected in a highly heterogeneous fluvial succession, and this provides valuable insight for the planning of ongoing and future CCS projects (e.g., Gippsland Basin, Australia).

Numerous prior studies have examined the behaviour of a CO₂ plume and its effects on cumulative injected CO₂ volumes and injection rates, considering controls such as relative permeabilities (Bennium and Bachu, 2005; Bachu, 2001; Sifuentes, 2009; Moodie et al., 2016), horizontal and vertical permeability ratios (Meyer and Krause, 2006), supercriticality of CO₂, and its behaviour under specific pressure and temperature conditions (Hagbakhsh et al., 2013). However, research questions on the importance of facies and architectural controls remain largely unaddressed. Although the dynamic behaviour of highly heterogeneous successions has been thoroughly documented for conventional hydrocarbon reservoirs (Cabello et al., 2018; Willis and Sech, 2018; Puig et al., 2019), only a limited number of studies have

considered CO₂ injection in high-sinuosity fluvial channel deposits (Frykman et al., (2009); Issautier et al., (2013); Sun, et al., 2023).

5.2 Aim and Objectives

The aim of this chapter is to assess how variability in the geological realism of facies models – through its controls on petrophysical properties – affects dynamic simulations of CO₂ injection. Different scales of heterogeneities (macroscale and mesoscale) incorporated within previously built facies models using SNESIM and DEESSE (Chapter 3) will be considered in order to examine their potential impact on carbon capture and storage (CCS) potential. Specific objectives of this chapter are as follows: i) the utilisation of PAFD introduced and explained in Chapter 4 as a tool that delivers petrophysical analogue data for fluvial deposits applicable for the creation of property models of value in assessing CO₂ storage potential in underground reservoir successions; ii) dynamic simulation for analyses of the behaviour of injected supercritical CO₂. Plume behaviour, injection rates and cumulative storage are analysed and compared between the 3-facies (macroscale) and 5-facies (mesoscale) models presented in Chapter 3 to evaluate the impact of smaller-scale heterogeneities.

5.3 Methodology: Property Modelling

A property model is obtained by populating a 3D grid with petrophysical properties whose distributions are constrained on the modelled facies. The distribution of petrophysical properties in the 3D grid and the particular modelling approach can be variably chosen depending on the type of input data and petrophysical properties of interest. For this study, no well-log data are used to condition the property models. Instead, trends between different properties (depth, porosity, and permeability) are based on the adoption of values derived from suitable geological analogues. The property models will be built considering trends that describe correlation between different properties (depth-porosity and porosity-permeability) and spatial relationships (often expressed by vertical and lateral trends) between different rock types (facies).

PAFD (Chapter 4) will be applied to derive petrophysical trends associated with model elements defined previously via the construction of the facies

models in Chapter 3. In this study, PAFD is used in the following ways: i) the identification of analogue datasets of petrophysical properties (porosity and permeability); and ii), the identification of correlations and spatial trends for petrophysical properties of specified rock types or facies. Property models for porosity and permeability are generated based on the previously created facies models of Case 7 and Case 8 of Chapter 3 (**section 3.3.6.1 and 3.3.6.2**) (**Figure 5.1**).

Porosity and permeability models were created in Schlumberger Petrel™ software by adopting and following conventional industry workflows. Property modelling is typically performed stochastically using different methodologies. In this study, the Petrel™ algorithm “Sequential Gaussian Random Function Simulation” (GRFS) was used to simulate all realisations for porosity and permeability models in combinations with co-kriging based on secondary variables to account for trends.

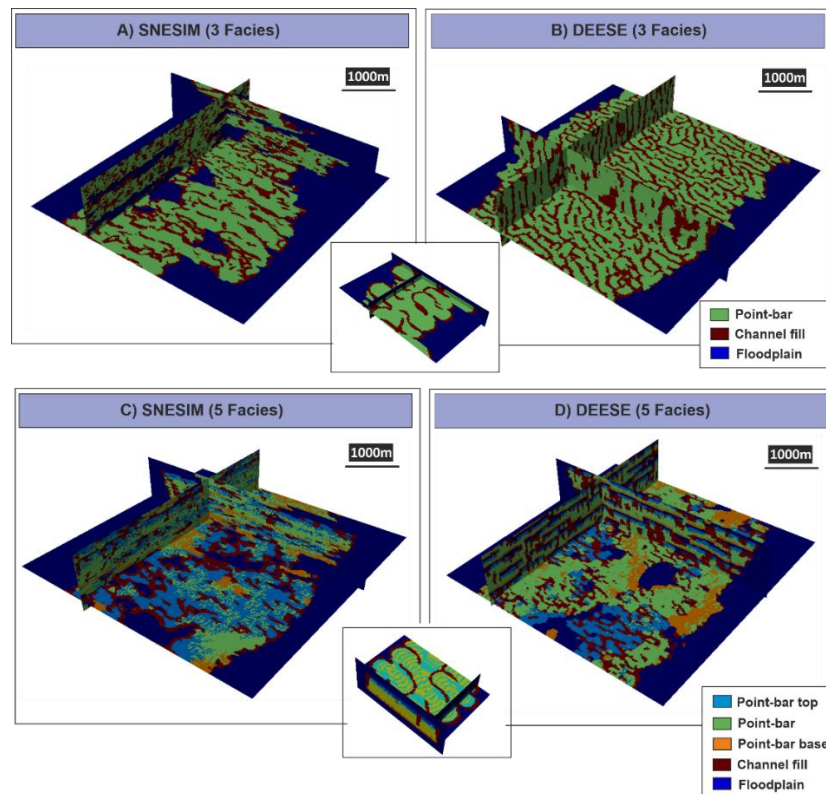


Figure 5.1 Four realisations selected for property modelling.

Four realisations from the cases 7 and 8 of the MPS facies models of Chapter 3, selected to be populated with petrophysical properties (porosity and permeability). The small figure in the middle of both realisations for SNESIM and DEESE corresponds to the training image used for the simulations.

The GRFS algorithm fully honours well data (a feature that is not needed in this study since no wells were utilised), as well as input distributions, variogram models and trends. The variogram models and the distributions are used to reproduce local variations of a given property. The GRFS algorithm is patented by Schlumberger and is based on the classical Sequential Gaussian Simulation (SGS; [Deutsch and Journel, 1997](#)). The GRFS algorithm controls anisotropy in the simulations by the calibration of a variogram model to establish threshold values for the spatial ranges in X, Y and Z directions. In this research, the major, minor, and vertical variogram ranges that define property anisotropy in the model are defined based on visual analysis of the size of point-bar features observed within the previously built facies models. An exponential variogram model was used for all property models in this study.

The GRFS algorithm used here is conditioned to secondary data. Each of the rock types of the facies model exhibits different trends. Correlations between different properties (e.g., depth, porosity, and permeability) in PAFD (Chapter 4) are used as secondary data. Regression analysis equations are taken as functions (transforms) for inference of the independent variable. The coefficient of determination (R^2) is used to evaluate the strength of correlation. Values below 0.3 were considered as poorly correlated for this study in based to standard petrophysical practices for porosity-permeability relationships ([Serra, 2008](#)).

A depth-porosity transform for each of the rock types is used to create porosity models (3D porosity volumes). For permeability models, a combination between porosity-permeability transforms and the previously modelled 3D porosity volumes for each of the rock types are used to deliver permeability models. No horizontal trends are incorporated in the simulations. The most important inputs utilised for the construction of porosity and permeability models are summarised in the **Table 5.1**.

For both the 3-facies and 5-facies property models (Chapter 3), a single reservoir zone was modelled, using a grid of 250 cells along X, 250 cell along Y and 50 cells along Z. The cell size is 20 m along X, 20 m along Y and 1 m along Z. This grid may be considered representative of area of investigation of 5,000 m in X and Y and 50 m of thickness. The chosen cell size results in

vertical resolution increased by a factor 20 relative to the horizontal. This ratio was considered as optimal for preserving all levels of lithological heterogeneity depicted in the facies models, including, vertical fining-upward facies variation trends, for example. The top of the modelled gridded volume is allocated to a subsurface depth of to 2,350 m; the base is allocated to 2,400 m.

		Porosity		Permeability	
		Variogram Ranges	Secondary Data	Variogram Ranges	Secondary Data
3 Facies	SNESIM	200x200x5	Transform (Co-kriging)	200x200x5	Transform + 3D Volume Porosity (Co-kriging)
	DEESSE	250x250x5	Transform (Co-kriging)	250x250x5	Transform + 3D Volume Porosity (Co-kriging)
5 Facies	SNESIM	300x300x5	Transform (Co-kriging)	300x300x5	Transform + 3D Volume Porosity (Co-kriging)
	DEESSE	250x250x5	Transform (Co-kriging)	250x250x5	Transform + 3D Volume Porosity (Co-kriging)

Table 5.1 Summary for simulations performed for porosity and permeability models.

Table summarising the experimental variogram ranges used for GFRS (major direction x minor direction x vertical direction corresponding to the distance where the experimental variogram levels off adjusted to the point-bar dimensions expressed in meters) and secondary data used to condition the simulations.

For the 3-facies models, the rock types selected for the facies modelling correspond to categories of architectural elements of a meandering fluvial system. These are: i) mud that accumulates in undisturbed floodplain areas; ii) sand deposited in point-bar settings in the main sand fairway of the channel belt, and that constitute the main reservoir rock; iii) mud-prone channel-fill deposits that can act as baffles or barriers to the flow between the main sandy

point-bar deposits. The petrophysical database (PAFD) has been interrogated to return data relating to geological analogues for which core data are known and which record these lithological types. **Table 5.2** indicates the filters applied to PAFD for the extraction of porosity and permeability values. For the 3-facies property modelling, data that exclusively relate to point-bar deposits were extracted. For floodplain and channel-fill deposits, an effective porosity of 0 and an effective permeability of 0 was input into the model as constant values. This means that, in practice, the floodplain and channel-fill deposits behave as non-permeable barriers in the 3-facies models.

		Rock Types-3 Facies (Excluded categories)
		Point-bar
PAFD Subgroups	Geomorphic Settings 1	Non-channelised
	Geomorphic Settings 2	Low sinuosity channel
	Dominant Formative River Platform	Anastomosing, braided and fluvial-undifferentiated
	Architectural Elements	Undiff, Bar Undiff

Table 5.2 Query 1: Analogue identification (Point-Bars)

Filters applied to PAFD (Petrophysical Analogue Fluvial Database) for obtaining data for specific lithological types (Point-bar, Channel-fill and Floodplain). The classes listed in the table indicate analogue categories (“subgroups”) that were excluded from the database. Outputs obtained applying these filters are shown in **Figure 5.2A**. For the Channel-fill and Floodplain rock types, effective porosity of 0 was applied as default.

The main objective for the database filters indicated in **Table 5.2** is the identification of geological analogues of fluvial point-bar deposits that can be used as a reference in the property modelling. PAFD outputs based on the application of these filters are reported in **Figure 5.2** where porosity and permeability values yield a relatively low R^2 value of 0.392 (**Figure 5.2A**). However, stringer correlation between porosity and permeability is seen for some of the individual formation rocks where the Latrobe Group, returns a R^2 value of 0.769 (**Figure 5.2B**). The Latrobe Group is therefore employed as a suitable analogue case-study example from which to derive a porosity-

permeability relationship, and with which to constrain the property models. Data on the Latrobe Group come from cores of the Tarwhine-1 well, located in the Gippsland Basin in the southeast of Australia ([WAPIMS database - Western Australia Department of Mines, Industry Regulations and Safety](#)). Further explanations as to why this analogue case study example is considered appropriate are given in the next section.

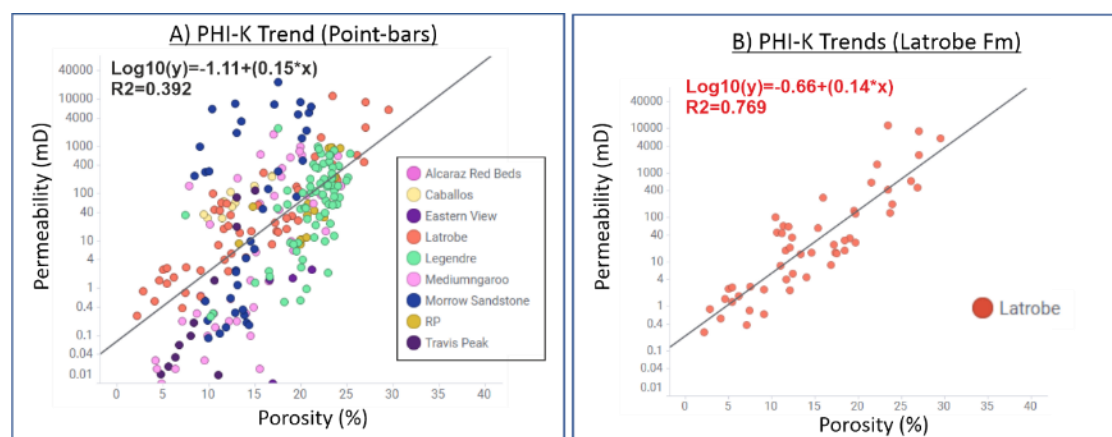


Figure 5.2 Porosity-Permeability Trends Dataset (Point-bars)

PAFD (Petrophysical Analogue Fluvial Database) outputs based on filters indicated in **Table 5.2**, showing (A) all porosity and permeability data associated with different rock formations included in the database (Alcaraz Fm, [Henares et al., 2016](#); Caballos Fm, [Castellanos, 1994](#); Eastern View Fm, Latrobe Fm, Legendre Fm, Mediumngaroo [WAPIMS](#); Morrow Sandstones, [Dolly and Mullarkey, 1996](#); RP, [Barde et al., 2002](#); Travis Peak, [Indiana University Database](#)) and (B) the Latrobe Group porosity and permeability data only.

5.3.1 The Latrobe Group

The geological analogue identified in the petrophysical database as a reference for this study is the Latrobe Group. Porosity and permeability values stored in PAFD are derived from the Tarwhine-1 well located in the Gippsland Basin, offshore southeast Australia (**Figure 5.3**). The Tarwhine-1 well intersects the Barracouta Formation, where the primary reservoir targets are located. The Barracouta Formation is part of the Halibut Subgroup, which is Late Cretaceous to Early Eocene in age (75 to 45 Ma). During this time, siliciclastic sediments were deposited in a rift-related extensional basin. This divergent regime created pervasive northwest-striking normal faults within the downthrown hanging wall blocks of which meandering fluvial, deltaic and marine systems were developed, and their successions were accumulated ([Bernecker et al., 2003](#)). The Barracouta Group records accumulation in an

upper coastal plain setting and includes fluvial sandstone and minor coal deposits. Overlying the Barracouta Group is the Kingfish Group, which records the accumulation of a lower coastal plain within which fluvio-deltaic and paralic systems developed (Holdgate and Gallagher, 2003).

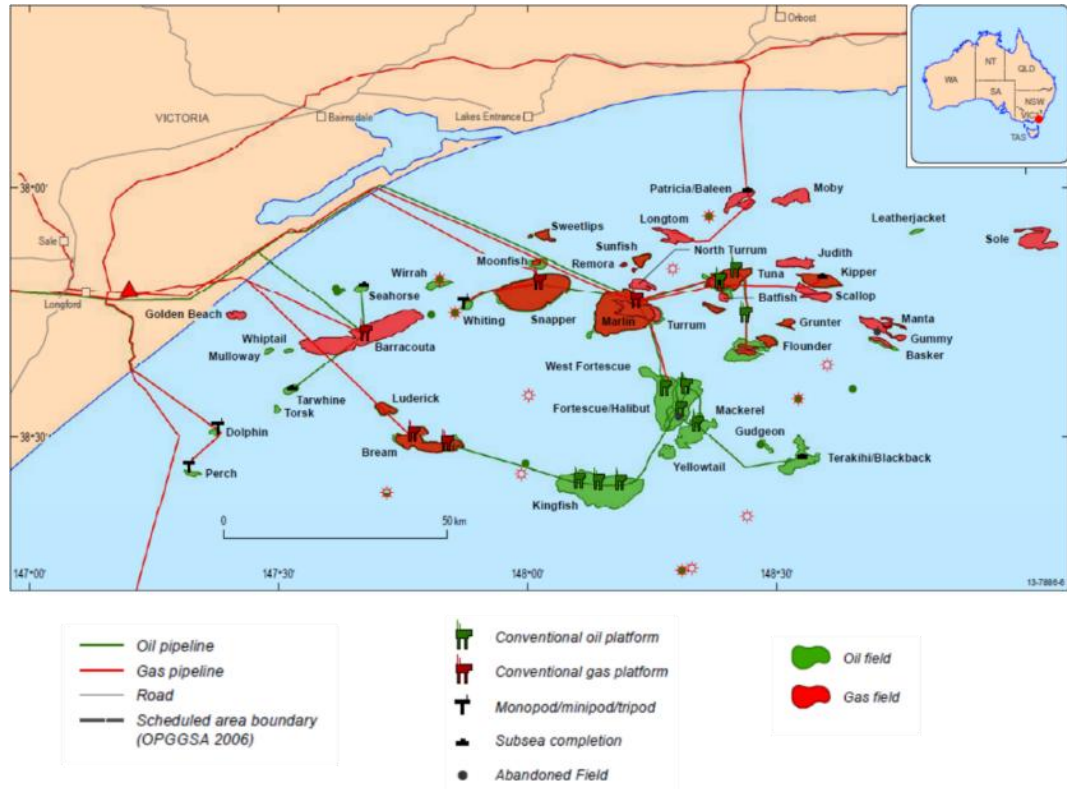


Figure 5.3 Petroleum Production facilities. Gippsland Basin

Location for Tarwhine-1 well within the Gippsland Basin (Petroconsultants, 1996).

The Barracouta Group comprises gas-prone reservoir rocks, whereas reservoir rocks of the Kingfish Group are more oil-prone (Moore et al., 1992). The Barracouta Group is deposited in a high-sinuosity fluvial system where lateral accretion features and fining-upward trends are identified in well logs (Walker and Cant, 1984) (Figure 5.4). Strong compartmentalisation of multiple stacked sandstones and shales has been recognised as largely due to the nature of meandering channel-belt deposition (O'Brien et al., 2008). The Latrobe Group sandstones are the primary reservoirs in the Gippsland Basin (Petroconsultants, 1996). Average porosities of fluvial sandstone bodies that comprise the reservoir rocks are 15-25%. These are sections commonly associated with texturally mature and moderately well-sorted sandstones.

More widely, most of the reservoirs located in the Gippsland Basin include multi-Darcy high-quality sandstones.

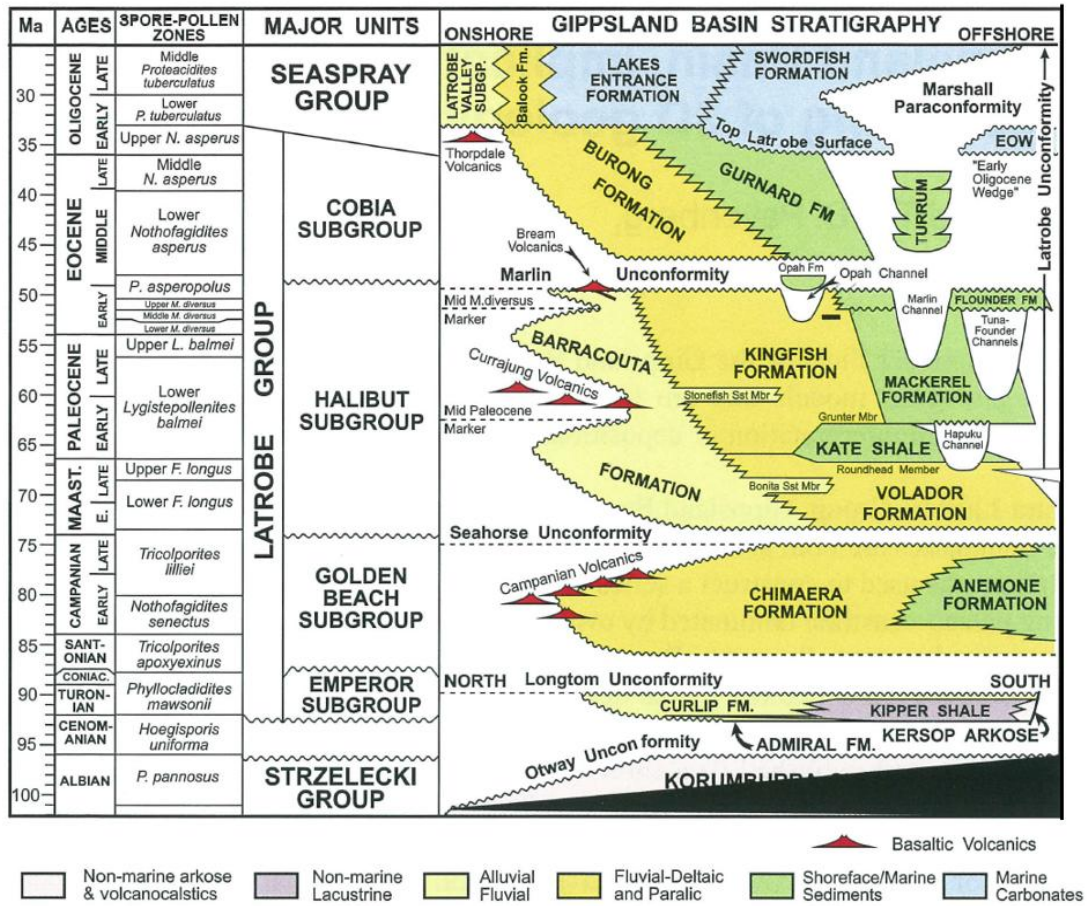


Figure 5.4 Latrobe Group (Stratigraphic units)

Stratigraphic units within the Latrobe Group. Modified from [Bernecker and Partridge \(2001\)](#) and [Riordan et al., \(2004\)](#).

Secondary porosity, due to dissolution of dolomite cement and associated with hydrocarbon emplacement, is the main porosity contributor in the Latrobe Fm. However, authigenic kaolinite growth, chlorite filling, quartz cementation and overgrowths have been observed occluding porosity ([Bunch et al., 2011](#)). Porosity versus depth cross-plots indicate a severe decline in porosity with depth; this limits the viability of the reservoir at approximately 4000 m at present-day depth ([Clark and Thomas, 1988](#)).

The Gippsland Basin has been extensively explored for hydrocarbons since the 1960s, when several giant oil and gas fields were found in the Kingfish

Fm, Snapper, Marlin and Barracouta fields, all located in the central and northern parts of the basin. Currently, several projects are investigating the suitability of this basin for the long-term storage of anthropogenic CO₂ in the subsurface (Quinn, 2022).

5.3.2 Porosity Models (3-Facies Simulations)

The methodology used to determine porosity-depth ranges associated with the simulations includes the determination of different compaction regimes related with the Latrobe Group; a function (transform) is derived for constraining porosity realisations. To this end, petrophysical data are extracted from PAFD by applying filters to the database. Depth-porosity values for the point-bar facies (sand bodies) are thus obtained (**Figure 5.5**). Filters have been applied as described in **Table 5.3**:

		Depth-Porosity Trend (compaction regime)
		Point-bar
PAFD Subgroups	Depositional Environment	Fluvial-deltaic
	Geomorphic Settings 1	Non-channelised
	Geomorphic Settings 2	Low sinuosity channel
	Dominant Formative River Planform	Anastomosing, braided
	Architectural Elements	Undiff

Table 5.3 Query 2: Porosity-Depth (3 facies)

Applied database filters for extracting porosity values related to depth and classified according to compaction regimes. The listed classes indicate categories associated with specific “subgroups” excluded from PAFD. Resulting database outputs are shown in **Figure 5.5**. The table only shows the filters applied to the Point-bar rock type. For the Channel-fill and Floodplain rock type an effective porosity of 0 was applied by default.

Different linear depth-porosity trends are observed corresponding to different compaction regimes (**Figure 5.5A**). For the determination of the point-bar depth-porosity trends, this study utilises the relationship that exists between porosity, depth, and rock compaction in the Latrobe Group. This choice is supported by a well completion report for the Tarwhine-1 well, which indicates reservoir rocks being subjected to moderate compaction (**Figure 5.5B**).

A depth-porosity trend function ($\phi = -0.0039 + (21.001depth)$) is then used to condition the 3-facies porosity models by the use of a secondary variable that drives porosity distribution in the static model (minimum and maximum values, as well as the mean and the standard deviation). For this particular case, minimum and maximum values of 0.11 and 0.12, respectively, a mean of 0.117, and a standard deviation of 0.05 are used as the porosity ranges within the modelled point-bar elements (**Figure 5.5B**).

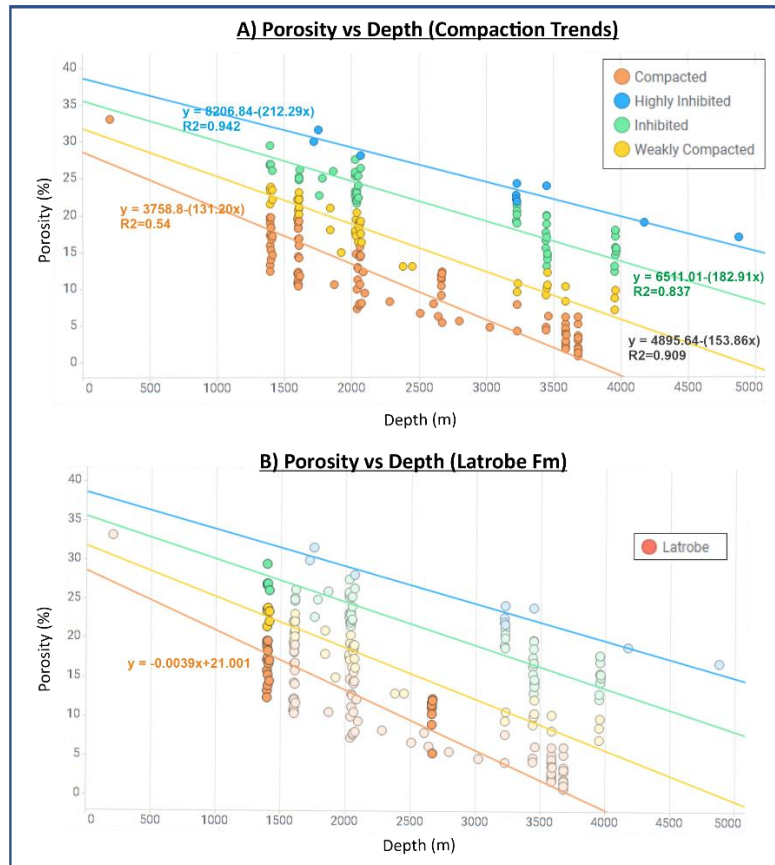


Figure 5.5 Porosity vs Depth Trends (compaction Regimes)

“A” Cross-plot indicating four different depth-porosity trends associated with query 2 (**Table 5.3**). Four transforms associated to strong correlation coefficients are obtained to condition porosity models. (B) Location of Latrobe Group within the porosity-depth dataset.

The trend is then applied to the simulations as a secondary variable (collocated co-kriging) in both SNESIM and DEESE facies models. For Channel-fill and Floodplain rock types, a constant (e.g., fixed) value of 0 for porosity was assigned in the static models. For the 3-facies scenario, variogram models were calibrated with respect to the size of the point-bar

features within the SNESIM and DEESSE frameworks (facies models). These are approximately 250m long (bend-axis) as observed in the original training image shown in Chapter 3 (3.3.6.1 section). **Table 5.1** includes the inputs used in the property modelling algorithm. No horizontal trend was included. **Figure 5.6** shows two representative realisations of resulting porosity distributions for SNESIM and DEESSE frameworks.

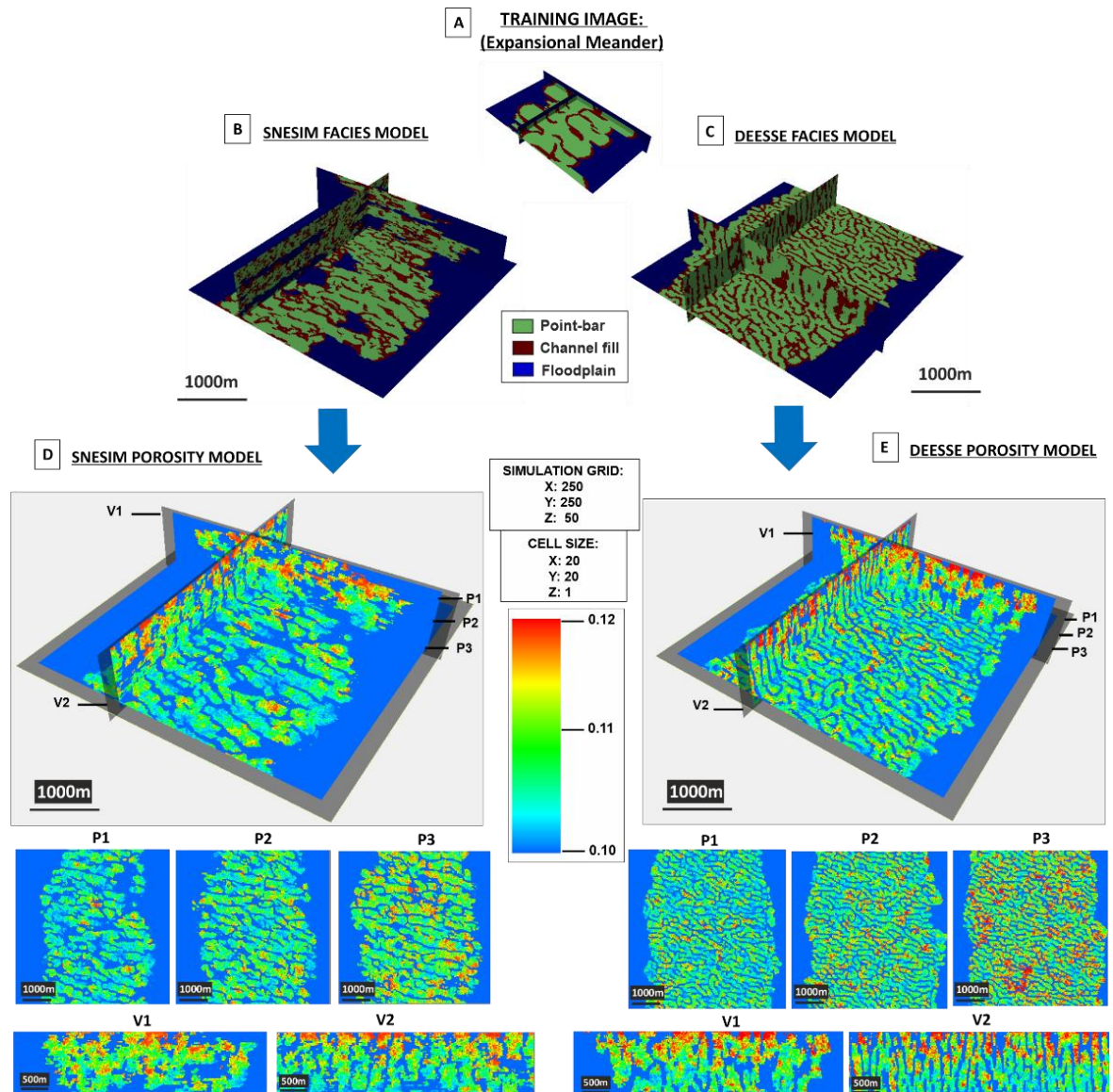


Figure 5.6 Porosity Models (3 Facies – SNESIM & DEESE)

Comparison between porosity models performed on SNESIM and DEESSE facies models. (A) shows the training image from which facies models (B) and (C) were made. These facies models are then used as the framework for the construction of porosity models (D) and (E). Different plan-view images (P1, P2 and P3) and vertical images (V1 and V2) are also shown.

5.3.3 Porosity Models (5-Facies Simulations)

A workflow similar to that used for the 3-facies porosity model was used for the 5-facies model grids. Again porosity-depth trends were adopted as secondary variables, and different functions (transforms) were chosen for each of the three different point-bar facies types (mesoscale heterogeneity level; see Chapter 3). These facies correspond to the following: i) the coarser basal part of the point-bar elements that accumulate near the channel thalweg; ii) sand-prone mid-point-bar deposits; and iii) finer-grained point-bar top deposits. These three categories are arranged according to a vertical fining-upward trend reproduced in each of the realisations.

		5 Facies porosity model (Point-Bar facies)	
		Point Bar base	Point Bar Top
PAFD (Subgroup)	Depositional Environment	Fluvial deltaic	
	Geomorphic Settings 1	Non-channelised	Non-channelised
	Geomorphic Settings 2	Low sinuosity channel	Low sinuosity channel
	Dominant Formative River Planform	Anastomosing, braided	Anastomosing, braided
	Architectural Elements	channel-fill, Mid-channel bar, splays, unconfined sheet body	Bar Undiff, Undiff
	Lithofacies		Gp, Sp, Sp-Sh
	Grain Size	Undiff, medium	
	Max. Grain size	Fine, medium	
	Sorting	Moderated sorted, moderated to well sorted, well sorted	
	Compaction Degree	Highly compacted, highly inhibited, undiff	Highly compacted, highly inhibited, Inhibited, and weakly compacted

Table 5.4 Query 3: Porosity-Depth (5 facies)

Filters applied to PAFD (Petrophysical Analogue Fluvial Database) for basal and top point-bar deposits, for derivation of data on porosity and associated depth. The reported classes indicate the categories (“subgroups”) excluded from the database (left classes). Resulting PAFD outputs are shown in **Figure 5.7**. For the mid-point-bar facies, the values previously determined for the Latrobe Group in **Figure 5.5B** (Query 2) were applied.

The two remaining facies types correspond to the following: i) the mud-prone floodplain deposits occurring between the channel belts; and ii) mud plugs representing abandoned channel fills. Porosity data for the point-bar basal and top facies types were extracted from PAFD, which was filtered on the attributes summarised in **Table 5.4**. The porosity values previously defined for the Latrobe Group point-bar deposits are used as the mid-point-bar facies type (**Figure 5.5B**).

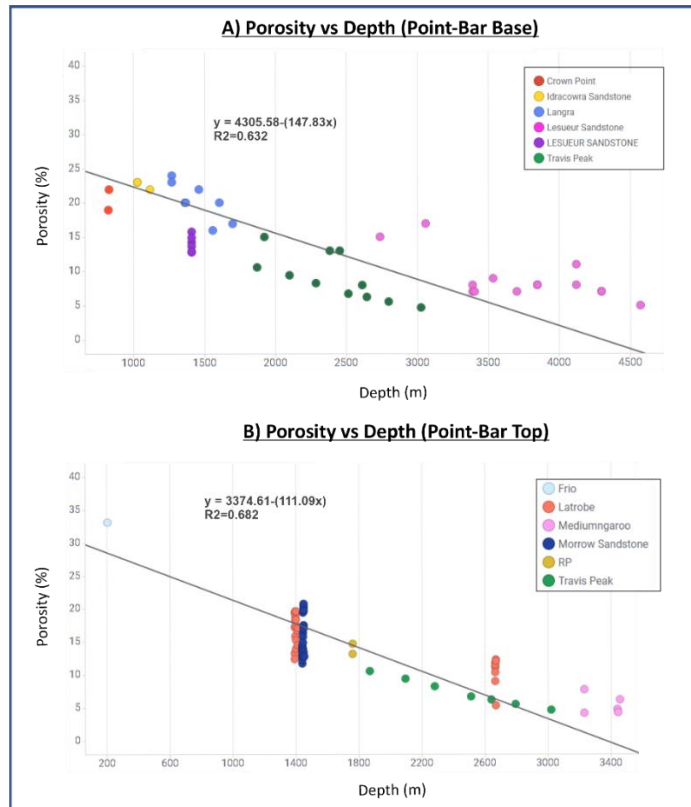


Figure 5.7 Porosity vs Depth Trends (Point-bar base and Point-bar top)

(A) Cross-plots of porosity vs depth that are used to constrain porosity models for basal point-bar (Crown Point Fm., Idracowra Fm, Langra Fm., Lesueur Fm, [WAPIMS](#); Travis Peak Fm., [Bartberger et al., 2003](#)) and point-bar top (B) facies (Latrobe Fm., Mediumngaroo Fm. [WAPIMS](#); Morrow Sandstones, [Dolly and Mullarkey, 1996](#); Frio Fm. [Indiana University Database](#), RP Fm., [Barde et al., 2002](#) and Travis Peak Fm., [Bartberger et al., 2003](#)). Both relationships are based on combination of analogue data from different successions.

Porosity-depth trends for basal point-bar and point-bar top facies are reported in **Figure 5.7**. A linear regression function based on data from several successions describes the depth-porosity trend; this has been used as a secondary variable for porosity modelling. The transforms to be used yield R^2

values of 0.632 and 0.682 for point-bar base and point-bar top, respectively. As was done for the 3-facies model, the porosity distribution in the 5-facies model is constrained by the obtained functions. For the mid-point-bar deposits the depth-porosity function for the Latrobe Group is considered ($\phi = -0.0039Depth + 21.001$; **Figure 5.5B**). Its application results in a minimum porosity value of 0.11, a maximum of 0.12 and a mean of 0.1174 ($0.05\sigma'$). For the point-bar base, the distribution of porosities resulting from the application of the chosen function ($\phi = 4305.58 - (147.83Depth)$) is characterised by a minimum of 0.12, a maximum of 0.14 and a mean of 0.1307 ($0.09\sigma'$). Finally for the point-bar top rock type ($\phi = 3374.61 - (111.09depth)$), the porosity ranges have a minimum value of 0.08, a maximum of 0.1 and a mean of 0.09 ($0.06\sigma'$).

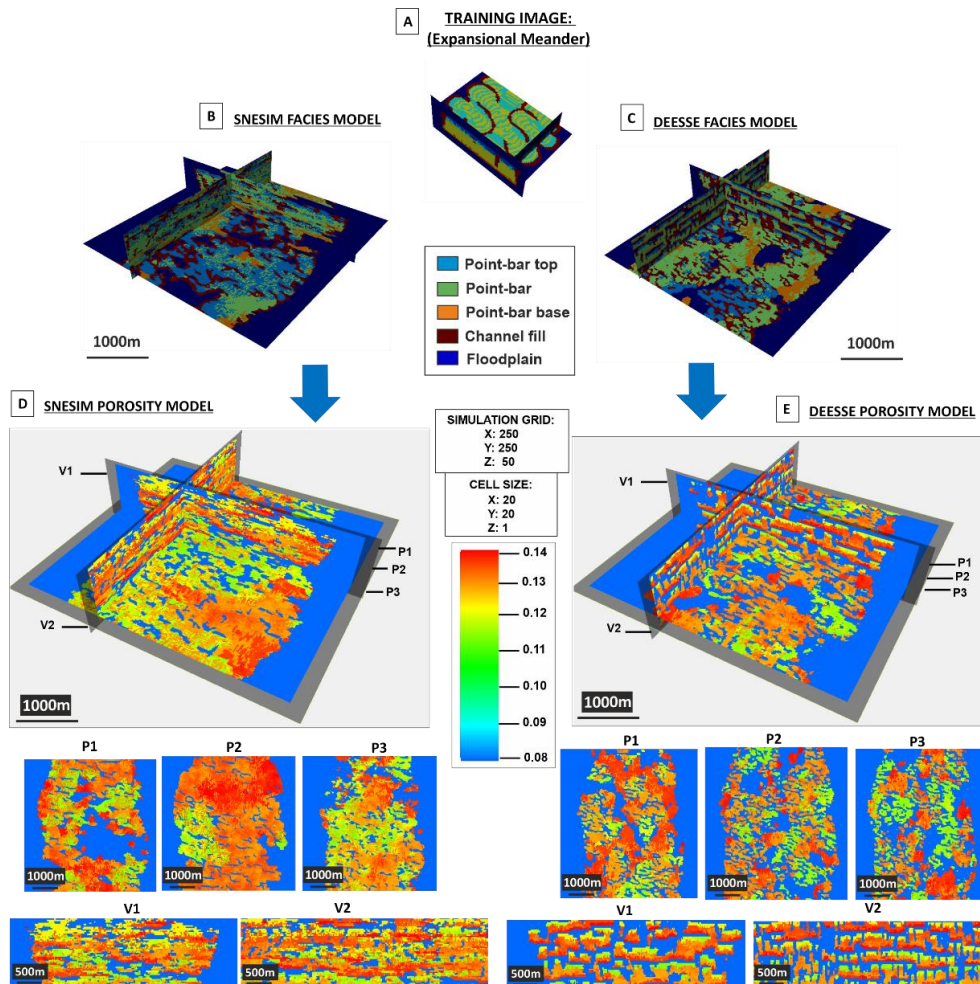


Figure 5.8 Porosity Models (5 Facies – SNESIM & DEESE)

Comparison between porosity models performed on SNESIM and DEESE facies models. (A) shows the training image from which facies models (B) and (C) were made. These facies models are then used as the framework for the construction of porosity models (D) and (E). Different plan-view images (P1, P2 and P3) and vertical images (V1 and V2) are also shown.

The variogram model and other parameters selected to constrain the models (co-kriged to the porosity-depth functions used as secondary data) are in **Table 5.1**. Similar to the 3-facies models, experimental variogram models were calibrated with respect to the size of the point-bar facies within the SNESIM and DEESSE frameworks (facies models). Some porosity realisations for the 5-facies models can be seen in **Figure 5.8**.

5.3.4 Permeability Models (3-Facies Simulations)

The approach taken to model permeability also includes the use of secondary data. Delivered realisations are presented in **Figure 5.9**:

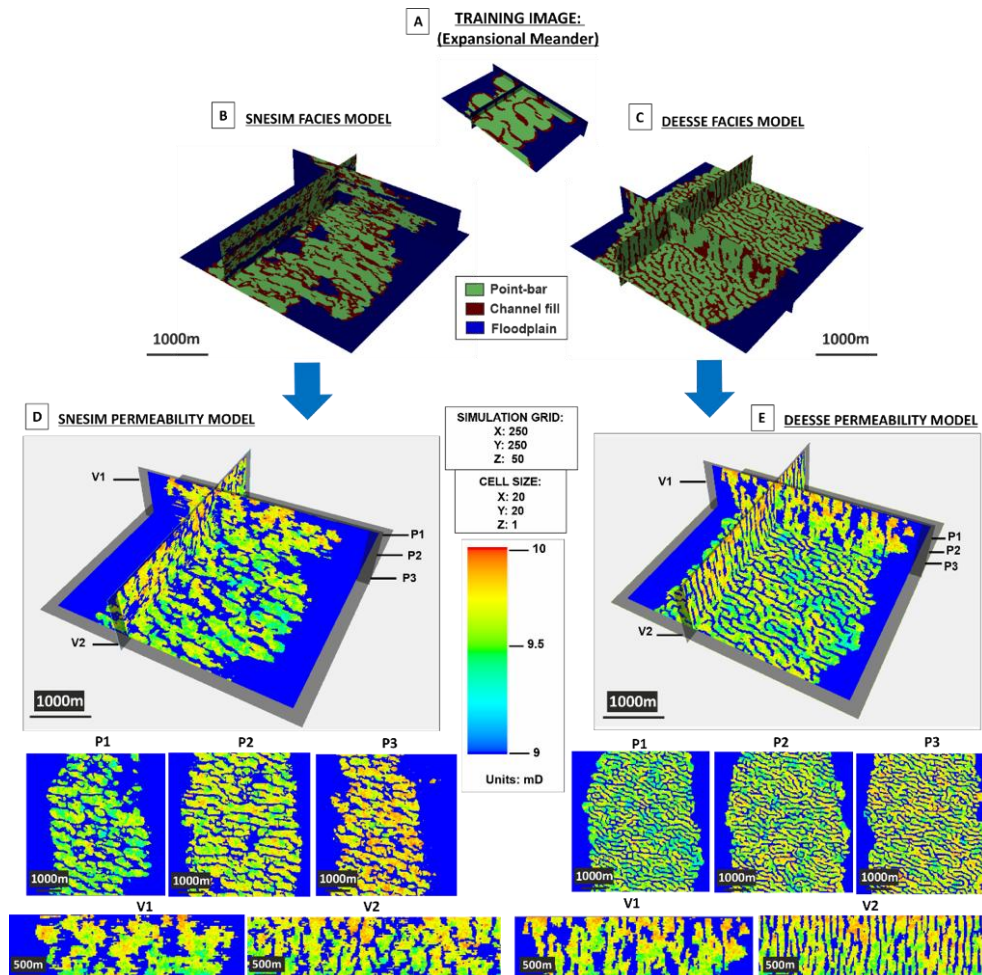


Figure 5.9 Permeability Models (3 Facies – SNESIM & DEESE)

Comparison between permeability models performed on SNESIM and DEESSE facies models. (A) shows the training image from which facies models (B) and (C) were made. These facies models are then used as the framework for the construction of porosity models (D) and (E). Different planview images (P1, P2 and P3) and vertical images (V1 and V2) are also shown.

For the 3-facies model, permeability modelling associated to the point-bar rock type was undertaken by using i) a porosity-permeability 1D trend derived from the Latrobe Formation ($\text{Log}_{10}(K) = -0.66 + (0.14\phi)$) (**Figure 5.2B**), and ii) a 3D trend (volume) whereby previously built porosity realisations are employed to condition the permeability values (**Figure 5.6 and Figure 5.8**). For the floodplain and channel-fills rock types fixed values of 0 mD apply. **Table 5.1** indicates the different parameters used to configure the GFRS simulations including the fit for the variogram model. The permeability transform indicates a range characterised by a maximum value of 10 mD and a minimum of 9 mD, with a mean of 9.6mD (0.17σ). The resulting static models exhibit i) an evident vertical permeability trend in the point-bar deposits, arising from the application of the chosen porosity-depth relationship, and ii) significant permeability variations in horizontal sections of the channel-belt deposits.

5.3.5 Permeability Models (5-Facies Simulations)

As in the 5-facies porosity models, three different permeability distributions need to be included for the point-bar base, mid-point-bar, and point-bar top lithologies. Therefore, the petrophysical database is filtered as summarised in **Table 5.5** to obtain porosity-permeability trends for basal point-bar and point-bar top facies. As a result, two different trends (transforms) are identified for point-bar base and point-bar top facies (**Figure 5.10A and B**). For the mid-point-bar facies, the Latrobe Group porosity-permeability relationship used for the 3-facies model is used (**section 5.3.2**).

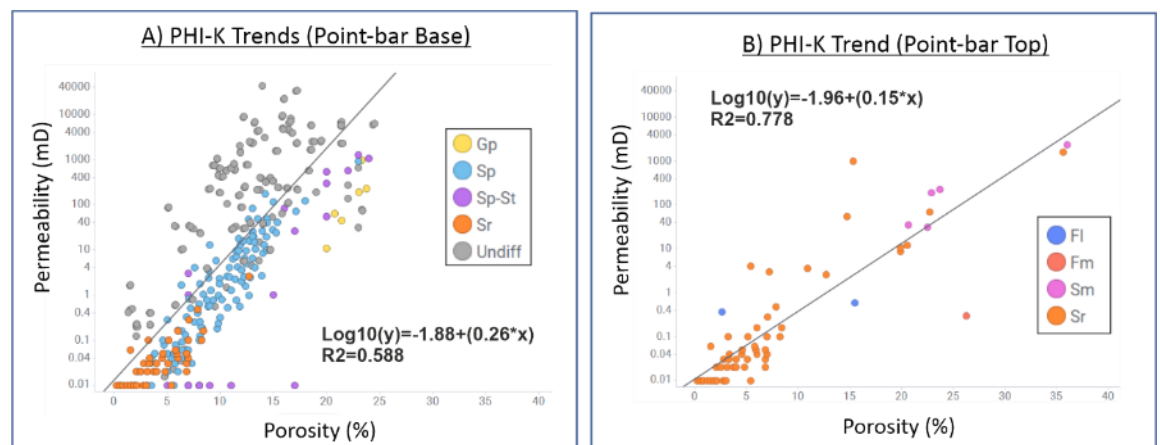


Figure 5.10 Depth-Porosity and Porosity-Permeability trends

Cross-plots of porosity vs permeability that are used to constrain permeability models for basal point-bar (A) and point-bar top (B) facies.

		5 Facies porosity model (Φ -K)	
		Point Bar base	Point Bar Top
PAFD (Subgroups)	Depositional Environment	Fluvial deltaic	
	Geomorphic Settings 1	Non-channelised	Non-channelised
	Geomorphic Settings 2	Low sinuosity channel	Low sinuosity channel
	Dominant Formative River Planform	Anastomosing, braided	Anastomosing, braided
	Architectural Elements	channel-fill, Mid-channel bar, splays, unconfined sheet body	
	Lithofacies		Gp, Sh, Sp, Sp-Sh, Sp-St, St
	Grain Size	Undiff	
	Max. Grain size	Fine, Medium	
	Sorting	Moderated sorted, moderated to well sorted, Well sorted	
	Compaction Degree	Highly compacted, highly inhibited,	

Table 5.5 Query 4: Porosity-Permeability trend (5 facies).

Filters applied to the petrophysical database (PAFD) for basal and top point-bar deposits, for derivation of data on porosity and permeability. listed classes indicate categories (“subgroups”) that have been excluded from the database (left classes). Resulting PAFD outputs are shown in **Figure 5.10**. For mid-point-bar facies, the values previously determined for the Latrobe Group in **Figure 5.2B** were applied.

The adopted porosity-depth relationship for the mid-point-bar rock type, takes the form $\text{Log}_{10}(K) = -0.66 + (0.14\text{Depth})$ (**Figure 5.2B**), and the permeability ranges takes a maximum value of 10mD, a minimum of 9mD and a mean of 9.6mD ($0.17 \sigma'$) was used. For the point-bar base rock type ($\text{Log}_{10}(K) = -1.88 + (0.26\phi)$) (**Figure 5.10A**), permeability varies from a maximum value of 37md to a minimum of 29mD, with a mean of 32.82mD ($1.94 \sigma'$).

Finally, for the point-bar top ($\text{Log}_{10}(K) = -1.96 + (0.15\phi)$) (**Figure 5.10B**), permeability ranges vary from a maximum value of 0.33mD to a minimum of 0.2mD, with a mean of 0.24mD ($0.015\sigma'$). Previously built porosity models for each of the 3 facies of the sandy point-bar elements are also used to co-krige

the simulations. The permeability ranges of the three point-bar lithologies do not overlap.

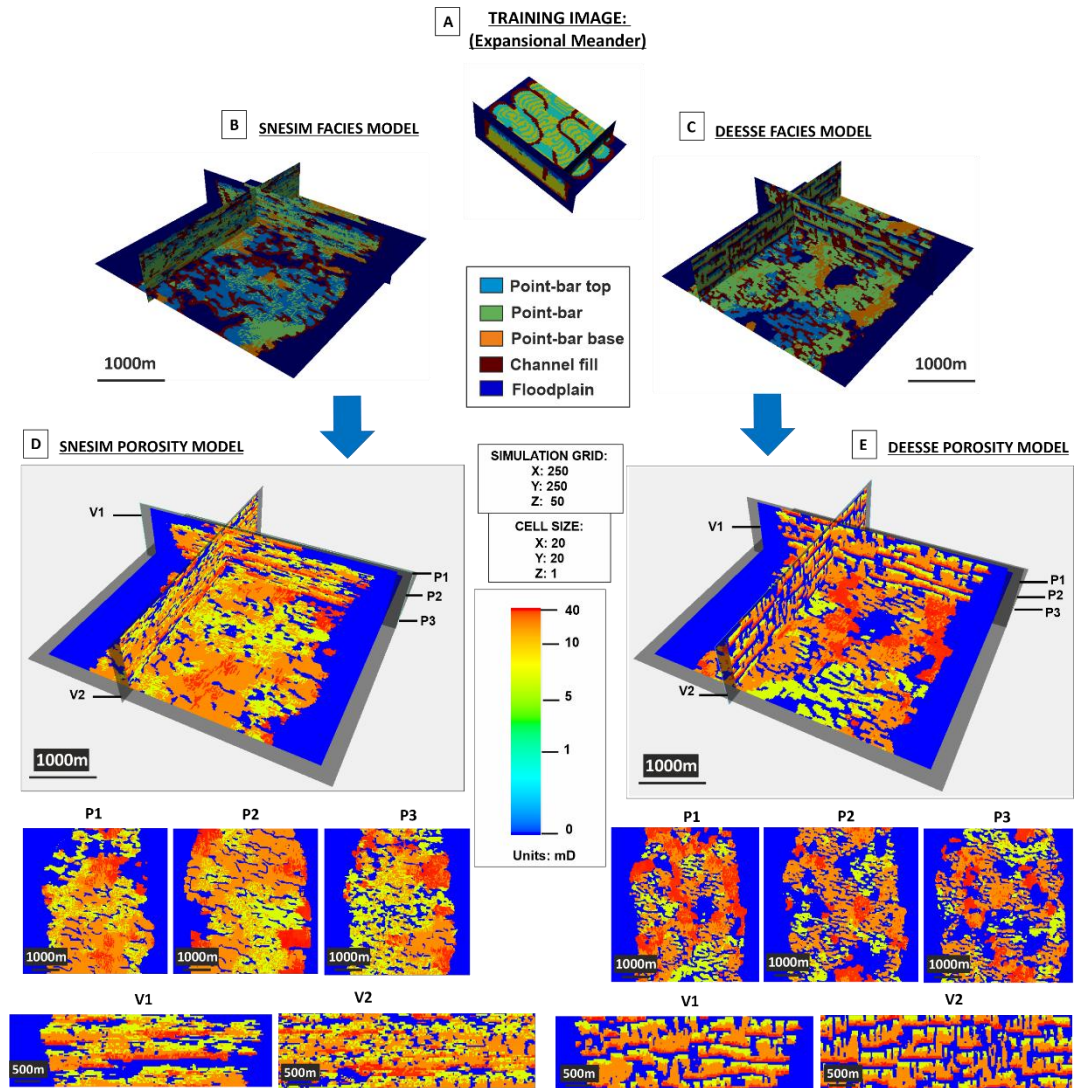


Figure 5.11 Permeability Models (5 Facies – SNESIM & DEESE)

Comparison between permeability models performed on SNESIM and DEESE facies models. (A) shows the training image from which facies models (B) and (C) were made. These facies models are then used as the framework for the construction of porosity models (D) and (E). Different planview images (P1, P2 and P3) and vertical images (V1 and V2) are also shown.

Primary observations that can be made from the delivered realisations (**Figure 5.11**) share with previous set of simulations (permeability models 3-facies in **section 5.3.4**) similarities with respect to the capturing of large-scale heterogeneities. These are the compartmentalisation made by the floodplain and channel-fill deposits (which are also forced to show 0 permeability values

in the simulations) in vertical and horizontal sections or stacked point-bars very well represented in vertical sections.

5.4 Dynamic Modelling

This section deals with the simulation of the dynamics of CO₂ (carbon dioxide) injection in the previously built static models. The study aims to determine how heterogeneities of a fluvial succession will impact the behaviour of a CO₂ plume. Injection rates and storage capacity will also be studied and compared between the 3-facies and 5-facies models.

5.4.1 Dynamic Model Configuration

The grid resolution of the facies and property models is maintained for the dynamic simulations. No upscaling was undertaken, in consideration of the need to capture detailed facies and petrophysical heterogeneity. Dynamic simulations were run using the Eclipse E300 simulator in Schlumberger Petrel®.

One injection well (INJ-1) is located at X:2250 and Y:2500. This is treated as a master well that is the main focus of the investigations. Additionally, a second injector (INJ-2) was created at X:2250 and Y:3450 to be used as a control well. Both penetrations were completed and the entire length from 2350 m to 2400 m was considered to be perforated.

A fluid-flow model including gas and water is adopted that considers existing fluid properties in the depleted gas field targeted by the Tarwhine-1 well at 2,350 m. The fluid-flow model corresponds to a standard pre-set of CO₂ gas and water. A constant water saturation of 0.98 (S_w) is considered as well as a gas saturation constant (S_g) equal to the inverse of water saturation ($S_g=1-S_w$). The reservoir is then initialised to be almost fully saturated with brine at the beginning of the simulations. Injected CO₂ and water solubility effects in the reservoir are considered in the simulations. CO₂ properties for density, viscosity, solubility, supercritical behaviour, etc. are based on experimental data that are typical for CO₂ storage conditions (12-250 degC and up to 600 bars) (Schlumberger Eclipse Manual, 2015; Haghbakhsh et al., 2013). No thermal exchange is considered in this model. The gas-water contact is

located above the interval of characterisation (2,300 m; Model Datum is at 2,350 m, and Target Datum equal to 2,400 m).

Maximum reservoir pressures in the model are set to 442.27 bar (1 bar=100 Kpa), in agreement with a calculated fracture gradient using sonic log data as pressure indicator downloaded from the [WAPIMS](#) database corresponding to the Tarwhine-1 well. The pore pressure at 2350 m is set as 281.9 bar (Eaton's Method). A geothermal gradient of 55°C/Km is selected based on data from the offset Snapper field ([Glenton, 1991](#)), the closest offset field where an accurate geothermal gradient was calculated. Temperatures from 129°C to 132°C are expected in the interval of investigation. A saline aquifer is considered to exist beyond the boundaries of the model.

The permeability and porosity models are used as input in the dynamic simulations. Permeability in K direction (vertical), I and J (horizontal) are considered to be equal. Relative permeabilities are considered in this study based on Corey's permeability curves ([Corey, 1954](#)) for each of the model elements present in the model and considering a compositional fluid model of gas and brine. Corey's relative permeability relationship, which was created to describe oil and gas flow in porous media, can effectively be applied to CO₂/brine flow ([Bennion and Bachu, 2006](#); [Moodie et al., 2014](#)). Using this approach, the residual water saturation (S_{wi}) and the residual gas saturation (S_{gr}) endpoints were calibrated for each of the rock types (facies) (**Figure 5.12**).

A standard compaction model for consolidated sandstones is calibrated using a minimum pressure of 262.10 bar (hydrostatic gradient at 2,350m) and a maximum pressure of 442.27 bar (fracture gradient at 2,350m). Rock compressibility is set to 0.0000145 bar. The previous porosity modelled in section 5.3.2 and 5.3.3 are also used to control porosity-depth dependencies in the rock compressibility model. No adsorption or J-function parameters were taken into account in this study.

A development strategy is considered where CO₂ is injected at a rate resulting in 430 bar bottom-hole pressure. The simulation time length considers the average life span of a CO₂-emitting coal-fired power station, which is

approximately 30 years. (Global CCS Institute, 2023). Therefore, three different time steps are evaluated for injection over 5, 10 and 30 years, for each of the realisations (SNESIM and DEESSE; 3 and 5 facies). The 5th year and 10th year times will be taken as intermediate steps for monitoring plume migration before the mature phase (>10 years) commences.

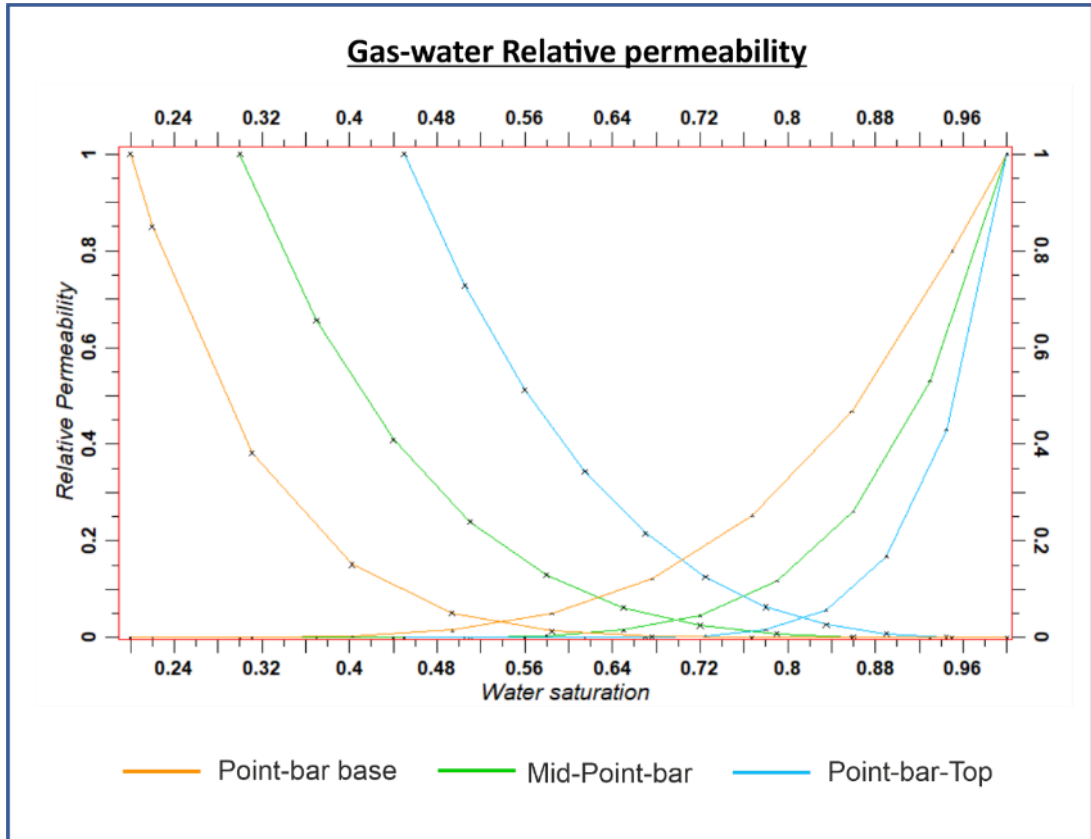


Figure 5.12 Relative Permeability for Point-bar facies.

Relative permeability and water saturation values for gas-water associated to each of the point-bar facies (Point-bar base, mid-point-bar, and point-bar top).

The grid consists of 3 million cells. Dynamic simulations were optimised to perform in a runtime that does not exceed 4 hours per 5 years of simulation time. To do so, a volume reduction was performed thanks to the creation of an "actinium" in Petrel®, to disregard grid cells having permeability values below 0.1 mD. This allows the dynamic models to run faster. Average simulation time for the 3-facies models using a conventional personal computer with a 6-core CPU (AMD Ryzen 5 3,600MHz), 16 GB RAM was approximately 45 minutes per year of simulation.

5.4.2 3Dynamic Models (3-Facies Simulations)

The 3-facies dynamic models incorporate macroscale heterogeneity consisting of facies that allow CO₂ flow (sandy point-bars deposits) and facies that act as barriers (channel-fill and floodplain deposits); these are expected to play a fundamental role in controlling the CO₂ plume behaviour. Overview summary results are presented in **Figure 5.13**.

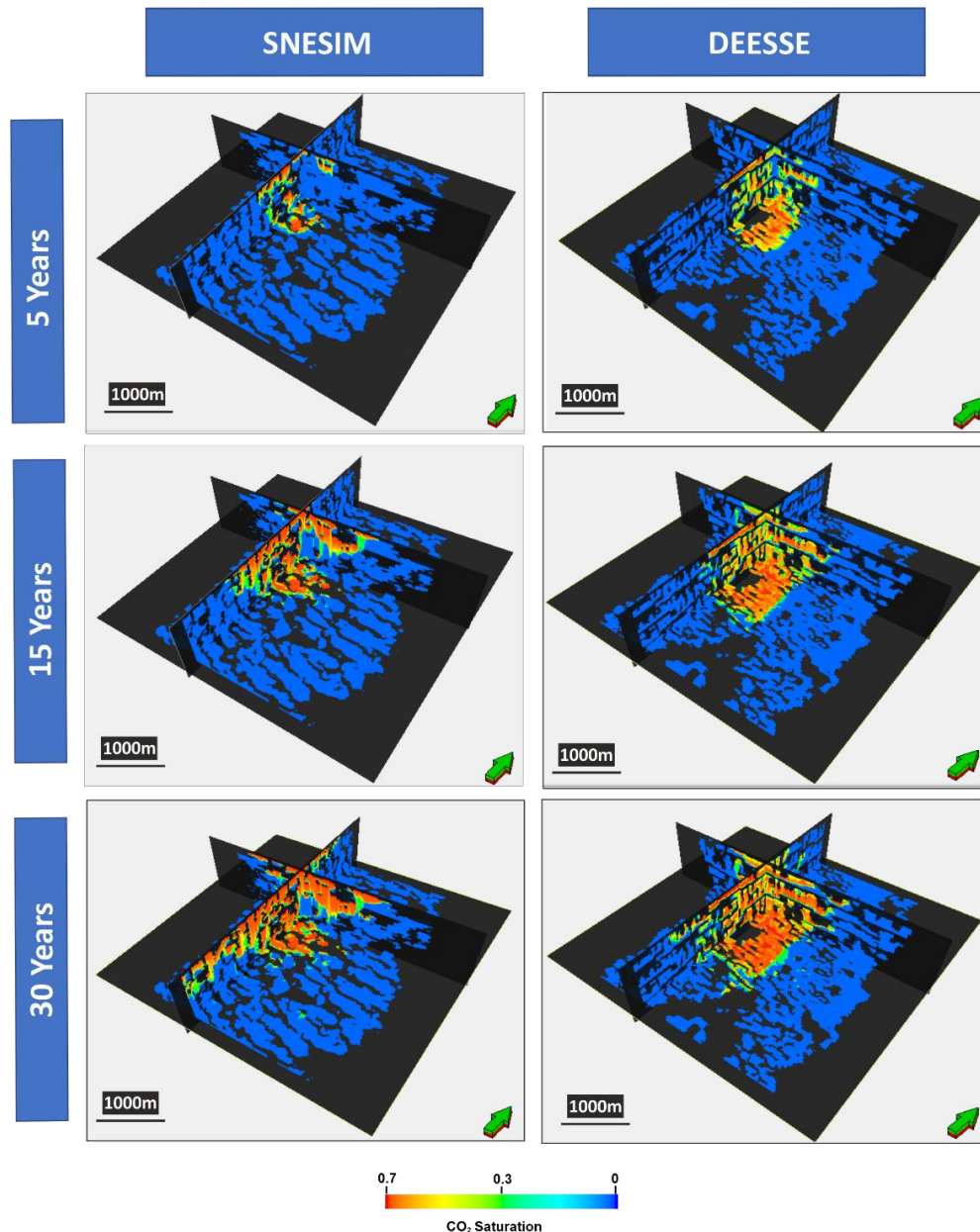


Figure 5.13 Dynamic Models - Summary (3 Facies – SNESIM & DEESE)

Comparison between dynamic simulations performed on 3-facies SNESIM and DEESSE models for periods of CO₂ injection of 5, 15 and 30 years at well INJ-1. A CO₂ plume (Saturation Gas) is observed spreading along different sections of the grid, displacing the brine that was originally present.

In both SNESIM and DEESSE simulations, outcomes over the first five years of injection show a rapid spread of the injected CO₂, which discontinuously and non-linearly flushes out the original brine starting from the original well location. The CO₂ plume front does not homogeneously spread as it progresses in the grid due to the presence of many non-permeable obstacles that it encounters. The plume, instead of growing radially around the well, expands in a tortuous manner. CO₂ patches related to small compartments can be also recognised in plan-view sections, where differences in CO₂ saturation and pressure can be distinguished. Differences with respect to the shape of the CO₂ plume in simulations run on the SNESIM and DEESSE models can be seen. The CO₂ plume migrates in the DEESSE static model taking a more finger-like morphology, compared to that in the SNESIM model (Figure 5.14).

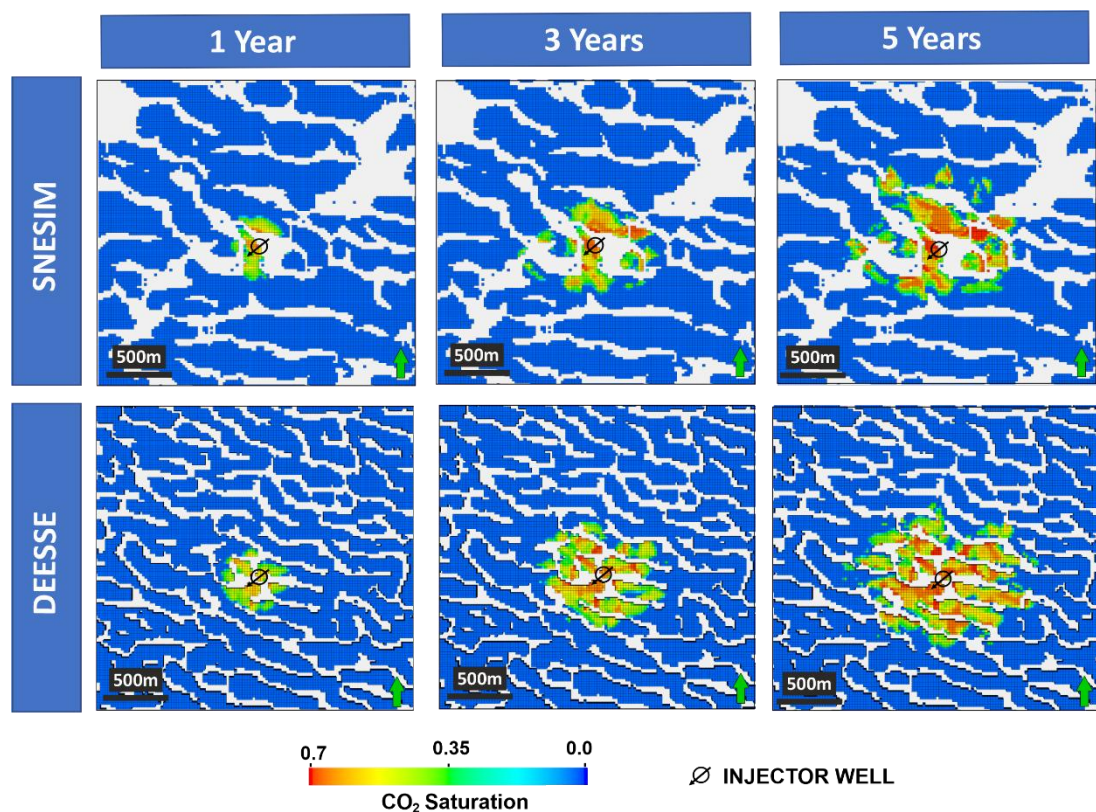


Figure 5.14 Plume evolution (Horizontal sections) (3-facies SNESIM and DEESSE models)

Comparison of CO₂ plume behaviour between simulations performed on SNESIM and DEESSE models in the first stages of injection (INJ-1 well). The blue colour indicates brine-saturated volumes. Barriers to flow are represented in white. Horizontal sections correspond to Z=21 (out of 50 slices).

Also, the CO₂ flow is conditioned to the shape and size of the non-permeable facies for both type of frameworks SNESIM and DEESSE, making the SNESIM features wider and longer than the DEESSE ones.

In vertical sections, the spreading of the CO₂ plume front appears affected by the numerous geological barriers it encounters on both SNESIM and DEESSE models (Figure 5.15). Small compartments are encountered in different sections. These commence filling at different time instances as the plume progresses in space. Various intraformational seals in the sandy fairway impact CO₂ storage at different vertical sections and cause pressure relief on the main uppermost seal.

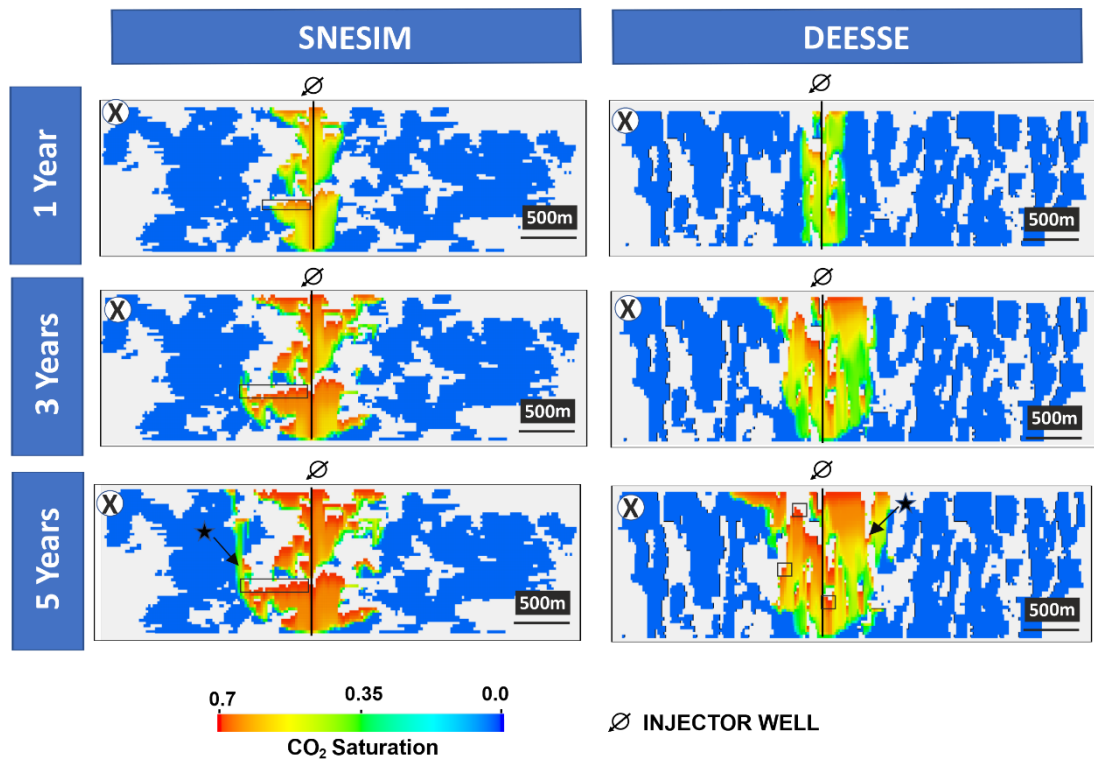


Figure 5.15 Plume shape (Vertical sections) at 5 years of injection (3-facies SNESIM and DEESSE models).

Comparison of CO₂ plume behaviour between simulations run on the SNESIM and DEESSE models in the first stages of injection (INJ-1 well). The blue colour indicates brine-saturated volumes. Black frames show compartments where CO₂ accumulated (higher saturation values) under intraformational seals. Star symbols highlight interconnections between compartments. Vertical sections correspond to Y=78, in agreement with the well INJ-1 cross-section location.

From the 5th to the 15th year of injection, clear CO₂ flow directions are identified following an E-W direction which spread at a faster horizontal rate as in the previous earlier stages. This is due to the deposition orientation of the sandy facies which are prevalently deposited perpendicular to the main channel-belt axis (E-W). However, in the area where the CO₂ injection takes place in the SNESIM simulations, compartments are oriented closer to the NW-SE direction. Preferential CO₂ paths agree with the bigger and thicker connected sandy deposit geometries that spread looking for lower pressure differentials (**Figure 5.16**).

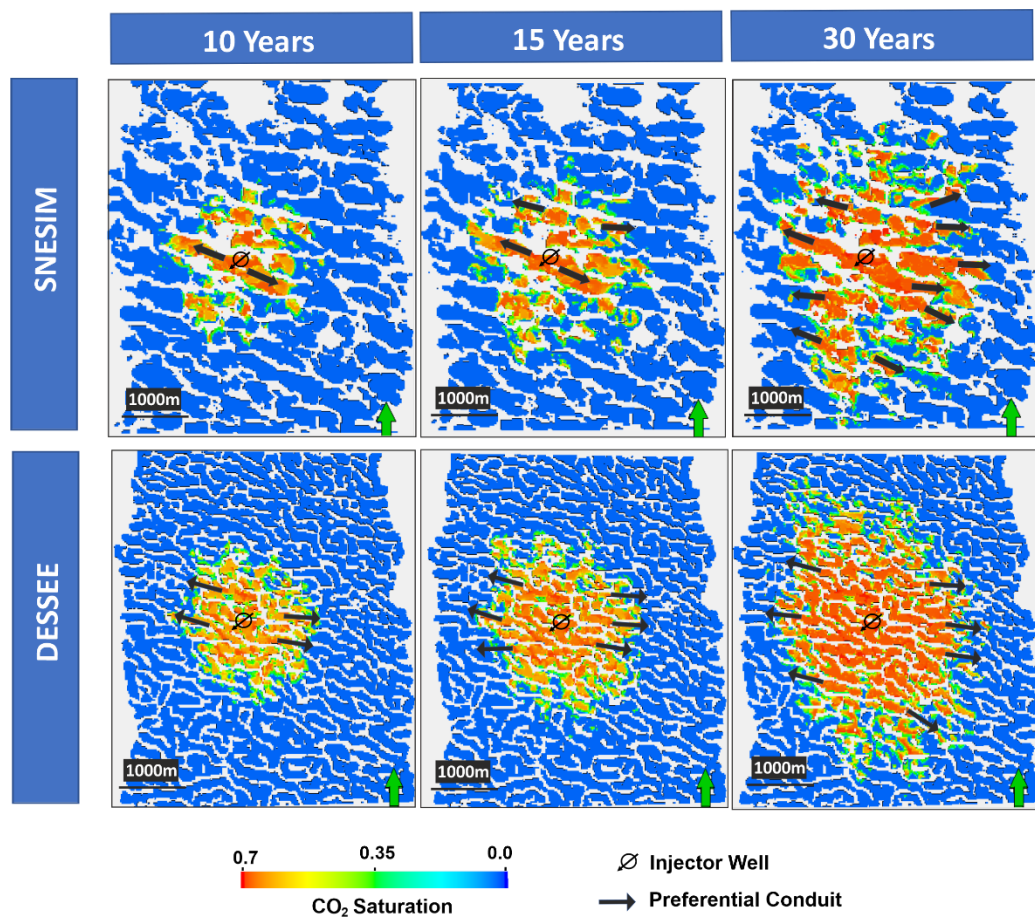


Figure 5.16 Plume shape (Horizontal sections) (3-facies SNESIM and DEESSE models) after 10, 15 and 30 years of injection.

Plume behaviour comparison between SNESIM and DEESSE simulations for 10, 15 and 30 years of continuous injection (INJ-1 well). The blue colour indicates brine-saturated volumes. Barriers to flow are represented in white. Horizontal sections correspond to Z=11 (out of 50 slices). Black arrows indicate preferential flow paths in agreement with sandy compartments geometries surrounded by channel-fill and floodplain deposits.

In vertical sections, the migration of CO₂ continues growing in a bell shape geometry for the SNESIM simulations and more triangular for the DEESSE realisations (Figure 5.17).

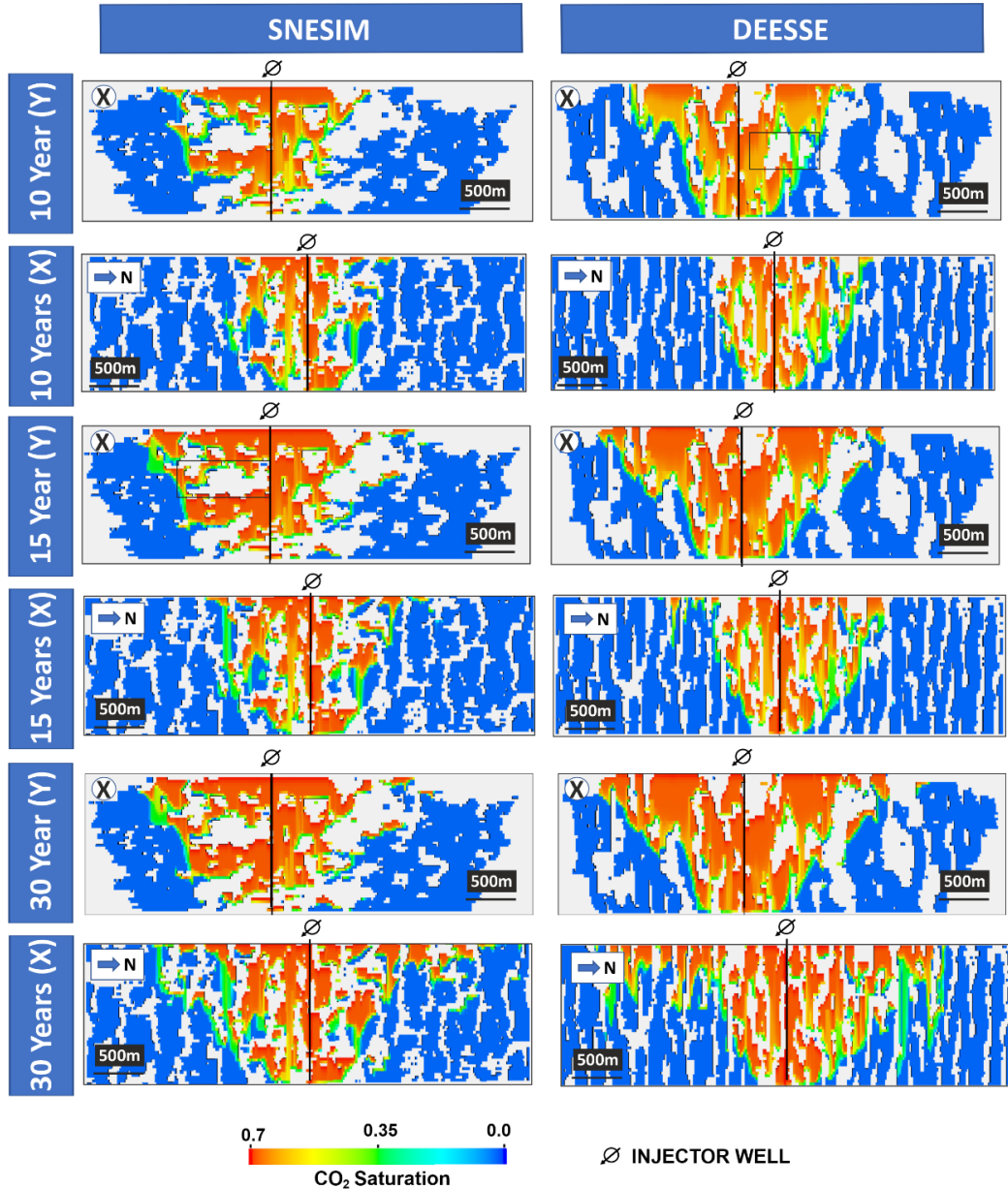


Figure 5.17 Plume shape (Vertical sections) after 10, 15 and 30 years of injection (3-facies SNESIM and DEESSE models).

Comparison of plume behaviour between simulations performed on SNESIM and DEESSE models, at the 10th, 15th and 30th year of injection. Vertical sections correspond to Y=78, and X=113 in agreement with the well INJ-1 cross-section location.

Similar behaviour to the first five years with respect trapping mechanisms due to the occurrence of intraformational seal continue. Different compartments

sealed by channel-fill and floodplain deposits tend to be filled up to spill points through which flow eventually progresses to a neighbouring connected compartment. Although CO₂ saturation and pressures are slightly higher at shallower depths during the 15 years of injection, it is evident that both properties are homogeneously distributed along the vertical sections avoiding high values of pressure or CO₂ saturation over the caprock. This is due to the presence of channel-fill and floodplain deposits that push the CO₂ plume to further displace horizontally. The CO₂ saturation value measured at the top of the caprock and minor intraformational seal is approximately 0.75. Pressures of 420 bar are recorded closed to the injection site, which are well below the value of 442.27 bar corresponding to the fracture pressure for the corresponding fracture gradient (**Figure 5.18**).

For the subsequent injection time, up to the 30 years of total simulation time, very similar results are seen for the SNESIM and DEESSE models (**Figure 5.17**). The CO₂ plume keeps displacing the brine from the already defined preferential pathways that were occupied in the previous years. The horizontal displacement occurs at a slower rate compared to the first years of injection. The only noticeable difference is that in the DEESSE model the CO₂ tends to spread radially, whereas in the SNESIM model the CO₂ plume tends to spread oriented to thicker and wider preferential pathways. This is again due to the differences existing in terms of amount and shapes of channel-fill facies (barriers to CO₂ flow) included in the SNESIM grid which makes pathways more tortuous and, hence reaching farther locations. It is confirmed that the main trapping mechanism observed is driven by the underlying stratigraphical framework.

5.4.2.1 Pressure Distribution

In the first five years of injection, the CO₂ flows around local barriers spreading in all directions, though connections linking sand-prone volumes. Pressure is higher in sandy point-bar elements flanked and surrounded by non-permeable channel-fill deposits. Very few full compartments where the CO₂ does not reach are found during the first years of injection which is another indicator of well-connected sand deposits. This is also supported by the pressure patterns that can be observed in **Figure 5.18** where only few compartments are indicated, and pressure homogeneously distribute along the entire grid.

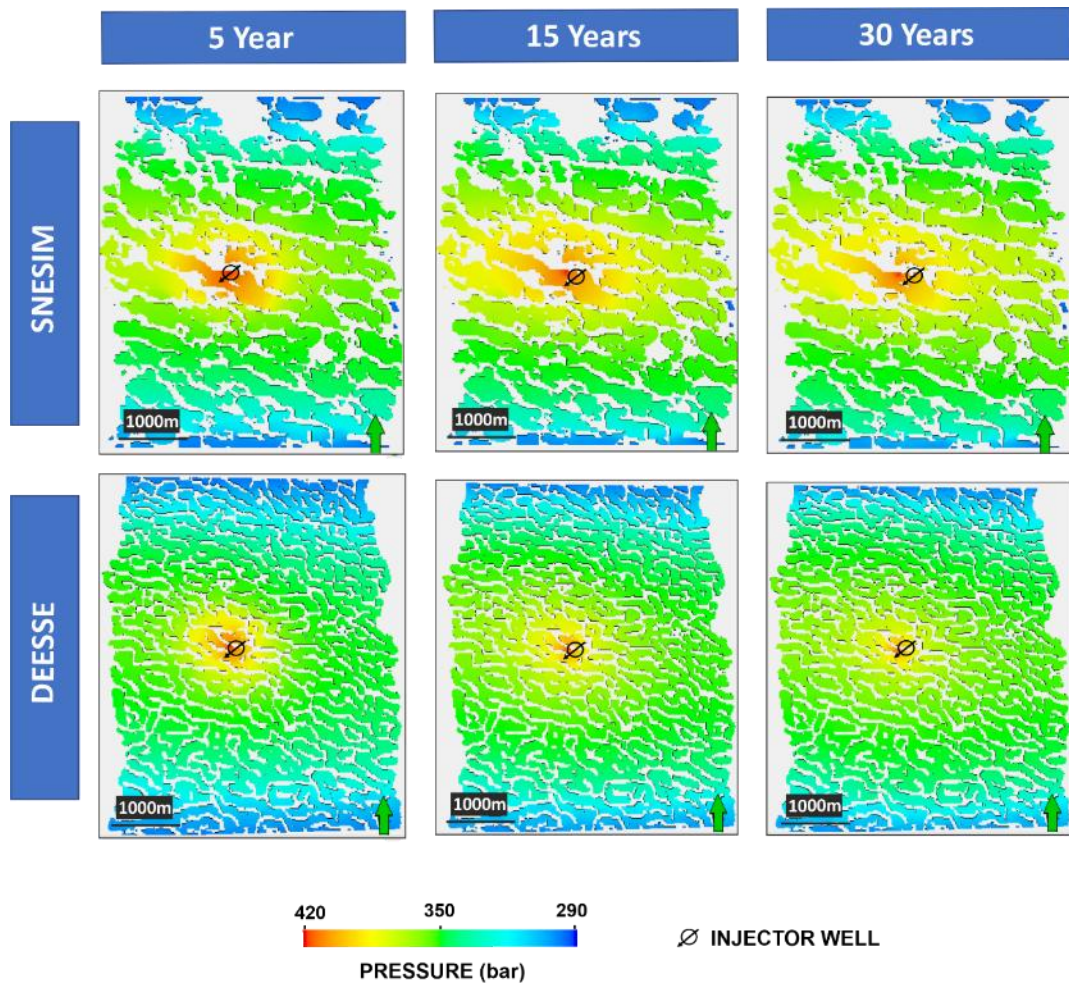


Figure 5.18 Pressure distribution over the area of investigation (3-facies SNESIM and DEESSE models) after 5, 15 and 30 years of injection.

Comparison of pressure values at the upper sections of the reservoir (Z=11) for SNESIM and DEESSE models for different years of injection, indicating a homogeneous distribution of pressure throughout the entire grid; this is especially the case for the DEESSE simulations (INJ-1 well).

Also, the SNESIM simulations have higher pressure values compared with DEESSE, especially in proximity of the injector well. In the SNESIM model, this is due to presence of thicker and wider flow barriers located closer to the area of influence of the well, which affect sand connectivity and CO₂ flow pathways. On the contrary, the DEESSE facies framework, with higher sandstone connectivity, is characterised by flow conduits that exert a more efficient pressure relief. In both simulations, pressure values decrease through time, meaning that during the first years of injection, higher values of pressure are observed. Vertical sections also show many pressure and CO₂-saturation anomalies, corresponding to the effects of intraformational seals that support the CO₂ column at different vertical sections in the reservoir.

5.4.3 Dynamic Models (5-Facies Simulations)

Figure 5.19 summarises the plume behaviour for the time steps of 5, 15 and 30 years, for the 5-facies models in which point-bar deposits are differentiated into point-bar base, mid-point-bar, and point-bar top facies.

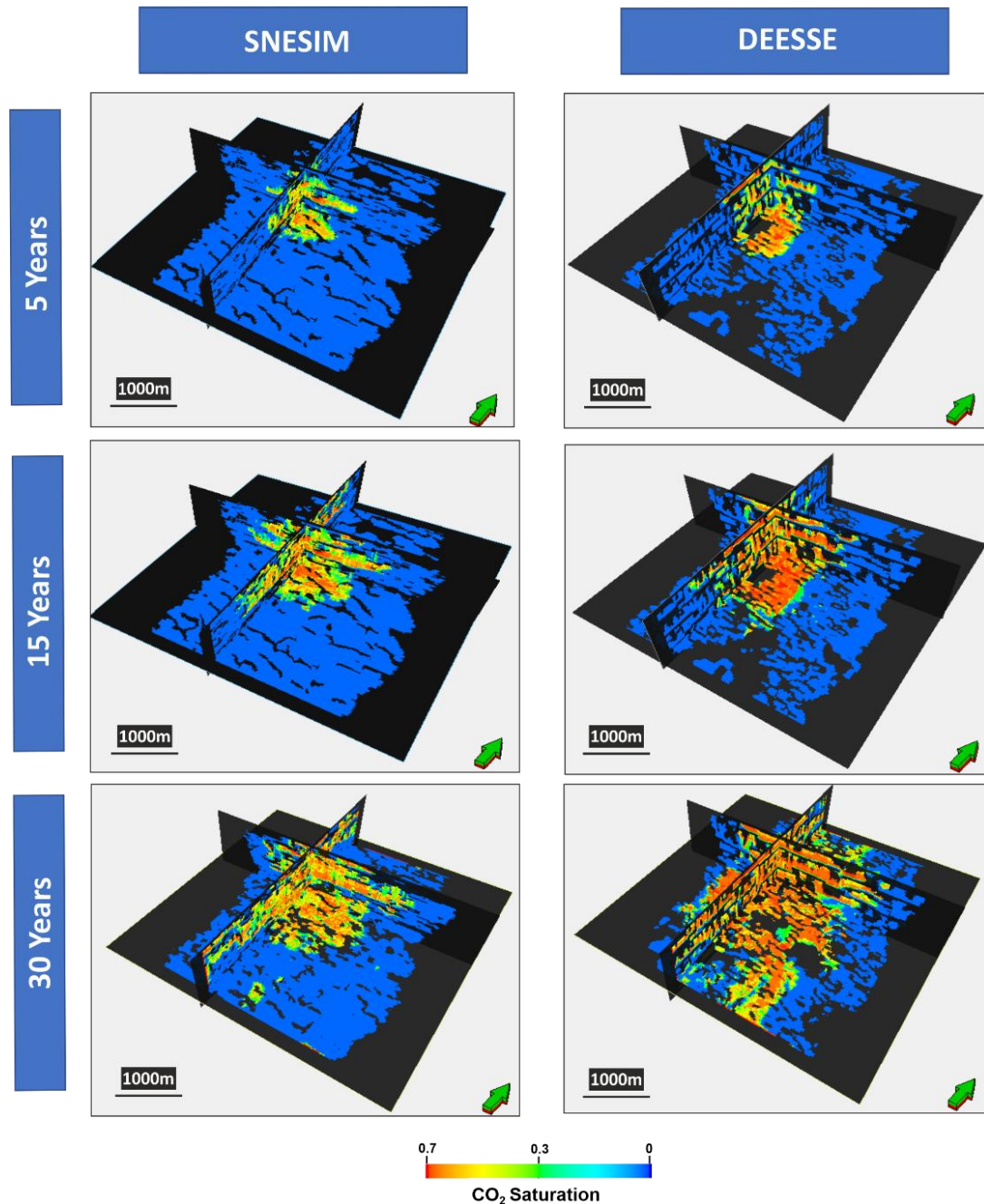


Figure 5.19 Dynamic simulations (5-Facies SNESIM & DEESSE models)

Comparison between dynamic simulations performed on 5-facies SNESIM and DEESSE models for a period of continuous CO₂ injection of 5, 15 and 30 years (INJ-1 well). A CO₂ plume (shown by CO₂ saturation values) is observed to spread to different sections of the grid displacing the brine that was originally in place.

The early stages of injection (first five years) for the 5-facies models show that the CO₂ flow is mainly controlled by the existence of flow barriers in proximity of the wells (channel-fill and floodplain deposits) and by connectivity and geometries of sand-prone facies. In contrary with the previously described 3-facies scenario, the SNESIM geometries for sandy deposits appear bigger and better connected closed to the area of influence of the well; more limited compartmentalisation is observed. Conversely, the DEESSE model includes a larger fraction of channel-fill deposits; thus, sand-prone volumes are smaller and more poorly connected. Therefore, more prominent pathways commence development in the SNESIM simulation whereas the DEESSE simulation indicates only incipient creation of preferential pathways at the end of year 5. The plume propagates faster in wider and thicker sandy conduits (**Figure 5.20 and 5.21**).

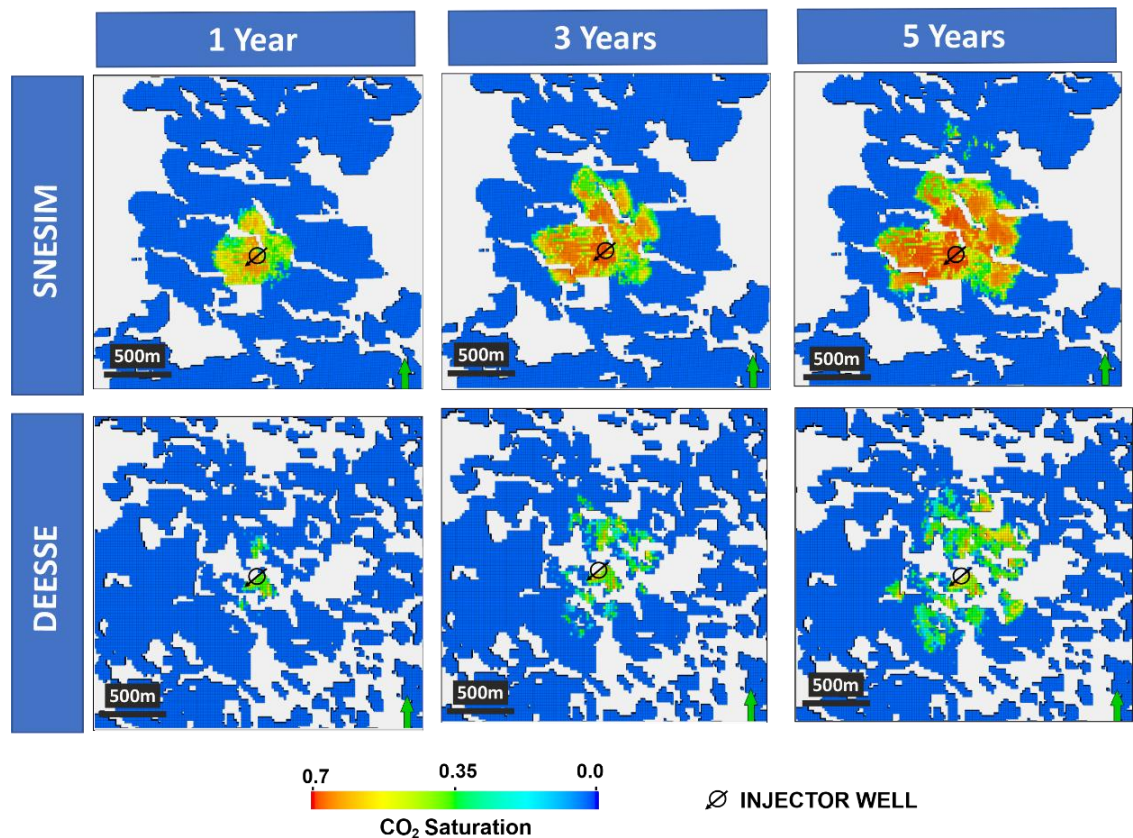


Figure 5.20 Plume shape (Horizontal sections) (5-facies SNESIM and DEESSE models) for early injection stages.

Comparison in plume behaviour between 5-facies SNESIM and DEESSE models in the first stages of simulated injection (INJ-1 well). The blue colour indicates brine-saturated volumes. Barriers to flow are represented in white. Horizontal sections correspond to a shallow Z=2 (out of 50 depth slices).

In the 5-facies models, the direction, speed, and regime of propagation of CO₂ is also dependent on the type of facies forming the point-bar features. This effect is readily recognisable from the 5th year of injection. **Figure 5.21** shows a plan-view section of the SNESIM and DEESSE simulations where the CO₂ flow is preferentially channelled through higher-permeability facies (point-bar base and mid-point-bar deposits).

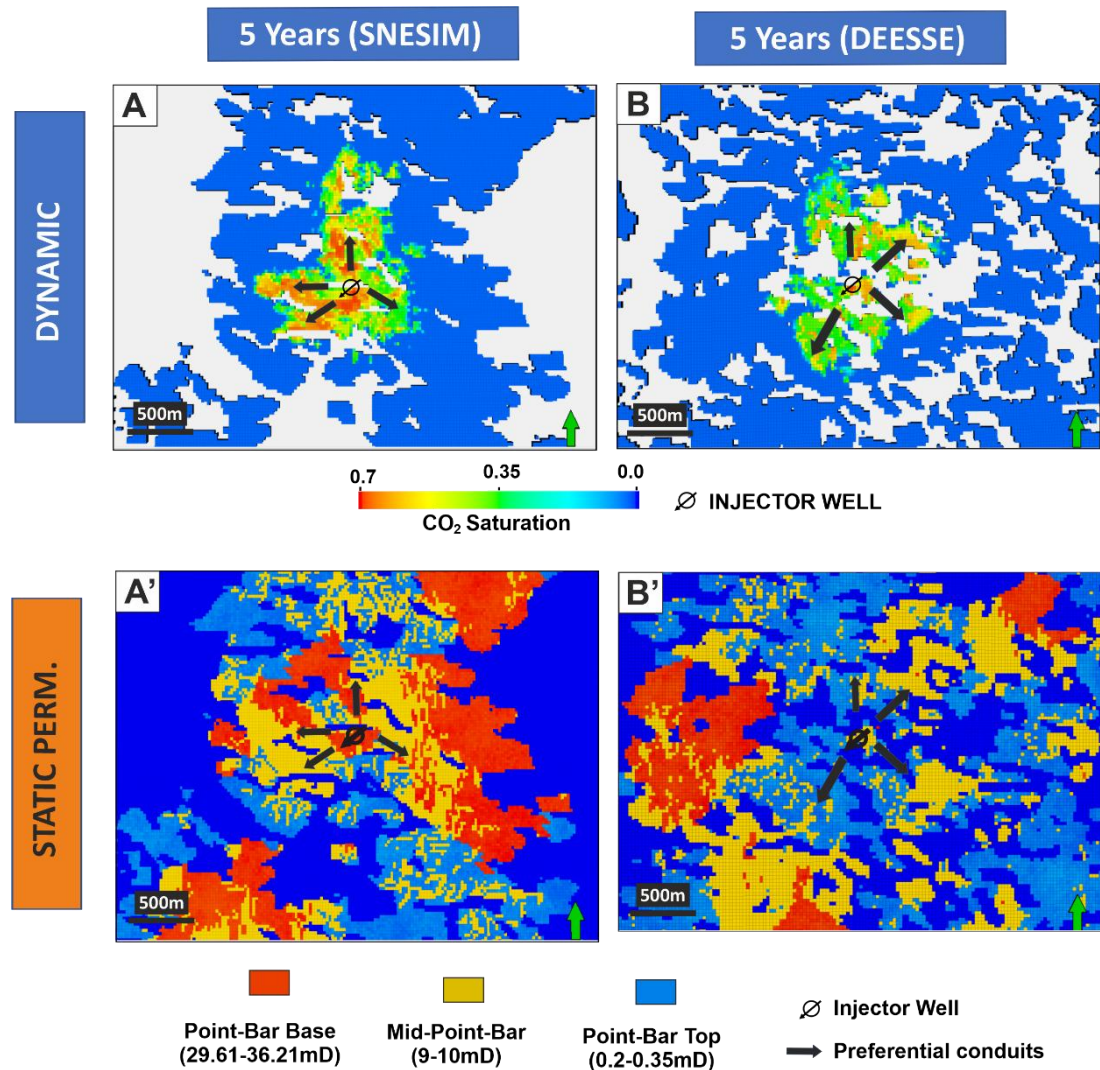


Figure 5.21 Plume shape (horizontal sections) compared with permeability model sections for early injection stages.

Comparison between the dynamic simulations (A and B) for SNESIM and DEESSE and their corresponding permeability sections (A' and B') at Z=2 (INJ-1 well). Arrows show preferential CO₂ flow pathways and circles highlight good quality rock types where the CO₂ moves to.

Vertical sections also indicate specific displacement of CO₂ in relation with the occurrence of higher-permeability rock types for the first five years of injection.

Observations confirmed how the direction and speed of the plume is influenced by facies contained within the amalgamated sandstones bodies (**Figure 5.22**). Also, the main trapping mechanism observed is controlled by the underlying stratigraphical framework.

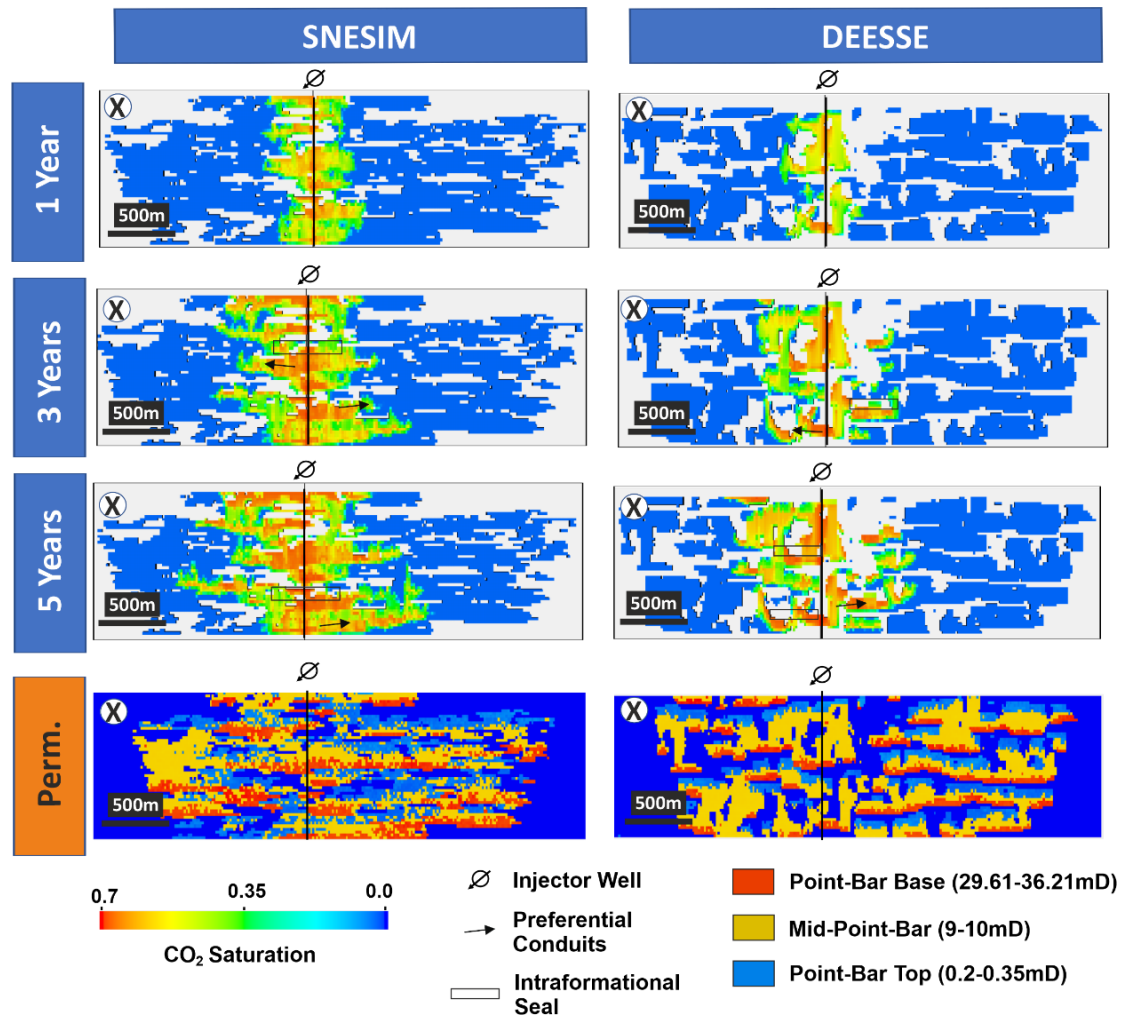


Figure 5.22 Plume shape (vertical sections) (5-facies SNESIM and DEESSE models) for early injection stages compared with permeability model sections.

Comparison between the dynamic models for SNESIM and DEESSE and their corresponding permeability sections (below) at Y=78 (INJ-1 well). Black frames indicate the location of intraformational seals which sustain the CO₂ column at different depths. CO₂ plume directions indicated with black arrows.

Furthermore, comparing the results with the 3-facies model vertical section counterparts, the CO₂ plume seems to move faster through the 5-facies models. The seeking out of preferential CO₂ paths is considerably more clearly defined in the 5-facies model and it is directly associated to the

deposition of point-bar base and mid-point bar facies. Previous observations taking place in the 3-facies model analysis (macroscale level of heterogeneity) can still be observed here. These are the effects of compartments of different sizes created by the channel-fill deposits and the muddy floodplain materials which provoke the CO₂ flow moving tortuously in the model. Connectivity effects and the details in terms of the effects of intraformational seals relieving the uppermost seal from high pressures can be also observed in the simulations.

The evolution of the CO₂ plume from the 5th to the 15th year seen on the horizontal sections of the SNESIM and DEESSE models is characterised by continued propagation of the plume fronts and the creation of new flow pathways in which the CO₂ flows more rapidly due to the presence of point-bar base and mid-point bar facies (**Figure 5.23**), which act as thief zones. By contrast, the point-bar top facies behave as baffles pushing the CO₂ front towards flow conduits and experience low saturation values due to capillary effects.

In vertical sections (**Figure 5.24**), the effects of lithological heterogeneity on CO₂ flow and saturation are also evident. This is due to the differences in relative permeabilities that exist between both rock types and evidences a second type of trapping mechanism due to capillary effects, being the point-bar base facies prone to allocate more quantity of gas than the mid-point bar facies. Subsequently, two gas fronts (according to gas saturation ranges) corresponding to the point-bar base and mid-point-bar according to different ranges of gas saturation.

Additionally, the occurrence of point-bar top facies, that also include a characteristic range of saturation values, makes the CO₂ plume to displace further horizontally. This is an important difference that exist against 3-facies model where the plume dispersion horizontally is more symmetrical and does not displace horizontally as far as the 5-facies model plume. Also, this behaviour added to the effects of the intraformational seals (non-permeable channel-fill and overbank deposits) helps to sustain the CO₂ column at different vertical sections in the simulations (**Figure 5.23 and Figure 5.24**).

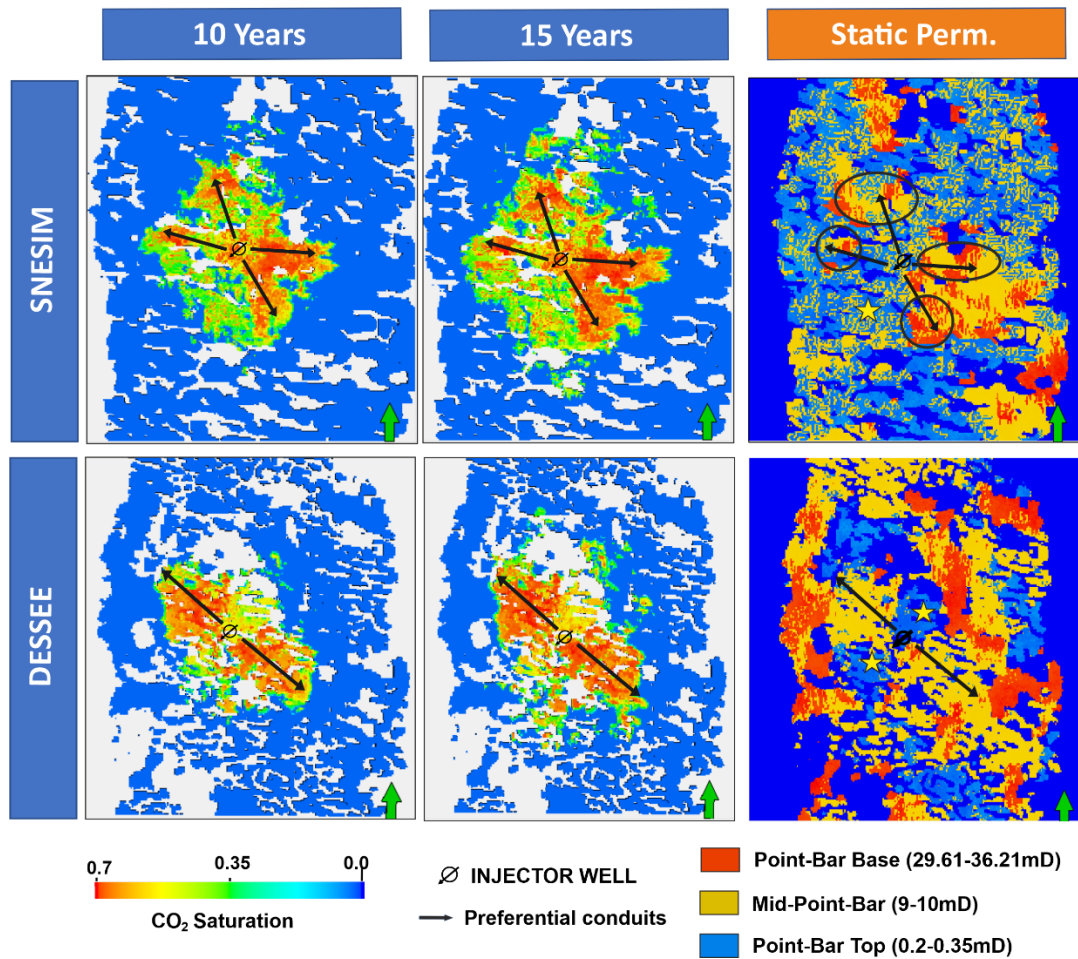


Figure 5.23 Plume shape analysis (horizontal sections) compared with permeability model sections (10- 15 years of injection).

Dynamic models for SNESIM and DEESSE compared to permeability sections at Z=12 and Z=26 respectively. The CO₂ front plume continue its progression through preferential conduits (arrows) in agreement with the deposition of the point-bar base (red) and mid-point-bar (yellow) whereas when the point-bar top is intersected by the flow the plume slows down. Circles indicate those sections in the simulations where higher concentration of CO₂ are located related with the appearance of point-bar top and mid-point bar facies.

Moreover, horizontal displacements are also associated to higher level of heterogeneities in based to the appearance of more numerous channel-fill deposits leading to the creation of effective preferential conduits. These are prominently created in the SNESIM simulations. Furthermore, in those places where the sandy point bars are well developed and the three different types of rock types take place, the fining-upward trend can be distinguished in based to the gas saturation intake differences too (**Figure 5.24**).

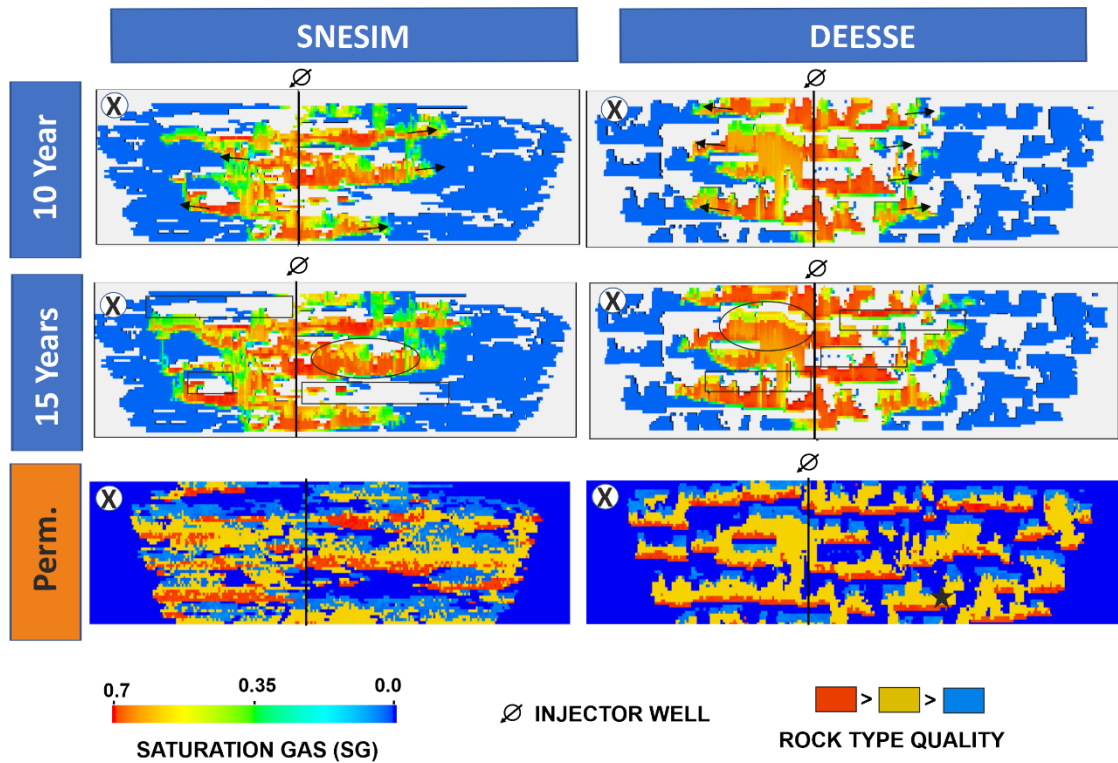


Figure 5.24 Plume shape (Vertical sections) (10- and 15-years injection-5-facies-SNESIM and DEESSE)

Plume behaviour comparison between SNESIM and DEESSE simulations during the 10th and the 15th year of injection (INJ-1 well). Arrows indicate preferential pathways and plume fronts following the presence of point-bar base and mid-point-bar facies. The squares represent intraformational seals made from floodplain and channel fill deposits (barriers to the flow). The circle highlights a section where the fining upward trend can be observed in terms of gas saturation effects and stars correspond to the baffle effects created by point-bar top facies on the flow of CO₂ through the rocks. Vertical sections correspond to Y=125.

In the following 15 years, and up to the 30 years of the total elapsed simulation time, the plume keeps growing asymmetrically but longitudinally to the main channel-belt axis in both the SNESIM and DEESSE grids. This asymmetric growth is mainly controlled by heterogeneity in terms of capillarity (relative permeabilities) and by the geometry of preferential conduits to flow (**Figure 5.25**). In comparison with simulations run on the 3-facies models, the plume spreads over a larger area in both the SNESIM and DEESSE 5-facies model.

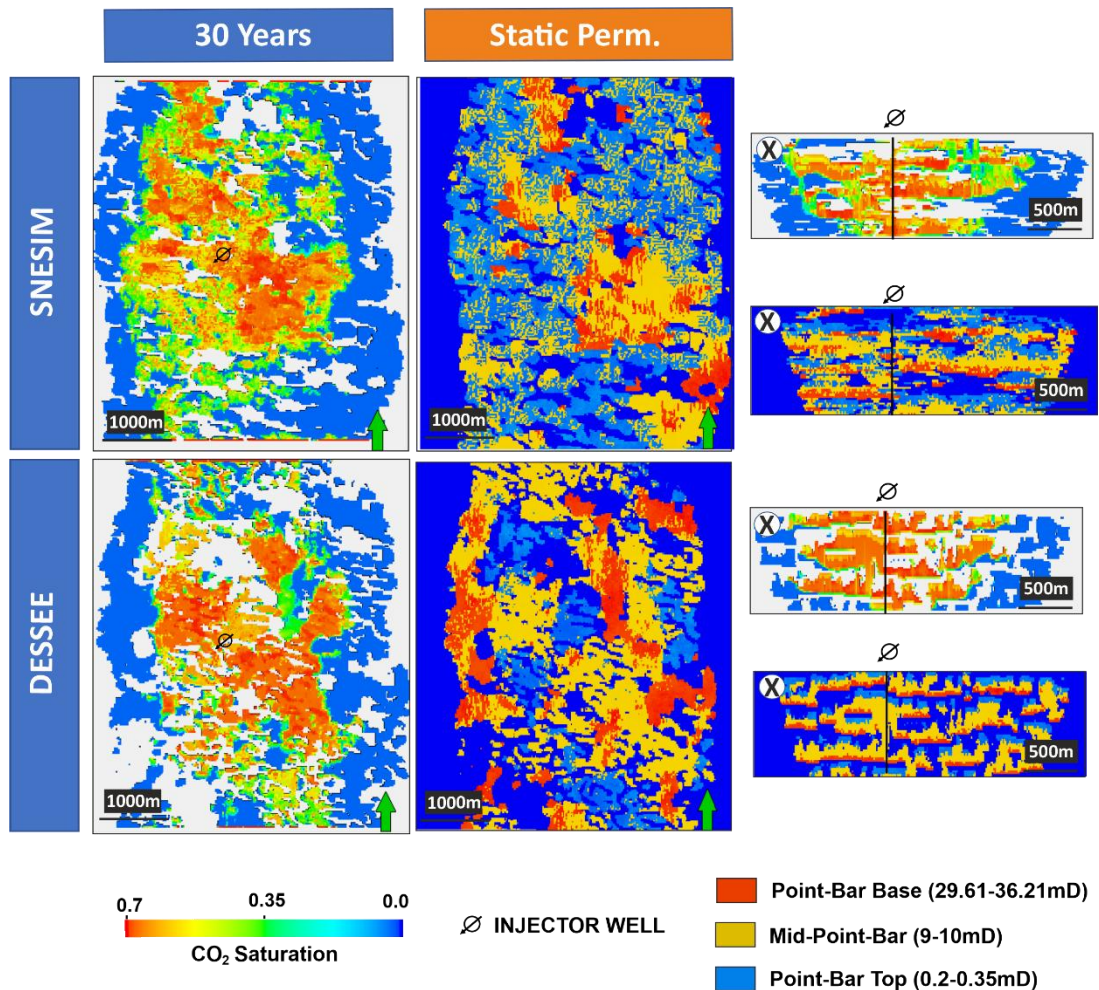


Figure 5.25 Plume shape in horizontal and vertical sections at 30 years of injection (5-facies SNESIM and DEESSE models)

CO₂ plume behaviour at the 30 years' injection period as seen on different horizontal (Z=12 for SNESIM and Z=26 for DEESSE) and vertical (Y=125) sections.

5.4.3.1 Pressure Distribution

In terms of pressure distribution for the first years of injection, results are different for the SNESIM and DEESSE models. The SNESIM model, which exhibits better sand connectivity and a smaller number of barriers to flow, especially near the area of influence of the well, experiences lower pressure values than the DEESSE model. Also, pressure dissipation throughout the years is more significant in the SNESIM model than in the DEESSE model, accommodating pressure values easily and faster along the entire grid. In vertical sections, even if higher pressures are found at shallower depths, the pressure regime is quite well distributed within the reservoir thickness. The pressure data indicate modest compartmentalisation of point-bar deposits (**Figure 5.26**). Simulations reaching the second decade demonstrate an

increase in pressure over the entire grid (**Figure 5.26- 30years**), which means the entire reservoir starts to pressurise. Reservoir pressurisation timing is different for the SNESIM and DEESSE models; it takes place from years 22 and 26, respectively. This pressurisation event did not take place in the simulations run on the 3-facies models, which highlight the impact of the mesoscale heterogeneities incorporated in the 5-facies models.

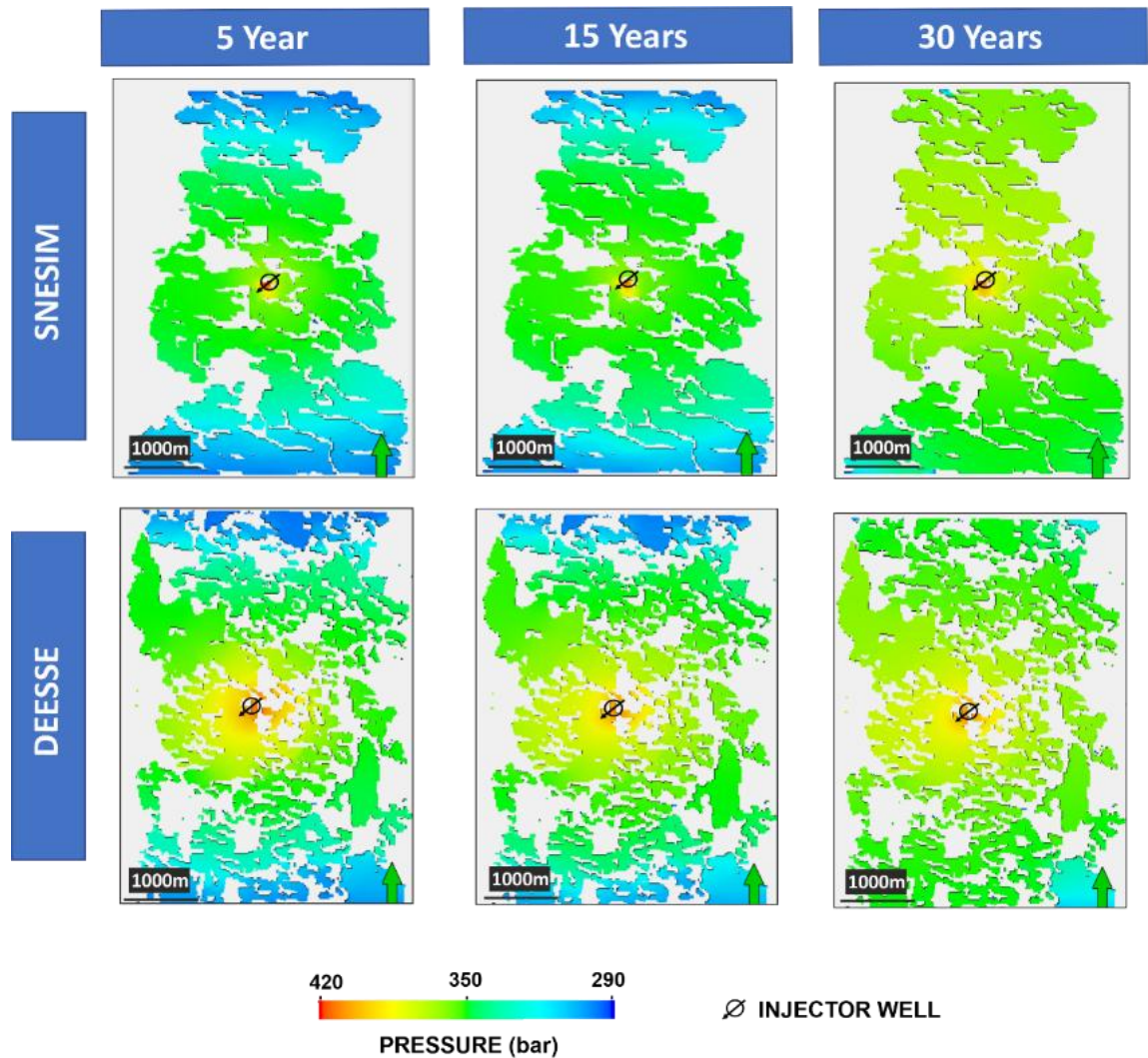


Figure 5.26 Pressure distribution over the area of investigation over time (5 facies SNESIM and DEESSE)

Pressure values at the upper sections of the reservoir ($Z=2$) for SNESIM and DEESSE simulations for different years of injection, indicating a homogeneous distribution of pressure throughout the entire grid between the 5th and 15th year. The 30th year figure indicates an increase of pressurisation in the entire grid in both the SNESIM and DEESSE models.

5.5.4 Storage and Injection Rates

To understand the storage capacity and injection rates of the simulations performed in this study, different cross-plots are evaluated so a comparison between 3- and 5-facies models can take place. Furthermore, additional information from another injector well located at 2250X and 3450Y (INJ-2) is used to understand location-related behaviour. For the 3-facies models, **Figure 5.27** indicates that there is an important discrepancy between observations at INJ-1 and INJ-2. The cumulative CO₂ injection at INJ-2 is similar for both SNESIM and DEESSE grids (**Figure 5.27A**). However, cumulative values for INJ-1 are different for the SNESIM and DEESSE frameworks, and themselves differ compared to INJ-2 results. In **Figure 5.27B**, it can be seen that higher injection rates correspond to larger cumulative injected volumes, and vice versa. Discrepancies between the four scenarios reflect location dependencies and the effect of specific types of heterogeneity (mainly amount and shapes of barriers to flow) on storage capacity and injection rate.

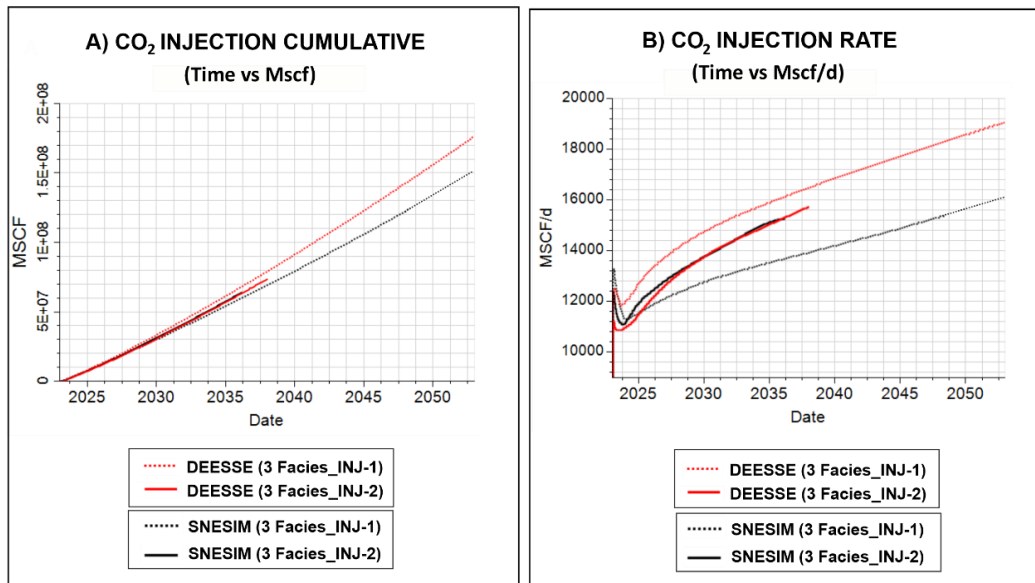


Figure 5.27 Cumulative injected volume and injection rate plots (3-facies models)

(A) and (B) compare simulations performed with SNESIM (black colour) and DEESSE (red colour) frameworks but also including INJ-1 (dotted patterns) and INJ-2 (Continuous patterns) for gas injection cumulative volumes and gas injection rates respectively. Simulation duration reach only 15 years for the INJ-2 cases, but it is enough to project a trajectory for the next year to come. INJ-2 simulation period is approximately 10 years.

The highest Injection rates rate associated with the highest cumulative volumes is seen in the simulation run on the DEESSE 3-faces model, for well INJ-1. The position of this well, which is drilled through well-connected sand volumes, results in larger injected volumes due to the creation of efficient preferential pathways since very early injection stages. Different stages of injection rates can be identified. First, gas injection rates display a rapid increase in the first few months, followed by a subsequent slowdown. This is explained by a rapid increase in pressure that is mainly induced by the bottom-hole pressure injection effects (430 bar) during the first months. Subsequently, a decrease in injection rates occurs, which is due to the dissolution of CO₂ in the reservoir brine. Afterwards, as the pore volume becomes saturated in CO₂, a phase of CO₂ is formed in the reservoir leading to the lift of Injection rates. Finally, as CO₂ saturation keeps increasing, the CO₂ Injection rates are mainly controlled by the effect of relative permeabilities that progressively become higher improving the injection rates in a sustained manner through the following years.

Dependencies between sandbody connectivity and well injection perforated intervals are also studied in this research (**Figure 5.28**).

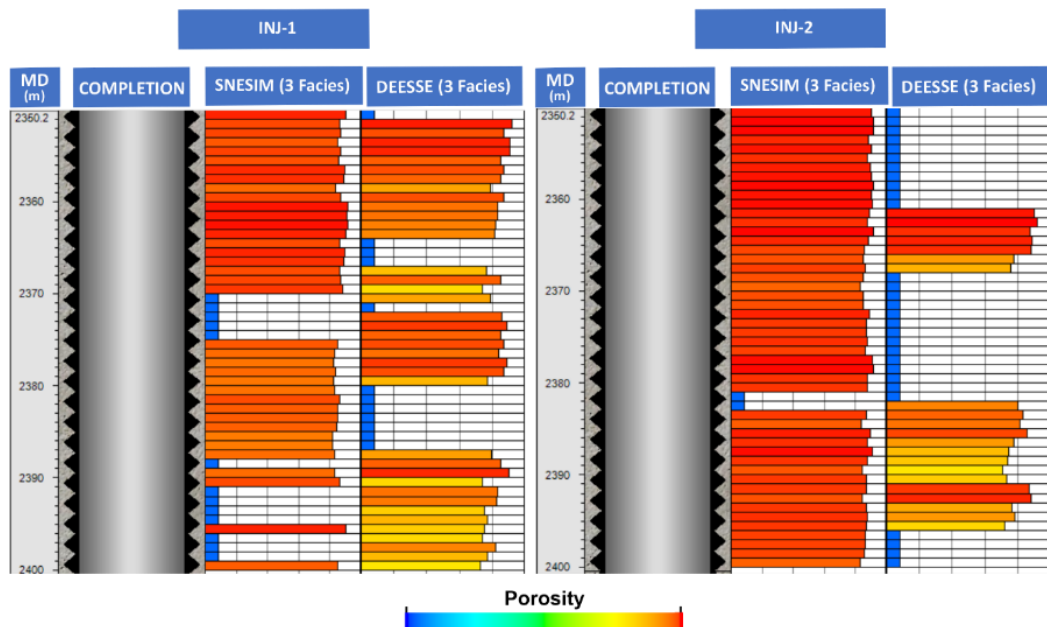


Figure 5.28 Perforated intervals associated with INJ-1 and INJ-2 for the four static models.

Porosity property displayed against the perforated intervals of the INJ-1 well for each of the models considered for dynamic simulations (3-facies models).

However, even if higher injection rates could be considered to be related to larger effective surface contacts (ratios between sand-prone and perforated intervals), in the early injection phases (<5 year) a direct association with overall CO₂ cumulative and Injection rates rate values is not recognised.

Regarding storage capacity, cross-plots for the 5-facies models (SNESIM and DEESSE simulations) associated with INJ-1, results were very similar (**Figure 5.29A**). However, a noteworthy behaviour is observed in the last years of injection, when both cumulative rates are attenuated, especially in simulations run on SNESIM models (**Figure 5.29B**). This is due to a marked decrease in injection rates in the last year of injection due to the pressurisation of the entire reservoir (**Figure 5.26- 30 years**). Also, injection rates associated with early years of injection are significantly different for SNESIM and DEESSE. Although the DEESSE simulations experience a similar behaviour to the ones previously displayed in the 3-facies model, the SNESIM model describes first a smaller increase of Injection rates in the first months, followed by a very rapid attenuation event that resumes shortly after at a fast rate. The injection rates for the SNESIM simulations overtake the DEESSE rates in year 3 (2025), when both models increase simultaneously their rates thereafter.

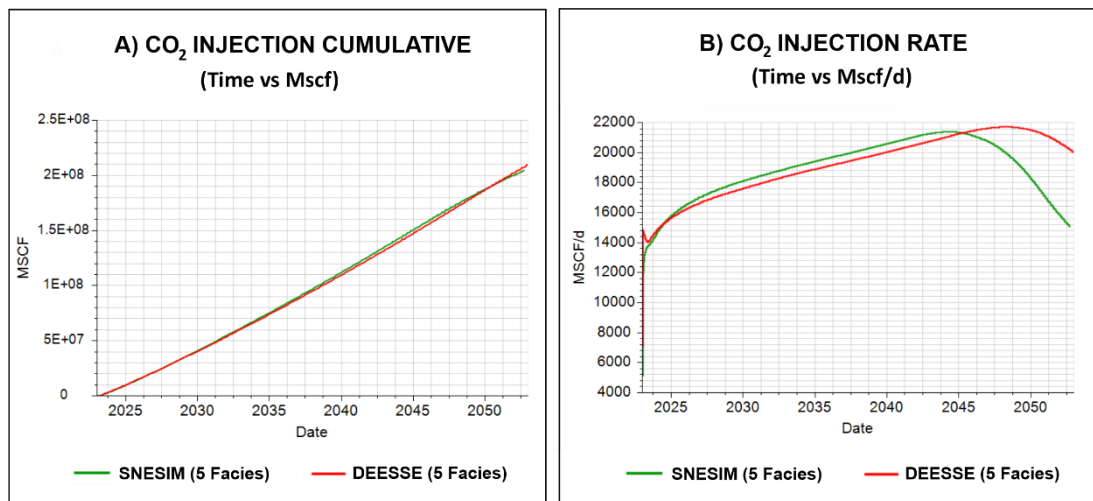


Figure 5.29 Injection cumulative and Gas Injection rate plots (5 facies models)

(A) indicates the CO₂ volumes injected throughout the 30 years of constant injection for SNESIM and DEESSE simulations. (B) shows the gas injection rates during the 30 years simulated for both SNESIM and DEESSE simulations.

This behaviour is explained as the larger sand connectivity that exist in the SNESIM 5-facies model with respect the DEESSE one, and the absent of significant barriers to the flow close to the well's area of influence. Because of this, the maximum solubility of CO₂ within the reservoir brine is reach earlier. It is observed, the type of heterogeneities located close to the well's area of influence condition early stages delivering different types of injection rate patterns.

A different analysis was performed to compare storage capacity and injection rates between 3-facies and 5-facies models using only the INJ-1 well (**Figure 5.30**).

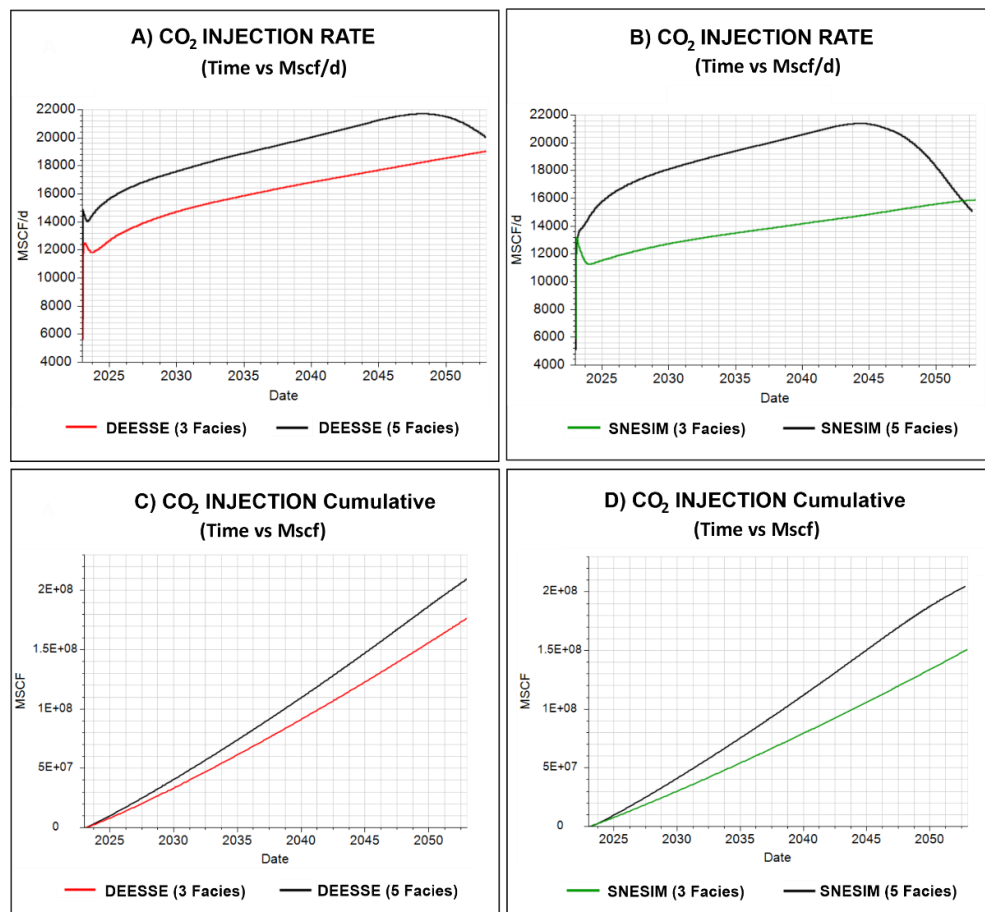


Figure 5.30 Cumulative injected volumes and injection rates through time (3 facies vs 5 facies models)

(A) and (B) compare CO₂ gas injection rates during the 30 years simulated for both SNESIM and DEESSE. Differences between the 3- and 5-facies models can be seen. (C) and (D) indicates cumulative volumes injected throughout the 30 years for SNESIM and DEESSE simulations associated to 3-facies and 5-facies models.

Larger CO₂ volume cumulations and higher Injection rates always correspond with the 5-facies models for both SNESIM and DEESSE. This is why the static porosity and permeability overall values are higher for the 5-facies models than for the 3-facies models. In terms of injection rates, the DEESSE simulations differences between the 3-facies and 5-facies are in terms of injected volume per day but not in profile shape, with the exception of the later stages where CO₂ injection in the 3-facies model do not reach to pressurise the entire reservoir (**Figure 5.30A**). In the case of the SNESIM models, important differences in the profile shape can be seen in the comparison between the 3-facies and 5-facies models. The SNESIM 3-facies model seems to follow the same patterns observed in the DEESSE simulations, but the dynamic behaviour of the 5-facies model is peculiar. This is due to higher connectivity rates between the sand deposits and lack of significant barriers to the CO₂ flow close to the proximities of the injector well's area of influence in the 5-facies model (**Figure 5.30B**). Therefore, associated with higher injection rates and higher cumulative CO₂ values, a relationship can be established with recorded pressures close to the well's area of influence (INJ-1).

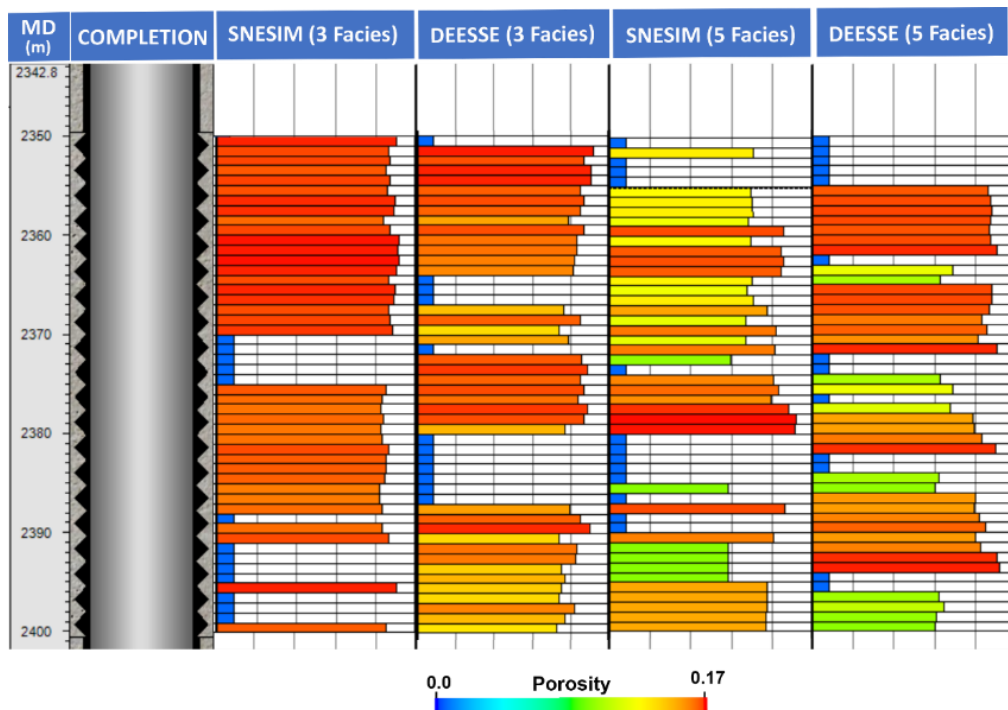


Figure 5.31 Perforated intervals associated with each of the dynamic models in INJ-1 well.

Porosity of the perforated intervals of the INJ-1 well for each of the models considered for dynamic simulations.

Also, the 3-facies SNESIM model showed significantly higher pressures than the DEESSE 3-facies simulations throughout the 30 years of injection (**Figure 5.18 vs Figure 5.26**), which correspond also with lower injection rates and cumulative storage values. This is again related to the type of heterogeneities and rock types encountered by the CO₂ plume in the well surroundings. Again, as confirmed in **Figure 5.31**, well profiles including better or worse surface connection to porous rocks did not play a fundamental role at controlling neither injection rates nor storage capacity. The location of the injector well ensures immediate connectivity flow with sandy deposits in more than 75% of its surface for all models. No major significances for overall porosities exist apart from punctual depths relating SNESIM and DEESSE frameworks.

5.6 Discussion

Visual inspection of differences in simulation outputs reveals the impact of large and mesoscale levels of heterogeneities on the displacement of a CO₂ plume. The 3-facies model incorporates large-scale heterogeneity associated with sandbody compartmentalisation by muddy channel-fill and floodplain deposits (Pickup et al., 1994), which is commonly considered in conventional reservoir models in the oil and gas industry (Pranter et al., 2007; Willis and Sech, 2019; Colombera, 2017). However, consideration of mesoscale heterogeneities associated with the facies organisation of point-bar deposits (point-bar base, mid-point-bar and top point-bar) enables a more accurate representation of lithological controls on fluid flow.

Heterogeneities that occur at even smaller scale (microscale. **Section 2.2.2**) are not captured by the porosity or permeability models in this study. An example for this scale of investigation is the permeability anisotropy of cross-bedded sandstones (Hurst and Rossvoll, 1991), which has been demonstrated in simulations by Dodge et al., (1997). Also, Pickup et al., (2002), highlighted how the ratio of low to high permeability laminae will impact the effective permeability of reservoir rocks. This is where low permeability beds are thin relative to high permeability beds, such that their impact is less compared to cases where beds are of similar thickness. This resolution is often ignored in permeability studies or industry workflows for static and dynamic models. Nevertheless, in static models for architecturally complex reservoir successions, such as those produced by meandering fluvial

systems, small-scale features will be of secondary importance as a control on fluid flow, relative to the connectivity of sand-prone deposits (Riordan et al., 2004; Tyler and Finley, 1991; Keogh et al., 2014). Therefore, micro or bed-scale lithological heterogeneity was ignored in this research. At the same time, the impact of diagenesis or fractures on petrophysics was not taken into account either, even though the employed petrophysical database (PAFD, Chapter 4) could in principle be used for deriving data associated with diagenetic effects. Furthermore, finer scale mud drapes contained in sand-prone volumes, which may affect the CO₂ plume behaviour, was also not considered in this study; it is proposed that these are considered in further investigations. This point is considered as a potential future investigation to continue this research.

Dynamic simulations run on both SNESIM and DEESSE static models demonstrate how the tortuosity of channel-fill deposits and presence of packages of floodplain deposits determine irregularity in the advancement of the plume front, in both 3-facies and 5-facies models. This type of plume evolution has been identified as a process that favours dissolution of CO₂ within the brine, as it increases the exchange surface between the reservoir water and the plume (Issautier et al., 2013; 2014; Zhang and DePaolo, 2017; Bachu et al., 2007; Al-Khdheewi et al., 2017b). However, it will also slow down the rate of spread of the CO₂ plume and hinder the development of early flow pathways (Puig et al., 2019; Willis and Sech, 2018b).

Although local sandbody compartmentalisation is recognised in the modelling grid, connectivity between sand deposits is generally high: the mudstone layers encountered in the model by the CO₂ plume are not sufficiently continuous in 3D to completely compartmentalise the reservoir unit; this is aligned with geological understanding, although not necessarily applicable to all meander-belt architectures (Colombera et al., 2017). This style of compartmentalisation and the related patterns of sandbody connectivity control the pressure distribution in the reservoir and the plume behaviour, especially in the first years of injection when pressures close to the well exert a stronger influence compared to later years. Compartmentalisation and sand connectivity are controlled by the net-to-gross ratios considered in the facies modelling stage, which vary across the four different scenarios considered in this study.

Important implications with respect to reservoir pressures can be drawn from observations made on vertical sections of the simulations. Pressures exhibit important vertical variations in the reservoir due to the presence of intraformational seals (channel-fill mud plugs and floodplain mudstones), which support a proportion of the CO₂ column thereby relieving the pressure exerted over the uppermost caprock. This can be beneficial with respect to preservation of seal integrity and prevention of chemical effects that the CO₂ may induce in the seal rocks (Espinoza et al., 2017).

With respect to injection rates, an interesting behaviour is observed in the early stages of injections for simulations on both SNESIM and DEESSE 3-facies models. Through time, CO₂ injection is controlled by initial bottom-hole pressure, dissolution of CO₂ in brine, creation of an independent CO₂ phase and relative-permeability changes. The bottom-hole pressure is equal for both SNESIM and DEESSE models (430 bar); yet differences in the facies models and with respect to the position of the well result in differences in injection rates in the different models. The observed behaviour is in line with previous research undertaken by different authors where heterogeneities, relative permeabilities, bottom-hole pressure, solubility conditions, and associated injection rates control the plume behaviour (Bennion and Bachu, 2005; 2008; Kumar et al., 2004; Nguyen et al., 2017).

A refinement of this study can be envisaged based on improved consideration of relative permeability relationships, since these have been shown as crucial approximately after the third year of injection in controlling the development of preferential pathways and overall plume spread. Apart from the Corey's relative permeability relationships used in this study, other popular functions have been successful when applied to CO₂ flow, such as the Van Genuchten function (Van Genuchten, 1980). Also, different authors have demonstrated the importance of developing bespoke relative-permeability functions for specific rock types as a way to obtain more realistic results (Dana et al., 2002; Krevor et al., 2012). These considerations highlight the need to better constrain relative permeabilities in future works of this type.

Also, this study sought to evaluate the spread of a CO₂ plume by buoyancy, diffusion and dispersion as the dominant transportation mechanisms (Moodie et al., 2016). However, this research does not consider the plume behaviour

when injection stops. Dissolution or mineralisation processes that may occur decades or even hundreds of years after injection are ignored. These long-term effects may need to be considered in further studies and for real-world examples, to minimise risks of CO₂ leakage to the surface (Bachu et al., 2001).

5.7 Conclusions

This study aimed to elucidate the importance of depositional heterogeneities at different scales and their representation in static models by application of geomodelling tools on petrophysical heterogeneities and resulting dynamic flow behaviour, for successions of meandering fluvial systems (Chapter 5). The sedimentary architecture modelled using SNESIM and DEESSE as detailed in Chapter 3 were employed to investigate the impact of large-scale and mesoscale heterogeneities on the behaviour of an injected CO₂ plume constraint to petrophysical parameters delivered by PAFD (Chapter 4). The study culminates in the following conclusions:

- Geological heterogeneities of successions of meandering fluvial systems control the behaviour of the CO₂ plume, trapping efficiency, injection rates and ultimately storage capacity.

The geometry of mud-prone channel-fill and floodplain deposits control the tortuosity of flow of the CO₂ plume, which can be beneficial for CCS projects since the plume surface area is a factor that facilitates dissolution in the brine.

-

In the static models, there exists connectivity between sand-prone point-bar compartments, which varies as a function of the net-to-gross ratio thereby controlling injection rates and storage capacity.

-

Abandoned channel-fill and floodplain mudstones create intraformational barriers that determine vertical variability in saturation levels and pressures. The resulting pressure distribution reduces the pressure exerted directly on the caprock, preserving its integrity, and preventing chemical reactions that may lead to leakages.

-

Plume behaviour is mainly controlled by the underlying facies model framework in the dynamic models. Heterogeneities of fluvial successions control CO₂ storage capacity and saturation. Dissolution

appears to be restricted to early injection phases before a separate CO₂ phase emerges.

-

Main trapping mechanism acknowledged in this study correspond to capillary effects associated with the occurrence of certain types of rock types or facies. The mesoscale or 5-facies model accurately represent the intra point-bar trapping mechanisms associated to each of the model elements which spatially distribute different CO₂ saturation content. The 3-facies model do not capture these effects.

-

The direction, speed, and regime of propagation of a CO₂ plume is strongly controlled by mesoscale (intra-point-bar) lithological heterogeneities that are commonly overlooked in subsurface modelling workflows. Higher permeability lower-bar facies act as preferential CO₂ pathways (thief zones), whereas point-bar top facies may act as baffles that retard CO₂ flow.

-

The point-bar top facies play a fundamental role in this specific setting where i) hinders CO₂ to move upwards sustaining the CO₂ column or ii) pushes the CO₂ plume to move horizontally in the space. This effect has implications on the horizontal distance that the CO₂ plume can extend in the simulation grid (larger than the one observed in the 3-facies model) but also the redistribution of pressures and gas saturation in the vertical section contributing to relief the uppermost caprock from a higher pressure coming from the CO₂ column alongside the multiple barriers encountered in the model (channel-fill and floodplain deposits).

-

The geometry, position, and the amount of channel-fill and floodplain deposits (barriers to the flow) existing in the grid with respect the location of the well will drastically condition the CO₂ Injection rates and final cumulative volumes.

Higher injection rates are associated with higher cumulative injected volumes. However, injection rates indicate that through time the injected plume is controlled by different processes; namely, in chronological ordered: i) bottom-hole pressure, ii) CO₂ dissolution in brine, iii) creation of a new CO₂ phase and iv) relative-permeability dependencies. The duration of each of this stage is fundamentally controlled by the existing connectivity and absence or presence of flow barriers near the well.

-

The analogue petrophysical database presented in Chapter 4 (PAFD) has been proven useful for assisting the construction of property models for dynamic simulation.

-

The successions of meandering fluvial systems have great potential for the long-term storage of CO₂ in the subsurface. Understanding the impact of the large-scale and mesoscale heterogeneities they contain is a key prerequisite for assessing the viability of CCS projects.

6. Discussion

To complement the detailed and focused discussions that are integrated within each of chapters 3, 4 and 5, Chapter 6 considers the following topics: i) the challenges and limitations of MPS geomodelling methods; ii) the scopes of application of the petrophysical database presented in Chapter 4; iii) fluvial successions generated by meandering rivers as potential target reservoirs for long-term underground carbon sequestration.

6.1 Challenges and Limitations of MPS Geomodelling

Chapter 3 demonstrated how a workflow built on the principles of facies modelling can appropriately characterise the sedimentary heterogeneity inherent in fluvial successions generated as the accumulated products of meandering rivers (Montero et al., 2021). However, this Thesis highlights some of the numerous hurdles and limitations faced by geomodellers using MPS methods. Specifically, these relate to i) the construction of a valid training image that can appropriately represent the chief lithological components of the reservoir in 3D, and ii) the time-consuming trial-and-error calibration process required to couple appropriately MPS codes to training images. These two essential requirements of the MPS modelling workflow recurrently hinder geomodellers and restrict the adoption of MPS codes as mainstream modelling methods.

Different approaches to promote the use of MPS algorithms have been made to minimise the time spent and effort required in the construction of training images. The utilisation of training image libraries has been advocated by different authors (Caers, 2001; Chugunova et al., 2008; Pyrcz et al., 2008; Mariethoz and Caers, 2015) and software platforms such as Schlumberger Petrel® or Halliburton SEM®, now include a selection of training-image libraries that aim to facilitate the uptake of MPS methods by geomodellers. Yet, many existing training-image libraries are limited in their realism and are not necessarily tailored to particular classes of lithological succession. Objective 1 in this research targets the practical issue of building sophisticated and specialised training-image libraries, and their application to generated better informed reservoir models. This is achieved with the construction of a training-image library including 24 examples for fluvial meandering successions (Figure 6.1).

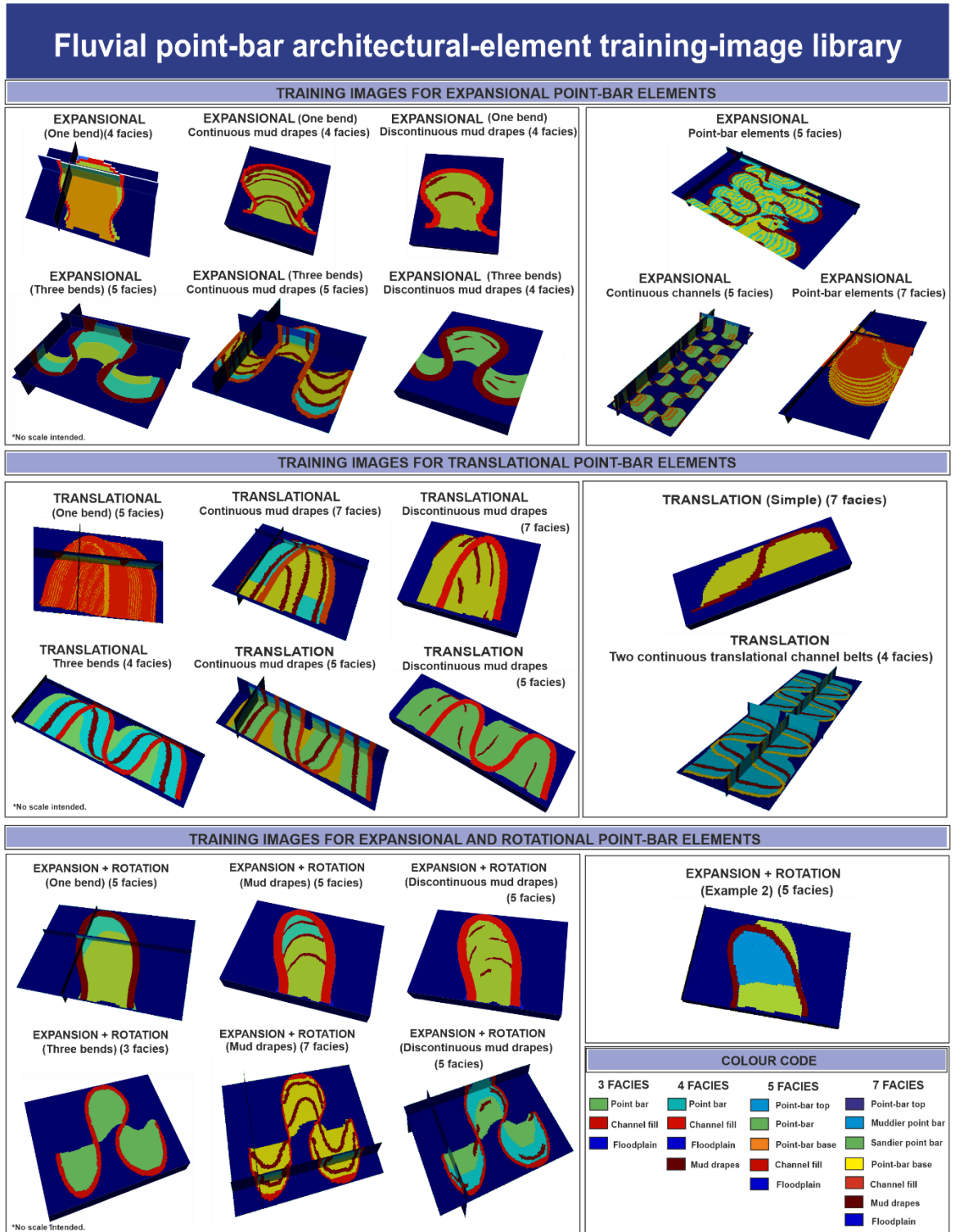


Figure 6.1 Training-image library (examples)

Training-image library including 24 samples classified by meander transformation type causing point-bar growth (expansion, translation, expansion and rotation). Different versions exist that include different types of facies (3, 4, 5 and 7-facies) illustrated by different colours. The library includes both examples with single point-bar elements and examples with channel-belt reaches consisting of repeated point-bar elements.

As highlighted in Chapter 2, the application of stationary training images is desired in MPS modelling (Strebelle, 2002; Comunian et al., 2012; Ringrose and Bentley, 2015); otherwise, original patterns located in the training images may not be reproduced in simulations. However, most geological processes are by nature non-stationary. This research continues the work of previous authors that have worked with non-stationary training images and incorporated trends in the resulting models following different techniques (e.g., the application of auxiliary variable maps: Chugunova and Hu (2008); Honarkhah and Caers, (2012)). Yet, this study advances the modelling workflow further in that it additionally incorporates trends within the training images themselves. The different tests performed in Chapter 3 (Objectives 2 and 3) indicate success at reproducing certain patterns. Examples can be the point-bar fining-upwards trend which is well reproduced in most of the Cases included in **section 3.3.1 to 3.3.6**, or the expansional point-bar growth features properly recorded in simulations (Case 2, **section 3.3.2**). However, more research is needed in this domain, specifically to understand better the boundaries of non-stationarity weights directly incorporated within training images. An example for further investigations can be the trends included within translational systems (Case 5, **section 3.3.6**) which were not adequately delivered in simulations by this study.

Another important limitation corresponds to the usage of auxiliary variable maps. These, even if they have been proven to be very useful at driving the simulation of different trends in this research, inevitably lead to a mismatching between the final facies model target proportions and the training image target proportions. The amount of mismatch was acceptable for this study because a key objective was the reproduction of channel-belt geometries and gross-scale sedimentary architecture, rather than the requirement to match exactly element proportions from training images. However, in other applications, the training image may represent a base-case for element proportions that needs to be honoured in resultant simulations. In these scenarios current MPS methods will be challenged if auxiliary variables are used (Tahmasebi, 2018).

Furthermore, uncertainties relating to the construction of training images require special attention. Commonly, the construction of training images is a manual development that requires various iterations. During this process, multiple checks on the three-dimensional volume will take place as well as numerous inspections over the target fractions for each of the model

elements. This is done to ensure optimum stratigraphical resolution and make sure specific statistical values are appropriately encapsulated within the training images. This represents an important issue since the process is highly subject to human bias. To mitigate this issue, this research introduces a new approach from which training images are developed as the result of 3D forward-stratigraphical models (PB-SAND, [Yan et al., 2017](#)) informed by quantitative information delivered by a relational database describing lithological aspects of many known fluvial systems and their preserved successions (FAKTS, [Colombera et al., 2012a; 2012b; 2013; 2017](#)). The process is not fully automated and requires manual input and guidance across multiple interactions. However, it offers an opportunity to further automate the process and eliminate human inclinations from the generation of the training images themselves. Future investigations with respect to the automation of the construction of bias-free training images by the application of machine learning algorithms (ML) have been already proposed by [Mitten et al., \(2020\)](#). These authors argue that a 3D training dataset constituted by multiple cross-sectional and plan-view planes belonging to specific reservoir rocks can inform a ML algorithm to later dictate the creation of training images. Although this may be possible in the foreseeable future, current developments for ML applications related to geoscience are far from offering the high degree of reliability required. An example can be seen in the current developments of simpler 1D log interpretation tools for which various service companies are currently developing software tools (e.g., the Assisted Lithology Interpretation tool – ALI® Halliburton, [Montero et al., 2019](#)). Although results are promising, the large geological variability at different scales currently prevents ML algorithms from delivering appropriate automated results.

The lack of clear QC/QA guidelines to validate training images and coupled MPS configurations demonstrates another important limitation for the adoption of MPS methods. The following questions remain. What are acceptable levels of stationarity in a training image? To what extent must a particular feature within a training image be repeated for the image overall to be considered stationary? These are examples of questions to which full answers have yet to be provided by code developers or by the geomodelling community more generally. Ambiguous statements such as “...for the given data template and the given training image the number of data events is too small” ([Comunian et al., 2012. p 63](#)) or “...the maximum data search template retained should not be taken too small, otherwise large-scale structures of the

training image would not be reproduced” (Strebelle, 2002. p.10) abound in the MPS-related literature. What is meant by “small” in this context? Such ambiguity in the messaging makes it especially difficult for geomodellers to adopt MPS methods as part of a reliable workflow.

With respect to the process of setup MPS modelling algorithms, multiple authors have highlighted the lack of standardised workflows with which to couple training images and MPS codes. Every case seems to be unique and requires configurations to overprint MPS controls upon specific reservoirs in three dimensions (Comunian et al., 2012; Tahmasebi and Sahimi, 2015a; Honarkhah and Caers, 2012). Although, Chapter 3 includes both a training-image library with ready-to-use samples and a comprehensive guide to couple training images with MPS codes (SNESIM and DEESSE) (Table 6.1), it is very likely that further configurations that differ from those indicated in this study will be required in different case-scenarios. This represents an important issue with the reutilisation of training images within any training-image library and associated MPS model recipes which currently can only be considered as “starting points or first references” in MPS simulations.

		SNESIM	DEESSE	Runtime
TRAINING IMAGE CALIBRATION	Number of cells	Upscale/Downscale from original TI number of cells to a size that properly define the dimensions of meandering features within the simulation grid.		The larger the n ^o of cells in TI, the longer the runtime/realisation
		The size of the TI with respect the size of the grid will determine the size of model elements		
	Number of Facies	Most of MPS modelling algorithms worked optimally with 4 to 5 facies		The more the n ^o of facies included as inputs, the larger the runtime/realisation
	Facies Proportions	Servosystem “ λ ” = 0 ensures TI proportions are honoured		
	Auxiliary Variable	Trends added overrides original TI proportions		
	Number of Nodes (N)	Structural and geometrical patterns are better honoured in realisations where larger number of N are included		The larger the N, the longer the runtime/realisation

	Template	Search Mask:	Search Neighbourhood:	The larger the template, the longer the time per realisation
		Elliptical template ($x=y \neq z$) delivered the best results		
		Factor of 1) number of cells in TI 2) the size and shape of the elements inside the TI required to be captured		
		The larger the template's radius, and the bigger N is, better the fluvial patterns included in the training image are reproduced in the simulation		
		Search radius 1.5 times bigger than the largest channel feature in TI (normally bend axis) delivered the best results		
OPTIMISATION	Multigrids	4 multigrids determined as optimum		Combination of the three works as runtime optimizers. Multigrids and subgrids can be use instead of making the template larger. The bigger RE, the longer the runtime
	Subgrids	4 Subgrids determined as optimum		
	Replicates (RE)	5 to 10 replicates as optimum		
	Maximum Fraction (F)		Pattern-reproduction improves when N is larger, DT is closer to 0, and F is closer to 1. Best results obtained when: F= 0.3-0.5; DT= 0.15-0.20	Reducing the F from 1 improves runtime. However, large reductions of F may lead to under sampling.
	Distance Threshold (DT)			The lower the DT, the more the runtime/realisation
AUX MAPS	TAU models	The higher TAU2 relative to TAU1, the higher the influence of the soft probability data.		
	Search radius (SR)	SR > 10 as optimum		The smaller the SR and DTR, the longer the runtime/realisation
	Deactivation threshold radius (DTR)	DTR > 5 as optimum		

Table 6.1 MPS modelling recipes (meandering fluvial systems)

Model recommendations with respect to the parameters controlling training image calibration, optimisation, and the utilisation of auxiliary maps in SNESIM and DEESSE. Important notes regarding runtime are also given.

6.2 PAFD Applications

The database of analogue petrophysical data (PAFD, Petrophysical Analogue Fluvial Database) presented in Chapter 4 was shown to work efficiently and effectively to provide quantitative petrophysical values to each of the facies types included in property models (Chapter 5; Objective 4 and 5). Different choices for suitable reservoir rocks were given. Between them, the Alcaraz Fm ([Henares et al., 2016](#)), the Caballos Fm ([Castellanos, 1994](#)), the Eastern View Fm, the Legendre Fm, the Mediumngaroo Fm ([WAPIMS](#)), the Morrow Sandstones ([Dolly and Mullarkey, 1996](#)), the RP Fm ([Barde et al., 2002](#)), and the Travis Peak Fm. ([Indiana University Database](#)) were delivered in the same query for the search of representative point-bar analogue data (Chapter 5, **section 5.3**, Query 1). However, the Latrobe Group (Gippsland Basin, Australia) was selected as a preferred analogue, as defined by core data evaluated from the Tarwhine-1 well and because of its potential to allocate CCS projects ([Chadwick et al., 2008](#)). As a result, realistic porosity and permeability inputs associated to each of the model elements (point-bar base, mid-point-bar and point-bar top) in the facies models, allowed the characterisation of each of them as representative rock types (Chapter 2, **section 2.1.6**). Additionally, the dynamic simulations performed in Chapter 5 proved the distinctive hydraulic behaviour under CO₂ fluid flow (Objective 6) for every rock type in the model.

Moreover, PAFD also includes a record of the existence of continuous wireline/LWD logs associated with core data. This can be useful if continuous petrophysical analysis are required. For the case of the Tarwhine-1 well a suite of logs derived from Quad-Combo analysis was located associated to the data source ([WAPIMS](#) database). Continuous logs were scanned from the original sources and petrophysical interpretations were contemplated to upscale porosity and permeability signatures in property models. This is another valid scenario to inform the previously built facies models. However, a decision was made to not use well logs to condition property models and continue with the application of transforms as secondary data extracted from PAFD instead. This was a decision based on the unconditionality of the experiments carried out in Chapter 3 where no well data is utilised. The investigation is oriented to those similar cases in an early exploration context where limited data or no data at all is handled and petrophysical data from an analogue case-study are required.

With respect to the chosen PAFD architecture for the developed database using a simple static spreadsheet, this investigation determined there was no need to implement more sophisticated designs to store and manage the multiple datasets handled by this study (e.g., a relational database architecture was not deemed necessary). Limitations like scalability, querying, data connectivity, data volume constraints, etc, are widely recognised spreadsheet issues as they make them difficult to use for relating complex type of datasets. However, with appropriate tools in place a simple spreadsheet like the one designed in this investigation, can be as versatile as any other more sophisticated relational database. Spotfire® from TIBCO is used in this research as both analytics and data visualisation software. Complex queries and filtering operations are simplified while useful visualisation dashboards are enabled. Spotfire® also helped to keep the database groomed and free from duplications.

Applications of PAFD presented in Chapter 4 expand beyond the identification of a suitable analogue rock to constrain property models (Chapter 5). It can also be potentially applied in different contexts associated within the reservoir modelling workflow. These are direct applications on the model conceptualisation process and on the input and data QC stages of a reservoir model (see **section 4.4**).

6.2.1 Model Conceptualisation

Professionals working on model conceptualisation will seek to employ information from one or more analogue rock succession(s) that possess similar characteristics to the subsurface succession under investigation. This is one of the earliest stages of the reservoir modelling workflow and is usually subject to uncertainty due to lack of hard and soft data. Therefore, analogue data can be useful to predict the geological background and understand the petrophysical framework needed to support subsurface evaluation and risk assessment (Tarek, 2020). In the case of fluvial reservoirs, it is important to understand the characteristics of sand bodies, including their geometries and connectivity, alongside their associated petrophysical properties. Therefore, analogue databases should be filtered accordingly (on metadata, stratigraphic, tectonic basin type, etc). Hypothetical examples to demonstrate how PAFD of Chapter 4 can contribute to the “model concept” stage is presented in the following case examples.

6.2.1.1 CASE 1: Model Conceptualisation for Prospect Definition

Superimposed channel-belt components exhibiting features arising from and related with systematic lateral migration of channels have been identified in seismic sections to occur in a standard terrestrial rift valley setting as described by a geoscientist (**Figure 6.2**).

The project is in a very early exploration stage and a model concept is needed to support the definition of a prospect. Filters are applied to PAFD (“*mobile channel belt system*”, “*divergent regime*”, and “*terrestrial valley*”) to identify suitable analogues that may be associated with potential reservoir rocks and to enable the subsequent identification of its key components and features in the subsurface (e.g., horizontal and vertical distribution). PAFD then delivers information referring to different attributes describing internal organisation, architecture, and petrography ultimately related with petrophysical data. This information is displayed in terms of proportions of sedimentary units that may be present in this prospect (**Figure 6.3**). It is important to note that these outputs are only useful to get a sense of where the associated petrophysical data in the database come from. They are not representative of any particular fluvial system, and its contribution is to complement the definition of model elements.

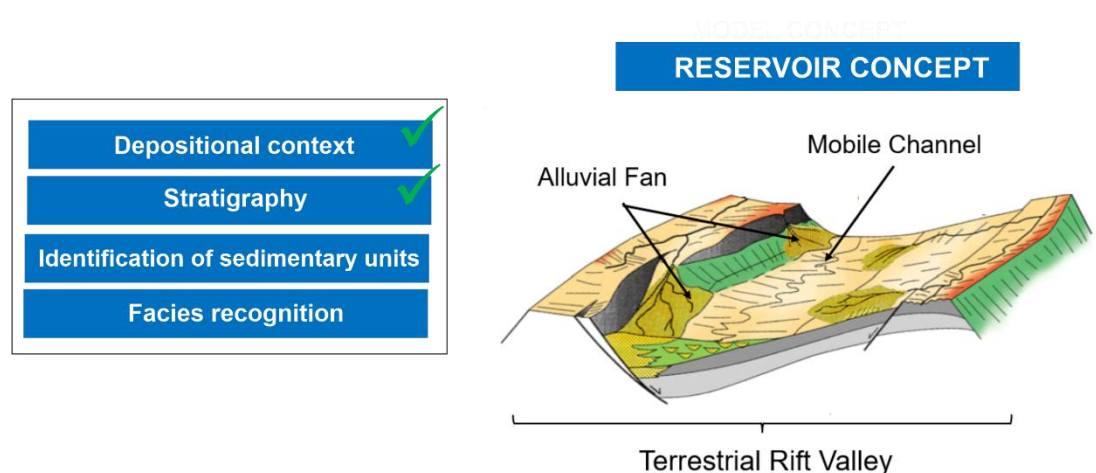


Figure 6.2 Case 1: Mobile Channel Belt

A mobile channel belt system included within a terrestrial rift valley setting (modified from [Gabrielsen and Steel, 1995](#)). PAFD (Petrophysical Analogue Fluvial Database) will be interrogated to deliver different types of information. The depositional context and stratigraphy are marked as ticked, as they are used to filter the database.

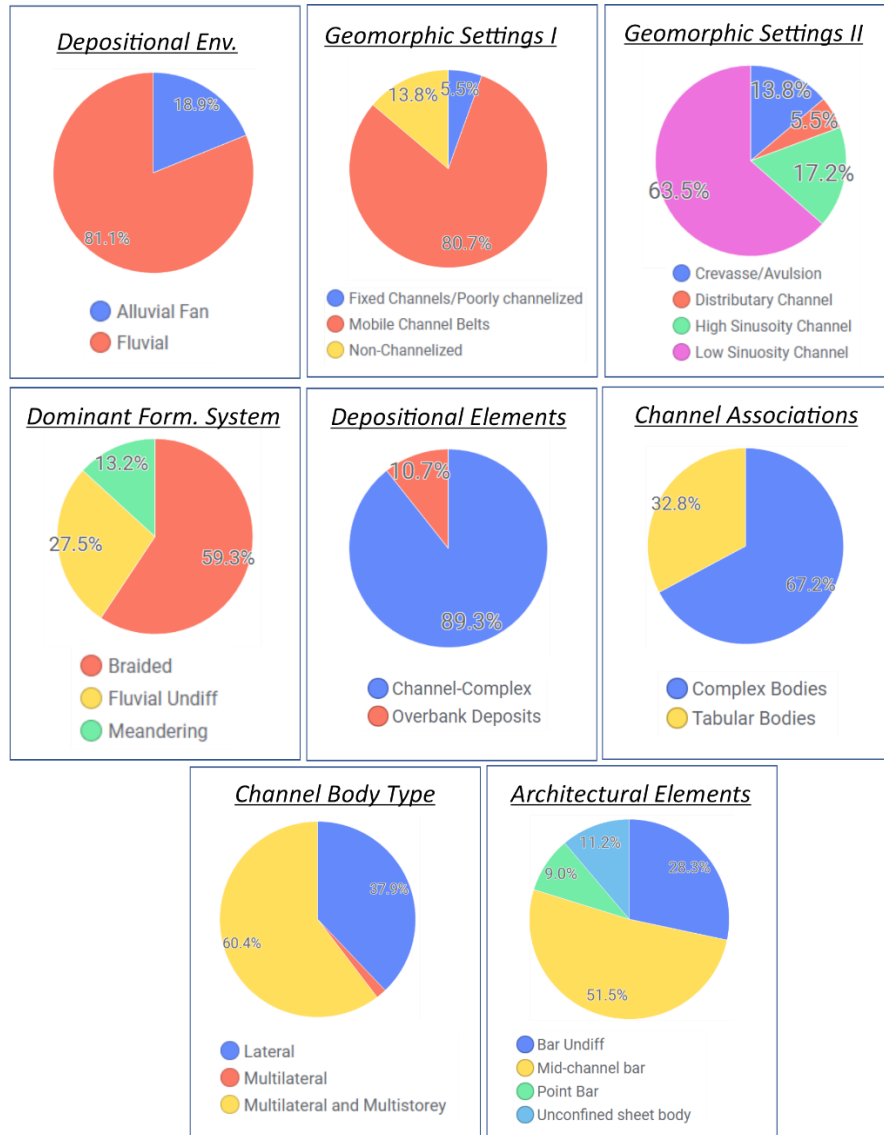


Figure 6.3 Model Elements identification

PAFD (Petrophysical Analogue Fluvial Database) outputs on proportions of observations corresponding to various subgroups aiming to complement the definition the model elements (sedimentary units) to be included in the reservoir model. Filters applied on the database corresponds with 1) *Tectonic-plate Setting*: “terrestrial rift valley”. 2) *Depositional Environment*: “fluvial-deltaic” category excluded, 3) *Dominant Process Influence*: “fluvial” only (“aeolian mixed”, “lacustrine” and “marine” excluded). N=1,114 entries are delivered by this query.

Subsequently, the geoscientist considers low-sinuosity braided channel systems as likely located in the area of investigation and the “braided” filter is therefore applied to the *Dominant Formative System* subgroup. This way, PAFD returns information regarding the lithofacies, and petrographic data related with braided systems in the database which may help to complement the facies recognition phase (**Figure 6.4**).

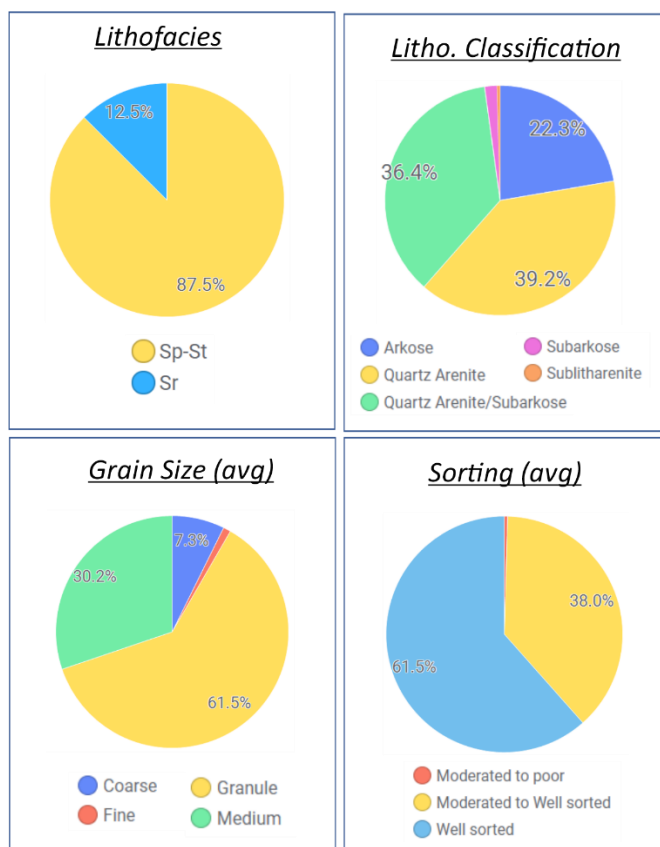


Figure 6.4 Facies Recognition (Braided)

Proportions of observations associated with different subgroups for the “braided” category identified as model elements. Filters applied on the database corresponds with 1) *Tectonic-plate setting*: “terrestrial rift valley”, 2) *Depositional Environment*: “fluvial-deltaic” category excluded, 3) *Dominant Process Influence*: “fluvial” only (“aeolian mixed”, “lacustrine” and “marine” excluded) and 4) *Dominant Form. System*: Only “braided”. N=661 for the four displayed pie charts.

Furthermore, PAFD helps to predict the reservoir in terms of its petrophysical properties, where **Figure 6.5** shows porosity-permeability cross-plots for different categories of analogues. The plots indicate a very large cloud of points which include sufficient values of porosity and permeabilities so regressions can be obtained for different reservoir model purposes (e.g., secondary variable data applied to property modelling).

The application of a colour code applied to porosity and permeability values (X and Y respectively) helps to better understand different relationships. For instance, **Figure 6.5A** includes a porosity-permeability plot with highlighted formation names. At this stage a decision can be made to consider 1) picking one of the analogue rock formations and continue with further studies focused

on that specific example (as done in Chapter 5 with the Latrobe Fm.), or 2) continue with a “combined analogue” analysis that includes various analogue rock data related with the implemented query.

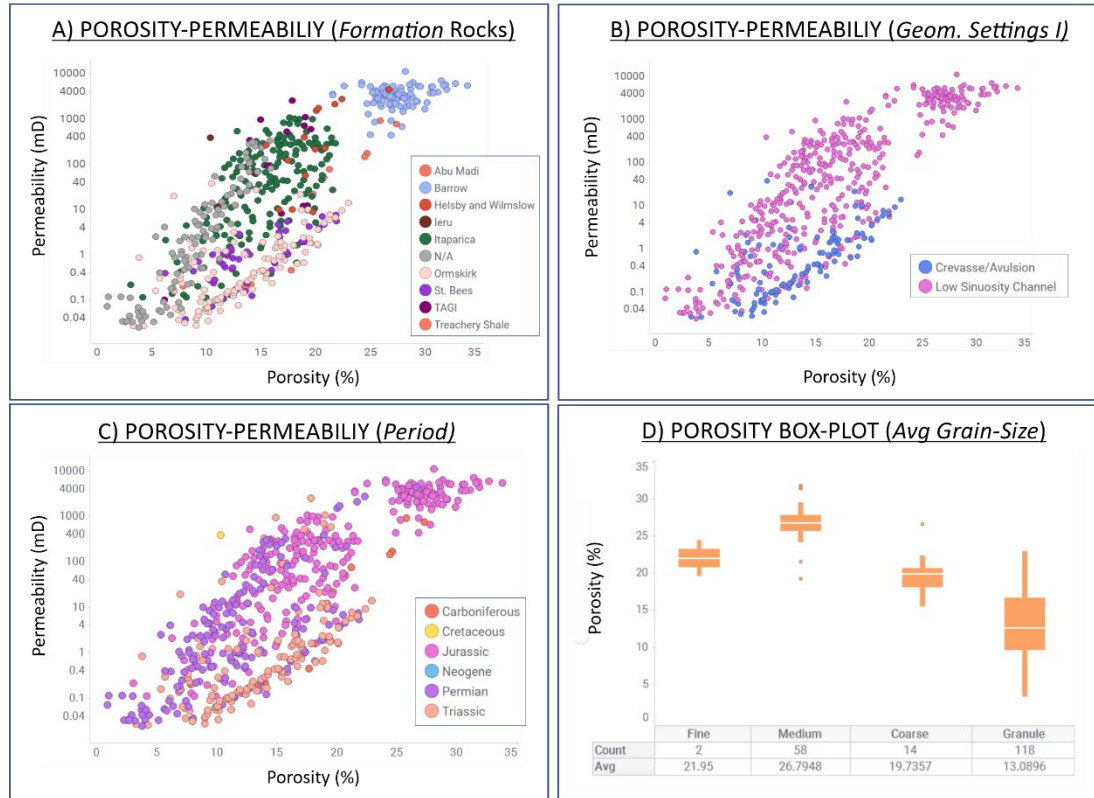
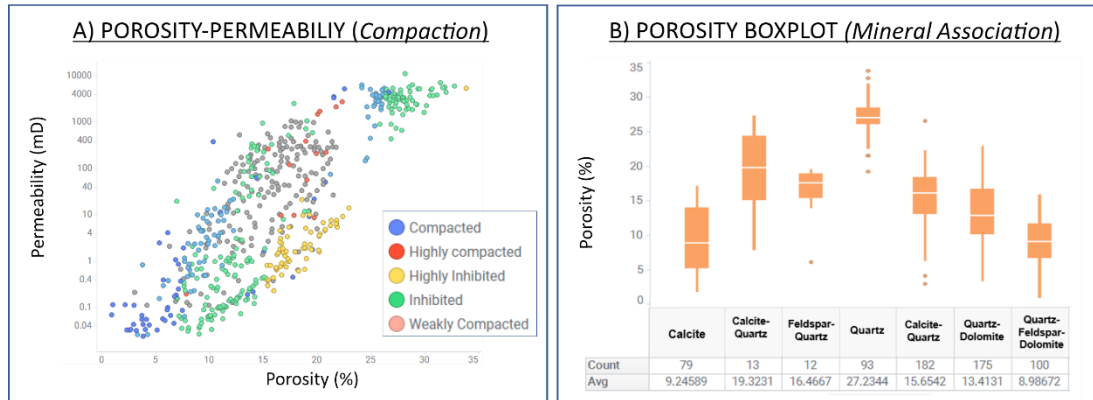


Figure 6.5 Porosity and permeability charts

(A), (B) and (C) present porosity-permeability cross-plots for different categories of analogues. (D) shows porosity boxplots for different classes of *Grain-Size*. Same filters used in the query described in **Figure 6.4** applies. N=661 applies to all charts in this figure.

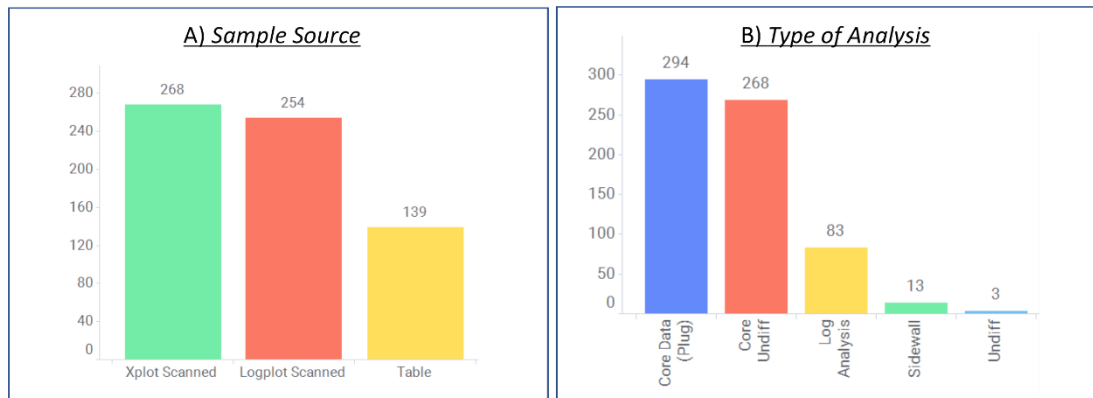
Results can also be evaluated in terms of diagenetic imprint. **Figure 6.6A** shows the mechanical compaction effects on porosity and permeability values. Also, the permeability and porosity values are related to different mineral associations (**Figure 6.6B**). The presence of quartz in the matrix appears to be the most important diagenetic chemical cementation process; this appears to be associated with higher values of porosity in this filtered dataset.

PAFD also stores metadata, including attributes describing data sources, so that associated uncertainties can be evaluated.



(6) Figure 6.6 Porosity and permeability charts shows a porosity-permeability cross-plotted for different *Compaction* categories. (B) shows boxplots for porosity distributions associated with different types of cementation processes (*Mineral Association*). The same filters as used in the query described in **Figure 6.4** are applied. N=661 for both cross-plot (A) and boxplot (B).

Figure 6.7 displays the *Sample Sources* and the *Type of Analysis* subgroups for the 661 records returned by PAFD upon application of the stated filters. These correspond with 268 records associated with “*scanned cross-plots*”, 254 entries belonging to “*logplots scanned*” and 139 coming from “*table*” sources.



(6) Figure 6.7 Uncertainty Analysis (Data source) shows a histogram plot where different sample sources are represented. (B) shows a histogram plot for the different *Type of Analysis* included in the database Same filters used in the query described in **Figure 6.4** applies. N=661 entries for both histogram plots.

With this information, highly reliable data sources can be selected, focussing for example on data coming from the “*table*” category, as these include RCA (Routine Core Analysis) and SCAL (Special Core Analysis) values (**Figure**

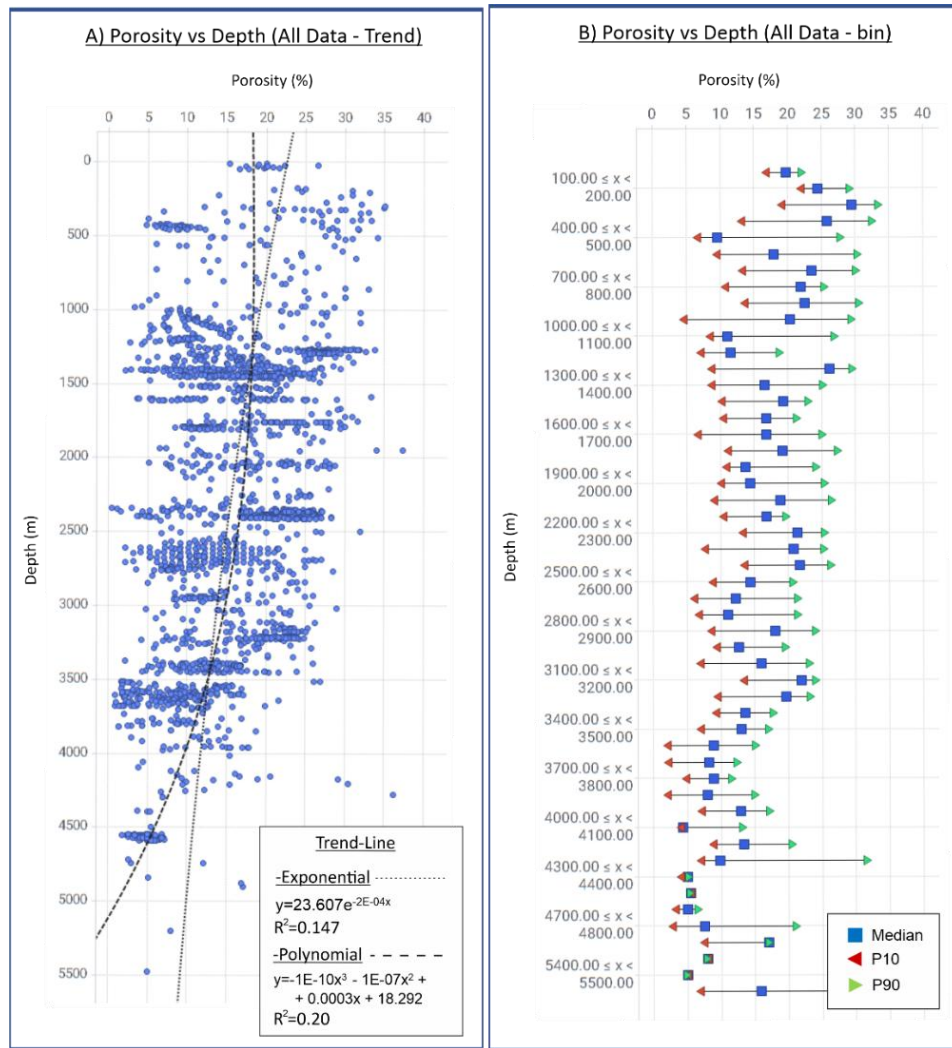
6.7A). Similarly, under *Type of Analysis*, records coming from plugs (“*core data*”) will be more accurate than those coming from 1D wireline logs or “*sidewall*” core sources (**Figure 6.7B**).

6.2.2 Porosity and Permeability Inputs for Reservoir Modelling

PAFD can be used to make porosity and permeability predictions based on various fluvial characteristics included in the database (e.g., porosity and permeability values related to “Gp-Lithofacies”). These porosity and permeability parameters can serve as direct inputs to reservoir models, but they are also applicable for a QC of petrophysical interpretations which are required to be validated by offset well data or analogue rock data, including similar rock types. Various case-scenarios are discussed below for different parameters included in the database.

6.2.2.2 CASE 2: Porosity-Depth Trends

Multiple studies have determined relationships between porosity and depth in sandstones, whereby the porosity tends to decrease with depth (Maxwell, 1964; Selley, 1978; Bloch, 1991). This means that prediction of unknown porosity from known depth can be attempted if sediment compaction of a sand-prone formation is well understood. The relationship between porosity and depth in sandstones is controlled by different factors including lithology, depositional facies, grain size, packing, age, and diagenesis (physical compaction and cementation). However, porosity reduction down to 2.5-3 km is mainly due to mechanical compaction, for which texture plays a significant role (Ramm, 1992). At depths greater than 3 km, quartz cementation becomes a key factor controlling porosity reduction (Ehrenberg, 1990; Ramm, 1992; Ryseth and Ramm, 1995). Temperature and pressure are also key controls; however, the devised database does not account for these variables explicitly. In early exploration phases, else in data-poor situations more generally, analogue data can assist depth-porosity studies (Ramm and). With more than 2,298 records of depth and porosity, from 298 wells and 85 rock formations, PAFD can yield depth trends or ranges of porosity values for specific depth intervals. As example, **Figure 6.8A** shows two depth-porosity relationships using exponential and third-degree polynomial functions.



(6) Figure 6.8 Depth-Porosity trends Porosity values as a function of depth based on the entire database. Two trend-lines are calculated. (B) Porosity-depth plot in which depths are binned into 100 m classes and median (e.g., P50), P10 and P90 porosity are shown (N=2,294).

It is common to consider similar trend functions for predicting porosity values at specific depths of investigation (Ramm and). Furthermore, as shown in **Figure 6.8B**, outputs can be derived in terms of descriptive statistics (e.g., median, different percentiles) of porosity measurements, linked with depth. As an example, considering the exponential trend of **Figure 6.8A**, a porosity of approximately 15% is calculated at 3,000 m. On the contrary, the binned plot (**Figure 6.8B**) returns, for the same depth, a porosity median of 12.4%, a P10 of 8.2% and a P90 of 18.8%. This statistical approach may represent a more useful display of uncertainties restricted to a particular depth bin rather than to larger statistical distribution represented by a low R^2 trend-line.

6.2.2.3 CASE 3: Porosity vs Depth Applied to “CASE-1”

In this example application, the same filters applied to the database in Case 1 are considered, to obtain a porosity-depth relationship constrained to different compaction regimes and defined by a trend line (**Figure 6.9A**). Significant data gaps in the 0-1,000 m and 1,600-3,250 m depth ranges exist, which causes uncertainty in the regression.

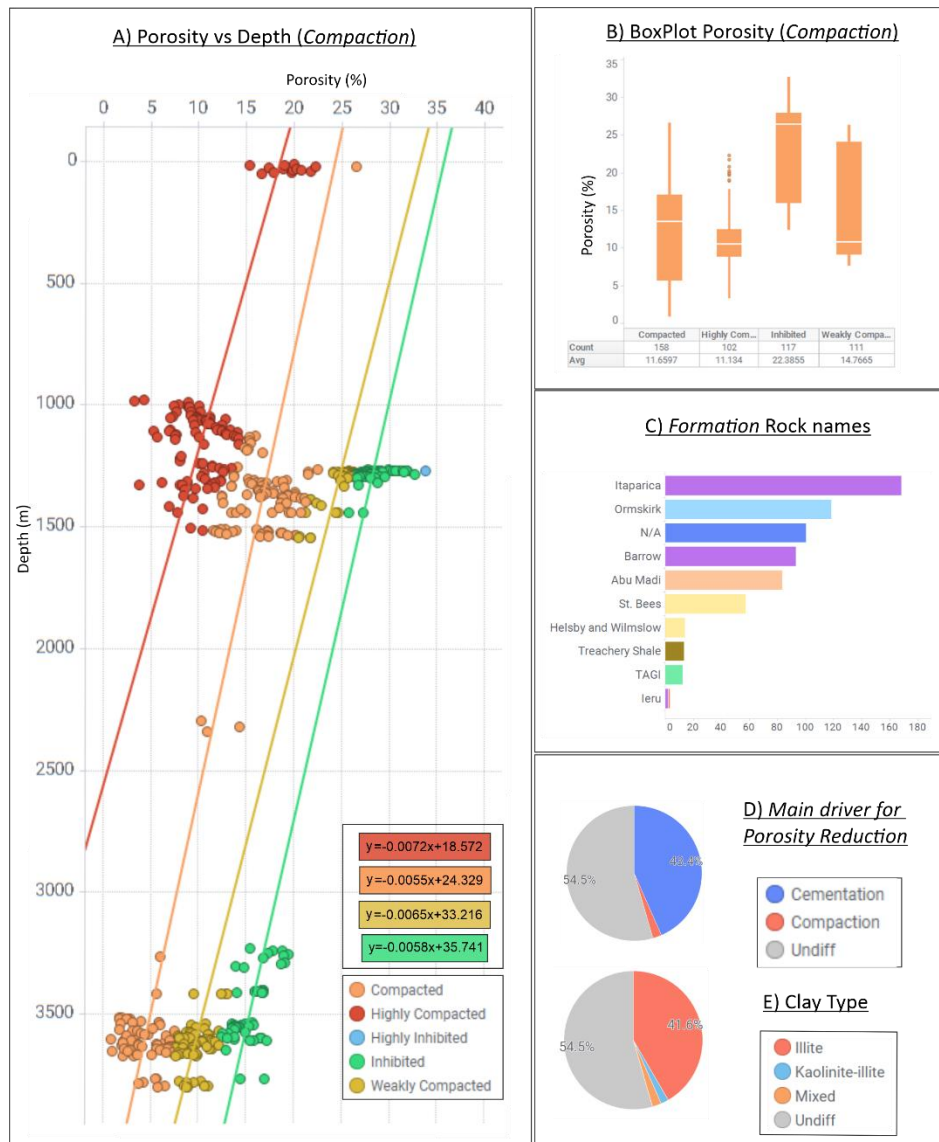


Figure 6.9 Depth-Porosity trends

PAFD (Petrophysical Analogue Fluvial Database) outputs obtained applying the same filters as in Case 1. (A) Depth-porosity cross-plots for variable mechanical compaction. (B) Boxplots for porosity distributions related to degrees of mechanical compaction. (C) Quantification of the amount of data by rock formation. (D) and (E) Pie-charts referring to main driver for porosity reduction and main diagenetic clay type, respectively. N=489.

By contrast, data are abundant in the 1,000-1,500 m and 3,250-3,750 m depth ranges. **Figure 6.10B** displays a boxplot where porosity distributions are classified for each of the compaction regimes. The chart in **Figure 6.10C** reports the different rock formations from which data are extracted to obtain the porosity-depth trends; it is seen that the Itaparica Fm is the succession associated with the largest amount of data. **Figure 6.10D** shows pie-charts indicating the main driver for porosity reduction, showing that cementation is the most important factor (43.4%), whereas physical compaction only dominates in 2.1% of cases. **Figure 6.10E** indicates proportions of the main diagenetic clay type, showing that illite is the main type of clay.

6.2.2.4 CASE 4: Porosity and Permeability Trends (Transforms)

Transforms from the exhibited porosity and permeability trends can be calculated by regression. These can be later utilized in larger workflows (e.g., secondary data to constraint property modelling). The higher the R^2 the better the relationship between porosity and permeability. In the cases where the relationship can be considered strong enough, theoretical and empirical models can be applied (Wyllie and Rose, 1950; Kozeny, 1927; Carman, 1937).

However, porosity-permeability relationship often exhibits a very low R^2 . For instance, different porous media may be characterised by similar ranges of porosity but different permeability distributions. This is due to the multiple factors that interplay to control the permeability distribution of geological media (e.g., grain size, sorting packing, compaction, dissolution) (Serra, 2008; Tiab et al., 2015). In these cases, petrophysicists will try to determine pore-throat dependencies in capillary pressure analysis (porous plate or mercury injection analysis), since this is a better indicator of porosity-permeability dependencies (Tiab et al., 2015; Cannon, 2015).

PAFD, with 3,809 values pairing both porosity and permeability properties, can be interrogated to find trends that relate porosity and permeabilities. Analogue porosity-permeability data related with multiple formation rocks can be evaluated cross plotted to various fluvial characteristics (**Figure 6.10**).

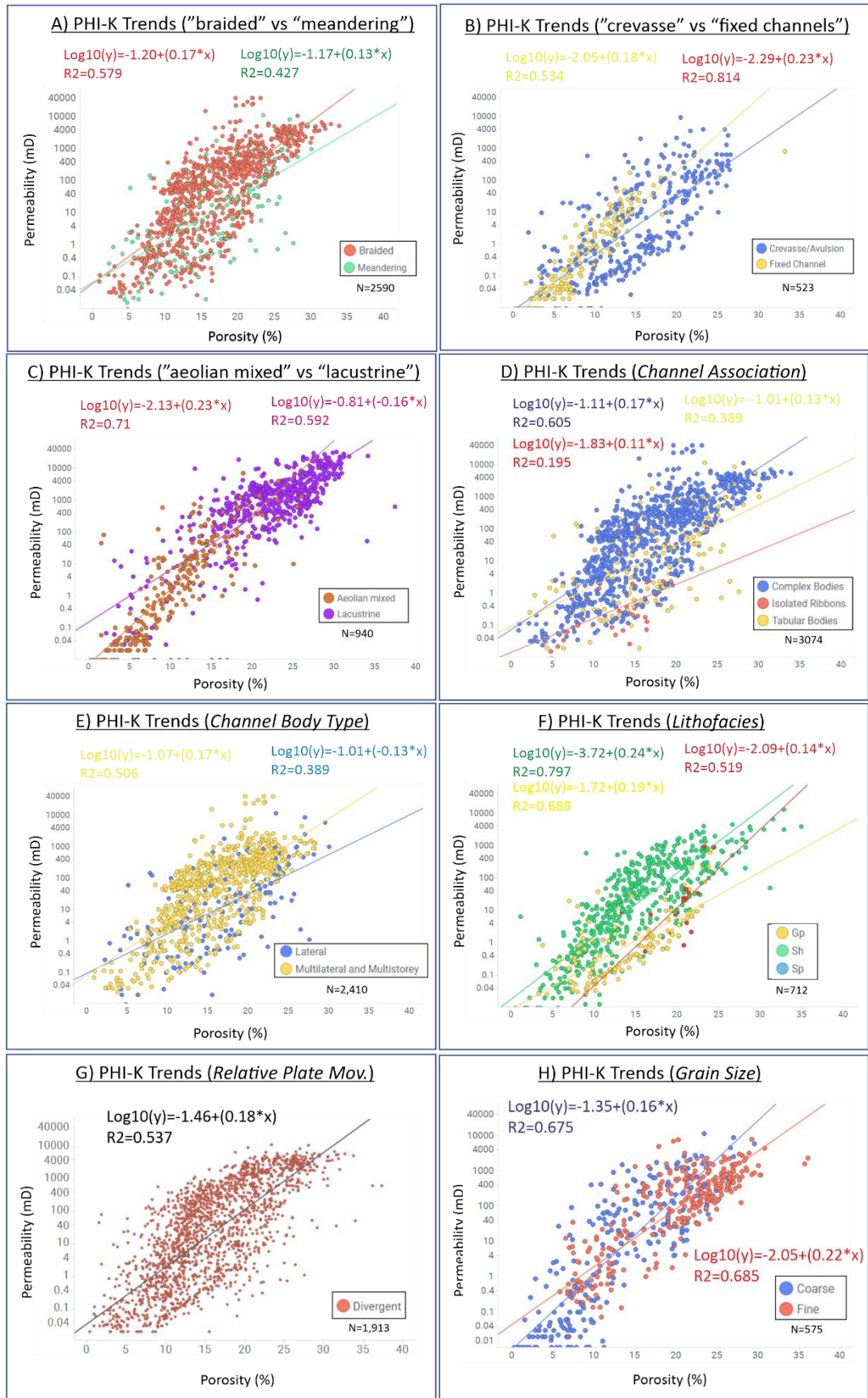


Figure 6.10 Porosity-Permeability trends

Porosity and permeability cross-plots for different categories of analogues considered in the database.

6.2.2.5 CASE 5: Porosity-Permeability Trends (Applied to “CASE-1”)

For Case-5 same filters as used for Case-1 and Case-3 are applied to determine porosity and permeability trends with respect to different categories in PAFD. **Figure 6.11** shows different cross-plots where multiple trend-lines are calculated with respect their R^2 value. It is Important to note the presence of low R^2 values. Below 0.30 the relationship can be considered non-compliant with standard petrophysical workflows (Serra, 2008). However, it can generally be observed that a strong porosity-permeability trend can be differentiated for “channel complexes” whereas “overbank deposits” show a more dispersed distribution (**Figure 6.11A**). Lithofacies related with both “channel complexes” and “overbank deposits” can be identified in **Figure 6.11B** where only the corresponding points for “Gp” and “Sp” are visible (“undiff” category hidden). **Figure 6.11C** stands for various Grain Size categories where also the “undiff” categories are hidden and less data points are displayed. Finally, **Figure 6.11D** shows the trends corresponding to the three most important Formation Rock names so that relationships corresponding with a specific analogue (case study) in the database can be understood.

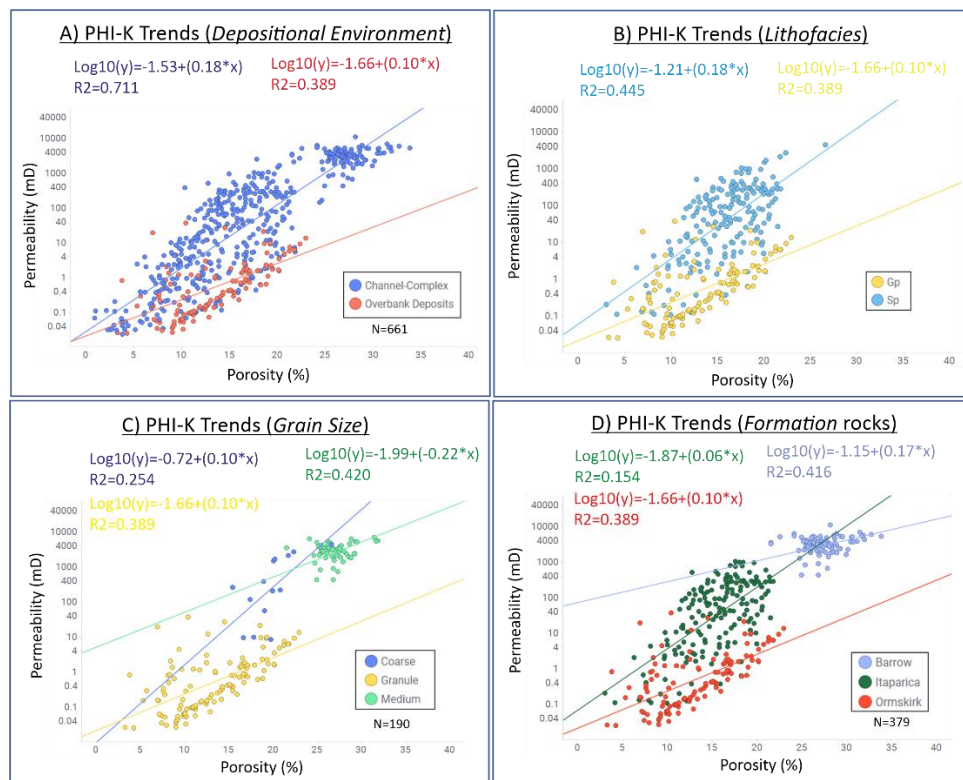


Figure 6.11 Porosity-Permeability trends (Case-1)

Porosity and permeability trends for various fluvial characteristics. Comparison between some selected trends is indicated.

6.2.2.6 CASE 6: Thresholds (Cut-off) Selection

Cut-off values must be selected prior to the definition of net and pay criteria so reservoir and non-reservoir intervals can be discriminated in well-log evaluations. Cut-offs will have a significant impact on the economical assessment of a project as it determines the in-place reserves of a given reservoir. Different techniques can be applied for the characterisation of cut-offs. Sensitivity analysis that uses statistical procedures can be applied (Serra, 2008; Glover, 2022; Crains, 2023). Yet, cross-plots are routinely used by petrophysicists to deterministically justify cut-off values cross-plotting different properties (e.g., porosity-permeability or volume of clay- porosity) (Worthington, 2005; Serra, 2008).

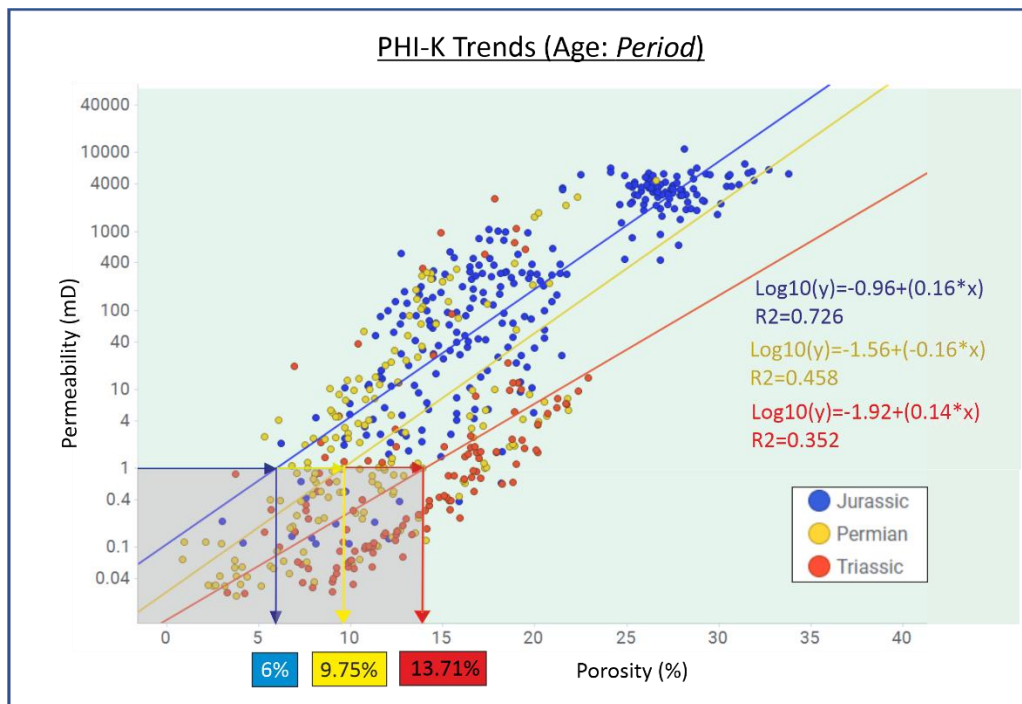
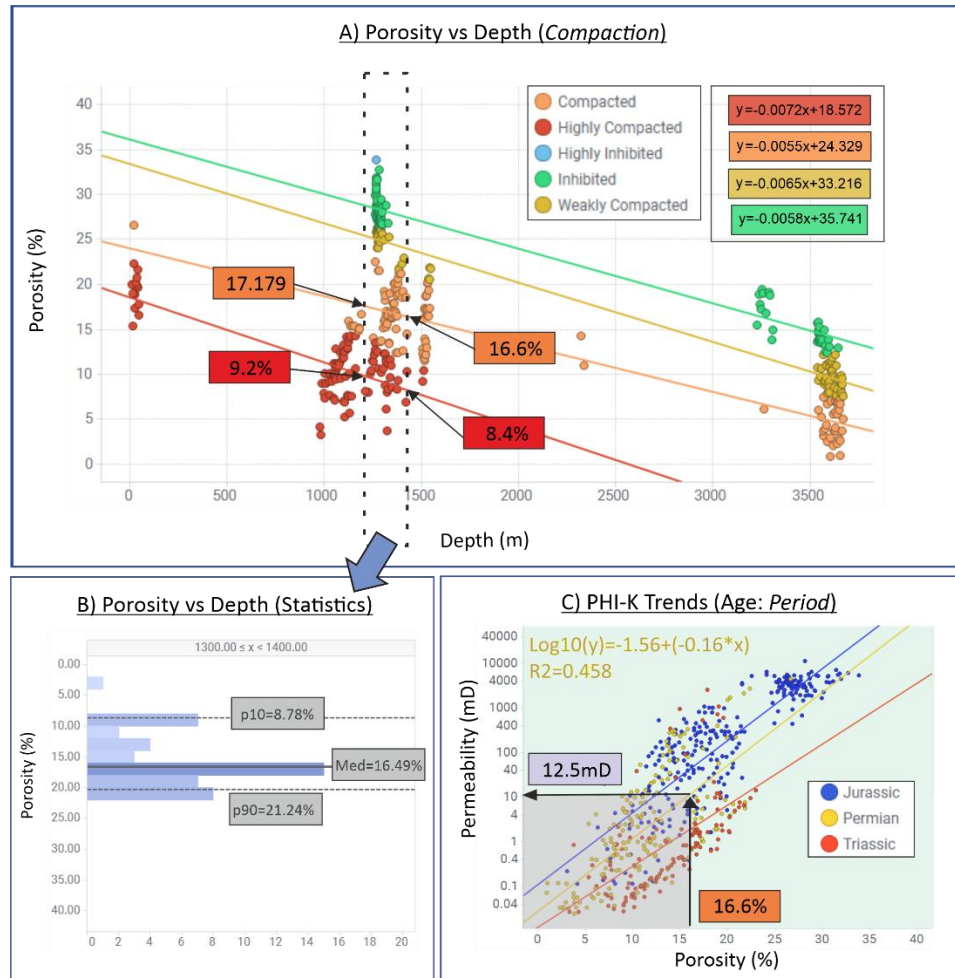


Figure 6.12 Porosity-Permeability trends (Porosity cut-off identification)

Porosity cut-offs represented graphically using 1mD permeability for the Jurassic, Permian and Triassic trend lines. Green shade represents the net area and the grey one the “non-reservoir” area. N=489

Core data coming from RCA (Routine Core Analysis) and SCAL (Special Core Analysis) are preferable for this purpose, as they are more reliable type of data. However, when core data are not available, analogue information can alternatively be used to justify the cut-off selection. **Figure 6.12** shows porosity-permeability trends related with different geological periods (Permian, Triassic and Jurassic) for a combined groups of different reservoir

rocks that apply to the Case-1 query. A permeability cut-off of 1 mD is being considered as an example of minimum value for commercial-scale fluid-flow into the borehole. PLT (production logging tools) tests can be used to calculate permeability cut-offs accurately, but the database currently does not include this type of data. Therefore, three different porosity cut-offs are determined which correspond with 6%, 9.75% and 13.71 for the Jurassic, Permian and Jurassic respectively.



(6) Figure 6.13 Porosity-Permeability trends (Permeability cut-o(A) calculated porosity values for the depth ranges (1200-1400 m). (B) porosity statistical evaluation for the depth range 1200-1400 m. (C) porosity-permeability trend used for the determination of a permeability cut-off based on 16.6% porosity and related to the Permian trend-line. N=489

By contrast, if no minimum permeability values for flow can be identified with commercial-flow parameters, PAFD also can deliver permeability cut-off values. A workflow that can be applied for the calculation of permeability will

include two steps: i) determination of porosity values using depth-porosity relationships (cf. Cases 2 and 3) and ii) using porosity-permeability trends to obtain permeability values (cf. Cases 4 and 5). **Figure 6.13** considers the previously described dataset obtained by filtering the database as in Case 1, presenting it in a depth-porosity plot. Depth-porosity trend-lines related to depth ranges of 1,300-1,400 m are calculated, and, as an example, trend-lines are selected for porosity calculations for the “highly compacted” and “compacted” classes (**Figure 6.13A**). As an alternative, the dataset is analysed to obtain the median, p10 and p90 values, which correspond with 8.78%, 16.49% and 21.24% porosity respectively (see **Figure 6.13B**).

Any of these two approaches to select porosity values that will be carried forward to the next step can be chosen, involving determination of the porosity-permeability trend. For this particular case, the 16.6% porosity associated with the compacted trend-line (minimum porosity) is selected as a cut-off in **Figure 6.13C**. The Permian trend-line yields a permeability cut-off of 12.5mD (green area: net; grey area: non-reservoir).

6.3 Meandering Fluvial Systems and CCS Suitability

In terms of CCS projects, the suitability of highly heterogeneous successions, such as those produced by meandering fluvial systems is debated. They are often compared and challenged against more homogeneous types of lithological successions (e.g., successions representing the deposits of low-sinuosity, multi-threaded braided rivers) ([Issautier et al., 2014](#); [Sun et al., 2022](#); [2023](#)). This study attempts to elucidate the potential of the preserved successions of meandering fluvial systems for CCS projects (Objective 8).

Fluvial meandering successions can be characterised by types of sedimentary units that exhibit high values of porosity, permeability, thickness, and areal extent, which have been proven to collectively ensure storage capacity (e.g., Sweetwater field (Wyoming, USA) and Little Creek field (Louisiana, USA), [Werren et al., 1990](#); Tarwhine field (Victoria, Australia), [WAPIMS](#)). Storage capacity in meandering systems is mainly restricted to the occurrence of relatively sand-prone point-bar deposits which are variable in size ([Posamentier and Allen, 1997](#); [Miall, 1996](#); [2016](#); [Colombera, 2017](#)). Furthermore, as a rule of thumb, it is understood that the bigger the river was,

the larger the point-bar sandbodies were deposited (Carter, 2003; Colombera, 2017). To understand the potential of this type of reservoir rocks and as example, each of the individual targets in the depleted Widuri Field in the Java Sea where Pertamina and Exxon Mobile are currently undertaking CCS studies, included point-bar elements of 1,220-1,500m diameter. Corresponding total oil production in only one well targeting this type of rocks approximated 3.2 MMbbls. In contrast, sand-prone point-bar elements targeted in the Jonah Gas field in Wyoming (US) are estimated to have individual point-bar element dimensions between 60 to 210m wide (Shanley, 2004). **Table 6.2** displays a comparison between thickness and width in meandering rivers against other fluvial environments (Gibling, 2006). It is shown how meandering systems can form sufficiently large and extensive reservoir systems, but its high dimensional variability is also highlighted. However, the measurements included in the table correspond to modern analogues and not their preserved deposits that are commonly remnants of what might once have been larger bars, else in some cases can be components of several bars that are amalgamated.

Reservoir System	Thickness	Width
<i>Meandering Rivers</i>	<i>Common range: 4-20m</i>	<i>Common range: 0.3-3 km; most < 3 km</i>
Low Sinuosity Rivers	Common range: 5-60m; most < 60m	Common range 0.5-10 km; many > 1 km
Fluvial Deltaic (Distributive Channels)	Common range: 3-20m; most < 20m	Common range: 10-300 m most < 500 m

Table 6.2 Thickness and width comparison

Table comparing thickness and width for modern meandering rivers against low sinuosity and fluvial deltaic systems. Modified from Gibling (2006).

However, to ensure reservoir volumes that make these successions economically viable (<\$20/tonne of CO₂ sequestered), connectivity between many point-bars sandbodies need to take place to combine larger sandy pathways enabling static connectivity of porous volumes (Willis 1989; 2019). Unfortunately, the presence of mud plugs (channel-fill deposits) and the intercalation of other non-permeable and non-porous material like floodplain deposits within sand-prone rock types decreases the potential storage volume

in meandering fluvial systems. Furthermore, vertical and horizontal heterogeneities mainly represented by the chaotically occurrence of these fine sediments within the sandbodies will significantly worsen the reservoir properties in comparison with more homogeneous reservoir successions (Tyler and Finley, 1991; Miall, 1996; Corbett et al., 2012). **Table 6.3** includes a list of reservoir systems separated in based to the lateral and vertical level of heterogeneities where meandering fluvial systems take place among the domain of higher heterogeneities.

		LATERAL HETEROGENEITY		
		LOW	MODERATE	HIGH
VERTICAL HETEROGENEITY	LOW	-Wave-dominated Delta -Barrier Core -Barrier Shoreface -Sand-rich Shoreface	-Delta-Front Mouth Bar -Proximal Delta Front -Tidal Deposits -Mud-rich Strand Plain	-Back Barrier -Fluvial -Delta
	MODERATE	-Aeolian -Wave-modified Delta (Distal)	-Shelf Bars -Alluvial Fans -Fan-Delta -Lacustrine Delta -Distal delta Front -Wave-modified Delta (proximal)	-Braided System -Tide-dominated -delta
	HIGH	-Basin-floor Turbidites	-Braid Delta	-Meandering Systems -Fluvially-dominated Delta -Submarine Fans

Table 6.3 Classification for reservoir heterogeneities (clastic reservoirs)

A classification for vertical and lateral heterogeneities corresponding to the main clastic reservoir is displayed. Meander belt systems taking place within the higher level of heterogeneities for both horizontal and vertical (Hamilton et al., 1998; Barton et al., 2004).

Although successions of meandering fluvial systems may be limited in terms of storage capacity and may be affected by issues related with injection rates, compared to more homogeneous successions, they may be better suited in terms of safety and efficiency of CO₂ storage. Once sufficient volumetrics to store CO₂ is ensured, the risk of leakage is evaluated. To do so, the impermeable layer of rock (known as a caprock) is analysed in based to its capability to hold a CO₂ column in the subsurface as well as other type of trapping mechanisms. Whilst a CO₂ plume in a homogeneous environment

will tend to migrate vertically towards shallower depths exerting significant amount of pressure on the uppermost only caprock, the heterogeneities contained in fluvial meandering successions may act to dissipate pressures horizontally (**Figure 5.22**, Chapter 5: Objective 7). This is due to the large amount of low permeable fine sediments that act as intraformational seals, which can alleviate pressures sustained by the main caprock. Additionally, the trapping mechanism caused by capillary differences between the rock types also contributes to extend the CO₂ plume horizontally redistributing the pressure exerted over the main caprock (**Figure 5.23**, Chapter 5: Objective 7).

High reservoir heterogeneities in a reservoir makes predictions or interpretations of injected fluids in the reservoir harder to estimate and most importantly in the case of meandering systems leads to a decrease in injection rates (**Figure 5.27**, Chapter 5). In fact, it might be significant, as operators might decide to increase bottom hole pressures to maintain injection rates, potentially leading to wellbore integrity issues ([Rutqvist et al., 2010](#)). Careful and detailed monitoring of injection rates in successions of meandering fluvial systems might be required, so that operators can identify where volumes are allocated with respect to each of the stages/clusters in the wellbore. Currently application of Distributed Acoustic Sensing technology (DAS) is being applied to monitor CO₂ injection in rocks ([Sadigov et al., 2017](#)).

Dissolution, residual, capillary, mineralisation and structural/stratigraphical are the most important trapping mechanisms of CO₂ that control the CO₂ plume behaviour ([Bachu et al., 2007](#); [Shukla et al., 2010](#)). However, this study mainly focuses on analysis regarding structural/stratigraphical, dissolution and capillary processes. These are the main trapping mechanisms acknowledged during early decades of injection (30 years in agreement with the average life of a coal power station) ([Moodie et al., 2016](#)). In the case of mineralisation, reactive transport simulations were not performed. Further dissolution processes are also considered beyond the scope of this investigation, since they usually start thousands of years after injection ([Zhang et al., 2013](#)). However, the tortuous pathways followed by the CO₂ plume around channel-fill and floodplain deposits acting as barriers to the flow will presumably increase the chance of dissolution and chemical reactions within the reservoir contributing to the trapping of CO₂.

Objectives 7 and 8 of this Thesis aimed to determine whether fluvial successions deposited by meandering rivers can be suitable candidates for CCS project. This study demonstrates the efficiency and effectiveness of heterogeneous successions at storing anthropogenic CO₂. If storage capacity cut-offs do not set the economic viability of a CCS project, fluvial meandering successions can be suitable candidates, and arguably preferable over more homogenous types of reservoirs. However, operators should be aware that decision making should be supported by a sound reservoir model that accounts for different forms of heterogeneities. The inclusion of macroscale heterogeneities only (cf. 3-facies models) may not result in realistic dynamic predictions. This study proves the dependency of CO₂ behaviour in the subsurface on mesoscale heterogeneities and recommends their inclusion in reservoir models (cf. 5-facies models).

7. Conclusions

7.1 Overview

This research has introduced, explained, and discussed a series of novel techniques and methodologies that may be applied to construct reservoir models that are able to predict and characterise the anatomy of subsurface sedimentary reservoir architectures in greater detail than has hitherto been typically possible. In accomplishing this, the emphasis has been to ensure realistic facies representation within sedimentary successions that develop as the preserved products of the evolution of meandering fluvial systems. The investigation focuses on the importance of devising realistic facies models that accurately provide an appropriate geological framework on which dynamic CO₂ flow simulations are performed. Lithological and architectural heterogeneity was effectively characterised in the constructed facies models. The following aspects played a fundamental role in ensuring geological realism in the developed reservoir models: i) the capabilities of the chosen modelling tools (e.g., modelling methods based on MPS – Multi-Point Statistics); ii) the quality of the input data (hard and soft data derived from a bespoke and purpose-designed and developed petrophysical database – PAFD, Petrophysical Analogue Fluvial Database); and iii) decision-making in the steps undertaken throughout this research (e.g., choice of injector-well placement in CO₂ dynamic simulations).

The conclusions of this study are presented below in three subsections addressing the research questions presented in the Introduction chapter of this Thesis. These correspond to the respective outcomes of Chapter 3 (facies modelling workflow), Chapter 4 (petrophysical database) and Chapter 5 (property and CO₂ dynamic models). **Figure 7.1** graphically summarises this research.

7.2 Facies Modelling Workflow

Meandering fluvial systems generate accumulated sedimentary successions that are highly heterogeneous with respect to lithology type (Allen, 1963; Miall, 1985; 2016; Dreyer et al., 2009; Bridge, 2003; Gibling, 2006). As such, simulating the complex internal sedimentary architecture of the accumulated and preserved deposits of this class of sedimentary environment and

expressing it in 3D geocellular models is challenging. The hierarchical workflow devised, developed and applied in this research has enabled the delivery of a novel modelling approach that can be applied to model reservoir successions characterised by meander-belt sedimentary successions. When dealing with meandering fluvial systems, the accurate representation of the geometries of the different model elements is a primary objective. Multi-point Statistics (MPS) approaches were chosen as the stochastic methods to be used to simulate 3D models in this research mainly because of their ability to appropriately reproduce complex curvilinear geometries. The widely applied SNESIM (Strebelle, 2000) and the more novel DEESSE algorithms (Straubhaar et al., 2020) were selected to perform the tasks for this first part of the Thesis (Chapter 3).

7.2.1 Training-Image Library Development (Objective 1)

“The development of a library of training-images – from which MPS modelling algorithms can borrow geological patterns for modelling meandering fluvial systems – based on forward stratigraphic modelling software.”

Multipoint Statistics geocellular modelling algorithms require digital reservoir representations called training images as principal inputs (Guardiano and Srivastava, 1993). A comprehensive training-image library has been developed as part of this research to address Objective 1. This library includes different samples depicting different types of meander evolution (expansion, translation, rotation and combinations thereof). The training-image library provides ready-to-use training images to be applied to MPS simulations. In this study, training images have been created using a combination of related methods and techniques. These include the following: i) 3D training images quantitatively informed by the Fluvial Architecture Knowledge Transfer System (FAKTS), a relational database that incorporates sedimentological data from modern and ancient analogue fluvial successions (Colombera et al., 2012a; 2012b; 2013; 2017). ii) PB-SAND (Point-Bar Sedimentary Architecture Numerical Deduction), a forward stratigraphic model devised to reconstruct and predict the complex spatial-temporal evolution of a variety of meandering river behaviours (Yan et al., 2017; 2020a; 2021). This numerical modelling software has been used to construct realistic training images in a time-efficient manner; in total, 24 specific types of sedimentary architecture arising from various classes of fluvial meandering system have been constructed. These

examples have been included in the training-image library. The process employed in the construction of training images is semi-automatic. Importantly, the developed workflow largely eliminates human biases that are commonly incorporated within training images.

7.2.2 Application of Training Images to SNESIM and DEESSE Codes (Objective 2)

“The application of the training images to two widely employed MPS modelling algorithms: SNESIM and DEESSE.”

The devised novel workflow has addressed the most important factors to be considered and incorporated in facies models for successions of meandering fluvial systems, and that are commonly misrepresented or difficult to reproduce in MPS models. These are as follows: i) highly sinuous channelised features; ii) specific sedimentary architectures known to be associated with each of the model architectural elements; iii) the implementation and representation of appropriate types of heterogeneity; and iv) representation of the overall net-to-gross ratio to be included for representation of overall sand and shale volumes. To ensure that these attributes are appropriately incorporated, modelling recipes coupling training images with SNESIM and DEESSE simulation parameters are employed. Moreover, the use of auxiliary variables that describe facies probabilities associated with different grid regions (probability grids) has allowed the incorporation and modelling of trends and provides a means to control the spatial distribution of variables such as net-to-gross-ratios. Target runtime was monitored to ensure that simulations could be delivered within a reasonable timeframe (<10min runtime for the 5-facies model).

To appropriately use MPS algorithms, a statistically valid training image is required as input. This includes a requirement of stationarity (a spatial process in which all statistical properties of an attribute depend only on the relative locations of attribute values) so that a template pattern can be derived from the training images (Deutsch and Journel, 1998; Caers and Zhang 2004). However, many geological features are, by their nature, non-stationary. The degree to which some levels of non-stationarity can be handled by MPS methods has been investigated. Results reveal that certain types of non-stationarity, such as the fining-upward grain-size trend that is typical in point-

bar elements, or the growth of expansional point bars included within the training images, can successfully be reproduced in simulations under specific circumstances (e.g., parameters associated with a specific MPS method in combination with auxiliary variable maps) (Montero et al., 2021).

7.2.3 Modelling Heterogeneity in Meandering Fluvial Systems (Objective 3)

“The creation of fluvial meandering reservoir models that consider scenarios encompassing macroscale and mesoscale levels of sedimentary heterogeneity.”

The sedimentary architectures and associated horizontal and vertical distributions of lithological types are incorporated within and represented by different facies models. Four different scales of lithological heterogeneity are commonly identified and modelled for meandering fluvial systems: megascale, macroscale, mesoscale and microscale (Tyler and Finley, 1991). Of these, this research has focused in detail on the macroscale and mesoscale levels of heterogeneity. These are represented by the 3-facies model (macroscale) and the 4-facies and 5-facies models (mesoscale) in Chapter 3 and in Montero et al., (2001).

The 3-facies models simulate the main characteristics identifiable in the successions of meandering rivers at the scale of well spacing (>1km to several km in lateral extent). These are relatively more porous sandy point-bar elements and relatively less-porous and permeable channel-fill and floodplain elements. This is likely the most important scale to quantify in facies models in many cases but is also the most challenging because inter-well heterogeneities are commonly present at scales that are too fine to be observable in seismic reflection datasets and too large to be appropriately described by well data (e.g., wireline logs, core data). The 4- and 5-facies models incorporate the mesoscale level of heterogeneity resolution into the models. Lithological heterogeneities included at this level correspond to lithological types, stratification types and bedding contacts of different types. Although this level of heterogeneity can be reasonably accurately recognised in subsurface reservoir successions in the vertical direction using cores or well logs, it is commonly disregarded by geomodellers who tend to group similar types of facies (e.g., different types of sand and silt deposits that occur

vertically arranged within point-bar elements). However, this study demonstrates how heterogeneities present in fluvial facies successions at the mesoscale may significantly impact flow properties. Therefore, property models and dynamic simulations need to account for such heterogeneities.

Realisations were evaluated qualitatively against the training images. In this study, for the 3-, 4- and 5-facies models, observable patterns can be summarised as follows.

- Plan-view sections show complex morphologies displaying a labyrinth-like appearance mainly created by the channel-fill deposits. Sandy point-bar bodies are distributed horizontally juxtaposed to each other and are realistically populated displaying typically crescentic shapes. Point-bar orientations relative to the axis of a channel belt (e.g., specular, and asymmetrical) honour geometries and features included in the 3D training images. This level of realism is achieved in all types of created facies models (3-, 4- and 5-facies).
- The presence and expected distribution of compartments within the channel-belt area can be clearly observed in vertical sections. These are vertically stacked and amalgamated point-bar facies sometimes separated by channel-fill and sheet-like floodplain deposits that limit sand connectivity in vertical sections. This particular distribution in combination with horizontally juxtaposed sand bodies may lead to the creation of isolated compartments that will impact overall reservoir connectivity.
- Continuous, curvilinear, narrow, and channelised geometries are associated with channel-fill deposits (mud plugs). These are low-porosity, low-permeability facies that can act as lateral and vertical barriers to the flow. The length and continuity of this type of facies is different for each type of facies model. They appear to be longer and displaying bigger loops for the 3-facies models than for the 4-facies and 5-facies models where their loop dimensions are smaller.
- Floodplain or overbank deposits display sheet-like continuous forms. They appear as vertical barriers to the flow and contribute to vertical compartmentalisation of sandy point-bar deposits.
- The 4-facies models incorporated thick accumulations of mud drapes in the point-bar compartments, which represent another type of baffles

to flow and are important to take into consideration when modelling meandering fluvial systems.

- The 5-facies models incorporate different types of sand deposits within point-bar deposits in vertical sections. These are the point-bar base, mid-point bar and point-bar top facies leading to a vertical fining-upward trend characteristic of meandering fluvial systems. Their inclusion increases the level of geological realism of the models. The point-bar deposits are horizontally limited by clay plug deposits (channel fills) and sometimes vertically by the occurrence of overbank deposits. This results in the partial enclosure of the sandy point-bar facies by low-permeability rocks.
- In horizontal sections, the 5-facies models display patchy features associated with different point-bar sections. Although chaotically distributed patches of point-bar deposits may be expected in successions of this type, these patterns were not originally present in the training images. Attempts were made to control the horizontal distribution of different point-bar regions using probability grids.
- Morphologies characteristic of expanding meander bends are observed in point-bar deposits of the 5-facies models. These are convex-bank accretion packages, which can be clearly distinguished in horizontal slices. However, translational features associated with counter-point bar fines related to bars associated with downstream translating meanders, present in the training images, were not replicated in the models.
- Variations in facies proportions and net-to-gross ratio in specific grid regions were mainly controlled using probability maps. They proved to be effective at controlling MPS facies models. However, auxiliary variable maps override the original target proportions of the training image.

In terms of qualitatively defined geological realism, this study does not find major differences between the SNESIM and DEESSE algorithms. The performance of both mainly depends on the combination of input parameters, type of architecture being modelled, and number and types of facies considered. A calibration process is always required to assign the most

appropriated parameters involved in the scanning-simulation process for both SNESIM and DEESSE.

7.2.4 Strengths, Weaknesses and Opportunities

The devised workflow can be used in real-world scenarios where facies models for meandering fluvial systems are required. The created workflow addresses the principal issues faced by geomodellers using MPS methods. These are the creation of a suitable training images and the parametrisation process. Results from this study show how training images can be informed quantitatively but also delivered through a geometric forward stratigraphic modelling software that enables the simulation of internal sedimentary architectures. This process ensures a degree of objectivity in the creation of training images. With respect to the model parameterisation, this study identifies certain parameters that work best when employing MPS methods using training images for successions of meandering rivers; however, additional bespoke trial-and-error tuning is usually required. Similarly, the reutilisation of specific training images for different case-studies, may require re-adaptation to ensure applicability to other contexts. This is to be expected given the highly heterogeneous nature of the successions being modelled, for which considerable architectural variability is usual. As a result, generalised models may not be always applicable.

The workflow has also potential to be adapted to situations where seismic data are available. Probability maps based on seismic properties can be extracted and used as soft data for model conditioning. Furthermore, the application of deterministic well data can be utilised to constrain the MPS methods and ensure improved realism in their outputs.

7.3. PAFD, Petrophysical Analogue Fluvial Database

A database that includes fluvial characteristics with petrophysical properties has been built. This is introduced and explained in Chapter 4. This was a necessary requirement that targets to inform specific model elements in facies models with specific petrophysical parameters (mainly porosity and permeability).

7.3.1 The Development of a Petrophysical Database (Objective 4)

“The development of a database that can be applied to describe fluvial characteristics in terms of quantitative petrophysical properties.”

PAFD (Petrophysical Analogue Fluvial Database) achieved its main purpose of providing petrophysical data (mainly porosity and permeability) from a large number of geological analogues, categorised with respect to fluvial facies and metadata (location, lithostratigraphy, petrography, stratigraphic architecture, tectonic settings, etc.), among other attributes. Data included in PAFD allow differentiation of different scales and types of lithological heterogeneity (macro, meso and microscale).

Model elements contained in the facies models (Chapter 3) are populated with properties (porosity and permeability) derived from the developed database. To do so, PAFD was employed to examine relationships between characteristics of fluvial successions and analogue petrophysical data, selecting analogues relevant to meandering fluvial systems.

7.3.2 Petrophysical Database for Fluvial Successions (Objective 5)

“The utilisation of PAFD as a tool that delivers petrophysical analogue data linked to fluvial deposits for the development of realistic property models that can be later utilised to simulate CO₂ fluid-flow through each of the model elements.”

Among different options, the Latrobe Group, located in the Gippsland Basin (Australia) is identified as an appropriate rock analogue for this study. Depth-porosity-permeability transforms are determined from a data analytics process in which different types of cross-plots, histograms, pie charts and boxplots are utilised. Furthermore, calculated transforms are included as auxiliary data to constraint porosity and permeability geostatistical simulations to complete the static geological model.

7.3.3 Strengths, Weaknesses and Opportunities of the Database

The developed database PAFD contains a total of 4,262 entries, coming from public domain sources (e.g., peer-reviewed publications, government databases). It includes both well and outcrop data. This data volume was considered sufficient for the scopes of this Thesis, but the database can be readily extended. PAFD is intended to support searches dedicated to “quick-look” or early exploration cases where quantitative data are scarce or absent.

Apart from its use in property modelling, different potential fields of application of PAFD include the following strengths (and opportunities).

- Conceptual modelling with respect to the classification of stratigraphic intervals, definition of classes of sedimentary units (proportions) and recognition of facies related with sedimentary processes.
- Determination of effective cut-offs or thresholds from which net reservoir criteria are defined (e.g., correct characterisation of a net thickness derived from porosity and permeability).
- Porosity and permeability predictions associated with particular sets of fluvial characteristics.

For these three points, some examples relevant for early stages of exploration and during reservoir appraisal are included in Chapter 6.

Among the weaknesses associated with the petrophysical database, the following limitations are noted.

- The database is a collection of spreadsheets. Although the PAFD structure has been proven efficient for the applications illustrated in Chapters 4, 5 and 6, inherent issues exist that are related to scalability, querying, data connectivity and data-volume constraints. Further work could be undertaken to migrate the current content to a relational database format, for which rules of normalisation apply.
- Public-domain data reliability. The majority of the data included in the database belongs to public-domain peer-reviewed datasets. Although

reported petrophysical data are generally reliable, these may have been wrongly extracted or affected by subjectivity in interpretation. Furthermore, uncertainties or errors in the original data sources may have occurred. A recommendation for data content growth in PAFD will be to include only core-plug data that were previously analysed and filtered from laboratory raw sources. This type of data is more reliable and is subject to reduced uncertainties compared to other sources (e.g., scanned cross-plots).

- Amount of available data remaining following the application of several filters. The number of observations returned after application of several filters may not be sufficiently large for the application at hand. This can be solved by the addition of more content to the database.

7.4 Property and Dynamic Models of CO₂ Injection

The creation of dynamic models for the analysis of injected supercritical CO₂ fluid-flow within a highly heterogeneous succession produced by a fluvial meandering system is undertaken in Chapter 5.

7.4.1 CO₂ Property and CO₂ Dynamic Model building (Objective 6)

“The creation of dynamic models for the analysis of injected supercritical CO₂ fluid-flow within a highly heterogeneous succession produced by a fluvial meandering system.”

Macroscale (3-facies models) and mesoscale (5-facies models) levels of heterogeneities of the successions of meandering fluvial systems are populated with porosity and permeability data in facies models obtained using SNESIM and DEESSE. The GRFS (Sequential Gaussian Random Function Simulations) is used where variograms are configured in based on the size of point-bar features observed within the previously built facies models in Chapter 3. Final outputs are used to feed dynamic models of the injection of CO₂ to evaluate the impact of different types of heterogeneities on fluid flow, injection rates and storage volumes (Objective 6). No further upscaling is attempted prior to dynamic modelling as the utilised grid configuration in facies and property models appropriately fit the targeted level of resolution (macro and mesoscale heterogeneities).

7.4.2 CO₂ Dynamic Model Assessment (Objective 7)

“An assessment of how variability in the geological realism of facies models impacts petrophysical properties (porosity and permeability) and ultimately influences the results of dynamic simulations of CO₂ injection. Determination of plume behaviour, injection rates and storage behaviour for scenarios considering macroscale mesoscale heterogeneities.”

The results of this investigation have highlighted how dynamic CO₂ simulations are influenced by the underlying facies framework. Geological realism in terms of an accurate facies model proved to be fundamental in controlling CO₂ plume displacement through the rocks, injection rates and cumulative injected volumes. The following characteristics were observed in the dynamic simulations:

- Compartments associated with sandy point-bars encased by mud-prone rocks (channel-fill deposits) were found in the simulations. Although completely isolated compartments may hinder CO₂ storage, pressure models indicate effective connectivity between amalgamated sand volumes. It is recognised that low-porosity and low-permeability muddy layers do not fully compartmentalise sandy volumes in 3D. The degree of compartmentalisation is largely controlled by the net-to-gross ratio assigned in the very early stages of facies modelling.
- The geometry and occurrence of channel-fill deposits control the tortuosity exhibited by the CO₂ plume. It is determined that meander loops created by channel-fill deposits using MPS methods (SNESIM and DEESSE) and properly reproduced in facies models played a significant role in the dynamic simulations. This degree of geological realism cannot commonly be captured adequately by means of other stochastic methods (e.g., SIS).
- Simulations show that dynamic CO₂ storage efficiency and injection rates vary depending on the injection well location. This is due to the arrangement, position and the amount of mud-prone rocks (barriers to the flow) encountered by the CO₂ within the area of influence of the well. Both CO₂ storage efficiency and injection rates decrease with increasing presence of channel-fill and overbank deposits. Furthermore, the speed and shape of the CO₂ plume vary in space, as the CO₂ fluid-flow moves through different types of permeable rocks within the grid. Preferential pathways can be created that are oriented according to the occurrence of certain rock types, namely the point-bar

base and mid-point-bar deposits; point-bar top facies tend to hinder the flow instead.

- Capillary effects were recognised as the most important trapping mechanisms during the CO₂ dynamic simulations. It is therefore important to properly define model elements within a reservoir model by their hydraulic properties related to rock types. Although in certain circumstances there might be a similarity between lithologies and the rock typing criteria, a geomodeller should be aware of their differences. The separation of different types of sand deposits within point-bar elements in corresponding rock types (point-bar base, mid-point-bar and point-bar top) was proven satisfactory, as each of them showed a distinctive flow behaviour.
- Higher storage capacity was directly associated with higher injection rates. However, injection rates did not behave homogeneously for the simulated 30-year period. Injection rates evolve from total dependency on bottom-hole pressure at the beginning of the operation to, shortly after, becoming controlled by CO₂ brine dissolution effects in the reservoir. Then, a new and independent CO₂ phase appears that seems to be controlled by relative-permeability dependencies related to capillary effects. The duration of each of these stages is fundamentally controlled by the connectivity and presence of flow barriers near the area of influence of the well.

The evaluation and comparison of simulations based on the 3-facies and 5-facies models permits identification of the role played by different levels of heterogeneities. The injection of CO₂ behaves quite differently in a scenario where 5 facies are simulated compared to the simulation of 3 facies. The following points summarise those features that are only seen to emerge in dynamic simulations of the 5-facies models.

- CO₂ plume displacement. The behaviour of the CO₂ plume is highly influenced by the mesoscale (intra-point-bar) lithological heterogeneities, which are commonly overlooked in standard subsurface modelling workflows. The creation of two CO₂ gas fronts mainly controlled by the point-bar base and mid-point bar facies are observed. Special attention should be given to the lower-bar facies that behave as a thief-zone, facilitating the initiation and further propagation of preferential CO₂ pathways. On the contrary, point-bar top facies act as baffles that retard CO₂ flow. The shape (vertically and horizontally)

exhibited by the CO₂ plume is also conditioned by the encountered type of sands.

- Caprock pressure relief. The presence of the point-bar top facies acting as baffles to the flow lead to a significant readdressing of the CO₂ plume horizontally. This effects further mitigates the pressures exerted by the CO₂ column over the main caprock.
- Further horizontal distribution. The injected CO₂ is observed to travel larger horizontal distances in comparison with the 3-facies model. This is caused by the presence of preferential conduits oriented along the point-bar base and mid-point-bar facies volumes.
- Capillary trapping. Capillary trapping differences due to the presence of three different type of porous and permeable rock types within the sandy point-bar lead to different trapping differences highlighted by different CO₂ saturation ranges.
- Redistribution of pressures along the grid. Reservoir pressurisation effects were observed at the end of the third decade of continuous injection in the 5-facies model. No sign of reservoir pressurisation effects where observe in the 3-facies model in the same period of time.

This study highlights the need to consider mesoscale types of heterogeneities in reservoir models for meandering fluvial systems. The unconditional and experimental models carried out in this Thesis have demonstrated the need for an accurate facies model able to capture different levels of heterogeneities in meandering fluvial systems. In addition to the large-scale heterogeneities considered by many authors to be indispensable components to be included in facies models, this investigation demonstrates how mesoscale heterogeneities are also important such that they ought to be included in facies models. It is imperative to adequately characterise the facies organisation of point-bar deposits (point-bar base, mid-point-bar and point-bar top) to enable a more accurate and realistic representation of the CO₂ fluid flow in the subsurface.

7.4.3 Strengths, Weaknesses and Opportunities of CO₂ Modelling

Dynamic simulations of the fate of CO₂ injection into sedimentary reservoir volumes undertaken in this Thesis focused on the first 30 years of injection. The study demonstrates how the stratigraphic architecture and related capillary pressure effects control the behaviour of injected CO₂ in the subsurface. However, other effects, such as dissolution or mineralisation, also take place at the same time or in subsequent years; these are not considered by this study. Therefore, further studies on these processes and on simulation behaviours over timespans longer than 30 years are required.

The dynamic models highlight the importance of capillary pressure constraints in CO₂ fluid flow. These are controlled by the chosen relative permeabilities associated with each of the model elements. This study chose experimental values to differentiate rock types, modified based on theoretical quality criteria without considering any particular geological analogue. Hence, more research can take place in this domain in the future.

7.4.4 Suitability of Reservoir Successions for CCS and Other Applications (Objective 8)

“Evaluation of the effectiveness of meandering fluvial successions as potential storage reservoirs for the long-term, safe sequestration of anthropogenically generated CO₂, thereby reducing and mitigating the effects of anthropogenic CO₂ emissions to the atmosphere.”

In terms of their suitability as long-term and large-scale repositories for CCS, meandering fluvial reservoir successions should be considered as prime CO₂ reservoirs candidates: they offer clear advantages with regard to effectiveness and safety, in spite of their debated potential as CCS reservoirs (Sun et al., 2023). This investigation demonstrates that, compared to more homogeneous types of reservoirs, successions of meandering fluvial systems may be preferable in certain circumstances. Their pros and cons are summarised below.

- Successions of meandering fluvial systems can provide sufficient interconnected storage capacity to make a CCS project economically viable. This is especially the case where individual sandy point-bar

elements are connected with each other. Nonetheless, storability will be reduced by point-bar compartmentalisation. Furthermore, the high presence of mud-prone rocks (channel-fill and overbank deposits) may lead to significantly reduce net volumes.

- The development of channel-fill and floodplain deposits will lead to the development of intraformational seals of different sizes that vertically redistribute the pressure exerted over the main caprock by the CO₂ gas column. Chemical reactions between caprock and CO₂ that may induce leaks are also reduced. Horizontal pressure redistribution effects are also seen to take place in succession of this type. The point-bar top facies can baffle the flow displacing the injected CO₂ away and relieving the pressure exerted on the main caprock.
- The tortuosity of flow paths caused by the occurrence of mud-prone rocks will increase the plume surface area, thereby increasing the chance of CO₂ dissolution, ensuring storage of CO₂ within the reservoir rock. This is due to an increase of the exchange surface between the reservoir brine and the CO₂ plume.

Calculations regarding the exact storage capacities for different reservoir units are challenging. The amount of worldwide subsurface CO₂ storage capacity remains uncertain. To evaluate such uncertainties effectively, robust facies models that incorporate mesoscale-level heterogeneities are required to inform decision-making with respect to the suitability of potential CCS reservoir projects, especially in highly heterogeneous environments such as fluvial meandering reservoirs. Furthermore, a thorough assessment of caprock integrity is also required. Although CCS activities are required to reduce emissions from industrial actions, there are multiple economic hurdles and potential risks associated with these activities, which need to be thoroughly evaluated. For instance, the cost of equipment and materials needed to separate and transport CO₂ can be prohibitively high. Hence, subsidies need to be provided ([Global CCS institute, 2021](#)). An important incentive for the use of this technology is offered by the use of CO₂ to support enhance oil recovery (EOR). Operators may buy waste industrial CO₂ and inject it in the subsurface for these purposes. Another important factor is the public perception of large-scale CCS activities, which may be viewed negatively. Public awareness currently remains low and feel reluctant to support is lacking for carbon storage locations near their properties ([Shell Sustainability Report 2019](#)). Although risks relating to CO₂ transportation

accidents are relatively low, leaks from pipelines are possible. These may lead to threat to human life. Caprock leakage related issues are also a possibility, which may lead to soil and groundwater contamination. Seismicity associated with CO₂ injection has also been documented close to storage sites (IPCC, 2022).

7.5 Suggested Future Works

Some possible topics of future research arising from the findings of this thesis are summarized below.

- **Machine Learning Applications.** Additional further research in the application of machine learning for the creation of training images may lead to a full automation of the process. Special attention must be given to development of a required dedicated and specialised training dataset to be utilised via machine learning approaches. Such investigation should be oriented to the determination of key reservoir analogues that will facilitate the discovering and the learning of key patterns.
- **Non-Stationarity.** Methods and strategies to address current limitations in the reproduction of non-stationary geological architectures in the modelling of sedimentary successions produced by high-sinuosity channel systems should be investigated. The application of probability maps shown in this study was a suitable approach in certain situations (e.g., point-bar elements related to meander bends undergoing expansion). However, more refined and improved techniques can be devised in the future, potentially based on the combination of different auxiliary variables (e.g., probability, rotation, scaling).
- **Facies model validation.** In this study, evaluation of the performance of algorithms SNESIM and DEESSE was mostly performed as a qualitative visual inspection of their outputs (e.g., simulation of compartments created by channel-fill deposits). Future research might be directed to the utilization of conditioning data (e.g., well data) or the use of outcrop analogues for quantitative assessments of MPS realisations.
- **Implementation of the Petrophysical Analogue Fluvial Database (PAFD), as a relational database.** Analogue Fluvial Database (PAFD) as a relational database. Currently, PAFD is a spreadsheet with multiple data fields. Future work could be directed towards re-structuring this dataset as a relational database that honours principles of normalization (Codd, 1970). This new relational database format could be incorporated in the existing FAKTS database (Colombera et al., 2013), such that the large volume of quantitative petrophysical data could be tied to associated fluvial sedimentary units.

- **Simulator selection.** The underground storage of large volumes of CO₂ requires analysis of complex multiphase physical and chemical behaviours. Dynamic simulations performed in this Thesis utilized the Eclipse E300 simulator of Schlumberger Petrel®, whereby CO₂ conditions and properties were introduced manually. However, a new and dedicated version for CO₂ dynamic evaluations has been recently introduced in a recent version of Petrel®, CO2STORE. This new software simulator package offers improvements in various modelling aspects (e.g., modelling of dissolution and physical properties of hydrocarbon components in thermal simulations). The software tool accommodates a wide variety of modelling scenarios. Future research might focus upon running dynamic simulations using this latest package release.
- **Improved Characterization of Relative Permeability associated with rock typing.** This Thesis used default relative permeability curves associated with rock types considered for the dynamic simulations (e.g., lower point-bar, mid-point-bar and point-bar top). However, the effect of related capillary pressure in controlling CO₂ plume displacement in a subsurface succession suggests that more realistic experimental data are required to investigate this domain in more detail. Future research might incorporate real-case relative permeability curves tied to each of the principal rock types. An initial focus of research might be on relative permeabilities observed in geological analogues documented in the literature and associated with each of the rock types.
- **Application of hard data and soft data.** In this Thesis, facies modelling, property modelling and CO₂ dynamic simulations were performed unconditionally, i.e., no hard data or well data were employed. To constrain the realism of outputs relating to plume behaviour, injection rates and storage capacity, application of the workflows to real-world case studies is desired. Future research may involve the use of well-derived hard data from fluvial successions (e.g., petrophysical data) in combination with secondary transforms (as defined in this study). Data from multiple wells will be required, ideally to be used in parallel with soft data (e.g., seismic attributed in the form of secondary/auxiliary data). Moreover, further studies of this type could be applied to outcrop analogues, such as the Pont de Montanyana outcrop of point-bar deposits from the southern Pyrenees ([Cabello et al., 2018](#)).

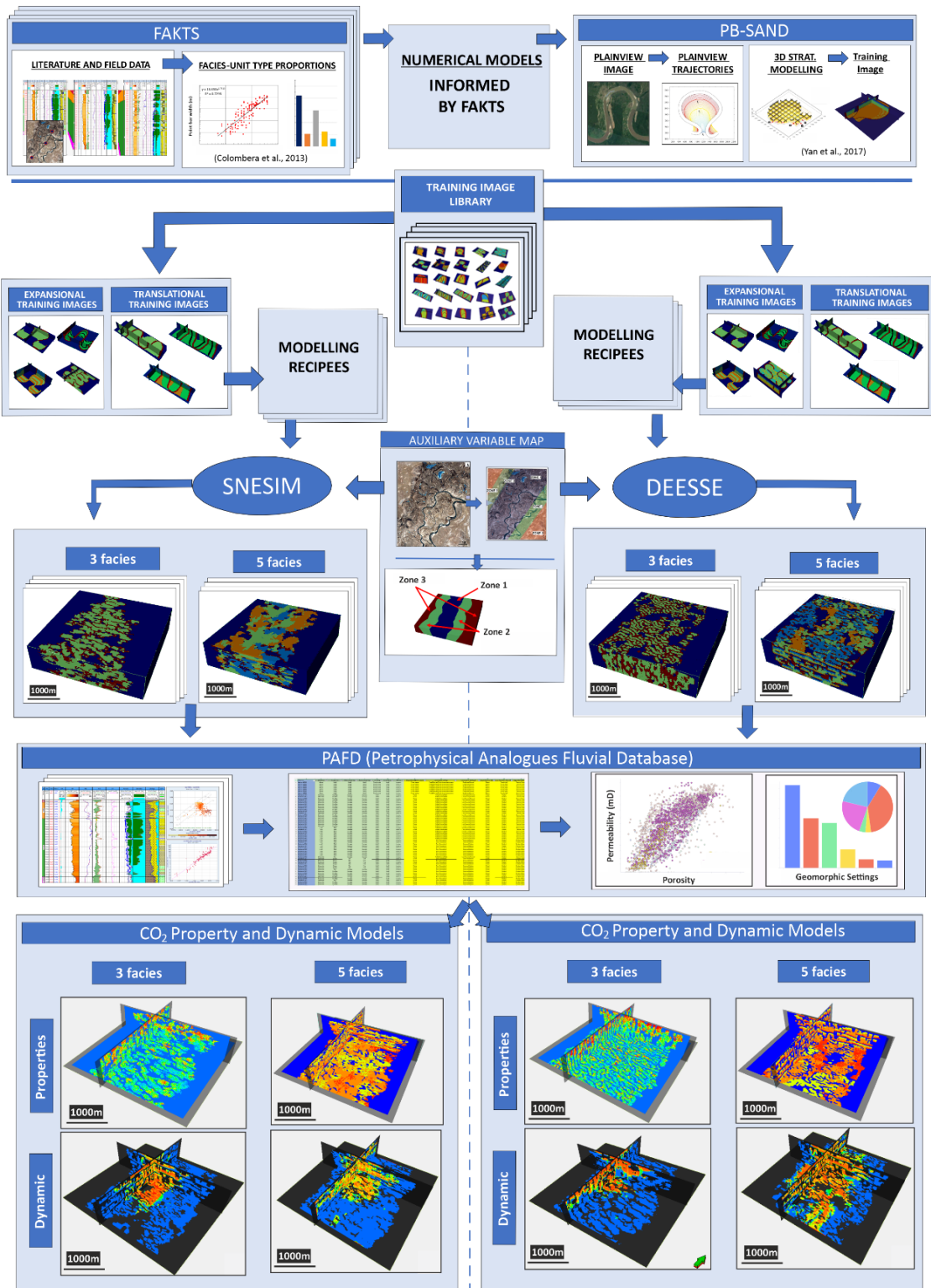


Figure 7.1. Graphical workflow summarising this Thesis research.

Graphical summary of the steps carried out in this Thesis where facies models are created using a novel workflow to be later informed by properties (porosity and permeability) using PAFD (Petrophysical Analogue Fluvial Database) with the intent to generate property and CO₂ dynamic models.

References

- Abbaszadeh M., Fujii H., Fujimoto F. (1996) Permeability prediction by hydraulic flow units – theory and applications. *SPE Form Eval* 11(4), 263-271.
<https://doi.org/10.2118/30158-PA>
- Abercrombie H.J., Hutcheon I.E., Bloch J.D., Caritat P.D. (1994) Silica activity and the smectite-illite reaction. *Geology*, 22(6), 539-542.
[https://doi.org/10.1130/0091-7613\(1994\)022<0539:SAATSI>2.3.CO;2](https://doi.org/10.1130/0091-7613(1994)022<0539:SAATSI>2.3.CO;2)
- Al-Baldawi, B.A. (2015) Building A 3D Geological Model Using Petrel Software for Asmari Reservoir, Southeastern Iraq. *Iraqi Journal of Science*, 56, 1750-1762.
- Al-Khdheawi E. A, Vialle S., Barifcani A., Sarmadivaleh M., Iglauer S. (2017) Impact of reservoir wettability and heterogeneity on CO₂-plume migration and trapping capacity. *International Journal of Greenhouse Gas Control*, 58, 142-158.
<https://doi.org/10.1016/j.ijggc.2017.01.012>
- Al-Mudhafar, W., Rao, D. (2015) Production Controls Optimization of Gas Assisted Gravity Drainage (GAGD) Process.: 68th Annual Session of the Indian Institute of Chemical Engineers (CHEMCON, 2015).
- Alabert, F.G., Massonnat, G.J. (1990) Heterogeneity in a complex turbiditic reservoir: Stochastic modeling of facies and petrophysical variability. SPE paper presented at the SPE Annual Technical Conference & Exhibition, New Orleans, LA. SPE 20604.
- Allaby, M. (2013) Aeolian processes (aeolian processes). A dictionary of geology and earth sciences (Fourth ed.). Oxford University Press, 634pp.
[10.1093/acref/9780199653065.001.0001](https://doi.org/10.1093/acref/9780199653065.001.0001)
- Alcalde, J., Flude, S., Wilkinson, M., Johnson, G., Edlmann, K., Bond, C.E., Scott, V., Gilfillan, S.M.V., Ogaya, X., Haszeldine, R.S. (2018) Estimating geological CO₂ storage security to deliver on climate mitigation. *Nature Communications*, 9, 2201.
<https://doi.org/10.1038/s41467-018-04423-1>
- Alcalde, J., Heinemann, N., Mabon, L., Worden, R., Hazel E., Maver O., Marko E., Ghanbari, S., Swennenhuis, F., Mann, I., Walker, T., Gomersal, S., Bond, Clare A., Haszeldine, R S., James, A., Mackay, E., Brownsort, P., Faulkner, D., Murphy, S. (2019) Acorn: Developing Full-chain Industrial Carbon Capture and Storage in a Resource- and Infrastructure-Rich Hydrocarbon Province. *Journal of Cleaner Production*, 233(1), 963-971.
<https://doi.org/10.1016/j.jclepro.2019.06.087>
- Alessio L., Bourdon L., Coca S. (2005) Experimental design as a framework for multiple realisation history matching: F6 further development studies. SPE paper presented at SPE Asia Pacific Oil and Gas conference and exhibition, Jakarta. SPE-93164-MS.
<https://doi.org/10.2118/93164-MS>
- Alexander, J. (1993) A discussion on the use of analogs for reservoir geology. In: Ashton, M. (ed.) *Advances in Reservoir Geology*. Geological Society, London, Special Publications, 69, 175-194.
- Alexander, J., Gawthorpe, R.L. (1993b) The complex nature of a Jurassic multistorey, alluvial sandstone body, Whitby, North Yorkshire, in North, C.P., and Prosser, D.J.,

eds., Characterization of Fluvial and Aeolian Reservoirs: Geological Society of London, Special Publication 73, 125-143.

Allen, J.R.L. (1963) The classification of cross-stratified units, with notes on their origin. *Sedimentology*, 2(2), 93-114.

<https://doi.org/10.1111/j.1365-3091.1963.tb01204.x>

Allen, J.R.L. (1964) Studies in fluvial sedimentation: six cyclothems from the lower old red sandstone, Anglo Welsh Basin. *Sedimentology* 3(3), 163-198.

<https://doi.org/10.1111/j.1365-3091.1964.tb00459.x>

Allen, J.R.L. (1965a) A review of the origin and characteristics of Recent alluvial sediments. *Sedimentology*, 5(2), 89-191.

<https://doi.org/10.1111/j.1365-3091.1965.tb01561.x>

Allen, J.R.L., (1965b) The sedimentation and paleogeography of the old red sandstone of anglesy, North Wales. *Proceedings of the Yorkshire Geological Society*, 35(2), 139.

<https://doi.org/10.1144/pyqs.35.2.139>

Allen, J.R.L. (1978) Studies in fluvial sedimentation: An exploratory quantitative model for the architecture of avulsion-controlled alluvial suites: *Sedimentary Geology*, 21(2), 129-147.

[https://doi.org/10.1016/0037-0738\(78\)90002-7](https://doi.org/10.1016/0037-0738(78)90002-7)

Ambrose, W.A., Lakshminarasimhan, S., Holtz, M.H., Núñez-Lopez, V., Hovorka, S.D., Duncan, I. (2008) Geologic factors controlling CO₂ storage capacity and permanence: case studies based on experience with heterogeneity in oil and gas reservoirs applied to CO₂ storage. *Environ. Geol.*, 54(8), 1619-1633.

<https://doi.org/10.1007/s00254-007-0940-2>

Altameemi, A.M.H., Alzaidy, A. (2018) Geological Modeling Using Petrel Software for Mishrif Formation in Noor Oil Field, Southeastern Iraq. *Iraqi Journal of Science*, 59, 1600-1613.

<https://doi.org/10.24996/ij.s.2018.59.3C.7>

Araújo A.L.S., Fernandes B.R.B, Drumond F.E.P., Araujo R.M., Lima I.C.M., Gonçalves A.D.R., Marcondes, F., Sepehrnoori, K. (2016) 3D Compositional reservoir simulation in conjunction with unstructured grids. *Process Systems Engineering, Braz. J. Chem. Eng* 33(2), 347-360.

<http://dx.doi.org/10.1590/0104-6632.20160332s20150011>

Aretz, A., Bär, K., Götz, A.E. Sass I. (2016) Outcrop analogue study of Permian geothermal sandstone reservoir formations (northern Upper Rhine Graben, Germany): impact of mineral content, depositional environment and diagenesis on petrophysical properties. *International Journal of Earth Science*, 105, 1431–1452.

<https://doi.org/10.1007/s00531-015-1263-2>

Arnold, D., Demyanov, V., Rojas, T., Christie, M., (2019) Uncertainty Quantification in Reservoir Prediction: Part 1—Model Realism in History Matching Using Geological Prior Definitions. *Mathematical Geosciences*, 51(2), 209-240.

<https://doi.org/10.1007/s11004-018-9774-6>

Atabek R. (2021) Sustainability consideration during the design and construction of geological disposal. Woodhead Publishing Series in Energy: Sustainability of Life Cycle Management for Nuclear Cementation-Based Technologies, 339-383.
<https://doi.org/10.1016/B978-0-12-818328-1.00006-X>.

Athy, L.F. (1930) Density, Porosity and Compaction of Sedimentary Rocks. Bulletin of the American Association of Petroleum Geologists (AAPG Bulletin), 14, 1-24.

Aziz, K., Settari, A. (2002) Petroleum reservoir simulation. Elsevier Applied Science, 342pp.
<http://www.worldcat.org/oclc/49352809>

Baas J.H., McCaffrey W.D., Knipe R.J. (2005) The Deep-Water Architecture Knowledge Base: towards an objective comparison of deep-marine sedimentary systems. Petroleum Geoscience, 11(4), 309-320.
<https://doi.org/10.1144/1354-079304-642>

Bachu S. (2001) Geological sequestration of anthropogenic carbon dioxide: applicability and current issues. In: Geological perspectives of global climate change, Author(s): Lee C. Gerhard, William E. Harrison, Bernold M. Hanson, 285-303.
<https://doi.org/10.1306/St47737>

Bachu, S., Bonijoly, D., Bradshaw, J., Burruss, R., Holloway, S., Christensen, N.P., Mathiassen, O.M. (2007) CO₂ storage capacity estimation: methodology and gaps. Int. J. Greenh. Gas Control, 1(4), 430-443.
[https://doi.org/10.1016/S1750-5836\(07\)00086-2](https://doi.org/10.1016/S1750-5836(07)00086-2)

Bachu, S., Bennion, B. (2008) Effects of in-situ conditions on relative permeability characteristics of CO₂-brine systems. Environmental Geology, 54, 1707-1722.
<https://doi.org/10.1007/s00254-007-0946-9>

Ballin P.R., Faria R.T., Becker M.R., Carrasco B.N., Teixeira P.W., (1997) Reservoir Studies in Fluvial Deposit: From Outcrops to Stochastic Characterization and Flow Simulation. SPE paper presented at the Latin American and Caribbean Petroleum Engineering Conference, Rio de Janeiro, Brazil. SPE-39000-MS.
<https://doi.org/10.2118/39000-MS>

Bär K., Reinsch T., Bott J. (2020) P³ - PetroPhysical Property Database – a global compilation of lab measured rock properties. Earth System Science Data 12(4), 2485-2515.

Barker J.W., Thibeau S. (1997) A critical review of the use of pseudo relative permeabilities for upscaling. SPE Reservoir Engineering 12(5), 138-143.
<https://doi.org/10.1007/s10596-015-9503-x>

Barton M., O'Byrne C., Pirmez C., Prather B., Van der Vlugt F. (2004) Understanding hydrocarbon recovery in deep water reservoirs: modeling outcrop data in the third dimension. Paper presented at the AAPG Annual Convention, Dallas, Texas, USA.

Bear, J. (1972) Dynamics of Fluids in Porous Media. American Elsevier Publishing Company, New York, 764pp.

Bennion B., Bachu S. (2005) Relative permeability characteristics for supercritical CO₂ displacing water in a variety of potential sequestration zones in the Western Canada sedimentary basin. SPE Annual technical conference and exhibition held in Dallas, Texas, SPE-95547-MS.

<https://doi:10.2118/95547-MS>

Bennion B., Bachu S. (2008) Drainage and imbibition relative permeability relationships for supercritical CO₂/brine and H₂S/brine systems in intergranular sandstone, carbonate, shale and anhydrite rocks. SPE Reservoir Evaluation & Engineering, 11, 487-496.

<https://doi.org/10.2118/99326-PA>

Bentley M.R., Woodhead T.J. (1998) Uncertainty handling through scenario-based reservoir modelling. SPE paper presented at the SPE Asia Pacific conference on Integrated Modelling for Asset Management, Kuala Lumpur, SPE-39717-MS.

<https://doi.org/10.2118/39717-MS>

Bentley M.R., Elliott A.A. (2008) Modelling flow along fault damage zones in a sandstone reservoir: an unconventional modelling technique using conventional modelling tools in the Douglas Field Irish Sea UK. SPE paper presented at SPE Europe/EAGE conference and exhibition. Society of Petroleum Engineers, Rome, SPE-113958-MS.

<https://doi:10.2118/113958-MS>

Bernecker, T., Partridge, A.D. (2001) Emperor and Golden Beach Subgroups: The onset of Late Cretaceous sedimentation in the Gippsland basin, SE Australia. PESA Eastern Australasian Basins Symposium, 391-402.

Bierkins M.F., (1996) Modelling hydraulic conductivity of a complex confining layer at various spatial scales. Water Resources Research, 32(8), 2369-2382.

<https://doi.org/10.1029/96WR01465>

Bischoff, A., Adam, L., Dempsey, D., Nicol, A., Beggs, M., Rowe, M.C., Bromfield, K., Stott, M., Villeneuve, M. (2021) Underground hydrogen storage in sedimentary and volcanic rock reservoirs: Foundational research and future challenges for New Zealand. EGU General Assembly, 19-30.

<https://doi.org/10.5194/egusphere-egu21-3496>

Bloch S. (1991) Empirical prediction of porosity and permeability in sandstones American Association of Petroleum Geologist Bulletin, 75, 1145-1160.

Bluck, B.J. (1971) Sedimentation in the meandering River Endrick. Scottish Journal of Geology, 7(2), 93-138.

<https://doi.org/10.1144/sjg07020093>

Blum, M.D., Törnqvist, T.E. (2000) Fluvial responses to climate and sea-level change: a review and look forward. Sedimentology, 47(s1), 2-48.

<https://doi.org/10.1046/j.1365-3091.2000.00008.x>

Bodard, J.M., Wall, V.J., Cas. R.A.F. (1984) Diagenesis and the evolution of Gippsland Basin reservoirs. The APEA Journal, 24, 314-335.

Bond, G.C., Kominz, M.A., Sheridan, R.E. (1995) Continental terraces and rises, in Busby, C.J., and Ingersoll, R.V., eds., Tectonics of sedimentary basins. Oxford, Blackwell Science, 149-178.

Brandsæter I., Ringrose P. S., Townsend C. T., Omdal S. (2001) Integrated modeling of geological heterogeneity and fluid displacement: Smørbukk gas-condensate field, Offshore Mid-Norway. SPE paper presented at the SPE Reservoir Simulation Symposium, Houston, Texas, SPE-66391-MS.

<https://doi.org/10.2118/66391-MS>

Bourbiaux B., Basquet R., Cacas M.C., Daniel J.M., Sarda S. (2002) An integrated workflow to account for multiscale fractures in reservoir simulation models: implementation and benefits. SPE paper presented at Abu Dhabi international petroleum exhibition and conference, Abu Dhabi, United Arab Emirates, SPE-78489-MS.

<https://doi.org/10.2118/78489-MS>

Brice, J.C. (1974) Evolution of meander loops. GSA Bulletin, 85(4), 581-586.

[https://doi.org/10.1130/0016-7606\(1974\)85<581:EOML>2.0.CO;2](https://doi.org/10.1130/0016-7606(1974)85<581:EOML>2.0.CO;2)

Bridges, P.H., Leeder M.R. (1976) Sedimentary model for intertidal mudflat channels, with examples from the Solway Firth, Scotland. Sedimentology, 23(4), 533-552.

<https://doi.org/10.1111/j.1365-3091.1976.tb00066.x>

Bridge, J., Leeder, M.A. (1979) Simulation model of alluvial stratigraphy. Sedimentology, 26(5), 617-644.

<https://doi.org/10.1111/j.1365-3091.1979.tb00935>

Bridge, J.S., Mackey, S.D. (1993a) A revised alluvial stratigraphy model. In: Alluvial Sedimentation (Eds M. Marzo and C. Puigdefabregas), Int. Assoc. Sedimentology Special Publication, 17, 319-336.

<https://doi.org/10.1002/9781444303995.ch22>

Bridge, J.S. (2003) Rivers and Floodplains. Forms, Processes, and Sedimentary Record. Blackwell, Oxford, 491pp.

<https://doi.org/10.1002/jgs.856>

Bridge, J.S. (2006) Fluvial facies models: Recent developments. In: Posamentier, H.W. & Walker, R.G. (eds) Facies Models Revisited. SEPM. Special Publication, 84, 85-170.

Brierley, G.J. (1996) Channel morphology and element assemblages: A constructivist approach to facies modelling. In: Carling, P.A. & Dawson, M.R. (eds) Advances in Fluvial Dynamics and Stratigraphy. Wiley, Chichester, 263-298.

Bristow, C.S. (1987) Brahmaputra River: channel migration and deposition. In: Recent developments in fluvial sedimentology (Eds. E.G. Ethridge, R.M. Flores and M.D. Harvey). SEPM Special Publication, 39, 63-74.

Brookfield, M.E. (2008) Principles of Stratigraphy. Wiley-Blackwell, 368pp.

Buchanan, T.J., Somers, W.P. (1969) Discharge measurements at gaging stations: U.S. Geological Survey Techniques of Water-Resources Investigations, book 3, chapter A8, 65p.

<https://pubs.usgs.gov/twri/twri3a8/>

Budinis, S., Krevor, S., Dowell, N.M., Brandon, N., Hawkes, A. (2018) An assessment of CCS costs, barriers and potential. Energy Strategy Reviews, 22, 61-81.

<https://doi.org/10.1016/j.esr.2018.08.003>

Bunch, M.A., Backe, G., Kaldi, J. (2011) Geological appraisal of an onshore CO₂ storage prospect. Energy Procedia, 4, 4625-4632.

Bryant S., Blunt M.J. (1992) Prediction of relative permeability in simple porous media. *Physical Review A*, 46(4), 2004-2011.

<https://doi.org/10.1103/physreva.46.2004>

Cabello, P. Dominguez, D., Murillo-López, M., López-Blanco, M. Garcia-Sellés, D., Cuevas, J., Marzo M. and Arbués, P. (2018) From conventional outcrop datasets and digital outcrop models to flow simulation in the Pont de Montanyana point-bar deposits (Ypresian, Southern Pyrenees). *Marine and Petroleum Geology*, 94, 19-42.

<https://doi.org/10.1016/j.marpetgeo.2018.03.040>

Caers, J., Journel, A.G. (1998) Geostatistical quantification of geological information for a fluvial type North-Sea reservoir: SPE paper presented at the SPE Annual Technical Conference and Exhibition, Houston, Texas. SPE-56655-MS.

<https://doi.org/10.2118/56655-MS>

Caers, J. (2001) Geostatistical reservoir modelling using statistical pattern recognition, *Journal of Petroleum Science and Engineering*. 29(3-4), 177-188.

[https://doi.org/10.1016/S0920-4105\(01\)00088-2](https://doi.org/10.1016/S0920-4105(01)00088-2)

Caers J. (2003) History matching under training image based geological model constraints. *SPE Journal* 8(3), 218-226.

<https://doi.org/10.2118/74716-PA>

Caers J., Zhang T. (2004) Multiple-point geostatistics: a quantitative vehicle for integration geologic analogs into multiple reservoir model, integration of outcrop and modern analog data in reservoir models. Stanford University, Stanford Centre for Reservoir Forecasting. Stanford, CA 94305-2220.

Caers, J., Zhang, T. (2004) Multiple-point geostatistics: a quantitative vehicle for integrating geologic analogs into multiple reservoir models. In: G. M. Grammer, P. M. Mitch Harris, & G. P. Eberli, eds., *Integration of outcrop and modern analogs in reservoir modeling*. AAPG Memoir, 80(80), 383-394.

Caers, J. (2008) *Petroleum Geostatistics*. Computers and Geosciences, 34(3), 299-300.

<https://doi.org/10.1016/j.cageo.2007.07.002>

Caers J. (2011) *Modeling uncertainty in the earth sciences*. Wiley-Blackwell, 248pp.

<https://doi.org/10.1007/s11004-012-9432-3>

Cannon S., (2015) *Petrophysics: A Practical Guide*. Petrophysics: A Practical Guide, John Wiley & Sons, 201pp.

<https://doi.org/10.1002/9781119117636>

Cannon, S. (2018) *Reservoir Modelling: A practical guide*. Wiley Blackwell, 312pp.

<https://doi.org/10.1002/9781119313458.fmatter>

Cant D., Walker R., (1978) Fluvial processes and facies sequences in the sandy braided South Saskatchewan River, Canada. *Sedimentology* 25(5), 625-648.

<https://doi.org/10.1111/j.1365-3091.1978.tb00323.x>

Cardwell W.T., Parsons R.L. (1945) Average permeabilities of heterogeneous oil sands. *Trans.*, 160(1), 34-42.

<https://doi.org/10.2118/945034-G>

Carlson, M.R. (2006) Practical reservoir simulation: using, assessing, and developing results. PennWell Publishing Company, 378pp.

Carman, P.C. (1937) Fluid Flow through Granular Beds. *AIChE*, 15, 150.

Carter, D.C. (2003) 3-D seismic geomorphology: Insights into fluvial reservoir deposition and performance, Widuri field, Java Sea: *AAPG Bulletin*, 87(6), 909-934.

Carvajal, G., Boisvert, I., Knabe, S. (2014) A Smart Flow for SmartWells: Reactive and Proactive Modes. Paper presented at the SPE Intelligent Energy Conference & Exhibition, Utrecht, The Netherlands, SPE-167821-MS.

<https://doi.org/10.2118/167821-MS>

Chadwick R.A., Arts R., Bernstone C, May F., Thibeau S., Zweigel P. (2008) Best Practice for the Storage of CO₂ in Saline Aquifers. Keyworth, Nottingham: British Geological Survey Occasional Publication,14.

Chandler M.A., Kocurek G., Goggin D.J., Lake L.W. (1989) Effects of stratigraphic heterogeneity on permeability in eolian sandstone sequence, Page Sandstone, Northern Arizona American. Association of Petroleum Geologists Bulletin, 73, 658-668.

Chiereci G.L. (1994) Principles of petroleum reservoir engineering Springer, Berlin, 2, 398pp.

<https://doi.org/10.1007/978-3-642-78243-5>

Chiles J.P., Delfiner P. (2012) Geostatistics: Modelling Spatial Uncertainty. John Wiley & Sons, 714pp.

<http://dx.doi.org/10.1002/9781118136188>

Chugunova, T.L., Hu, L.Y. (2008) Multiple-point simulations constrained by continuous auxiliary data. *Mathematical Geosciences*, 40(2), 133-146.

<https://doi.org/10.1007/s11004-007-9142-4>

Clark, A.B.S., Thomas, B. M. (1988) The Intra-Latrobe Play: a case history from the Basker/Manta block (VIC/P19), Gippsland Basin. *The APEA Journal*, 28, 100-112.

Codd, E.F. (1970) A Relational Model of Data for Large Shared Data Banks. *Communications of the ACM*, 13, 377-387.

<https://doi.org/10.1145/362384.362685>

Colombera, L., Mountney, N.P., McCaffrey, W.D. (2012a) A relational database for the digitization of fluvial architecture concepts and example applications. *Petroleum Geoscience*, 18(1), 129.

<http://dx.doi.org/10.1144/1354-079311-021>

Colombera, L., Felletti, F., Mountney, N.P., McCaffrey, W.D. (2012b) A database approach for constraining stochastic simulations of the sedimentary heterogeneity of fluvial reservoirs. *AAPG Bulletin*, 96(11), 2143-2166.

<https://doi.org/10.1306/04211211179>

Colombera, L., Mountney, N.P., McCaffrey, W.D. (2013) A quantitative approach to fluvial facies models: methods and example results. *Sedimentology*, 60(6), 1526-1558.

<https://doi.org/10.1111/sed.12050>

Colombera, L., Mountney, N.P., Felletti, F., McCaffrey, W.D. (2014) Models for guiding and ranking well-to-well correlations of channel bodies in fluvial reservoirs. AAPG Bulletin, 98, 1943-1965.

<https://doi.org/10.1306/05061413153>

Colombera, L., Mountney, N.P., McCaffrey, W.D. (2015) A meta-study of relationships between fluvial channel-body stacking pattern and aggradation rate: implications for sequence stratigraphy. *Geology*, 43, 283-286.

<https://doi.org/10.1130/G36385.1>

Colombera, L., Mountney, N.P., Howell, J.A., Rittersbacher, A., Felletti, F., McCaffrey, W.D., (2016) A test of analog-based tools for quantitative prediction of large-scale fluvial architecture. AAPG Bulletin, 100, 237-267.

<https://doi.org/10.1306/11181514227>

Colombera L, Mountney N.P., Russell C.E, Shiers M.N., McCaffrey W.D. (2017) Geometry and compartmentalization of fluvial meander-belt reservoirs at the bar-form scale: quantitative insight from outcrop, modern and subsurface analogues. *Marine and Petroleum Geology*, 82, 35-55.

<https://doi.org/10.1016/j.marpetgeo.2017.01.024>

Colombera L., Mountney N.P., Howell J.A., Rittersbacher A., McCaffrey W.D. (2016) Geological Modeling of Outcrop Successions to Assess Analog – Based Predictions of the Sedimentary Heterogeneity in Fluvial Reservoirs. AAPG Search and Discovery, 41771.

Colombera, L., Mountney, N.P., Russell, C.E., Shiers, M.N., McCaffrey, W.D. (2017) Geometry and compartmentalization of fluvial meander-belt reservoirs at the bar-form scale: Quantitative insight from outcrop, modern and subsurface analogues. *Marine and Petroleum Geology*, 82, 35-55.

<https://doi.org/10.1016/j.marpetgeo.2017.01.024>

Colombera, L., Yan, N., McCormick-Cox, T., Mountney, N.P. (2018) Seismic-driven geocellular modeling of fluvial meander-belt reservoirs using a rule-based method. *Marine and Petroleum Geology*, 93, 553-569.

<https://doi.org/10.1016/j.marpetgeo.2018.03.042>

Colombera, L., Mountney, N.P. (2019) The lithofacies organization of fluvial channel deposits: A meta-analysis of modern rivers. *Sedimentary Geology*, 383, 16-40.

<https://doi.org/10.1016/j.sedgeo.2019.01.011>

Comunian A., Renard P., Straubhaar J. (2012) 3D multiple-point statistics simulation using 2D training images. *Computers and Geosciences*, 40, 69-65.

<https://doi.org/10.1016/j.cageo.2011.07.009>

Corbett P.W.M, Jensen J.L. (1992) Estimating the mean permeability: how many measurements do you need? *First Break* 10(3), 89-94.

Corbett P.W.M., Ringrose P.S., Jensen J.L., Sorbie K.S. (1992) Laminated clastic reservoirs: the interplay of capillary pressure and sedimentary architecture. SPE paper presented at the SPE Annual Technical Conference and Exhibition, Washington, D.C., SPE-24699-MS.

<https://doi.org/10.2118/24699-MS>

Corbett, P., Hamdi, H., Gurav, H. (2012) Layered fluvial reservoirs with internal fluid cross flow: A well-connected family of well test pressure transient response. *Petroleum Geoscience*, 18(2), 219-229.

<https://doi.org/10.1144/1354-079311-008>

Corey A.T. (1954) The interrelation between gas and oil relative permeabilities. *Producers Monthly*, 19, 38-41.

Cosentino L. (2001) *Integrated reservoir studies*. Editions Technip, Paris, 310pp

Cosgrove G.I.E., Colombera L., Mountney N.P. (2021) A database of Aeolian Sedimentary Architecture for the characterization of modern and ancient sedimentary systems. *Marine and Petroleum Geology*, 127, 104983.

<https://doi.org/10.1016/j.marpetgeo.2021.104983>

Crains R. (2023) *Crain's Petrophysical Handbook*.

<https://spec2000.net/index.htm>

Cressie, N. (1993) *Statistics for spatial data*. Wiley Interscience, 928pp.

Crichlow, H.B. (1978) *Modern reservoir engineering: A simulation approach*. Englewood Cliffs, 354pp.

<http://www.worldcat.org/oclc/636084916>

CrowdFlower Data Science report (2016)

https://visit.figure-eight.com/rs/416-ZBE-142/images/CrowdFlower_DataScienceReport_2016.pdf

Curry, W.H. (1972) South Glenrock oil field, Wyoming pre-discovery thinking and post discovery description. In R. E. King, ed., *Stratigraphic oil and gas fields Classification, exploration methods, and case histories*. AAPG Memoir 16, 415-427.

Dai Z., Zhang S., Wang Y., Li X., Cao H. (2014) Short-term safety risk assessment of CO₂ geological storage projects in deep saline aquifers using the Shenhua CCS Demonstration Project as a case study. *Environmental Earth Sciences*, 73, 7571-7586.

<https://doi.org/10.1007/s12665-014-3928-8>

Dake L.P. (2001) *The practice of reservoir engineering (Rev edition)*. Elsevier, Amsterdam, 572pp.

Dana E., Skoczylas, F. (2002) Experimental study of two-phase flow in three sandstones. I. Measuring relative permeabilities during two-phase steady-state experiments, *International Journal of Multiphase Flow*, 28(11), 1719-1736,

[https://doi.org/10.1016/S0301-9322\(02\)00090-3](https://doi.org/10.1016/S0301-9322(02)00090-3).

Danskin, W.R., Freckleton, J.R. (1992) Groundwater flow modeling and optimization techniques applied to high groundwater problems in San Bernardino, California, in selected papers in the hydrological science, S. Subitzky (ed.), *US Geological Survey Water-Supply, Paper No. 2340*, 165-177.

Danskin W.R., McPherson K.R., Woolfenden L.R. (2006) *Hydrology, description of computer models, and evaluation of selected water-management alternatives in the San Bernardino area, California*. USGS Publications Warehouse, 2005-1278.

<https://doi.org/10.3133/ofr20051278>

Darcy, H.P.C. (1856) *Les Fontaines Publiques de la Ville de Dijon: Exposition et Application des Principes a Suivre et des Formulesa Employer dans les Questions de Distribution d'Eau*. Paris. In: Dalmont, V., Ed., 647pp.

De Vries, L., Carrera J., Falivene O., Gratacos O., Slooten L. (2009) Application of multiple point geostatistics to non-stationary images. *Mathematical Geoscience*, 41(1), 29-42.

Dean, L. (2008) Volumetric Estimation in R., Mireault, L. Dean, *Reservoir Engineering for Geologists: Canadian Society of Petroleum Geologists Reservoir Magazine*, 2011-14,

<http://large.stanford.edu/courses/2013/ph240/zaydullin2/docs/fekete.pdf>

Deutsch, C.V. (1992) *Annealing Techniques Applied to Reservoir Modeling and the Integration of Geological and Engineering (Well Test) Data*. PhD thesis, Stanford University, Stanford, 325pp.

Deutsch, C.V., Wang, L. (1996) Hierarchical object-based stochastic modeling of fluvial reservoirs. *Mathematical Geology*, 28(7), 851-880.

<https://doi.org/10.1007/BF02066005>

Deutsch, C.V., Journel, A.G. (1997) *GSLIB Geostatistical Software Library and User's Guide*. Oxford University Press, New York, second edition, 369pp.

<https://doi.org/10.1017/S0016756899531774>

Deutsch, C.V. (2002) *Geostatistical Reservoir Modeling (Applied Geostatistics)*. Oxford University Press Inc, 376pp.

<https://doi.org/10.1007/s11004-008-9188-y>

Desberats A.J. (1987) Numerical estimation of effective permeability in sand-shale formations. *Water Resources Research* 23(2), 273-286.

[https://doi.org/10.1016/S0074-6142\(08\)62821-1](https://doi.org/10.1016/S0074-6142(08)62821-1)

Dewey, J.F. (1980) Episodicity, sequence and style at convergent plate boundaries. *Geological Association of Canada Special Paper*, 20, 553-573.

Dickinson, W.R. (1974a) Sedimentation within and beside ancient and modern magmatic arcs. *Society of Economic Paleontologists and Mineralogists Special Publication*, 19, 230-239.

Dickinson, W.R., Seely, D.R. (1979) Structure and stratigraphy of forearc regions. *American Association of Petroleum Geologists Bulletin*, 63, 2-31.

Dickinson, W.R. (1976a) Plate tectonic evolution of sedimentary basins. *American Association of Petroleum Geologists Continuing Education Course Notes Series* 1, 62pp.

https://doi.org/10.1007/978-94-011-1614-5_16

Dodge, C.F., Holler, D.P., Meyer, R.L. (1971) Reservoir heterogeneities of some Cretaceous Sandstones. *AAPG Bulletin*, 55, 1814-1828.

Dreyer, T. (1990) Sand body dimensions and infill sequences of stable, humid-climate delta plain channels. In: Buller, A. T., Berg, E., Hjelmeland, O., Kleppe, J., Torsæter, O. & Aasen, J. O. (eds) *North Sea Oil and Gas Reservoirs – II*. Graham & Trotman, London, 337-351.

https://doi.org/10.1007/978-94-009-0791-1_29

Dreyer, T. (1993) Quantified fluvial architecture in ephemeral stream deposits of the Esplugafreda Formation (Palaeocene), Tremp-Graus Basin, northern Spain. In *Alluvial Sedimentation*, 337-362.

<https://doi.org/10.1002/9781444303995.ch23>

Dolson J. (2016) Understanding Oil and Gas Shows and Seals in the Search for Hydrocarbons. Springer-Verlag, 486pp.

<https://doi.org/10.1007/978-3-319-29710-1>

Dott, R.H. (1964) Wacke, Greywacke and Matrix – What Approach to Immature Sandstone Classification? *Journal of Sedimentary Petrology*, 34, 625-632.

Durán, E.L., Adam, L., Wallis, I.C., Barnhoorn, A.: Mineral Alteration and Fracture Influence on the Elastic Properties of Volcaniclastic Rocks, *Journal of Geophysical Research, Solid Earth*, 124, 25pp.

<https://doi.org/10.1029/2018JB016617>

Durkin, P.R., Hubbard, S.M., Boyd, R.L., Leckie, D.A. (2015) Stratigraphic expression of intra-point-bar erosion and rotation. *Journal of Sedimentary Research* 85, 1238-1257.

<https://doi.org/10.2110/jsr.2015.78>

Durkin, P.R., Hubbard, S.M., Holbrook, J., Boyd, R. (2017) Evolution of fluvial meander belt deposits and implications for the completeness of the stratigraphic record. *Geological Society of America Bulletin* 130(5), 721-739.

<https://doi.org/10.1130/B31699.1>

Durlofsky L.J. (1991) Numerical calculations of equivalent grid block permeability tensors for heterogeneous porous media. *Water Resources Research* 27(5), 699-708.

<https://doi.org/10.1029/91WR00107>

Durlofsky, L.J. (2003) Upscaling of geocellular models for reservoir flow simulation: a review of recent progress. 66th EAGE Conference and Exhibition – Workshops, cp-133-00001.

<https://doi.org/10.3997/2214-4609.201405607>

Ehrenberg, S.N. (1995) Measuring sandstone compaction from modal analyses of thin sections: how to do it and what the results mean: *Journal of Sedimentary Research*, A65, 369-379.

Eiken O., Ringrose P., Hermanrud C., Nazarian B., Torp T.A., Hoier L. (2011) Lessons learned from 14 years of CCS operations: Sleipner, In Salah and Snøhvit. *Energy Procedia*, 4, 5541-5548.

<https://doi.org/10.1098/rsfs.2019.0065>

Ekran S., Aasen J.O. (2000) Steady-state upscaling. *Transport in Porous Media*, 41(3), 245-262

<https://doi.org/10.1023/A:1006765424927>

Engie, H.D., Howell, J.A., Buckley, S.J. (2010) Quantifying clinothem geometry in a forced-regressive river-dominated delta, Panther Tongue Member, Utah, USA. *Sedimentology*, 57, 1750-1770.

<https://doi.org/10.1111/j.1365-3091.2010.01164.x>

England, W.A., Townsend, C. (1998) The effects of faulting on production from a shallow marine reservoir – a study of the relative importance of fault parameters. SPE paper presented at the Society of Petroleum Engineers Annual Technical Conference and Exhibition, New Orleans, Louisiana, USA. Paper SPE-49023.

<https://doi.org/10.2118/49023-MS>

Equinor's Volve Field Dataset. Complete set of data from a North Sea oil field available for research, study and development purposes.

<https://www.equinor.com/energy/volve-data-sharing>

Ertekin, T, Abou-Kassem, King G.R. (2001) Basic Applied Reservoir Simulation, SPE Textbook Series, 7, 406pp.

Espinoza, D.N., Santamarina, J.C. (2017) CO₂ breakthrough-caprock sealing efficiency and integrity for carbon geological storage. *Int. J. Green. Gas Contro*, 1 66, 218-229.

<https://doi.org/10.1016/j.ijggc.2017.09.019>

Fanchi, J.R. (2001) Principles of applied reservoir simulation. Houston, Tex: Gulf Publications, 378pp.

<http://www.worldcat.org/oclc/471519143>

Farmer, C.L. (1988) The generation of stochastic fields of reservoir parameters with specified geostatistical distributions. In: Edwards, S., and King, P.R., eds., *Mathematics in oil production*, Clarendon Press, Oxford, 235-252.

Feynman R.P., Leighton R.B., Sands M.L. (1963) *The Feynman lectures on physics*, Addison-Wesley Pub. Co, 458pp.

Fielding, C.R., Crane, R.C. (1987) An application of statistical modelling to the prediction of hydrocarbon recovery factors in fluvial reservoir sequences. In: *Recent Developments in Fluvial Sedimentology* (Eds F.G. Ethridge, R.M. Flores and M.D. Harvey). SEPM Special Publications, 39, 321-327.

Flett, M., Gurton, R., and Weir, G. (2007) Heterogeneous saline formations for carbon dioxide disposal: Impact of varying heterogeneity on containment and trapping. *Journal of Petroleum Science and Engineering*, 57(1–2), 106-118.

<https://doi.org/10.1016/j.petrol.2006.08.016>

Flint, S.S., Bryant, I.D. (1993) *The geologic modeling of hydrocarbon reservoirs and outcrop analogs*. John Wiley & Sons Ltd, 269pp.

Folk, R.L. (1968) *Petrology of Sedimentary Rocks*. Hemphill Publishing Co., Austin, 184pp.

Folk, R.L. (1974) *Petrology of Sedimentary Rocks*. Hemphill Publishing Co., Austin, 170pp.

<http://hdl.handle.net/2152/22930>

Fredsøe J. (1978) Meandering and braiding of rivers. *Journal of Fluid Mechanics* 84, 609–624.

Friend, P.F. (1983) Towards the field classification of alluvial architecture or sequence. In *Modern and Ancient Fluvial Systems* (eds J.D. Collinson and J. Lewin). International Association of Sedimentologists, Special Publication 6, 345-354.

<https://doi.org/10.1002/9781444303773.ch28>

Frykman P., Bech N., Sørensen A., Nielsen L., Nielsen C., Kristensen L., Bidstrup T. (2009) Geological modeling and dynamic flow analysis as initial site investigation for large-scale CO₂ injection at the Vedsted structure, NW Denmark. *Energy Procedia*, 1(1), 2975-2982.

<https://doi.org/10.1016/j.egypro.2009.02.074>

Gabrielsen, R.H., Steel, R.J., Nottvedt, A. (1995) Subtle traps in extensional terranes; a model with reference to the North Sea. *Petroleum Geoscience* 1, 223-235.

Gay, G.R., Gay, H.H., Gay, W.H., Martinson, H.A., Meade, R.H., Moody, J.A., (1998) Evolution of cutoffs across meander necks in Powder River, Montana, USA. *Earth Surface Process and Landforms* 23(7), 651-662.

[https://doi.org/10.1002/\(SICI\)1096-9837\(199807\)23:7<651::AID-ESP891>3.0.CO;2-V](https://doi.org/10.1002/(SICI)1096-9837(199807)23:7<651::AID-ESP891>3.0.CO;2-V)

Gershenzon, N., Ritzi, R., Dominic, D., Mehnert, E. (2017) Effective constitutive relations for simulating CO₂ capillary trapping in heterogeneous reservoirs with fluvial sedimentary architecture. *Geomechanics and Geophysics for Geo-Energy and Geo-Resources*, 3.

<https://doi.org/10.1007/s40948-017-0057-3>

Ghazi S., Mountney N.P. (2009) Facies and architectural element analysis of a meandering fluvial succession: The Permian Warchha Sandstone, Salt Range, Pakistan. *Sedimentary Geology*, 221(1-4), 99-126.

<https://doi.org/10.1016/j.sedgeo.2009.08.002>.

Ghinassi, M., (2011) Chute channels in the Holocene high-sinuosity river deposits of the Firenze plain, Tuscany, Italy. *Sedimentology* 58(3), 618-642.

<http://dx.doi.org/10.1111/j.1365-3091.2010.01176.x>

Ghinassi, M., Ielpi, A., Aldinucci, M., Fustic, M. (2016) Downstream-migrating fluvial point bars in the rock record. *Sedimentary Geology*, 334, 66-96.

<https://doi.org/10.1016/j.sedgeo.2016.01.005>

Gilman, J.R., Brickey, R.T., and Red, M.M. (1998) Monte Carlo Techniques for Evaluating Producing Properties. SPE paper presented at the SPE Rocky Mountain Regional/Low-Permeability Reservoirs Symposium, Denver, Colorado. SPE-39926-MS.

<http://dx.doi.org/10.2118/39926-MS>

Gilman J.R., Ozgen C. (2013) Reservoir Simulation: History Matching and Forecasting. SPE Books, 120pp.

Gibling, M. (2006) Width and Thickness of Fluvial Channel Bodies and Valley Fills in the Geological Record: A Literature Compilation and Classification. *Journal of Sedimentary Research*, 76(5), 731-770.

<https://doi.org/10.2110/jsr.2006.060>

Gibson-Poole, C., Svendsen, L., Underschultz, J., Watson, M., Ennis-King, J., Ruth, P., Nelson, E., Daniel, R. Cinar, Y. (2008) Site characterisation of a basin-scale CO₂ geological storage system: Gippsland Basin, southeast Australia. *Environmental Geology*, 54, 1583-1606.

<https://doi.org/10.1007/s00254-007-0941-1>

Gier, S., Worden R.H., (2008) Diagenesis and reservoir quality of Miocene sandstones in the Vienna Basin, Austria. *Marine and Petroleum Geology*, 25(8), 681-695.

<https://10.1016/j.marpetgeo.2008.06.001>

Glenton, P.N., Sutton, J.T., McPherson, J.G., Fittall, M.E., Moore, M.A., Heavysege, R.G., Box, D. (2013) Hierarchical approach to facies and property distribution in a

basin-floor fan model, Scarborough Gas Field, Northwest Shelf, Australia. Paper presented at the 6th International Petroleum Technology Conference, Beijing, China.

Global Statistics of CCS (2020) Global CCS Institute.

<https://www.globalccsinstitute.com/wp-content/uploads/2021/03/Global-Status-of-CCS-Report-English.pdf>

Glover P. (2022) Petrophysics. Paul Glover Petrophysics ebook.

<https://pdfprodocs.vip/download/4330427-paul-glover-petrophysics>

Gluyas J.G., Swarbrick R.E. Petroleum Geoscience. Wiley-Blackwell, 2021.

Goovaerts P. (1997) Geostatistics for Natural Resources Evaluation, Oxford University Press, 483pp.

<https://doi.org/10.1017/S0016756898631502>

Górniak K., (1997) The role of diagenesis in the formation of kaolinite raw materials in the Santonian sediments of the North-Sudetic Trough (Lower Silesia, Poland). Applied Clay Science. 12(4), 313-328.

Grammar, G.M. Harris, P.M. Eberli G.P. (2004) Integration of outcrop and modern analogs in reservoir modeling, integration of modern and outcrop analogs in reservoir modeling: overview and examples from the Bahamas, American Association of Petroleum Geologists, Memoirs, ed. By G.M. Grammar, P.M. Harris, G.P. Eberli, 80, 1-22.

Guardiano, F.B., Srivastava, R.M. (1993) Multivariate Geostatistics: Beyond Bivariate Moments. In: Soares, A. (eds) Geostatistics Tróia '92. Quantitative Geology and Geostatistics, 5, 133-144.

https://doi.org/10.1007/978-94-011-1739-5_12

Haghighbakhsh R., Soleymani H., Raeissi S. (2013) A simple correlation to predict high pressure solubility of carbon dioxide in 27 commonly used ionic liquids, The Journal of Supercritical Fluids, 77, 158-166.

<https://doi.org/10.1016/j.supflu.2013.02.022>.

Haghighbakhsh R., Parvaneh K., Raeissi S., Shariati A. (2018) A general viscosity model for deep eutectic solvents: The free volume theory coupled with association equations of state. Fluid Phase Equilibria, 470,193-202.

<https://doi.org/10.1016/j.fluid.2017.08.024>.

Haldorsen H.H. (1986) Simulator parameter assignment and the problem of scale in reservoir engineering. In: Lake LW, Carroll HB (eds) Reservoir characterization. Academic Press, 293-34.

<https://doi.org/10.1016/B978-0-12-434065-7.50016-2>

Haldorsen, H.H. and Macdonald, C.J. (1987) Stochastic modelling of underground reservoir facies. SPE paper presented at the SPE Annual Technical Conference and Exhibition, Dallas, Texas. SPE-16751-MS

<https://doi.org/10.2118/16751-MS>

Haldorsen H.H., Damsleth E. (1990) Stochastic modelling. Journal of Petroleum Technology, 42(4), 404-412.

<https://doi.org/10.2118/20321-PA>

Hamilton, D., Holtz, P., Ryles, T. (1998) Approaches to identifying reservoir heterogeneity and reserve growth opportunities in a continental scale bed-load fluvial system: Hutton Sandstone, Jackson field, Australia. AAPG Bulletin, 82, 2192-2219.

Harding A., Strebelle S., Levy M., Thorne, J., Xie, D., Leigh, S., Preece, R., Scamman, R. (2004) Reservoir Facies Modelling: New Advances in MPS. Quantitative Geology and Geostatistics Geostatistics Banff, 14(1), 245-265.

Heller, P.L., Paola, C. (1996) Downstream changes in alluvial architecture: An exploration of controls on channel-stacking patterns. Journal of Sedimentary Research, 66, 297-306.

<https://10.1306/D4268333-2B26-11D7-8648000102C1865D>

Hickin, E.J. (1993) Fluvial facies models: a review of Canadian research. Progress in Physical Geography. Earth and Environment, 17(2), 205-222.

<https://doi.org/10.1177/03091333930170020>

Hohn M.E. (1999) Geostatistics and petroleum geology. 2nd edition. Kluwer, Dordrecht, 243pp.

Holbrok, J.M. (2001) Origin, genetic interrelationships, and stratigraphy over the continuum of fluvial channel-form bounding surfaces: an illustration from middle Cretaceous strata, southeastern Colorado. Sedimentary Geology, 144(3-4), 179-222.

[https://doi.org/10.1016/S0037-0738\(01\)00118-X](https://doi.org/10.1016/S0037-0738(01)00118-X)

Holbrook, J., Scott, R.W., Oboh-Ikuenobe F.E. (2006) Base-level buffers and buttresses: a model for upstream versus downstream control on fluvial geometry and architecture within sequences. Journal of Sedimentary Research 76(1), 162-174.

<https://doi.org/10.2110/jsr.2005.10>

Holden L, Hauge R, Skare Ø, Skorstad A (1998) Modeling of fluvial reservoirs with object models. Mathematical Geology, 30(5), 473-496.

<https://link.springer.com/article/10.1023/A:1021769526425>

Holdgate, G., Gallagher, S. (2003) Tertiary. A period of transition to marine basin environments. Geology of Victoria. Geological Society of Australia Special Publication, 23, 289-335.

Honarkhah M. and Caers J. (2010) Stochastic Simulation of Patterns Using Distance-Based Pattern Modeling. Mathematical Geosciences, 42, 487-517.

<https://doi.org/10.1007/s11004-010-9276-7>

Hooke, J.M. (1979) An analysis of the processes of riverbank erosion. Journal of Hydrology, 42(1-2), 39-62.

[http://dx.doi.org/10.1016/0022-1694\(79\)90005-2](http://dx.doi.org/10.1016/0022-1694(79)90005-2)

Hooke, J.M. (1980) Magnitude and distribution of rates of riverbank erosion. Earth Surface Processes, 5(2), 143-157.

<http://dx.doi.org/10.1002/esp.3760050205>

Hovadik, J.M. and Larue, D.K., (2007) Static characterization of reservoirs: refining the concepts of connectivity and continuity. Petroleum Geoscience, 13(3), 195-211.

<http://dx.doi.org/10.1144/1354-079305-697>

Howell, J.A., Skorstad, A., MacDonald, A., Fordham, A., Flint, S., Fjellvoll, B., Manzocchi, T. (2008) Sedimentological parameterization of shallow-marine reservoirs *Petroleum Geoscience* 14, 17-34.

<https://doi.org/10.1144/1354-079307-787>

Howell J.A., Martinus A. and Good T.R. (2014) The application of outcrop analogues in geological modelling: a review, present status and future outlook Howell, John A. et al., Geological Society, London, Special Publications, 387(1), 1-25.

<https://doi.org/10.1144/SP387.12>

Hubbard, S.M., Smith, G.D., Nielsen, H., Leckie, A.D., Fustic, M., Spencer, J.R., Bloom, L. (2011) Seismic geomorphology and sedimentology of a tidally influenced river deposit, lower Cretaceous Athabasca Oil Sands, Alberta, Canada. *AAPG Bulletin*, 95, 1123-1145.

<http://dx.doi.org/10.1306/12131010111>.

Hurst, A. and Rossvoll, K.J., (1991) Permeability variations in sandstones and their relationship to sedimentary structures. In: Lake, L. W., Carroll, H. B. Jr. and Wesson, T. C. (Eds), *Reservoir Characterization II*, Academic Press, 166-196.

Huysmans M. and Dassargues A. (2006) Hydrogeological modeling of radionuclide transport in low permeability media: a comparison between Boom Clay and Ypresian Clay. *Geostatistics for Environmental applications* 50(1), 122-131.

<https://doi.org/10.1007/s00254-006-0191-7>

Ide S., Jessen K, Franklin M. (2007) Storage of CO₂ in saline aquifers: Effects of gravity, viscous, and capillary forces on amount and timing of trapping, *International Journal of Greenhouse Gas Control*, 1(4), 481-491.

[https://doi.org/10.1016/S1750-5836\(07\)00091-6](https://doi.org/10.1016/S1750-5836(07)00091-6).

Ielpi, A., Ghinassi, M. (2014) Planform architecture, stratigraphic signature and morphodynamics of an exhumed Jurassic meander plain (Scalby Formation, Yorkshire, UK). *Sedimentology* 61(7), 1923-1960.

<https://doi.org/10.1111/sed.12122>

Iglauer, S. (2018) Optimum storage depths for structural CO₂ trapping. *Int. J. Greenh. Gas Control* 77, 82-87.

<https://doi.org/10.1016/j.ijggc.2018.07.009>

Indiana University Database

<https://maps.indiana.edu/metadata/Geology/extras/Petroleum-Wells.html>

Ingersoll, R.V. (1988) Tectonics of sedimentary basins. *Geological Society of America Bulletin*, 100, 1704-1719.

Ingersoll, R.V., and Busby, C.J. (1995) Tectonics of sedimentary basins, in Busby, C.J., and Ingersoll, R.V., eds., *Tectonics of sedimentary basins*. Oxford, Blackwell Science, 1-51.

IPCC report 2022

<https://www.ipcc.ch/report/ar6/wg2/>

Isaaks E.H., Srivastava R.M. (1989) *Introduction to applied geostatistics*. Oxford University Press, Oxford, 413pp.

Issautier B., Fillacier S., Le Gallo Y. Audigane P, Chiaberge C., Viseur S. (2013) Modelling of CO₂ Injection in Fluvial Sedimentary Heterogeneous Reservoirs to assess the Impact of Geological Heterogeneities on CO₂ Storage Capacity and Performance. *Energy Procedia*, 37, 5181-5190.

<https://doi.org/10.1016/j.egypro.2013.06.434>.

Issautier, B.S., Viseur S., Audigane, P. and Nindre, Y.M. (2014) Impacts of fluvial reservoir heterogeneity on connectivity: Implications in estimating geological storage capacity for CO₂. *International Journal of Greenhouse Gas Control*, 20, 333-349.

Issautier, B., Viseur, S., Audigane, P., Chiaberge, C., Le Nindre, Y.-M., (2016) A new approach for evaluating the impact of fluvial type heterogeneity in CO₂ storage reservoir modeling. *Comptes Rendus Geosci.* 348, 531-539.

<https://co2re.co/FacilityData>.

Jackson, R. (1976) Depositional model of point bars in the lower Wabash River. *Journal of Sedimentary Research*, 46(3), 579-594.

<https://doi.org/10.1306/212F6FF5-2B24-11D7-8648000102C1865D>

Jackson, M. D., Valvatne, P. H., Blunt, M. J. (2003) Prediction of wettability variation and its impact on flow using pore- to reservoir-scale simulation. *Journal of Petroleum Science and Engineering*, 39, 231-246.

[https://doi.org/10.1016/S0920-4105\(03\)00065-2](https://doi.org/10.1016/S0920-4105(03)00065-2)

Jensen J.L., Lake L.W., Corbett P.W.M., Goggin D.J. (2000) *Statistics for petroleum engineers and geoscientists*, 2nd edn. Elsevier, 338pp,

Johnston S., Holbrook J. (2018) *Toggling between expansion and translation*. Willey Online Library.

<https://doi.org/10.1002/9781119424437.ch3>

Johnston, S., Holbrook, J. (2019) Toggling between expansion and translation: The generation of a muddy-normal point bar with an earthquake imprint. In M. Ghinassi, L. Colombera, N.P. Mountney, A.J. Reesink (Eds.), *Fluvial meanders and their sedimentary products in the rock record*. International Association of Sedimentologists Special Publication, 48, 47-80.

<https://doi.org/10.1002/9781119424437.ch3>

Jordan O.D., Mountney N.P. (2010) Styles of interaction between aeolian, fluvial and shallow marine environments in the Pennsylvanian to Permian lower Cutler beds, south-east Utah, USA. *Sedimentology*, 57(5), 1357-1385

<https://doi.org/10.1111/j.1365-3091.2010.01148.x>

Journel A.G., Deutsch C.V., Desbarats A.J (1986) Power averaging for block effective permeability. SPE paper presented at SPE California regional meeting, California, SPE paper 151282.

<https://doi.org/10.2118/15128-MS>

Journel A.G. Alabert F.G. (1990) New method for reservoir mapping. *Journal of Petroleum Technology* 42(2), 212-218

<https://doi.org/10.1023/A:1007563907124>

Journel, A.G. (1993) Geostatistics: Roadblocks and challenges. In Soares, A., ed., *Geostatistics: Troia '92*, Kluwer Academic, 5, 213-224.

https://doi.org/10.1007/978-94-011-1739-5_18

Journel, A. (2002) Combining knowledge from multiple information sources: An alternative to traditional data independence hypotheses. *Mathematical Geology*, 34(5), 573-596.

<https://doi.org/10.1023/A:1016047012594>

Journel, A.G. and Zhang, T. (2006) The necessity of a multiple-point prior model. *Mathematical Geology*, 38(5), 591-610.

<https://doi.org/10.1007/s11004-006-9031-2>

Juanes, R., Spiteri, E.J., Orr, F.M., and Blunt, M.J. (2006) Impact of relative permeability hysteresis on geological CO₂ storage, *Water Resources Research*, 42(12).

<https://doi.org/10.1029/2005WR004806>

Kearey P., Brooks M., Hill I. (2013) *An Introduction to Geophysical Exploration* John Wiley & Sons. 288pp.

Kelkar M. and Perez G. (2002) *Applied geostatistics for reservoir characterization*, Society of Petroleum Engineers, 264pp.

Keogh, K.J., Martinius, A.W., Osland, R. (2007) The development of fluvial stochastic modelling in the Norwegian oil industry: a historical review, subsurface implementation and future directions. *Sedimentary Geology*, 202(1-2), 249-268.

<https://doi.org/10.1016/j.sedgeo.2007.05.009>

Keogh, K. J., Leary, S. (2014) Data capture for multiscale modelling of the Lourinha~ Formation, Lusitanian Basin, Portugal: an outcrop analogue for the Staffjord Group, Norwegian North Sea. *Geological Society, London, Special Publications*, 387(1), 27-56.

<http://dx.doi.org/10.1144/SP387.11>

King M.J., Mansfield M. (1999) Flow simulation of geologic models. *SPE Reservoir Evaluation Engineering*, 2(4), 351-367.

<https://doi.org/10.2118/57469-PA>

Kinsman, D.J.J. (1975) Rift valley basins and sedimentary history of trailing continental margins, in Fischer, A.G. and Judson, S., eds., *Petroleum and global tectonics*. Princeton, NJ, Princeton University Press, 83-126.

Kirk, M. (1983) Bar development in a fluvial sandstone (Westphalian 'A'), Scotland. *Sedimentology*, 30 (5), 727-742.

<https://doi.org/10.1111/j.1365-3091.1983.tb00706.x>

Klinkenberg, L.J. (1941) *The Permeability of Porous Media to Liquids and Gases*. Drilling and Production Practice, New York, API-41-200.

Kozeny, J. (1927) Ueber kapillare Leitung des Wassers im Boden. *Sitzungsber Akad. Wiss., Wien*, 136(2A), 271-306.

Krevor S.C.M., Pini R., Zuo L., Benson S.M. (2012) Relative permeability and trapping of CO₂ and water in sandstone rocks at reservoir conditions. *Water Resources Research*, 48(2), W02532.

<https://doi.org/10.1029/2011WR010859>

Krishnan, S., Boucher, A., Journel, A. (2004) Evaluating Information Redundancy through the TAU model. *Geostatistic Banff*, 1037-1046.

https://doi.org/10.1007/978-1-4020-3610-1_108

Krige, D.G. (1951a) A Statistical Approach to Some Mine Valuation and Allied Problems on the Witwatersrand. MSc (Eng) thesis, Univ. of the Witwatersrand, Johannesburg.

Krynine, P.D. (1948) The megascopic study and field classification of sedimentary Rocks. *Journal of Geology*, 56, 130-165.
<https://doi.org/10.1086/625492>

Kumar, A., Sah, B., Singh, A.R., Deng, Y., He, X., Kumar, P., Bansal, R.C. (2017) A review of multi criteria decision making (MCDM) towards sustainable renewable energy development. *Renewable and Sustainable Energy Reviews*, 69, 596-609.
<https://doi.org/10.1016/j.rser.2016.11.191>

Labourdette, R. (2011) Stratigraphy and static connectivity of braided fluvial deposits of the lower Escanilla Formation, south central Pyrenees, Spain. *American Association of Petroleum Geologists Bulletin*, 95, 585-617.

Labourdette, R. (2008) LOSCS' lateral offset stacked channel simulations: towards geometrical modelling of turbidite elementary channels. *Basin Research*, 20, 431-444.
<https://doi.org/10.1111/j.1365-2117.2008.00361.x>

Lander R. H., Walderhaug O. (1999) Predicting Porosity through Simulating Sandstone Compaction and Quartz Cementation. *AAPG Bulletin*, 83(3), 433-449.

Larsen, J. (2004) The effects of dissolved CO₂ on coal structure and properties. *International Journal of Coal Geology*, 57, 63-70.
<https://doi.org/10.1016/j.coal.2003.08.001>

Larue, D., Hovadik, J. (2006) Connectivity of channelized reservoirs: A modelling approach. *Petroleum Geoscience*, 12(4), 291-308.
<https://doi.org/10.1144/1354-079306-699>

Lasseter, T.J. (2002) A New Approach for the Efficient Construction of 3D Geological Models for Reservoir Applications. Paper E03, Proceedings of the Eighth European Conference on the Mathematics of Oil Recovery, Freiberg, Germany.

Le Coz, M., Genthon, P., and Adler, P.M. (2011) Multiple-point statistics for modelling facies heterogeneities in a porous medium: The Komadugu-Yobe alluvium, Lake Chad Basin, *Mathematical Geoscience*, 43, 861-878.
<https://doi.org/10.1007/s11004-011-9353-6>

Leeder, M.R. (1978) A quantitative stratigraphic model for alluvium, with special reference to channel deposit density and interconnectedness. *Canadian Society of Petroleum Geologists Memoir*, 5, 587-596.

Leopold B. and Wolman M. (1960) River meanders. *Bulletin of the geological society of America*, 71, 769-794.

Leverett M.C. (1941) Capillary behaviour in porous solids. *Transactions of the AIME*, 142, 159-172.

Li, D., Myra A.D. (1997) Cut-off or Separation? A New Approach to Distinguish Reservoir Rock from Non-Reservoir Rock for Reservoir Modeling and Simulation.

SPE paper presented at the SPE Rocky Mountain Regional Meeting, Casper, Wyoming. SPE-38380-MS.

<https://doi.org/10.2118/38380-MS>

Li B., Friedman F. (2005) Novel multiple resolutions design of experiment/response surface methodology for uncertainty analysis of reservoir simulation forecasts. SPE paper presented at the SPE Reservoir Simulation Symposium, The Woodlands, 2005. SPE-92853-MS.

<https://doi.org/10.2118/92853-MS>

Liu, Y., Harding, A., Gilbert, R. and Journel, A.G. (2004) A Workflow for Multiple-point Geostatistical Simulation. In: Leuangthong O. and Deutsch C.V. (eds) Geostatistics Banff 2004. Quantitative Geology and Geostatistics, 14(25), 245-254.

https://doi.org/10.1007/978-1-4020-3610-1_25

Liu, Y. (2006) Using the SNESIM program for multiple-point statistical simulation. Computers & Geosciences, 32(10), 1544-1563.

<https://doi.org/10.1016/j.cageo.2006.02.008>

Liu, Y., Harding, A., Gilbert, R. and Journel, A.G. (2004) A Workflow for Multiple-point Geostatistical Simulation. In: Leuangthong O. and Deutsch C.V. (eds) Geostatistics Banff. Quantitative Geology and Geostatistics, Springer, Dordrecht, 14(25), 245-254.

https://doi.org/10.1007/978-1-4020-3610-1_25

Liu, Y. (2006) Using the SNESIM program for multiple-point statistical simulation. Computers & Geosciences, 32(10), 1544-1563.

<https://doi.org/10.1016/j.cageo.2006.02.008>

Lucia, F., Kerans C., Jennings J. (2013) Carbonate Reservoir Characterization. Journal of Petroleum Technology, 55, 70-72.

<https://doi.org/10.2118/82071-JPT>

Lunt, I. A., Bridge, J.S., Tye, R.S. (2004) A quantitative, three-dimensional depositional model of gravelly braided rivers. Sedimentology, 51, 377-414.

<https://doi.org/10.1111/j.1365-3091.2004.00627.x>

Luthi, S.M., Flint, S.S. (2013) The application of outcrop-based research boreholes for reservoir modelling: potential, challenges and pitfalls. In: Martinus, A. W., Howell, J. A. & Good, T. R. (eds) Sediment- Body Geometry and Heterogeneity: Analogue Studies for Modelling the Subsurface. Geological Society, London, Special Publications, 387, 233-246.

<https://doi.org/10.1144/SP387.6>

Ma, S., Zeybek, M.M., and Kuchuk, F. (2014) Static, dynamic data integration improves reservoir modeling, characterization. Oil & Gas Journal, 112(9), 82-82.

Ma, Y. Zee (2019) Quantitative Geosciences: Data Analytics, Geostatistics, Reservoir Characterization and Modeling. Springer Cham, 640pp.

<https://doi.org/10.1007/978-3-030-17860-4>

Mackey, S.D., Bridge, J.S. (1995). Three-dimensional model of alluvial stratigraphy; theory and applications. Journal of Sedimentary Research, 65(1B), 7-31.

<https://doi.org/10.1306/D42681D5-2B26-11D7-8648000102C1865D>

Maharaja, A., (2008) Tgenerator: Object-based training image generator. *Computers Geosciences*, 34(12), 1753-1761.

<https://doi.org/10.1016/j.cageo.2007.08.012>

Mallet J.L. (2008) *Numerical earth models*. European Association of Geoscientists and Engineers (EAGE), Houston, 147.

Manchuk, J.G., Lyster, S.J. and Deutsch, C.V. (2011) A Comparative Study of Simulation Techniques with Multiple Point Statistics: The MPS Beauty Contest. CCG Annual Report 13, Paper 107.

Mariethoz G., Caers J. (2015) *Multiple-point geostatistics: stochastic modeling with training images*. Wiley Library, 364pp.

<https://10.1002/9781118662953>

Mariethoz, G., Renard, P. and Straubhaar, J. (2010) The Direct Sampling method to perform multiple point geostatistical simulations. *Water Resources Research*, 46(11), 1-14.

<https://doi.org/10.1029/2008WR007621>

Marshak, S. (2009) *Essentials of Geology* (3rd ed.). W.W. Norton & Company, 628pp.

Marzo, M., Puigdefabregas, C. (eds) *Alluvial Sedimentation*. International Association of Sedimentologists, Special Publications, 17, 337-362.

<https://doi.org/10.1002/9781444303995.ch23>

Matheron, G. (1960) *Traite de geostatistique appliquee*, tome 1. *Memoires de Bureau de Recherches Geologiques et Minières*, no. 14. Editions Technip, Paris. English translation: *Treatise on Applied Geostatistics*, Kennecott Copper Corporation, Salt Lake City, Utah.

Matheron G (1963) Principles of geostatistics. *Economic Geology* 58(8), 1246–1266

<https://doi.org/10.2113/gsecongeo.58.8.1246>

Mattax, C.C. and Dalton, R.L. (1990) *Reservoir Simulation*, Society of Petroleum Engineers, SPE Monograph, 13.

Maučec, M., Yarus, J., Chambers, R. and Shi, G. (2011) Modeling of Reservoir Properties with Grid-less Continuity Field Interpolation. Ninth International Geostatistics Congress, Oslo.

<http://geostats2012.nr.no/pdfs/1745375.pdf>

Maxwell J.C. (1964) Influence of depth, temperature, and geologic age on porosity of quartzose sandstone *American Association Petroleum Geological Bulletin*, 48, 697-709.

McDonnell, K.L. (1978) Transition matrices and the depositional environments of a fluvial sequence. *Journal of Sedimentary Research*, 48(1), 43-48.

<https://doi.org/10.1306/212F73F1-2B24-11D7-8648000102C1865D>

Medici G., West L.J., Mountney N.P. (2019) Sedimentary flow heterogeneities in the Triassic U.K. Sherwood Sandstone Group: Insights for hydrocarbon exploration. *Geological Journal Ruffell A* (eds.), 54(3), 1361-1378

<https://doi.org/10.1002/gj.3233>

Meerschman E., Pirot G., Mariethoz G., Straubhaar J., Van Meirvenne M. and Renard, P. (2013) A practical guide to performing multiple-point statistical simulations with the Direct Sampling algorithm. *Computers & Geosciences*, 52(28), 307-324.
<https://doi.org/10.1016/j.cageo.2012.09.019>

Meyer, R., Krause, F.F. (2006) Permeability Anisotropy and Heterogeneity of a Sandstone Reservoir Analogue: An Estuarine to Shoreface Depositional System in the Virgelle Member, Milk River Formation, Writing-on-Stone Provincial Park, Southern Alberta. *Bulletin of Canadian Petroleum Geology*, 54, 301-318.
<https://doi.org/10.2113/gscpgbull.54.4.301>

Miall, A.D. (1977) Lithofacies Types and Vertical Profile Models in Braided River Deposits: A Summary. In: Miall, A.D., Ed., *Fluvial Sedimentology*, Geological Survey of Canada, Calgary, 597-604.

Miall, A.D. (1978) Lithofacies Types and Vertical Profile Models in Braided River Deposits: A Summary. In: Miall, A.D., Ed., *Fluvial Sedimentology*, Memoir 5, Canadian Society of Petroleum Geologists, Calgary, 597-604.

Miall, A.D. (1985) Architectural-Element Analysis: A New Method of Facies Analysis Applied to Fluvial Deposits. *Earth-Science Reviews*, 22(4), 261-308.
[http://dx.doi.org/10.1016/0012-8252\(85\)90001-7](http://dx.doi.org/10.1016/0012-8252(85)90001-7)

Miall, A.D. (1988) Architectural elements and bounding surfaces in fluvial deposits: anatomy of the Kayenta Formation (Lower Jurassic), southwest Colorado. *Sedimentary Geology*, 55(3-4), 233-262.
[https://doi.org/10.1016/0037-0738\(88\)90133-9](https://doi.org/10.1016/0037-0738(88)90133-9).

Miall, A.D., Tyler, N. (1991) The Three-Dimensional Facies Architecture of Terrigenous Clastic Sediments and its Implications for Hydrocarbon Discovery and Recovery. *Journal of Petroleum Science and Engineering*, 8(3), 237-238.
<https://doi.org/10.2110/pec.87.40.0333>

Miall, A.D. (1996) *The Geology of Fluvial Deposits. Sedimentary Facies, Basin Analysis and Petroleum Geology*. Springer, 582pp.
<https://doi.org/10.1007/978-3-662-03237-4>

Miall, A.D. (2014) *Fluvial Depositional Systems*. Springer, 317pp.
<https://doi.org/10.1007/978-3-319-00666-6>

Miall, A.D. (2016) *Stratigraphy: A Modern Synthesis*. Springer, 454pp.
<https://doi.org/10.1007/978-3-319-24304-7>

Milliken W.J., Levy M., Strebelle S.B., Zhang Y. (2008) The effect of geologic parameters and uncertainties on subsurface flow: deepwater depositional systems. SPE Western Regional and Pacific Section AAPG Joint Meeting, SPE 114099.
<https://doi.org/10.2118/114099-MS>

Mintzberg H. (1990) The design school: reconsidering the basic premises of strategic management. *Strategic Management Journal*, 11(3), 171-195.

Mirzadeh, S., Chambers, R., Carvajal G., Singh, A, Maučec M., Knabe, Al-Jasmi S., Ismail D., (2014) Reservoir Simulation Design Strategy for Next-Generation Multi-level Assisted History Matching, 4, 10.2523/17518-MS.
<https://www.istor.org/stable/2486485>

Mitten, A.J., Mullins J., Pringle J.K., Howel J.K., Clarke S.M. (2020) Depositional conditioning of three-dimensional training images: improving the reproduction and representation of architectural elements in sand-dominated fluvial reservoir models." *Marine and Petroleum Geology*, 113, 104156.

<https://doi.org/10.1016/j.marpetgeo.2019.104156>

Montero, J., Zhang J., Baines G. (2019) Rapid Lithology Interpretation From wireline data. *Exploration Insights* (Halliburton, Landmark): Predicting into the Unknown with source-to-sink scaling relationship. October edition.

<https://joom.ag/7r0e/p20>

Montero J.M., Colombera L., Yan, N., Mountney N.P. (2021) A workflow for modelling fluvial meander-belt successions: Combining forward stratigraphic modelling and multi-point geostatistics, *Journal of Petroleum Science and Engineering*, 201, 108411.

<https://doi.org/10.1016/j.petrol.2021.108411>

Mountney N.P., Howell J., Flint S., Jerram D.A. (1998) Aeolian and alluvial deposition within the Mesozoic Etjo Sandstone Formation, northwest Namibia. *Journal of African Earth Sciences*, 27, 175-192.

[https://doi.org/10.1016/S0899-5362\(98\)00056-6](https://doi.org/10.1016/S0899-5362(98)00056-6)

Mountney N.P., Heme de La Cote VJP (2022) A classification scheme for sedimentary architectures arising from aeolian-fluvial system interactions: Permian examples from southeast Utah, USA. *Aeolian Research*, 58, 100815.

<https://doi.org/10.1016/j.aeolia.2022.100815>

Moodie, N., Pan, F., Jia, W., McPherson, B. (2016) Impacts of relative permeability formulation on forecasts of CO₂ phase behavior, phase distribution, and trapping mechanisms in a geologic carbon storage reservoir. *Greenhouse Gases: Science and Technology*, 7, 241-258.

<https://doi.org/10.1002/ghg.1610v>

Moore, P.S., Burns, B.J., Emmett, J.K., and Guthrie, D.A. (1992) Integrated source, maturation and migration analysis, Gippsland Basin, Australia; *The APEA Journal*, 32(1), 313-324.

Morad S., Ketzer J.M., L.F. De Ros (2013) Linking Diagenesis to Sequence Stratigraphy: An Integrated Tool for Understanding and Predicting Reservoir Quality Distribution. *Linking Diagenesis to Sequence Stratigraphy*, 1-36.

Mordensky, S.P., M.C. Villeneuve, B.M. Kennedy, M.J. Heap, D.M. Gravley, J.I. Farquharson, and T. Reuschlé (2018) Physical and mechanical property relationships of a shallow intrusion and volcanic host rock, Pinnacle Ridge, Mt. Ruapehu, New Zealand, *Journal of Volcanology and Geothermal Research* 359, 1-20.

<https://doi.org/10.1007/s00531-015-1263-2>

Moscariello A. (2017) Alluvial fans and fluvial fans at the margins of continental sedimentary basins: Geomorphic and sedimentological distinction for geo-energy exploration and development. *Geological Society London Special Publications* 440(1), SP440.11.

<https://doi.org/10.1144/SP440.11>

Nanda N.C. (2016) *Seismic Data Interpretation and Evaluation for Hydrocarbon Exploration and Production*. Springer, 304pp.

<https://doi.org/10.1007/978-3-030-75301-6>

Nanson, G.C. and Hickin, E.J. (1983) Channel migration and incision on the Beatton River. *Journal of Hydraulic Engineering*, 109(3), 327-337.

[https://doi.org/10.1061/\(ASCE\)0733-9429\(1983\)109:3\(327\)](https://doi.org/10.1061/(ASCE)0733-9429(1983)109:3(327))

Nanson, G.C. and Page, K. (1983) Lateral Accretion of Fine-Grained Concave Benches on Meandering Rivers. In *Modern and Ancient Fluvial Systems* (eds J.D. Collinson and J. Lewin).

<https://doi.org/10.1002/9781444303773.ch10>

Nghiem, L., Collins, D.A., and Sharma, R. (1991) Seventh SPE Comparative Solution Project: Modelling of Horizontal Wells in Reservoir Simulation. SPE Symposium on Reservoir Simulation, Anaheim, California, SPE-21221-MS.

<http://dx.doi.org/10.2118/21221-MS>

Nguyen M., Zhang X., Ning W., Jun L., Xiaochun L., Zhang Y., Philip S. (2017) An object-based modeling and sensitivity analysis study in support of CO₂ storage in deep saline aquifers at the Shenhua site, Ordos Basin. *Geomechanics and Geophysics for Geo-Energy and Geo-Resources*, 3, 293-314.

<https://doi.org/10.1016/j.esr.2018.08.003>

Nichols, G. (2009) *Sedimentology and Stratigraphy* Second Edition. West Sussex: John Wiley & Sons Ltd, 432pp.

Nielsen, L.H., Johannessen, P.N. (2001) Accretionary, forced regressive shoreface sands of the Holocene-Recent Skagen Odde spit complex, Denmark: a possible outcrop analogue to fault-attached shoreface sandstone reservoirs. In: Martinsen, O.J., Dreyer, T. (Eds.), *Sedimentary Environments Offshore Norway Palaeozoic to Recent*, Norwegian Petroleum Society Special Publications, 10, 457-472.

[https://doi.org/10.1016/S0928-8937\(01\)80028-X](https://doi.org/10.1016/S0928-8937(01)80028-X)

Norouzi A., Gluyas J., Babaei M. (2022) CO₂-plume geothermal in fluvial formations: A 2D numerical performance study using subsurface metrics and upscaling, *Geothermics*, 99(4), 40-54.

<https://doi.org/10.1016/j.geothermics.2021.102287>

Nordahl, K., Ringrose, P.S., Wen, R. (2005) Petrophysical characterization of a heterolithic tidal reservoir interval using a process-based modeling tool. *Petroleum Geoscience*, 11, 17–28.

<https://doi.org/10.1144/1354-079303-613>

Nordahl, K., Ringrose, P., Wen, R. (2005) Petrophysical characterization of a heterolithic tidal reservoir interval using a process-based modelling tool. *Petroleum Geoscience*, 11(1), 17-28.

<https://doi.org/10.1144/1354-079303-613>

Nordahl, K., Messina, C., Berland, H., Rustad, A.B., Rimstad, E. (2014) Impact of multiscale modelling on predicted porosity and permeability distributions in the fluvial deposits of the Upper Lunde Member (Snorre Field, Norwegian Continental Shelf). In: Martinius, A. W., Howell, J. A. & Good, T. R. (eds) *Sediment-Body Geometry and Heterogeneity: Analogue Studies for Modelling the Subsurface*. Geological Society, London, Special Publications, 387(1), 85.

<http://dx.doi.org/10.1144/SP387.10>

North, C.P. (1996) The prediction and modelling of subsurface fluvial stratigraphy. *Advances in Fluvial Dynamics and Stratigraphy* (Eds P.A. Carling and M.R. Dawson), Chichester, UK. John Wiley & Sons, 395-508.

North, C.P., Davidson, S.K. (2012) Unconned alluvial ow processes: recognition and interpretation of their deposits, and the significance for palaeogeographic reconstructions. *Earth-Science Reviews*, 111(1-2), 199-223.

<https://10.1016/j.earscirev.2011.11.008>

O'Brien, G.W., Tingate, P.R., Divko G., Harrison, M.L., Boreham, C., Keyu L., Arian, N., Skladzien, P. (2007) First order sealing and hydrocarbon migration processes, Gippsland Basin, Australia: Implications for CO₂ geosequestration. *PESA Eastern Australasian Basins Symposium III*, 1-28.

Office for National Statistics, 2023

<https://www.ons.gov.uk/>

Olea E. (1999) *Geostatistics for Engineers and Earth Scientists*, Kluwer Academic Publishers, 303pp.

<https://doi.org/10.1080/00401706.2000.10485748>

Oliver, D.S., Reynolds, A.C., Liu, N. (2008) *Inverse Theory for Petroleum Reservoir Characterization and History Matching*. Cambridge University Press, Cambridge, 394pp.

<https://doi.org/10.1017/CBO9780511535642>

Olsen, H., (1989) Sandstone-body structures and ephemeral stream processes in the Dinosaur Canyon Member, Moenave Formation (Lower Jurassic), Utah, U.S.A. *Sedimentary Geology*, 61, 207-221.

[https://doi.org/10.1016/0037-0738\(89\)90058-4](https://doi.org/10.1016/0037-0738(89)90058-4)

Omre, H. (1991) Stochastic models for reservoir characterization, in Kleppe, J., Skjaeveland, S.M., eds., *Recent advances in improved oil recovery, methods for North Sea Sandstones reservoirs*, Norwegian Petroleum Directorate, Stavanger, Norway.

Orton, G.J., Reading, H.G. (1993) Variability of deltaic processes in terms of sediment supply, with particular emphasis on grain size. *Sedimentology*, 40(3), 475-512.

<https://doi.org/10.1111/j.1365-3091.1993.tb01347.x>

Oscar E. (1923) *Outline of ground-water hydrology, with definitions*. USGS Numbered Series, 494.

<https://10.3133/wsp494>

Pan, J.G.S., (2000) Integrated 3D seismic inversion and volume visualization for reservoir characterization and reserve estimation. *SEG Technical Program Expanded Abstracts*, 1489-1492.

<https://doi.org/10.1190/1.1815688>

Peng C.Y., Gupta R. (2005) Experimental design and analysis methods in multiple deterministic modelling for quantifying hydrocarbon in place probability distribution curve. SPE paper presented at SPE Asia Pacific conference on Integrated Modelling for Asset Management, Kuala Lumpur. SPE-87002-MS

<https://doi.org/10.2118/87002-MS>

Pettijohn, F.J., Potter, P.E. and Siever, R. (1973) Sand and Sandstones. Springer Verlag, New York, 553pp.

<https://doi.org/10.1007/978-1-4612-1066-5>

Petroconsultants (1996) Petroleum Exploration and Production Database. Petroconsultants Inc., [database available from Petroconsultants, Inc., P.O. Box 740619, Houston, TX 77274-0619]

Pickup, G.E., Ringrose, P.S., Forrester, M. M., Jensen, J.L., and Sorbie, K.S., (1994) The Geopseudo Atlas: Geologically based upscaling of multiphase flow. Paper presented at the European Petroleum Computer Conference, Aberdeen, UK, SPE 27565, 277-289.

<https://doi.org/10.2118/27565-MS>

Pickup G. E., Ringrose P.S., Corbett P.W.M., Jensen J.L., Sorbie K.S. (1995) Geology, geometry and effective flow. *Petroleum Geoscience* 1(1), 37-42.

<https://doi.org/10.1144/petgeo.1.1.37>

Pickup G.E. and Stephen K.S. (2000) An assessment of steady state scale-up for small-scale geological models. *Petroleum Geoscience*, 6(3), 203-210.

<https://doi.org/10.1144/petgeo.6.3.203>

Pickup G.E., Ringrose P.S., Sharif A. (2002) Steady-state upscaling: from lamina-scale to full-field model. *SPE J5*, 208-217

<https://doi.org/10.2118/62811-PA>

Pola A., Crosta G.B, Fusi N., Castellanza, R. (2014) General characterization of the mechanical behaviour of different volcanic rocks with respect to alteration. *Engineering Geology*, 169, 1-13.

<https://doi.org/10.1016/j.enggeo.2013.11.011>

Posamentier, H.W. (2001) Lowstand alluvial bypass systems: incised vs unincised. *AAPG Bulletin*, 85(10), 1771-1793

<https://doi.org/10.1306/8626D06D-173B-11D7-8645000102C1865D>

Posamentier, H.W. and Allen, G.P. (1999) Siliciclastic Sequence Stratigraphy: Concepts and Applications. *Geological Magazine*, 138(5), 619-630.

<https://doi.org/10.2110/csp.99.07>

Potter, P.E. (1967) Sand bodies and sedimentary environments: a review: *American Association of Petroleum Geologists Bulletin*, 51, 337-365.

Pourfard, M., Abdollahifard, M.J., Faez, K., Motamedi, S.A., Hosseinian T. (2016) PCTO-SIM: Multiple-point geostatistical modeling using parallel conditional texture optimization. *Computers & Geosciences*, 102, 116-138.

<https://doi.org/10.1016/j.cageo.2016.12.012>

Pranter, M.J., Hewlett, A.C., Cole, R.D., Wang, H., Gilman, J. (2013) Fluvial architecture and connectivity of the Williams Fork Formation: use of outcrop analogues for stratigraphic characterization and reservoir modelling. In: Martinius, A. W., Howell, J. A. & Good, T. R. (eds) *Sediment-Body Geometry and Heterogeneity: Analogue Studies for Modelling the Subsurface*. Geological Society, London, Special Publications, 387(1), 57-83.

<http://dx.doi.org/10.1144/SP387.1>

Priddy, C.L. and Clarke, S.M. (2021) Spatial variation in the sedimentary architecture of a dryland fluvial system. *Sedimentology*, 68, 2887-2917.

<https://doi.org/10.1111/sed.12876>

Puig J.M., Cabello P., Howell J., Arbués P. (2019) Three-dimensional characterisation of sedimentary heterogeneity and its impact on subsurface flow behaviour through the braided-to-meandering fluvial deposits of the Castissent Formation (late Ypresian, Tremp-Graus Basin, Spain). *Marine and Petroleum Geology*, 103, 661-680.

<https://doi.org/10.1016/j.marpetgeo.2019.02.014>

Pyrzcz M. J. and Deutsch, C. V. (2002) *Geostatistical Reservoir Modeling*. Oxford University Press, New York, 376 pp.

Pyrzcz, M.J., Boisvert, J.B. and Deutsch, C.V. (2008) A library of training images for fluvial and deepwater reservoirs and associated code. *Computers & Geosciences*, 34(5), 542–560.

<https://doi.org/10.1016/j.cageo.2007.05.015>

Pyrzcz, M.J., Boisvert, J.B. and Deutsch, C.V. (2008) A library of training images for fluvial and deepwater reservoirs and associated code. *Computers & Geosciences*, 34(5), 542-560.

<https://doi.org/10.1016/j.cageo.2007.05.015>

Pyrzcz, M.J., and Deutsch, C.V. (2014) *Geostatistical Reservoir Modeling*. Second Edition. Oxford University Press, 448pp

https://doi.org/10.1007/978-94-011-1739-5_12

Pyrzcz, M.J., White, C.D. (2015) Uncertainty in reservoir modeling. *Interpretation*, 3(2), 7-19.

<https://doi.org/10.1190/INT-2014-0126.1>

Quinn, M. (2022) Carbon capture and storage: a review of Australian projects. *APPEA Journal* 62(1) 334-341.

<https://doi.org/10.1071/AJ21161>

Ramm M. (1992) Porosity depth trends in reservoir sandstones; Theoretical models related to Jurassic sandstones offshore Norway. *Marine Petroleum Geology*, 9(5), 553-567.

[https://doi.org/10.1016/0264-8172\(92\)90066-N](https://doi.org/10.1016/0264-8172(92)90066-N)

Ramm, M., Bjørlykke, K. (1994) Porosity/depth trends in reservoir sandstones: Assessing the quantitative effects of varying pore-pressure, temperature history and mineralogy, Norwegian Shelf data. *Clay Minerals*, 29(4), 475-490.

<https://doi:10.1180/claymin.1994.029.4.07>

Rasmussen A. F., Sandve T., Kai B., Lauser A., Hove J., Skaflestad B., Klöfkorn R., Blatt M., Rustad A., Sævareid O., Knut-Andreas L., Thune A. (2012) The Open Porous Media Flow reservoir simulator. *Computers & Mathematics with Applications*, 81, 159-185.

<https://doi.org/10.1016/j.camwa.2020.05.014>

Reading, H.G. (1986) *Sedimentary Environments and Facies*. Blackwell Scientific Publications, 615pp.

Reading, H.G. (2001) Clastic Facies Models: A Personal Perspective. *Bulletin of the Geologic Society of Denmark*, 48, 101-125.

Remy, N., Boucher, A. and Wu, J. (2009) *Applied Geostatistics with SGEMS. A user's guide*. Cambridge University Press, 264pp.
<https://doi.org/10.1017/CBO9781139150019>

Renard, P.H., de Marsily G. (1997) Calculating equivalent permeability: a review. *Advances in Water Resources*, 20(5-6), 253-278.
[https://doi.org/10.1016/S0309-1708\(96\)00050-4](https://doi.org/10.1016/S0309-1708(96)00050-4)

Riaz, A., Cinar, Y. (2014) Carbon dioxide sequestration in saline formations: part I. Review of the modeling of solubility trapping. *Journal of Petroleum Science and Engineering* 124, 367-380.
<https://doi.org/10.1016/j.petrol.2014.07.024>

Ringrose P.S. (2008) Total-property modeling: dispelling the net-to-gross myth. *SPE Reservoir Evaluation and Engineering*, 11, 866-873.
<https://doi.org/10.2118/106620-PA>

Ringrose P., Roberts D.M., Raikes S., Gibson-Poole C., Iding M., Østmo S., Taylor M., Bond C., Wightman R., Morris J. (2011) Characterisation of the Krechba CO₂ storage site: critical elements controlling injection performance. *Energy Procedia*, 4, 4672-4679.
<https://doi.org/10.1016/j.egypro.2011.02.428>

Ringrose, P., Bentley, M. (2015) *Reservoir Model Design: A practitioner's guide*. Springer Science & Business Media B.V., Berlin. 260pp.
<https://doi.org/10.1007/978-94-007-5497-3>

Riordan, S. J., Lang S. C. and Payenberg, T. (2004) Sequence stratigraphy of the intra-Latrobe Group, Flounder Field, Gippsland Basin. Implications for the building and upscaling of 3D geological models. *PESA Eastern Australasian Basins Symposium II*, 523-536.

Riou, J., and Hocker C. (2015) Practical recommendations for successful application of the MPS facies modelling method. SPE Paper presented at the Abu Dhabi International Petroleum Exhibition and Conference, Abu Dhabi, UAE. SPE-177675-MS.
<https://doi.org/10.2118/177675-MS>

Rittersbacher, A., Buckley, S.J., Howell, J.A., Hampson, G.J., Vallet, J. (2013) Helicopter-based laser scanning: a method for quantitative analysis of large-scale sedimentary architecture. In: Martinius, A. W., Howell, J. A. & Good, T. R. (eds) *Sediment-Body Geometry and Heterogeneity: Analogue Studies for Modelling the Subsurface*. Geological Society, London, Special Publications, 387(1), 185.
<http://dx.doi.org/10.1144/SP387.3>

Rojas, T., Demyanov, V., Christie, M., Arnold, D. (2012) Reducing uncertainty in modelling fluvial reservoirs by using intelligent geological priors. Paper presented at the Ninth Geostatistical Congress, Oslo.
<http://geostats2012.nr.no/pdfs/1747975.pdf>

Russell, C.E., Mountney, N.P., Hodgson, D.M. and Colombera, L. (2019) A novel approach for prediction of lithological heterogeneity in fluvial point-bar deposits from analysis of meander morphology and scroll-bar pattern. In: Ghinassi, M., Colombera,

L., Mountney, N.P. and Reesink, A.J., eds., *Fluvial Meanders and their Sedimentary Products in the Rock Record*. International Association of Sedimentologists, Special Publication, 48, 385-418.

<https://doi.org/10.1002/9781119424437.ch15>

Rust, B.R. (1982) Sedimentation in fluvial and lacustrine environments. In: Sly, P.G. (eds) *Sediment/Freshwater Interaction*. Developments in Hydrobiology, 9, 59-70.

https://doi.org/10.1007/978-94-009-8009-9_6

Rutqvist, J., Vasco, D., Myer, L., (2010b) Coupled reservoir-geomechanical analysis of CO₂ injection at In Salah, Algeria. *International Journal of Greenhouse Gas Control*, 4, 225-230.

Ryseth A., Ramm M. (1996) Alluvial architecture and differential subsidence in the Staffjord Formation, North Sea, prediction of reservoir potential. *Petroleum Geoscience*, 2(3), 271-287.

<https://doi.org/10.1144/petgeo.2.3.271>

Sadigov T., Thiruvankatanathan P., Sheydayev A. (2017) Application of Distributed Acoustic Sensing DAS Technology in Identification and Remediation of Sand Producing Zones in OHGP Completion. SPE paper presented at the SPE Annual Caspian Technical Conference and Exhibition, Baku, Azerbaijan, SPE-188991-MS

<https://doi.org/10.2118/188991-MS>

Santos, S., Schiozer, D. (2017) Assessing the Value of Information According to Attitudes Towards Downside Risk and Upside Potential. 79th EAGE Conference and Exhibition, SPE Europec.

Schlumberger® (2018) Manual “ECLIPSE Reservoir Simulation Software, Technical Description.” Version 2018.1.

Schlumberger® (2018) Manual “Petrel Geology”, “Petrel Advanced”, “Petrel Modelling”. Version 2018.1.

Schumm, S.A., (1963) A Tentative Classification of Alluvial River Channels. U.S. Geological Survey Circular 477, 10pp.

<https://pubs.usgs.gov/circ/1963/0477/report.pdf>

Scherer M. (1987) Parameters influencing porosity in sandstones: A model for sandstone porosity prediction. *American Association of Petroleum Geologist Bulletin*. 71, 485-491.

Sclater J.G., Christie P. (1980) Continental stretching: An explanation of the Post-Mid-Cretaceous Subsidence of the Central North Sea Basin. *Journal of Geophysical Research Atmospheres*, 85(B7), 3711-3739.

<https://DOI:10.1029/JB085iB07p03711>

Selley R.C. (1978) Porosity gradients in the North Sea oil-bearing sandstones. *Journal of Geological Society*. London, 135,119-132

Sengor, A.M.C., Burke, K., and Dewey, J.F. (1978) Rifts at high angles to orogenic belts: tests for their origin and the upper Rhine graben as an example. *American Journal of Science*, 278, 24-40.

Sengor, A.M.C. (1995) Sedimentation and tectonics of fossil rifts, in Busby, C.J., and Ingersoll, R.V., eds., Tectonics of sedimentary basins. Oxford, Blackwell Science, 53-117.

Serra, O. (1986) Fundamentals of Well Log Interpretation, the Interpretation of Logging Data, Elsevier, 684pp.

Serra, O., Serral L. (2007) Well Logging and Reservoir Evaluation. Editions Techhnip, 330pp

Serra, O. (2008) Well Logging Handbook. Editions Techhnip, 609pp.

Serra, O., Serra L. (2010) Well Logging and Geology. Serralog, 436pp.

Shanley, K.W. (2004) Fluvial reservoir description for a giant, low-permeability gas field: Jonah field, Green River Basin, Wyoming, U.S.A., in J. W. Robinson and K. W. Shanley, eds., Jonah field: Case study of a giant tight-gas fluvial reservoir: AAPG Studies in Geology, 52, 159-182.

Sharp M. J. (2003) Heterogeneity of Fluvial Systems--Control on Density-Driven Flow and Transport. February Environmental and Engineering Geoscience 9(1), 5-17.
<https://doi.org/10.2113/9.1.5>

Sheets, B.A., Hickson, T.A. & Paola, C. (2002) Assembling the stratigraphic record: depositional patterns and time-scales in an experimental alluvial basin. Basin Research, 14(3), 287-301.
<https://doi.org/10.1046/j.1365-2117.2002.00185.x>

Shell sustainability report (2019).
<https://reports.shell.com/sustainability-report/2019/>

Shiers M.N., Mountney N.P., Hodgson D.M., Cobain S.L. (2014) Depositional controls on tidally influenced fluvial successions, Neslen Formation, Utah, USA. Sedimentary Geology, 311, 1-16.
<https://doi.org/10.1016/j.sedgeo.2014.06.005>

Shukla R., Ranjith P., Haque A., Choi, X. (2010) A review of studies on CO₂ sequestration and caprock integrity, Fuel, 89(10), 2651-2664,
<https://doi.org/10.1016/j.fuel.2010.05.012>.

Sichel, H.S. (1952) New methods in the statistical evaluation of mine sampling data. Bull. Inst. Min. Metall., 261-288.

Sifuentes, W., Blunt, M.J. and Giddins, M.A. (2009) September. Modeling CO₂ Storage in Aquifers: Assessing the key contributors to uncertainty. In SPE Offshore Europe Conference and Exhibition, SPE-123582
<https://doi.org/10.2118/123582-MS>

Singh V.P., Cavanagh A., Hansen H., Nazarian B., Iding M., Ringrose P.S. (2010) Reservoir modeling of CO₂ plume behaviour calibrated against monitoring data from Sleipner, Norway. SPE paper presented at the SPE Annual Technical Conference and Exhibition, Florence, Italy. SPE-134891-MS.
<https://doi.org/10.2118/134891-MS>

Soleimani, M., Shokri, B.J. (2015) 3D static reservoir modeling by geostatistical techniques used for reservoir characterization and data integration. *Environmental Earth Sciences*, 74(2), 1403-1414.

<https://doi.org/10.1007/s12665-015-4130-3>

Soltanian M.R., Hajirezaie S., Hosseini S.A., Dashtian H., Amooie M.A., Meyal A., Ershadnia R., Ampomah W., Islam A., Zhang X. (2019) Multicomponent reactive transport of carbon dioxide in fluvial heterogeneous aquifers. *Natural Gas Science and Engineering*, 65, 212-223.

<https://doi.org/10.1016/j.ingse.2019.03.011>

Spiteri, E.J., Juanes, R., Blunt, M.J., and F.M. Orr. (2005) Relative Permeability Hysteresis: Trapping Models and Application to Geological CO₂ Sequestration. SPE paper presented at the SPE Annual Technical Conference and Exhibition, Dallas, Texas, SPE-96448-MS.

<https://doi.org/10.2118/96448-MS>

Srivastava, R.M., (1994) An overview of stochastic methods for reservoir characterization. In Yarus, J. M., and Chambers, R. L., eds., *AAPG Computer Applications in Geology No. 3, Stochastic modeling and geostatistics: Principles, methods and case studies*. American Association of Petroleum Geologists, Tulsa, OK, p. 3-16.

Stalker L., Gent D.V., NGL Project Team (2014) South West Hub CCS Project in Western Australia - characterization of a Greenfield site. *Energy Procedia*, 63, 5041-5050.

<https://doi.org/10.1016/j.egypro.2014.11.534>

Stolum H.H. (1996) River meandering as a self-organization process. *Science* 271(22), 1710-1713.

<https://doi.org/10.1126/science.271.5256.1710>

Stonecipher, S. A. (2000) *Applied Sandstone Diagenesis—Practical Petrographic Solutions for a Variety of Common Exploration, Development, and Production Problems*. SEPM Short Course Notes, 143pp.

Straubhaar, J., Renard, P., Mariethoz, G., Froidevaux, R. and Besson, O. (2011) An improved parallel multiple-point algorithm using a list approach. *Mathematical Geosciences*, 43(3), 305-328.

<https://doi.org/10.1007/s11004-011-9328-7>

Straubhaar, J., Walgenwitz, A. and Renard, P. (2013) Parallel Multiple-point Statistics Algorithm Based on List and Tree Structures. *Mathematical Geoscience*, 45(2), 131-147.

<https://doi.org/10.1007/s11004-012-9437-y>

Strebelle, S. (2000) *Sequential Simulation Drawing Structures from Training Images*, Ph.D. thesis, Department of Geological and Environmental Sciences, Stanford University, Stanford.

Strebelle, S., Journel, A. (2001) Reservoir modeling using multiple-point statistics. SPE paper presented at the SPE Annual Technical Conference and Exhibition, New Orleans, Louisiana. SPE-71324-MS

<https://doi.org/10.2118/71324-MS>

Strebelle, S. (2002) Conditional simulation of complex geological structures using multiple-point statistics. *Mathematical Geology*, 34(1), 1-21.

<https://doi.org/10.1023/A:1014009426274>

Strebelle S. (2006) Sequential simulation for modeling geological structures from training images. In: Coburn T.C., Yarus JM, Chambers R.L. (eds) *Stochastic modeling and geostatistics: principles, methods and case studies—volume II: AAPG computer applications in geology*, 5, 139-149.

Strick R.J.P., Ashworth P.J., Awcock G., Lewin J. (2018) Morphology and spacing of river meander scrolls. *Geomorphology*, 310, 57-68.

<https://doi.org/10.1016/j.geomorph.2018.03.005>.

Summerfield, M. A. (1987) Neotectonics and landform genesis. *Progress in Physical Geography: Earth and Environment*, 11(3), 384-397.

<https://doi.org/10.1177/030913338701100305>

Sun, X., Alcalde, J., Bakhtbidar, M., Elío, J., Vilarrasa, V., Canal, J., Ballesteros, J., Heinemann, N., Haszeldine, S., Cavanagh, A., Vega-Maza, D., Rubiera, F., Martínez-Orio, R., Johnson, G., Carbonell, R., Marzan, I., Travé, A., Gomez-Rivas, E., (2021a) Hubs and clusters approach to unlock the development of carbon capture and storage – Case study in Spain. *Applied Energy*, 300, 117418.

<https://doi.org/10.1016/j.petrol.2021.108411>

Sun, X., Gomez-Rivas, E., Cruset, D., Alcalde, J., Munoz-Lopez, D., Cantarero, I., Martín-Martín, J.D., John, C.M., Trave, A., (2022) Origin and distribution of calcite cements in a folded fluvial succession: The Puig-reig anticline (south-eastern Pyrenees). *Sedimentology*, 69, 2319-2347.

<https://onlinelibrary.wiley.com/doi/10.1111/sed.12994>

Sun X., Cao Y., Liu K., Alcalde J., Cabello P., Travé A., Cruset D., Gomez-Rivas E. (2023) Effects of fluvial sedimentary heterogeneity on CO₂ geological storage: Integrating storage capacity, injectivity, distribution and CO₂ phases, *Journal of Hydrology*, 617, 128936.

<https://doi.org/10.1016/j.jhydrol.2022.128936>

Tahmasebi P, Sahimi M (2015a) Reconstruction of nonstationary disordered materials and media: watershed transform and cross-correlation function. *Physical Review E*, 91, 32401.

<https://doi.org/10.1103/PhysRevE.91.032401>

Tahmasebi, P. (2018) Multiple Point Statistics: A Review. In: Daya Sagar, B., Cheng, Q., Agterberg, F. (eds) *Handbook of Mathematical Geosciences*. Springer, Cham, 613-643.

https://doi.org/10.1007/978-3-319-78999-6_30

Tarek A. G., Ganat O. (2020) *Petroleum Reservoir Analogues*. Springer Briefs in Applied Sciences and Technology book series, 94pp.

<https://doi.org/10.1007/978-3-030-45250-6>

Tchelepi H.A., Jenny P., Lee C., Wolfsteiner C. (2005) An adaptive multiscale finite volume simulator for heterogeneous reservoirs. SPE paper presented at the SPE reservoir simulation symposium, The Woodlands, Texas, SPE-93395-MS.

<https://doi.org/10.2118/93395-MS>

Tiab D. and Donaldson E.C. (2003) *Petrophysics: Theory and Practice of Measuring Reservoir Rock and Fluid Transport Properties: Second Edition*. Gulf Professional Publishing – Elsevier, 894pp.

<https://doi.org/10.1016/C2014-0-03707-0>

Thomas, R.G., Smith, D.G., Wood, J.M., Visser, J., Calverley-Range, E.A. and Koster, E.H. (1987) Inclined heterolithic stratification — terminology, description, interpretation and significance. *Sedimentary Geology*, 53(2), 123-179.

[https://doi.org/10.1016/S0037-0738\(87\)80006-4](https://doi.org/10.1016/S0037-0738(87)80006-4)

Thorntwaite C.W. (1931) The Climates of North America: According to a New Classification. *Geographical Review*, 21, 4, 633-655

<https://www.jstor.org/stable/i210646>

Towler B.F. (2002) *Fundamental principles of reservoir engineering*, SPE textbook series. Richardson, Tex.: Henry L. Doherty Memorial Fund of AIME, Society of Petroleum Engineers, 8, 232.

Tyler, N. and Findley, R.J. (1991) Architectural controls on the recovery of hydrocarbons from sandstone reservoirs. In: Miall, A.D., Tyler, N. (Eds.), *The Three-dimensional Facies Architecture of Terrigenous Clastic Sediments and Its Implications for Hydrocarbon Discovery and Recovery*. Concepts in Sedimentology and Palaeontology. Society for Sedimentary Geology. SEPM (Society for Sedimentary Geology), 1-5.

<https://doi.org/10.2110/csp.91.03.0001>

Tyson S. (2007) *An Introduction to Reservoir Modeling*. Piper's Ash Ltd., 238pp.

Tye, R.S. (2004) Geomorphology: An approach to determining subsurface reservoir dimensions. *American Association of Petroleum Geologists Bulletin*, 88(8), 1123-1147.

Tucker M.E. (1996) *Sedimentary Rocks in the Field*, 2nd ed. The Geological Field Guide Series. John Wiley & Sons, 153pp.

United Nations Climate Change.

<https://unfccc.int/>

Va P.R., R.M. Mitchum, Jr., S. Thompson, S. (1977) Seismic Stratigraphy and Global Changes of Sea-Level, Part 2: The Depositional Sequence as a Basic Unit for Stratigraphic Analysis. In: Payton, C.E., Ed., *Seismic Stratigraphy—Applications to Hydrocarbon Exploration*, American Association of Petroleum Geologists Memoir, 26, 53-62.

<https://doi.org/10.1306/M26490C5>

Van de Lageweg, W.I., Schuurman, F., Cohen, K.M., van Dijk, W.M., Shimizu, Y. and Kleinhans, M.G. (2016) Preservation of meandering river channels in uniformly aggrading channel belts. *Sedimentology*, 63, 586-608.

<https://doi.org/10.1111/sed.12229>

Van Genuchten, M.T. (1980) A Closed-Form Equation for Predicting the Hydraulic Conductivity of Unsaturated Soils. *Soil Science Society of America Journal*, 44, 892-898.

<https://doi.org/10.2136/sssaj1980.03615995004400050002x>

Van Wagoner J.C., Mitchum R.M., Campion K.M., Rahmanian V.D. (1990) Siliciclastic sequence stratigraphy in well logs, core, and outcrops: concepts for high-resolution correlation of time and facies. American Association of Petroleum Geologists Methods in Exploration Series, 7,55.

Vakarelov, B.K., Ainsworth, R.B. and Nanson, R.A. (2010) A Novel Database-Driven Approach to Shallow Marine Classification: Towards Building a Knowledge Base. AAPG New Orleans.

Vakarelov B.K. and Ainsworth B.R. (2013) A hierarchical approach to architectural classification in marginal-marine systems: Bridging the gap between sedimentology and sequence stratigraphy. APPG Bulletin, 97(7), 1121-1161.
<https://doi.org/10.1306/11011212024>

Voormeij, D., Simandl, G. (2003) Geological and Mineral CO₂ Sequestration Options: A Technical Review, 1, 265-275.

Wackernagel, H. (2003) Multivariate Geostatistics, Springer, 388pp.
<https://doi.org/10.1007/978-3-662-05294-5>

Wakefield O.J.W., Mountney N.P. (2013) Stratigraphic architecture of back-filled incised-valley systems: Pennsylvanian–Permian lower Cutler beds, Utah, USA. Sedimentary Geology, 298, 1-16.
<https://doi.org/10.1016/j.sedgeo.2013.10.002>

Walker, R.G. and Cant, D.J. (1979). Facies models 3. Sandy fluvial systems. In Facies Model. Ed. R.G. Walker, Geoscience Canada, 3(1), 23-31.

Walker, R.G. (1984) General introduction: facies, facies sequences and facies models. In: Facies Models (Ed. R.G. Walker), 2nd edn, Geological Association of Canada Reprint Series. Geological Association of Canada, Toronto, 1-9.
<https://cir.nii.ac.jp/crid/1571135650747572736>

WAPIMS database. Western Australia Department of Mines, Industry Regulations and Safety
<https://wapims.dmp.wa.gov.au/WAPIMS/Search/Wells#>

Wang L., Yin Y., Feng W., Duan T., Zhao L., Zhang W. (2019) A training image optimization method in multiple-point geostatistics and its application in geological modeling. Petroleum Exploration and Development, 46(4), 739-745.
[https://doi.org/10.1016/S1876-3804\(19\)60231-4](https://doi.org/10.1016/S1876-3804(19)60231-4).

Wang R., Colombera L., Mountney N.P. (2019) Geological controls on the geometry of incised-valley fills: Insights from a global dataset of late-Quaternary examples. Sedimentology, 66(6), 2134-2168.
<https://doi.org/10.1111/sed.12596>

Weber, K. J., Mandl, G., Pilaar, W. F., Lehner, F., Precious, R. G. (1978) The role of faults in hydrocarbon migration and trapping in Nigerian growth fault structures. SPE paper presented at the SPE Offshore Technology Conference, Houston, Texas, May 1978.
<https://doi.org/10.4043/3356-MS>

Weber K.J. (1986) How heterogeneity affects oil recovery. In: Lake L.W., Carroll H.B. (eds) Reservoir characterisation. Academic Press, 487-544.
<https://doi.org/10.1016/B978-0-12-434065-7.50021-6>

Weber, K.J. (1987) Computation of initial well productivities in aeolian sandstone on the basis of a geological model, Leman gas field, U.K. In: Tillman, R. W. & 24 J. A. Howell et al., Downloaded from <http://sp.lyellcollection.org/> at Statoil on July 3, 2014
Weber, K.J. (eds) Reservoir Sedimentology. Society of Economic Paleontologists and Mineralogists, Special Publications, 40, 333-354.

<https://doi.org/10.2110/pec.87.40.0333>

Weber, K.J., Van Geuns, L.C. (1990) Framework for constructing clastic reservoir simulation models: *Journal of Petroleum Technology*, 42(10), 1248-1297.

https://pure.manchester.ac.uk/ws/portalfiles/portal/188966368/FULL_TEXT.PDF

Wentworth, C.K. (1922) A Scale of Grade and Class Terms for Clastic Sediments. *Journal of Geology*, 30, 377-392.

<https://doi.org/10.1086/622910>

Werren E.G., Shew R.D., Adams E.R. (1990) Meander-Belt Reservoir Geology, Mid-Dip Tuscaloosa, Little Creek Field, Mississippi. *Sandstone Petroleum Reservoirs*, 403pp.

https://doi.org/10.1007/978-1-4613-8988-0_5

Weydt L.M., Ramírez-Guzmán A.A., Pola A., Lepillier B., Kummerow J., Mandrone G., Comina C., Deb P., Norini G., Gonzalez-Partida E., Avellán D.R. Macías J.L, Bär K., Sass I. (2012) Petrophysical and mechanical rock property database of the Los Humeros and Aocolco geothermal fields (Mexico). *Earth Syst. Sci. Data*, 13, 571-598.

Williams G.A. and Chadwick R.A. (2017) An improved history-match for layer spreading within the Sleipner plume including thermal propagation effects. *Energy Procedia*, 114, 2856-2870.

<https://doi.org/10.1016/j.egypro.2017.03.1406>.

Willis, B.J. (1989) Paleochannel reconstructions from point bar deposits: a three-dimensional perspective. *Sedimentology*, 36(5), 757-766.

<https://doi.org/10.1111/j.1365-3091.1989.tb01744.x>

Willis, B.J. and Sech, R.P. (2018a) Quantifying impacts of fluvial intra-channel-belt heterogeneity on reservoir behaviour. In *Fluvial Meanders and Their Sedimentary Products in the Rock Record* (eds M. Ghinassi, L. Colombera, N.P. Mountney, A.J.H. Reesink and M. Bateman), 543-572.

<https://DOI:10.1002/9781119424437.ch20>.

Willis, B.J. and Sech, R.P. (2018b). Emergent facies patterns within fluvial channel belts. In *Fluvial Meanders and Their Sedimentary Products in the Rock Record* (eds M. Ghinassi, L. Colombera, N.P. Mountney, A.J.H. Reesink and M. Bateman), 509-542

<https://doi.org/10.1002/9781119424437.ch19>

Willis, B.J., Sech, R.P. (2019). Emergent facies patterns within fluvial channel belts. In M. Ghinassi, L. Colombera, N.P. Mountney, & A.J. Reesink (Eds.), *Fluvial meanders and their sedimentary products in the rock record*. International Association of Sedimentologists Special Publication, 48, 509–542.

<https://doi.org/10.1002/9781119424437.ch19>

Wood, J.M. (1989). Alluvial architecture of the upper Cretaceous Judith River Formation. Dinosaur Provincial Park. Alberta. Canada. *Bulletin of Canadian Petroleum Geology*, 37(2), 169–181.

<https://doi.org/10.35767/gscpgbull.37.2.169>

Wood, L.J., (2004) Predicting tidal sand reservoir architecture using data from modern and ancient depositional systems. In: Grammer, G.M., Harris, P.M., Eberli, G.P. (Eds.), *Integration of Outcrop and Modern Analogs in Reservoir Modeling*, AAPG Memoir, 80, 45-66.

Worden, R.H. and Burley, S. D. 2009. Sandstone Diagenesis: The Evolution of Sand to Stone. *Sandstone Diagenesis: Recent and Ancient* (pp.1 - 44) Chapter: 1. <https://doi.org/10.1002/9781444304459.ch>

Worthington P.F. (2001) Scale effects on the application of saturation-height functions to reservoir petrofacies units. *SPE Reservoir Evaluation Engineering* 4(5), 430-436.

<https://doi.org/10.2118/63139-MS>

Wynn T., Stephens E. (2013) Data constraints on reservoir concepts and model design. Presented at the Geological Society conference on Capturing Uncertainty in Geomodels – Best Practices and Pitfalls, Aberdeen.

Wyllie M.R.J., Rose W.D. (1950) Some theoretical considerations related to the quantitative evaluation of the physical characteristics of reservoir rock from electric log data. *Trans AIME* 189, 105p.

Xu, W., Tran, T.T., Srivastava, R.M., Journel, A.G (1992) Integrating seismic data in reservoir modeling: the collocated cokriging alternative. In 67th Annual Technical Conference and Exhibition, Washington, DC, Society of Petroleum Engineers. SPE Paper 24742, 833-842.

<https://doi.org/10.2118/24742-MS>

Yan N., Mountney N.P., Colombera, L. and Dorrell, R.M. (2017) A 3D forward stratigraphic model of fluvial meander-bend evolution for prediction of point-bar lithofacies architecture, *Computers and Geosciences*, 105(7), 65-80.

<https://doi.org/10.1016/j.cageo.2017.04.012>

Yan, N., Colombera, L., Mountney, N.P., Dorrell, D.M. (2019) Three-dimensional modelling of fluvial point-bar architecture and facies heterogeneity using analogue data and associated analysis of intra-bar static connectivity: application to humid coastal-plain and dryland fluvial systems. In: Ghinassi, M., Colombera, L., Mountney, N.P. and Reesink, A.J., eds., *Fluvial Meanders and their Sedimentary Products in the Rock Record*. International Association of Sedimentologists, Special Publication, 48, 475–508.

<https://doi.org/10.1002/9781119424437.ch18>

Yan N., Colombera L., Mountney N.P. (2020a) Three-dimensional forward stratigraphic modelling of the sedimentary architecture of meandering-river successions in evolving half-graben rift basins. *Basin Research* 32(1), 68-90.

<https://doi.org/10.1111/bre.12367>

Yan N., Colombera L., Mountney N.P. (2021) Evaluation of Morphodynamic Controls on the Preservation of Fluvial Meander-belt Deposits. *Geophysical Research Letters*. 48(16).

Yarus J.M., Chambers R.L. (1994) Stochastic modeling and geostatistics. Principles, methods, and case studies. *AAPG computer applications in geology*. American Association of Petroleum Geologists (AAPG), 1, 379pp.

<https://doi.org/10.1306/CA51063>

Yarus, J.M., Srivastava, R.M., Gehin, M., Chambers, R.L. (2009) Distribution of properties in a 3D volumetric model using a maximum continuity field, PCT Patent, WO 2009/151441 A1.

Yarus, J.M., Chambers, R.L. (2010) Practical Geostatistics – An Armchair Overview for Petroleum Reservoir Engineers, SPE 103357, Journal of Petroleum Technology, 58(11), 78-86.

<https://doi.org/10.2118/103357-JPT>

Yarus, J., Chambers R., Fei, J. (2016) Apply two-way cluster analysis to select candidate reservoir models from multiple realizations. SPE intelligent energy conference & exhibition, Utrecht, The Netherlands, SPE-167821-MS.

<https://doi.org/10.2118/167821-MS>

Zaitlin, B.A., Dalrymple, R.W., Boyd, R., (1994) The stratigraphic organization of incised valley systems associated with relative sea-level change. In: Dalrymple, R.W., Boyd, R., Zaitlin, B.A. (Eds.), Incised-Valley Systems: Origin and Sedimentary Sequences. SEPM Special Publication, 51, 45-62.

Zhang, S., Depaolo, D. (2017) Rates of CO₂ Mineralization in Geological Carbon Storage. Accounts of chemical research, 50.

<https://10.1021/acs.accounts.7b00334>

Appendix A: 48 Case-studies Included in the Database (References)

CASE 1: Amthor, J.E., Okkerman, J. (1998) Influence of Early Diagenesis on Reservoir Quality of Rotliegende Sandstones, Northern Netherlands. AAPG Bulletin, 82(12), 2246–2265.

<https://doi.org/10.1306/00AA7F04-1730-11D7-8645000102C1865D>

CASE 2: Atkinson, C.D., McGowen J.H., Bloch S., Lundell L.L., and Trumbly P. N. (1990) Braidplain and deltaic reservoir, Prudhoe Bay Field, Alaska. In Sandstone Petroleum Reservoirs, Barwis J.H., McPherson J.G., and Studlick J.R.J., eds, Springer-Verlag, 205-224.

[10.11648/j.earth.20211003.11](https://doi.org/10.11648/j.earth.20211003.11)

CASE 3: Anjos S.M., Leite Sombra C., de Souza R.S. and Waick R.N. (1990) Potencial de reservatorios profundos da formacao Pendencia, bacia Potiguar Emersa. Geoci. Petrobras, Rio de Janeiro, 5(4), 509-530.

CASE 4: Barde J.P., Chamberlain, P., Galavazi, M., Gralla, P., Harwijanto, J., Marsky, J., Van den Belt, F. (2002) Sedimentation during halokinesis: Permo-Triassic reservoirs of the Saigak Field, Precaspian Basin, Kazakhstan. Petroleum Geoscience. 8(2), 177-187.

<https://doi.org/10.1144/petgeo.8.2.177>

CASE 5: Bartberger C.E., Dyman T.S., and Condon S.M. (2003) Potential for deep basin-centered gas accumulation in Travis Peak (Houston) Formation, Gulf Coast Basin, U.S.A. Bulletin USGS, 2184-E.

<https://doi.org/10.3133/b2184E>

CASE 6: Bloch S., McGowen J.H., Duncan J., R; Brizzolara D.W. (1990) Porosity Prediction, Prior to Drilling, in Sandstones of the Kekiktuk Formation (Mississippian), North Slope of Alaska. AAPG Bulletin 74(9), 1371-1385.

<https://doi.org/10.1306/0C9B24CF-1710-11D7-8645000102C1865D>

CASE 7: Bloomfield J.P., Moreau M.F., Newell A.J. (2006) Characterisation of permeability distributions in six lithofacies from the Helsby and Wilmslow sandstone formations of the Cheshire Basin, UK. Geological Society, London, Special Publications, 263(1), 83-101.

<https://doi.org/10.1144/GSL.SP.2006.263.01.04>

CASE 8: Bowker K.A., Jackson W.D. (1989) The Weber Sandstone at Rangely Field, Colorado. Rocky Mountain Association of Geologists Petrogenesis and Petrophysics of Selected Sandstone Reservoirs of the Rocky Mountain Region. Rocky Mountain Association of Geologists, 65- 80.

CASE9: Bruhn, C., De Ros, L. (1987) Formação Sergi: evolução dos conceitos e tendências na geologia dos reservatórios. Boletim de Geociências da Petrobras, 1, 25-40.

CASE 10: Alan P.B., Robert M.C., Webb J.C. (2009) Analysis of Critical Permeability, Capillary Pressure and Electrical Properties for Mesaverde Tight Gas Sandstones from Western U.S. Basins. US DOE # DE-FC26-05NT42660.

<http://www.kgs.ku.edu/mesaverde>

CASE 11: Canfield, R.W., Bonilla, G., Robbins, R.K. (1982) Sacha oil field of Ecuadorian Oriente. AAPG Bulletin, 66, 1076-1090.

CASE 12: Castellanos, H.R. (1994) A geological and engineering reservoir characterisation of the Caballos Formation (Cretaceous), Puerto Colon, Field Putumayo Basin, Colombia. Thesis, Texas A&M University.

CASE 13: Cowan, G. Bradney, J. (1997) Regional diagenetic controls on reservoir properties in the Millom accumulation: implications for field development. Geological Society, London, Special Publications, 124(1), 373-386.

<https://doi.org/10.1144/GSL.SP.1997.124.01.22>

CASE 14: Garcia, A., De Ros, L., Souza, R., Bruhn, C. (1990) Potencial de reservatórios profundos na Formação Serraria, Bacia de Sergipe-Alagoas. Boletim De Geociências Da Petrobras, 4, 467-488.

CASE 15: Dickey, P. A. (1992) La Cira-Infantas Field--Colombia Middle Magdalena Basin. AAPG Special Volumes. TR: Structural Traps VII, 323-347

CASE 16: Dixon S.A., Summers D.M., Surdam R.C. (1989) Diagenesis and Preservation of Porosity in Norphlet Formation (Upper Jurassic), Southern Alabama. AAPG Bulletin, 73(6), 707-728.

<https://doi.org/10.1306/44B4A24E-170A-11D7-8645000102C1865D>

CASE 17: Dolly E.D. and Mullarkey J.D. (1996) Hydrocarbon production from low contrast, low resistivity reservoirs, Rocky Mountain and Mid-Continent regions. Log examples of subtle plays: Rocky Mountain Association of Geologists, 290pp.

CASE 18: Dolson, J., Burley, S., Sunder, V., Kothari, V., Naidu, B., Whiteley, N., Farrimond, P., Taylor, A., Direen, N., Ananthakrishnan, B., John M., (2015). The Discovery of the Barmer Basin, Rajasthan, India, and its petroleum geology. AAPG Bulletin, 99(3).

<https://10.1306/10021414045>.

CASE 19: Elfigih, O.B. (2000) Regional diagenesis and its relation to facies change in the Upper Silurian, Lower Acacus Formation, Hamada (Ghadames) Basin, Northwestern Libya. Thesis, Memorial University of Newfoundland.

CASE 20: Estupiñán, J., Marfil, R., Delgado, H.A., Permanyer, A. (2007) The Impact of carbonate cements on the reservoir quality in the Napo Fm sandstones (Cretaceous Oriente Basin, Ecuador). Geologica Acta. 5, 89-108.

CASE 21: Abdel-Fattah, Mohamed (2014) Petrophysical characteristics of the Messinian Abu Madi Formation in the Baltim East and North fields, Offshore Nile Delta, Egypt. Journal of Petroleum Geology, 37(2), 183-194.

<https://doi.org/10.1111/jpg.12577>

CASE 22: Ferreira, H. (2000) The development of two integrated reservoir studies to improve field performance. Texas A&M University ProQuest Dissertations Publishing, 9968868.

CASE 23: Garcia, A., De Ros, L., Souza, R., Bruhn, C. (1990) Potencial de reservatórios profundos na Formação Serraria, Bacia de Sergipe-Alagoas. Boletim De Geociências da Petrobras, 4, 467-488.

CASE 24: Guangming J. (1992) Laojunmiao Field- People's Republic of China, Jiuquan Basin, Gansu Province. Scientific Research Institute of Petroleum Exploration and Development. Beijing, People's Republic of China. AAPG Datapages, TR Structural Traps VII, A0201.

CASE 25: Henares, S., Caracciolo, L., Viseras, C., Fernandez, Yeste, L. M. (2016) Diagenetic constraints on heterogeneous reservoir quality assessment: A Triassic outcrop analog of meandering fluvial reservoirs. AAPG Bulletin, 100(9).

CASE 26: Higgs K.E., Arnot M.J., Browne G.H., Kennedy E.M. (2010) Reservoir potential of Late Cretaceous terrestrial to shallow marine sandstones, Taranaki Basin, New Zealand. Marine and Petroleum Geology, 27(9), 1849-1871.

<https://doi.org/10.1016/j.marpetgeo.2010.08.002>

CASE 27: Indiana University database. IU Bloomington Libraries.

http://webapp1.dlib.indiana.edu/virtual_disk_library/index.cgi/5389627

CASE 28: Ávalos H., Alvarez V.M., Arroyo J., Hernández T., Arévalo I. (2006) Shallow Reservoirs and The Gas-Effect, Tinta 3 Well, An Oligocene And Eocene Case In Burgos Basin, Mexico. Paper presented at the SPWLA 47th Annual Logging Symposium, Veracruz, Mexico, SPWLA-2006-MMM.

CASE 29: Hunt J.W., Guthrie D.A., Dodman A.P. (1990) Jackson Field-Australia Cooper-Eromanga Basins, Central Australia. AAPG Special Volumes. TR: Structural Traps IV: Tectonic and Nontectonic Fold Traps. 217-253.

CASE 30: Kassab, M.A., Hassanain I. M., Salem, A.M. (2014) Petrography, diagenesis and reservoir characteristics of the Pre-Cenomanian sandstone, Sheikh Attia area, East Central Sinai, Egypt. *Journal of African Earth Sciences*, 96, 122-138.

<https://doi.org/10.1016/j.jafrearsci.2014.03.021>.

CASE 31: Keller, M., Bohnsack D., Koch R., Hinderer, M., Hornung J., Al Ajmi H., Abu Amarah B. (2019) Outcrop Analog Studies of the Wasia–Biyadh and Aruma Aquifers in the Kingdom of Saudi Arabia. In book: *Siliciclastic reservoirs of the Arabian plate* (Chapter 10) Publisher: R. J. Steel and O. M. Soliman, American Association of Petroleum Geologists. AAPG Memoir, 116, 317-382.

<https://doi.org/10.1306/13642171M1183514>

CASE 32: Khalifa M., Morad S. (2012) Impact of structural setting on diagenesis of fluvial and tidal sandstones: The Bahi Formation, Upper Cretaceous, NW Sirt Basin, North Central Libya, *Marine and Petroleum Geology*, 38(1), 211-231.

<https://doi.org/10.1016/j.marpetgeo.2011.05.006>.

CASE 33: Negreiros, J. H. C. (1990) Arenitos da formação Itaparica no extremo nordeste da bacia do recôncavo: sedimentação, evolução diagenética e características de reservatório. *Boletim de Geociências, Petrobras*, 4(2), 137-134.

CASE 34: Olausson S., Beck L., Falt L.M., Graue E., Jacobsen K.G., Malm O.A., South D. (1992) Gullfaks Field-Norway East Shetland Basin, Northern North Sea". AAPG Special Volumes. TR: Structural Traps VI, 55-83.

CASE 35: Graham and Trotman (1986) Petroleum Geology of Northwest Europe. Proceedings of the 3rd Conference on Petroleum Geology of Northwest Europe Held at the Barbican Centre, London. edited by J. Brooks and K.W. Glennie, 2, 1219pp.

CASE 36: Ramon, J.C., and Fajardo A. (2006) Sedimentology, sequence stratigraphy, and reservoir architecture of the Eocene Mirador Formation, Cupiagua field, Llanos Foothills, Colombia. In P. M. Harris and L. J. Weber, eds., Giant hydrocarbon reservoirs of the world: From rocks to reservoir characterisation and modelling. AAPG Memoir 88/SEPM Special Publication, 433-469.

CASE 37: Reynolds, A.D., Simmons M., Bowman M.B.J., Henton, J., Brayshaw, A.C., Ali-Zade, A.A., Guliyev, I., Suleymanova, S.F., Ateava, E.Z., Mamedova, D.N., Koshkarly, R. O., (1998) Implications of outcrop geology for reservoirs in the Neogene productive series: Apsheron peninsula, Azerbaijan. AAPG Bulletin. 82, 25-49.

CASE 38: Rossi, C., Kälin, O., Arribas, J., Tortosa, A. (2002) Diagenesis, provenance and reservoir quality of Triassic TAGI sandstones from Ourhoud Field, Berkine (Ghadames) Basin, Algeria. Marine and Petroleum Geology, 19, 117-142.

[https://doi.org/10.1016/S0264-8172\(02\)00004-1](https://doi.org/10.1016/S0264-8172(02)00004-1)

CASE 39: Rowan R. (1992) Silver Springs/Renlim Field-Australia Bowen Basin, Queensland. AAPG Special Volumes. TR: Structural Traps VI, 219-238.

CASE 40: Saad, A., and de Groot M. (2010) Lower Safa Sedimentological Study, New Insights in the Reservoir Quality Distribution of the Obaiyed Field, Western Desert, Egypt. SPE paper presented at the North Africa Technical Conference and Exhibition, Cairo, Egypt, SPE-128015-MS.

<https://doi.org/10.2118/128015-MS>

CASE 41: Schmid S., Worden R.H., Fisher Q.J (2004), Diagenesis and reservoir quality of the Sherwood Sandstone (Triassic), Corrib Field, Slyne Basin, west of Ireland. *Marine and Petroleum Geology*, 21(3), 299-315.

<https://doi.org/10.1016/j.marpetgeo.2003.11.015>.

CASE 42: Ruble T.E., George S.C., Lisk M., Quezada R.A., (1998) Organic compounds trapped in aqueous fluid inclusions, *Organic Geochemistry*, Volume 29(1-3), 195-205.

[https://doi.org/10.1016/S0146-6380\(98\)00090-4](https://doi.org/10.1016/S0146-6380(98)00090-4).

CASE 43: Stephen V., Clare D., Keith R., Aliyeva, E. (2010) Contrasting Pliocene fluvial depositional systems within the rapidly subsiding South Caspian Basin; a case study of the palaeo-Volga and palaeo-Kura River systems in the Surakhany Suite, Upper Productive Series, onshore Azerbaijan. *Marine and Petroleum Geology*, 27(10), 2079-2106.

<https://doi.org/10.1016/j.marpetgeo.2010.09.007>

CASE 44: WAPIMS (Western Australia Department of Mines, Industry Regulation and Safety database.

<https://wapims.dmp.wa.gov.au/WAPIMS/Search/Wells#>

CASE 45: Warren E.A., Pulham A.J. (2001) Anomalous Porosity and Permeability Preservation in Deeply Buried Tertiary and Mesozoic Sandstones in the Cusiana Field, Llanos Foothills, Colombia. *Journal of Sedimentary Research*, 71(1), 2–14.

<https://doi.org/10.1306/081799710002>

CASE 46: Winn, S. (1993) Australian Petroleum Systems. Australian Geological Survey Organisation. Papuan Basin module, *Australian*, 3, no. 1994/13.

CASE 47: Wolela, A. (2010) Diagenetic evolution of the Anisian-Pliensbachian Adigrat Sandstone, Blue Nile Basin, Ethiopia. *Journal of African Earth Sciences*, 56(1), 29-42.

<https://doi.org/10.1016/j.jafrearsci.2009.05.005>

CASE 48: Yaliz A. (1997) The Douglas Oil Field. Geological Society, London, Special Publications, 124, 399-416.

<https://doi.org/10.1144/GSL.SP.1997.124.01.24>

Appendix B: Published Version of Chapter 3

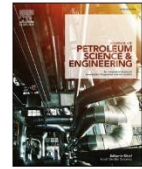
Journal of Petroleum Science and Engineering 201 (2021) 108411



Contents lists available at ScienceDirect

Journal of Petroleum Science and Engineering

journal homepage: <http://www.elsevier.com/locate/petrol>



A workflow for modelling fluvial meander-belt successions: Combining forward stratigraphic modelling and multi-point geostatistics

Jose M. Montero^{*}, Luca Colomera, Na Yan, Nigel P. Mountney

Fluvial & Eolian Research Group, School of Earth and Environment, University of Leeds, Leeds, LS2 9JT, UK

ARTICLE INFO

Keywords:

Facies modelling
Multi-point statistics
SNESIM
DEESSE
Training image
Meandering fluvial system

A new workflow has been developed for modelling reservoir successions that comprise fluvial meander-belt deposits, based on algorithms that employ multi-point statistics (MPS). A library of training images – from which MPS modelling algorithms can borrow geological patterns for modelling fluvial meandering systems – has been built. The training images incorporate sedimentary architectures relating to point-bar deposits accumulated by fluvial meander-bend expansion and translation, as observed in high-sinuosity river systems and their preserved deposits in the geological record. The training-image library has been developed using a forward stratigraphic modelling software (PB-SAND) that simulates fluvial meander-bend evolution and resulting point-bar facies organization, and which has been constrained using sedimentological data from geological analogues.

The training images are applied to two widely employed MPS modelling algorithms: SNESIM and DEESSE. Solutions to common issues encountered in MPS modelling workflows have been established through optimization of modelling settings for SNESIM and DEESSE. Auxiliary variables are used to simulate common facies trends. Application of the training-image library through the developed workflows for SNESIM and DEESSE has been tested; the sensitivity of unconditional simulation results to input parameters has been analysed to define modelling recipes, consisting of sets of appropriate modelling parameters for use with each training image and modelling algorithm. The creation of fluvial reservoir models that are geologically realistic using MPS algorithms remains challenging, but the proposed approach holds promise.

1. Introduction

Static models depicting the sedimentary architecture of subsurface successions are required to visualize the possible distribution of different properties associated with the rock volume being characterized, to determine volumetric capacities, and for well and production planning (Ringrose and Bentley, 2015). Facies models are used to depict the distribution and the geometry of rock types and constitute the framework on which petrophysical parameters are populated in a digital three-dimensional grid (Caers, 2005; Cannon, 2018; Honarkah et al., 2010). Facies models simplify lithological heterogeneity, but nevertheless provide a reasonable framework with which to model flow properties (Harding et al., 2004; Walker et al., 1979). To address the considerable uncertainty regarding properties of the bulk reservoir volume, including uncertainty associated with geological heterogeneities at multiple scales, stochastic modelling methods are routinely employed (Ma, 2019; Caers, 2001). Several classes of stochastic methods exist for facies modelling: variogram-based methods (i.e., based on two-point statistics), object-based methods, and methods based on

multi-point statistics (MPS) (Pyrzc and Deutsch, 2014; Pyrcz et al., 2008).

Since the 1980s, geomodellers have relied preferentially on variogram- and object-based methods to model different depositional environments, using indicator variograms and Boolean objects, respectively (Guardiano and Srivastava, 1993). However, techniques based on two-point statistics are not especially effective at capturing and reproducing complex geological patterns, such as curvilinear shapes (Journel, 1993; Strebelle, 2000; Strebelle and Journel, 2001). By contrast, object-based methods do permit the reproduction of bodies with complex shapes, but commonly are unable to honour conditioning well data, particularly for densely drilled reservoirs (Deutsch et al., 1996). Techniques based on multi-point statistics (MPS) allow reproduction of complex geological patterns while simultaneously honouring well data, but require suitable and realistic training images to be used as simplified digital representations of the heterogeneities of a reservoir rock (Strebelle and Journel, 2001). A library of suitable training images should, ideally, incorporate stationary features, i.e., patterns that are homogeneous, repeated and not confined to specific locations in the grid.

^{*} Corresponding author.

E-mail address: ejmm@leeds.ac (J.M. Montero).

<https://doi.org/10.1016/j.petrol.2021.108411>

Received 12 May 2020; Received in revised form 12 December 2020; Accepted 12 January 2021

Available online 23 January 2021

0920-4105/© 2021 Elsevier B.V. All rights reserved.

However, the geological bodies that training images seek to model are inherently non-stationary, because the properties of rock types are variable in space (Caers and Zhang, 2004). To enable the reproduction of geological non-stationarity through the application of stationary training images, MPS modelling algorithms employ auxiliary variables that describe how geological properties should vary in space; this permits the incorporation of geological trends in the modelling grids (Chugunova and Hu, 2008).

A workflow that incorporates an MPS approach, a library of training images constructed using analogue data and forward stratigraphic modelling, and the use of auxiliary variable maps has here been developed to support the construction of facies models for a common type of hydrocarbon reservoirs: high-sinuosity meandering fluvial successions. These facies models incorporate geological features that are commonly difficult to reproduce with traditional subsurface modelling workflows. The application of training images has been optimized for two MPS algorithms: SNESIM (Strebelle, 2002) and DEESSE (Mariethoz et al., 2010); these algorithms are adopted in this work because they are widely used in the hydrocarbon industry, thanks to their availability in commercial software. For the construction of the training images, a stratigraphic forward modelling approach to simulating geological complexity in meandering fluvial systems and their accumulated successions has been employed (Yan et al., 2017), constrained with data from a wide range of known geological analogues (Colombera et al., 2012a, b).

The aim of this study is to develop and employ a workflow for the generation of unconditional reservoir models that capture the complex lithological heterogeneity inherent in meandering fluvial reservoir successions at multiple scales (Fig. 1). Primary research objectives are as follows: (i) creation of a library of training images that incorporate the main sedimentological and stratigraphic features of meandering fluvial systems and their accumulated deposits; (ii) demonstration of how the training images included in the library can be constrained in terms of their geological realism through the use of data from many known examples stored in a relational database, and of how suitable examples can be selected from the library according to the specifications of different

geomodelling cases; (iii) development of an efficient modelling workflow whereby appropriate training images are selected from the library and used to undertake MPS-based simulations.

2. Background: MPS modelling and training images

Geomodellers commonly rely on pixel-oriented facies-modelling tools based on two-point statistics, which are constrained on indicator variogram models that describe the spatial continuity of the modelling categories ('facies') (Deutsch and Journel, 1998). However, the variogram is merely a measure of continuity, and does not capture significant geological characteristics, such as shape, facies transitions and connectivity (Caers and Zhang, 2004). This is especially problematic, for example, when modelling sinuous channelized bodies. Object-based algorithms are also popular within the geomodelling community. They build geological realizations by placing 3D objects with specific geometries (e.g., ellipsoids, crescents, channels) onto the simulation grid (Bridge and Leeder, 1979; Haldorsen and Damsleth, 1990; Omre, 1991). Object-based methods successfully render the complex geometries of geobodies that are common in fluvial, deltaic and turbiditic successions. However, it may be difficult or impossible to condition the models to subsurface data, particularly in cases where these data are densely distributed, as in the case of seismic surveys or dense well arrays (Ringrose and Bentley, 2015).

By contrast, geomodelling methods based on multiple-point statistics (MPS), which are pixel-based, capture textures by considering more than two points (cells) simultaneously, allowing the reproduction of complex, non-linear spatial correlation (Strebelle, 2000). Overall, the MPS approach combines the strengths of other pixel-based methods (i.e., perfect conditioning to subsurface data) and of object-based methods (i.e., the ability to reproduce complex geological shapes) (Guardiano and Srivastava, 1993; Liu et al., 2005) making them suitable to model fluvial systems with sinuous channel fills and belts.

Following early attempts at using stochastic methods based on MPS in the geosciences (Farmer, 1988; Deutsch 1992; Xu et al., 1992), Guardiano and Srivastava (1993) first proposed a direct (non-iterative)

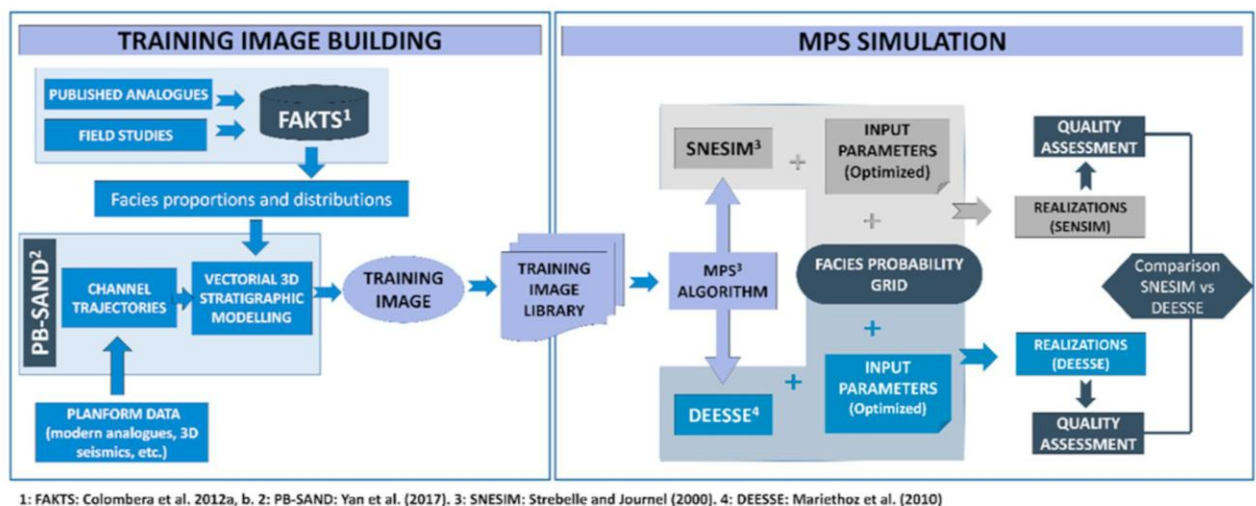


Fig. 1. Workflow describing the process for building a training-image library for MPS facies simulations and its application to two different MPS algorithms. The workflow consists of two stages: (i) the creation of training images and (ii) their application to SNESIM (Single Normal Equation SIMulation) and DEESSE (DS, Direct Sampling) (Strebelle, 2002; Mariethoz et al., 2010). The left-hand side of the workflow demonstrates how the training images are built through a novel approach for the synthesis of geological knowledge of the sedimentary architecture of successions deposited by meandering fluvial systems, by using a forward stratigraphic model (PB-SAND) (Yan et al., 2017) constrained using analogue data from a sedimentological database (FAKTS) (Colombera et al., 2012a, b). The box on the right-hand side summarizes the application of the training images for MPS modelling, as undertaken in this work, utilizing input parameters and facies-probability grids that are optimized for the reproduction of features of reservoir architecture typical of meandering fluvial systems. As part of this work, assessment of algorithm outputs and comparisons between realizations of SNESIM and DEESSE are also undertaken.

MPS algorithm for stochastic simulations. Initial incarnations of MPS modelling algorithms were highly demanding on CPU time, and this issue significantly limited the use of the method. However, Strebelle and Journé (2000) implemented the efficient SNESIM (Single Normal Equation SIMulation) algorithm, which rendered the approach practical by significantly decreasing computer resource requirement. Other MPS algorithms have been created since, including DEESSE (Mariethoz et al., 2010) and IMPALA (Straubhaar et al., 2013). In this study, both SNESIM and DEESSE are used in the devised modelling workflows.

2.1. MPS and training images

A type of input required by MPS algorithms is the so-called 'training image' (TI), which can be defined as a 2D or 3D cellular model acting as a digital representation of the geological architecture of the reservoir interval that needs to be modelled. Therefore, a TI includes the perceived heterogeneity of the geological media, incorporating the geometries, connectivity, spatial distribution and relationships of geobodies (Journé and Zhang, 2006). Training images can be built using satellite images of modern analogues, idealized models representing the fundamental architectural features of a particular depositional system, or outputs of object-based modelling algorithms or forward stratigraphic models; this last approach has been taken in this work, as explained below.

An MPS algorithm scans a TI to draw patterns that it then replicates across a modelling grid. Once a statistical pattern is acquired from the TI, the MPS algorithm assigns conditional probability distributions of the random variables performing a multi-point analysis of the grid. Training images should ideally honour requirements of stationarity so that patterns can be readily reproduced by MPS modelling algorithms. To meet the assumption of stationarity, TIs are required to have the following attributes: (i) that spatial patterns are reasonably homogeneous over the entire TI (Maharaja, 2008); (ii) that patterns should be repeated throughout the volume or area of the TI; (iii) that sedimentological features in the form of facies and their properties should ideally not be confined to specific locations within parts of a TI, but should instead be distributed throughout the TI grid (Meerschman et al., 2013).

Dealing with geological non-stationarity is one of the main issues faced by geomodellers who employ MPS methods for facies modelling. Since most geological processes in nature result in non-stationary patterns or distributions, the creation and application of suitable TIs is one of the main factors that limit the uptake of MPS modelling algorithms for purposes of subsurface modelling. Because of the stationarity requirements of MPS modelling algorithms, complex geological trends are not readily reproducible in the resulting reservoir models. To enable the reproduction of realistic stratigraphic architectures, MPS modelling inputs include various types of secondary data (auxiliary variables) that can be employed to reproduce spatial trends (Remy et al., 2009; Straubhaar et al., 2011).

MPS methods might be well suited to modelling reservoirs hosted in fluvial successions that represent the product of high-sinuosity river systems, as they allow reproducing complex morphologies such as those of the deposits of meandering rivers (e.g., point bars, channel fills). However, MPS reservoir modelling usually requires extensive effort on model set-up through a 'trial-and-error' approach, whereby the geomodeller performs several simulations to optimize the input parameters with consideration of the outputs being sought.

2.2. Sedimentary heterogeneity in the deposits of meandering river systems

A library of training images that incorporate the main sedimentological and stratigraphic features of meandering fluvial systems should ideally incorporate heterogeneities at different scales. Significant sedimentary heterogeneities that can be observed in fluvial successions deposited by meandering rivers occur at a range of spatial scales, and

include those relating to: (i) stratigraphic architecture determined by the distribution of channel-belt and floodplain deposits; (ii) internal architecture of channel belts determined by the distribution of channel-fill and point-bar deposits; (iii) intra-bar variations in the relative proportion of sand and mud, vertically and horizontally. Such lithological heterogeneities have long-been recognized in the deposits of meandering rivers (Jackson, 1976). From an applied perspective, such lithological heterogeneities are important because they affect fluid-flow behaviour over a range of scales (Corbett et al., 2012; Hovadik and Larue, 2007).

Some common examples of complex sedimentary architectures that give rise to the configuration and the lithological heterogeneity in the deposits of meandering fluvial systems are depicted in Fig. 2; their origins and form are summarised below.

- The migration of river channels over time results in erosion of sediments from the outer bank and sedimentation occurring via accretion on the inner bank. The gradual lateral accretion of successive units forms a point bar on the inner part of a developing meander loop. In sand-rich fluvial systems, resultant accumulated lateral-accretion architectural elements commonly form volumetrically significant sand-bodies with good reservoir potential composed internally of a coset of lateral-accretion units. Each lateral-accretion unit may be separated from its neighbouring unit within the overall point-bar element by thin lower-permeability beds. Commonly, such beds take the form of drapes on successive bar-front surfaces, which themselves accumulate during episodes of reduced flow in the aftermath of flood events (Miall, 2016).
- Some lateral-accretion units are characterized by 'inclined heterolithic stratification' (IHS), a term introduced to describe shallow-dipping heterogeneous point-bar deposits whose strata show original depositional dip (Thomas et al., 1987). Muddy IHS, in either fluvial or tidally influenced channels, may represent baffles that can hinder or impede fluid flow in otherwise sand-prone point-bar deposits (Hubbard, 2011).
- Different styles of baffling can be developed within a laterally accreting point-bar element. The distribution of intra-bar-scale heterogeneities is dependent, in part, on the growth mechanisms of the point bars and on the trajectories of the formative meanders. For example, unlike meanders undergoing simple expansion (i.e., lateral growth), translating (i.e., downstream migrating) meanders are characterized by areas where deposition takes place on concave banks, leading to the deposition of mud-prone counter-point-bar deposits (Ielpi and Ghinassi, 2014; Nanson and Page, 1983).
- High-sinuosity fluvial-channel deposits commonly display fining-upward sequences in which the coarsest-grained sediment accumulations are deposited in the lower portions of point-bar units. These results from energy dissipation associated with the helical flow in the channel (Miall, 2016). Moreover, sediments forming point-bar deposits also commonly display a trend of downstream decrease in grain size, especially downstream of a meander-bend apex, in relation to changes in flow direction around the bend (Bluck, 1971; Wood 1989).

These commonly occurring types of lithological heterogeneity give rise to different forms and degrees of non-stationarity, which need to be accounted for (i) in TIs that seek to depict the range of architectural styles common in point-bar deposits associated with meandering-river succession, (ii) by means of auxiliary variable maps intended to enable effective training-image application, and (iii) in resulting MPS models (de Vries et al., 2009).

3. Methodology

A workflow has been developed for the creation of training images and their application to MPS simulations. A detailed explanation of the

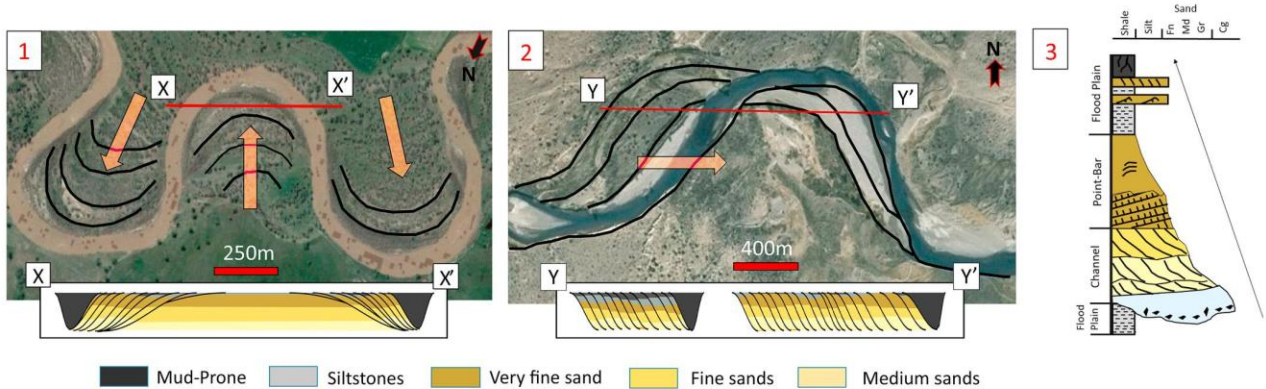


Fig. 2. Two examples of point bars and their deposits associated with meanders undergoing expansion (1-Powder River, US (45°19'34.43"N-105°31'43.43"W) and translation (2-Chubut River, Argentina (42°31'26.33"S-70°32'53.24"W). Cross-sections resulting from PB-SAND forward stratigraphic model runs (X-X' and Y-Y') show accreted deposits with typical fining-upward trends (3). Red arrows indicate the accretion trajectory of point bars associated with the different types of meander transformations. Grainsize categories are for illustration only and may vary considerably in natural examples. These two images are shown to illustrate accretion geometries associated with meander expansion and translation, as incorporated in the training images constructed and employed in this work. (For interpretation of the references to colour in this figure legend, the reader is referred to the Web version of this article.)

steps undertaken for building the TIs is provided. Six different TIs are then utilized to demonstrate their use in MPS simulations with SNESIM and DEESSE, making use of auxiliary variables to achieve the desired

trends in facies distribution and orientation.

To construct TIs that include fundamental features of the facies architecture of fluvial point bars and meander belts, a workflow has been

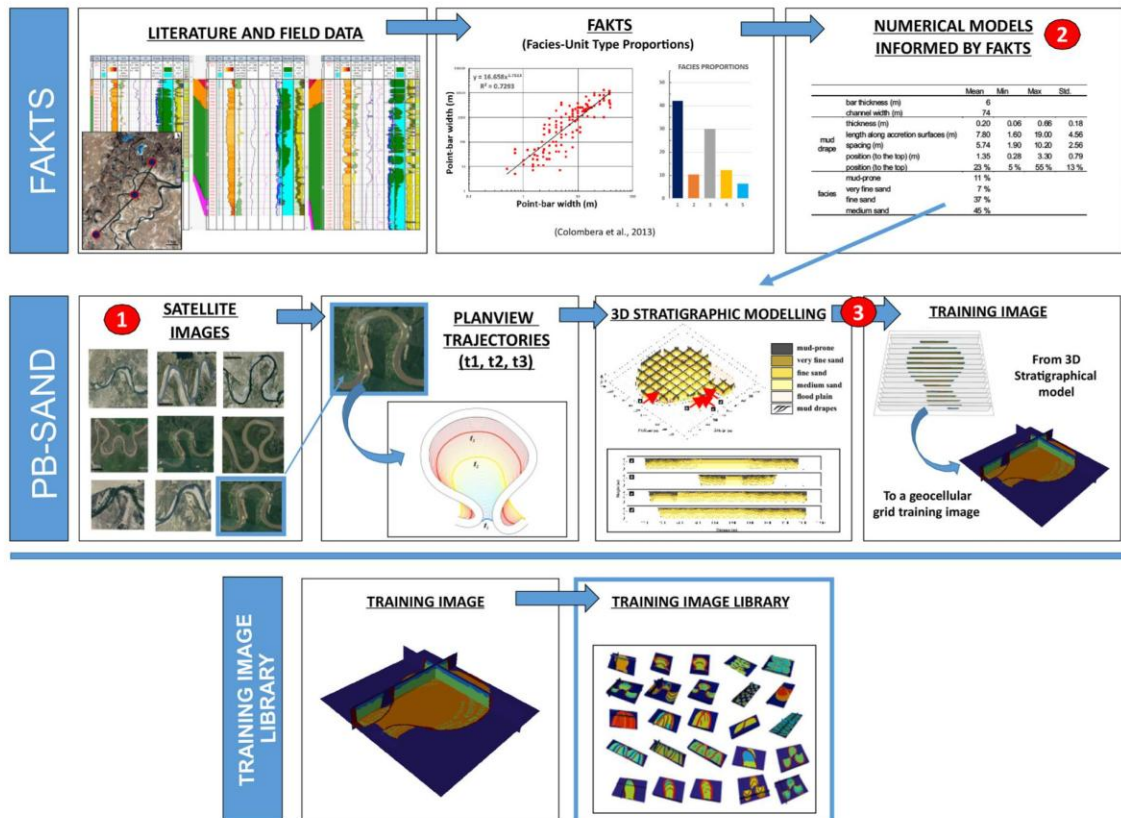


Fig. 3. A training image is created following a three-step process, as follows: (1) derivation of quantitative information on facies architecture from geological analogues stored in FAKTS (e.g., facies proportions, channel geometry), to be employed as input to PB-SAND; (2) specification of trajectories tracking channel planform evolution (e.g., as captured from time-lapse satellite images), to be fed as input to PB-SAND; (3) PB-SAND simulation of meander-belt facies architectures, whereby geometries of bar accretion are modelled deterministically and facies distributions are simulated stochastically. 3D vector models produced by PB-SAND are then converted into gridded geocellular models that can be used as MPS training images. A set of training images is created using this workflow that serves as a training-image library.

established (Fig. 3) whereby a forward stratigraphic model of meander-belt sedimentary architectures (Point-Bar Stratigraphic Architecture Numerical Deduction; PB-SAND (Yan et al., 2017, 2019, 2020) has been informed by sedimentological data drawn from a relational database (Fluvial Architecture Knowledge Transfer System; FAKTS (Colombera et al., 2012a, 2012b; 2013, 2017). The joint application of PB-SAND and FAKTS allows reproduction of the sedimentological features of interest in this particular study. Of note, TIs have been created that embody different styles of sedimentary architecture that are common in high-sinuosity fluvial environments, associated with different modes of meander transformation. Utilizing this workflow, a TI library has been created that includes different TIs representing idealized stratigraphic architectures applicable to different modelling scenarios (Fig. 3).

3.1. PB-SAND

The Point-Bar Sedimentary Architecture Numerical Deduction (PB-SAND), coded in Matlab and C#, is a forward stratigraphic model designed to reconstruct and predict the complex spatial-temporal evolution of a variety of meandering river behaviours. The software simulates the complex spatio-temporal migratory evolution of fluvial meanders, their generated bar forms and the associated lithofacies distributions that accumulate as heterogeneous fluvial successions (Yan et al., 2017).

PB-SAND can be applied to explore and gain improved understanding of relationships between evolutionary channel trajectories and preserved lithofacies distributions, allowing reproduction of the stratigraphic heterogeneity of fluvial meandering systems at different temporal and spatial scales and in three dimensions.

Based on time-lapse plan-view trajectories of channel courses (e.g., as captured from satellite images; cf. Fig. 2) PB-SAND can reconstruct the channel-belt sedimentary architectures that arise from the complex spatio-temporal evolution of meandering rivers; facies characteristics in the modelled architectures will reflect the type of meander-bend transformation, the channel sinuosity, the stream-wise distance away from meander apices, and the position of inflection points of a meander loop (Yan et al., 2019). In addition to the centrelines that track the course of a river channel at different times, PB-SAND requires definition of several other parameters, which vary depending on the type of meander-bend transformation, and which include the river-channel hydraulic geometry (maximum bankfull depth, width) and descriptions of the types and arrangement of lithologies forming point-bar and channel-fill deposits (Yan et al., in press). Inputs to constrain channel-form and bar geometries can be acquired from different sources such as well data (electrical logs, core data, etc), field-based measurements from outcrops and modern systems, satellite images, or – as done in this study – from a relational database (FAKTS) that stores the required inputs.

3.2. FAKTS

The Fluvial Architecture Knowledge Transfer System (FAKTS) is a MySQL relational database that stores quantified sedimentological data from modern systems and analogue ancient fluvial successions (Colombera et al., 2012a, b; 2013, 2017). FAKTS satisfies the long-recognized need for inclusion of quantitative inputs in facies models, which improves the value of facies models as a reference for comparison, interpretation and subsurface prediction.

FAKTS uses end-member styles of fluvial geomorphology to classify facies models by type of facies, facies associations and facies relationships that tend to occur in a particular environment. FAKTS allows determination of appropriate geological analogues to subsurface reservoir successions (Colombera et al., 2012a). This is the case that applies for this particular research where FAKTS provides the required inputs to PB-SAND.

3.3. Construction of training images

The TIs constructed in this work are scale-independent, hence only a relative scaling between channel-fill and barform deposits is specified, on the basis of analogue data from FAKTS (Colombera et al., 2012a, b; 2013, 2017, 2018). In PB-SAND outputs, the stratigraphic complexity of point-bar deposits is characterized by bar-accretion geometries and the presence of genetically related channel fills, sitting in a background of fine-grained overbank deposits. By default, a representative fining-upward point-bar succession is modelled, though the facies trends can be customized. PB-SAND incorporates a number of facies types specified by users, and which relate to different grainsize categories (e.g., gravel, clay). Additional lithofacies types include the following: (i) mud that is deposited on accretion surfaces to form drapes during stages of low energy or slack water; (ii) mud that accumulates in undisturbed floodplain areas between point-bar elements; and (iii) conglomerates or breccias that accumulate on the channel thalweg floor as a result of localized reworking of channel banks (e.g., intraformational mud-clast breccias) (Miall, 1996).

In this study, training images that incorporate three, four or five facies were created for the purpose of testing different geomodelling scenarios. PB-SAND outputs are vector-based, grid-free graphics. This output is converted to a 3D geocellular grid, which can be outputted as an ASCII format text file or GSLib file for importing into industry-standard software applications. The resulting TIs are idealized and scale independent. Examples of the produced training images can be seen in Fig. 4.

Although MPS modelling codes are known to work best with stationary training images, all the 3D training images created for the purpose of this research represent inherently non-stationary fluvial architectures. This means that some of the lithological trends (e.g., point-bar fining-upward) are incorporated in the training image itself. However, the reproduction of other forms of non-stationarity (e.g., spatial variations in proportions of deposits) is only attempted through the application of auxiliary variables when performing MPS simulations (see below).

3.4. Training-image selection

From PB-SAND outputs, two geometric frameworks were selected that are representative of meander-belt architectures associated with meander translation and expansion, respectively (Fig. 4). For each of these two architectural frameworks, a set of three alternative TIs were created using a different number of facies. The aim of this is to simulate different categories of lithology and different types of facies trends, each of which serves a different geomodelling purpose.

- 1) **Three-facies training image.** In this case, the training image only incorporates lithological categories representing point-bar (sand-prone), floodplain (mud-prone) and channel-fill (mud-prone) deposits. A TI of this type is applicable in contexts of prospect evaluation, or where intra-point-bar sedimentary heterogeneity is considered negligible or not important.
- 2) **Four-facies training image.** In addition to the previously mentioned facies, training images of this type also include a separate category for muds that are deposited as drapes on the bar fronts and that are thus oriented along lateral-accretion surfaces. Therefore, these training images include: point-bar (sand-prone), floodplain, channel-fill and bar-front-mud (all mud-prone) facies. A TI of this type is applicable in contexts requiring assessment of intra-point-bar compartmentalization.
- 3) **Five-facies training image.** Three additional types of sandy facies within point-bar (meander expansion and translation) and counterpoint-bar (meander translation) deposits are defined in terms of grainsize (coarse, medium and fine sands) to portray fining-upward (meander expansion and translation) and downstream-

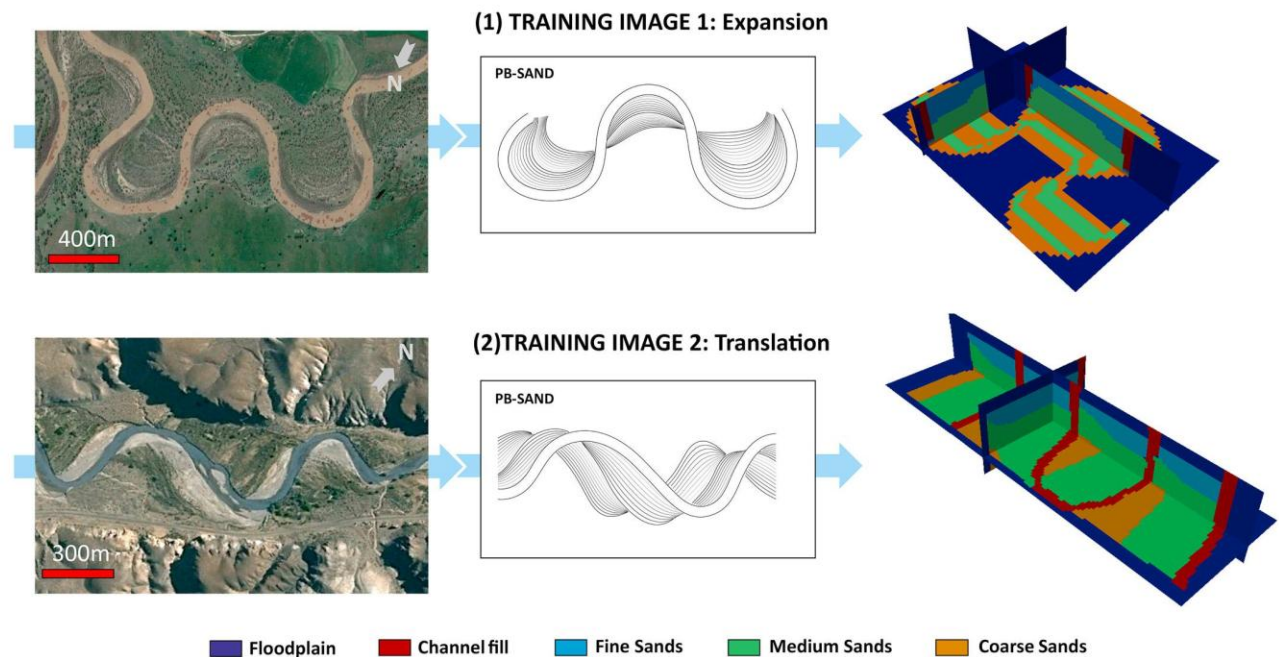


Fig. 4. Two training images selected from the training-image library, which incorporate channel belts associated with two different scenarios of meander transformation: 1) meander expansion (mean sinuosity 1.55) and 2) meander translation (mean sinuosity 3.03). PB-SAND outputs of reconstructed planform evolution are also shown in the middle, showing the plan-view expression of accretion surfaces resulting from channel migration through time. The legend at the bottom applies to the gridded TIs shown on the right-hand side. Satellite imagery of meanders undergoing expansion and translation are shown for comparison.

fining (meander translation) trends. A TI of this type is applicable in situations where prediction of intra-point-bar petrophysical heterogeneity is deemed important.

The size of the geobodies that are to be modelled in the simulation grid is determined by the number of cells and the cell size of the training image, in accordance with the number of cells and cell size of the simulation grid. Vector-based output from PB-SAND can be rasterized at any resolution. The larger the size and/or resolution (number of cells) of the TI, the longer it will take to complete a realization using it. Since an objective of this study is to develop a workflow that delivers a realization in less than 10 min – a runtime considered to be standard in industry – using a standard desktop computer (of 2019 vintage), upscaling of the training images is required. Training-image grid upscaling may result in significant loss of sedimentological detail, but the TIs included in the library are all scale-independent, allowing users to set a resolution that preserves the desired features.

3.5. MPS algorithms: SNESIM and DEESSE

The training images have been applied in workflows for the simulation of meandering fluvial systems using the modelling algorithms SNESIM (Strebelle, 2002) and DEESSE (Mariethoz et al., 2010). A calibration process based on trial and error has been employed to determine appropriate inputs for parameters that control TI scan and grid simulation, for both SNESIM and DEESSE. This has been achieved by trialling different values for input parameters, with consideration of runtime performance. Some of these parameters are similar or equivalent for SNESIM and DEESSE (e.g., search mask/neighbourhood) others are unique and only apply to a particular code (e.g., number of replicates in SNESIM, distance threshold “ t ” in DEESSE).

The numbers of facies in the training images have a significant impact on the computational time of both SNESIM (Strebelle, 2002) and DEESSE (Mariethoz et al., 2010). Input parameters have been adjusted to a runtime target of 10 min or less. The same facies proportions for the

different facies included in the training images have been specified as the target proportions for realizations of both SNESIM and DEESSE. In SNESIM, the modelled facies proportions are allowed to vary from the input facies proportions if the servosystem value ‘ λ ’ is different from 0, or if a trend is included using an auxiliary variable. For this study, the servosystem value was set to 0.5, and probability grids were employed, so a discrepancy between target and output proportions is expected.

The number of nodes considered during scan and simulation depends on the size and shape of the search mask or neighbourhood, i.e., of geometric templates defined as a set of cells with elliptical, circular or rectangular shape, and specified in terms of radius, azimuth, strike and rake. The larger the search mask, the longer the time per realization (Meerschman et al., 2013). In DEESSE, the radius of the search neighbourhood can vary according to the number of nodes that are being simulated. (i.e., the size of the radius will progressively decrease when the number of simulated nodes increases). A number of strategies have been introduced for optimizing search-mask or search neighbourhood definition. Riou et al. (2015), in application to channelized architectures, proposed the application of a search radius of 1.5 times the width of the largest channel units, and recommended isotropic search neighbourhoods as the most robust option for capturing some of the patterns expected in fluvial meandering systems.

In SNESIM, so-called ‘multigrids’ and ‘subgrids’ are used to configure the search mask so as to store the conditional probabilities efficiently. The purpose is to capture large-scale structures using a relative small search mask with a relatively small number of nodes. The larger the multigrid size the fewer the nodes that need to be considered in a particular grid. In this study, four multigrids have been used to run the simulations, as preliminary work indicated that this setting results in reasonably short runtime; the four multigrids have each been divided into four subgrids, which allow locating a larger number of conditioning data during simulation. The runtime increases with increasing minimum number of replicates (Strebelle, 2002); a minimum number of replicates between 5 and 10 has been chosen.

In the TI-scan process performed by DEESSE, a distance threshold ‘ t

is used to define the tolerance within which a pattern is recognized to match; the maximum fraction of TI to scan ('f') can also be specified (Mariethoz et al., 2010). Runtime increases with decreasing values of 't' and increasing values of 'f' (Meerschman et al., 2013). In DEESSE, the combination of number of nodes (n), distance threshold (t), and maximum scanned fraction (f) will have a significant impact on computation time. Therefore, changes to these parameters will need to be considered jointly. According to Meerschman et al. (2013) important considerations can be made as follows: (i) pattern-reproduction performance improves when 'n' is larger, 't' is closer to 0, and 'f' is closer to 1, but at the expense of realization runtime; (ii) variations in 't' and 'n' influence significantly the degree to which the patterns from the training image are reproduced in the simulation grid. However, 'f' has a much smaller effect on the simulation quality; (iii) reducing the scanned fraction 'f' of the TI allows substantial computational gains without degrading pattern reproduction as long as the TI contains a large enough number of reproducible patterns; (iv) a small 'f' value for TIs may lead to TI under-sampling and thus affect simulation results, but usually results in large computation gains without substantial decrease in simulations quality. The choice of input parameters to DEESSE was guided by these considerations. Table 1 includes all the parameters used for every simulation presented in this study.

3.6. Auxiliary variables (trends)

To employ the TIs for modelling the stratal architecture of a particular fluvial meandering system, a hierarchical approach to facies modelling has been taken. This is in part achieved through the use of auxiliary variables as means to force the incorporation of expected or desired geological features within the models.

For obtaining representative statistics, MPS algorithms commonly require stationary TIs. However, sedimentary bodies and associated facies characteristics and distributions tend to vary in space, i.e., are non-stationary. To be able to incorporate – at least in part – non-stationary features in the simulations, auxiliary variable grids (Chugunova and Hu, 2008) have been employed. Auxiliary variables are gridded properties that describe a spatial trend in the property being modelled. They also facilitate the reproduction of nested architectures, whereby simulations are undertaken at multiple scales, to enable reproduction of heterogeneities.

Auxiliary variables in the form of 2D or 3D grids are routinely used for forcing the reproduction of spatial variations in modelled properties at different levels (e.g., in mean body thickness, grainsize). These

auxiliary variables allow resultant models to account for non-stationarity relating to scaling effects (scaling maps that describe variations in space of the scale of certain features), variations in orientations of architectural elements (rotation maps), variations in the facies proportions (probability maps), and differentiation of regions characterized by different types of lithological heterogeneities (region maps). Probability maps are used as part of the proposed workflow to facilitate the reproduction of geological features associated with the channel belts of meandering rivers.

In the proposed workflow, probability maps have also been used to ensure realistic spatial transitions between facies, particularly between channel-belt and floodplain facies, and the reproduction in the simulations of specific sedimentological features, such as planform cut-bank geometries, and variations in facies proportions. Auxiliary variables also facilitate the incorporation of relationships between small-scale and large-scale features in a reservoir model (see below).

Auxiliary variable grids have been used in the developed workflow, consisting of grids that specify the probability of modelling categories. The object-based modelling tool of Schlumberger Petrel® was used to create probability regions. These regions represent: (i) the axial part of a sand fairway that could represent an amalgamated channel belt or valley fill (90% probability of channel deposits); (ii) an area that can only be occupied by floodplain deposits (100% probability of occurrence of mud-prone overbank sediments); and (iii) a buffer area that is defined with the scope to reproduce realistic channel-to-overbank transitions, whereby the channel belts would have some rugosity in planform and mud plugs would border the outer side of the belts (see Fig. 5). The same probability grids have been applied to all simulations, but a total of 3 different grids for each of the 3 TI types (3, 4 and 5 facies) have been created, which will differ with respect to probability values assigned to each region (cf. Tables in Fig. 5).

The functioning of probability grids differs between SNESIM and DEESSE. In SNESIM, auxiliary variables are applied based on TAU models (Journel, 2002). The probability of A jointly conditioned on B and C becomes a function of the marginal probability of A and of the two probabilities of A separately conditioned on B and C. This function depends on a parameter τ that measures the degree of redundancy between events B and C with respect to event A (Krishnan et al., 2004). Parameters that act as weights, named Tau2 and Tau1, can be controlled so that the higher Tau2 relative to Tau1 the higher is the influence of soft-probability data in controlling simulation results.

In DEESSE two main parameters control simulation outputs: the support radius (SR) and the deactivation threshold radius (DTR). The

Table 1

The parameters employed in the simulations whose outputs are discussed. SM: Search Mask, SN: Search Neighbourhood N: Nodes, Serv: Servosystem, Rep: Number of replicates, MG: Multigrids, SG: Subgrid, Tau: Tau Model weight values, SN: Search Neighbourhood, DT: Distance Threshold, F: maximum fraction of TI to scan, SR: Support Radius and DTR: Deactivation Threshold Radius.

		SNESIM input parameters							DEESSE input parameters					
		SM	N	Serv	Rep	MG	SG	Tau	SN	N	DT	F	SR	DTR
Meander expansion TIs	Case 1	2000x 2000y 10z	60	0.5	10	4	4	2, 1	20x 20y 8z	30	0.15	0.3	7	5
	Case 2	2000x 2000y 10z	60	0.5	10	4	4	2, 1	20x 20y 8z	30	0.2	0.3	10	8
	Case 3	4000x 3000y 4z	60	0.5	10	4	4	2, 1	20x 20y 4z	30	0.2	0.3	10	6
Meander Translation TIs	Case 4	5000x 5000y 10z	60	0.5	5	4	4	2, 1	20x 20y 5z	30	0.2	0.5	12	10
	Case 5	5000x 5000y 10z	60	0.5	5	4	4	2, 1	18x 18y 4z	35	0.15	0.5	10	7
	Case 6	5000x 5000y 5z	60	0.5	5	4	4	2, 1	15x 15y 5z	40	0.15	0.5	10	8

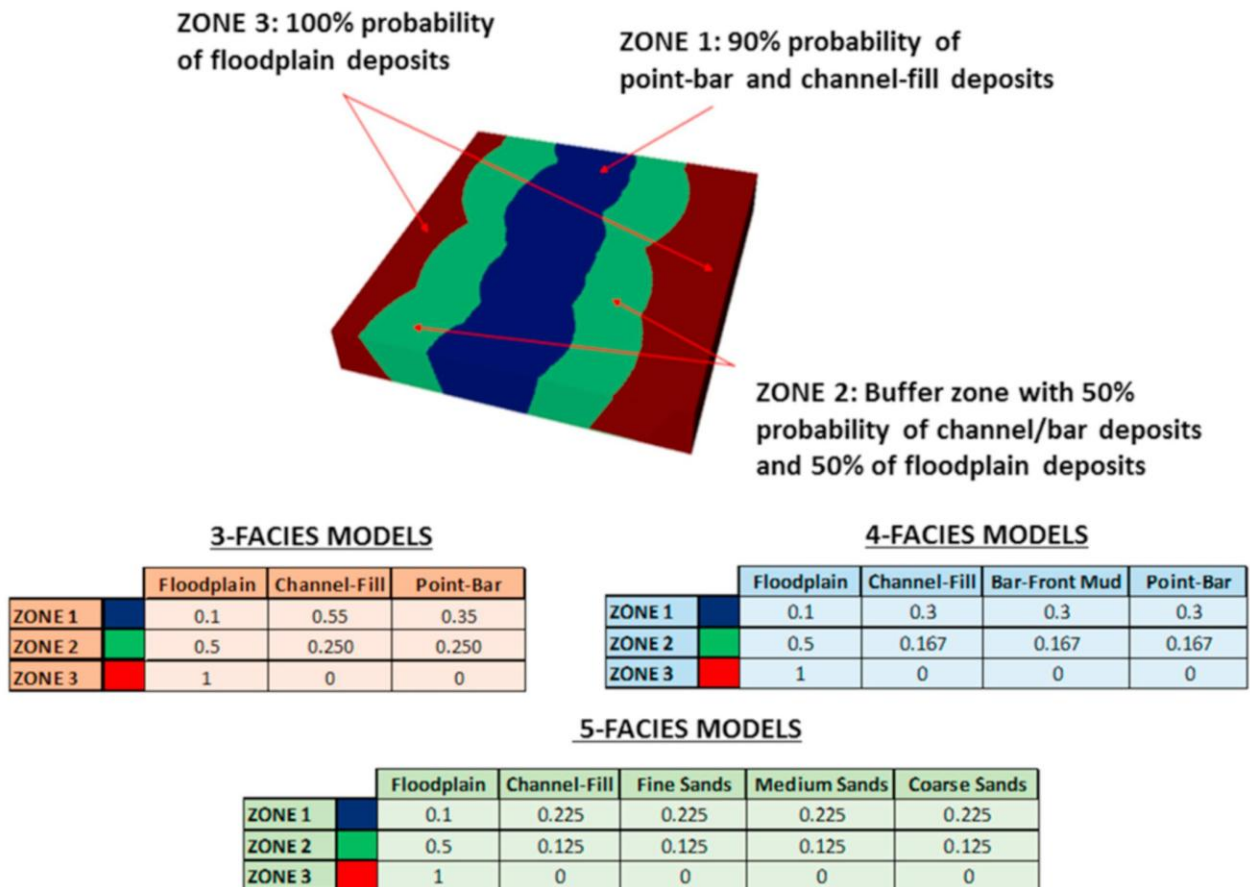


Fig. 5. Example of a probability grid that may be applied to reproduce facies distributions in a channel-belt or valley-fill unit. In the grid, 3 different zones are created, within which the probability of occurrence of the facies varies. The tables represent the 3 different probability scenarios that will be used in the application of training images that include 3, 4 and 5 facies (see main text and Table 1).

simulation process will randomly pick a data event “X” (i.e., a pattern formed by a certain number of cells) in the simulation grid, and will then try to find a similar data event considering (i) the patterns in the training images, (ii) the previously populated categories in the simulation grid, and (iii) the probabilities stored in the probability map. SR is used to identify patterns in the nodes that have been previously populated. If within the SR distance there are more informed nodes than the number of nodes, the nodes closest to “X” are those that will be populated in the realizations.

At the beginning of the simulation, prior to any cells being populated in the simulation grid, the algorithm populates facies that are recognized directly from the training image conditioned on the probabilities in the probability grid. At this stage the SR is equal or smaller than the actual search radius (RA). However, towards the end of the simulation, when most of the simulation grid is populated with informed nodes, if the RA is smaller than the DTR distance, the probability constraint mechanism is stopped. The selection of appropriate SR and DTR is a critical step when dealing with auxiliary variables in DEESSE, as it significantly affects the quality and the computation time per realization.

3.7. Model configuration and input tuning

Training images have been used that incorporate the two channel-belt geometries shown in Fig. 4, which are representative of channel-belt reaches composed of three meander bends and associated point-bar and channel-fill deposits, placed in a background of fine-grained

floodplain sediment. The two architectural frameworks represent simple meander belts that are respectively undergoing meander expansion and translation. For each of these two frameworks, three different sets of modelling categories (hereafter termed ‘facies’, for sake of simplicity) have been considered (Table 1). Each of these sets involves different number and types of facies. The three cases are as follows: (i) 3-facies case (point-bar, channel-fill and floodplain deposits); (ii) 4-facies case (point-bar deposits, channel-fill deposits, continuous bar-front muds and floodplain deposits); and (iii) 5-facies case (coarse point-bar sands, medium point-bar sands, fine point-bar sands, channel fill and floodplain deposits). These facies configurations have been selected to run unconditional simulations, such as those that would be run for modelling undrilled prospects, since unconditional realizations are ideal for assessing the degree to which TI patterns are reproduced (Rojas et al., 2012; Manchuk et al., 2011; Manchuk and Deutsch, 2012).

Unconditional simulations were performed to establish preferred modelling recipes that can be paired to each training image and to each MPS modelling algorithm. SNESIM and DEESSE were run on a simulation grid with the following dimensions: 250 cells along X, 250 cells along Y and 50 cells along Z. The cell size for the simulation grid was set to X:Y:Z ratios of 20:20:0.25.

The parameters selected for every simulation in SNESIM and DEESSE, based on trial and error and aiming for a runtime below 10 min, are shown in Table 1.

Results are analysed and discussed according to qualitative criteria that allow evaluation of aspects of sedimentary architecture whose

reproduction in the simulations is desirable. These are: (i) planform sinuosity and continuity of deposits with curvilinear geometries such as channel fills and bar-front muds; (ii) cross-sectional channelized geometry and adjacency to point-bar facies for channel-fill deposits, which act to compartmentalize point-bar sands; (iii) vertical fining-upward trends in point-bar deposits, in cases where different grain-size categories of point-bar sediments are considered; (iv) planform concavity of abandoned-channel fills being oriented towards the belt axis when placed at the transition to the overbank domain; and (v) outward fining in point-bar elements associated with expansional meanders. Additionally, for training images embodying the products of meander translation, the presence of counter-point-bar deposits (which are typically finer grained than corresponding point-bar deposits) associated with concave-bank accretion is also evaluated.

4. Results

Here, an evaluation of the modelling outputs that would be generated upon application of training images created using the proposed workflow is presented. Results are shown below for the six cases that result from applying (i) the two sets of training images reflecting contrasting channel-belt accretion geometries and (ii), for each set, three facies configurations, as explained above (Section 3.4; Fig. 4). The training images were retrieved from the training-image library constructed following the workflow explained above (Sections 3.1-3.3; Fig. 3). The application of training images in MPS simulations was tested using SNESIM and DEESSE, constrained through the parameters and auxiliary variable described above (Sections 3.5-3.7). Outputs of SNESIM and DEESSE are compared in terms of degree of pattern reproduction and CPU performance.

Twenty realizations were generated for each of the six simulation cases. In the figures (Figs. 6-11), only one of these realizations is presented for each of the six cases. The results of the qualitative assessment of modelling outputs are also indicated in Figs. 6-11.

4.1. Case 1: meander expansion (3 facies)

Upon application of this TI, in both SNESIM and DEESSE realizations (Fig. 6) sinuous channel-fill deposits appear relatively continuous, locally display loop geometries, and compartmentalize the sand-fairway zone where point-bar deposits are located. Stratigraphic compartmentalization created by sinuous channel-fill deposits is also evident in vertical sections of realizations delivered by SNESIM. DEESSE realizations appear slightly different in vertical sections, in which more vertically elongated features are present. Overall, both SNESIM and DEESSE reproduce meandering loops typical of mud-filled plugs representing abandoned channel-fill segments over a sand fairway (fluvial channel belt).

4.2. Case 2: meander expansion (4 facies)

Case 2 was simulated using a larger training image (number of cells: 165 along x, 175 along y, 60 along z) to test the effects of image resolution in populating geobodies with better defined geometries in the selected simulation grid (Fig. 7). SNESIM simulations delivered results in less than 7 min, on average. However, for simulations performed according to the devised workflow using DEESSE, in order to complete simulations within the 10-min runtime target, the TI had to be set to a lower resolution ($76 \times 80 \times 30$). Although DEESSE realizations contain geobodies that are significantly smaller than those generated by SNESIM due to the different size of the TI, realizations are relatively similar in terms of geological patterns they incorporate. Curvilinear shapes are evident in plan-view sections, corresponding to channel-fill deposits and mud-front facies. Channel-fill deposits create compartments separating volumes of point-bar facies, but lack the expected continuity in both SNESIM and DEESSE realizations. Plan-view sections show bar-front muds that are sinuous and delineate a second type of compartments within the point-bar facies, separating different sand-prone packages. Compartmentalization by thick mud-prone packages that drape accretion surfaces are also evident in most of the realizations. In vertical

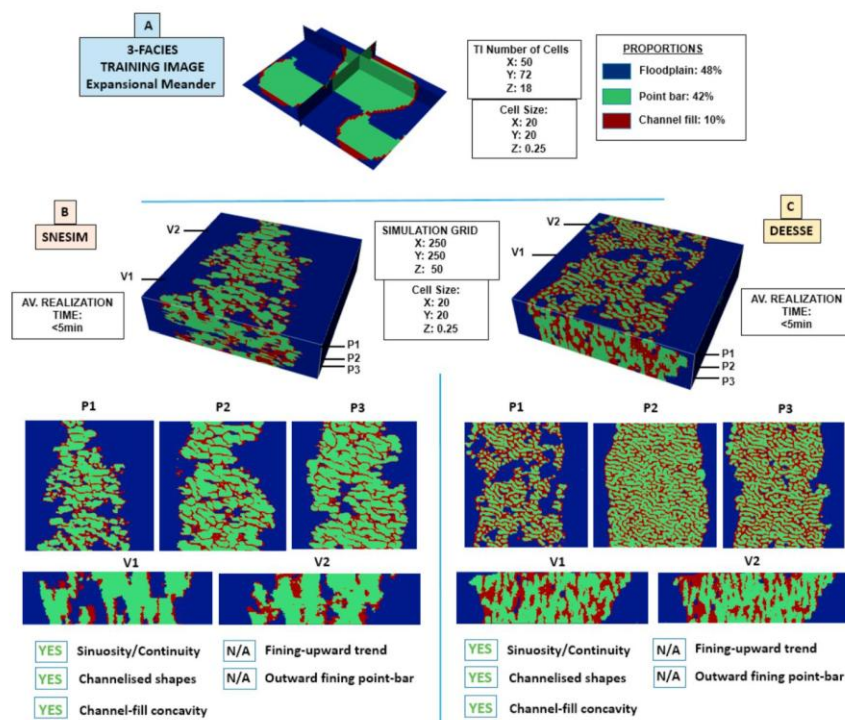


Fig. 6. Representative simulation results for the 3-facies training image for meander belts with expansional meanders (case 1). (A) Employed training image. Number of cells, cell size and proportions are indicated. Simulations performed for SNESIM (B) and DEESSE (C) are presented as block models in perspective view, together with 3 plan-view sections (P1, P2 and P3) and 2 vertical sections (V1 and V2) for each. A summary of the number of cells for the simulation grid is reported between part B and C. Below the vertical sections, a qualitative assessment of the realizations is presented for each simulation method.

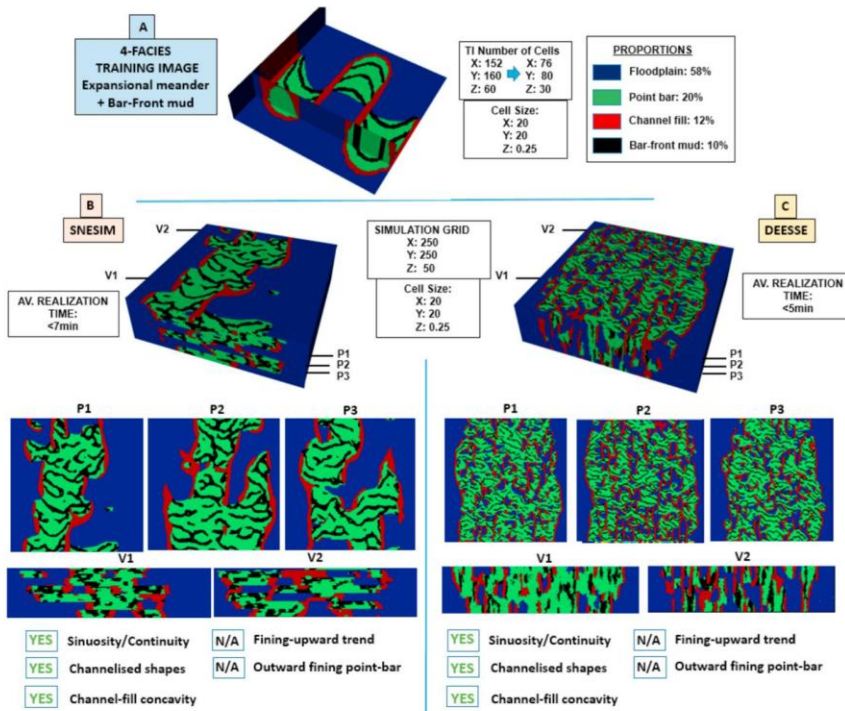


Fig. 7. Representative simulation results for the 4-facies training image for meander belts with expansional meanders (case 2). (A) Employed training image. Number of cells, cell size and proportions are indicated. Simulations performed for SNESIM (B) and DEESSE (C) are presented as block models in perspective view, together with 3 plan-view sections (P1, P2 and P3) and 2 vertical sections (V1 and V2) for each. A summary of the number of cells for the simulation grid is reported between part B and C. Below the vertical sections, a qualitative assessment of the realizations is presented for each simulation method.

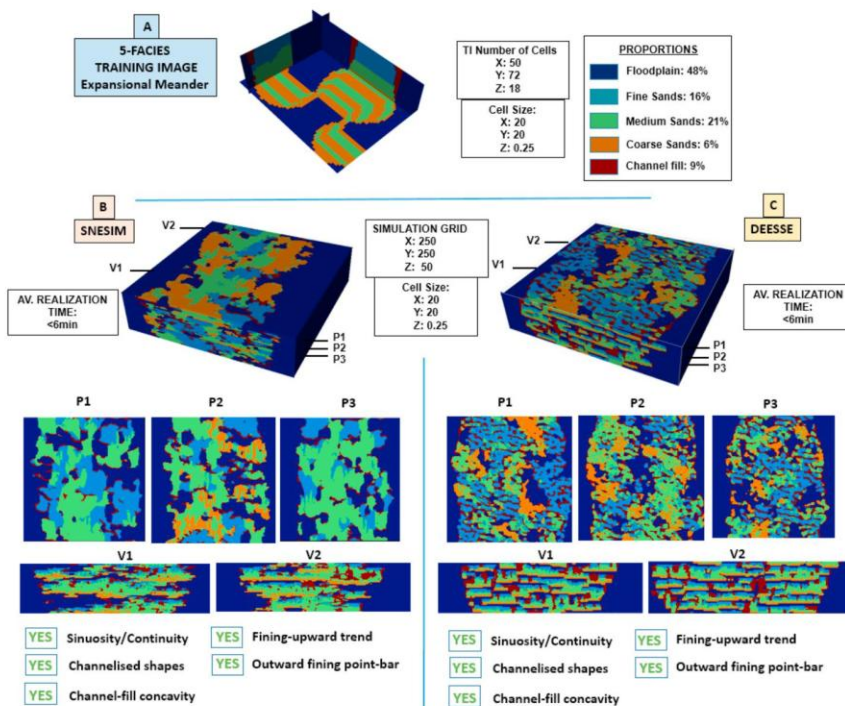


Fig. 8. Representative simulation results for the 5-facies training image for meander belts with expansional meanders (case 3). (A) Employed training image. Number of cells, cell size and proportions are indicated. Simulations performed for SNESIM (B) and DEESSE (C) are presented as block models in perspective view, together with 3 plan-view sections (P1, P2 and P3) and 2 vertical sections (V1 and V2) for each. A summary of the number of cells for the simulation grid is reported between part B and C. Below the vertical sections, a qualitative assessment of the realizations is presented for each simulation method.

sections, channel-fill deposits exhibit a channelized shape. However, both channel-fill and bar-front-mud bodies are excessively elongated vertically in DEESSE simulations, similarly to Case 1.

4.3. Case 3: meander expansion (5 facies)

These simulations attempted to model different types of sandy point-bar facies including the characteristic fining-upward trend common in expansional point-bar elements (Fig. 8).

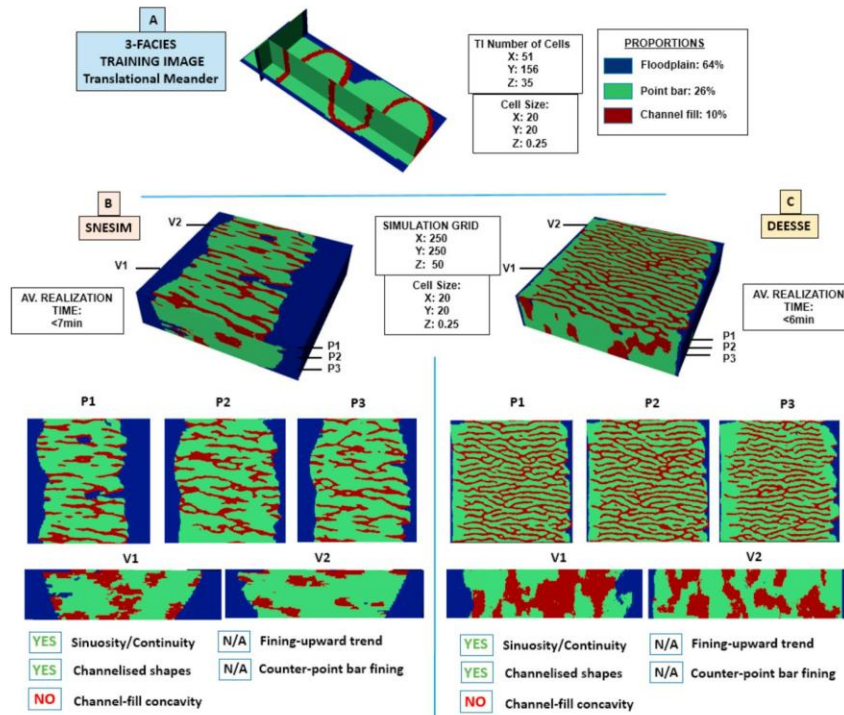


Fig. 9. Representative simulation results for the 3-facies training image for meander belts with downstream translating meanders (case 4). (A) Employed training image. Number of cells, cell size and proportions are indicated. Simulations performed for SNESIM (B) and DEESSE (C) are presented as block models in perspective view, together with 3 plan-view sections (P1, P2 and P3) and 2 vertical sections (V1 and V2) for each. A summary of the number of cells for the simulation grid is reported between part B and C. Below the vertical sections, a qualitative assessment of the realizations is presented for each simulation method.

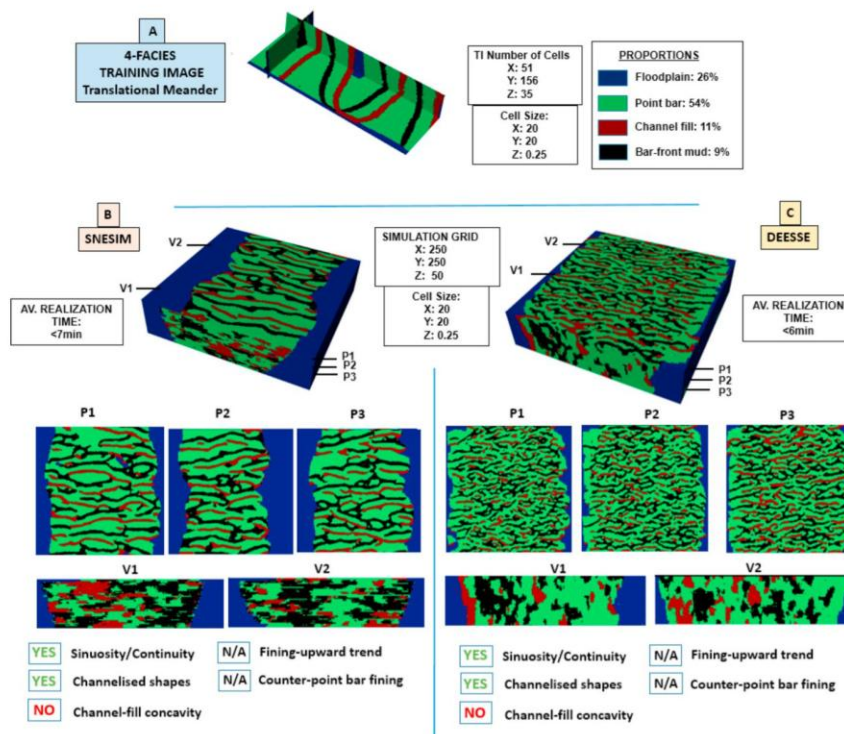


Fig. 10. Representative simulation results for the 4-facies training image for meander belts with downstream translating meanders (case 5). (A) Employed training image. Number of cells, cell size and proportions are indicated. Simulations performed for SNESIM (B) and DEESSE (C) are presented as block models in perspective view, together with 3 plan-view sections (P1, P2 and P3) and 2 vertical sections (V1 and V2) for each. A summary of the number of cells for the simulation grid is reported between part B and C. Below the vertical sections, a qualitative assessment of the realizations is presented for each simulation method.

In horizontal sections, realizations created by both SNESIM and DEESSE demonstrate the simulated lateral juxtaposition of different point-bar elements deposited through the sand-fairway region. Channel-fill deposits are seen as remnant channel-fill plugs that have limited

continuity and sinuosity; these only locally compartmentalize point-bar sands, as is common in many documented successions.

Vertically, a fining-upward trend has been successfully reproduced by both SNESIM and DEESSE, with channel-deposits located at the

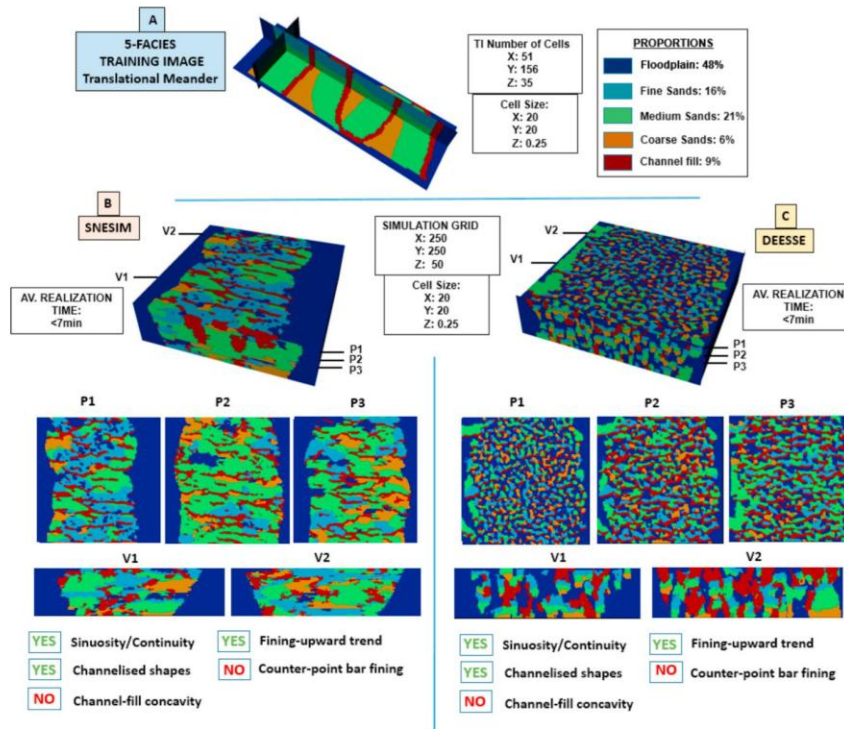


Fig. 11. Representative simulation results for the 5-facies training image for meander belts with downstream translating meanders (case 6). (A) Employed training image. Number of cells, cell size and proportions are indicated. Simulations performed for SNESIM (B) and DEESSE (C) are presented as block models in perspective view, together with 3 plan-view sections (P1, P2 and P3) and 2 vertical sections (V1 and V2) for each. A summary of the number of cells for the simulation grid is reported between part B and C. Below the vertical sections, a qualitative assessment of the realizations is presented for each simulation method.

margins of point-bar units. Model outputs are characterized by vertically stacked bar-and-channel deposits locally separated by remnants of overbank deposits, such that point-bar tops are mostly preserved.

In general terms, realizations performed using both SNESIM and DEESSE show aspects of geological realism; it is possible to differentiate different types of sand-prone units located in isolated compartments. No major differences in runtime were observed between SNESIM and DEESSE.

4.4. Case 4: meander translation (3 facies)

On horizontal planes, simulations performed using both SNESIM and DEESSE demonstrate channel-fill geobodies that appear as low-sinuosity linear features that are oriented perpendicular to the direction of the sand-fairway axis (Fig. 9) and that are laterally discontinuous. Compartments are locally created by the channel-fill deposits, which do not however exhibit loop geometries. In vertical sections, channelized features are recognizable as channel deposits in simulations delivered by SNESIM. However, DEESSE realizations include oversized channel-fill geobodies. Overall, geometries of geobodies produced by SNESIM and DEESSE differ from the ones in the original training image. Notably, channel-fill deposits appear overly elongated along a direction that is perpendicular to the sand-fairway axis.

4.5. Case 5: meander translation (4 facies)

Similar to Case 4, considerable time was required to satisfactorily tune input parameters to DEESSE. Both SNESIM and DEESSE realizations produced using this TI (Fig. 10) include channel-fill geobodies and mud-prone packages that appear as low-sinuosity ribbons elongated perpendicularly to the sand-fairway axis, similarly to Case 4. Both mud-prone packages and channel-fill deposits interrupt the continuity of sandy point-bar deposits. However, similarly to the 3-facies scenario, channel-fill meander-loop elements are rarely reproduced, since channel fills appear as continuous features perpendicular to the channel-belt

axis. Furthermore, delivered realizations included sharp transitions between floodplain and channel-belt facies, and in most of the cases simulations incorporated less than 50% of floodplain facies, as embodied in the probability grid selected for this simulation (Fig. 5). In vertical sections, channel-fill deposits rendered by DEESSE have more unrealistic shapes and aspect ratios that those generated by SNESIM.

4.6. Case 6: meander translation (5 facies)

These realizations include different types of bar deposits (grain-size categories) located within the channel belt (Fig. 11). Compartmentalization determined by muddy abandoned channel-fill deposits is oriented dominantly perpendicular to the channel-belt axis. However, similarly to cases 4 and 5, the continuity of abandoned channel-fill elements is limited. Sinuous abandoned channel-fill features are absent in both SNESIM and DEESSE outputs.

Similar to previous cases, considerable time was required for effective parameterization. For DEESSE, the chosen values for SR (Search Radius) and DTR (Deactivation threshold radius) gave rise to patchy and chaotic geobodies, and resulted in proportions of floodplain facies in the sand-fairway region that do not honour the probability grid (i.e., floodplain deposits represent over 10% of this region; cf. Fig. 5).

Vertical sections display sandbody compartmentalized by channel-fill deposits. The point-bar fining-upward trend is not typically evident in either SNESIM or DEESSE outputs. The lack of a clear differentiation between different point-bar bodies makes it difficult to ascertain the reproduction of downstream facies trends within them. Overall, the geobodies bear little resemblance to the patterns present in the TIs.

5. Discussion

The intent of this research was not to test modelling algorithms through a systematic assessment of their performance, with the aim to provide definitive guidance on parameter tuning; work of this type already exists, as applied to both SNESIM and DEESSE (Liu, 2006;

Meerschman et al., 2013). Rather, we determined the ability of these MPS modelling methods to reproduce the types of geological architectures that are characteristic of successions deposited by meandering fluvial systems, since this is a geological context to which MPS is often applied (Rojas et al., 2012; Manchuk et al., 2011; Manchuk and Deutsch, 2012; Arnold et al., 2019), but which is characterized by heterogeneities that are intrinsically non-stationary (Nanson and Page, 1983; Thomas et al., 1987; Alpak and Barton, 2014; Russell et al., 2019). Concurrently, this work:

- (i) provides a test of the suitability of the proposed forward stratigraphic modelling software (PB-SAND; Yan et al., 2017, 2019, 2020; Colombera et al., 2018) as a training-image creator, which allows producing trends that would not be readily generated using general-purpose tools (e.g., Maharaja, 2008);
- (ii) outlines a workflow that is applicable in cases where a framework exists of the larger-scale architecture of a fluvial succession, consisting of the distribution of large-scale channelized geobodies representing channel belts or valley fills, within which sedimentary heterogeneity needs to be predicted; in reservoir-modelling situations, this framework may be established based on outputs of other modelling efforts (e.g., object-based modelling) linked with MPS in a hierarchical fashion, or by defining channelized geobodies recognizable in 3D seismic cubes; in this way, regions of the reservoir volumes can be defined that can be utilized in the same manner as the probability grids adopted to generate the unconditional realizations discussed in this work.

As applied to SNESIM and DEESSE using training images that incorporate 3 facies only (representing point-bar, channel-fill and overbank deposits) and that relate to channel-belt architectures associated with simple meander expansion, the proposed workflows were effectively employed to model the distribution of channel-fill deposits. The resultant simulated outputs reveal the presence and expected distribution of compartments within meander-belt deposits.

Similar results were observed when using 4-facies training images for expansional point bars, where thick accumulations of mud are also simulated within the point-bar compartments. The successful application of training images incorporating 3 and 4 facies are particularly important as these types of simulation are the preferred scenarios for many simulations of fluvial reservoir successions. When feeding a dynamic simulation, these static models will effectively discriminate facies that act as barriers to fluid flow (floodplain, channel-fill and bar-front mud) from more permeable reservoir volumes (point-bar deposits).

By contrast, the application of training images that incorporate 3, 4 and 5 facies relating to channel-belt architectures associated with meander translation returned realizations that contained discontinuous string-shaped channel-fill geobodies arranged perpendicular to the axis of the sand fairway, rather than units that are continuous and sinuous in planform, as was expected. Also, trends incorporated in the training image such as downstream or upward fining do not seem to be well replicated by either SNESIM or DEESSE. This highlights limitations in the application of these codes to reproduction of trends of this type.

The 5-facies simulations were performed for the two different types of training images. Contrary to the 3-facies training images, the aim for this set of model runs was to simulate a scenario where three different types of bar deposits (sands forming reservoir units) can be differentiated from two types of mud-prone units (channel-fill and floodplain facies – typically non-net reservoir). For both SNESIM and DEESSE, the implemented fining-upward trend is recognized in all the realizations, allowing effective differentiation of different vertically stacked, genetically related bars and channel fills. Channelized shapes are also recognized in the vertical section. However, a decrease in sinuosity and continuity of channel-fill deposits has been acknowledged in the horizontal planes. Loops are rarely distinguished, unlike in 3- and 4-facies simulations obtained using the training images related to expansional

meanders. Moreover, simulations appear patchy where different types of point-bar facies are populated in sandy compartments. Runtime for these types of simulations were significantly higher than for the 3- and 4-facies simulations. However, all realizations were still generated in less than 10 min based on the chosen inputs.

Based on the qualitative criteria of geological realism considered in this work, an algorithm – SNESIM or DEESSE – that performs consistently better cannot be indicated. Rather, the manner in which features incorporated in the training images are reproduced by either algorithm appears to depend on a combination of input parameters, type of architecture being modelled, and number and types of facies considered.

The simulations performed in this research are not associated with a specific physical scale. The size and resolution of the TIs were important factors in the simulations for dictating geological realism and runtime. The relative size of the TI (number of cells) with respect to the relative size of the simulation grid was calibrated to the size of geobodies to be reproduced in the realizations. For example, the reproduction of large-scale patterns requires training images whose size might be close to the size of the simulation grid. Modelled channelized features will tend to be discontinuous in planform if the TI is smaller than the modelling grid. However, if the training image includes small-scale features that must be reproduced in the simulation grid, a larger number of cells is required (Caers and Zhang, 2004). However, the greater the number of cells in the training image, the greater the runtime needed to perform the simulations in both SNESIM and DEESSE. The size of the geobodies is controlled by the number of cells in the training image with respect to the number of cells in the simulation grid.

Differences were observed in runtime when SNESIM and DEESSE needed to handle training images with larger number of cells. An example of the differences can be seen in cases 2 and 5 where DEESSE realizations required significantly longer runtime than those created using SNESIM. In these cases, the input parameters employed initially resulted in runtime that exceeded the established 10 min threshold per realization, so a further upscaling was performed to create a coarser TI for use in DEESSE simulations.

The iterative process by which parameters are optimized in order to deliver relatively realistic realizations within the target runtime is time-consuming, and likely represents a barrier to the widespread uptake of this method by geomodellers. On the basis of the experience acquired through this work, some recommendations can be made that can be used to guide modelling practice, as follows:

- (i) Both the Search Mask (SNESIM) and the Search Neighbourhood (DEESSE) should be set to a size that is sufficiently large to allow the algorithm to borrow the required patterns from the training image along horizontal axes. This study always considered search masks and search neighbourhood values that span the number of cells needed to cover the full amplitude of a meander bend (point bar). Working with large 3D training images often results in excessive runtime.
- (ii) To speed up the modelling effort, it is recommended that parameter tuning is initially performed on 2D grids with any given orientation (X, Y or Z).
- (iii) Calibrating the use of the probability grids in DEESSE can be time-consuming. Unlike SNESIM, which only requires the choice of a TAU model, DEESSE demands setting the weight of the probability grid in the simulations, which requires a search radius (SR) and deactivation threshold radius (DTR) to be optimized simultaneously. A recommendation can be made for a calibration of probability grids starting from values of SR and DTR that are relatively high (>10); smaller values for SR and DTR resulted in excessive runtime.

6. Conclusions

A hierarchical workflow for the application of MPS modelling

algorithms (SNESIM and DEESSE) has been tested by modelling sedimentary architectures that are characteristic of high-sinuosity fluvial meandering systems. The hierarchical approach involves the use of 3D training images for 2 different scenarios (associated with fluvial systems development via bar expansion and translation respectively), each incorporating either 3, 4 or 5 facies. Training images were built using a forward stratigraphic model (PB-SAND) partly conditioned on geological-analogue data borrowed from a sedimentological database (FAKTS), together with auxiliary variables that describe facies probability and input parameters to the algorithms that are optimized for delivering realizations in less than 10 min on a standard desktop personal computer. The proposed workflow can be employed in real-world reservoir modelling scenarios through the use of probability grids constrained on seismic geobodies, or through linkage to outputs of object-based modelling.

The comparison between unconditional realization generated using SNESIM and DEESSE enables evaluation of their performance in modelling fluvial successions, assuming a target runtime of up to 10 min. Realizations have been assessed qualitatively against (i) the training images, and (ii) known characteristics of sedimentary architectures of high-sinuosity river systems. Analysis of simulation results indicate what geological features of meandering fluvial successions arising from expansional and translational point-bar development are reproduced.

Planform curvilinear and channelized geometries in the cross-section are sometime evident in modelled channel-fill deposits. Furthermore, under certain modelling inputs, modelled sand-prone point-bar facies take the form of compartments that are juxtaposed horizontally and vertically. This modelling set up is applicable to simulate the architecture of meandering reservoir successions requiring prediction of the degree of stratigraphic compartmentalization of effective net reservoir units by mud plugs. Fining-upward trends incorporated in the 5-facies training image for expansional bars are successfully reproduced by both SNESIM and DEESSE. This modelling approach finds application to reservoir models requiring finer-scale petrophysical characterization of point-bar deposits, especially in contexts of enhanced oil recovery. However, for simulations based on training images associated with translational meanders, the desired differentiation of counter-point bar fines and the geometry of channel-fill meander loops were not readily replicated.

Geomodelling workflows that employ MPS simulations recommend use of stationary training images and incorporation of trends by using auxiliary variable maps. This study demonstrates that geological trends that are incorporated in the training image itself (e.g., point-bar fining-upwards) can be reproduced in some circumstances. Moreover, this research highlights the potential value of a comprehensive training-image library for fluvial depositional systems (cf. [Pyrz et al., 2008](#)), from which geomodellers could select training images and associated modelling recipes based on types of heterogeneities that need to be modelled and target runtime.

Credit author statement

Jose Montero: conceptualization, methodology, validation, formal analysis, writing original-draft preparation. Luca Colomera: conceptualization, validation, supervision, writing-review and editing. Nigel Mountney: validation, resources, supervision, writing-review and editing. Na Yan: software, supervision.

Declaration of competing interest

The authors declare that they have no known competing financial interests or personal relationships that could have appeared to influence the work reported in this paper.

Acknowledgements

We thank AkerBP, Areva (now Orano), BHPBilliton, Cairn India (Vedanta), ConocoPhillips, Chevron, CNOOC, Equinor, Murphy Oil, Occidental, Saudi Aramco, Shell, Tullow Oil, Woodside and YPF for their financial support of the Fluvial & Eolian Research Group at the University of Leeds. We also thank our project partner Petrotechnical Data Systems for their support. Luca Colomera has been supported by NERC (Catalyst Fund award NE/M007324/1; Follow-on Fund NE/N017218/1). We would also like to thank Philippe Renard and Julien Straubhaar (University of Neuchatel) for providing an academic license to DEESSE, and Alessandro Comunian (University of Milan) for providing feedback. Two anonymous reviewers are thanked for their constructive comments.

References

- Alpak, F., Barton, M.D., 2014. Dynamic impact and flow-based upscaling of the estuarine point-bar stratigraphic architecture. *J. Petrol. Sci. Eng.* 120, 18–38. <https://doi.org/10.1016/j.petrol.2014.05.020>.
- Arnold, D., Denysanov, V., Rojas, T., Christie, M., 2019. Uncertainty quantification in reservoir prediction: Part 1—model realism in history matching using geological prior definitions. *Math. Geosci.* 51 (2), 209–240. <https://doi.org/10.1007/s11004-018-9774-6>.
- Bluck, B.J., 1971. Sedimentation in the meandering river Endrick. *Scott. J. Geol.* 7 (2), 93–138. <https://doi.org/10.1144/sjg07020093>.
- Bridge, J., Leeder, M.A., 1979. Simulation model of alluvial stratigraphy. *Sedimentology* 26 (5), 617–644. <https://doi.org/10.1111/j.1365-3091.1979.tb00935>.
- Caers, J., 2001. Geostatistical reservoir modelling using statistical pattern recognition. *J. Petrol. Sci. Eng.* 29 (3–4), 177–188. [https://doi.org/10.1016/S0920-4105\(01\)00088-2](https://doi.org/10.1016/S0920-4105(01)00088-2).
- Caers, J., 2005. *Petroleum Geostatistics*. Society of Petroleum Engineers.
- Caers, J., Zhang, T., 2004. Multiple-point geostatistics: a quantitative vehicle for integrating geologic analogs into multiple reservoir models. In: Grammer, G.M., Mitch Harris, P.M., Eberli, G.P. (Eds.), *Integration of Outcrop and Modern Analogs in Reservoir Modeling*, vol. 80. AAPG Memoir, pp. 383–394.
- Cannon, S., 2018. *Reservoir Modelling: A Practical Guide*. Wiley Blackwell.
- Chugunova, T.L., Hu, L.Y., 2008. Multiple-point simulations constrained by continuous auxiliary data. *Math. Geosci.* 40 (2), 133–146. <https://doi.org/10.1007/s11004-007-9142-4>.
- Colomera, L., Mountney, N.P., McCaffrey, W.D., 2012a. A relational database for the digitization of fluvial architecture concepts and example applications. *Petrol. Geosci.* 18 (1), 129. <https://doi.org/10.1144/1354-079311-021>.
- Colomera, L., Felletti, F., Mountney, N.P., McCaffrey, W.D., 2012b. A database approach for constraining stochastic simulations of the sedimentary heterogeneity of fluvial reservoirs. *AAPG (Am. Assoc. Pet. Geol.) Bull.* 96 (11), 2143–2166. <https://doi.org/10.1306/04211211179>.
- Colomera, L., Mountney, N.P., McCaffrey, W.D., 2013. A quantitative approach to fluvial facies models: methods and example results. *Sedimentology* 60 (6), 1526–1558. <https://doi.org/10.1111/sed.12050>.
- Colomera, L., Mountney, N.P., Russell, C.E., Shiers, M.N., McCaffrey, W.D., 2017. Geometry and compartmentalization of fluvial meander-belt reservoirs at the bar-form scale: quantitative insight from outcrop, modern and subsurface analogues. *Mar. Petrol. Geol.* 82, 35–55. <https://doi.org/10.1016/j.marpetgeo.2017.01.024>.
- Colomera, L., Yan, N., McCormick-Cox, T., Mountney, N.P., 2018. Seismic driven geocellular modeling of fluvial meander-belt reservoirs using a rule-based method. *Mar. Petrol. Geol.* 93, 553–569. <https://doi.org/10.1016/j.marpetgeo.2018.03.042>.
- Corbett, P., Hamdi, H., Gurav, H., 2012. Layered fluvial reservoirs with internal fluid cross flow: a well-connected family of well test pressure transient response. *Petrol. Geosci.* 18 (2), 219–229. <https://doi.org/10.1144/1354-079311-008>.
- De Vries, L., Carrera, J., Falivene, O., Gratacos, O., Slooten, L., 2009. Application of multiple point geostatistics to non-stationary images. *Math. Geosci.* 41 (1), 29–42. <https://doi.org/10.1007/s11004-008-9188-y>.
- Deutsch, C.V., 1992. *Annealing Techniques Applied to Reservoir Modeling and the Integration of Geological and Engineering (Well Test) Data*. PhD Thesis. Stanford University, Stanford, CA.
- Deutsch, C.V., Journel, A.G., 1998. *GSLIB. Geostatistical Software Library and User's Guide*, second ed. Oxford University Press, Oxford, New York. <https://doi.org/10.1017/S0016756899531774>. x + 369 pp. + CD-ROM.
- Deutsch, C.V., Wang, L., 1996. Hierarchical object-based stochastic modeling of fluvial reservoirs. *Math. Geol.* 28 (7), 851–880. <https://doi.org/10.1007/BF02066005>.
- Farmer, C.L., 1988. The generation of stochastic fields of reservoir parameters with specified geostatistical distributions. In: Edwards, S., King, P.R. (Eds.), *Mathematics in Oil Production*. Clarendon Press, Oxford, pp. 235–252.
- Guardiano, F.B., Srivastava, R.M.no, 1993. Multivariate geostatistics: beyond bivariate moments. In: Soares, A. (Ed.), *Geostatistics: Troia '92*. Kluwer Academic Publishers, Dordrecht, pp. 133–144.
- Haldorsen, H., Damsleth, E., 1990. Stochastic modelling. *J. Petrol. Technol.* 42 (4), 404–412.
- Harding, A., Strebelle, S., Levy, M., Thorne, J., Xie, D., Leigh, S., Preece, R., Scamman, R., 2004. Reservoir facies modelling: new advances in MPS. *Quantitative Geology and Geostatistics Geostatistics Banff* 14.

- Honarkhah & Caers, 2010. Stochastic simulation of patterns using distance-based pattern modeling. *Math. Geosci.* 42, 487–517. <https://doi.org/10.1007/s11004-010-9276-7>.
- Hovadik, J.M., Larue, D.K., 2007. Static characterization of reservoirs: refining the concepts of connectivity and continuity. *Petrol. Geosci.* 13 (3), 195–211. <https://doi.org/10.1144/1354-079305-697>.
- Hubbard, S.M., Smith, D.G., Nielsen, H., Leckie, D.A., Fustic, M., Spencer, R.J., Bloom, L., 2011. Seismic geomorphology and sedimentology of a tidally influenced river deposit, Lower Cretaceous Athabasca oil sands, Alberta, Canada. *AAPG (Am. Assoc. Pet. Geol.) Bull.* 95 (7), 1123–1145. <https://doi.org/10.1306/12131010111>.
- Jelpi, A., Ghinassi, M., 2014. Planform architecture, stratigraphic signature and morphodynamics of an exhumed Jurassic meander plain (Scalby Formation, Yorkshire, UK). *Sedimentology* 61 (7), 1923–1960. <https://doi.org/10.1111/sed.12122>.
- Jackson, R., 1976. Depositional model of point bars in the lower Wabash River. *J. Sediment. Res.* 46 (3), 579–594. <https://doi.org/10.1306/212F6FF5-2B24-11D7-8648000102C1865D>.
- Journel, A.G., 1993. Geostatistics: roadblocks and challenges. In: Soares, A. (Ed.), *Geostatistics: Troia '92*. Kluwer Academic, Dordrecht, pp. 213–224. https://doi.org/10.1007/978-94-011-1739-5_18.
- Journel, A., 2002. Combining knowledge from multiple information sources: an alternative to traditional data independence hypotheses. *Math. Geol.* 34 (5), 573–596. <https://doi.org/10.1023/A:1016047012594>.
- Journel, A.G., Zhang, T., 2006. The necessity of a multiple-point prior model. *Math. Geol.* 38 (5), 591–610. <https://doi.org/10.1007/s11004-006-9031-2>.
- Krishnan, S., Boucher, A., Journel, A., 2004. Evaluating information redundancy through the TAU model. *Geostatistic Banff 1037–1046*. https://doi.org/10.1007/978-1-4020-3610-1_108.
- Liu, Y., 2006. Using the Snesim program for multiple-point statistical simulation. *Comput. Geosci.* 32 (10), 1544–1563. <https://doi.org/10.1016/j.cageo.2006.02.008>.
- Liu, Y., Harding, A., Gilbert, R., Journel, A.G., 2005. A workflow for multiple-point geostatistical simulation. In: Leuangthong, O., Deutsch, C.V. (Eds.), *Geostatistics Banff 2004. Quantitative Geology and Geostatistics*, vol. 14. Springer, Dordrecht, pp. 245–254. https://doi.org/10.1007/978-1-4020-3610-1_25 (25).
- Ma, Y., Zee, 2019. *Quantitative Geosciences: Data Analytics, Geostatistics, Reservoir Characterization and Modeling*. Springer.
- Maharaja, A., 2008. Tgenerator: object-based training image generator. *Comput. Geosci.* 34 (12), 1753–1761. <https://doi.org/10.1016/j.cageo.2007.08.012>.
- Manchuk, J.G., Deutsch, C.V., 2012. Modeling of the McMurray formation using MPS tied to tidal range. *CCG Annual Report 14*. Paper 108.
- Manchuk, J.G., Lyster, S.J., Deutsch, C.V., 2011. A comparative study of simulation techniques with multiple point statistics: the MPS beauty contest. *CCG Annual Report 13*. Paper 107.
- Mariethoz, G., Renard, P., Straubhaar, J., 2010. The Direct Sampling method to perform multiple point geostatistical simulations. *Water Resour. Res.* 46 (11), 1–14. <https://doi.org/10.1029/2008WR007621>.
- Meerschman, E., Pirot, G., Mariethoz, G., Straubhaar, J., Van Meirvenne, M., Renard, P., 2013. A practical guide to performing multiple-point statistical simulations with the Direct Sampling algorithm. *Comput. Geosci.* 52 (28), 307–324. <https://doi.org/10.1016/j.cageo.2012.09.019>.
- Miall, A.D., 1996. *The Geology of Fluvial Deposits: Sedimentary Facies, Basin Analysis and Petroleum Geology*. Springer.
- Miall, D., 2016. *Stratigraphy: A Modern Synthesis*. Springer.
- Nanson, G.C., Page, K.J., 1983. Lateral accretion of fine-grained concave benches on meandering rivers. In: Collinson, J.D., Lewin, J. (Eds.), *Modern and Ancient Fluvial Systems: International Association of Sedimentologists*, vol. 6. Special Publication, pp. 133–143. <https://doi.org/10.1002/9781444303773.ch10>.
- Omre, H., 1991. Stochastic models for reservoir characterization. In: Kleppe, J., Skjæveland, S.M. (Eds.), *Recent Advances in Improved Oil Recovery, Methods for North Sea Sandstones Reservoirs*. Norwegian Petroleum Directorate, Stavanger, Norway.
- Pyrzc, M.J., Deutsch, C.V., 2014. *Geostatistical Reservoir Modeling*. Oxford University Press. https://doi.org/10.1007/978-94-011-1739-5_12.
- Pyrzc, M.J., Boisvert, J.B., Deutsch, C.V., 2008. A library of training images for fluvial and deepwater reservoirs and associated code. *Comput. Geosci.* 34 (5), 542–560. <https://doi.org/10.1016/j.cageo.2007.05.015>.
- Remy, N., Boucher, A., Wu, J., 2009. *Applied Geostatistics with SGEMS. A User's Guide*. Cambridge University Press. <https://doi.org/10.1017/CBO9781139150019>.
- Ringrose, P., Bentley, M., 2015. *Reservoir Model Design: A Practitioner's Guide*. Springer.
- Riou, J., Hocker, C., 2015. Practical Recommendations for Successful Application of the MPS Facies Modelling Method. *SPE Abu Dhabi*. <https://doi.org/10.2118/177675-MS>.
- Rojas, T., Demyanov, V., Christie, M., Arnold, D., 2012. Reducing uncertainty in modelling fluvial reservoirs by using intelligent geological priors. In: *Paper Presented at the Ninth Geostatistical Congress*. Oslo.
- Russell, C.E., Moutney, N.P., Hodgson, D.M., Colombera, L., 2019. A novel approach for prediction of lithological heterogeneity in fluvial point-bar deposits from analysis of meander morphology and scroll-bar pattern. In: Ghinassi, M., Colombera, L., Moutney, N.P., Reesink, A.J. (Eds.), *Fluvial Meanders and Their Sedimentary Products in the Rock Record*, vol. 48. International Association of Sedimentologists, Special Publication, pp. 385–418. <https://doi.org/10.1002/9781119424437.ch15>.
- Straubhaar, J., Renard, P., Mariethoz, G., Froidevaux, R., Besson, O., 2011. An improved parallel multiple-point algorithm using a list approach. *Math. Geosci.* 43 (3), 305–328. <https://doi.org/10.1007/s11004-011-9328-7>.
- Straubhaar, J., Walgenwitz, A., Renard, P., 2013. Parallel multiple-point statistics algorithm based on list and tree structures. *Math. Geosci.* 45 (2), 131–147. <https://doi.org/10.1007/s11004-012-9437-y>.
- Strebelle, S., 2000. *Sequential Simulation Drawing Structures from Training Images.. Ph. D. Thesis Department of Geological and Environmental Sciences, Stanford University, Stanford*.
- Strebelle, S., 2002. Conditional simulation of complex geological structures using multiple-point statistics. *Math. Geol.* 34 (1), 1–21. <https://doi.org/10.1023/A:1014009426274>.
- Strebelle, S., Journel, A., 2001. Reservoir Modeling Using Multiple-point Statistics: Society of Petroleum Engineers Annual Technical Conference and Exhibition. *SPE Paper*, New Orleans. <https://doi.org/10.2118/71324-MS>, 71324: 11.
- Thomas, R.G., Smith, D.G., Wood, J.M., Visser, J., Calverley-Range, E.A., Koster, E.H., 1987. Inclined heterolithic stratification — terminology, description, interpretation and significance. *Sediment. Geol.* 53 (2), 123–179. [https://doi.org/10.1016/S0037-0738\(87\)80006-4](https://doi.org/10.1016/S0037-0738(87)80006-4).
- Walker, R.G., Cant, D.J., 1979. Facies models 3. Sandy fluvial systems. In: Walker, R.G. (Ed.), *Facies Model*, vol. 3. *Geoscience Canada*, pp. 23–31, 1.
- Wood, J.M., 1989. Alluvial architecture of the upper cretaceous judith river formation. *Dinosaur provincial park. Alberta. Canada. Bull. Can. Petrol. Geol.* 37 (2), 169–181. <https://doi.org/10.35767/gscpgbull.37.2.169>.
- Xu, W., Tran, T.T., Srivastava, R.M., Journel, A.G., 1992. Integrating seismic data in reservoir modeling: the collocated cokriging alternative. In: *67th Annual Technical Conference and Exhibition. Society of Petroleum Engineers. SPE Paper*, Washington, DC, pp. 833–842. October 24742.
- Yan, N., Colombera, L. and Moutney, N.P., Controls on fluvial meander-belt thickness and sand distribution: insights from forward stratigraphic modelling, *Sedimentology*, (in press).
- Yan, N., Moutney, N.P., Colombera, L., Dorrell, R.M., 2017. A 3D forward stratigraphic model of fluvial meander-bend evolution for prediction of point-bar lithofacies architecture. *Comput. Geosci.* 105 (7), 65–80. <https://doi.org/10.1016/j.cageo.2017.04.012>.
- Yan, N., Colombera, L., Moutney, N.P., Dorrell, D.M., 2019. Three-dimensional modelling of fluvial point-bar architecture and facies heterogeneity using analogue data and associated analysis of intra-bar static connectivity: application to humid coastal-plain and dryland fluvial systems. In: Ghinassi, M., Colombera, L., Moutney, N.P., Reesink, A.J. (Eds.), *Fluvial Meanders and Their Sedimentary Products in the Rock Record*, vol. 48. International Association of Sedimentologists, Special Publication, pp. 475–508. <https://doi.org/10.1002/9781119424437.ch18>.
- Yan, N., Colombera, L., Moutney, N.P., 2020. Three-dimensional forward stratigraphic modelling of the sedimentary architecture of meandering-river successions in evolving half-graben rift basins. *Basin Res.* 31 (2), 213–404. <https://doi.org/10.1111/bre.12367>.

Appendix C: Supplementary Files

Supplementary .csv file is attached including the developed database including petrophysical properties for fluvial successions.

Petrel Project is attached where the various simulations performed by this research can be found.